Hans-Jörg Fecht
Markus Mohr   *Editors*

Metallurgy in Space

Recent Results from ISS

TMS

Springer

The Minerals, Metals & Materials Series

The Minerals, Metals & Materials Series publications connect the global minerals, metals, and materials communities. They provide an opportunity to learn about the latest developments in the field and engage researchers, professionals, and students in discussions leading to further discovery. The series covers a full range of topics from metals to photonics and from material properties and structures to potential applications.

More information about this series at http://www.springer.com/series/15240

Hans-Jörg Fecht • Markus Mohr
Editors

Metallurgy in Space

Recent Results from ISS

TMS

Springer

Editors
Hans-Jörg Fecht
Institute of Functional Nanosystems
Ulm University
Ulm, Germany

Markus Mohr
Institute of Functional Nanosystems
Ulm University
Ulm, Germany

Foreword by Alexander Gerst

MacGyver Is Melting Metals in Space

During my first mission to the International Space Station (ISS), called "Blue Dot," it was one of my main tasks to install the electromagnetic levitator (EML) in ESA's magnificent Columbus laboratory. This furnace represents one of the most impressive material science experiments in space. It can heat a metallic alloy to 2200 °C and then cool and solidify it rapidly, while the molten droplet remains freely suspended and undisturbed in the experiment chamber. This is impossible to achieve on Earth.

Material scientists study these free-floating droplets in order to obtain characteristic thermophysical properties of the molten alloy in its liquid state. These thermophysical property data are needed for the development of computer models that simulate industrial production processes on Earth. Consequently, this increases the production efficiency and the quality of end products and reduces the energy consumption in line with major global efforts of green energy. It is a good example for why we sometimes have to go to a strange and hostile place like space to improve things down here on Earth.

As a result, the better material performance on Earth leads to reduced energy consumption and greenhouse gas emissions, for example, in advanced turbines for aircraft and land-based power generation. Other materials that were studied by scientists all around the world using the material science laboratory on board the ISS are, for example, high-strength steels, low-weight titanium-alloys for a wide range of applications from aerospace to biomedicine, new semiconductors for photovoltaics, and new metallic glass alloys designed for future rovers on the Moon and Mars.

From this impressive list of potential benefits that can be obtained by operating a device like EML on ISS, you can probably estimate the "weight" on the shoulders of an astronaut who is given the complex task to install such a device. In contrary to the assumption of most humans on Earth, an astronaut's biggest fear is not to end up in a

fireball during launch (even though admittedly that is also not a nice thought, it is relatively unlikely) but to make a mistake that endangers the success of the many invaluable experiments, designed and built by hundreds of engineers and scientists over the course of many years. To disappoint them would be a true failure for us.

You can now probably imagine the feeling of terror that I had when, during the installation of EML, I realized that one of the launch fasteners that secured the hardware from the massive vibrations during its launch was stuck and couldn't be removed. What was even worse, it prevented the final assembly of EML, and therefore it threatened the entire project – just a single tiny bolt, in a very difficult place to access. But what followed was one of the finest examples of what an international team of experts can achieve when they all work together.

A crisis team was formed, consisting of our mission ground team, engineers, and me, the astronaut in orbit. In the following weeks, we went through various options of removing the stuck bolt and meticulously analyzed the risks of each approach. In the end, ground teams allowed me to go ahead with the option we called "MacGyver," which, needless to say, was my favorite: I got the GO to cut off the bolt with a metal saw blade, using a very special liquid to catch and prevent metal shavings from contaminating the station's atmosphere – a dab of shaving gel from my personal hygiene kit. In my imagination I could see my childhood hero nodding at me with a smile.

Almost exactly 4 years later, I returned to the International Space Station for my second mission, called "Horizons," as the Commander of Expedition 57. One of the first things I did when arriving on ISS was to visit my favorite workplace in space, the ever-so-magnificent Columbus laboratory. And what I saw made me smile. I could see that the EML was still in its place, where I left it several years before, and it was still running flawlessly. It was operated very successfully and routinely by the international science team, conducting hundreds of experiment runs in the last years, for the benefit of humans on planet Earth. Hence, I am very excited about the results that the scientists have obtained on board the ISS and that are presented in this book.

European Space Agency, Directorate of   Alexander Gerst
Human Robotic Exploration
Programmes, LEO Exploration Group,
ESTEC, Noordwijk, the Netherlands

Foreword by Matthias Maurer

Future Metallurgy in Space

The International Space Station is a unique laboratory that allows experiments not possible on Earth. In the fall of 2021, I will go to the International Space Station (ISS) for my mission "Cosmic Kiss." Especially as a material scientist, I am excited to become directly involved with the materials science experiments in ESA's Columbus module.

For a long time, material scientists focused their investigations on the relation between mechanical and physical properties of solids related to their microstructures. Very soon, the importance of the defining steps for the microstructure, the processing route from the liquid melt to the final product, was recognized. Hence, in order to achieve new advancements in material science, a deeper understanding of the properties of the molten state is of key importance.

Due to the high reactivity of most metallic melts, the investigation of liquid metals is best done by container-less methods. The weightlessness in the International Space Station allows the easy positioning of liquid metallic droplets. Furthermore, the absence of gravity allows precise measurements that are not possible on Earth. The obtained thermophysical properties of the investigated metallic alloys are used to answer basic scientific questions and are further utilized for the simulation of industrial production processes and the development of new materials.

The upcoming experiments in the EML on board the International Space Station are concerned with materials that will improve life on Earth and also increase our abilities for space exploration. These experiments will improve steels for applications in energy conversion and electro-mobility, titanium alloys for 3D-printed biomedical implants, new metallic glasses for 3D printing of advanced structural, and functional components for several industries, including space flight and exploration.

I am looking forward to the materials science experiments in the Columbus module, and I am very enthusiastic to support the continuation of the successful experiments that have been performed until now and are presented in this book.

European Space Agency, Directorate of   Matthias Maurer
Human Robotic Exploration
Programmes, LEO Exploration Group,
EAC, Cologne, Germany

Preface

Evolution of matter in the universe is one of the key elements related to our fundamental understanding of the formation of the planets and stars and life on Earth, and hence, has always evoked very keen interest in the scientific community. The natural forces existing on Earth, such as pressure, gravity, and strong or weak magnetic forces, are either absent or present in significantly different magnitude outside the Earth's atmosphere. It is intuitive that formation of solids in outer space must have been through an entirely different environment and influence than what we can experiment with on Earth. Thus, experiments to determine thermophysical and thermochemical properties of common elements and compounds, of inorganic and organic in origin and nature, are essential to develop a fair understanding of the genesis and behavior of matter in outer space and simulate the same on Earth through rigorous modeling.

This volume, entitled *Metallurgy in Space*, with selected chapters devoted to fundamental aspects of various intrinsic properties (melting/boiling point, viscosity, conductivity, diffusion coefficient, specific heat, and crystal structure), properties of pure solids (elements, alloys, and compounds), and response to external stimuli like temperature, pressure, and magnetic or electrical fields, both in reduced gravity condition in space and with usual gravitational environment on Earth, is absolutely essential. One of the highlights of this book arises from the articles dealing with experiments conducted in the International Space Station (ISS) and results obtained thereof concerning studies on various important thermophysical parameters of interest, which are not only unique but simply not known so far. These results and trends will greatly influence and impact our basic understanding in physical sciences as well as research and innovations in materials science and engineering in the future.

A variety of industries – information technology, aerospace, automotive, bio-medical, and basic and new materials manufacturing – need technological innovations, which attain high-value-added and high-quality products and at the same time environmental consciousness and regulations in a multibillion-dollar market. In recent years, the trend in developing new products moved from the traditional

trial-and-error approach to computer-based modeling, for example, for high-temperature melt processing which represents almost 100% of all metal production technologies. This has become possible by the increase in computer power, but it is still hampered by a lack of available and appropriate liquid property data as reliable input parameters since – in a thermodynamic sense – "entropy wins at high temperature."

Recent progress in containerless levitation and processing techniques can overcome the experimental difficulties and enable measurements of various properties of "free-floating" metallic drops in the stable and undercooled liquid state in the high-temperature limit (in contrast to the famous Millikan experiment at Caltech about 100 years ago on oil drops at ambient conditions).

With respect to this exciting development, truly international and multi-disciplinary materials science projects (ThermoProp/ThermoLab – ISS) have been conceived over the last decades and supported by the various space agencies worldwide. Materials investigated include metallic alloys and composites, intermetallics, semiconductors, and glasses in the high-temperature limit. Basic metal physics aspects are considered as well, such as the atomic structure of complex multi-component liquids, their relation to macroscopic properties of the liquid phase, and the thermodynamics and kinetics of phase formation from the liquid which is of relevance for industrial alloy design.

The measurements and investigations were performed and are still continuing onboard the International Space Station. Using the high-precision electromagnetic levitation device ISS-EML in the COLUMBUS module, the experimental temperature-time window available can be sufficiently extended to about 2200 °C for more than 10,000 s. In this temperature-time regime, performance of controlled surface excitations, temperature modulation (A.C. calorimetry), and other techniques become reality in the high-temperature liquid state. The analysis based on high-precision video and temperature measurements as well as other sensing devices allows a in-depth study of a free-floating hot metallic liquid drop in equilibrium with different atmospheres for the first time ever.

Besides basic scientific insight, this knowledge becomes also relevant for modern industrial processes such as high-precision casting, welding, 3D printing, energy conversion, and "green" processing. The experimental set-up is embedded in a truly international and world-renowned team of scientists in the field of thermophysics and the development of new materials in order to achieve the best science. Furthermore, the awareness and interest about the scope and need for such benchmark experiments allows to extend our deeper understanding of the origin and genesis of matter in space and evolution of properties of solids in space and on Earth. The future is wide open.

Ulm, Germany   Hans-Jörg Fecht
Ranchi, Jharkhand, India   Indranil Manna

Contents

Contributors

Winfried Aicher Airbus Defence and Space, Friedrichshafen, Germany

Livio Battezzati Dipartimento di Chimica, Università di Torino, Torino, Italy

Gwendolyn P. Bracker Department of Mechanical and Industrial Engineering, University of Massachusetts, Amherst, MA, USA

Jürgen Brillo Institut für Materialphysik im Weltraum, Deutsches Zentrum für Luft- und Raumfahrt (DLR), Köln, Germany

Qing-Ping Cao International Center for New-Structured Materials (ICNSM), State Key Laboratory of Silicon Materials, and School of Materials Science and Engineering, Zhejiang University, Hangzhou, People's Republic of China

Quentin Champdoizeau Faculty of Engineering – Chemical and Materials Engineering Department, University of Alberta, Edmonton, AB, Canada

Yannick Champion CNRS, Grenoble INP, SIMaP, University of Grenoble Alpes, Grenoble, France

Bernd Damaschke I. Physikalisches Institut, Georg-August-Universität Göttingen, Göttingen, Germany

Angelika Diefenbach Microgravity User Support Center, Deutsches Zentrum für Luft- und Raumfahrt (DLR), Köln, Germany

Alex Dommann Center for X-Ray Analytics, Empa Swiss Federal Laboratories for Materials Science and Technology, Dübendorf, Switzerland

Hans-Jörg Fecht Institute of Functional Nanosystems, Ulm University, Ulm, Germany

Hiroyuki Fukuyama Institute of Multidisciplinary Research for Advanced Materials (IMRAM), Tohoku University, Sendai, Japan

Anup K. Gangopadhyay Washington University in St. Louis, St. Louis, MO, USA

Alexander Gerst European Space Agency (ESA), Directorate of Human Robotic Exploration Programmes, LEO Exploration Group, ESTEC, Noordwijk, the Netherlands

Donatella Giuranno Institute of Condensed Matter Chemistry and Technologies for Energy, National Research Council (CNR-ICMATE), Genoa, Italy

Hani Henein Faculty of Engineering – Chemical and Materials Engineering Department, University of Alberta, Edmonton, AB, Canada

Taketoshi Hibiya Graduate School of System Design and Management, Keio University, Yokohama, Kanagawa, Japan

Douglas C. Hofmann Materials Development and Manufacturing Technology Group, NASA Jet Propulsion Laboratory/California Institute of Technology, Pasadena, CA, USA

Robert W. Hyers Department of Mechanical and Industrial Engineering, University of Massachusetts, Amherst, MA, USA

Takehiko Ishikawa Japan Aerospace Exploration Agency, Tsukuba, Ibaraki, Japan

Jian-Zhong Jiang International Center for New-Structured Materials (ICNSM), State Key Laboratory of Silicon Materials, and School of Materials Science and Engineering, Zhejiang University, Hangzhou, People's Republic of China

William L. Johnson Keck Engineering Laboratories, California Institute of Technology, Pasadena, CA, USA

Kenneth F. Kelton Washington University in St. Louis, St. Louis, MO, USA

Manoj Kumar Department of Metallurgical and Materials Engineering, Indian Institute of Technology Kharagpur, Kharagpur, West Bengal, India
CSIR – Institute of Minerals and Materials Technology, Bhubaneswar, Odisha, India

Georg Lohöfer Institut för Materialphysik im Weltraum, Deutsches Zentrum für Luft- und Raumfahrt (DLR), Köln, Germany

Yuansu Luo I. Physikalisches Institut, Georg-August-Universität Göttingen, Göttingen, Germany

Jyotsna Dutta Majumdar Department of Metallurgical and Materials Engineering, Indian Institute of Technology Kharagpur, Kharagpur, West Bengal, India

Indranil Manna Department of Metallurgical and Materials Engineering, Indian Institute of Technology Kharagpur, Kharagpur, West Bengal, India
Birla Institute of Technology, Mesra, Ranchi, Jharkhand, India

Douglas M. Matson Department of Mechanical Engineering, Tufts University, Medford, MA, USA

Matthias Maurer European Space Agency (ESA), Directorate of Human Robotic Exploration Programmes, LEO Exploration Group, EAC, Cologne, Germany

Markus Mohr Institute of Functional Nanosystems, Ulm University, Ulm, Germany

Antonia Neels Center for X-Ray Analytics, Empa Swiss Federal Laboratories for Materials Science and Technology, Dübendorf, Switzerland

Rada Novakovic Institute of Condensed Matter Chemistry and Technologies for Energy, National Research Council (CNR-ICMATE), Genoa, Italy

Shumpei Ozawa Department of Advanced Materials Science and Engineering, Chiba Institute of Technology, Narashino, Chiba, Japan

Paul-François Paradis I.N.O., Quebec-city, QC, Canada

Konrad Samwer I. Physikalisches Institut, Georg-August-Universität Göttingen, Göttingen, Germany

Michael P. SanSoucie Materials and Processes Laboratory, Metallic Materials & Processes Division (EM30), NASA Marshall Space Flight Center (MSFC), Huntsville, AL, USA

Seshadri Seetharaman Royal Institute of Technology, Stockholm, Sweden

Wim Sillekens European Space Agency – ESTEC, Noordwijk, the Netherlands

Wolfgang Soellner Airbus Defence and Space, Friedrichshafen, Germany

Takao Tsukada Department of Chemical Engineering, Tohoku University, Sendai, Japan

Xiao-Dong Wang International Center for New-Structured Materials (ICNSM), State Key Laboratory of Silicon Materials, and School of Materials Science and Engineering, Zhejiang University, Hangzhou, People's Republic of China

Masahito Watanabe Department of Physics, Gakushuin University, Toshima, Tokyo, Japan

Rainer Willnecker Microgravity User Support Center, Deutsches Zentrum für Luft- und Raumfahrt (DLR), Köln, Germany

Rainer Wunderlich Institute of Functional Nanosystems, Ulm University, Ulm, Germany

Xue-lin Wang International Center for New-Structured Materials (ICNSM), State Key Laboratory of Silicon Materials, and School of Materials Science and Engineering, Zhejiang University, Hangzhou, People's Republic of China

Dong-Xian Zhang International Center for New-Structured Materials (ICNSM), State Key Laboratory of Silicon Materials, and School of Materials Science and Engineering, Zhejiang University, Hangzhou, People's Republic of China

Chapter 1
Introduction

Hans-Jörg Fecht

1   General

Material scientists originally devoted most of their efforts to studying the solid state of materials, their microstructure, and their mechanical and thermal properties. However, in the last 10–20 years, a change in paradigm has taken place, and the importance of the liquid phase has been recognized. In this regard, it is interesting to note that almost 100% of all metallic products are, at some stage, produced through solidification and casting processes. Consequently, this field of new materials, processes, and products constitutes a major backbone to industries worldwide.

Solidification from the melt leaves its fingerprints in the final material, and hence it is of utmost importance to understand the properties of the molten state and its solidification behavior. The prominent feature of fluids, namely, their ability to flow and to form free surfaces, poses the main difficulty in their theoretical description. The physics of fluids is governed by the Navier-Stokes equation and by the ubiquitous presence of convection. In addition, when dealing with metallic materials, the high temperatures involved lead to experimental difficulties, the most trivial but also most fundamental being the suitability of available containers.

Besides the atomic scale inherent to condensed matter and the intermediate scales associated with the solidification microstructures, fluid flow driven by gravity generally occurs in the melt at the macroscopic level so that the relevant length scales in casting are widespread from the atomic size (capillary length, crystalline defects such as dislocations, attachment of atoms, etc.) to the meter size of the ingot (fluid flow, spacing of dendrite side branches, etc.).

Accordingly, to produce materials that meet ever-higher specific requirements and performance, the solidification processing of structural and functional materials

H.-J. Fecht (✉)
Institute of Functional Nanosystems, Ulm University, Ulm, Germany
e-mail: hans.fecht@uni-ulm.de

has to be controlled with ever-increasing precision. It can be foreseen that materials for tomorrow will be optimized in their design and underlie more efficient production conditions, availability of scarce resources, and cleaner processes.

The interactive feedback between experiments and sophisticated computer simulations developed within the last 10 years that now drives the design and processing of materials is reaching performances never been seen in the past. Thus, it becomes possible to control and optimize the defect and grain structure at critical patches of components. Here, two major aspects are most essential for the continued improvement of materials processing with increasing requirements on composition, microstructure, and service achievements, which often implies the breaking of technology barriers:

- The reliable determination of the thermophysical properties of metallic melts in order to understand the fundamentals of complex melts and their influence on the nucleation of ordered phases.
- The reliable determination of the formation and selection mechanisms at microstructure scales in order to understand the fundamentals of casting and other solidification processes (foundry, welding, brazing, atomization,...). This also requires accurate knowledge of thermophysical properties.

2   Scientific Challenges

Casting is a non-equilibrium process by which a liquid alloy is solidified. The liquid-solid transition is driven by the departure from thermodynamic equilibrium, where no change can occur. From the standpoint of physics, casting thus belongs to the vast realm of out-of-equilibrium systems, which means that, rather than growing evenly in space and smoothly in time, the solid phase prefers to form a diversity of microstructures.

Actually, the relevant length scales in casting are widespread over ten orders of magnitude. At the nanometer scale, the atomic processes determine the growth kinetics and the solid-liquid interfacial energy, and crystalline defects such as dislocations, grain boundaries, and voids are generally observed. Macroscopic fluid flow driven by gravity or imposed by a stimulus (electromagnetic field, vibration, etc.) occurs in the melt at the meter scale of the cast product. The characteristic scales associated with the solidification microstructures are mesoscopic, i.e., intermediate, ranging from dendrite tip/arm scale (1–100 μm) to the grain size (mm–cm). It follows that the optimization of the grain structure of the product and inner microstructure of the grain(s) during the liquid-to-solid phase transition is paramount for the quality and reliability of castings, as well as for the tailoring of new advanced materials for specific technological applications.

On this basis, the quantitative numerical simulation of casting and solidification processes is increasingly demanded by manufacturers, compared to the well-established but time-consuming and costly trial-and-error procedure. It provides a
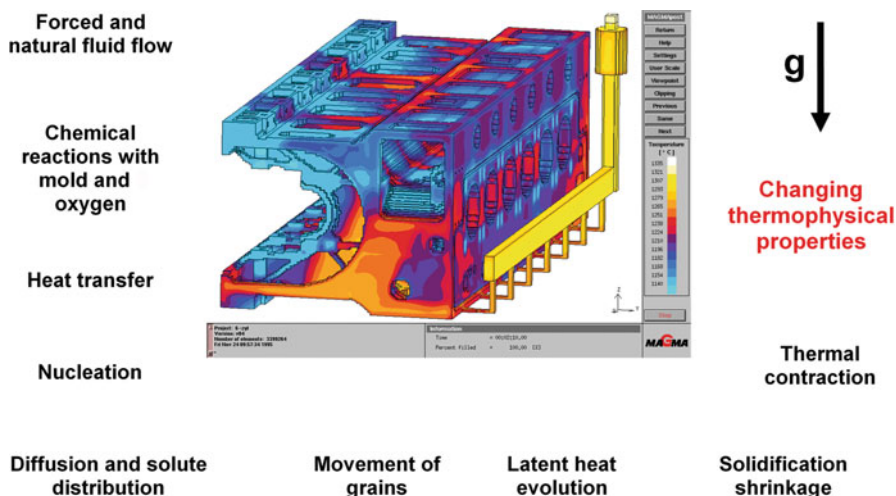
Fig. 1.1 A wide range of fundamental events during casting of complex components – here, a car engine with varying local temperatures. (Courtesy MagmaSoft)

rapid tool for the microstructural optimization of high-quality castings, in particular where process reliability and high geometric shape accuracy are important (see, e.g., Fig. 1.1 exhibiting cast structural components and the temperature distribution during casting of a car engine block). Any improvement of numerical simulation results in improved control of fluid flow and cooling conditions that enable further optimization of the defect and grain structure as well as stress distribution at critical patches of components. Through the control of unwanted crystallization events, it becomes even possible to produce completely new materials with a controlled amorphous (glassy) or nanocomposite structure.

3   Microgravity Space Conditions and Containerless Processing

The paucity of thermophysical property data for commercial materials as well as materials of fundamental interest is a result of the experimental difficulties arising at high temperatures. Some of these data can be obtained more or less accurately by conventional methods, in particular for non-reactive metals such as noble metals. High-precision measurements, however, on chemically highly reactive melts at the temperatures of interest require the application of containerless processing techniques and the use of high-precision non-contact diagnostic tools.

By eliminating the contact between the melt and a crucible, accurate surface nucleation control and the synthesis of materials free of surface contamination become possible. For highly reactive metallic melts, electromagnetic levitation

Fig. 1.2 Electromagnetic processing on the ground (left) and in microgravity (right) – the latter allowing controlled investigations of fully spherical liquid metallic samples (6.5–8 mm diameter) with a wide range of sophisticated analytical equipment. (Courtesy DLR)

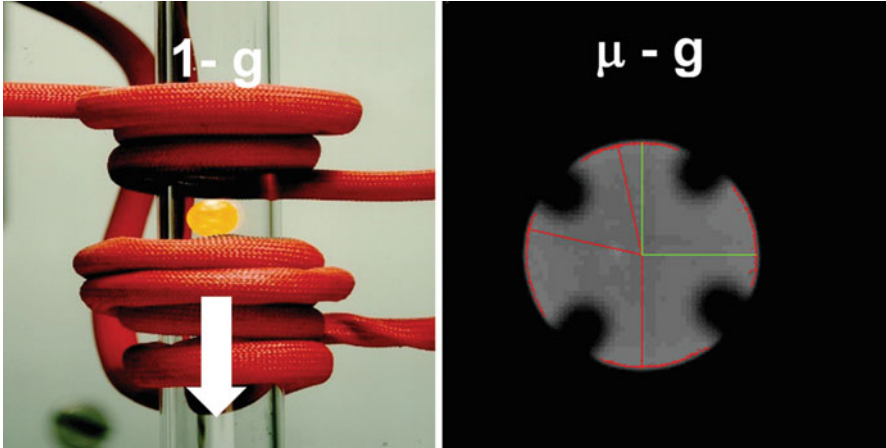(EML) is a well-developed containerless technique that offers several advantages over alternative levitation methods (electrostatic levitation, gas-phase levitation) due to the direct coupling of the high-intensity radiofrequency electromagnetic field with the sample.

Ground-based experiments using electromagnetic levitation have achieved limited success in measuring thermophysical properties of liquid alloys, since the high electromagnetic field B required to lift the sample against gravity (Lorentz force $F \propto \nabla B^2$) also causes excessive heating and turbulence due to induced eddy currents. In contrast, under microgravity conditions, much smaller levitation forces are needed since the force of gravity no longer has to be overcome. In fact, in space, only a weak positioning field is required.

This means that heating effects, magnetic pressure, melt turbulence, and asphericity of the molten drop are significantly reduced, allowing considerably more accurate results to be obtained or making such experiments possible at all. As an example, Fig. 1.2 shows a comparison between a specimen levitated in a ground-based em-levitation (left) and a liquid specimen positioned under reduced gravity conditions in an em-levitation device on board a parabolic flight (right). As compared to the specimen levitated on the ground, the specimen positioned under reduced gravity exhibits no detectable deviation from a spherical shape.

The motivation for performing benchmark experiments in the microgravity environment thus is straightforward and at a high level of scientific innovation. Firstly, in space it is possible to suppress the gravity-induced effects of fluid flow and more subtle sedimentation effects during solidification. Therefore, the contribution to fluid flow and heat transport in the melt can be investigated without the complications of buoyancy-driven thermo-solutal convection and sedimentation/flotation.

Secondly, the space environment on long time scales allows the application of containerless processing techniques, such as electromagnetic levitation. Levitated melts can be controlled effectively at temperatures up to 2200 °C, which in turn enables critical liquid parameters to be measured much more accurately and in a larger temperature range as compared to the earth laboratory.

Experience with parabolic flights (μg duration 10–20 s) and TEXUS rocket flights (μg duration ca. 180 s) already indicated that some aspects of the experiments could be successfully performed, but μg times are far too short to reach thermal equilibrium and measurements in the adiabatic regime. Expanding the experimental time-temperature window through the use of the International Space Station (ISS) opens a completely new realm of space experimentation. The main advantages in this regard can be summarized as follows:

- Avoidance of any chemical reactions with a metallic or ceramic container
- Decoupling of electromagnetic heating and positioning fields, therefore minimized levitation forces and, thus, controlled heating and reduced liquid convection in comparison with 1-g gravity conditions on earth
- Achievement of fully spherical samples
- Control of the sample environment (and cooling rate) in vacuum (better than 10^{-8} Torr) or inert gas atmosphere
- Extended periods of processing time (>10,000 s) in a temperature range between 700 and 2200 °C.
- Considerably improved accuracy of the measurements.

4   Experimental Program

The processing of metallic alloys (a combination of two or more elemental metals) through melting and casting techniques, whereby the molten material is poured or forced into a mold and allowed to harden, was invented several thousand years ago. Today, this processing is still an important step in the industrial production chain for a wide range of products. The end products often need to perform well and retain their integrity under extreme circumstances, particularly when used at high temperatures or when the product must be as light as possible in order to conserve energy. To produce these high-performance materials, the process must be closely controlled for the sake of both optimal design and efficiency of production.

The production and fabrication of alloys together with the casting and foundry industry generate a considerable amount of wealth. For example, the 10 million tons of castings produced in 1 year within the European Union is worth about 20 billion Euros. To continue generating this kind of turnover, the casting and foundry industry relies on the design and creation of advanced materials, which is accomplished by using sophisticated computer codes to control the metallurgical processes. These days everyone is looking for the next great breakthrough that leaps forward in technology that revolutionizes the way business is done. The answer may lie in a

surprising place: space. In the last years, a scientific program has been established by the European Space Agency (ESA) using weightlessness as an important research tool on parabolic flights, on sounding rockets, and, most recently, on the International Space Station.

Experiments performed in microgravity enable the study of the relevant volume and surface-dependent properties free of certain restrictions of a gravity-based environment. In space it is possible to suppress gravity's effects on the flow of molten metals and on sedimentation during solidification. Without gravity's interference, it is possible to isolate other properties for investigation, such as diffusion and how it contributes to mass and heat transport in the melt without the gravity-associated complications of certain solute ingredients being more buoyant than others.

Using advanced experimental techniques to gather data on the intricate processes of melting and casting brings us closer to the design of new materials with better performance. Such advanced products can range from meter-sized objects to micrometer-sized powders, for example:

- Energy-efficient turbine components for the aerospace industry and land-based power plants.
- Powder production to improve catalytic performance of modern fuel cells and advanced combustion engines.
- High-strength metals with added functionalities.
- Precision casting of detailed shapes for electronic casings.
- Low-weight and high-strength materials for modern space vehicles within the space exploration programs.
- Medical implants.

In order to perform the necessary experiments, it is important to have access to extended periods of reduced gravity. A crucial ISS facility is the electromagnetic levitator (EML). As fantastic as it sounds, this equipment does precisely what the name implies: levitated molten metals. The EML permits containerless melting and solidification of alloy samples. Furthermore, the EML is equipped with highly advanced diagnostic tools that permit accurate measurements of thermophysical properties, as well as direct observation of the experiment during flight by high-speed videography.

As the products we make become more sophisticated, it follows that their production processes must keep up. Advancements in liquid processing techniques have enabled the industry to create products such as jet engines, spacecraft, and medical implants, but society's push for continually stronger, lighter, and more efficient products requires that next great leap.

Part I
Programmatic, Facility and Infrastructure

Chapter 2
ESA's Materials Science in Space Programme

Wim Sillekens

1 Introduction

Within ESA, its member and cooperating states are working together on space research and technology and their space applications. Activities relating to the exploration destinations Low-Earth Orbit, Moon and Mars are integrated into a single European Exploration Programme (E3P), of which the "Science in Space Environment" (SciSpacE) element is concerned with the scientific research on the ISS, non-ISS space platforms and space-environment analogues. SciSpacE and its preceding "European Programme for Life and Physical Sciences in Space" (ELIPS) are and have been providing the scientific communities in the relevant disciplines with experiment opportunities using these platforms since the start of ISS utilisation at the turn of the century and as an extension of the initial European microgravity programmes going back to the 1980s. Descriptions and results of these experiments are archived in a publicly accessible and searchable ESA repository [1].

The overall motivation for conducting science in a space environment is that this reveals features of terrestrial life and physical processes that cannot be observed and/or controlled on Earth. Aspects of interest include – but are not limited to – the reduced-gravity condition, the otherwise extreme conditions (in their possibly wide sense, ranging from radiation and temperature variations to remoteness and confinement) and the vantage point for Earth as well as for deep space.

Research activities that are being developed and conducted in this context are correspondingly diverse. These research activities are being guided by the so-called science roadmaps (or research agendas) that have been established by the European scientific communities for the respective domains and are documented in [2] – with an updated second issue that now also includes the Moon and Mars destinations to be

W. Sillekens (✉)
European Space Agency – ESTEC, Noordwijk, the Netherlands
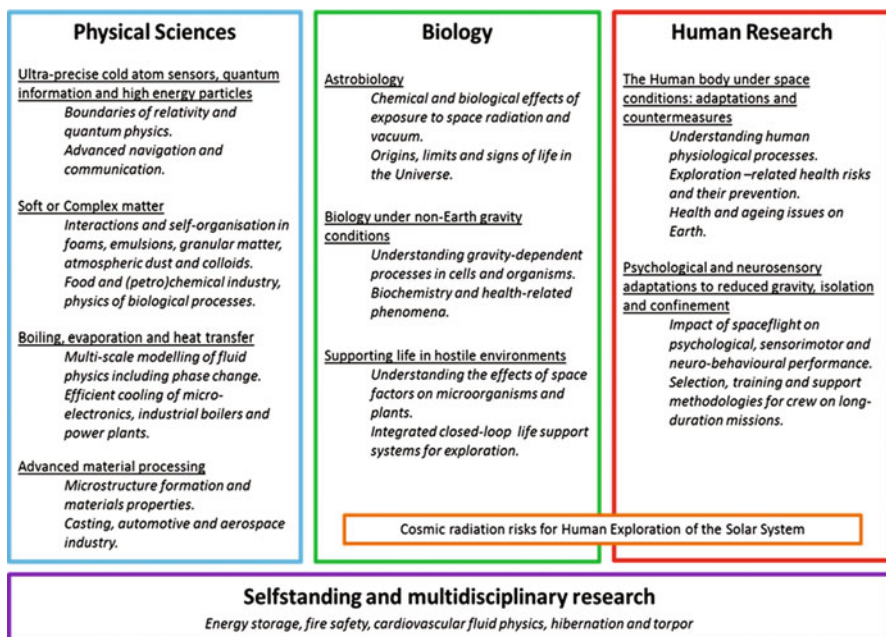e-mail: wim.sillekens@esa.int

Physical Sciences	Biology	Human Research
Ultra-precise cold atom sensors, quantum information and high energy particles *Boundaries of relativity and quantum physics. Advanced navigation and communication.* **Soft or Complex matter** *Interactions and self-organisation in foams, emulsions, granular matter, atmospheric dust and colloids. Food and (petro)chemical industry, physics of biological processes.* **Boiling, evaporation and heat transfer** *Multi-scale modelling of fluid physics including phase change. Efficient cooling of micro-electronics, industrial boilers and power plants.* **Advanced material processing** *Microstructure formation and materials properties. Casting, automotive and aerospace industry.*	**Astrobiology** *Chemical and biological effects of exposure to space radiation and vacuum. Origins, limits and signs of life in the Universe.* **Biology under non-Earth gravity conditions** *Understanding gravity-dependent processes in cells and organisms. Biochemistry and health-related phenomena.* **Supporting life in hostile environments** *Understanding the effects of space factors on microorganisms and plants. Integrated closed-loop life support systems for exploration.*	**The Human body under space conditions: adaptations and countermeasures** *Understanding human physiological processes. Exploration –related health risks and their prevention. Health and ageing issues on Earth.* **Psychological and neurosensory adaptations to reduced gravity, isolation and confinement** *Impact of spaceflight on psychological, sensorimotor and neuro-behavioural performance. Selection, training and support methodologies for crew on long-duration missions.*

Cosmic radiation risks for Human Exploration of the Solar System

Selfstanding and multidisciplinary research
Energy storage, fire safety, cardiovascular fluid physics, hibernation and torpor

Fig. 2.1 ESA's top-level roadmap themes for Low-Earth Orbit research activities

published in 2021. Roadmap themes are structured as shown in Fig. 2.1, with materials science being covered in the physical sciences box under the title Advanced Material Processing. Here, the implication of a reduced-gravity environment (typically $<10^{-3}$ g) is that no buoyancy/sedimentation and thereby that diffusive conditions exist in experiments involving multiple phases such as in solidification, as well as in a variety of other physical sciences experiments.

This chapter is dedicated to the materials science in space programme as supported by ESA. Following a general outline in terms of research topics and (on-orbit) facilities that have been realised or are being planned, particular attention is given to the activities relating to electro-magnetic levitation, being a major constituent of the reported research in this book. The latter includes brief descriptions of how the research is organised, which samples are selected and what research outputs have been generated to date. Finally, benefits for Earth and industrial relevance of the investigations in this materials science programme are addressed in broad terms.

2 The Materials Science Programme

As outlined above, a reduced-gravity environment offers specific opportunities for experiments involving a phase transition and aiming to study phenomena that are obscured in experiments on Earth by buoyance/sedimentation and the convection resulting from that. For materials science this means that the field of solidification physics is of particular interest.

Figure 2.2 lists the main topical scientific challenges in this domain. As one of the first steps – and often even the single step – in the processing of materials, solidification from the melt inevitably leaves its fingerprints in the (semi)-finished product. Hence, it is essential to understand the properties of the molten state and the solidification mechanisms in order to tailor the processing route and to achieve satisfying microstructures to meet functional performance requirements.

Advances in these areas are key to further improve the quantitative and predictive modelling and simulation of liquid-state manufacturing processes. This is to the benefit of the industrial manufacturing of semi-finished products (e.g. slab, billet, bloom, ingot) and shape castings, as well as of processes entailing rapid solidification such as high-pressure die casting, strip casting, welding, atomisation, spray forming and additive manufacturing (3D printing). Enhanced process control implies an increase in production efficiency and a reduction of energy consumption and scrap material, rendering these manufacturing processes more efficient and sustainable. Also, reductions in weight or improvements in (mechanical) performance may be achieved through optimised casting.

Deriving from these overall scientific challenges, ESA's materials science roadmap identifies the following major research areas of interest for reduced-gravity experimentation:
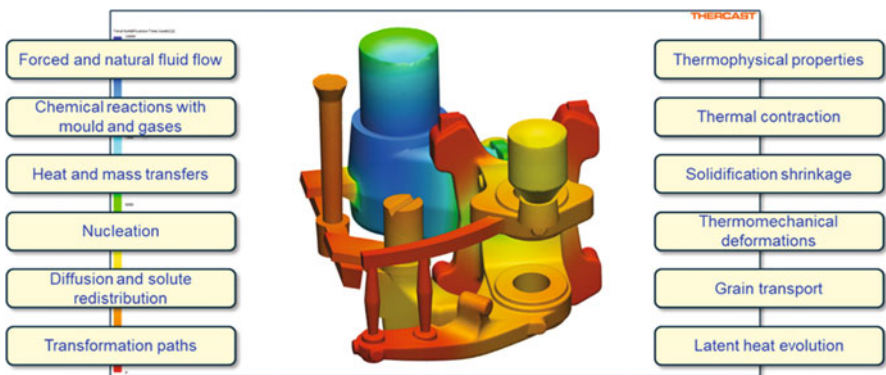

Fig. 2.2 Fundamental aspects of casting a complex component, here shown in relation to the total solidification time predicted for a steering knuckle (Image: Courtesy of S. Andrietti (TRANSVALOR))
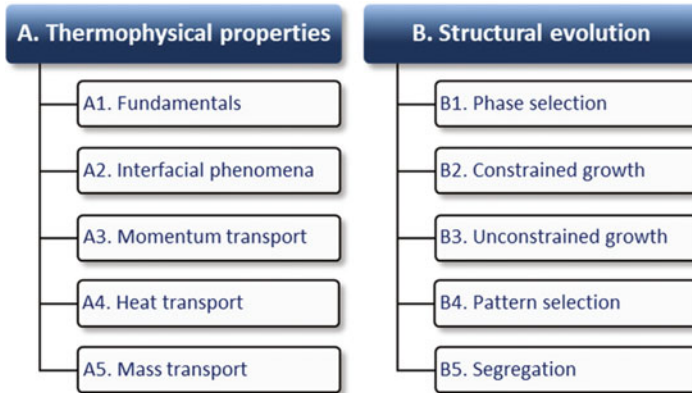
Fig. 2.3 Physical phenomena from processing and properties to solidification (micro)-structure in materials

- The reliable determination of the *thermophysical properties* of (metallic and other) materials, notably of melts.
- The investigation of *structural evolution* in materials during liquid-solid phase transition, requiring the reliable determination of the formation of phases and of selection mechanisms at the relevant length scales.

Figure 2.3 depicts the physical phenomena distinguished within these areas. For each of these, several (sub)-topics are identified with a rationale for space experimentation. Pattern selection (B4), by means of random example, consists of the topics of dendritic growth, peritectic growth and eutectic growth. These topics are further specified and described in relation to the underlying mechanisms in the concerned roadmap document.

Through ESA's E3P and its predecessor programmes, several materials science facilities have meanwhile been developed and are being operated on board the ISS. Typically, they are designed as multi-user and multi-purpose facilities, meaning that they are accessed by multiple science teams to enable experiments with distinctly different research objectives and experiment protocols. The facilities are introduced below, with some further details listed in Table 2.1:

- *Materials science laboratory (MSL)*. This facility is for metal-alloy solidification and crystal growth of semiconductor materials. A rod-shaped sample is molten and then directionally solidified while being moved in axial direction versus the heating elements under a maintained thermal gradient. Processed samples are downloaded for microstructural evaluations. The MSL is operational since 2009 and is located in NASA's Materials Science Research Rack in the Destiny module. It is being utilised under a joint implementation plan between ESA and NASA.
- *Electro-magnetic levitator (EML)*. This facility is for containerless processing of liquid metals and semiconductor materials. An electrically conductive spherical

Table 2.1 Key features of ESA's materials science facilities for solidification physics on board the ISS

Aspect	Materials science laboratory	Electro-magnetic levitator	Transparent alloys	X-ray facility
Research area(s)	Directional solidification	Containerless processing	Directional solidification	Directional/isothermal solidification[a]
Heating	Bridgman furnace	Induction system (separate positioning coil)	Bridgman furnace	Gradient furnace, isothermal furnace
Hardware options	Two exchangeable furnace inserts; rotating magnetic field	Trigger needle, chill-cooling plate (oxygen sensing and control system)		Exchangeable micro-focus X-ray source
Sample exchange	Individual sample cartridges	Carrousel with 18 samples	Individual sample cartridges	Individual sample cartridges
Sample geometry	Rod-like 3D (e.g. ∅8 mm)	Spherical (∅6–8 mm)	Rectangular 3D (e.g. thickness 1–10 mm)	Flat quasi-2D (thickness ~0.2 mm)
Sample materials	Wide range of material types and alloy compositions (metals, semiconductors)	Wide range of material types and alloy compositions (metals, semiconductors)	Organic model alloys (e.g. SCN-DC) with optical transparency	Metallic alloy systems and compositions (e.g. Al-based alloys) with adequate X-ray contrast
Operating temperature	≤1400 °C	≤2100 °C	≤170 °C	≤900 °C
Runs per sample	Single	Multiple	Multiple	Multiple
Control parameters	Temperatures (hot/cold zones), sample translation speed, magnetic field	Coil voltages (including modulation and pulses), processing atmosphere	Temperatures (hot/cold zones), sample translation speed	Temperatures (hot/cold zones), sample translation speed
Diagnostics	Thermocouples	Optical cameras, pyrometer, sample coupling electronics	Optical cameras (resolution ~1 μm), thermocouples	Trans-illumination: camera with scintillator (resolution ~3–5 μm), thermocouples
Post-flight sample analysis	Full suite of analytical tools (including 3D numerical model validation)	Full suite of analytical tools (including 3D numerical model validation)	None (mostly not needed)	Additionally possible

[a]Other experiment types (diffusion, foaming, etc.) are to follow in due time

sample is molten and maintained in place by an electro-magnetic field. Distinct heating-cooling cycles enable high-accuracy measurements of thermophysical properties (specific heat capacity, surface tension, viscosity, etc.) and the study of solidification kinetics (undercooling and nucleation, growth velocity, etc.). The

EML is operational since 2015 and is located in the European Drawer Rack in the Columbus module. The facility and its extensions and sample batches are a co-development of DLR and ESA. It is being utilised under an agreement between ESA, NASA and Roscosmos.

- *Transparent alloys (TA)*. This facility is for solidification of organic substances serving as transparent analogues for metallic alloys. Flat samples are molten and then directionally solidified in a fashion similar to MSL but under the in situ observation of the solidification dynamics by optical means. TA is operational since 2018 and is being utilised for successive experiment campaigns in NASA's Microgravity Science Glovebox in the Destiny module.

- *X-ray facility (XRF)*. Being in the development stage still, this facility is for metal-alloy solidification as well as for other experiment types using a micro-focus X-ray source for in situ diagnostics. For materials science, it is building on heritage from previous parabolic flight and sounding rocket missions involving trans-illumination (radiography) experiments on directional and isothermal metal-alloy solidification, diffusion in metallic melts and metal foaming.

In addition, SciSpacE enables access to other ESA platforms (parabolic flight, sounding rocket), including ground-based facilities (drop tower, large diameter centrifuge) for preparatory and supplementary research.

3   EML Activities

Electro-magnetic levitation in space has a long heritage. An EML can be operated under terrestrial conditions as well, but in a reduced-gravity environment, the required levitation/positioning power is much lower. This means that the molten sample better retains its spherical shape and that convection (fluid flow) remains limited, leading to a higher accuracy of the measurements than on ground and enabling the study of phenomena undisturbed by gravitational effects. Moreover, the regime of undercooling (i.e. metastable region of the phase diagram) becomes better accessible.

Early missions under TEMPUS[1] denominator were in SpaceLab using the IML-2 (1994) and MSL-1 (1997) facilities; on sounding rockets TEXUS 42 (2005), TEXUS 44 (2008) and TEXUS 46 (2009); and in parabolic-flight campaigns (since the late 1980s and with technical improvements continued regularly by DLR to date). Techniques and methods for specific (property) measurements and evaluations were developed among others, and exploratory scientific investigations were conducted in reduced gravity. This then led to the development and operation of the ISS-EML and the associated sample batches in recent years.

---

[1] "Tiegelfreies ElektroMagnetisches Prozessieren Unter Schwerelosigkeit" in German ("Containerless electromagnetic processing in zero-gravity" in English translation).

ESA's research in the physical sciences is organised through projects selected in so-called Announcements of Opportunity (AO). Each with their own scientific scope and objectives, these projects are commonly initiated in parallel with the conceptual and actual development of the scientific payloads. In that sense they are typically long-standing projects for which scientific yield is ramping up with these payloads becoming operational. To confirm scientific relevance and interest, AO projects are subject to recurring 3-yearly external reviews. The project pool for materials science currently consists of some 20 different research projects, involving international teams from universities, research organisations and industry that are not only limited to the ESA member states subscribing to this programme but also include other participants from across the globe. The following AO projects (acronyms and full titles) are involved in EML activities:

- *CCEMLCC*: Chill cooling for the electro-magnetic levitator in relation to continuous casting of steels
- *COOLCOP*: Undercooling and demixing of copper-cobalt alloys (*merged with LIPHASE*)
- *Electrical resistivity*: Electrical resistivity measurement of high-temperature metallic melts (*completed*)
- *ICOPROSOL*: Thermophysical properties and solidification behaviour of undercooled Ti-Zr-Ni liquids showing an icosahedral short-range order
- *LIPHASE*: Liquid-phase separation in metallic alloys (*merged with COOLCOP*)
- *MAGNEPHAS*: Study and modelling of nucleation and phase selection phenomena in undercooled melts – application to magnetic alloys of industrial relevance
- *METCOMP*: Metastable solidification of composites – novel peritectic structures and in situ composites
- *MULTIPHAS*: Multiphase solidification – eutectic and intermetallic solidification and glass formation
- *NEQUISOL*: Non-equilibrium solidification, modelling for microstructure engineering of industrial alloys
- *OXYTHERM*: Thermophysical properties of liquid alloys under oxygen influence
- *PARSEC*: Peritectic alloy rapid solidification with electro-magnetic convection
- *SEMITHERM*: Investigations of thermophysical properties of liquid semiconductors in the melt and in the undercooled state under microgravity conditions
- *THERMOPROP*: Thermophysical properties of liquid metals for industrial process design

In addition, several other research projects are involved through agreements with other space agencies: ELFSTONE and its predecessor LODESTARS, QUASI and USTIP (for NASA) and PERITECTICA (for Roscosmos).

Matters of common interest to the EML community are being addressed in the Investigators Working Group (IWG), in which all science teams with accepted experiments as well as executives of the agencies and other involved parties are represented. This includes not only the discussion of programmatic and operational

issues but also the presentation of acquired results and sharing of lessons learnt. Overall goal of this scientific coordination forum is to maximise science return within the scope of available resources. More information on the IWG is given in [3, 4].

Sample materials for the successive ISS-EML sample batches are selected by peer review from research proposals following a dedicated AO and at a pace in line with the development and processing of the sample batches. Samples have to be qualified for flight on the ISS by precursor TEMPUS parabolic flight or the like, demonstrating technically sound and safe levitation processing in reduced gravity. Tables 2.2,

Table 2.2 EML sample batch 1 overview: prime proposer (●) and other interested projects (○)

ID no.	Sample designation	CCEMLCC	COOLCOP	Elec. resist.	ICOPROSOL	LIPHASE	MAGNEPHAS	METCOMP	MULTIPHAS	NEQUISOL	OXYTHERM	PARSEC	SEMITHERM	THERMOPROP	ELFSTONE	QUASI	LODESTARS	USTIP
1	Al40Ni60									●				○		○		
3	Cu75Co25		●													○		
4	Cu89Co11		●													○		
6	Fe45Co55						●					○			○	○		
7	Fe50Co50						●					○			○	○		
9	FeCr21Ni19											○		●			○	
10	Ni13.8Al6.6Cr7.6Co2.1Ta1.6W1.0Re1.0Mo0.05Hf *(LEK94)*													●				
11	Ni5Al8Cr5Co6Ta8W2Mo1.5Ti *(MC2)*													●				
12	TiAl6V4													●				
13	Zr70Cu13Ni9.9Al10.3Nb2.8 *(VIT106A)*								○					●		○		
14	Ni96Ta4+Ta2O5							●										
15	Ni98Ta2+Ta2O5							●										
18	Zr									○				●				
21	Zr57Nb5Cu15.4Ni12.6Al10 *(VIT106)*								○					○		●		
22	Nd18Fe73B9						●					○						
23	NiCr2Co3Mo0.4Al5.7Ti0.2Ta8W5Nb0.1Hf0.03Re6 *(CMSX-10)*													●				
42	Al40Ni60									●				○		○		
43	Cu75Co25		●													○		

Table 2.3 EML sample batch 2 overview: prime proposer (●) and other interested projects (○)

ID no.	Sample designation	CCEMLCC	COOLCOP	Elec. resist.	ICOPROSOL	LIPHASE	MAGNEPHAS	METCOMP	MULTIPHAS	NEQUISOL	OXYTHERM	PARSEC	SEMITHERM	THERMOPROP	ELFSTONE	QUASI	LODESTARS	USTIP
2	Al75Ni25									●				○				
5	FeC0.05Si0.2	●												○				
16	Ge												●			○		
17	Si50Ge50												●			○		
20	FeC0.9Si0.2	●												○				
24	Al65Ni35									●				○				
25	Al89Cu11									●				○				
27	Cu50Zr50								●					○		○		
28	Cu67Co33		●													○		
29	Fe90B10						●					○		○	○			
30	Si25Ge75													●		○		
34	Zr52.5Cu17.9Ni14.6Al10Ti5 (LM105)													●		○		
36	Zr64Ni36			●								○				○		○
38	Zr-O(0.1)		○							○			○	●	○			
39	Ti39.5Zr39.5Ni21				●							○		○	○	○		
40	Fe60Co40						●					○				○		
44	Ti48.5Al47.6Nb2Cr1.9													●				
45	Fe57.8Ni19.2Mo10C5B8													●				

2.3 and 2.4 give the respective overviews of the sample batches 1, 2 and 3 (each consisting of 18 samples) along with the involved research projects. Altogether the samples cover a wide range of material classes (steels, superalloys, aluminium alloys, titanium alloys, bulk metallic glasses, high-entropy alloys, semiconductor materials and so on) for diverse application areas and include model alloys (research materials) as well as commercial alloys. Sample batches 1 and 2 were processed in the periods 2015–2018 and 2017–2021, respectively, with reprocessing of samples and intermediary swaps between the batches involved as well. Processing of sample batch 3 is to start in 2021. Sample batch 4, which also includes samples from newly entering research projects, is in preparation.

The scientific output of the EML activities has meanwhile accumulated to hundreds of publications and covers PhD/MSc theses, journal papers, conference

Table 2.4 EML sample batch 3 overview: prime proposer (●) and other interested projects (○)

ID no.	Sample designation	CCEMLCC	COOLCOP	Elec. resist.	ICOPROSOL	LIPHASE	MAGNEPHAS	METCOMP	MULTIPHAS	NEQUISOL	OXYTHERM	PARSEC	SEMITHERM	THERMOPROP	ELFSTONE	QUASI	LODESTARS	USTIP
31	Si75Ge25												●			○		○
41	Zr47Cu47Al6												○	○	○	●		○
47	FeC1.5Mn 0.6Si0.6Cr 12Mo1V1	●												○				
48	FeC1.5Mn0.6 Si0.6Cr 12Mo1V1	●																
50	Ti45Zr45Ni10				●									○	○	○		○
52	Co38.5Si61.5					●						○			○			○
56	Al96Fe4								●					○	○			○
57	Si95Ge5								●				○					○
66	Ti50Al50						○					●			○			○
67	Fe90Ni10						●					○			○			○
70	Zr80Pt20							○								●		○
81	Pt57.5Cu14. 7Ni5.3P 22.5													●		○		○
83	Fe25Cr25 Ni25Co25													●				○
84	Fe72Cr17Ni11										○			○	●			○
86	Fe72Cr13Ni15										○			○	●			○
90	FeSi3													●				○
93	ZrSn1.3Fe0.2 Cr0.1O0.13													●				○
94	ZrNb2.5O0.11Fe(x)													●				○

papers and other contributions (such as presentations and posters). Figure 2.4 gives the breakdown of documented published works during the past two decades for the various research projects. About half of these publications are (peer-reviewed) journal papers. Notably this inventory does not only consider publications relating to the ISS-EML but also to EML experiments on sounding rocket, parabolic flight and other microgravity platforms, on-ground (preparatory and reference) work and on modelling. A comprehensive list of publications, updated to the time of its publishing, is included as an annex to this book.
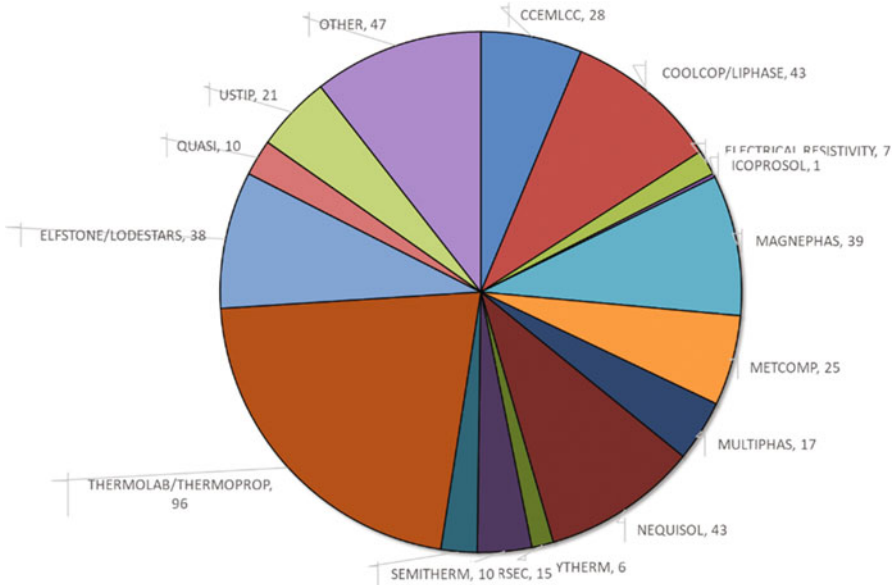
Fig. 2.4 EML-related publication output since 2001 – total count: 446, of which 8 PhD/MSc theses, 18 book chapters, 241 journal papers, 57 conference papers with presentations and 122 other contributions (presentations, posters, etc.)

4   Benefits for Earth and Industrial Relevance

The outcome of ESA's space research programme on materials science consists of benchmark data on thermophysical properties of (metallic and other) melts and the structural evolutions during the liquid-to-solid phase transition. These experimental data are of an unprecedented accuracy and reliability due to their origination in a reduced-gravity environment. This information results in both a better understanding of the fundamental solidification mechanisms and validation of theoretical models describing these mechanisms, as well as in more accurate data to feed into these models. As implemented into simulation software, this enables scientists to deepen their insights and industrial manufacturers to better design and control their processes. Thus, microstructures of materials and thereby their mechanical and physical properties can be better forecast, and novel routes can be explored upfront virtually rather than empirically. Among others, this is to the benefit of conventional continuous and shape casting (for semi-finished and finished products, respectively); investment casting including directional and single-crystal production methods, spray forming, gas atomisation (for powder production) and other deposition techniques (for coatings); and additive manufacturing through the liquid state.

The materials that are addressed in this programme can broadly be categorised as follows.

Fig. 2.5 World production
of metals from ore
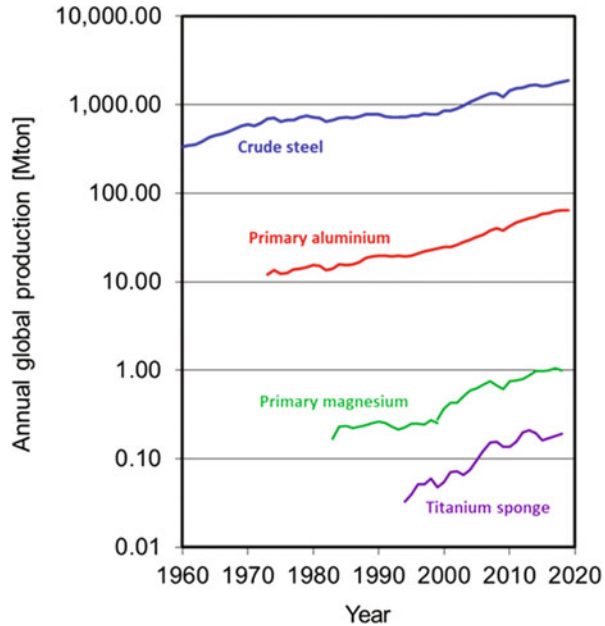
- *Structural materials*. Metals that are used for structural applications include steel and aluminium. Figure 2.5 – compiled from various sources [5–9] – shows that the global production of these metals is steadily growing for many decades now and that since the turn of the millennium this growth is even accelerating in pace. Metal production and manufacturing activities are major drivers for the economy. To save on resources and limit waste, the recycling of these metals has tradition-ally been high and is increasing still. Steel and aluminium alloys are used extensively due to their favourable combination of mechanical properties (strength and toughness) at low to moderate costs. This includes durable goods such as for building/infrastructure and for automotive, as well as goods with short cycle times such as for packaging. With steel being a traditional material of choice for construction and cars, aluminium has now firmly established itself as well for notably the latter due to its light-weighting potential. Competition between steel and aluminium in certain application areas such as automotive body parts came with several advancements in materials like dual-phase steels and (paint) bake-hardening aluminium alloys, to name just a few. Magnesium alloys are used for light-weight automotive and electronics applications (casings), and titanium alloys are used for corrosion-resistant high-strength applications (jet engine parts), among others. Besides structural applications, such metals are also used in other domains such as for energy applications (electrical steel) and biomedical applications (stainless steel and titanium implants).
- *High-performance materials*. Certain engineering materials have to serve under extreme conditions, be it at very high or low temperatures, very high mechanical/ dynamical loading or a very corrosive or otherwise aggressive environment but

most commonly being a combination of these. In line with that, they are also called materials for extreme environments. To withstand such diverse conditions, a variety of metallic and non-metallic material classes have been and are being further developed; the following is limited though to those sub-sets that are of relevance in the current context. High-temperature materials like (nickel-, cobalt- or iron-based) superalloys are used in aircraft jet engines and land-based gas turbines and are thus enablers for long-distance mobility and energy generation. Drivers for alloy development are creep, fatigue and oxidation resistance but also light-weighting; manufacturing challenges consist in geometric structures becoming more and more complex due to the integration of advanced cooling concepts, the exploration of additive manufacturing processes and so on. Advancements for these aerospace and power applications are to further increase energy efficiency, reduce emissions and enhance service lifetime. Non-degradable bio-passive materials like cobalt-chromium alloys, nickel titanium ("nitinol"), stainless steel and titanium alloys are used for implantable medical devices such as for hip replacements and cardiovascular stents. Here, alloy and manufacturing developments aim for enhanced biocompatibility and in-service performance; additive manufacturing technologies are of interest for low-volume series and one-offs, such as for trauma surgery. Advancements in implant materials contribute to the quality of healthcare (less invasive interventions and patient discomfort) and thus add to the quality of life, notably in aging societies.

- *Functional materials*. Among these there are materials that have one or more properties that can be significantly changed in a controlled fashion by external stimuli; an important category which is of interest here is that of the semiconductor materials. Commonly consisting of crystalline inorganic solids, their electronic properties depend controllably on impurities (doping) and defects, and with that their quality depends heavily on the solidification process with which they are manufactured. Silicon is the most common semiconductor material in integrated circuits and solar cells. Other semiconductor materials such as germanium, gallium arsenide and cadmium telluride are also of importance for computers and photovoltaics, as well as for detectors. With that, this category of materials is essential for ICT and (renewable) energy applications. Magnetic materials such as Nd-Fe-B permanent magnets and Fe-Si soft magnets are yet another example of functional materials, of relevance to applications in the same domain.

- *Novel materials*. Besides the established material classes, there are novel materials and alloy concepts that could become game changers for existing and future applications due to their unprecedented properties. These materials have no substantial market volume or share to date (although niche applications exist), but have a potential for that pending their further research and development. Bulk metallic glasses (BMGs) are metallic alloys that solidify in a non-crystalline, amorphous state and by that exhibit properties like exceptional hardness, elasticity and corrosion resistance. BMGs can be based on zirconium or copper but are also developed with titanium, iron, palladium and platinum. They are of interest for application in aircraft, spacecraft and car components; gears, fashion and sport

equipment; as well as in medical devices. Several companies are already adopting manufacturing processes – requiring distinct solidification rates – to produce BMG components. These processes include conventional casting, injection moulding and liquid-state additive manufacturing. Besides structural components, BMGs are also of interest as coating materials. High-entropy alloys (HEAs) are materials that deviate from the conventional alloying paradigm in that they are formed by mixing equally large proportions of four or more chemical elements (thus exhibiting high configurational entropy in their crystalline state). This can be used to design materials with considerably improved strength-to-weight ratio, fracture toughness and/or corrosion resistance versus conventional alloys. Commensurate with this approach, the number of conceivable alloying combinations is astronomical, but FeCrMnNiCo, NiCrFeCoAl and TiVZrNbTa are among the best-known examples. Potential applications for HEAs (also called concentrated multi-component alloys) are in harsh environments such as in aircraft turbines, as well as in space exploration. The crystal-lattice distortion typical for HEAs may also be used for solid-state (interstitial) hydrogen storage, presenting a possible other avenue for development.

5   Conclusion

ESA has consistently been developing a reduced-gravity research programme on physical and life sciences for several decades. For materials science, the programme presently provides experiment opportunities to about 20 ESA (plus associated NASA and Roscosmos) research projects, each with their own scientific objectives and activities on specific topical challenges in the field. Altogether the project consortia gather hundreds of materials scientists from academia as well as from industry and from across the globe. The programme is currently using three materials science facilities on board the ISS (with a further one in development), as well as various scientific payloads for other ESA platforms. Among these, the ISS-EML is since 2015 being successfully operated and is providing a steady stream of original scientific results for the successively processed sample batches that cover a wide spectrum of structural, high-performance, functional and novel materials. Acquired scientific results – as also presented in this book – advance the fundamental understanding in solidification physics (thermophysical properties, structural evolutions) and serve to validate and enhance modelling capabilities.

References

1. Erasmus Experiment Archive. https://eea.spaceflight.esa.int/portal/
2. N.N., *Roadmaps for Future Research: A Redefinition of Strategic Goals for Future Space Research on the ISS and Supporting Research Platforms,* (European Space Agency, Directorate of Human Spaceflight and Robotic Exploration, 2016). http://esamultimedia.esa.int/docs/HRE/SciSpacE_Roadmaps.pdf
3. I. Egry, D. Voss, Present activities of the investigators working group (IWG) for the electromagnetic levitator (EML) on ISS: A status report. J. Jpn. Soc. Microgravity Appl. **27**(4), 178–182 (2010). https://doi.org/10.15011/jasma.27.4.178
4. D.M. Matson, Maximizing scientific return from shared facilities working in space: ESA's investigator working group for the ISS-EML facility. Int. J. Microgravity Sci. Appl. **37**(3), 370301 (2020). https://doi.org/10.15011/jasma.37.3.370301
5. World Steel Association. https://www.worldsteel.org/steel-by-topic/statistics/steel-statistical-yearbook.html
6. The International Aluminium Institute. https://www.world-aluminium.org/statistics/primary-aluminium-production/#data
7. International Magnesium Association. https://www.intlmag.org (1983–1999)
8. U.S. Geological Survey. https://www.usgs.gov/centers/nmic/magnesium-statistics-and-information (1999–2018, excluding US)
9. U.S. Geological Survey. https://www.usgs.gov/centers/nmic/titanium-statistics-and-information (excluding US)

Chapter 3
The Electromagnetic Levitator Facility (EML) on Board the ISS

Wolfgang Soellner and Winfried Aicher

1 Introduction

The EML facility, developed by Airbus Defence and Space under contracts to ESA and DLR, has been installed and commissioned on the International Space Station (ISS) in 2014 (see Fig. 3.1). It is integrated within the European module Columbus in the European Drawer Rack (EDR) using up to two-thirds of the volume.

With EML being a multi-user and multi-purpose facility, it allows the strong international Investigator Working Group to complement their research with an unmatched opportunity in gathering precision data of melts. This not only improves the understanding of solidification processes and the physics of melts but also has an industrial benefit.

Material properties measured to precision in space are used in modelling of earthbound casting processes for quality enhancement and cost reduction of high-tech casting parts.

The purpose for performing these measurements in space under microgravity (µg) is derived from the electromagnetic levitation principle which allows processing of the samples without contact to a container. The sample is placed in the centre of a coil system which is part of an oscillating RF circuit and generates an RF electromagnetic field. The interaction of eddy currents induced in the sample by the electromagnetic field leads to a displacement force keeping the sample at the centre of the coil system. Heating is achieved by ohmic losses of the eddy currents flowing in the sample. In ground-based experiments, the required levitation force and thus the electromagnetic field strength to counteract gravity are so large that many materials are melted just by applying the field to position them. Heating and positioning of the sample are hence not independent, and the undercooled regime

W. Soellner (✉) · W. Aicher
Airbus Defence and Space, Friedrichshafen, Germany
e-mail: wolfgang.soellner@airbus.com

25
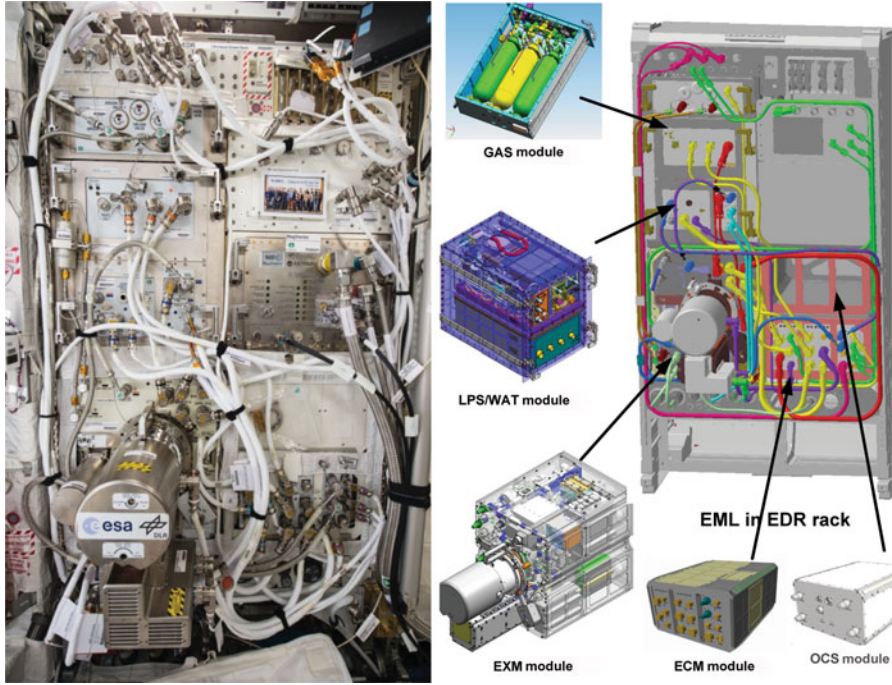
Fig. 3.1 EML installed in EDR in the European module Columbus of the ISS. EML covers the full left side and lower third on the right side of EDR. The future OCS module is shown shaded

of samples with low melting temperatures is not accessible. Furthermore, the electromagnetic pressure exerted by the strong fields leads to strong convection and a deformation of the liquid samples which are not compatible with many experiment objectives such as the determination of viscosity and surface tension. The need for lower electromagnetic field strengths thus becomes evident which means that gravity has to be largely eliminated in order to perform experiments with undisturbed samples over a wide temperature range (refer to Fig. 3.2) [1].

The EML facility supports five classes of experiments covering a wide range of scientific objectives. An overview of the experiment classes and the main physical parameters that are measured is provided in Fig. 3.3. Common to all experiments is the use of contactless diagnostic means to measure the scientifically interesting sample properties. Hence, the EML optical instruments and their relevant control electronics play the most important role in terms of scientific data acquisition besides the acquisition of standard EML housekeeping data. To enhance the precision of measurements concerning class E experiments, electrical conductivity, the dedicated instrument Sample Coupling Electronics (SCE) was developed.
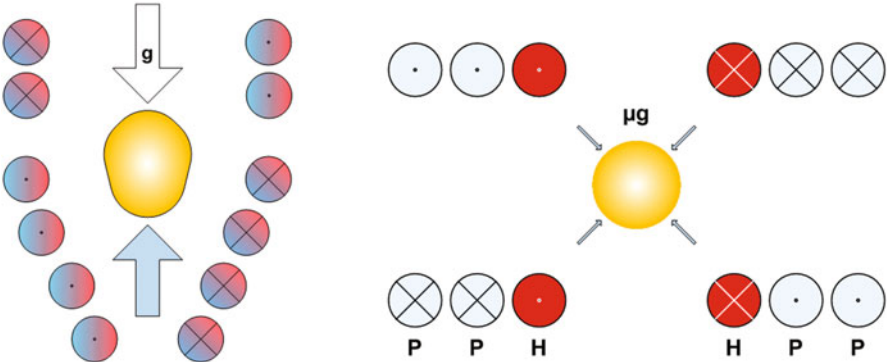
Fig. 3.2 Principle design of levitation coils for levitation under 1g (left) and μg (right). Note that this illustrative sketch simplifies the EML flight coil working principle w.r.t. the superimposing of independent heater (H) and positioner (P) currents generating the respective dipole (H) and quadrupole (P) fields
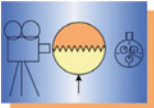
Class A: Undercooling and nucleation
Solidification front speed, nucleation statistics, phase selection and morphology
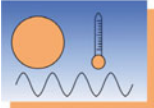
Class B: Modulation calorimetry
Heat capacity, heat of fusion, total hemispherical emissivity, thermal transport coefficients, fraction solid

Class C: Surface oscillations
Surface tension, viscosity
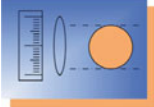
Class D: Size measurement
Thermal expansion
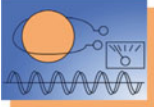
Class E: Electrical coupling
Electrical conductivity
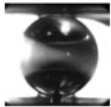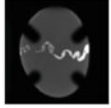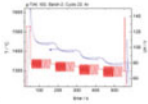
Fig. 3.3 EML experiment classes

2   The EML Mission Scenario

The EML facility is operated following a tele-science concept in a semi-automated manner from operators on ground relying on live data and live video transmission. EML is also planned to stay on board the ISS for many years with recurring experiments being supplied. Thus, a program was established to mirror this scenario by a lifecycle of one group of experiments, called batch, shown in Fig. 3.4.

Each batch consists of 18 samples, each being housed in a dedicated sample holder which differs depending on science needs and sample size. These 18 holders in turn are contained in a sample chamber which constitutes one part of EML's ultra-high vacuum environment for experiment conduction. Such a sample chamber can be uploaded and attached by crew to the facility on board the ISS. After all samples have been processed, the sample chamber can be downloaded allowing sample return to the scientist for post-process analyses.

Together with each experiment batch, a dedicated experiment ground support program (GSP) is launched preparing the vast amount of facility parameters allowing the semi-automated processing of the samples.
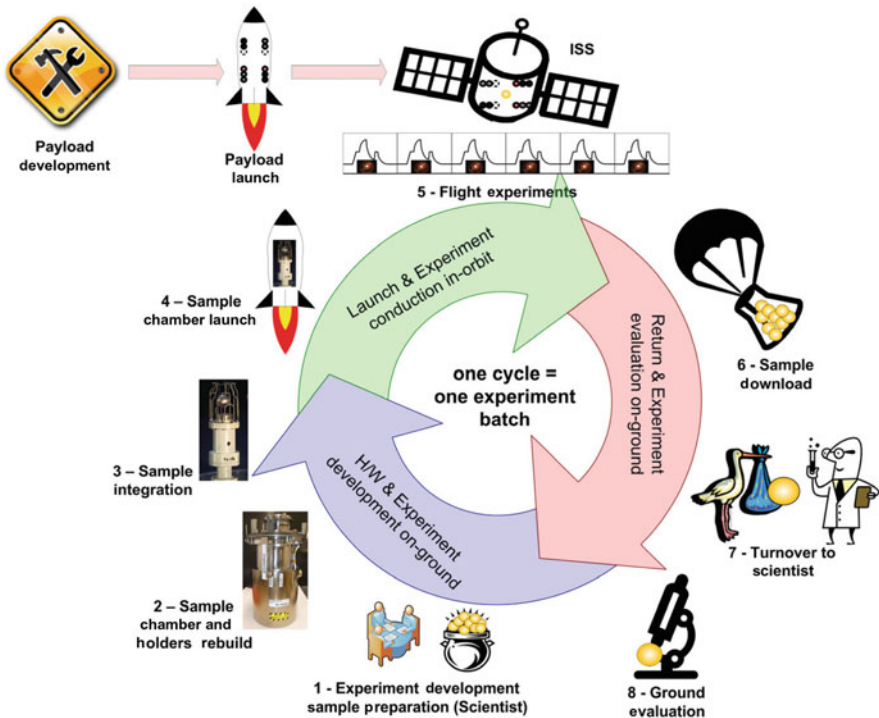
Fig. 3.4 EML mission scenario, showing the complete lifecycle of the experiments from experiment preparation to post-flight evaluation, one cycle is equal to one experiment batch

3   EML Facility Overview

The facility is designed modular to fit into its hosting rack EDR. The current four modules and their purpose are given in Table 3.1, whereas their allocation in the rack is depicted in Fig. 3.1. In the following focus is placed on the Experiment Module (EXM) as the experiments are conducted therein and because it also houses the diagnostic instruments which are of most importance to the scientific reader. More details have been provided in [2–5]. Note, after the removal of another experiment which was hosted in EDR until late 2020, the remaining free rack volume becomes available to hold the future fifth EML module called Oxygen sensing and Control System (OCS).

   The densely integrated EXM houses the core experiment chamber with all diagnostics, RF coil system, mechanisms and samples and defines the payload's capabilities with respect to the experiment. It is the biggest and most complex module of the four. Central part of it is a stainless steel ultra-high vacuum chamber, to which the exchangeable sample chamber (SCH) is being flanged upon upload to the ISS (refer to blue-lined rectangle in Fig. 3.5). The process atmosphere is either ultra-high vacuum or high-purity (99.9999%) noble gas, argon or helium or a mixture of these. The pressure inside the two chambers can be varied between 10^{-8} and 400 mbar during the experiment runs. Furthermore, the EML gas distribution system offers the possibility of a closed-loop gas circulation, in order to either apply a smooth gas flow onto the sample during the experiment or to flush particles and dust into a filter afterwards. Figure 3.5 provides a block diagram as overview on the facility functions provided by the EXM and its various subsystems such as pyrometer; two cameras; digital video system (DVS); gas and vacuum systems with their sensors, valves and pumps; illumination; mirrors in the optical path; and the RF oscillating circuit called coil system module (CSM). The 3D CAD view insert illustrates where the detachable SCH and the high-speed camera (HSC) are mounted to the front of the EXM protruding into the cabin. The inserted photo illustrates EXM's integration density when including gas pipes and harness.

Table 3.1   EML modules and their purpose – the future module OCS is indicated in grey italic

No.	EML module	Main function
1	Gas Supply Module (GAS)	Storage and distribution of the noble gases
2	Levitation Power Supply/Water Pump Module (LPS/WAT)	Provision of RF voltage to the RF coil generating the electromagnetic fields. Secondary cooling loop to subsystems
3	Experiment Module (EXM)	Core experiment: comprising, e.g. vacuum chamber, RF coil, diagnostics, mechanisms, samples
4	Experiment Controller Module (ECM)	Data management and control, power distribution
5	*Oxygen sensing and Control System (OCS)*	*Provision and control of atmospheric condition in the EML process chamber w.r.t. to oxygen content*
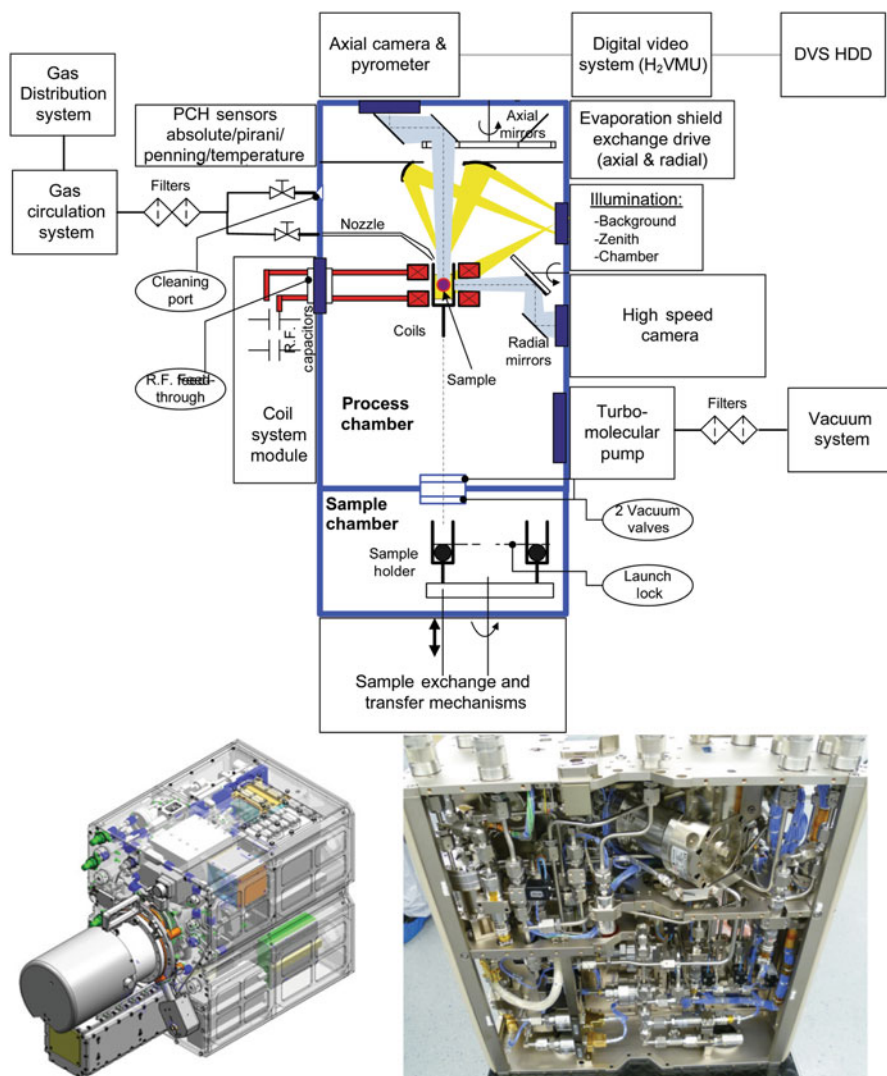
Fig. 3.5 Functional block diagram of EXM showing experiment-driven functions. The 3D CAD view insert shows the SCH and the HSC being mounted to EXM's front panel, whereas the photo on the bottom right shows the integration density

The coils generating the electromagnetic fields are shown in Fig. 3.6 within the process chamber. The design of the coil is such that the radiofrequency (RF) currents generating the positioning and heating fields are superimposed within the same coil, thereby achieving a high concentricity of both fields and hence an optimized positioning of the sample. The positioning field is of quadrupole type with low heating efficiency and operates at about 140 kHz, whereas the heating field is of
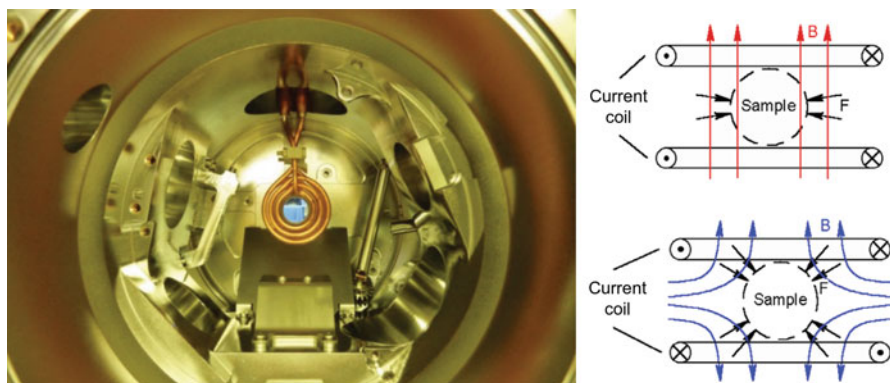
Fig. 3.6 (Left) Internal view into EML process chamber with the RF coils in the centre. (Right) The inserts show the principle of the two RF currents and their related RF fields being superimposed in one coil but shown here separately for clarity reasons (positioner = blue, heater = red)

dipole type with low forces on the sample and operates at about 380 kHz. Depending on the sample material and process environment heating rates of about 100 K/s can be applied, allowing sample temperatures of up to 2100 °C to be reached within 1 min. Both heater and positioner voltages can be varied as linear functions of time.

EML accommodates 18 samples (6–8 mm diameter) per sample chamber (SCH). The samples are housed in individual sample holders mounted to a carousel within the SCH. With a mechanism, a sample can be selected and transferred from the storage position to process position within the RF coil. The sample holder design allows contactless free floating during the experiment run, while a contact of the levitated sample with the RF coil is prevented in case of any inadvertent excessive acceleration, and as well the sample containment during launch is assured by the sample holders and dedicated locking mechanisms.

Two basic types of holders are available: the cage type and the cup type, which have slit openings on the top and side of the cylinder for sample observation by the EML diagnostic instruments. Common to both types is a ceramic foot on top of which the sample confinement is mounted. The selected silicon nitride ceramic is thermo-shock resistant and compatible with highly reactive melts. The cage design uses rhenium wires with a geometry that minimizes coupling to the RF fields. For EML Batch 2, a third type, called chill-cool-plate sample holder, was developed. This is a sub-type of the cup sample holder with a closed lid on top instead of the clover leaf-shaped opening. This plate is used in the experiment as heat sink for the sample contacting it by purpose and hence starts to solidify at this point with a higher cooling rate as the sample's heat is transferred to the sample holder. For temperature monitoring by the EML pyrometer, a central boring of 1 mm diameter was introduced into the chill-cool-plate allowing just enough room for the pyrometer's optical path to pass through.

Fig. 3.7 (Left) EML sample chamber. (Top right) Three sample holder types: cage, cup and chill-cool-plate. (Bottom right) View inside sample chamber's vacuum part with sample carousel holding 18 dummy sample holders and the sample launch lock mechanism

The samples are integrated into the sample holders inside a glove box on ground under controlled noble gas atmosphere (argon 99.9999%) and are then transferred to the sample chamber again under the same controlled noble gas atmosphere. Figure 3.7 shows the sample chamber with samples integrated, ready for launch, the three sample holder types and an SCH internal view.

In support of contactless undisturbed levitation, EML offers as the main sample diagnostics three optical systems: a fast digital pyrometer and two digital video cameras, in orthogonal views. One camera is integrated together with the pyrometer in a single instrument using the same optical path but separating the infrared spectrum from the visible light by a beam splitter. This instrument observes the sample in axial direction of the coil system. The second camera, called HSC (high-speed camera), observes the sample from a radial direction, i.e. imaging it through the 8-mm-wide slit between the two induction coil windings.

Special care was taken in the development of the entire optical path considering the cameras and all optical elements deriving high performance in support of the different experiment goals. As Tables 3.2 and 3.3 show, both cameras are able to observe fast sample surface oscillations for measurement of surface tension and

Table 3.2 Key performance data of EML camera in axial view direction

Sensor: CMOS, resolution 1280 × 1024 pixel	Various fields of view, resolutions and maximum frame rates, e.g.:	
Digitalization: 10 bit/pixel	10 × 10 mm:	704 × 704 pixel @ 50 Hz
Global shutter, fixed or auto exposure	10 × 10 mm:	352 × 352 pixel @ 150 Hz
Frame rate enhancing by subsampling 2 × 2 (i.e. pixel reduction by factor 4)	8 × 8 mm:	280 × 280 pixel @ 200 Hz
	18 14 mm:	1280 × 1024 pixel @ 15 Hz
Focal point of optics: 1.7 mm above sample equator towards the pole	Optical resolution:	15.6 µm/line

Table 3.3 Key performance data of EML high-speed camera in radial view direction

Sensor: CMOS, resolution 800 × 600 pixel	Various fields of view, resolutions and maximum frame rates, e.g.:	
Digitalization: 14 bit/pixel	10 × 10 mm:	600 × 608 pixel @ 8500 Hz
Global shutter, fixed or auto exposure	10 × 10 mm:	250 × 250 pixel @ 30 kHz
Frame rate enhancing by pixel reduction	13 × 10 mm:	800 × 600 pixel,
Focal point of optics: 1.7 mm in front of sample equator towards the pole	Optical resolution:	17.5µm/line
Real-time analogue NTSC video output for process control	Recording duration of 8 GB camera memory: 600 × 608 pixel @ 200 Hz: 58.2 s	
Internal 8 GB ring memory for high-speed video acquisition, download to EML mass memory after experiment	600 × 608 pixel @ 8500 Hz: 1.37 s 256 × 256 pixel @ 10 KHz: 6.48 s 256 × 256 pixel @ 30 KHz: 2.16 s	
Triggering of recording by temperature event recognition (recalescence detection)		

viscosity. The HSC provides additionally a high-speed acquisition mode of up to 30,000 fps (achieved by pixel reduction) to visualize the solidification front growth. By the focal plane's position slightly in front of the sample's equator, the observation benefits from the high resolution at the sample surface and allows edge detection on sub-pixel resolution at the sample's equator by offline image analysis. Even if sample movements of ±1 mm occur, the optical systems allow to measure relative size changes better than $7*10^{-5}$ supporting thermal expansion measurements. Moreover, the beam splitter is a dedicated development matching the camera's sensitivity in the near-infrared regime and thus supports the sample observation at relatively low temperatures when the sample is not visible for the naked eye. Both cameras provide also the possibility of thermal radiation mapping due to the high digitalization which can be used to display temperature distribution across the sample in false colours by offline ground video processing.

The sensitive EML pyrometer complements the camera diagnostics providing fast and stable measurements over a wide temperature and sample emissivity range (see Table 3.4). It also provides the input to the recalescence detection algorithm providing the stop trigger to HSC to capture the fast solidification event.

Table 3.4 Key performance data of EML pyrometer

Wavelength range: 1.45…1.8 μm	Temperature resolution (for emissivity = 0.05)
Measurement rate: 100 Hz	$\leq$0.1 K (>600 °C)
Measurement range: 300–2100 °C	<0.5 K (500–600 °C)
Emissivity: 0.05...1.00	<1.5 K (400–500 °C)
Integration time: 5 ms	<3.0 K (300–400 °C)
Measurement spot diameter: 0.8 mm	
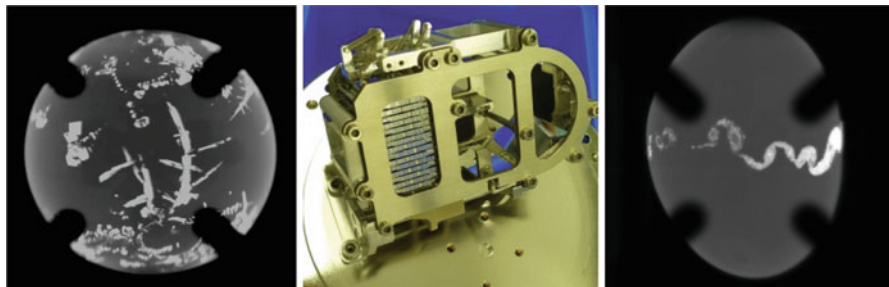
Fig. 3.8 (Left) SiGe sample solidifying. (Middle) Axial evaporation shield mechanism holding 24 exchangeable mirrors with a total of 48 reflective surfaces. (Right) Sample performing surface oscillation in axial direction after stimulation by a heater pulse

The HSC includes the possibility to provide a replay of the acquired event hold in its internal high-speed memory buffer at various speeds. This feature allows the user to verify if the fast solidification was captured by the automatism and if not to decide whether or not algorithm parameters to be reprogrammed on the fly before cycle repetition. This is also an advantage from operational point of view because after the HSC buffer content is stored into a file this file can only be viewed after downlink to ground and re-generation (offline process of approx. 1 day).

To protect the optical viewports from metallic vapour and dust deposition stemming from the molten sample, two sophisticated mechanisms have been developed allowing the first mirror of a double-mirror system to be exchanged when needed. Figure 3.8 (middle) shows the relevant mechanism of the axial optical path within the EML process chamber providing 48 individual mirror sides to be exchanged automatically and precisely without an impact on the optical path. Additionally, Fig. 3.8 shows two example images of levitated samples during solidification (left) and during surface oscillation (right).

EML offers as well a variety of stimuli for the said experiment classes. Nucleation can be triggered by a zirconia-coated trigger needle integrated in the sample holder; all other excitations are contactless via the RF fields, e.g. heater pulses of different shape, heater sine voltage amplitude or sine power modulation, heater sine frequency sweep, free definable modulation for heater and positioner.

4   EML Experiment and Facility Control Concept

A typical experiment consists of several individual melt cycles each having its own distinct temperature time profile, camera and stimuli settings according to the scientific need which typically differs significantly between experiments and partly also from cycle to cycle. Hence, EML offers the user a high degree of flexibility by a large number (several hundreds) of freely adjustable experiment parameters per cycle, accumulating to tens of thousands per experiment. These parameters are defined by the user in a development process on ground (refer to ground support program in Chap. 4) and put into a large parameter set which is then uplinked as a file to EML and used by the experiment handler to run the experiment in a semi-automatic fashion. This means ground operators initiate the automated process by telecommand and the experiment handler follows the parameter set's timely script acting on all EML subsystems accordingly. While ground operators observe the telemetry and the floating sample on the live video downlinked from EML on-board video systems, the operators can interact with the on-board process control to initiate further process steps or terminate the cycle.

Even though the facility monitors the process and the relevant subsystems by sophisticated software supervision and dedicated hardware circuitry, such tele-science operation warrants high emphasis on the entire video chain from end to end. Hence, as part of the EML mission, the dedicated video ground support equipment was developed re-generating both EML live video streams in real time.

The high-resolution and high-speed video acquired during experiment runs is stored on board within dedicated controllers of each camera. Downlink of these large data amounts is performed offline, after the experiment, and also fed into the video ground equipment to generate the scientific video files as one major EML mission product.

5   EML Program Achievements and Recent Enhancements

Since the start of regular science operations, two complete batches of experiments have been conducted since, processing 36 samples with a total of more than 2000 individual melt cycles developed and a large fraction thereof successfully processes on-orbit.

The operation of EML is performed by MUSC in Cologne (refer to Chap. 4) with the support of Airbus Defence and Space w.r.t. maintenance, upgrades, enhancements and troubleshooting. The installation, on-orbit commissioning, the operational concept of EML and first results obtained in Batch 1 have been described in [4]. After completion of the last Batch 1 experiments, the sample chamber #1 returned to ground in summer 2019, and the samples were de-integrated from

SCH within the EML glovebox's pure environment and subsequently returned to the scientist for analysis. In parallel operations on Batch 2 experiments in sample chamber #2 (launched in 2017) continued until its planned end in spring 2021.

5.1 Sample Coupling Electronics (SCE)

The measurement of the sample's temperature-dependent electrical conductivity in the molten state is one goal of EML experiments. In principle this measurement can be achieved by using the housekeeping data of the LPS providing the RF power to the coil system in which the sample levitates and is heated by the eddy currents. However, the accuracy of this method is limited as the phase shift between RF current and voltage is not available at the LPS.

Thus, it was decided to build the SCE as the dedicated instrument for this type of measurement (see Fig. 3.9). The development is based on a laboratory model and measurement principles established by DLR (Institut für Materialphysik im Weltraum). The SCE measures the critical parameters directly at the coil system module with high precision taking also the temperature of the capacitor in the oscillating circuit into account. Especially challenging for the electronics development was the measurement of the settle changes (order of 10^{-4}) of the RF circuit's electrical properties on top of the large background provided by the RF power supply. The SCE was installed in EML flight facility in February 2017 and is since then successfully used for EML Batch 2 experiments.
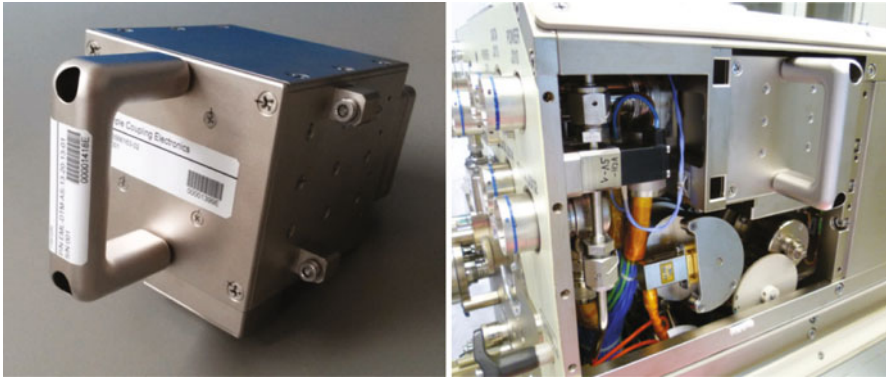
Fig. 3.9 (Left) SCE flight model. (Right) SCE ground model integrated in EML ground facility Experiment Module (EXM)

5.2 High-Speed Camera Operating System (HSC-OS)

Soon after the EML facility started its operation in orbit, it turned out that the amount of video data recorded with the HSC by the scientists is factors higher than anticipated in the mission scenario. As a consequence, the data transfer times from the HSC's volatile memory to the HSC-OS were very long consuming a big part of the available operation time per shift. Thus, the amount of melt cycles, and the amount of science, which can be performed with the EML facility per shift, was limited by the HSC to HSC-OS transfer speed.

Out of this situational analysis and the desire to perform more experiments in shorter time, the need for speed was derived and the upgrade of the HSC-OS to the second generation was started in spring 2016.

Boundary conditions were that the new hardware had to fit exactly into the existing EML architecture in terms of volume, power consumption, cooling concept and data interfaces, and harness routing but at the same time include internally a new board-level architecture supporting higher data throughput. With the new architecture, not only the data transfer from camera to the hard disk was increased by factor 10, but also the data amount to be transferred to ground can be reduced by factors up to 10 without negative influence on the scientific evaluation of most experiments. The compression board also allows lossless compression which still leads to data reduction of factor 2 and is used for some scientific evaluations being more sensitive to information loss by compression. The new unit (see Fig. 3.10) was launched to ISS and installed in EML in summer 2018 and provides successfully since then the scientific data for EML Batch 2.
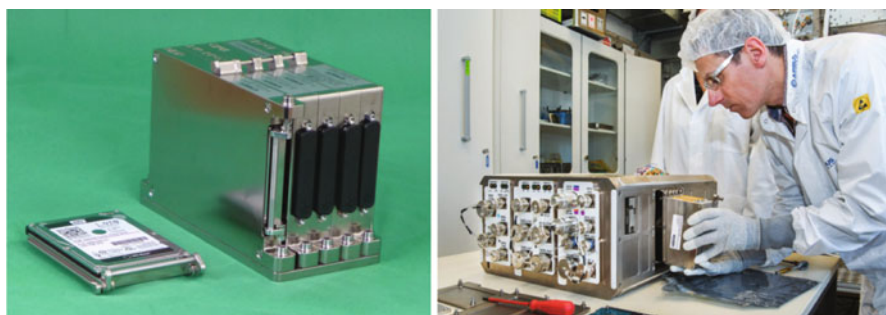
Fig. 3.10 (Left) HSC-OS second-generation flight model. (Right) Installation of HSC-OS in EML ground model Experiment Control Module (ECM)

5.3   EML Batch 3 Sample Chamber and Holders and GSP

Due to the interlaced on-board processing of Batches 1 and 2, it became evident that sample chamber #1 would not be available on ground in time considering its refurbishment and readiness for Batch 3. Hence, it was decided to build a third sample chamber (SCH) for flight identical to the other two in order to support continuous resupply of new experiment samples to EML maintaining an on-orbit operation scenario without long interruptions. Also new sample holders were manufactured for Batch 3 to match the need derived from the scientific objectives. In parallel to the hardware manufacturing, ground support program (GSP) was launched. A major GSP output was the preparation and test of flight like samples leading to certified flight sample production with controlled sample properties and eventually to flight sample delivery by the scientists for integration into the SCH. As the next step in the GSP, the experiment parameter development, validation and acceptance for the first sub-Batch 3.1, consisting of six experiments, took place. The data product is ready for upload. The process for sub-Batch 3.2, consisting of seven experiments, is currently under finalization and acceptance.

In the meantime, the SCH and the sample holders where manufactured, tested and accepted by ESA and the sample integration could be performed under the known high-purity conditions using the EML-dedicated glovebox flooded with argon of 99.9999% purity and moisture/oxygen control below 1 ppm (refer to Fig. 3.11). The filled and accepted Batch 3 SCH was delivered in January 2021 to the cargo integrator for launch preparation. It is expected to arrive on ISS by early summer 2021 allowing the timely continuation of on-orbit experiment with the already developed Batch 3 parameters (see above) after the last Batch 2 (sub-Batch 2.5) is finished.

Fig. 3.11   Sample integration process using the EML glovebox

6   Future Enhancements to EML

As described in more detail in [6], Airbus Defence and Space is currently developing the Oxygen sensing and Control System (OCS) to further enhance the EML mission success by enlarging the EML science scope and community. With the OCS the sample's thermo-physical properties measured by the employed EML techniques shall be determined also in dependence of the oxygen partial pressure in the process atmosphere. The OCS shall be installed as an individual module in a locker of EDR, as shown in Fig. 3.1, and will be connected to the EML gas loop front panel connectors by flex lines. This allows feeding the EML process gas through OCS to measure the incoming O_2 partial pressure and to control (add or remove oxygen) the outgoing O_2 partial pressure. In all other aspects, i.e. power, thermal, commanding and control, OCS will be fully independent from EML.

The OCS is based on an oxygen ion pump using heated zirconia (see Fig. 3.12) and is able to measure and control hereby the O_2 partial pressure in the range from 10^4 to 10^{-15} Pa. The sensor's functional principle is hereby the measurement of the NERNST potential between an O_2 reservoir (ambient) and a gas atmosphere with lower oxygen content separated by a heated ceramics wall. When inverting this scenario, i.e. applying an external voltage to the electrodes, it is possible to transfer oxygen through the heated ceramics wall in both directions from ambient to the process gas or vice versa depending on voltage polarity. This leads to a so-called oxygen pump.

The system's core unit is the Oxygen Management Unit (OMU) which houses two zirconia tubes as depicted in Fig. 3.12 serving as oxygen sensor and as oxygen sensor/pump. They are surrounded by a heater tube and accordingly thermal radiation shields and isolation to reduce thermal losses. The OMU is part of the OCS internal gas loop including also a gas circulation pump to feed the EML process gas through the OMU and back into the EML process chamber. The pump is similar to the one already used in EML. OCS second major part is the control unit (CU) which houses all the electronics to operate and control the OMU and the OCS internal components. The CU represents also the electrical interface to EDR (power and data). Both major parts and the internal components are integrated in a drawer
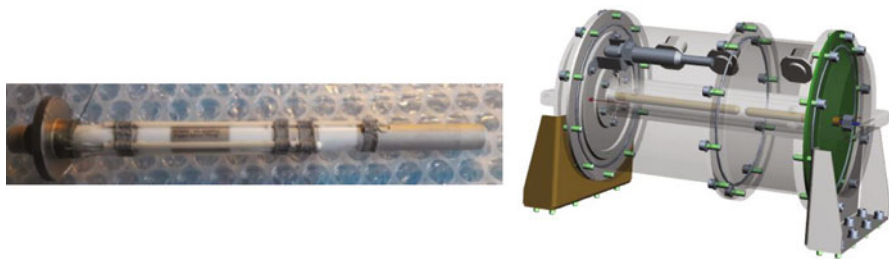
Fig. 3.12 (Left) Picture of integrated oxygen pump and oxygen sensor of OCS prototype. (Right) 3D CAD view of the Oxygen Management Unit (OMU) housing the oxygen pump
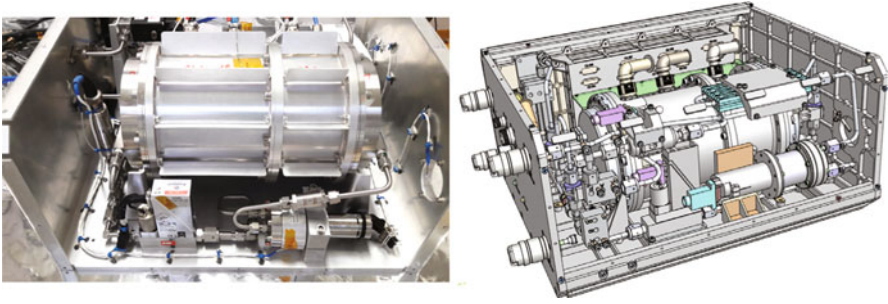
Fig. 3.13 (Left) Elegant breadboard (PDR status) of the OCS locker with Oxygen Management Unit (OMU). (Right) 3D CAD view of OCS (CDR status)

structure (see Fig. 3.13) providing the mechanical and thermal (air-cooling) interface to EDR. The OCS project is currently in phase C expecting the critical design review (CDR) early summer 2021. The OCS flight model is foreseen to be available by end of 2023 to be launched to ISS and used from EML Batch 4 onwards.

7 Conclusions

Following several years of development and the launch to the International Space Station (ISS) in 2014, the electromagnetic levitator (EML) today is a reliable facility for on-orbit experiments related to materials science of liquid metals, alloys and semiconductors inside the Columbus module of the ISS. In order to keep the facility up to date on a scientific level, additional diagnostic capabilities have been added in the recent years, and others are currently under development. With the Batch 3 sample chamber being launched by mid-2021, new experiment samples are available to continue successful operation for scientific achievements.

The ongoing EML sustaining engineering provides maintenance of the facility to keep the facility in a very good operational state until its end of life time recently extended to 2030. Just recently the second gas module was refurbished, tested and filled with the high-purity noble gases argon and helium and is now ready for launch as a resupply for the consumed gas resource within gas module #1. The re-built and exchange of the gas circulation pump planned for fall 2021 serve as the second example for the profound engineering service provided. Thus, future experiment batches may rely on the full performance of the EML facility as described herein.

References

1. A. Seidel, W. Soellner, C. Stenzel, Materials science investigations using electromagnetic levitation. J. Phys. Conf. Ser. **327**, 012015 (2011)
2. W. Soellner et al., EML-containerless processing facility for materials science research onboard the ISS. J. Jpn. Soc. Microgravity Appl. **27**, 4 (2010)
3. A. Seidel, W. Soellner, C. Stenzel, EML – An electromagnetic levitator for the international space station. J. Phys. Conf. Ser. **327**, 012057 (2011)
4. B. Glaubitz et al., The Electro-Magnetic Levitator (EML) onboard the ISS – An overview and outlook, Deutscher Luft- und Raumfahrtkongress, Rostock, Germany, 22–24 Sept. 2015
5. W. Soellner, 164th ISIJ Meeting, Ehime University, Matsuyama, Japan, 18 Sept. 2012
6. W. Aicher, Future capabilities of the Electromagnetic Levitator (EML) on-board the ISS: Oxygen sensing and Control System (OCS), International Astronautical Congress (IAC), Bremen, Germany, 2018, 1–5 October, IAC-18.A2.2.5.7x43087 (2018)

Chapter 4
Operations of the Electromagnetic Levitator: From Spacelab to the ISS

Rainer Willnecker and Angelika Diefenbach

1 Introduction

Electromagnetic levitation techniques in combination with contactless diagnostics was found a sophisticated means for undercooling experiments on liquid metals and alloys and determination of their thermophysical properties. In 1986, the first results on pure metals and alloys showed the outstanding suitability of this technique and its significant potential for scientific investigations on the physical properties of metallic liquids [1]. Further ground-based experiments gave evidence for new applications of electromagnetic levitation. In combination with fast infrared pyrometry, the investigation of unknown metastable phase formation in undercooled liquids, growth velocity determination and nucleation path identification became feasible [2, 3].

New digital camera and intelligent image processing techniques paved the way for additional scientific research areas like viscosity, surface tension and density measurements of improved accuracy [4]. Of utmost importance, the development of contactless calorimetry methods opened the broad field of measurements of thermophysical properties on undercooled liquid materials for basic and applied research [5].

Experiment limitations on ground and the beginning of international microgravity programs opened a new era for electromagnetic levitation by its use in space. Since very large levitation forces are necessary to suspend liquid samples in the earth gravity field, the experiments prove to be restricted to high-melting metals. Sample deformation from strong magnetic fields prevents high precision measurements on the material's physical properties. Advantages of this technique in low-gravity fields

R. Willnecker (✉) · A. Diefenbach
Microgravity User Support Center, Deutsches Zentrum für Luft- und Raumfahrt (DLR), Köln, Germany
e-mail: rainer.willnecker@dlr.de

Fig. 4.1 First TEMPUS laboratory model

became obvious and moved into focus of space programs. The first microgravity project was set up by the German Space Agency DLR (formerly DARA 'Deutsche Agentur für Raumfahrtangelegenheiten') called 'TEMPUS' ('tiegelfreies elektromagnetisches Positionieren unter Schwerelosigkeit'). Industry (formerly Dornier Friedrichshafen, latterly Airbus D&S) was targeted with the development of the first electromagnetic levitation apparatus for application in the space environment [5]. Figure 4.1 shows the first TEMPUS laboratory model delivered to the Microgravity User Support Center (MUSC) at DLR in Cologne, which was used for the preparation program of future experiments under microgravity conditions. In 1988 short-term parabolic flight experiments at the Ellington Airfield in Houston were performed to test and verify successfully this technique under reduced gravity conditions. A particular technical emphasis was led on the generation of electromagnetic fields to position and heat the samples independently by two coil systems. Forces could be reduced under low-gravity conditions by two orders of magnitude, and it was possible to decouple the sample stability forces from the heating forces, thus allowing a lower heat input into the samples leading to a temperature control in the regime down to about 600 K. With this finding, new classes of sample materials like low-melting glass forming eutectics became possible for investigation of their interesting properties in the region of high levels of undercooling near the glass transition.

In 1989, a first test flight of TEMPUS on a sounding rocket mission was undertaken. The 6-min microgravity flight time was aimed to verify the sample

stability and to perform the first full melting and solidification experiment on a Fe-Ni sample. While the stability test went successful, the sample could not be molten due a fault of the high-frequency heating generator. Nevertheless, the technical results reached, and the high science potential of this technique led to a wide-ranging utilisation planning of electromagnetic levitation techniques under microgravity conditions for the future years up to the Space Station era.

2   International Collaboration on Electromagnetic Levitation in Space and Space Agencies Programs

The chapter of electromagnetic levitation in low-earth orbit was formally opened with a bi-lateral agreement between NASA and DARA in 1990 on the flight of the TEMPUS facility on board the International Microgravity Laboratory Spacelab Mission (IML-2). The cooperation was based on a 'no exchange of funds' scenario and covered the design, development, integration, verification and implementation of the TEMPUS instrument to fly on the 14-day Spacelab mission with the Space Shuttle Columbia. The scientific utilisation scenario foresaw the equal share of resources between the eight investigator teams from the USA and Germany, who participated in the mission in July 1994. Twenty-two samples of different materials were flown, and in total 26 experiments were performed. TEMPUS was operated for about 200 h. Figure 4.2 shows NASA astronaut Donald Thomas supporting TEMPUS operations. The experiment classes included undercooling and nucleation investigations, surface and viscosity measurements by oscillating drop technique, specific heat determination by power modulation and solidification experiments on quasi-crystal forming alloys [6]. The sample stability was found the most critical part of the experiments and subject to improvement for the subsequent utilisation of TEMPUS on the Spacelab Mission 'Materials Science Laboratory' (MSL-1R).

The mission MSL-1 and MSL-1R in 1997 were based on the continuation of the NASA-DLR agreement with the participation of nine investigator teams. Research topics were expanded by measurements of the thermal expansion of glass-forming alloys and thermophysical properties of advanced materials in the undercooled liquid state. An improved coil design greatly reduced the coil misalignments and allowed for a better stability of the liquid drops. As another important lesson learnt from the IML-2 mission, the experiments during MSL-1R were performed in periods of less crew activities providing the best environmental conditions of reduced microgravity disturbances. Due to these measures, during MSL-1R, all 22 samples could be processed almost flawlessly without sample positioning problems.

After the successful TEMPUS Spacelab missions in 1997, the plan for the evolution of electromagnetic levitation on the new platform International Space Station (ISS) was elaborated programmatically. It was decided to develop an 'electromagnetic levitator' (EML) based on the TEMPUS heritage as a second-generation payload for the Columbus module. An agreement between DLR and the European

Fig. 4.2 NASA Astronaut
D. Thomas operating
TEMPUS on board the
Space Shuttle Mission
STS-83. (Photo: NASA)

Space Agency in 1998 on the common development and utilisation of EML for the ISS was reached and gave prospect to materials science experiments in the next decade in low-earth orbit until 2020+. An ESA-NASA agreement on the share of EML utilisation and consumption resources opened the access to EML for US investigator groups, thus continuing the collaboration concept of the TEMPUS era. This gave the fundament for future international cooperation in materials sciences using electromagnetic levitation in space for the growing field of thermophysical properties. With this long-term perspective, microgravity application programs could be started, and a strong involvement of industry in applied research using EML was initiated. Particularly the field of materials thermophysical properties was stimulated by an intense collaboration between universities and industries, which the results described in this book remarkably demonstrate.

EML finally was launched to the ISS with the Automated Transfer Vehicle (ATV-5) from French Guiana and installed in EDR (European Drawer Rack) inside the European Columbus module during the 'blue-dot' mission of ESA Astronaut Alexander Gerst in Nov. 2014 (Fig. 4.3). Due to the complexity of the payload, installation on board took about 3 days. EML was built as a multi-purpose facility, providing the capacity for 18 scientific specimens to be uploaded per batch. After the successful payload commissioning, the first experiments started in March 2015.

Fig. 4.3 ESA Astronaut A. Gerst during EML installation in Columbus in 2014. (Photo: ESA)

3   TEMPUS Operations in the Spacelab Era

The Microgravity User Support Center (MUSC) of DLR in Cologne has been charged with the preparation and operation of experiments in TEMPUS and later EML from the cradle of electromagnetic levitation techniques in space. During IML-2, TEMPUS operations were executed by a combined team of ground personnel from the payload developer, the investigator groups and operators from the MUSC, all located at the Huntsville Operations Support Center (HOSC) in Alabama [7]. A dedicated science operation area (SOA) was provided by NASA to the international investigator and operator teams close to the main control room dedicated to the mission control team (Fig. 4.4).

Voice and video interfaces could be used for communication with the mission control team and the crew on board. Unique data interfaces were established to the dedicated TEMPUS-provided ground systems for experiment monitoring and commanding. Communication between S/L and ground was realised by two 'Tracking and Data Relay Satellites' (TDRS) as relay to the NASA ground terminals in White Sands, where the data from the Shuttle and S/L was received and distributed to the Mission Control Center in Houston and to the HOSC in Huntsville via ground cable links (Fig. 4.5). A longer LOS (loss of signal) time of about 15 min always occurred during each Shuttle earth orbit when passing the region of the Indian Ocean where no coverage to the available TDRS system can be realised for data downlink to earth. The implemented TDRS system is still in use today for the communication with the ISS.

Fig. 4.4 TEMPUS console at NASA HOSC
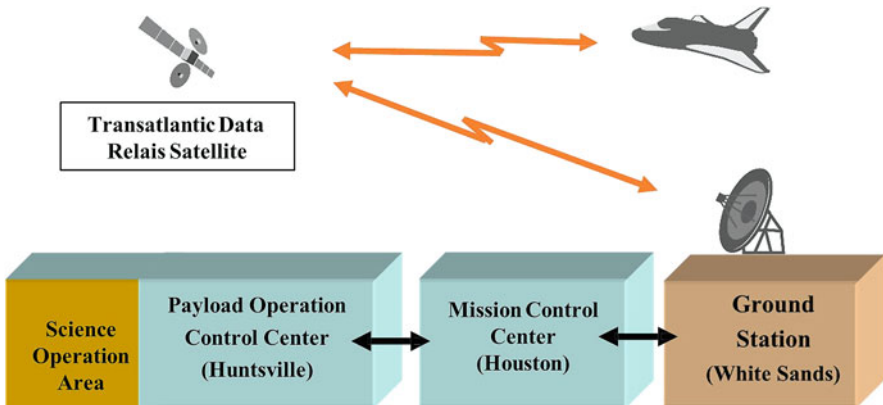
Fig. 4.5 Spacelab overall data path

Compared to the majority of other S/L payloads, TEMPUS had demanding resource requirements. Data downlink rate for TEMPUS housekeeping and science data was about 480 kB/sec. Video bandwidth for the two TEMPUS cameras (analogue PAL and NTSC signals) was scaled to 10 Mb/sec in total, which was the full Spacelab video capacity during running TEMPUS experiments. The power consumption of the TEMPUS payload reached about 2500 Watt at maximum, which was about 50% of the available power resources for the Spacelab at this time. TEMPUS experiments were always characterised by a highly interactive execution approach to optimise the experiment performance and to obtain the best results. Dedicated software tools for experiment commanding were developed for the benefit of the scientific investigators. Experiment sequence could be changed flexibly to consider results from the precursor science runs, and even single experiment control parameters (e.g. heating or positioning power of the levitation experiments, pulse

settings for oscillating drop investigations, camera settings, etc.) could be changed during experiment execution. The data run time between ground and space segment was reduced to a minimum of about 3 s including the command acknowledge signal received on ground. During the IML-2 mission, more than 36,000 commands were sent to operate the TEMPUS experiments, which was about 50% of the total number of the entire commands sent to Spacelab during the whole mission.

For the Spacelab mission MSL-1R, the operation concept was enhanced for the first time by a remote operation demonstration. Video, video conferencing and science data was provided via public Internet to DLR in Cologne, where a remote science and engineering team observed the experiments and supported the operator teams at the main Control Center in Huntsville. The videoconferencing was established by Windows 95 PCs and an integrated VISTACOM board, by which a transmission rate of about 384 Kb/sec could be made available. The stability and temporal overload situation of the public Internet at that time did not allow to rely yet on the Internet for mission critical operation. Nevertheless, the result was a pathfinder for later remote operation concepts, which were consequently investigated and followed over the years and which are state of the art in today's space experiment operation concepts superseding the monolithic operation concepts of the 1990s.

4 Electromagnetic Levitator on Board the ISS: Main Payload Subsystems for Experiment Operations

The core elements of the EML payload on board the ISS consist of the process chamber containing the coil system for sample positioning and heating, a vacuum-gas system allowing experiment processing under high-vacuum conditions or clean noble gases (He or Ar), a power supply unit and the Experiment Controller Module (ECM) housing the payload computer connected via EDR to the Columbus LAN system. A sample wheel with 18 samples is located in a sample chamber below the process chamber, from where the selected sample can be slowly moved with its holder into the centre of the coil system by commanding from ground. Figure 4.6 shows the EML ground model integrated in EDR at MUSC in Cologne. A detailed description on the payload subsystems is given in Chap. 3 of this book. The below emphasis is laid on to the components relevant for payload and experiment operations.

The coil system is connected to two independent RF generators operating at frequencies of around 330 kHz and at around 170 kHz to generate a heating dipole field and to build up a positioning quadrupole field. Generators can be operated automatically via scripts or manually from ground by adjusting the coil control voltages. In addition, the EML device contains the sample coupling electronics (SCE), which enables the measurement of the heating generator current, voltage, phase shift and frequency with high accuracy, enabling the determination of the sample's apparent impedance and hence its electrical conductivity. EML visual

Fig. 4.6 EML ground
model at MUSC
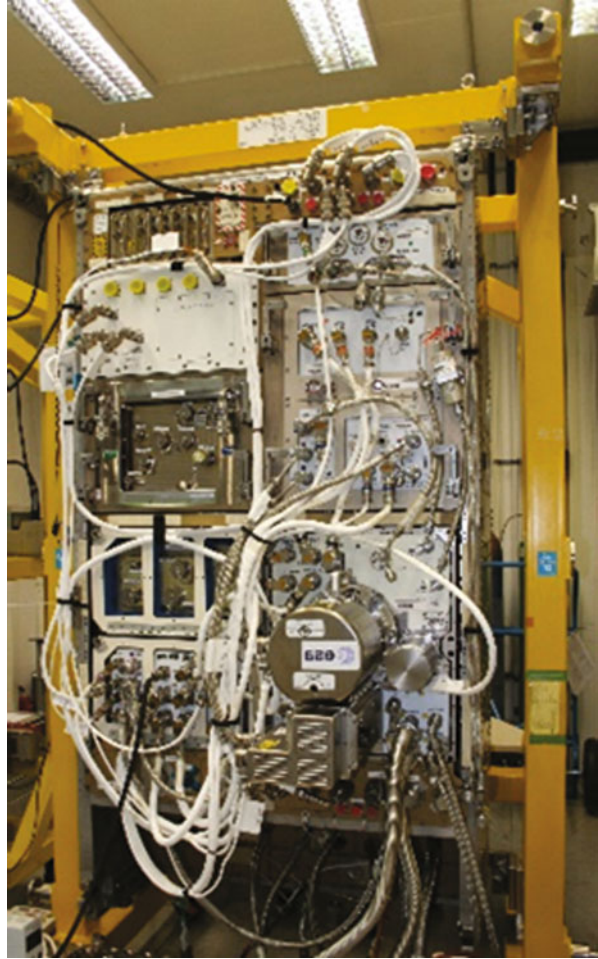
sample observation is performed by two camera systems. The process chamber is
equipped with a high-resolution, high-speed camera, incorporating an optical
pyrometer in the axial viewing direction and another high-speed camera looking
from a radial direction onto the sample. The radial camera offers a maximum frame
rate of 20 kHz, allowing to record the advancing of the solidification front. Typi-
cally, the cameras are operated at frame rates of 150 and 200–400 Hz for the
observation of surface oscillations of the liquid sample. Optical density measure-
ments are performed with lower frame rates (~40 Hz), allowing a higher contrast and
resolution.

The axial camera, a Loglux i5, has embodied a sensor with at least 1000×1000
pixel resolution (1 MegaPixel); for the 1000×1000 pixel resolution of the video
camera, the camera/optical system enables a relative resolution of 2×10^{-4} for
sample size measurements. The pixel rate is not less than 20 MegaPixels/second and

should also be able to operate with a frame rate of 200 Hz. The nominal field of view is 10×10 mm, with the possibility to both increase and decrease the field of view by electronic means (selectable by telecommand) up to at least 14×14 mm, in which case achievable frame rate is higher or lower than for the nominal field of view, respectively.

The radial camera, a Phantom V7.3 High-Speed camera, has two operational modes and delivers both analogue NTSC video and a high-speed digital video signal. Its own controller, the HSC-OS, is connected via Ethernet to the EDR hub. Supported video format of the high-speed camera is the CINE format. The HSC frame rate is selectable by telecommanding in steps between 200 Hz and 190.5 kHz. Depending on the frame rate, the picture resolution is between 800×600 and 32×32 pixels, with an image depth of 8 bit or 14 bit. The camera has a relative resolution of sample size measurements of equal or less than 2×10^{-4}. The video camera has embodied features to adjust the exposure of the sensor to the varying illumination levels due to the changing sample temperatures and illumination conditions, automatically or by commanding from the facility and experiment control electronics. The minimal field of view is 10×10 mm, but it is possible to both increase and decrease the field of view by electronic means (selectable by telecommand) up to at least 10×13 mm, in which case achievable frame rate is higher or lower than for the nominal field of view, respectively. The HSC has two optical operation modes (recalescence and oscillation mode). The mode can be selected by pushing a lever in the according direction (crew task), which internally moves the optical lens system. The respective positions in combination with the selected chip resolution allow to determine the optical field of view. HSC-OS provides a hard disk drive (HDD) for storage of video clips. Further, it provides wavelet compression of videos by software to reduce the amount of data for downlink. Compression and later downlink of compressed video are done offline in experiment pauses by the third EML HSSL (SpaceWire) interface to EDR VMU. The camera allows the user to playback files held in the camera's ring memory via the NTSC interface allowing the user to have a quick look on the scientific recording before the ring memory content is transferred to the HSC-OS for further processing and downlink. For real-time video, the HSC has an analogue output that directly connects to the EDR VMU for downlink.

Beside the video data, the payload housekeeping and science data is transmitted to ground via the ISS Ku-Band. Payload data is typically transmitted at a rate of 1 Hz, and specific payload HK and science data are measured at higher rates. These are heater and positioner voltage, supply current and frequency, sample coupling electronics channels, gas atmosphere absolute pressure, sample holder position (all at 10 Hz) and pyrometer temperature of the sample (100 Hz). The housekeeping and science data contain all payload subsystem information and, as the main source for experiment monitoring and later science evaluation, the contactless measured sample temperature data from the pyrometer.

The pyrometer is available for temperature measurement in axial direction. The pyrometer together with its optics has a measurement spot of 0.8 mm diameter on the sample surface, and the spot is aligned within a radius of 0.3 mm from the centre of

the nominal sample position. The wavelength of pyrometer is a narrowband from 1.45 to 1.8 μm. The temperature reading is in the range 600–2100 °C with a resolution better than 0.1 K for emissivity factors of 0.05–1.00. For temperatures below 600 °C down to the minimum temperature of 300 °C, the resolution depends on the selected emissivity factor. The frequency resolution is better than 0.01 Hz and 100 Hz data rate. The accuracy of the pyrometer is within ±5 K with respect to calibrated black body radiators over the complete measurement range.

5 ISS Mission Operation and EML Operations Implementation Concept

In the planning for European ISS exploitation, ESA decided to adopt a decentralised infrastructure for the operation of European payloads on board the ISS. Under the overall management of ESA, the network of European User Support and Operation Centres performs the majority of tasks related to the preparation and operations of experiments in multi-user facilities. USOCs like the MUSC in Germany are based on already existing national user centres. The USOCs are connected via an Interconnecting Ground Segment (IGS) to the Columbus Control Center at Oberpfaffenhofen in Germany, which became responsible for the Columbus system operation as well as the payload operation coordination. The Col-CC directly interfaces to the ISS lead control centre in Houston, since the Columbus resources are fully provided by the American segment of the station.

In this set-up experiment, preparation and verification, payload planning, payload operation and experiment execution are the responsibility of the USOCs. The centres are equipped with advanced generic operation infrastructures, including an electronic information exchange system for operation planning and changes, voice loops to communicate between the centres and with the crew on board as well as a telemetry (TM) system including video transmission and a telecommand (TC) system to monitor and control the payloads and execute the experiments. The interfaces between the USOCs and the Col-CC are realised by an Interconnecting Ground Segment (IGS), which is using MPLS (Multiprotocol Label Switching) as routing technique between them (Fig. 4.7).

Payload and experiment data are streamed to the remote control centres. While the data is routed by the IP protocol, the video signals are transmitted by dedicated lines and interfaces. Figure 4.8 shows the implementation for the EML data and video links from the payload on board to the MUSC. EML provides four video data streams from the two camera systems for sample observation and science evaluation. The live video signals from both cameras are downlinked to ground in compressed size near real time for experiment monitoring in a bandwidth of at least 12 Mb/s, which is comparable to the downlink rates in Spacelab. The science video signals are stored on board in the storage medium of both cameras (HDD and DVS) and transferred intermediately after the science session. This video data is downlinked
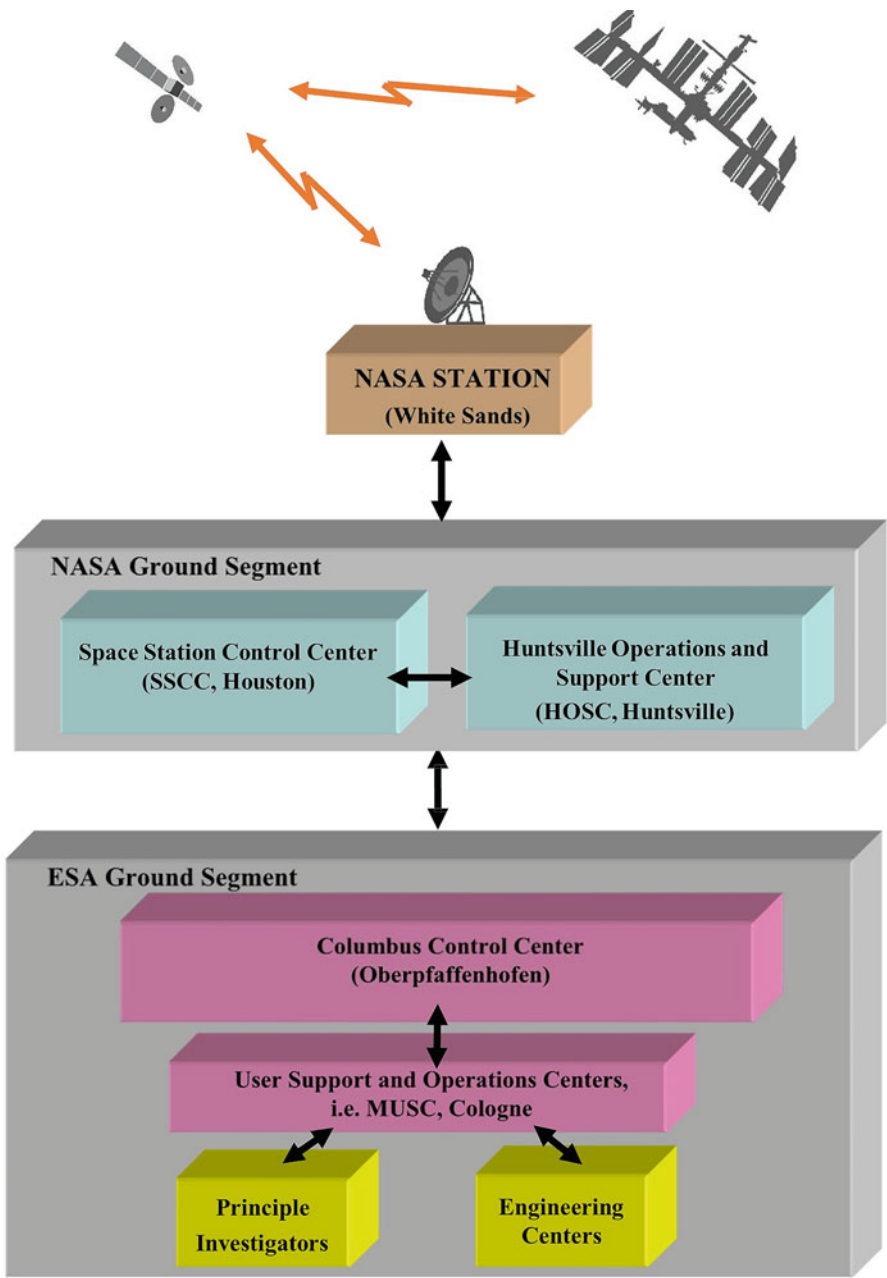
Fig. 4.7 ISS overall data path
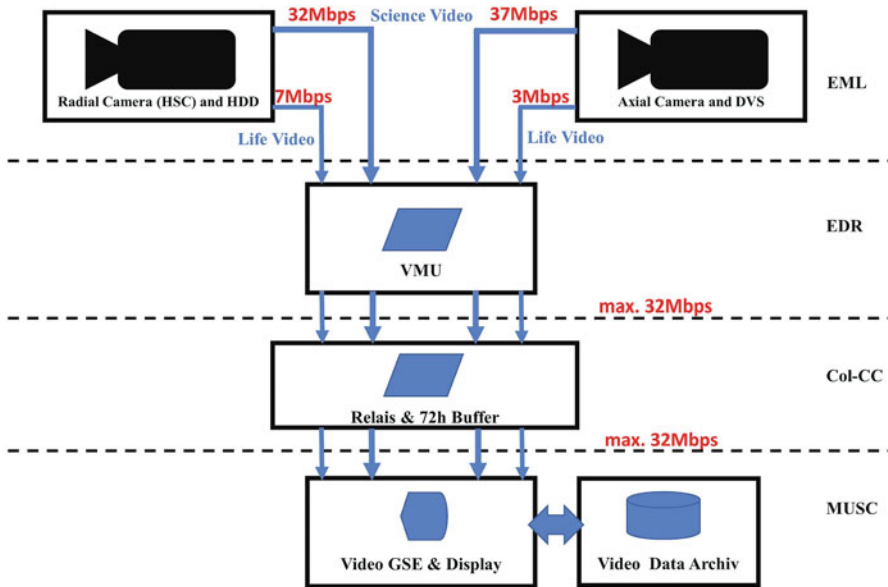
Fig. 4.8 Sketch of EML video data flow

at higher rates of 24–32 Mb/s through a high-rate data channel of the ISS. All video data is received by a Video Ground Support Equipment (VGSE) at MUSC, where the data is processed to readable mpeg or cine formats.

Special emphasis was laid on the signal turnaround times from ground to the EML payload on-board Space Station. The execution of on-orbit EML experiments requires near-real-time reactions from the ground operators based on information contained in the two video signals obtained from the EML cameras and science data in the medium rate telemetry of the payload. Therefore, a maximum delay time of 3 s is required.

Extensive signal run time tests were performed in 2013 to prove the feasibility of the intended experiment monitoring and control concept. These tests determined the time delay between the generation of a high-rate downlink packet by the EDR FM video management unit, the high-rate downlink (HRDL) interface and the reception on ground at the MUSC high-rate data front-end. The video signal delay in the transmission to ground is the sum of all delays in the data link, displayed in Fig. 4.6, from generation of video by the EML cameras to the display on the EML ground segment video equipment.

As outcome of these tests, it could be concluded that 92.5% of the data packets arrived with less than 2 s of transmission time. In average, the signal run times observed during EML utilisation in orbit, with changing on-board and ground configurations, always stayed within the demonstrated 3 s range.

6   Ground Infrastructure at the Microgravity User Support Center (MUSC) for EML Experiment Preparation and Operation

The MUSC user support concept has always been marked by a strong collaboration with the research laboratories and the payload engineering teams, from the initiation of feasibility tests for new experiments, through common development of novel diagnostics, and finally experiment preparation and operation. The support activities at MUSC were started for the TEMPUS missions first on the national level and later on moved to the European USOC concept for the EML utilisation. The remote operation concept by decentralised centres could develop very fast, driven by the technical evolution of the space ground segments with the availability of wide area networks and the growing World Wide Web technologies.

A key element in experiment preparation of human spaceflight experiments is the availability of a representative payload ground model, which is a functional fully identical to the flight model. This model serves the experiment development and verification. During experiment execution, it can be used for failure and anomaly investigations. A first TEMPUS laboratory model, consisting of the core parts of the facility, was provided in 1987 to MUSC. It was used for experiment feasibility tests, experiment verification programs on ground and parabolic flight experiments under short-time microgravity conditions. This model was used first in 1988 for test experiments on parabolic flight and later on in enhanced versions, regularly for ISS experiment preparation in European parabolic flight campaign on an Airbus 300 aircraft operated by Novespace in France. The same ground model concept was applied later for experiment preparation and verification of the TEMPUS S/L flights.

For ISS utilisation, a dedicated EML payload ground model and further operation tools were built. EML on board the Columbus module in the European segment of the Space Station is integrated in the European Drawer Rack. This rack provides the resources (power, cooling water, airflow) to operate EML and also the interfaces to monitor and command the facility and experiments. Figure 4.6 shows the EML ground model integrated in EDR at the MUSC, which is used for experiment verification, interface testing of new payload subsystems and failure investigation in case of anomalies occurred with the flight model.

Specific tools for the operation of EML on ISS were developed based on the experiences gathered during the Spacelab flights of the electromagnetic levitator TEMPUS. Since levitation experiments can be performed under vacuum condition, sample material evaporation was identified as a critical resource for EML. Evaporation is leading to cross-contamination between the processed samples, and in addition, sample material condenses on the levitation coil and peels off when a critical layer thickness is reached and can induce short circuits. Therefore a software program was developed, which autonomously calculates the evaporated material mass and the resulting thickness layer from the sample temperature-time profiles measured during the flight experiments. It compares the results with the precalculated and forecasted values from the experiment preparation program and

serves the operators to assess the compliance with the defined experiment resources in near real time. The critical thickness layer on the coils was found in the Spacelab flights at about 20 µm. This thickness is defined as the maximum layer on the coil and the limit for coil contamination throughout the lifetime of the EML payload on board the ISS.

A particularity and challenge of electromagnetic levitation experiment preparation is the lacking possibility to run representative experiments on ground with the EML facilities built for space utilisation. The generated electromagnetic forces are not suited to levitate the samples against the gravity field and therefore to verify the space experiments in an adequate environment; only solid samples can be tested, suspended in a sample holder, with minimum thermal contact to minimise external heat flow. The final sample behaviour has to be calculated by computer simulations considering the assumed properties of the liquid state. A so-called science reference simulator was developed for the prediction of the necessary electromagnetic power to levitate and heat the metallic samples and to reach the required temperature-time profile of the experiment. The simulator was developed by MUSC and made available to all investigators for experiment development. The necessary materials parameters of the solid and liquid samples are either measured in dedicated facilities (e.g. evaporation rates, emissivity) or assumed theoretically on the best available physical models (e.g. specific heat values in the liquid state). The levitation behaviour of all selected flight samples is finally verified during parabolic flight experiments in a functional identical flight equipment.

7 EML Space Experiments Preparation Flow

Operations preparation of space experiments is structured in several phases [8]. Based on the experiment requirement documents, which describe the experimental goals and their overall demands for execution, an operational assessment is performed confirming the experiment operation feasibility under the conditions of the flight carrier.

As a next EML-specific step, the detailed experiment protocols are defined by the determination of the control parameters of the EML payload; this is kept in a so-called EML science protocol. It includes all settings of the EML facility during flight including camera settings, the required temperature-time profile, parameters of the contactless pyrometer for temperature measurements and recalescence detection and recording, definition of short heating pulses for oscillating drop stimulations and, most prominent, establishment of heating modulations values for the determination of specific heat data of the samples and related thermophysical properties. Also, the process conditions of high-vacuum or noble gas environment are defined.

EML experiments consist of multiple melting events and subsequent measurement phases during cooling. Every EML sample will in average be subject to 50 thermal cycles. Each thermal cycle consists of 20 processing steps in average. Each processing step is defined by 39 parameters. EML limit parameters (LPs)
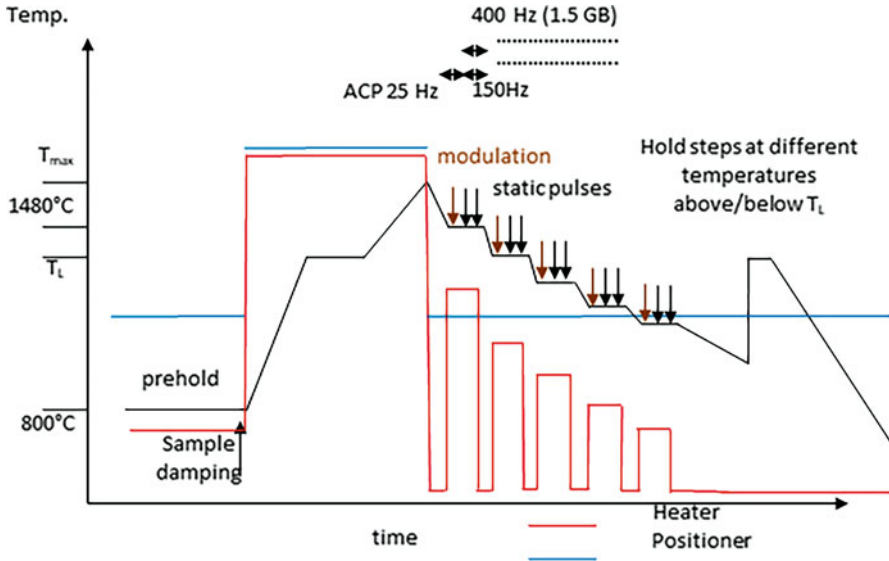
Fig. 4.9 Example of planned temperature-time profile (black) including the heating (red) and positioning control voltages (blue) as part of the science protocol showing specific heat measurements with the modulation calorimetry at five constant temperatures

provide an envelope for heater and positioner profiles during an EML experiment. An internal safety feature on board prevents heater and positioner voltages outside these limits. EML video files are needed to control the settings of both the ACP and HSC. They are developed for every thermal cycle.

Figure 4.9 depicts a representative example of one typical thermal cycle. Positioner control voltage is shown in blue, heater control voltage in red and the black line is the sample temperature. Measurement steps are indicated on different temperature levels during cooling.

In parallel to the science protocol definition, the relevant sample material properties are measured in ground-based facilities. This includes the temperature-dependent materials emissivities in the wavelength range of the pyrometer system, coupling coefficients between samples and the electromagnetic field as a function of temperature and the evaporation rates of the materials in the solid and, most importantly, in the liquid state. Thermophysical data like heat of fusion and heat capacities are taken from literature or physical models. All values are used in the EML science reference simulator to derive the necessary EPs and LPs including heating and positioning control parameter, modulation values and limit parameters for the experiment run under microgravity conditions in EML.

The verification of the defined experiment control parameters is performed in the EML ground model, which is fully functional representative to the flight model in orbit. The successful verification tests are the precondition for uploading the final parameter sets and video files to the EML flight model via file transfer for storage

and implementation in the EML payload. All experiment parameters are changeable via reprogramming from ground during on-orbit operations.

Planning requests for the EML resources in the Columbus module including crew time, power consumption, required video and data bandwidth and ventline demands for payload vacuum conditioning are gathered in advance to every 6-month increment on the Space Station. Increment resource allocations are agreed upon by the International Space Station partners, and respective monthly and weekly look-ahead plans are produced giving the operation timeline of each payload.

EML experiments are grouped into batches. One batch includes all experiments related to the maximum 18 samples integrated in the sample chamber of the payload. The sample chamber is changeable on board by the crew. Typically, the experiments of one batch are performed in the timeframe of about 2 years, before a new chamber is uploaded to the station via one of the ISS supply vehicles. Each sample can be processed many times, until the resources defined for the experiment are reached. One batch of experiments consists of about a thousand of melt cycles. For the first two experiment batches performed in EML until 2019, about 2000 individual melt cycles could be completed. EML batch 3 and 4 experiments are planned for the timeframe of 2020 until late 2023 with another 2000 cycles in preparation.

8   EML Experiment Operations on Board the ISS

EML is operated in a campaign mode. The roughly 1000 individual cycles of one batch are separated into smaller units, called sub-batches. Such a sub-batch consists of typically 12 weeks of on-orbit operation with a 24 h scheme during 5 days.

One week before the execution of any on-orbit activities, the timeline for the upcoming week is prepared by the international partners and consolidated by several planning reviews. This ensures the correct assignment of the required resources for each activity. EML experiments are especially demanding, as they, for example, have a high power consumption and heat rejection and require high-rate data downlink for the video images, an exclusive command window and connection to the Columbus vacuum line, all of which has to be coordinated with the other users in Columbus to deconflict potential overbooking of resources.

The experiments are always performed at night during crew sleep intervals to provide the least-disturbed microgravity environment on board the ISS. They are performed from the MUSC control room at DLR in Cologne by certified operators at the EML and EDR console. A ground controller position is completing the team for establishment the console settings, to monitor the interfaces to the external sits and to support the data and video link transmissions to the respective interfaces and archives. During the night shifts, when the experiments are performed in a highly interactive manner, the EML console is additionally staffed with a science support position. It has been the best practice that the responsible scientist as the decision-taking person for experiment commanding is also present. Figure 4.10 shows the EML console during experiment performance of the investigator group of

Fig. 4.10 EML science operations at MUSC with Prof. D. Matson
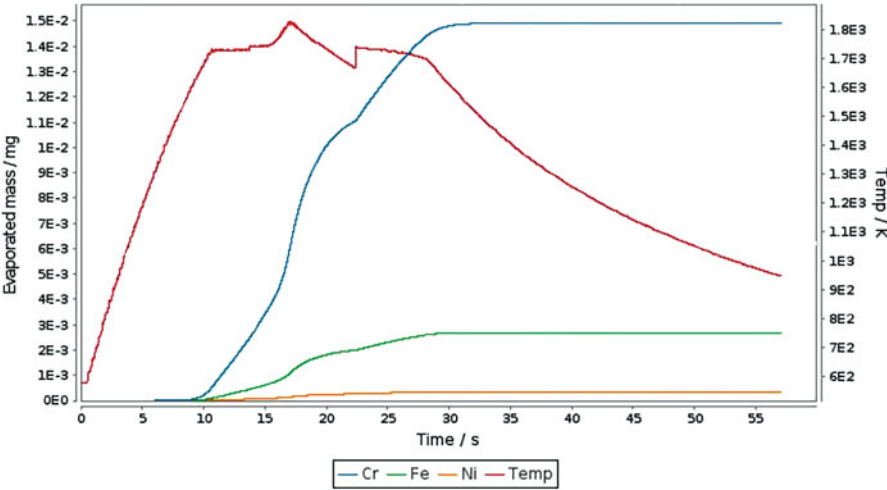
Fig. 4.11 Typical temperature-time profile of FeCrNi sample (Prof. D. Matson), showing also calculated evaporated mass per element

Prof. D. Matson. The investigator follows the experiment on console, has access to both the incoming facility data and the process video streams from the on-board cameras and can use the experiment simulator for fine-tuning the next experiment cycles. Figure 4.11 shows a typical experiment profile obtained on a FeCrNi sample. Temperature readings are shown in red, and evaporated sample material per component are shown in blue, green and orange colour.

With the restrictions imposed by the pandemic situation since spring 2020, it was agreed to focus the involvement of the investigator on a remote connection via video streaming of crucial experiment information and conferencing during EML operations. With this new concept tailored to the requirements of the scientific community, a continuation of the EML on-orbit operations has been assured.

Similar to levitation experiments on earth, the real-time execution of the individual thermal experiment cycles is not following a strictly deterministic line of events. For example, the level of undercooling achieved by a given sample in a given experiment cycle cannot be precisely predicted and will thus vary from one experiment cycle to the next. Interactive commanding to fine-tune heater and positioner control voltages and times to optimise the science output is thus one major key to successful science output.

Compared to other payloads, EML experiments are operated on very short time scales. The sample heating from ambient temperature via melt plateau to maximum temperature is usually in the order of seconds. Cooling the sample down and performing the scientific measurements are in the order of maximum several minutes until solidification occurs. While the sample is heated and the experiment is under way, the operators monitor the sample processing, judging the temperature profile, sample surface, sample stability and elongation while liquid. In case of unexpected events (e.g. sample picks up rotations or strong translational movements), a live reaction is needed, i.e. with a time scale for decisions also in the order of seconds. The operational scenario for EML has been customised to deal with these specific boundaries. Active sample processing is only started with a full set of telemetry, video and telecommand capability available, during AOS (acquisition of signal). EML itself monitors the so-called AOS/LOS flag and transfers the experiment into a hold step with only positioning power applied, if LOS (loss of signal) is detected.

The data stream including EML housekeeping and science telemetry on ground is monitored on a dedicated software tool with various customised graphic displays depicting, e.g. the experiment temperature/power-time profile or major EML subsystems. The EML live video data used for process control is monitored in the control room as PAL and NTSC signals and is stored in the local archive. Detailed description is given in the previous chapter on the signal run time tests. The science video data gathered during the crucial phase of the experiment are intermediately stored on board and are later downlinked via the high-rate data channel.

Commanding of the experiment for science optimisation is performed by the telecommand part of CD-MCS. Commands are sent either from editable tables or from graphical displays, which is the standard during science. It is not uncommon that 50 commands are sent before and during one individual experiment cycle, resulting in 500 commands during one single EML operation night. For highly demanding novel modulation experiments, a maximum of about 1900 commands per night was recently reached. Science video data downlink is performed during daytime, which is followed by the data conversion into readable formats and storage in the local archive.
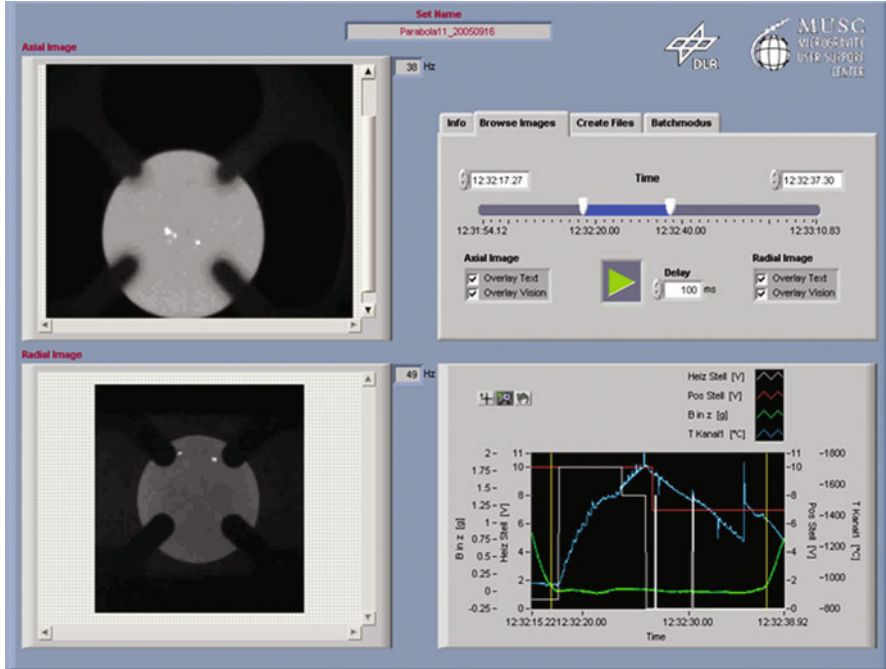
Fig. 4.12 Example of synchronised EML and video data in TeVi Tool

Distribution of all available scientific data to the investigators is ensured via the data and information archive system 'Hypertest' at MUSC [9]. Typically, 24 h after the experiment performance in orbit, all the necessary processed data are available on ground for evaluation. For that purpose, the data of the science runs are assembled individually per cycle and comprise:

– A comprehensive overview plot of the temperature/voltage/time profile
– Selected (PI discretion) housekeeping data in .csv
– Science video data of the crucial experiment phases in cine format and readable format (several days after the run, due to the required post-processing)

Since the science video files have to be demultiplexed and post-processed to be transformed into a standard readable format, they are made available for the scientific community within a few days. All other data are provided nearly in real time.

It is crucial to synchronise the available data streams for scientific evaluation. For that purpose, a special software tool 'TeVi' developed by MUSC is available to all investigators for the synchronous display of video and experiment science data [10]. Figure 4.12 shows the graphical user interface displaying radial and axial camera signals together with the recorded temperature-time profile of the experiment.

9 Summary and Outlook

Electromagnetic levitation under microgravity conditions is well established for solidification experiments and thermophysical properties measurements of metals and alloys since the first Spacelab flight of the TEMPUS facility in 1994. The ISS payload EML is integrated in the European Columbus module as a second-generation payload since the flight of ESA astronaut Alexander Gerst in 2014. The operation concept of EML is highly decentralised giving the possibility for investigators at their universities or laboratories to follow and control their experiments from remote sites. Experiment objectives have been expanded by sophisticated diagnostics, facility subsystems and on-ground control capabilities to new frontiers including investigations on advanced materials relevant for actual industrial processes and usage. Until 2020 the first two batches of experiments including 36 materials samples could be successfully processed. About 1500 experiment melting and solidification cycles were executed, and an even higher number of runs are envisioned for the next two experiment batches. One hundred twenty-three thousand commands have been sent to the ISS for EML experiment control to optimise and adapt the experiment execution to the needs of the scientists. EML was operational in orbit for about 6000 h.

Further enhancements of the payload are planned for the timeframe of 2023, in particular to study the impact of small proportions of gases like oxygen on the sensitive materials properties and to satisfy the evolving requirements from the user community.

Data from the space experiments will be stored and made publicly available in the near future. From one experiment batch about 5 terabytes of data is produced by the payload and stored on ground for scientific evaluation. ESA decided on a central ISS data archive to be realized at the Science Data Archive Center in Madrid. In close collaboration with MUSC, this archive will be established over the next years and will be open for all interested parties in the ESA member states.

References

1. R. Willnecker, D.M. Herlach, B. Feuerbacher, Containerless undercooling of bulk Fe-Ni melts. Appl. Phys. Lett. **49**(20), 1339–1341 (1986)
2. R. Willnecker, D.M. Herlach, B. Feuerbacher, Evidence of non-equilibrium processes in rapid solidification of undercooled melts. Phys. Rev. Lett. **62**, 2707–2710 (1989)
3. E. Schleip, R. Willnecker, D.M. Herlach, G.P. Görler, Measurements of ultra-rapid solidification rates in greatly undercooled bulk metals by a high speed photosensing device. Mater. Sci. Eng. A **98**, 39–42 (1988)
4. R. Wunderlich, H.J. Fecht, R. Willnecker, Power modulation technique for noncontact high-temperature calorimetry. Appl. Phys. Lett. **62**(24), 3111–3113 (1993)
5. I. Egry, Surface tension measurements of liquid metals by the oscillating drop technique. J. Mater. Sci. **26**, 2997–3003 (1991)

6. Team TEMPUS, Containerless processing in space, recent results, in *Lecture Note in Physics*, (Springer, Berlin, 1996), pp. 233–252
7. A. Diefenbach, M. Kratz, D. Uffelmann, R. Willnecker, Advanced user support programme – TEMPUS IML-2. Acta Astr. **35**(9), 719–724 (1995)
8. A. Diefenbach, S. Schneider, T. Volkmann, Experiment preparation and performance for the electromagnetic levitator (EML) onboard the International Space Station, in *Preparation of Space Experiments*, ed. by V. Pletser, (IntechOpen, 2020). https://doi.org/10.5772/intechopen.92406
9. S. Schwartze, R. Willnecker, *SpaceOps Conference* (AIAA, 2006), p. 2006-5886. https://doi.org/10.2514/6.2006-5886
10. R. Willnecker, S. Schneider, F. Münstermann, M. Pütz, W. Koerver, Digital video system for TEMPUS on parabolic flights. Space Technol. **26**, 73–79 (2006)

Chapter 5
Electrostatic Levitation on the ISS

Takehiko Ishikawa and Paul-François Paradis

1 Introduction

Microgravity environment obtained in space offers unique experimental conditions for materials sciences. Especially, liquid samples can be easily levitated and processed without crucibles in microgravity. However, excellent sample positioning is necessary for materials research to precisely heat samples and to measure accurately their temperatures as well as their thermophysical properties. For these reasons, space agencies have developed levitators and used them in long-duration microgravity platforms. For example, the National Aeronautics and Space Administration (NASA) developed acoustic levitators, and experiments on drop dynamics were conducted at room temperature during several space shuttle flights [1, 2]. The European Space Agency (ESA) flew electromagnetic levitators (EMLs) in two space shuttle missions, in which several alloy samples were levitated and melted at high temperatures [3, 4]. An upgraded version of the electromagnetic levitator was developed by ESA and is currently used in the International Space Station (ISS) [5, 6].

Due to its greater technical challenges, the development of electrostatic levitators was far behind those of acoustic and electromagnetic levitators. The development of an electrostatic levitation facility for the ISS started in 1993 at the Japan Aerospace Exploration Agency (JAXA), and the facility has been operational since 2016.

T. Ishikawa (✉)
Japan Aerospace Exploration Agency, Tsukuba, Ibaraki, Japan
e-mail: ishikawa.takehiko@jaxa.jp

P.-F. Paradis
I.N.O., Quebec-City, QC, Canada
e-mail: Paul-Francois.Paradis@ino.ca

This document briefly explains the electrostatic levitation method, the history of microgravity experiments, the development of the Japanese electrostatic levitation furnace in the International Space Station (ISS-ELF), and its current status.

2 Development History of Electrostatic Levitation

The history of the development of the electrostatic levitation method was described in detail in a review article published earlier [7]. This section will therefore focus on the development related to the microgravity experiments.

An electrostatic levitator was first designed in the 1970s in Germany through funding from the ESA [8]. Then, the first microgravity experiment on electrostatic levitation was conducted in 1988 using a sounding rocket (TEXUS 19) [9]. Even though the experiment failed due to a mis-alignment of one CCD camera (that acted as a position sensor), it nonetheless demonstrated that all components necessary for position control, heating, and temperature measurement could be packed in a small space and could operate with limited resources. Since the electromagnetic levitation method showed promise for materials science studies in microgravity, no further development was pursued in Europe.

Systematic, extensive, and fundamental research and development on ground-based facilities was carried out at the NASA Jet Propulsion Laboratory (JPL) in the 1980s and 1990s [10–12]. A high-temperature electrostatic levitation system was developed [13], and several materials including refractory metals and semiconductors were successfully levitated and melted in a high-vacuum environment.

Figure 5.1 depicts a schematic diagram of the electrostatic levitator used in JPL [13]. In this system, a charged sample can be levitated between the two disk electrodes (top and bottom electrodes), which are parallel and separated by about 10 mm. The sample position can be detected by projecting the sample's shadow onto a position sensor using a He-Ne laser. The position information is sent to a computer where the control signals are processed using a PID feedback control algorithm. The signals are then amplified and sent to the top electrode. In addition, four small electrodes distributed around the sample expected levitation location are used to

Fig. 5.1 Schematic diagram of the electrode configuration and active position control system used in the JPL high-temperature electrostatic levitator
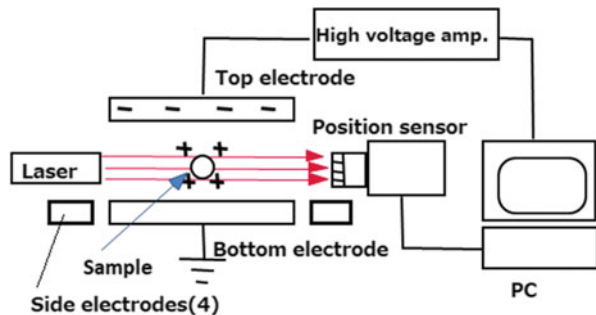
stabilize the sample position along the horizontal. Optical devices such as pyrometers, heating lamps or lasers, and observation cameras are aligned in the horizontal plane between the top and bottom electrodes.

In addition, fundamental techniques to measure thermophysical properties such as density [14], isobaric heat capacity [15], surface tension [16], viscosity [16], and electrical resistivity [17] with the levitation system were developed in JPL. Almost all electrostatic levitators currently working in the USA [18–20], Germany [21, 22], Japan [23], Korea [24], and China [25, 26] inherited from the JPL pioneering work. However, although JPL electrostatically levitated isothermal samples at room temperature during parabolic flights, no long-term microgravity facility was designed by JPL.

3 Development of the ISS-ELF in Japan

3.1 Phase 1

The Japanese space agency has started the development of an electrostatic levitation furnace for the ISS in 1993. A conceptual drawing of the levitation furnace is depicted in Fig. 5.2 [27]. It basically employed the JPL's parallel electrode configuration. However, both top and bottom electrodes were divided into four pieces. These eight electrodes were used for both vertical and horizontal position control. All optical devices (position sensors, heating lasers, pyrometers, cameras) were placed in a horizontal plane. Two position detectors were located orthogonally to each other to detect the sample position along the three dimensions. A levitated sample was heated by four heating lasers.
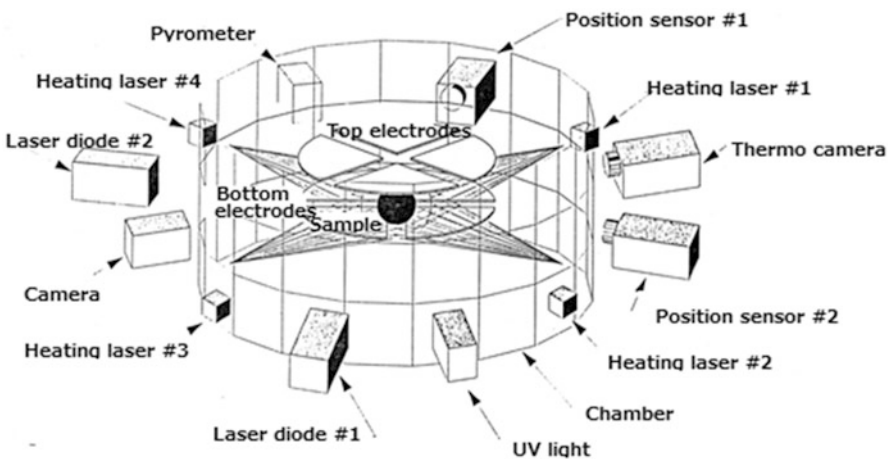
Fig. 5.2 Schematic representation of Japanese electrostatic levitation furnace designed around 1996

Fig. 5.3 Picture of an electrostatic levitation furnace flown in the sounding rocket TR-IA#7. Hardware design was similar to the one in Fig. 5.2, but the number of heating lasers was reduced to 2 due to size and power limitation
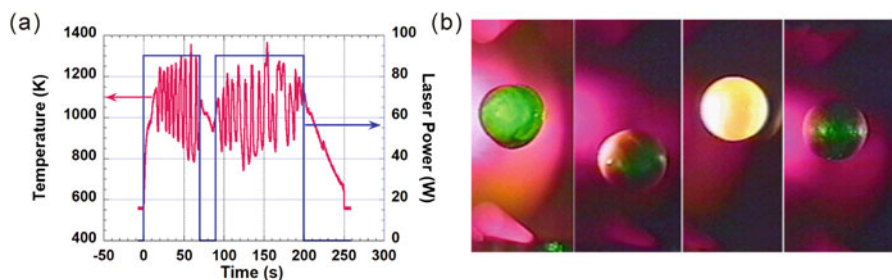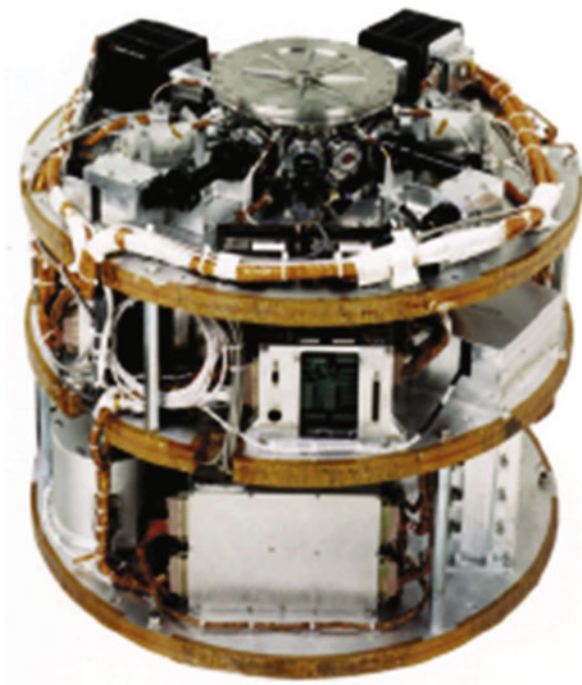
Fig. 5.4 (**a**) Temperature of the levitated sample in the sounding rocket experiment and (**b**) images of the sample during experiment. Sample position was not stable at elevated temperature

In order to evaluate the hardware and software, the first microgravity experiment of this electrostatic levitator was conducted using a sounding rocket (TR-IA) in 1997. Figure 5.3 illustrates the actual hardware [28]. During the free-fall part of the sounding rocket flight where microgravity condition was obtained, a spherical $BiFeO_3$ sample with a diameter of 5 mm was heated, melted, and solidified in a pressurized gaseous atmosphere.
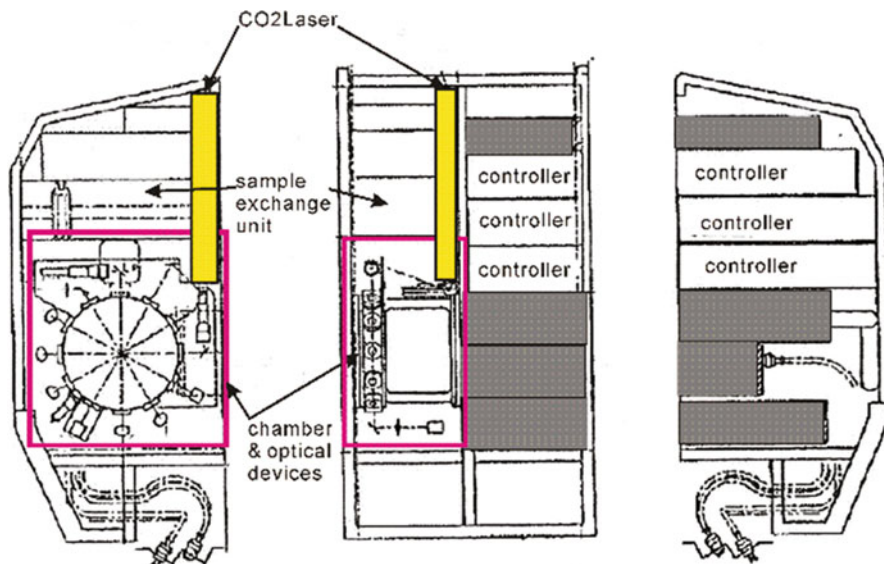
Fig. 5.5 Proposed layout of the ISS-ELF in the ISPR around 2000. A CO_2 laser (colored yellow) could not be fit inside of the ISPR, due to the bulky chamber (indicated red line)

Figure 5.4 shows the measured temperature as a function of time as well as snapshots of the levitated sample during the experiment [29]. The sample was levitated, then heated, and cooled twice. When the sample temperature increased, the amount of surface charge became much lower than the estimated value, and the control system could not cope with the sample stability. As a result, the sample could not be maintained in a fixed position, and the measured temperature fluctuated. Even though the sample was successfully levitated and melted in reduced gravity for the first time, it was recognized that stable levitation at elevated temperature was a huge technical issue that has to be solved.

The design of the ISS-ELF faced technical and financial problems around 2000. The layout of the ISS-ELF proposed at that time is shown in Fig. 5.5 [30]. However, the heating CO_2 laser was too large, and the chamber was very bulky. This prevented the levitator to be installed in an ISPR (International Standard Payload Rack), as all facilities in the ISS should. The chamber diameter was determined by the number of optical windows, while it was limited by the size of the rack. No additional optical devices could be allowed from the setup shown in Fig. 5.2 due to this constraint. In addition, the estimated cost was far beyond the budget, and the proposal could not be authorized.

3.2   Phase 2

In order to solve these problems, the development of a flight hardware was restarted
from the beginning. To specifically solve the technical problems found in the
sounding rocket experiment, a ground-based electrostatic levitator has been fabri-
cated based on the JPL's design, over which several key modifications were made to
accomplish stable sample levitation at extremely high temperatures. As a result,
refractory metals whose melting temperatures are above 2000 K were stably levi-
tated and melted, and their thermophysical properties such as density, surface
tension, and viscosity were obtained [31]. Figure 5.6 depicts the viscosity of molten
tungsten, tantalum, and rhenium as a function of temperature.

   Another ground-based facility was designed to be combined with a synchrotron
radiation source for the measurements of the atomic structures of molten metals at
high temperature. Due to the stringent space limitations imposed by the SPring-
8 beamlines, the chamber and optical system of this facility had to be downsized to
fit the experimental facility [32]. The development of this compact levitator was very
influential to the design of the future ISS-ELF.

3.3   Key Elements for the Space Facility

Based on the ground-based development, the ISS-ELF was completely re-designed.
Several key elements especially needed for operation in microgravity are described
below.

Fig. 5.6 Viscosities of refractory metals whose melting temperatures are above 3000 °C measured in a ground-based electrostatic levitator in JAXA
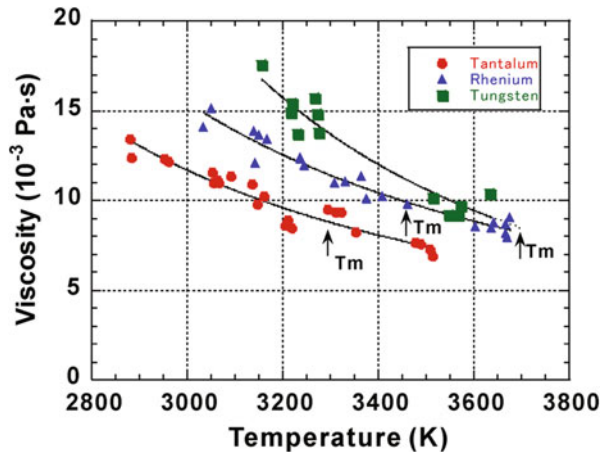
3.3.1   Electrodes/Chamber

In order to downsize the chamber, the configuration of electrodes and optical windows were fully re-designed [33]. Figure 5.7 shows the conceptual layout of the electrodes and optical windows. Three pairs of electrodes orthogonally located to each other control the sample position in three dimensions. Since there is no preferential gravity direction in the ISS, the diameters of all electrodes are identical and placed at nearly identical distances from the sample. The observation windows are also three-dimensionally distributed.

3.3.2   Heating Lasers

A compact heating laser with a high efficiency was one of the most critical components for the ISS-ELF because space and power are very limited. As far as the wavelength is concerned, CO_2 lasers emitting at a wavelength of 10.6 μm are the most efficient for oxide materials. However, commercially available CO_2 lasers were too big to be installed in the ISS-ELF. Moreover, since no suitable optical fibers were available for this wavelength, free-beam propagation had to be used. However, to introduce high-power laser beams to the chamber was very hard on an optical design standpoint, and it was almost impossible to design a system that withstands the ISS unique requirements such as large vibration spectrum during ascent and crew safety

Fig. 5.7 Configuration of electrodes and layout of optical windows in the ISS-ELF
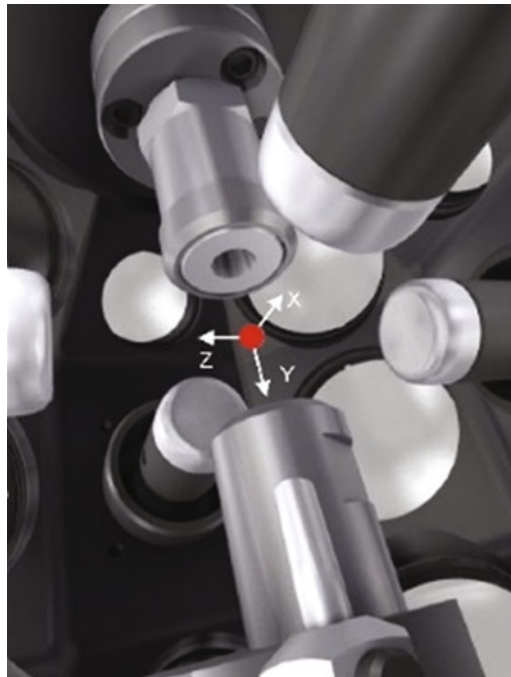
considerations. A compact semiconductor laser (n-LIGHT Pearl™ series) was nonetheless found that could meet the size and power requirements [33]. The only issue was with its emitting wavelength (980 nm). Generally, oxide materials will not absorb this wavelength well. Therefore, compatibility between samples and the heating laser had to be checked during the ground-based preparation.

3.3.3 Sample Insertion/Retrieval System

Sample handling from/to sample cartridge and the electrodes in microgravity is one of the key techniques that had to be developed. Figure 5.8 describes the sample handling operations in a ground-based facility. Before levitation, a sample remains stable on the bottom electrode due to gravity. After the levitation experiment, the processed sample can be retrieved to the sample holder beneath the bottom electrode using gravity. These operations cannot be used in microgravity.

Figure 5.9 shows the sample holding device used in the sounding rocket experiment. Two fingers made of spring plates held a sample [30]. A pushing rod (colored
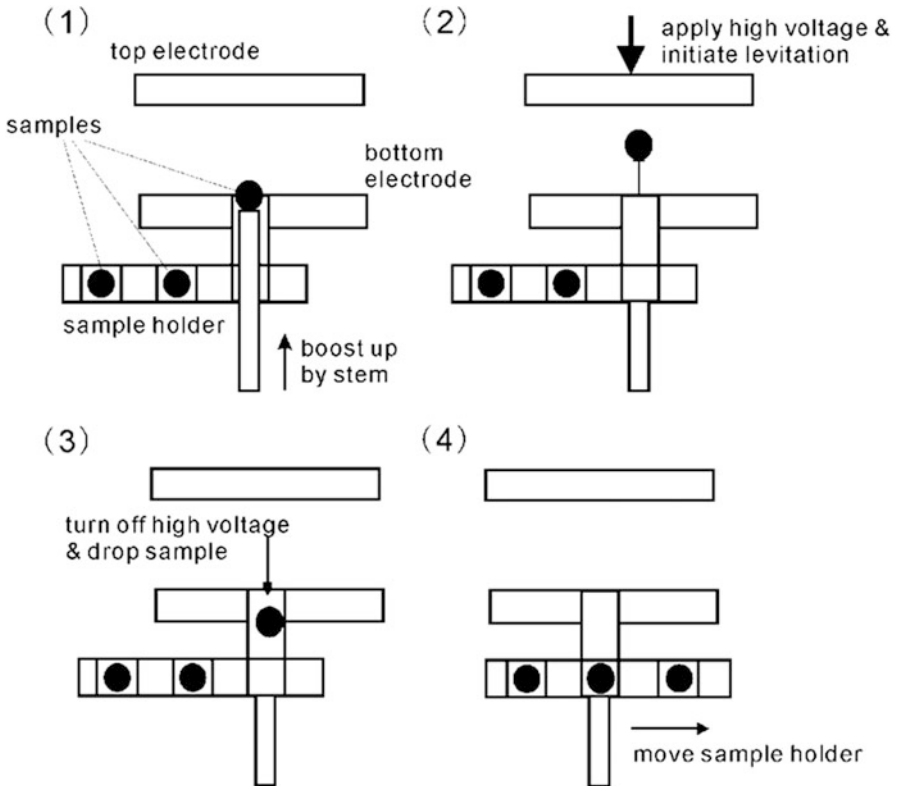
Fig. 5.8 Sample handling in the ground-based electrostatic levitators
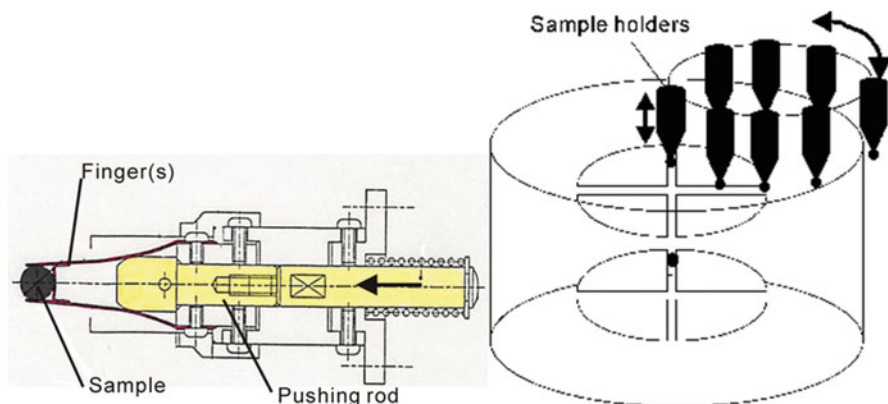
Fig. 5.9 Conceptual drawing of sample handling mechanism designed around 2000. Each sample was held by a holding device shown in the left. Eight to ten holding devices were installed in a carousel

yellow in Fig. 5.9a) opened the fingers and released the sample. In the design made around year 2000, a carousel composed of several sample holders were placed near the processing chamber (Fig. 5.9b). This design could not be accepted in terms of size, cost, as well as estimated crew time to exchange samples from/to the holders.

Figure 5.10 shows the current system concept of sample insertion and retrieval in microgravity. A sample is pushed by a rod and inserted into the levitation field. After the experiment, the sample will be thrown to the sample holder using the position control scheme. Then another pushing rod carries the sample back to the sample holder. The feasibility of this concept was confirmed during parabolic flight experiments where low gravity conditions were obtained for 20 s [30].

3.3.4 Removal of the High-Vacuum System

Even though the abovementioned efforts helped reduce considerably the mass and volume of the facility, some components had to be discarded due to the restriction of space, power, and budget. It was decided to remove a turbo molecular pump and the associated high-vacuum system implying that all the experiments should be conducted in gaseous environment. This decision was made based on the reasons described below.

As shown in Fig. 5.11, metal samples have been successfully levitated and melted, and their thermophysical properties have been measured using high-vacuum electrostatic levitators on ground [31]. Therefore, the necessity of microgravity environment is relatively less for this class of materials. In addition, metals and alloys can be handled by the electromagnetic levitator (EML) in the ISS.

On the other hand, oxide materials were very difficult to levitate or melt in 1-G, mainly because it was hard to accumulate enough electrical charges on the samples
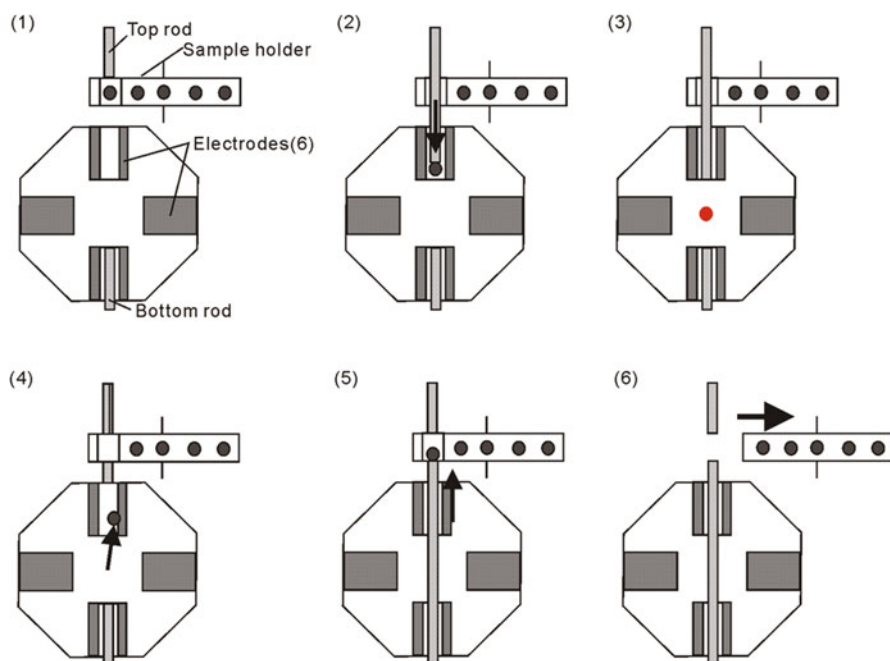
Fig. 5.10 Conceptual drawings of sample insertion and retrieval operations in the ISS-ELF
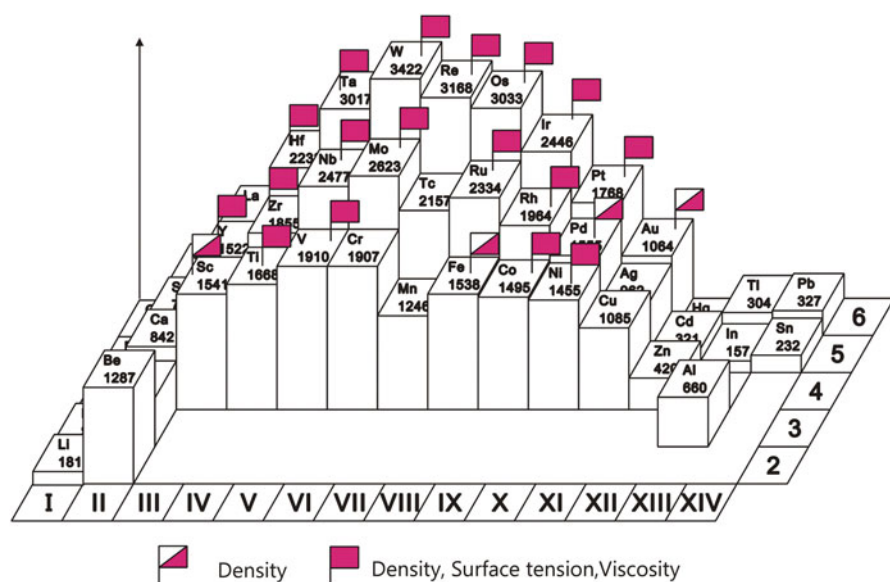
Fig. 5.11 Status of thermophysical property measurements of molten metal elements using ground-based electrostatic levitators. Elements are arranged in a periodic table, and their vertical heights represent their melting temperatures

and lift them against gravity. Moreover, oxide samples tended to lose their oxygen at elevated temperatures under high-vacuum condition. Also, since oxides are insulators, the EML could not handle them. Based on these reasons, the oxide samples became the main target for the ISS-ELF.

On the ground, inert gases could not be used for electrostatic levitation due to its high electric conductivity (high voltage between electrodes cannot be maintained before electrical breakdown appears). In addition, it was thought that microgravity would enable electrostatic levitation in Ar gas environment, where sample evaporation is suppressed, and would maintain stoichiometry of the alloys. Therefore, conducting experiments with Ar gas was set to be the secondary target.

4   Overview of the ISS-ELF [34]

The fabrication of the ISS-ELF started in 2011, and the flight hardware was flown to the ISS in late 2015. It became operational after crew operations in February 2016. Figure 5.12 shows an overview of the ISS-ELF. It weighs about 220 kg and is installed in the Multi-Purpose Small Payload Rack 2 (MSPR-2) as illustrated in Fig. 5.12. Since the MSPR-2 is shared with other experimental facilities, the ISS-ELF must be easily installed and removed from the rack. Electric power, avionics, air, cooling water, and communication signals are supplied from the ISS to the ISS-ELF through the MSPR-2.
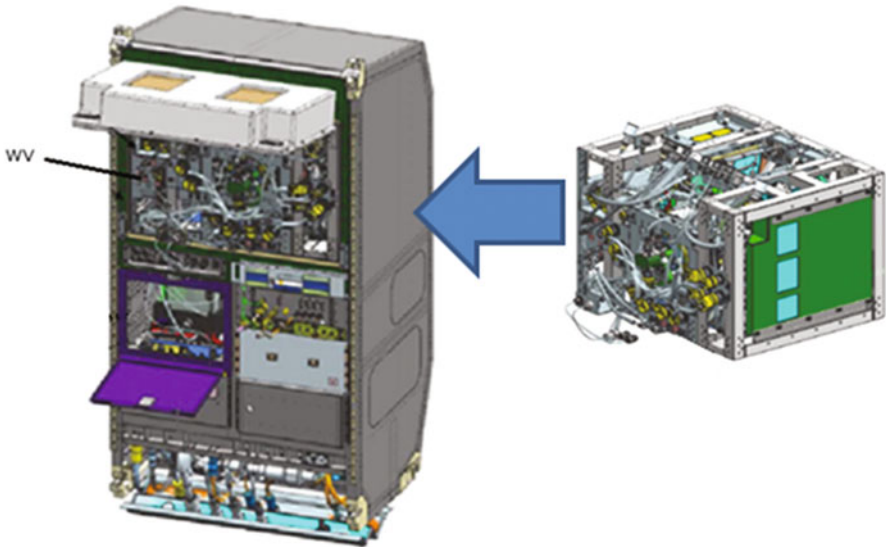
Fig. 5.12   Drawing of the ISS-ELF installed in the MSPR-2
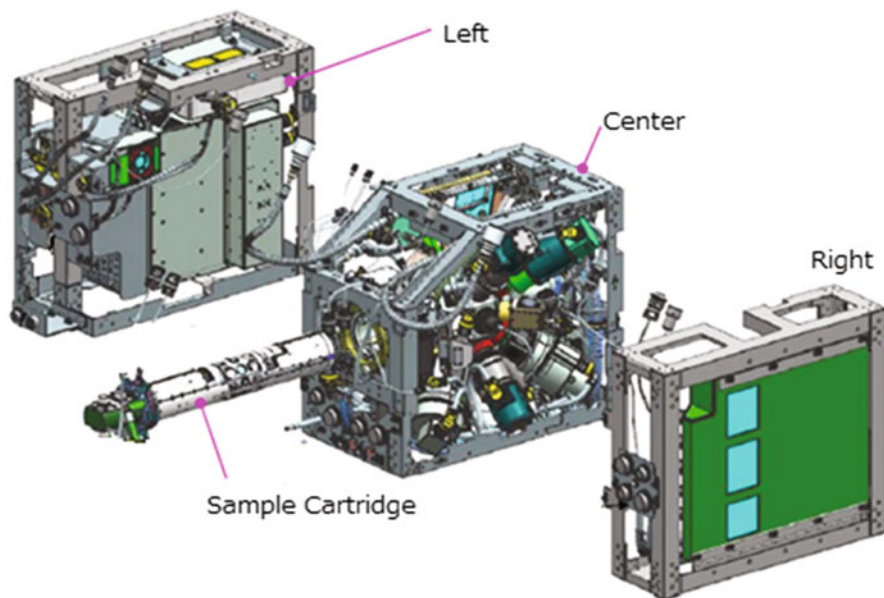
Fig. 5.13 The ISS-ELF in its shipping and launch configuration. The main part of the ISS-ELF is divided into three parts. The sample cartridge is also separately shipped

The main body of the ISS-ELF consists of three parts as shown in Fig. 5.13. The right part contains a computer called the "experiment controller," and the left part contains another one named the "position controller." The left part also contains the high-voltage amplifiers and the gas valve assembly. The center part is occupied by the processing chamber and optical devices that include the heating lasers, a pyrometer, and the observation cameras. All the optical devices are mounted on the chamber as illustrated in Fig. 5.14. The chamber is a polyhedron with 26 faces. It can be evacuated using a gas vent line to 500 Pa and pressurized up to 2×10^5 Pa. The ISS-ELF has the capabilities to measure the density, the surface tension, and the viscosity of molten samples.

4.1 Sample Cartridge and Sample Holder

The details of the sample cartridge are shown in Fig. 5.15. The sample cartridge can accommodate a sample holder which contains 15 samples. The size of the spherical samples is approximately 2 mm in diameter. The sample cartridge contains six electrodes among which a sample is levitated. Since there is no strong G-vector in microgravity, the size of these six electrodes is identical. The separation between the electrodes is 15 mm along the y-axis and 30 mm along both the x- and z-axes. An electrical potential of up to ± 3 kV can be applied to each electrode in dry air
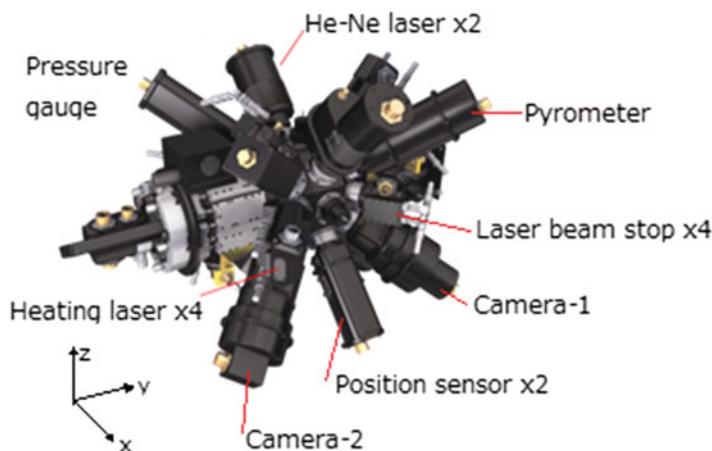
Fig. 5.14 Drawing of the ISS-ELF chamber and installed optical devices. Coordinates of the ISS-ELF (x, y, and z directions) are also indicated
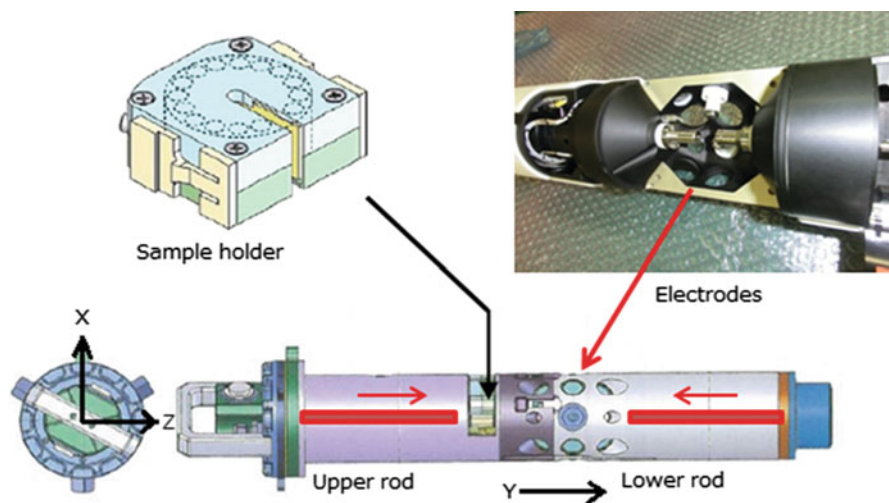
Fig. 5.15 Conceptual drawing of the sample cartridge. A sample holder (left top) is inserted in the cartridge, and upper rod transfers a sample to the levitation field (right top). The lower rod is used to return the sample back to the holder

atmosphere, whereas it is limited to 1.5 kV for an Ar environment to prevent electric discharge between electrodes. The sample cartridge has two pushing rods. They are used for sample insertion and retrieval as depicted in Fig. 5.10. By rotating the sample holder, the samples are exchanged from the processed sample to an unprocessed one. These operations are conducted from the ground through remote commands, thereby enabling to carry out experiments on all 15 samples continuously and without the requirement of crew operation. The sample cartridge is inserted into the chamber by crew members, as shown in Fig. 5.13.

4.2 Experiment and Position Control

The overall experiment sequence is controlled by the experiment controller. It activates and deactivates all other devices. It opens and closes gas valves to maintain atmospheric conditions in the chamber. It also measures the temperatures of all devices for safety. Finally, it records experiment and house-keeping data and transfers these data to the ground. The position controller is dedicated to the position control of the levitated samples. It also moves the rods and rotates the sample holder in the sample cartridge for sample insertion and retrieval.

The sample position control method, shown in Fig. 5.16, is the same as the original technique innovated at JPL. A collimated laser (He-Ne laser emitting at 638 nm) projects a shadow of the sample on a position sensor (Hamamatsu Intelligent Vision System) where vertical and horizontal coordinates are measured. Two sets of the projection laser and position sensor system are orthogonally placed to measure the tridimensional sample position (x, y, and z). The position signals are sent to the position controller where the sample position data are compared with the setting position (x_0, y_0, and z_0). The position control voltages (V_x, V_y, and V_z) are then calculated using the following PD (proportional-differential) control algorithm:
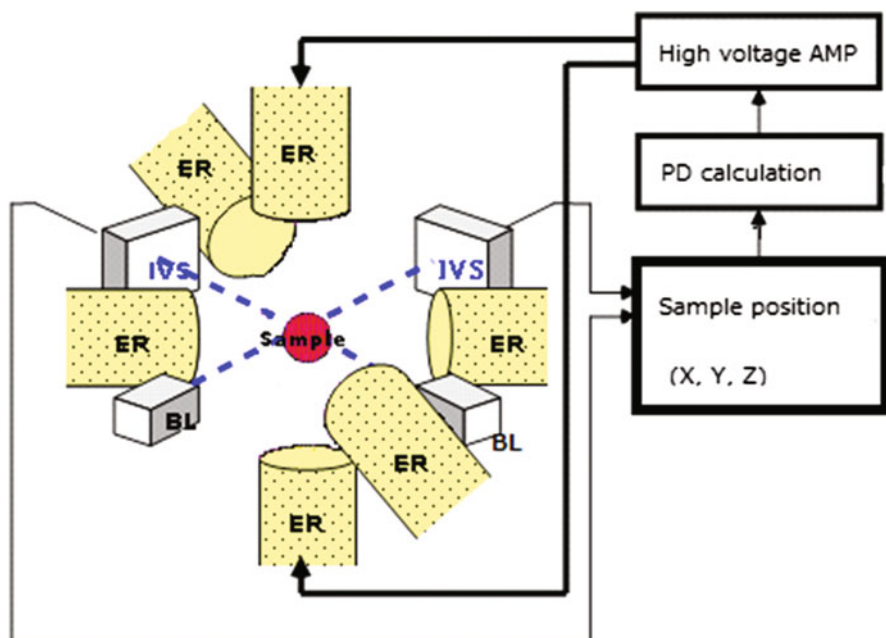
Fig. 5.16 Control diagram of the ISS-ELF

$$V_x = P_x(x - x_0) + D_x \frac{d(x - x_0)}{dt}$$
$$V_x = P_y(y - y_0) + D_y \frac{d(y - y_0)}{dt} \qquad (5.1)$$
$$V_z = P_z(z - z_0) + D_z \frac{d(z - z_0)}{dt}$$

where P and D indicate the proportional and differential control parameters, respectively. It shall be noted that the integral term usually used in normal PID control is removed (based on the results of the sounding rocket experiment) so that the control system remains stable in case of a sudden sample charge reduction. This feedback control is conducted with a frequency of 1000 Hz. The control parameters are adjustable from the ground commands.

4.3 Heating Lasers

The sample is heated by four semiconductor lasers (980 nm, 40 W power each). In order to obtain an excellent temperature homogeneity of the sample, these lasers are arranged in a tetrahedral heating configuration around the sample. Each laser power can be controlled by commands from the ground thorough the experiment controller. Laser beam stops are installed to absorb the laser radiation and to protect the chamber wall. The laser beams are focused (around 0.4 mm in diameter) at the sample position.

4.4 Optical Devices

The sample temperature can be measured by a commercial pyrometer (IMPAC IGA140) through a couple of sapphire windows. The pyrometer measures the radiation intensity from the sample over the 1.45–1.8 μm spectral range. Since the emissivity setting on the pyrometer cannot be changed from the ground command, it remains at 1.0. The measurement temperature range is from 300 to 3000 °C, with a 100 Hz frequency. The actual sample temperature can be determined using the temperature plateau occurring after recalescence and the known melting temperature of the sample. The pyrometer contains a built-in video camera with which it can be easily confirmed that the sample stays in the measuring spot of the pyrometer (Fig. 5.17a).

The ELF has two other cameras. Camera 1 (color) offers a wide view of the levitation field, including the electrodes, to help observe the sample behavior from insertion to retrieval (Fig. 5.17b). Camera 2 (a black-and-white camera with a non-telecentric zoom lens) gives a magnified image of a UV backlit sample
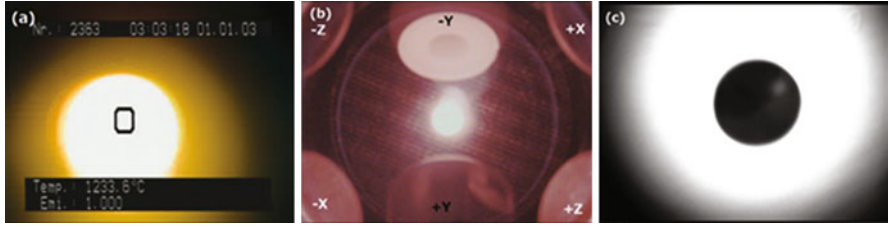
Fig. 5.17 A levitated sample observed by three cameras: (**a**) pyrometer, (**b**) image taken by camera 1, and (**c**) magnified sample image with UV back light

(Fig. 5.17c). Using the video images (taken at a rate of 60 Hz) of this camera, the density of the sample can be calculated.

4.5 Thermophysical Property Measurements

4.5.1 Density

The density was obtained using a computer-aided image analysis and the measurement of the sample mass after the experiment. The detailed method of image analysis was described in Ref. [14] but is shortly explained here for completeness. Once the sample was melted, it took a spherical shape due to surface tension (Fig. 5.17c). With the assumption that the sample is axisymmetric, the sample volume can be calculated from an image recorded by the camera. At first, 400 edge points are detected and converted to polar coordinates (R, θ). These points are then fitted with the spherical harmonic functions through sixth order as

$$R(\theta) = \sum_{n=0}^{6} c_n P_n(\cos \theta) \tag{5.2}$$

where $P_n(\cos\theta)$ are the n-th order Legendre polynomials, and c_n are the coefficients which are determined to minimize the value expressed as:

$$F = \sum_{j=1}^{400} \left\{ R_j - R_j(\theta) \right\}^2. \tag{5.3}$$

Then, the volume (V) is calculated by the following equation:

$$V = \frac{2\pi}{3} \int_0^{\pi} R^3(\theta) \sin \theta d\theta \tag{5.4}$$

The mass (m) of the processed sample is measured upon its return to Earth, and the density (ρ) is finally obtained from

$$\rho = \frac{m}{V}.$$ (5.5)

4.5.2 Surface Tension and Viscosity

Surface tension and viscosity of the sample can be measured using the oscillation drop method. The measurement technique is the same as the one implemented by JPL [16] and is depicted in Fig. 5.18. The drop oscillation of the molten sample is excited by superimposing a sinusoidal voltage on the electric field for a few seconds. After the termination of the excitation, the oscillation amplitude on the sample gradually decays due to its viscosity. A collimated laser beam, which creates a drop shadow for position sensing, is split in two beams, and one of the beams is directed to a circular photodetector. The oscillating drop amplitude can be measured as a fluctuation of the total laser power at the photodetector at a rate of 5000 Hz. From the measured signal, the characteristic oscillation frequency of the sample ω_c and the time constant of the amplitude decay τ are obtained. Using ω_c, the surface tension γ can be found from the following equation [35]:

$$\gamma = \frac{\rho r_0^3 \omega_c^2}{8},$$ (5.6)

where r_0 is the radius of the sample when a spherical shape is assumed. Similarly, using τ, the viscosity η can be found by [36].
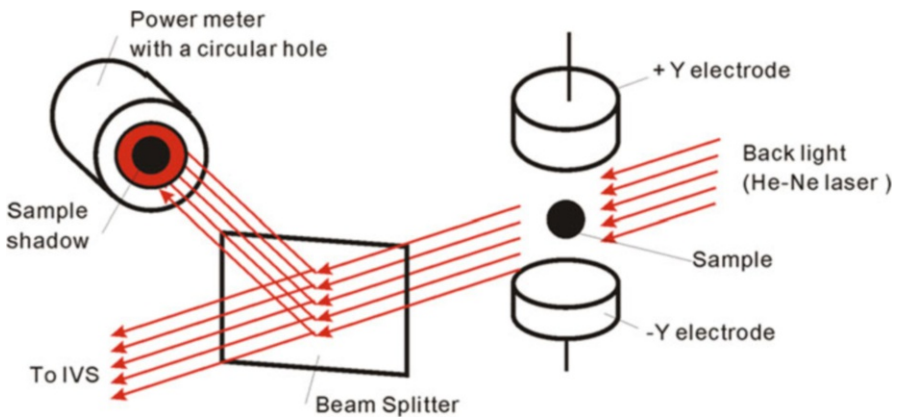
Fig. 5.18 Schematic drawing of drop oscillation measurement system

$$\eta = \frac{\rho r_0^2}{5\tau}.$$

(5.7)

With this method, the viscosity can be measured over the 0.5–100 mPa·s range.

5   Experimental Results of the ISS-ELF

Since February 2016, a functional checkout and initial experiments using metal and oxide samples have been conducted. Oxide samples including Al_2O_3 and rare-earth sesquioxides were melted under dry air, while zirconium samples were melted in an Ar gaseous environment.

5.1   Levitation of Solid Samples

Figure 5.19a shows a time-position (Y-direction) history of a stainless steel sphere during sample insertion. The sample position data were recorded at intervals of 0.1 s. The amount of the surface charge on the sample can be estimated using this sample position profile. Sample motion in the y-direction (y) is governed by the following simple equation:
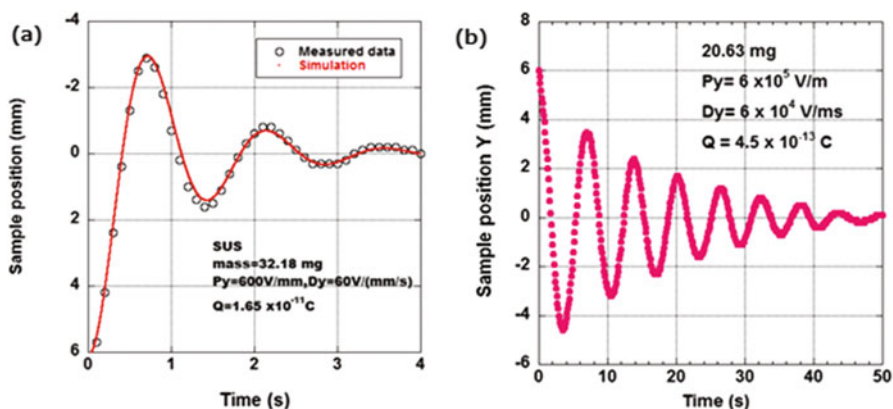
Fig. 5.19 Movement of samples (Y-direction) at initial insertion: (**a**) stainless steel sphere and, (**b**) Ga_2O_3. Estimated sample charges by simulation (red line) are 16.5 pC (stainless steel) and 0.45 pC (Gd_2O_3), respectively

$$m\frac{d^2y}{dt^2} = \frac{QV_y}{L_y},\tag{5.8}$$

where m is the sample mass, V_y is the control voltage between the top and bottom electrodes determined by Eq. (5.1), L_y is the distance between the top and bottom electrodes, and Q is the charge of the sample.

Numerical simulations were conducted by changing Q to find the best simulation that agrees with the measured sample motion. The best simulation result is plotted in Fig. 5.19a. The sample charge is estimated to be about 17 pC (10^{-12}C). In the ground experiments, a surface charge of around 200 pC is needed to levitate this stainless steel sample against gravity. In the case of a Gd_2O_3 sample (shown in Fig. 5.19b), the estimated amount of charge is as small as 0.45 pC. This confirmed that even though the sample surface charge is very small, position control using the Coulomb force is applicable in microgravity.

The sample position stability at room temperature was studied using image analysis. Still images of the stainless- steel sphere such that shown in Fig. 5.17c were captured from a video recorded for 30 s (900 frames). Each image was analyzed, and the centroid of the sample was determined. Sample movement in 30 s was found to be less than ± 40 μm.

Upon heating, position stability degrades due to the disturbances induced by the heating lasers. The sample position of a molten Al_2O_3 sample and the measured temperature as a function of time are shown in Fig. 5.20. By properly adjusting the control parameters, the position fluctuation was suppressed by about ± 100 μm during the time the sample was maintained above the melting temperature, as well as during rapid cooling. The fluctuation of temperature measurements was less than ± 20 K.
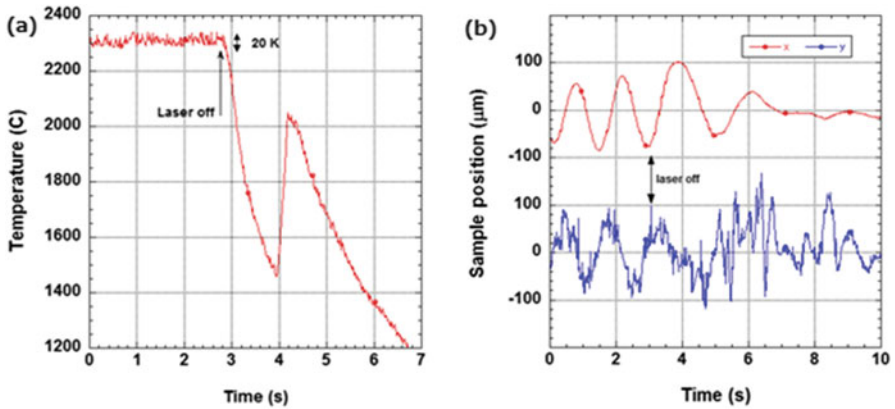
Fig. 5.20 (a) Typical temperature profile of molten Al_2O_3 sample and (b) its position fluctuation during rapid cooling. Position fluctuation is obtained from image analysis

5.2 Density Measurements

Al_2O_3 samples were used to evaluate the capabilities for density measurements. Each sample was levitated in dry air (2×10^5 Pa in pressure) and heated. When the sample was fully melted, all lasers were powered off to cool the sample. A typical temperature-time profile measured by the pyrometer is shown in Fig. 5.20b. When the heating lasers were turned off, the sample was cooled by radiation and conduction through the surrounding gas. After the sample reached the maximum undercooled temperature, it exhibited recalescence (a sudden temperature rise to its melting temperature) and solidified. After the experiment, the sample was successfully retrieved to the sample holder, which was later returned to Earth for analysis.

Magnified sample images recorded during the time period from a to b in Fig. 5.20b were analyzed to obtain the volume as a function of temperature. The mass of the processed samples was measured on the ground. Finally, the density data of alumina as a function of temperature were obtained. Figure 5.21 shows the measured density of molten Al_2O_3 as a function of temperature along with the reference data found in the open literature. Two alumina samples were used to validate the density measurements. The first sample (sample 1) was heated above 3000 K and was quickly cooled down to ensure that the sample was stable at high temperature. The second sample (sample 2) was heated to around 2600 K and maintained at this temperature for 10 min to check the long-term sample stability and the extent and influence of evaporation. The difference between values of sample 1 and sample 2 was about 2%, which is within the experimental uncertainties of our measurement system and method.

Fig. 5.21 Density of liquid Al_2O_3 as a function of temperature. Literature data are also plotted
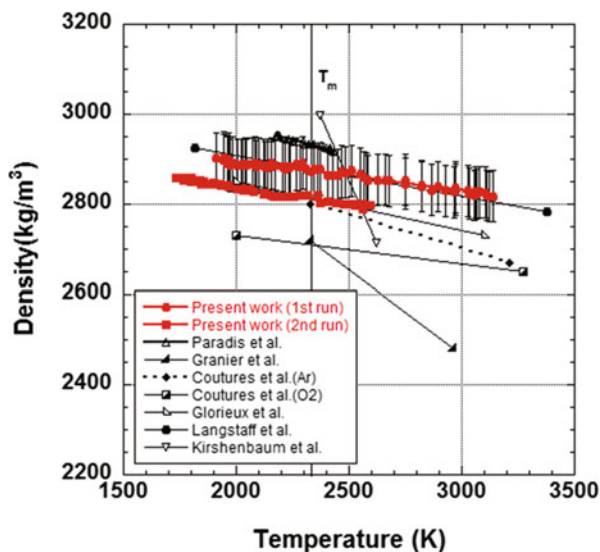
Table 5.1 Literature values of the density of liquid alumina

Density at T_m (10^3 kg·m^{-3})	Temperature coeff. (kg·m^{-3}·K^{-1})	Temperature (K)	References
2.87	−0.064	1913–3139	Present work (run-1)
2.81	−0.074	1732–2597	Present work (run-2)
2.9	−0.09	1900–3240	Langstaff [37]
2.93	−0.12	2175–2435	Paradis [38]
2.81	−0.107	2000–3100	Glorieux [39]
2.71	−0.0678	2000–3275	Coutures [40]
2.80	−0.151	2327–3210	Coutures [40]
2.72	−0.28	2323–2965	Granier [41]
2.69	−0.79	2320–3100	Zubarev [42]
2.55		2327	Wartenberg [43]
3.06		2327	Ikemiya [44]
3.06	−0.965	2323–3023	Shpil'rain [45]
2.98	−1.15	2325–2775	Elyutin [46]
3.03	−0.752	2323–2673	Rasmussen [47]
3.04	−1.15	2323–2828	Mitin [48]
3.05	−1.127	2375–2625	Kirshenbaum [49]
3.05		2327	Kozakevitch [50]
2.97		2327	Kingery [51]

The measured data show a good agreement with the literature data presented in Fig. 5.21 and listed in Table 5.1. In particular, the data of sample 1 are almost identical with those obtained by Langstaff et al. using an aerodynamic levitator. As a result, the validity of the density measurement method with the ISS-ELF has been confirmed.

The density of rare-earth sesquioxides (Er_2O_3, Gd_2O_3, Ho_2O_3, and Tb_2O_3) has been measured using the ISS-ELF [52–54]. The thermophysical properties of these samples have been rarely measured due to their high melting temperatures (above 2600 K). The measured density data as a function of temperature are depicted in Fig. 5.22 with the literature data and are summarized in Table 5.2. No reference value was found for Ho_2O_3 and Tb_2O_3. However, the densities of Er_2O_3 and Gd_2O_3 were measured with an aerodynamic levitator [55]. These density values are lower than our results. The discrepancies may be derived from the difference in the imaging methods. The ISS-ELF uses a UV back light technique to avoid the effect of strong irradiation from the high-temperature sample [56], while the other group directly observes the sample at high temperature, which probably introduces over-estimates on the sample volume measurements. The measured density shows a linear temperature dependence, and the results, listed in Table 5.2, can be fit with a 95% confidence of interval.
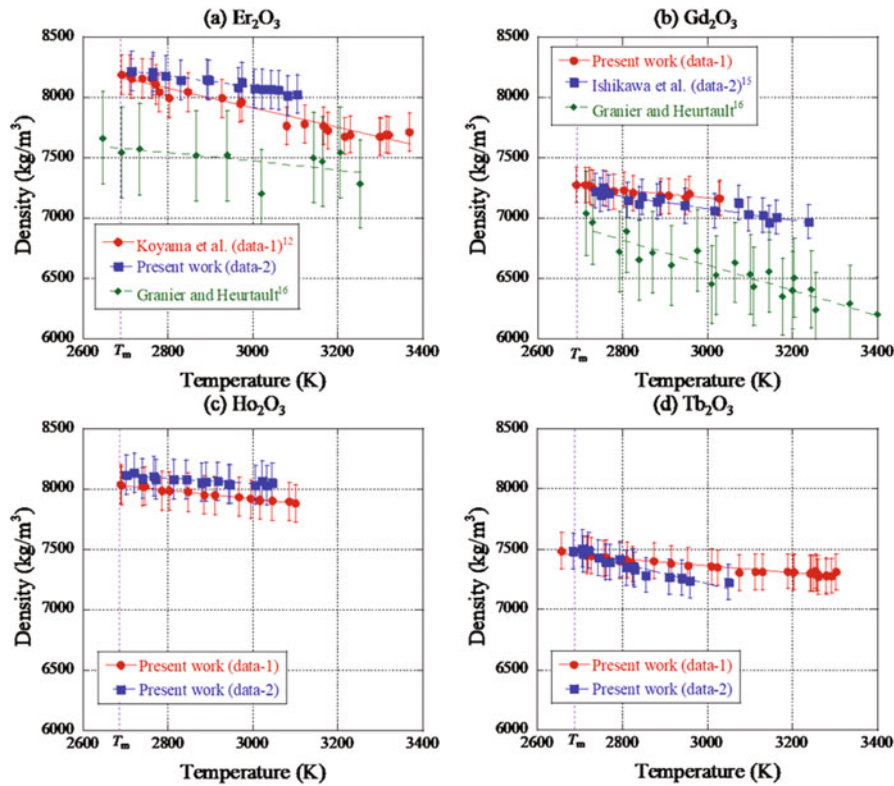
Fig. 5.22 Measured density of liquid lanthanoid sesquioxides and their temperature dependence

Table 5.2 Density of molten lanthanoid sesquioxides

	T_m (K)	Density at T_m (10^3 kg·m^{-3})	Temperature coeff. (kg·m^{-3}·K^{-1})	References
Gd$_2$O$_3$	2693	7.24 ± 0.28	-0.50 ± 0.09	[52, 54]
		7.27 ± 0.16	-0.33 ± 0.06	[54]
	(2713)	6.93 ± 0.34	-1.048 ± 0.112	[55]
Tb$_2$O$_3$	2683	7.45 ± 0.87	-0.28 ± 0.03	[54]
		7.48 ± 0.42	-0.85 ± 0.15	[54]
Ho$_2$O$_3$	2688	8.04 ± 0.84	-0.37 ± 0.03	[54]
		8.08 ± 0.19	-0.22 ± 0.07	[54]
Er$_2$O$_3$	2686	8.17 ± 0.25	-0.81 ± 0.08	[53, 54]
		8.23 ± 0.20	-0.48 ± 0.07	[54]
	(2698)	7.57 ± 0.53	-0.3273 ± 0.053	[55]

Precise density data are paramount to calculate other thermophysical properties. They are also needed for structural analyses to obtain pair distribution function ($g(r)$) from measured structure factors ($S(Q)$) by X-ray scattering experiments. The $g(r)$ of molten Er_2O_3 was obtained using our density data, and its characteristic liquid structure was obtained using molecular dynamics simulations [53]. Measurements of other rare-earth sesquioxides (Tm_2O_3, Yb_2O_3, and Lu_2O_3) will be conducted in the near future.

Under argon gaseous environment, zirconium samples were successfully levitated and melted. These molten samples were gradually oxidized due to the residual oxygen in argon (at least 3 ppm). To take advantage of this oxidization, densities of liquid Zr-O system and their dependence of oxygen concentration were measured [57]. The density of Zr-O with relatively low oxygen concentrations was measured with the ground-based facility with high vacuum [58], while that of high oxygen concentrations was obtained with the ISS-ELF. Oxygen concentrations in the processed samples were measured either though thermogravimetric analysis (TG) or X-ray photoelectron spectroscopy (XPS). The density of Zr-O system shows a negative concentration dependence as shown in Fig. 5.23a. The calculated molar volumes from density versus oxygen concentrations were depicted in Fig. 5.23b, where slight excess volumes were observed from the ideal $Zr-ZrO_2$ mixture.
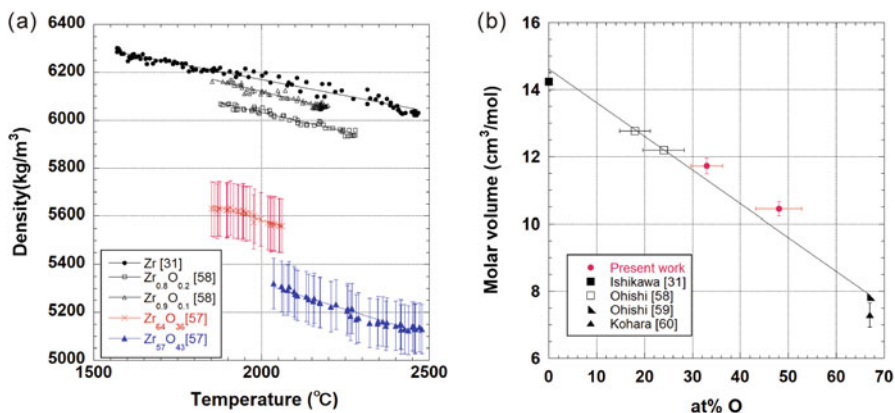
Fig. 5.23 Results of density measurement of Zr-O system: (**a**) densities as a function of temperature, (**b**) molar volume versus oxygen concentration. Molar volume of ZrO_2 (67 at% oxygen) was calculated from density values from Refs. [59, 60]
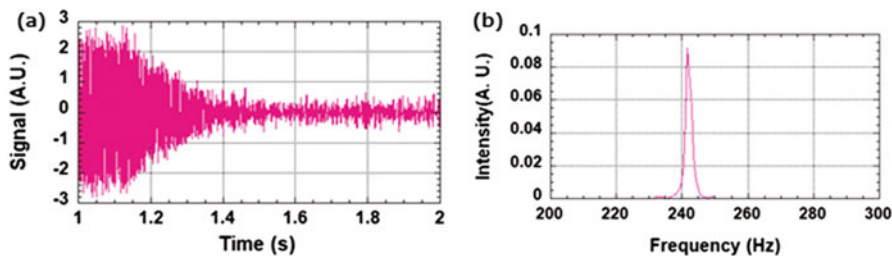
Fig. 5.24 (**a**) Typical oscillation signal obtained with liquid zirconium in the ISS-ELF. (**b**) A clear single peak frequency was obtained by the FFT analysis

5.3 Surface Tension and Viscosity Measurements

Surface tension and viscosity measurements through drop oscillations are more challenging than density measurements. In order to get a good signal, the position of a molten sample must be stable, while its surface deforms with a detectable amplitude. As described earlier, the amount of charge accumulated on the sample in microgravity is less than 10% of that on the ground experiments, which makes it difficult to induce sufficient surface oscillation using the electric field. Therefore, no surface tension or viscosity data have been published yet. Recently, good oscillation signals have been obtained for Zr (Fig. 5.24), Au, and oxide samples (Al_2O_3 and Tb_2O_3). The surface tension and viscosity will be determined after these samples are brought back to Earth and their masses are measured.

6 Conclusions

This report briefly summarized the development of the ISS-ELF carried out by the Japanese Aerospace Exploration Agency, described the current configuration of the ISS-ELF, and presented the experimental results. By conducting the experiments, several points to be improved were found. In particular, better oscillation signals should be obtained to improve surface tension and viscosity data and the oxidization occurring when processing in argon environment should be minimized. In addition, more stable levitations are desired to allow better measurements. Hardware and software modifications are currently being conducted, the development of the ISS-ELF being a never-ending process. Additional and better experimental results will be reported in future publications.

References

1. T.G. Wang, A.V. Anilkumar, C.P. Lee, K.C. Lin, Bifurcation of rotating liquid drops: Results from USML-1 experiments in Space. J. Fluid Mech. **276**, 389–403 (1994). https://doi.org/10.1017/S0022112094002612

2. T.G. Wang, A.V. Anilkumar, C.P. Lee, Oscillations of liquid drops: Results from USML-1 experiments in space. J. Fluid Mech. **308**, 1–14 (1996). https://doi.org/10.1017/S002211209600136X

3. I. Egry, Thermophysical property measurements in microgravity. High Temp.-High Press. **32**, 127–134 (2000)

4. G. Lohöfer, S. Schneider, I. Egry, Thermophysical properties of undercooled liquid $Co_{80}Pd_{20}$. Int. J. Thermophys. **22**, 593–604 (2001). https://doi.org/10.1023/A:1010701821392

5. Y. Luo, B. Damaschke, G. Lohöfer, K. Samwer, Thermophysical properties of a $Si_{50}Ge_{50}$ melt measured on board the International Space Station. Npj Microgravity **6**, 10 (2020). https://doi.org/10.1038/s41526-020-0100-5

6. M. Mohr, R. Wunderlich, Y. Dong, D. Furrer, H.-J. Fecht, Thermophysical properties of advanced Ni-based superalloys in the liquid state measured on board the International Space Station. Adv. Eng. Mater. **2019**, 1901228 (2019). https://doi.org/10.1002/adem.201901228

7. P.-F. Paradis, T. Ishikawa, G.-W. Lee, D. Holland-Moritz, J. Brillo, W.-K. Rhim, J.T. Okada, Materials properties measurements and particle beam interactions studies using electrostatic levitation. Mater. Sci. Eng. R **76**, 1–53 (2014). https://doi.org/10.1016/j.mser.2013.12.001

8. P.F. Clancy, E.G. Lierke, R. Grossbach, W.M. Heide, Electrostatic and acoustic instrumentation for material science processing in space. Acta Astronaut. **7**, 877–891 (1980). https://doi.org/10.1016/0094-5765(80)90077-6

9. E.G. Lierke, R. Grossbach, G.H. Frischat, K. Fecker, Electrostatic positioning for the containerless processing of a Li-silicate glass, in *Summary Review of Sounding Rocket Experiments in Fluid Science and Materials Sciences, esa SP-1132*, (1991), pp. 370–371

10. W.-K. Rhim, S.-K. Chung, M.T. Hyson, E.H. Trinh, D.D. Elleman, Large charged drop levitation against gravity. IEEE Trans. Ind. Appl. **IA-23**, 975–979 (1987). https://doi.org/10.1109/TIA.1987.4505016

11. W.K. Rhim, M. Collender, M.T. Hyson, W.T. Simms, D.D. Elleman, Development of an electrostatic positioner for space material processing. Rev. Sci. Instrum. **56**, 307 (1985). https://doi.org/10.1063/1.1138349

12. W.-K. Rhim, S.K. Chung, Isolation of crystallizing droplets by electrostatic levitation. Meth. Companion Meth. Enzymol. **1**, 118–127 (1990)

13. W.-K. Rhim, S.K. Chung, D. Barber, K.F. Man, G. Gutt, A. Rulison, R.E. Spjut, An electrostatic levitator for high-temperature containerless materials processing in 1-g. Rev. Sci. Instrum. **64**, 2961 (1993). https://doi.org/10.1063/1.1144475

14. S.K. Chung, D.B. Thiessen, W.-K. Rhim, A noncontact measurement technique for the density and thermal expansion coefficient of solid and liquid materials. Rev. Sci. Instrum. **67**, 3175 (1996). https://doi.org/10.1063/1.1147584

15. A.J. Rulison, W.-K. Rhim, A noncontact measurement technique for the specific heat and total hemispherical emissivity of undercooled refractory materials. Rev. Sci. Instrum. **65**, 695 (1994). https://doi.org/10.1063/1.1145087

16. W.-K. Rhim, K. Ohsaka, P.-F. Paradis, R.E. Spjut, Noncontact technique for measuring surface tension and viscosity of molten materials using high temperature electrostatic levitation. Rev. Sci. Instrum. **70**, 2796 (1999). https://doi.org/10.1063/1.1149797

17. W.-K. Rhim, T. Ishikawa, Noncontact electrical resistivity measurement technique for molten metals. Rev. Sci. Instrum. **69**, 3628 (1998). https://doi.org/10.1063/1.1149150

18. R.W. Hyers, J.R. Roger, A review of electrostatic levitation for materials research. High Temp.-High Press. **27**, 461–474 (2008). https://doi.org/10.1515/HTMP.2008.27.6.461

19. G.E. Rustan, N.S. Spyrison, A. Kreyssig, R. Prozorov, A.I. Goldman, Noncontact technique for measuring the electrical resistivity and magnetic susceptibility of electrostatically levitated materials. Rev. Sci. Instrum. **83**, 103907 (2012). https://doi.org/10.1063/1.4759021

20. N.A. Mauro, A.J. Vogt, K.S. Derendorf, M.L. Johnson, G.E. Rustan, D.G. Quirinale, A. Kreyssig, K.A. Lokshin, J.C. Neuefeind, K. An, X.-L. Wang, A.I. Goldman, T. Egami, K.F. Kelton, Electrostatic levitation facility optimized for neutron diffraction studies of high temperature liquids at a spallation neutron source. Rev. Sci. Instrum. **87**, 013904 (2016). https://doi.org/10.1063/1.4939194

21. T. Meister, H. Werner, G. Lohöfer, D.M. Herlach, H. Unbehauen, Gain-scheduled control of an electrostatic levitator. Control. Eng. Pract. **11**, 117–128 (2003). https://doi.org/10.1016/S0967-0661(02)00102-8

22. T. Kordel, D. Holland-Moritz, F. Yang, J. Peters, T. Unruh, T. Hansen, A. Meyer, Neutron scattering experiments on liquid droplets using electrostatic levitation. Phys. Rev. B **83**, 104205 (2011). https://doi.org/10.1103/physrevB.83.104205

23. P.-F. Paradis, T. Ishikawa, S. Yoda, Electrostatic levitation research and development at JAXA: Past and present activities in thermophysics. Int. J. Thermophys. **26**, 1031–1049 (2005). https://doi.org/10.1007/s10765-005-6683-y

24. H. Yoo, C. Park, S. Jeon, S. Lee, G.W. Lee, Uncertainty evaluation for density measurements of molten Ni, Zr, Nb and Hf by using a containerless method. Metrologia **52**, 677–684 (2015). https://doi.org/10.1088/0026-1394/52/5/677

25. L. Hu, H. Wang, W. Xie, B. Wei, Electrostatic levitation under the single-axis feedback control condition. Sci. China Phys. Mech. Astron. **53**, 1438–1444 (2010). https://doi.org/10.1007/s11433-010-4068-0

26. Q. Zhong, L. Yang, H. Li, Y. Tao, W. Wang, Z. Xu, C. Luo, A new 3D reconstruction method for the density measurement of ellipsoid levitated droplets with containerless technique. J. Mol. Liq. **316**, 113345 (2020). https://doi.org/10.1016/j.molliq.2020.113345

27. Y. Tsuchiya, K. Murakami, M. Yuzawa, Y. Awa, Y. Gotoh, S. Shimada, K. Yoshizawa, C. Tsukishima, H. Shimoji, Y. Tamagawa, Electrostatic levitator furnace for Japanese experiment module. J. Jpn. Soc. Microgravity Appl. **13**, 16 (1996). https://doi.org/10.15011/jasma.13.1.16

28. S. Yoda, N. Koshikawa, T. Nakamura, J. Yu, T. Nakamura, Y. Nakamura, S. Yoshitomi, H. Karasawa, T. Ikeda, Y. Arai, M. Kobayashi, Y. Awa, H. Shimoji, T. Morita, S. Shimada, Evaluation of the positioning control function of an electrostatic levitation furnace for the Space Station. J. Jpn. Soc. Microgravity Appl. **17**, 76 (2000). https://doi.org/10.15011/jasma.17.2.76

29. J. Yu, N. Koshikawa, Y. Arai, S. Yoda, H. Saitou, Containerless solidification of oxide material using an electrostatic levitation furnace in microgravity. J. Cryst. Growth **231**, 568–576 (2001). https://doi.org/10.1016/S0022-0248(01)01431-2

30. T. Ishikawa, J.T. Okada, P.-F. Paradis, Parabolic flight experiments on the development of an electrostatic levitation furnace for the International Space Station (ISS). Int. J. Microgravity Sci. **31**, 72 (2014). https://doi.org/10.15011/jasma.31.2.72

31. T. Ishikawa, J.T. Okada, P.-F. Paradis, Y. Watanabe, Thermophysical property measurements of high temperature melts using an electrostatic levitation method. Jpn. J. Appl. Phys. **50**, 11RD03 (2011). https://doi.org/10.1143/JJAP.50.11RD03

32. T. Masaki, T. Ishikawa, P.-F. Paradis, S. Yoda, J.T. Okada, Y. Watanabe, S. Nanao, A. Ishikura, K. Higuchi, A. Mizuno, M. Watanabe, S. Kohara, Compact electrostatic levitator for diffraction measurements with a two axis diffractometer and a laboratory x-ray source. Rev. Sci. Instrum. **78**, 026102 (2007). https://doi.org/10.1063/1.2435590

33. T. Ishikawa, J.T. Okada, P.-F. Paradis, M.V. Kumar, Towards microgravity experiments using the Electrostatic Levitation Furnace (ELF) in the International Space Station (ISS). Trans. JSASS Aerospace Technol. Jpn. **12 ists29**, Th-15-18 (2014). https://doi.org/10.2322/tastj.12.Th15

34. H. Tamaru, C. Koyama, H. Saruwatari, Y. Nakamura, T. Ishikawa, T. Takada, Status of the Electrostatic Levitation Furnace (ELF) in the ISS-KIBO. Microgravity Sci. Technol. **30**, 643–651 (2018). https://doi.org/10.1007/s12217-018-9631-8

35. L. Rayleigh, Proc. R. Soc. Lond. **29**, 71 (1879)

36. H. Lamb, *Hydrodynamics*, 6th edn. (Cambridge University Press, Cambridge, 1932), pp. 473–639

37. D. Langstaff, M. Gunn, G.N. Greaves, A. Marsing, F. Kargl, Aerodynamic levitator furnace for measuring thermophysical properties of refractory liquids. Rev. Sci. Instrum. **84**, 124901 (2013). https://doi.org/10.1063/1.4832115

38. P.-F. Paradis, T. Ishikawa, Y. Saita, S. Yoda, Non-contact thermophysical property measurements of liquid and undercooled alumina. Jpn. J. Appl. Phys. **43**, 1496–1500 (2004). https://doi.org/10.1143/JJAP.43.1496

39. B. Glorieux, F. Millot, J.-C. Rifflet, J.-P. Coutures, Density of superheated and undercooled liquid alumina by a contactless method. Int. J. Thermophys. **20**, 1085–1094 (1999). https://doi.org/10.1023/A:1022650703233

40. J.-P. Coutures, J.-C. Rifflet, P. Florian, D. Massiot, Rev. Int. Hautes Temp. Refract. **29**, 123 (1994)

41. B. Granier, S. Heurtault, Rev. Int. Hautes Temp. Refract. **20**, 31 (1983)

42. Y.V. Zubarev, V.I. Kostikov, B.S. Mitin, Y.A. Nagibin, V.V. Nishcheta, Izv. Akad. Nauk. SSSR Neorg. Mater. **5**, 1563 (1969)

43. H.V. Wartenberg, G. Wehner, E. Saren, Nach. Akad. Wiss. Goettingen **2**, 65 (1936)

44. N. Ikemiya, J. Umemoto, S. Hara, K. Ogino, Surface tension and densities of molten Al_2O_3, Ti_2O_3, V_2O_5 and Nb_2O_5. ISIJ Int. **33**, 156–165 (1993). https://doi.org/10.2355/isijinternational.33.156

45. E.E. Shpil'rain, K.A. Yakinovich, F. Tsitsarkin, Experimental study of the density of liquid alumina up to 2750 C. High Temp.-High Press. **2**, 191–198 (1973)

46. V.P. Elyutin, B.S. Mitin, I.S. Anisimov, Izv. Akad. Nauk. SSSR Neorg. Mater. **9**, 1585 (1973)

47. J.J. Rasmussen, Surface tension, density, and volume change on melting of Al_2O_3 systems, Cr_2O_3, and Sm_2O_3. J. Am. Ceram. Soc. **55**, 326 (1972). https://doi.org/10.1111/j.1151-2916.1972.tb11298.x

48. B.S. Mitin, Y.A. Nagabin, Zhur. Fiz. Khim. **44**, 1325 (1970)

49. A.D. Kirshenbaum, J.A. Cahill, J. Inorg. Nucl. Chem. **14**, 283 (1960). https://doi.org/10.1016/0022-1902(60)80272-2

50. P. Kozakevitch, Rev. Metal. **57**, 149 (1960)

51. W.D. Kingery, Surface tension of some liquid oxides and their temperature coefficients. J. Am. Ceram. Soc. **42**, 6–10 (1959). https://doi.org/10.1111/j.1151-2916.1959.tb09134.x

52. T. Ishikawa, C. Koyama, H. Saruwatari, H. Tamaru, H. Oda, M. Ohshio, Y. Nakamura, Y. Watanaebe, Y. Nakata, Density of molten gadolinium oxide measured with the electrostatic levitation furnace in the International Space Station. High Temp.-High Press. **49**(1–2), 5–15 (2020). https://doi.org/10.32908/hthp.v49.835

53. C. Koyama, S. Tahara, S. Kohara, Y. Onodera, D.R. Småbråten, S.M. Selbach, J. Akola, T. Ishikawa, A. Masuno, A. Mizuno, J.T. Okada, Y. Watanabe, Y. Nakata, K. Ohara, H. Tamaru, H. Oda, I. Obayashi, Y. Hiraoka, O. Sakata, Very sharp diffraction peak in nonglass-forming liquid with the formation of distorted tetraclusters. NPG Asia Mater. **12**, 43 (2020). https://doi.org/10.1038/s41427-020-0220-0

54. C. Koyama, T. Ishikawa, H. Oda, H. Saruwatari, S. Ueno, M. Oshio, Y.I. Watanabe, Y. Nakata, Densities of liquid lanthanoid sesquioxides measured with the electrostatic levitation furnace in the ISS. J. Am. Ceram. Soc. **104**, 2913–2918 (2021). https://doi.org/10.1111/jace.17674

55. B. Granier, S. Heurtault, Density of liquid rare-earth sesquioxides. J. Am. Ceram. Soc. **71**, C466 (1988). https://doi.org/10.1111/j.1151-2916.1988.tb07551.x

56. T. Ishikawa, P.-F. Paradis, S. Yoda, New sample levitation initiation and imaging techniques for the processing of refractory metals with an electrostatic levitator furnace. Rev. Sci. Instrum. **72**, 2490–2495 (2001). https://doi.org/10.1063/1.1368861

57. H. Oda, C. Koyama, M. Oshio, H. Saruwatari, T. Ishikawa, Density of molten zirconium -oxygen system measured with an electrostatic levitation furnace in the International Space Station. Int. J. Microgravity Sci. Appl. **37**, 370302 (2020). https://doi.org/10.15011/ijmsa.37.3. 370302

58. Y. Ohishi, T. Kondo, T. Ishikawa, J.T. Okada, Y. Watanabe, H. Muta, K. Kurosaki, S. Yamanaka, Thermophysical properties of Zr-O liquid alloys measured by electrostatic levitation. Int. J. Microgravity Sci. Appl. **35**, 350105 (2018). https://doi.org/10.15011/jasma. 35.1.350105

59. T. Kondo, H. Muta, K. Kurosaki, F. Kargl, A. Yamaji, M. Furuya, Y. Ohishi, Density and viscosity of liquid ZrO_2 measured by aerodynamic levitation technique. Heliyon **5**, e02049 (2019). https://doi.org/10.1016/j.heliyon.2019.e02049

60. S. Kohara, J. Akola, L. Patrikeev, M. Ropo, K. Ohara, M. Itou, A. Fujiwara, J. Yahiro, J.T. Okada, T. Ishikawa, A. Mizuno, A. Masuno, Y. Watanabe, T. Usuki, Atomic and electronic structures of an extremely fragile liquid. Nat. Commun. **5**, 5892 (2014). https://doi.org/10.1038/ncomms6892

Part II
Liquid Structure and Transition

Chapter 6
Atomic Structure in Metallic Liquids

Xiao-Dong Wang, Xue-lin Wang, Qing-Ping Cao, Dong-Xian Zhang, and Jian-Zhong Jiang

1 Introduction

Knowledge of structure, dynamics and thermophysical properties of metals in the liquid state is of fundamental importance when considering their practical applications, and in particular their structural evolution induced by temperature variation is a prerequisite for understanding the processes that occur in the formation of production from the melts. The study of liquid structure started in 1916 when Debye and Scherrer observed the XRD haloes from liquid benzene. Later, Zernike and Prins laid the modern theoretical foundation of radial distribution analysis of liquid diffraction pattern [1]. By using this analysis, Debye and Menke presented the first liquid structural data of mercury, which marked the beginning of a new era in metallic liquid structure research [2]. After nearly a century of immense efforts, advances in experimental equipment and techniques have provided more accurate experimental data on liquid structures, especially for the application of the third-generation synchrotron radiation sources with high intensity, high energy, and high resolution, largely enhancing structure analytical capacity. Simultaneously, the theoretical calculations have also made great progress, e.g., classical molecular dynamics (MD) simulation, ab initio MD simulation, and reverse Monte Carlo simulation, which provide effective approaches to studying the liquid structure on the microscopic length scales.

The liquid is one of the fundamental states of matter. However, there is still no idealized model to describe it. The typical characteristics of metallic liquids are ordered in the short range but disordered in the long range, which means it can

X.-D. Wang · X.-l. Wang · Q.-P. Cao · D.-X. Zhang · J.-Z. Jiang (✉)
International Center for New-Structured Materials (ICNSM), State Key Laboratory of Silicon Materials, and School of Materials Science and Engineering, Zhejiang University, Hangzhou, People's Republic of China
e-mail: jiangjz@zju.edu.cn
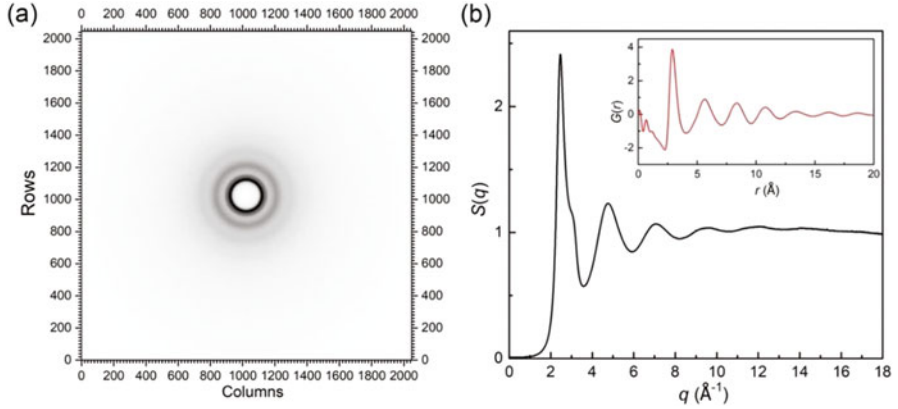
Fig. 6.1 (**a**) Raw data from liquid GaIn eutectic alloy collected at 300 K on Perkin Elmer 1621 detector at the beamline 11-ID-C at the Advanced Photon Source in 20 s of exposure time. (**b**) Structure factor and corresponding PDF in the inset, showing high quality at high q region in $S(q)$ and low r fluctuations in $G(r)$ caused by systematic and termination errors

neither be described by crystallographic theory with long-range periodic symmetry nor by van der Waals equation of completely disordered gas. Due to the complexity of liquid structure and limitations of experimental techniques, the studies of metallic liquid greatly lag behind that of solid state. In the past few decades, the knowledge on metallic liquids has been obtained mainly from various diffraction experiments, physical property measurements, and computer simulations. The pair distribution function (PDF) or radial distribution function (RDF) is a very useful method to describe the structure of disordered materials, including liquids and glasses, yielding the quantitative structural information on the nanoscale. The PDF exhibits the distribution of the distances between two atoms, which can be derived by the Fourier integral transformation from the structure factor, $S(q)$, obtained by X-ray, neutron, and electron diffraction experiments [2, 3], where q is the momentum transfer of scattering $q = 4\pi \sin \theta/\lambda$, θ is the diffraction angle, and λ is the wavelength of incident probe through

$$g(r) = 1 + \frac{1}{(2\pi)^3 \rho_0 r} \int_0^\infty 4\pi q^2 [S(q) - 1] \frac{\sin (qr)}{qr} dq \qquad (6.1)$$

where ρ_0 is the atomic number density. Figure 6.1 presents the raw diffraction data of liquid eutectic GaIn alloy collected at 300 K by a flat panel PerkinElmer 1621 detector at the beamline 11-ID-C of the Advanced Photon Source, USA, and corresponding processed data in the form of $S(q)$ and PDF. Apparently, the high-quality data usually have the good signal-to-noise ratio in the high q range on $S(q)$. By analyzing the PDF or RDF, one can gain the information of average interatomic distance and the nearest coordination number. It is recognized that both PDF and S (q) only provide the average values of structural information, which to some extent
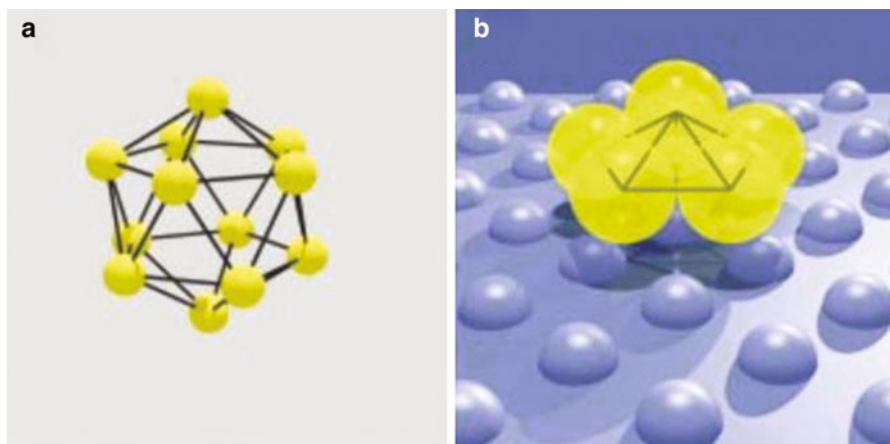
Fig. 6.2 (**a**) Polytetrahedral arrangement predicted for close-packed monatomic liquids. (**b**) Upper half (pentagonal) of the Pb icosahedron (**a**) captured by the potential landscape of the primitive Si (001) surface. (Reproduced from Ref. [8], with permission @ 2000 by Macmillan Magazines Ltd: Nature Communications)

restricts the possibility of a complete interpretation and deep understanding of the liquid structure. Fortunately, with advancing the computer power and various simulation methods, it is possible to investigate the liquid structure on the atomic scale via constructing the three-dimensional configurations. Considerable studies have reported that metallic liquids contain not only short-range clusters with different sizes and types but also medium-range ordered structures over the nearest neighbors.

As early as 1952, Frank [4] first proposed the concept of the icosahedral short-range order (ISRO) in metallic liquids, which contains 13 atoms and 20 equivalent tetrahedrons. When using the Lennard-Jones potential to describe atomic interactions, the icosahedral arrangement has a significantly lower energy than those of face-centered cubic and hexagonal close-packed structures with the same number of atoms. He speculated that the icosahedral structure plays a key role in stabilizing the liquid; that is why metallic liquids could largely be supercooled below their melting temperatures, as experimentally observed by Turnbull [5]. Later, some MD simulations confirmed this conjecture in monoatomic and binary Lennard-Jones liquids, in which the degree of ISRO increases with supercooling [6, 7]. Until early in this century, Reichert et al. [8] used the total internal reflection X-ray technique to experimentally observe the five-order local symmetric structure in liquid Pd close to a (001) surface of Si in Fig. 6.2 and predicated that this structural characteristic exists in all close-packed monoatomic liquids. By combining the electromagnetic levitation with neutron scattering or XRD, Schenk's group has systematically investigated the SRO of a variety of stable and supercooled liquids, Fe [9, 10], Ni [9, 10], Co [11], Ti [12], and Zr [9, 10]; binary alloys Co-Pd [13] and Ti-Fe [14]; as well as melts forming quasi-crystalline or polytetrahedral phases, such as Al-(Fe/Co)

[15] and Al-(Cu/Fe)-Co [10, 16]. They found all the investigated metallic liquids exhibit a small shoulder on the right side of the second peak in structure factor and confirmed that this particular feature is closely related to the existence of the ISRO. Similar results were reported in liquid Ni and Ti by Lee et al. [17], but the ISRO was significantly distorted in the liquid Ti. In recent years, although the ISRO has been intensively detected in many metallic liquids, it is not perfect as proposed by Frank [18]; instead having different degrees of distortion and defects and even its fraction varies largely in different systems [19–33]. For instance, Jakse et al. [34] applied the first-principle MD simulations to investigate the short-range order of liquid and supercooled Ta. They found although the liquid is dominated by fivefold symmetrical local structures, the fraction of ISRO is rare, mainly forming a complex polytetrahedral-type order that is very close to that of A15 phase and its fraction increases with increasing supercooling. Ding et al. [32] also argued that the full or complete ISRO that has 12 neighbors and 12 fivefold bonds dominated only in the specific systems, although the fivefold local symmetry may be universal in metallic liquids and glasses. Li et al. [35] have reviewed the recent developments of the fivefold local symmetry in metallic liquids and its key role in understanding of structure-property relationship, like glass transition, dynamic crossover phenomena, relaxation dynamics, and mechanical deformation.

When considering binary or even multicomponent metallic liquids, the liquid structure become more complex and diverse due to different contents, types, and atomic interactions between various elements. In addition to topological short-range order, there exists chemical short-range order that requires separated analyses of the local structure of different components. For example, Cheng et al. [36] and Ding et al. [32] reported that the full ISCO was the dominant local motif around Cu atoms in CuZr liquids, while the most popular short-range order around Zr was identified to be 16-coordinated Kasper polyhedra. Decreasing temperature leads to an increase in the number of Cu-centered full ISCO, showing a sharp increase near the glass transition temperatures. In contrast to Cu-Zr alloys, the Ni-Zr liquids contained relatively low fractions of ISCO. Holland-Moritz et al. [37] used neutron scattering technique, and Huang et al. [38] performed the first-principle MD simulations to investigate the structure of liquid $Ni_{36}Zr_{64}$ eutectic alloy. They found significant topological and chemical short-range orders in the liquid, and the local environments around Ni and Zr atoms were more complex than ISRO due to the strong directional interaction and large size difference between the two elements. Analogous results were reported by Ding et al. [39] who revealed that in $Mg_{65}Cu_{25}Y_{10}$ alloy the characteristic short-range order was dominated by Cu-centered bicapped square antiprisms and tricapped trigonal prisms instead of ISRO. Moreover, these local motifs showed weak temperature dependence with undercooling, quite different from the ISCO in Cu-Zr and Cu-Zr-Al systems. To reveal how different local orders are packed to form the three-dimensional disordered structures in metallic glasses, some structural models have been proposed, as reviewed in Ref. [40]. Among them, Miracle's efficient cluster packing model [41] and Sheng's quasi-equivalent cluster model [42] are two most popular models, in which the solute-centered clusters can be treated as the basic building blocks of metallic glasses, and the connection

between them in a certain packing scheme, such as fcc, icosahedral, and dense random packing by sharing solvent atoms in the shell, constitutes the medium-range order (MRO). Many theoretical studies have confirmed that these structural models are also suitable for the study of liquid structure. For example, the MD simulation results of the rapid cooling process of $Cu_{64.5}Zr_{35.5}$ liquids indicated that there existed a considerable number of MROs in the liquid above the melting temperature, which was formed by the connectivity of icosahedral clusters. Upon cooling, the MROs formed by different linking mechanisms, such as sharing vertex, edge, face, and pentagonal-cap, exhibited different growth trends [43]. In terms of the same simulation scheme, Fang et al. [44] discovered a Bergman-type MRO around Cu atoms in the liquid $Cu_{64.5}Zr_{35.5}$ alloy using the cluster alignment analysis, which are formed by the outward expansion of icosahedral clusters and develop with decreasing temperature. Using the ab initio MD simulation, Kang et al. [45] also confirmed the existence of MRO structure in liquid $Al_{75}Cu_{35}$ alloy by clustering the fivefold short-range ordered structures. Recently, neutron and XRD measurements reported the presence of a pronounced pre-peak at a small q range (1.5–2.0 Å^{-1}) of the structure factor in some liquid Al-based alloys, such as Al-TM (TM=Mn, Fe, Co, Ni, Cu, Ge) [46–50], Al-Fe-Co [16], Al-Fe-Ce [51], and $Zr_{80}Pt_{20}$ [52], which was interpreted as a diffraction peak broadening caused by MRO structures (~0.5–2.0 nm) composed of icosahedral clusters [51]. Although numerous studies have been performed to study liquid structures in various systems, in fact, no general physical model or theory has been developed to unambiguously describe how atoms are packed to form such short- and/or medium-range ordered structures without long-range periodicity.

This review is composed of a brief introduction of the short- and medium-range orders in metallic liquids in Sect. 1. Section 2 deals with some commonly used experimental and computational techniques to characterize the liquid structure. Section 3 summarizes the structural data of several representative metallic liquids which could be used in space and examines the correlation of structure with viscosity of Zr and ZrCu melts. Finally, a summary is presented in Sect. 4.

2   Experimental and Theoretical Methods

When a crystalline solid is exposed to X-rays, neutrons, or electrons, the regular repeating arrangement of atoms gives rise to the sharp diffraction or Bragg peaks in scattering experiments that can be used to identify the crystalline structure. In liquids or amorphous solids, the atoms are not arranged in a regular array. Despite lack of long-range atomic packing, they are not truly a random distribution of atoms and still exhibit a certain degree of short-range order, thereby producing a diffuse intensity peak in the scattering patterns. By analyzing the structure factor and PDF extracted from the scattering data, one can obtain the average structural information of the liquids and amorphous solids, e.g., the number of the nearest neighbors and the mean interatomic distance, whereas the direct construction of three-dimensional structure,

even locally, is very difficult only from the experimental point of view. Computer simulations and some theories of liquids have been confirmed to provide key insights to complement experimental investigations, not only giving reasonable predictions of material properties but also allowing the atomic-scale structural analyses by constructing the three-dimensional structure. However, the theoretical methods also have inherent limitations, such as limited time and length scales, as will be discussed below. To fundamentally understand the structure and properties of metallic liquids, the combination of experimental and theoretical methods has an advantage over either of them. Over a few decades, numerous experimental techniques and computer simulations have been developed to investigate the liquid structure in pure, binary, and ternary alloy systems, such as XRD, neutron scattering, X-ray absorption fine structure, classical MD simulation, ab initio MD simulation, and reverse Monte Carlo. Some review articles have provided an excellent description of various theories, methods, and experimental results [40, 53–55]. Here we just give a brief introduction to them.

2.1 Experimental Methods

2.1.1 X-Ray/Neutron Diffraction

X-ray and neutron diffraction technique are powerful tools to investigate the local and intermediate-range structure of liquids and amorphous solids. In particular, the state-of-the-art synchrotron-based X-ray sources possessing highly collimated, monochromatic, high-intensity, and high-resolution features as well as spallation neutron sources enable to measure highly accurate diffraction patterns of disordered systems up to the high q region. When combined with high-efficiency area detectors, it could achieve a continuous monitor of structural evolution as a function of time and temperature. Experimentally, the coherent scattered intensity, $I_c(q)$, is related to the total structure factor through the well-known relationship:

$$S(q) = \frac{\left\langle I_c(q) - |f(q)|^2 \right\rangle}{|\langle f(q) \rangle|^2} + 1 \tag{6.2}$$

where $\langle f(q) \rangle$ is the mean atomic scattering factor $\langle f(q) \rangle = \sum_\alpha c_\alpha f_\alpha(q)$, c_α is the atomic fraction of species (α) for XRD. For neutron diffraction, the mean coherent scattering length $\langle b \rangle = \sum_\alpha c_\alpha b_\alpha$ replaces $\langle f(q) \rangle$. Since X-rays and neutron are scattered by the electrons and nucleus, respectively, the scattering factor $f(q)$ is a function of q for X-ray, while bound coherent scattering length b, the q independent in the case of neutron. Note that when the scattering vector q approaches zero, the structure factor contains thermodynamic information for homogeneous liquids, i.e.,

isothermal compressibility, χ_T, which is a very useful parameter to test the consistency of theoretical calculations and experimental measurements [56]:

$$\lim_{q \to 0} S(q) = \rho k_B T \chi_T \qquad (6.3)$$

where ρ is the atomic number density, k_B is the Boltzmann constant and T is the absolute temperature.

The structure of disordered system can be described in real space in terms of PCF $g(r)$ which is a measure of the probability of finding an atom at a distance r away from a given reference atom. Given the electron density approximation, the $g(r)$ can be obtained by Fourier transformation of $S(q)$ over all values of q from zero to infinity, as defined in Eq. 6.2. However, in real experiments, the available q values are limited by instrument design to a range from q_{min} to q_{max} so from a practical perspective the equation is re-written as

$$g(r) = 1 + \frac{1}{(2\pi)^2 \rho_0 r} \int_{q_{min}}^{q_{max}} 4\pi q^2 [S(q) - 1] \frac{\sin(qr)}{qr} dq \qquad (6.4)$$

The quality of collimation usually determines q_{min}, and for most instruments, it is sufficiently small that the terms from the transformation can be negligible. The upper limit q_{max} has a significant impact on the Fourier transformation, especially at low r region of $g(r)$ where spurious oscillation appears when terminating the integration for a low q_{max} value [57–59]. In order to eliminate these termination ripples or errors, a large value of q_{max} is always expected in the practical experiments. However, it should be noted that extending the range of q might increase noise due to statistical errors, as discussed by Toby and Egami [57]; thus a suitable q_{max} has to be chosen by balancing termination error and noise. By using synchrotron radiation source at the ID-11-C at APS, we have succeeded in measuring structure factor of liquid GaIn up to $q \sim 20$ Å^{-1} with good statistics in Fig. 6.1, and consequently the high quality of PDF is obtained with low r fluctuations.

Another widely used correlation function in real space is the reduced PCF, $G(r)$, defined as

$$G(r) = 4\pi r \rho_0 (g(r) - 1) \qquad (6.5)$$

Compared with $g(r)$, the main advantage of $G(r)$ is that this function can be directly obtained from the Fourier transformation of $S(q)$ with no need of the average number density, ρ_0. Furthermore, at low r region, the slope of the function is proportional to ρ_0. When we performed a series of in situ XRD studies of temperature dependence of liquid structures, $G(r)$ has become a good choice for characterizing their structural evolution, especially if the liquid density is unknown. Radial distribution function (RDF(r)) is also one important structure parameter in describing the local structure of disordered system, given by

$$RDF(r) = 4\pi r \rho_0 r^2 g(r) \tag{6.6}$$

which can be integrated to obtain the average number of neighboring atoms in a coordination shell

$$\overline{n} = \int_{r_1}^{r_2} RDF(r) dr = \int_{r_1}^{r_2} 4\pi r \rho_0 r^2 g(r) dr \tag{6.7}$$

where r_1 and r_2 are the integration limits of the peak in $g(r)$. The atoms around a central atom are separated into shells of first, second, third, etc., with the increased distances with the central atom. The average number of atoms in the first shell is often called the nearest coordination number, CN for short, indicating a possible geometrical arrangement of the atoms surrounding a given atom or short-range order. It should be noted that the definition of the limits of the first shell is somewhat arbitrary and four methods are proposed in the literature, including fitting and integrating the area of the first symmetrical peaks in $rg(r)$ or $r^2g(r)$, integrating the area of the first peak up to the extrapolated abscissa of the right side of the first peak in RDF or to the first minimum between the first and second peaks in RDF, as reviewed by Waseda [60]. Figure 6.3 gives the schematic diagram of RDF for determining the CN. One could get different values by adopting different methods, and sometimes a more reasonable CN is expected by averaging them.

In simulations, Voronoi tessellation [61] provides another sophisticated approach to determine CN, which defines the minimum volume polyhedron around a given atom whose faces are composed of the perpendicular bisecting planes of the vectors pointing from the central atom to the neighbors. The total number of faces of a polyhedron is equivalent to the CN. To avoid the involvement of atoms beyond the first coordination shell, sometimes those small surface areas are ignored, or the cutoff radius of coordination sphere is predetermined according to the minimum between the first and second peaks in PDF. In our studies [62–66], we often evaluate the CN by integrating the area of the first peak up to the first minimum in RDF in Fig. 6.3d and the Voronoi analysis and find although different values might be obtained, that it does not affect the relative variations of CN with temperature or pressure. Similar conclusion was also supported by Schenk et al. who studied the temperature-dependent structural evolution in liquid zirconium [9].

For multicomponent alloys, only total structure factor or total PCF is not insufficient to describe the chemical and topological SRO in the disordered system. Therefore, it is necessary to extract information on element-resolved partial $S(q)$. In practice, there are a few somewhat different definitions of partial $S(q)$, such as Faber-Ziman formalism [67], Ashcroft-Langreth formalism [68], and Bhatia-Thornton formalism [69]. The most usual form for these partials is the Faber-Ziman (FZ) formalism, given by
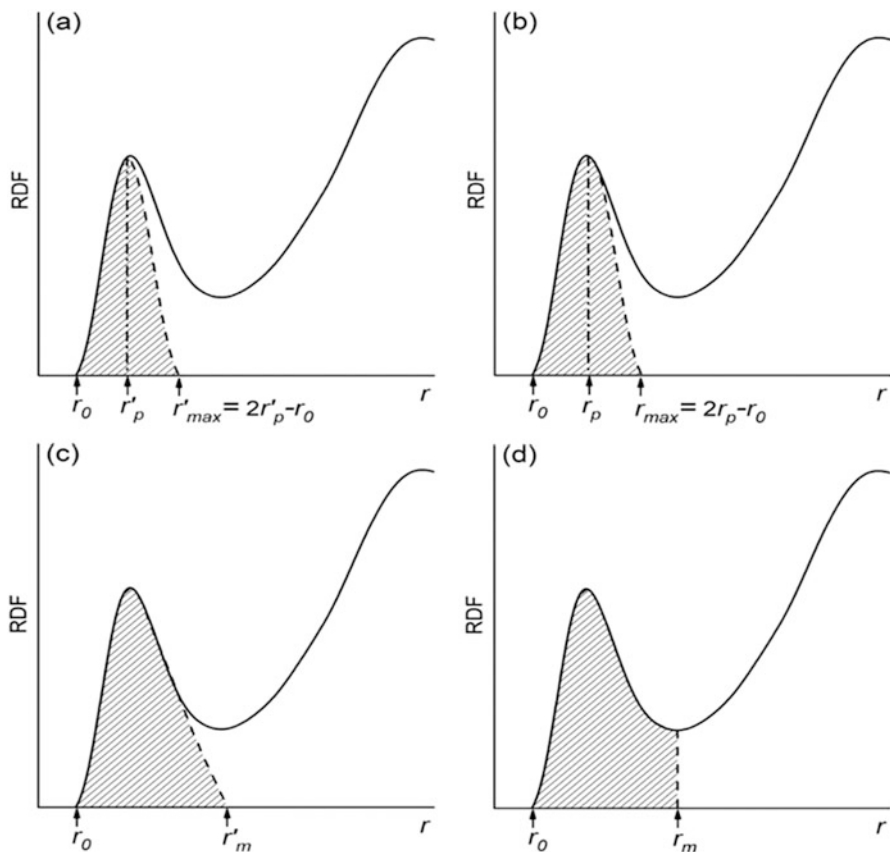
Fig. 6.3 Schematic diagrams of RDF for extracting the CN in terms of four different integration limits. r_0 is considered to be the left-hand edge in RDF. (**a**) r'_p and r_p denote the peak position of the first symmetrical peak in (**a**) $rg(r)$ and (**b**) $r^2 g(r)$ curves, respectively. r'_{max} and r_{max} are the corresponding right-hand integration limit of the first peak made symmetrical than on the left. r'_m and r_m are (**c**) the extrapolated abscissa of the right-hand side of the first peak in RDF and (**d**) the first minimum between the first and second peaks in RDF. (Reprinted from Ref. [60], with permission @1980 by McGraw-Hill Inc.)

$$S(q) = \sum\nolimits_{\alpha,\beta=1}^{n} c_\alpha c_\beta f_\alpha(q) f_\beta(q) \left(S_{\alpha\beta}(q) - 1 \right) \tag{6.8}$$

where α and β represent the different atomic species in the material with n chemical species, $S_{\alpha\beta}(q)$ is the FZ partial structure factors, and $f_\alpha(q)$ is the scattering factor of species α that has to be replaced by b_α in the neutron case.

The partial structure factors are related to the partial correlation function as follows:

$$S_{\alpha\beta}(q) = 1 + \rho_0 \int_0^\infty 4\pi r^2 \left[g_{\alpha\beta}(r) - 1 \right] \frac{\sin(qr)}{qr} dr \tag{6.9}$$

and

$$g_{\alpha\beta}(r) = 1 + \frac{1}{(2\pi)^3 \rho_0} \int_0^\infty 4\pi q^2 \left[S_{\alpha\beta}(q) - 1 \right] \frac{\sin(qr)}{qr} dq \tag{6.10}$$

Experimentally, it is possible to obtain the partial structure factors through anomalous XRD [55, 70] and isotopic substitution in neutron diffraction [55]. The atomic scattering factor is nearly independent of the X-ray energy except near the absorption edge of the atom. That means if one intentionally tunes the X-ray energy to the absorption edge of a particular element, the scattering spectrum from this element would vary strongly with energy, known as the anomalous scattering, while the scattering from other elements remains more or less constant. By taking advantage of this special nature of interaction between an atom and X-ray, one can solve the partial structure factors [71, 72]. For example, Waseda et al. [71] applied this technique combined with neutron diffraction pattern to derive the three partial structure factors of GeO_2 glass in Fig. 6.4a, b. But because the X-ray energy is limited in the vicinity of absorption edge of atom, the resulting data are often of low q_{max}. On the other hand, since the neutron scattering length of an element is usually different for different isotopes, isotopic substitution can be used to label a specific element without affecting the chemical composition and structure of the material. Taking a binary Ag_2Se alloy as an example performed by Barnes et al. [73] in Fig. 6.4c, d, all the partial structure factors are determined by obtaining the total neutron structure factor for three samples with the identical chemistry and structure but composed of different isotopes. In principle, by using isotopic substitution for every element, all the partial structure factors can be determined. However, it is difficult to implement in practice, especially if the sample contains more than two elements and the preparation is too difficult to ensure the identical structure. Despite the shortcomings of both methods, since neutron and X-ray interact with matter in different ways, a combination of them provides diffraction data with different contrasts. Salmon et al. offered a good example of the utility of a combination of neutron diffraction and XRD in determining the ion-valence electron partial structure factor and the valence electron form factor in liquid lithium [74], offering additional constraints on the RMC modeling to make the resulting configurations more reliable [53], as discussed in 3.2. In recent years, combined with various levitation techniques, the use of neutron diffraction or high-energy XRD has provided the best way to study the structure of the high-temperature and supercooled liquids [9, 10, 15, 17, 19, 75–77].
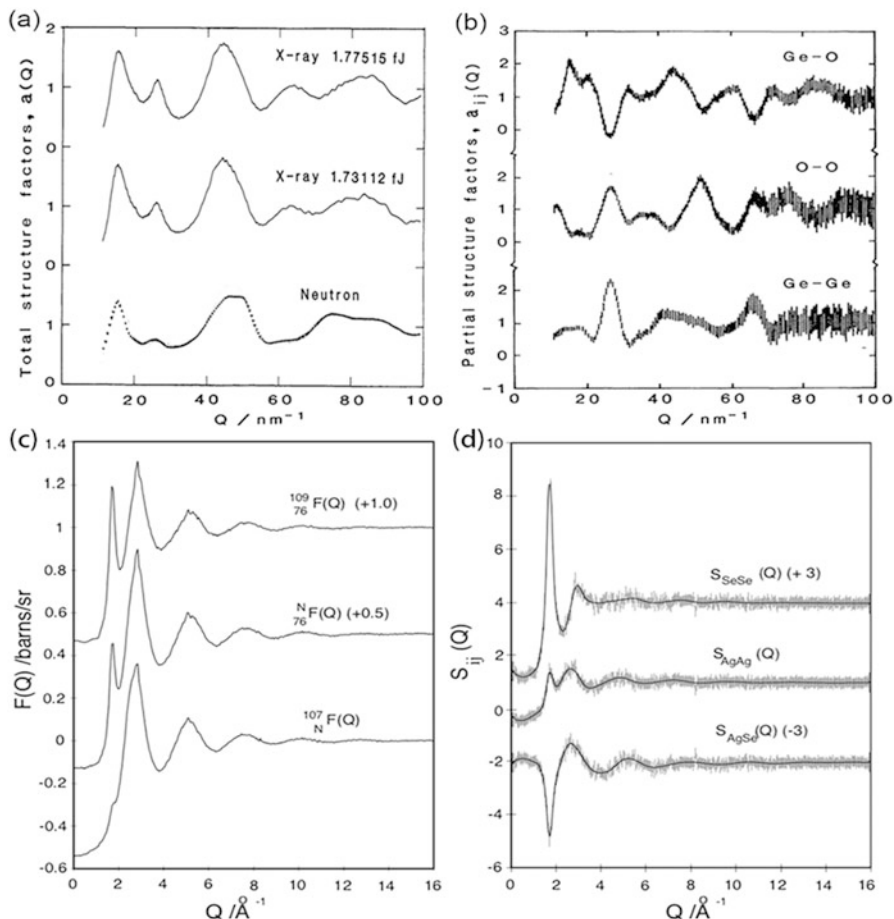
Fig. 6.4 (**a**) Three sets of the diffraction data of amorphous GeO_2 obtained from the anomalous X-ray scattering at the Ge K absorption edge and the conventional neutron diffraction measurements. (**b**) Three partial structure factors of GeO_2 glass estimated directly from the diffraction data of (**a**) (Reproduced from Ref. [71], with permission @1990 by The Japan Institute of Metals). (**c**) The total interference functions $F(q)$ measured by neutron diffraction experiments for liquid Ag_2Se samples with three different isotopic compositions. "Net" indicates the natural isotopic composition. (**d**) Experimental partial structure factor for liquid Ag_2Se alloys determined via the technique of neutron diffraction with isotopic substitution. (Reproduced from Ref. [73], with permission @1997 by IOP Publishing Ltd.)

2.1.2   X-Ray Absorption Fine Structure

Extended X-ray absorption fine structure (EXAFS), along with X-ray absorption near-edge structure (XANES), is a subset of X-ray absorption spectroscopy, which measures the absorption of X-rays by a sample as a function of X-ray energy. The X-ray absorption coefficient of a material can be given by

Fig. 6.5 X-ray absorption spectrum of Ga foil, including XANES and EXAFS
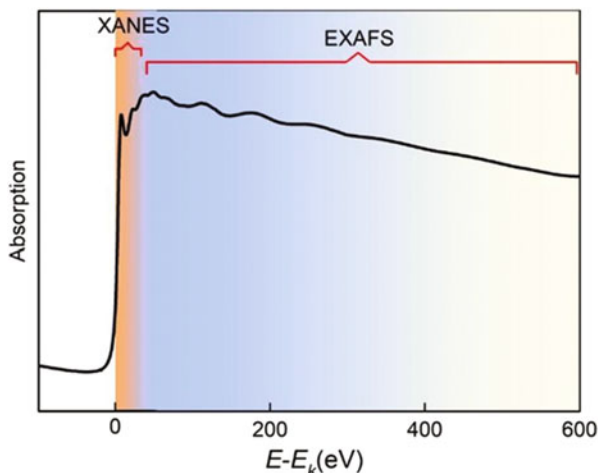
$$\mu(E) = \frac{1}{d} \ln\left(\frac{I_0}{I}\right) \tag{6.11}$$

where E is the X-ray photon energy, is the transmitted X-ray intensity in measurements, I_0 is the incident X-ray intensity, and d is the thickness of the sample. Generally, X-ray absorption coefficient of a material decays exponentially when the energy of the incident X-ray beam matches or is greater than the binding energy (E_0) of a bound electron of an atom. The electrons are emitted by the photoelectric effect described by Einstein, resulting in a sharp increase in X-ray absorption at specific energy E_0, the absorption edge of a particular element. Each element has a set of unique absorption edges corresponding to different excitation energies of its inner shell electrons. X-ray absorption fine structure (XAFS) refers to the oscillatory structure in the X-ray absorption coefficient just above an X-ray absorption edge in Fig. 6.5, which is attributed to a quantum interference phenomenon between the photoelectron from the excited core atom and the electrons in the surrounding non-excited atoms. Therefore, by measuring the XAFS spectrum, one can provide element-specific information on the local environment. The XAFS spectrum is defined as

$$\chi(E) = [\mu(E) - \mu_0(E)]/\Delta\mu_0 \tag{6.12}$$

where E is the X-ray energy, $\mu(E)$ is the absorption coefficient, $\mu_0(E)$ is the relatively smooth atomic-like background absorption, and $\Delta\mu_0$ is a normalization factor that arises from the net increase at the absorption edge.

The low-energy XAFS spectrum within the first 50 eV above the absorption edge is generally referred to as the XANES, which exhibits some strong absorption peaks (Fig. 6.5) dominated by the multiple scattering resonances, thus enabling the local chemical information in complex and disordered materials. Although the

fundamental multiple scattering formalism of X-ray absorption is well established, the interpretation and calculation of XANES are still a challenge [78]. In contrast, from approximately 50 to 1000 eV, above the absorption edge is termed the EXAFS, in which the photoelectron is scattered by a relatively simple way, mainly arising from the single scattering contributions [79]. The standard EXAFS function is given by

$$\chi(k) = \sum_R S_0^2 N_R \frac{|f(k)|}{kR^2} \sin(2kR + 2\delta_c + \phi)e^{-2R/\lambda(k)}e^{-2\sigma^2 k^2} \tag{6.13}$$

where k is the so-called photoelectron wave vector, R is the interatomic distance between the absorber atom and the neighboring atoms, N_R is the coordination number, $f(k)=|f(k)|e^{i\Phi(k)}$ is the backscattering amplitude, δ_c is central-atom partial-wave phase shift of the final state, $\lambda(k)$ is the energy-dependent photoelectron mean free path and σ represents the fluctuation in R by thermal motion and the structural disorder. A few ab initio computer codes have been developed for the calculation of experimental EXAFS, e.g., IFEFFIT program [80], and then by Fourier transforming the experimental $\chi(k)$ to the real space PCF, the local structural information around the absorber atom is extracted, including the coordination number and interatomic distance.

Although XAFS has been recognized as a suitable tool to probe the local structure of disordered system, it is rarely applied to metallic liquids, especially for the high-temperature liquids. That is largely due to the experimental difficulties in preparing the uniform and stable liquid specimen as thin as several micrometers to be penetrated by X-rays [81, 82]. Recently, in terms of tablet specimen with 10 mm diameter and 1 mm thickness that were prepared pressing the mixtures of the well-ground sample powder and boron nitride powder, Su et al. [83] successfully applied in situ EXAFS technique to explore the temperature dependence of local structural evolution around Au and Ga atoms in the liquid $Au_{44}Ga_{56}$ eutectic alloy. As shown in Fig. 6.6, a series of the k^2 – weighted $\chi(k)$ spectra of Au L_{III}-edge and Ga K-edge and corresponding nonphase-corrected R-space spectra were given in the temperature range of 800–1073 K. By analyzing the temperature-dependent peak areas that is related to the coordination number, they observed a significant local atomic packing change at about 970 K around Ga atoms. Similar conclusion was also supported by subsequent high-energy XRD and ab initio MD simulations.

2.2 Theoretical Methods

In the 1970s, the theory of liquids was rapidly developed for understanding and predicting the properties of simple liquids and their mixtures [84–86]. For a given interatomic potential of a simple liquid, its properties can be obtained from the methods of statistical mechanics [85], initially including various forms of perturbation theories, such as Barker and Henderson (BH) theory [87, 88]; Week, Chandler,
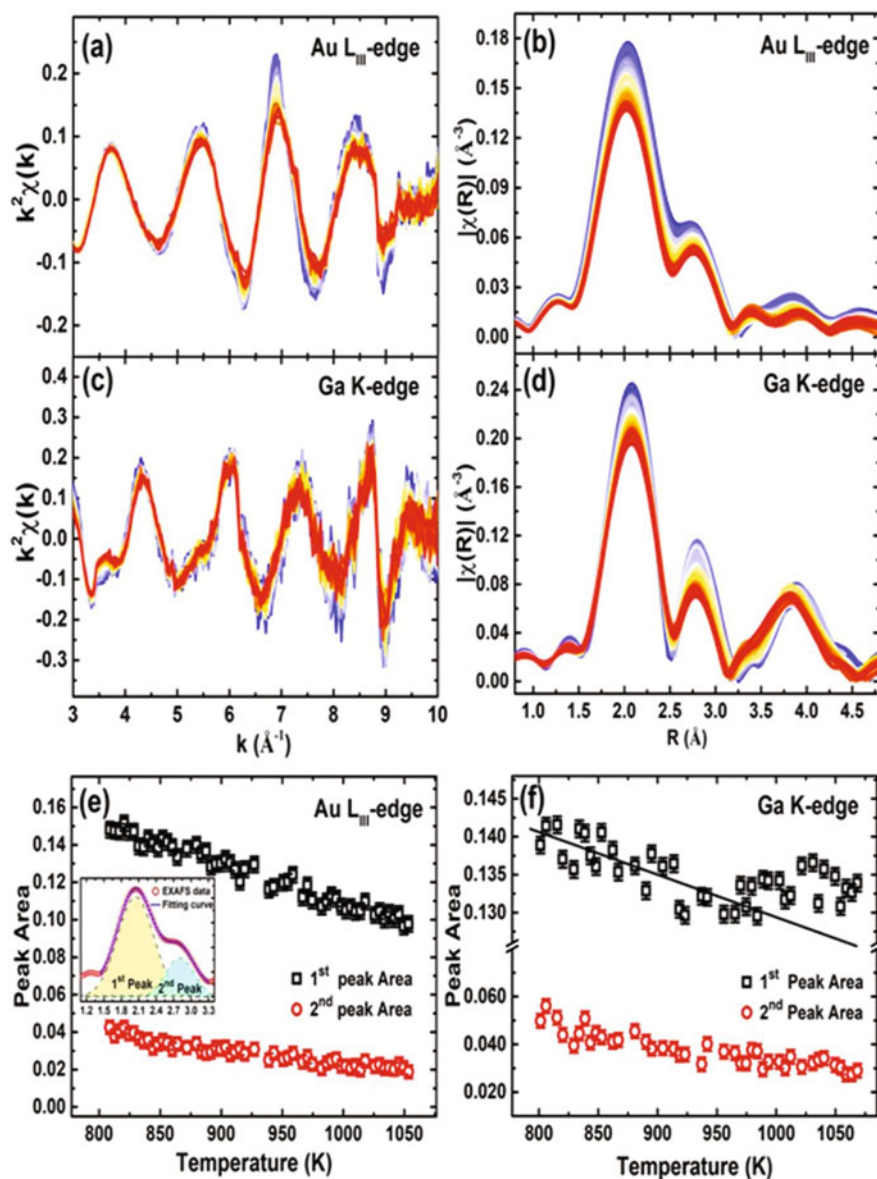
Fig. 6.6 (**a** and **c**) The k^2 – weighted (k) spectra of Au L$_{III}$-edge and Ga K-edge of liquid Au$_{44}$Ga$_{56}$ alloy obtained from in situ EXAFS in the temperature range of 800−1073 K, respectively. The blue and red lines represent the structure at low and high temperatures, respectively. (**b** and **d**) The nonphase-shift-corrected R-space spectra at the Au L$_{III}$-edge and Ga K-edge of liquid Au$_{44}$Ga$_{56}$ alloy by Fourier transform of k^2 – weighted spectra, respectively. (**e** and **f**) The temperature-dependent evolution of two peak areas of R-space spectra at the Au L$_{III}$-edge and Ga K-edge, respectively. (Reproduced from Ref. [83], with permission @2019 by the American Physical Society)

and Andersen (WCA) theory [89]; and optimized random-phase approximation (ORPA) [90], as well as some integral equations for PCFs, such as the Percus-Yevick (PY) approximation [91], mean spherical approximation (MSA) [92, 93], hypernetted-chain (HNC) approximation [94], and their modified forms, like hybridized mean spherical approximation (HMSA) [95] and modified hypernetted-chain (MHNC) approximation [96]. Recently, with the rapid development of modern computers, a variety of direct computer simulation techniques ranging from classical simulation techniques to quantum mechanical methods based on the density functional theory (DFT) ushered in a rapid development. For studies of metallic liquids, the most commonly used simulations include reverse Monte Carlo (RMC), classical MD simulation, and ab initio MD simulation (AIMD), which help construct and visualize the three-dimensional structure of the liquids.

RMC modeling technique has also been used successfully to model the structures of liquids and amorphous materials. The review of this technique and its application to metallic liquids and glasses has been given by McGreevy [53, 97]. The goal of RMC modeling is to produce a plausible structural model, also referred to as a configuration that can reproduce one or more sets of structural parameters, such as PCF and structure factor, derived from experimental measurements. Thus, RMC modeling is not a stand-alone computational method but relies on external input as constraints. There are many different sorts of experimental data that can be used with RMC modeling, such as structure factor and PCF from neutron, X-ray and electron diffraction, XAFS, fluctuation electron microscopy, and nuclear magnetic resonance signals. With the structure factor as the fitting parameter, the algorithm can be summarized as follows: (1) Create an initial configuration with periodic boundary conditions, and calculate the PCF $g^o(r)$ from the configuration. (2) Fourier transform $g^o(r)$ to structure factor $S^o(q)$, and calculate the difference between the measured $S_e(q)$ and predicted $S^o(q) \left(\chi_0^2 = \sum_{i=1}^{m} (S^o(q_i) - S^e(q_i))/\sigma^2(q_i) \right)$, where the sum is over the m experimental points and σ nominally represents the experimental error. Superscripts e, o, and the following n means experiment, old, and new configurations. (3) Randomly move atoms to generate a new configuration, and calculate the new structure factor $S^n(q)$ and difference $\left(\chi_0^2 = \sum_{i=1}^{m} (S^o(q_i) - S^e(q_i))/\sigma^2(q_i) \right)$. (4) If $\chi_n^2 < \chi_0^2$, it is accepted, namely, the new configuration becomes the old one; if $\chi_n^2 > \chi_0^2$, it is accepted with probability $\exp\left(-\left(\chi_n^2 - \chi_0^2\right)/2\right)$. When repeating steps 3 and 4, χ^2 will decrease gradually until it reaches a predetermined tolerance. Hereto, a resulting three-dimensional atomic configuration is achieved, which is consistent with the experimental data within a certain error. In order to obtain a physically stable and meaningful configuration, multiple independent data should always be fitted simultaneously [62, 98–100]. Although RMC modeling does not yield a unique configuration, it really helps provide structural information that is not accessible directly from the experiments as well as to understand the relationship between structure and some physical properties of interest. Specifically, since the random movement of atoms in RMC modeling is realized by probabilistic statistics, it tends to produce the most disordered structure that is consistent with the experimental structural parameters within the given tolerance and cannot simulate the dynamic properties of atoms.

In MD simulations, Newton's equations of motion are iteratively solved to obtain the time-dependent positions and trajectories of each atom from which it is possible to trace the atomic structure evolution as a function of time and temperature and to extract various thermodynamics parameters and correlation functions by using statistical mechanics and thermodynamics, thereby providing an effective means for calculating the structure, dynamic, and thermodynamic properties of metallic liquids under various conditions [101–105]. Depending on the forces between the atoms and their potential energies, there are two different MD approaches, namely, classical MD, which is based on the use of empirical interatomic potentials parametrized to experimental data, and AIMD, which often adopts density functional theory (DFT) to calculate the interactions among the atoms in the ensemble. The classical MD allows the simulation of a few millions of atoms over periods of a few microseconds, in which the preciseness strongly depends on the effectiveness of force field used in describing interaction between atoms [103–107]. One of the simplest force fields for simulating the metallic liquid is hard-sphere model proposed by Ashcroft and Lekner [108], which has only repulsive nature with one adjustable parameter, namely, the hard-sphere diameter. Later various modified pair potentials were developed by adding an attractive part that extends some distance away from the shell of the sphere [109], enabling us to calculate various properties of some simple liquids, like alkali metals and alkali earth metals, in a meaningful way, e.g., the predication of liquid structure in terms of the structure factor and PCF [110–117]. However, these pair potentials omit a crucial piece of the physics of metallic bonding and so fail to describe the non-simple metallic liquids that possess relatively complex electron structures. Until the end of the 1980s, a great progress has been made in many-body interaction potentials that include the effects of three or more atoms interacting with each other, such as the embedded-atom method (EAM) [118], tight-binding method (TBM) [119], the glue model (GM) [120], and the effective medium theory (EMT) [121]. As for the EAM potential, the total energy is represented by a sum of pair potentials and embedding energies for the atoms whose parameters can be tuned by fitting to some experimental bulk properties to accurately reproduce certain material properties [122]. However, it is not always sufficiently transferable to calculate new properties or new thermodynamics states.

AIMD methods, instead of empirical interatomic potential functions as input, utilize interatomic forces generated directly from the electronic structure calculations based on quantum mechanics, thereby yielding more accurate predictions of atomic structure as well as electronic properties than classical MD methods. Traditionally, the electronic structure is described by using Kohn-Sham (KS) formulation of the DFT [123]. In the Born-Oppenheimer (BO) methods to AIMD, the calculations of electronic structure and the atomic motion are carried out separately [124]. By self-consistently solving the KF formulation, one can obtain the ground-state electronic density and the resulting properties, such as energy, eigenvalue, and forces on the nuclei. The atomic motion follows classical Newton's equations of motion without considering the quantum effect. For each ion step (update of the ion positions), an explicit electronic minimization is required. In contrast to BO-MD, the Car-Parrinello method introduces fictitious electronic dynamical variables, writing an

extended Lagrangian for the system which leads to the coupled equations of motion for both ions and electrons [101]. After the initial standard electronic minimization, the fictitious dynamics of the electrons makes them approach the electronic ground state in the simulation process, thus avoiding resolving the KS formulation for each new ionic configuration. Obviously, the CP-MD simulations greatly save the computing resources compared to the BO-MD and have been successfully applied in describing the structural, dynamical, and electronic properties of metallic liquids. Although high accuracy for the energies, dynamics, and structure can be achieved using the Kohn-Sham version of DFT [123], it is always limited by high computational cost associated with the matrix diagonalization and orbital orthonormalization that limits studied ensembles very small about a few hundreds of atoms on a limited time scale (about picoseconds) [21, 27, 64, 123, 125–131]. To overcome this issue, the so-called orbital-free density functional theory (OF-DFT) has been developed in recent years due to its advantage in numerical simplicity and efficiency [132, 133]. The OF-DFT uses electron density as the sole variable in description of the electronic state and employs a kinetic energy density functional to evaluate the kinetic energy directly from the electron density, rather than electronic orbitals in the KS scheme. Although these simplifications make the OF-DFT less accurate than KS-DFT due to the lack of accurate approximations for the kinetic energy functional, it is possible to perform simulations with the larger number of atoms and longer runs. Studies on the thermodynamic properties and structure of several liquid metals, such as lithium [134, 135], cesium [136], aluminum [137], magnesium [138, 139], zinc [140], iron [141], and noble metals [142], have demonstrated its efficiency.

3   Structural Studies on Metallic Liquids

Since the pseudopotential theory of the crystal structures has been reviewed in 1970 by Heine and Weaire [143], some characteristic trends of the stable crystal structure of elements in periodic table were revealed [144], e.g., (i) the change from metallic structures in Groups I–III to more covalent structures in Groups IV–VI with decreasing coordination number; (ii) an increasing distortion in Group II with increasing the atomic number (Zn and Cd), culminating in a unique structure for Hg; and (iii) a similar phenomenon in Group III of a unique structure for Ga but then a return to a less distorted structure for In and finally to a close-packed structure for Tl as the atomic number increases. It was suggested that some of these trends might persist in the liquid state [145]. Hafner and Jank [115, 146–148] presented systematic investigations of the trends in the structural and electronic properties of liquid IIA, IIB, IIIA, IVA, and VA elements across the periodic table using classical MD calculations. They found that Group II elements from Mg to Hg (Mg, Zn, Cd, Hg) show an increasing distortion of the hard-sphere-like structures. The most pronounced manifestation of this trend is the shape change of the first peak in $S(q)$, from symmetrical as observed in Mg to asymmetrical in Zn, Cd, and Hg [146]. As for Group IVA elements from Si to Pb, a transition from the open, low-coordinated structures of

liquid Si and Ge (CN ~ 6–7) to the close-packed structures of liquid Sn and Pb (CN ~ 10–11) was revealed, accompanied by an electronic transition from a free-electron-like density of states with strong s-p hybridization in Si to well-separated *s* and *p* bands in liquid Pb [147]. The trend of trivalent elements in Group IIIA (Al, Ga, In, Tl) becomes much more complex both in the crystalline and liquid structures [115]. Structural changes are from a close-packed structure in Al (CN = 12 in fcc structure and 11.5 in the melt) to a somewhat loosely packed atomic structure in Ga (CN = 7 in orthorhombic -Ga and 9–10 in liquid Ga), then a return to more regular, close-packed structures in In and Tl (CN = 12 in bct-In, hcp-Tl, and 11.6 in both liquids). Contrary to this nonmonotonic variation in the atomic structure, the electronic density of states shows a gradual transition from a nearly free-electron model in liquid Al to a density of states with a pseudo-gap separating *s* and *p* bands in liquid and crystalline Tl. They argued that all these distorted or open, low-coordinated structures arise from the modulation of the random packing of atoms by the Friedel oscillations in the effective interatomic potentials, but these modulations are damped by relativistic effects, leading to a return to more closely packed liquid structures and to the formation of a characteristic "s-p gap" in the electronic spectrum.

Waseda [60, 110] summarized a large amount of diffraction data of pure elements in the liquid state just above their melting points and classified liquid structures into three different categories according to the shape of the main peak of static structure factor $S(q)$ or the PCF $g(r)$. The first class is the hard-sphere-like simple structure, which exhibits a very symmetrical main peak in both $S(q)$ and $g(r)$. The ratios of the positions between the second and the first peaks in these functions are about $q_2/q_1 = 1.86$ and $r_2/r_1 = 1.91$, and the nearest coordination number (CNs) varies between 9 and 11. Alkali metals (group I, Li-Rb), alkali earth metals (group II, Mg-Sr), Al, Pb, and most transition metals belong to this class. The second class is called the "distorted" liquid structure, which is characterized by the skewed main peak of $S(q)$ or $g(r)$. The ratios of peak positions for q_2/q_1 and r_2/r_1 slightly deviate from ideal values 1.86 and 1.91, respectively, and the CNs are between 10 and 11. The typical examples of this sort are Zn, Cd, Hg, In, and Tl. The third type has an "anomalous" structure, indicated as one shoulders or humps on the high q side of the first peak of $S(q)$ or subsidiary maxima in $g(r)$ located in between the two main maxima. The ratios of peak positions strongly show non-ideal values, and they have low CN around 9 and 10 (6 for Ge and Si). Ga, Si, Ge, Sn, and Bi fall into the type. Waseda's classification has been greatly recognized, but the results strongly depend on the liquid structure near the melting point. As for the liquid structures at the elevated temperatures and how large the temperature effect, more discussion will be given in the following.

Besides the consideration of the first peak of $S(q)$, a clear shoulder on the high q side of the second peak was observed in liquid Fe [9], Ni [9], Co [11], Ti [12], and Zr [9] by Schenk and co-workers who performed a series of energy-dispersive XRD or neutron scattering measurements combined with electromagnetic levitation technique, which becomes more pronounced with increasing the degree of undercooling. They applied some different geometries of local clusters, namely, bcc, fcc, hcp, icosahedron, and dodecahedron, to simulate the structure factor for large q values,

and found that only the ISRO, in particular the larger polytetrahedral aggregates (such as dodecahedra), can well reproduce the particular feature of the second oscillation. For several static and dynamic properties of the liquid 3d transition metals, readers can refer to a recent review given by Del Rio et al. [149]. As discussed in Section 2, the ISRO is believed to dominate the local structure of most pure metallic melts, like copper, but the question is why some elements display an asymmetrical form of the second peak in structure factor, while others do not. Thus next, we summarize more details on the existing experimental and theoretical structural information and properties of some metallic liquids, which have been used in space.

3.1 Magnesium (Mg) and Aluminum (Al)

Magnesium is considered as the simplest divalent metal, which belongs to the group of the alkaline-earth metals, among which magnesium has the lowest melting (923 K) and boiling point (1363 K). The static structure factor of liquid magnesium was first measured by Waseda using XRD technique at 953 K, which displays a very symmetrical principle peak at a position of about 2.42 Å^{-1} [60]. Takeda et al. [150] presented the first neutron diffraction data of liquid magnesium at 953 K and estimated the electron-ion correlations by utilizing the difference of structure factor compared with Waseda's data. It is well known that neutrons, being scattered by nuclei at the centers of ions, determine the ionic structure factor, while X-rays are scattered by electrons, which include both core electrons bound to ions and valence electrons surrounding them. In general, the measured structure factors derived from different scattering mechanisms are almost coincident within the experimental errors, but small differences can still be detected by sufficiently accurate measurements, from which the electron-ion and electron-electron correlations may be extracted. Recently, Tahara et al. [151] performed another X-ray and neutron diffraction experiments and discussed the static structure of liquid magnesium and the electron-ion correlation. The overall feature of new measured structure factors resembled with the earlier data of Waseda and Takeda, but the height of the first peak was larger, and the second oscillation exhibited an asymmetry shape that cannot be reproduced by the hard-sphere model. The peculiar feature of the second peak in structure factor was also found in several transition metals, such as Fe [9], Ni [9], Zr [9], Co [11], and Ti [12], which could be related to the icosahedral short-range order.

Many theoretical works have been reported to study the static structure and thermodynamic properties of liquid magnesium through the use of various effective interatomic potentials constructed either by fitting to experimental data or derived from some approximate theoretical models. Although the lack of consistency between various potentials in many aspects, such as the height of the positive hump beyond the minimum, the depth of potential valley at the nearest neighbor distance, and the strength of Friedel oscillation at the longer distance, it is possible to obtain a good description of liquid structure of magnesium. For example, 20 years

ago Hafner [146] calculated the atomic and electronic structures of the liquid divalent metals near the melting point, including magnesium, by using effective interatomic pair potential derived from the first-principle optimized plane wave (OPW) pseudopotentials of Harrison. The theoretical calculations for both static structure factor and PCF based on the classical MD simulation showed good agreement with the available XRD data of Waseda [60]. In addition, the electronic density of states (DOS) indicated that among all alkali earth metals, only liquid magnesium was reasonably well described by the nearly free-electron model. A deep minimum was observed in the DOS of liquid beryllium at the Fermi level, and the electron structures of calcium, strontium, and barium were much complicated due to the partial occupation of the d band. González et al. [152] presented the calculation of the liquid structure of the alkaline-earth metals (Be, Mg, Ca, Sr, and Ba) near their melting points by combing the neutral-pseudoatom (NPA) method-derived interionic pair potentials with the variational modified hypernetted-chain equation (VMHNC) theory of liquids. Their predicated results yielded good agreement with those of experimental data for all alkaline-earth metals, apart from the fact that the height of the main peak in the simulated structure factor and PDF was higher than those deduced from the experiments. By using the same effective pair potential, Alemany et al. [116] performed MD simulations to study the static structure and dynamic properties of liquid alkaline-earth metals (Mg, Ca, Sr, and Ba). Likewise, their simulated structure factor and shear viscosity were also consistent with the available experimental data. Kang [153] utilized the perturbative hypernetted-chain (PHNC) equation to model the liquid alkaline-earth metals (Be, Mg, Ca, Sr, and Ba) in combination with optimized nonlocal model potential (OMP) proposed by Shaw. A reasonable structure factor and PDF near melting point was predicated compared with experiments other than Ba. Recently, Wax et al. [117] performed another MD simulation to investigate the static structure, dynamic, and thermodynamic properties of liquid alkaline-earth metals (Be, Mg, Ca, Sr, and Ba), where an effective pair potential obtained from the second-order pseudopotential perturbation theory originally developed by Fiolhais et al. [154] was applied in the simulations. The agreement between the structure factor and binding energy obtained experimentally and by MD simulations was also satisfactory. However, different trends were observed in self-diffusion coefficient from Mg to Ba when compared with the results of Alemany et al. [116], which displayed a monotonous decrease, while Wax's calculations indicated that Mg has smaller self-diffusion coefficient than Ca. Different pair potentials produce the similar liquid structures but might result in different dynamic properties; thus the self-diffusion coefficient could be used as an effective variable to judge the quality of potentials applied. Unfortunately, the experimental data on dynamic properties are scarce for alkaline-earth metals; thus it cannot determine which potential is more reliable now.

The first-principle MD simulations were also undertaken to study the static structural and dynamic properties of liquid magnesium. The first Kohn-Sham ab initio MD (KS-AIMD) simulations of liquid magnesium were performed by de Wijs et al. [155] who used 90 atoms to calculate atomic and electronic structures near the melting point. Their calculations provided a correct description of liquid structure
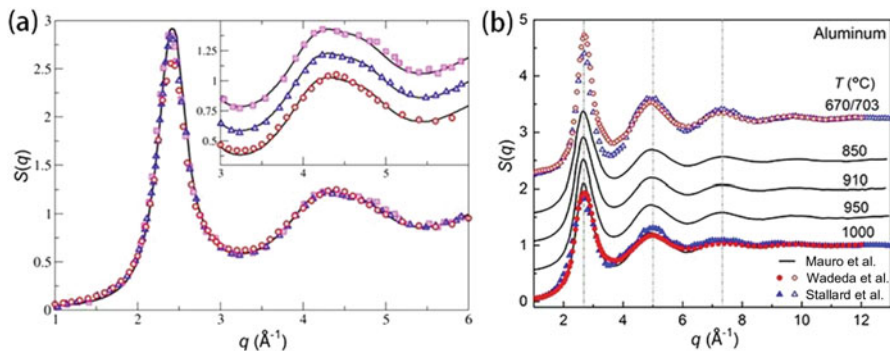
Fig. 6.7 (**a**) Static structure factor of liquid magnesium at 953 K. (Open circles) Experimental X-ray diffraction data from Waseda [60]. (Triangles and squares) Experimental X-ray diffraction and neutron scattering data at 973 K from Tahara et al. [151]. (Continuous line) OF-AIMD simulations calculated by Sengül et al. [139]. The inset shows the comparison of the second peak. (**b**) Static structure factor of liquid aluminum at various temperatures. (Continuous line) High-energy X-ray diffraction data measured by Mauro et al. [162]. (Filled and open circles) X-ray diffraction data from Waseda [60] at 670 °C and 1050 °C. (Filled and open triangles) Neutron scattering data from Stallard et al. [161] at 703 °C and 1029 °C

and the valuable insights into the ion-electron correlation. To reduce the computational cost, Anta et al. [138] used orbital-free ab initio MD (OF-AIMD) method to simulate the liquid magnesium, whose results were virtually coincident with those of KS-AIMD simulations. Later, Sengül and co-workers [139] also used OF-AIMD method to calculate several static and dynamic properties of liquid magnesium. As shown in Fig. 6.7a, their calculated structure factor well reproduced the XRD and neutron diffraction data of Tahara et al. [151], particularly for the height of the first peak and the asymmetrical shape of the second peak in structure factor. In addition, the OF-AIMD results indicated that the liquid magnesium was dominated by the fivefold symmetry containing a considerable amount of perfect and defective icosahedral short-range order. The calculated dynamic structure factor showed a reasonable agreement with the experimental IXS data of Kawakita et al. [156], and transport coefficients, i.e., self-diffusion coefficient (0.51 $\text{Å}^2 \text{ ps}^{-1}$) and shear viscosity (1.35 GPa), compared to the CMD results of Alemany et al. [116]. So far, the studies of liquid magnesium are confined near the melting point. Debela et al. [157] presented the detailed studies of temperature-dependent structural evolution of liquid magnesium by sorting to a series of AIMD calculations. During cooling from 1700 K to 900 K, they found that the interatomic distance and the nearest neighboring coordination number both increase in the liquid and undercooled liquid magnesium. Using various local structural analysis methods, they revealed that further cooling resulted in the formation of metastable body-centered cubic-like nuclei at about 800 K which finally transformed into stable hexagonal closed-packed phase at low temperatures. Such crystallization pathway was consistent with the predication by Alexander and McTague that bcc ordering near the melting point could be easily formed in the undercooled liquid of elements.

Aluminum is the most abundant metal and the third richest element in the earth's crust after oxygen and silicon. Due to its low density of 2.73 g/cm^3, high electric and thermal conductivity, excellent weldability, great strength, and good resistance to corrosion through surface passivation, aluminum, and its alloys have been extensively used in modern aerospace, automotive, transportation, and construction industries. Aluminum products are generally prepared by quenching the high-temperature melts; thus the deep understanding of its liquid structure and accurate control of the microstructure evolution in pure aluminum and aluminum-based alloys is of major importance in the production process for specific applications. At ambient condition, liquid aluminum crystallizes into the face-centered cubic structure with CN = 12 atoms at a distance of 2.86 Å.

Considerable experimental and theoretical studies have been made to explore and understand liquid structure and dynamics of aluminum near the melting temperature, but only a few focused on the structural change caused by temperature variation. The earlier studies on liquid structure of aluminum were performed by Gamertsfelder [158], Black and Cundall [159], and Fessler et al. [160] who used XRD technique to obtain the radial distribution function of liquid aluminum at several temperatures within the range of 670–1000 °C, but the quality of these data are poor. Later, Waseda et al. [60, 161] provided relatively accurate structure factor for liquid aluminum at 670, 750, and 1050 °C using XRD technique. As the temperature increases, the positions of the peaks of structure factor remain nearly unchanged, but their breadths significantly increase, and peak amplitudes decrease. The measured structure factors showed a very symmetrical main peak located at about 2.68 Å. The ratio (q_2/q_1) of the position of the first peak (q_1) to that of the second peak (q_2) is 1.85, in accordance with those of simple liquid metals, such as alkali metals which is rather well described by a dense random packing of hard spheres. The same ratio (q_2/q_1) value and variation of peaks were also revealed by Stallard and Davis [162] who first measured the structure factor in a large q region ($0<q<15$ Å^{-1}) using neutron diffraction technique at 703 °C and 1029 °C. Recently, Mauro et al. [163] used high-energy synchrotron XRD combined with electrostatic levitation techniques to produce a series of high-quality diffraction data and PCFs of liquid aluminum in the temperature range of 850 °C to 1000 °C in Fig. 6.7b. Consistent with previous studies, the primary peak position of structure factor remains nearly unchanged at about 2.68 Å^{-1} with increasing temperature, but the amplitude decreases significantly. Their atomic structural analyses by using reverse Monte Carlo simulations indicated that liquid aluminum contained a high degree of icosahedral order and a modest amount of body-centered cubic (bcc) order.

The hard-sphere model was the most commonly used to describe the simple liquid metals, for example, Ashcroft et al. [108] and Vahvaselkä [164] calculated the S(q) for hard spheres according to the Percus-Yevick equation with the packing density of 0.45, which reproduced the main peak of experimental S(q) of liquid aluminum at 667 °C. Later, Gopala Rao and Murthy [165] introduced a square-well potential on the hard-sphere reference system and reproduced the experimental

structure factor and radial distribution function of liquid aluminum at 670 °C and 750 °C. Molecular dynamic (MD) simulations were also used to investigate the liquid aluminum.

For example, Ebbsio et al. [166] reported the first MD simulations of structure and dynamics studies of liquid aluminum near the melting temperature using three different pair potentials in which two of them were deduced from nonlocal pseudopotentials and the other one based on local Ashcroft pseudopotential. Despite difference in shape of three potentials, the static structure factors and PDF obtained showed an overall similarity, which agreed with the experimental data, whereas the calculated dynamic structure factors deviated from the experiments. Hafner and Jank [115] systematically studied the atomic and electronic structures of the trivalent metals Al, Ga, In, and Tl by using classical MD simulations. Their MD results showed a complex trend in the liquid structures from Al to Tl as mentioned above. Moreover, the calculated structure factor and PCF in liquid aluminum based on a local empty-core potential and an optimized nonlocal pseudopotential with relativistic core functions both yielded an excellent agreement with experiment. Li et al. [167] simulated the cooling process of the liquid aluminum with different cooling rates by the use of a semi-empirical tight-binding potential. Their calculated PDF and local structural analyses revealed that the different cooling rate would lead to a different microstructure in the system, e.g., fast cooling rate favors the formation of amorphous structure, and slow cooling rate leads to crystallization. Similar studies on the solidification of liquid aluminum were also reported by Shen et al. [168] and Hou et al. [169] who pointed out that the liquid and glassy aluminum are predominated by icosahedral clusters, but the former overestimated the amount of face-centered cubic and hexagonal close-packed SROs compared with Hou's MD simulations [169] and Mauro's RMC results [163].

There exists a variety of pseudopotentials that are derived from first-principle calculations, or fitted and parameterized to certain experimental data, all of which should, in principle, yield similar results for any given property in the same system. However, the fact is that the choice of pseudopotential greatly affected the final results. As discussed by Jiang et al., they systematically examined the thermodynamic and structural properties of aluminum using MD simulations derived from seven embedded-atom potentials over a wide temperature range [170]. Consequently, they found MKBA potential [171] could yield the best liquid structure at 973 K, while MDSL [172], WKG [173], and ZJW potentials [174] predict either a little more ordered or disordered liquid structure in comparison with the XRD result. In addition, MKBA and MDSL potentials could give quite accurate prediction of thermodynamically equilibrated melting points and were confirmed much more suitable for the description of solid-liquid phase transition of aluminum than others.

To overcome the influence of pair potential option, a different approach based on the density functional theory (DFT) was developed, like Kohn-Sham ab initio MD (KS-AIMD) and orbital-free (OF)-AIMD simulations, which determined the liquid structure and properties via the self-consistent electronic structure calculations instead of model interaction potentials. For instance, Alemany et al. [126] studied the static, dynamic, and electronic properties of liquid aluminum near its triplet point

(1000 K) by means of 205-particle KS-AIMD simulations, giving results in good accordance with experiments. Appling the same scheme, Fang et al. [175] simulated the cooling process of liquid aluminum with 108 atoms and revealed the competition between icosahedral and face-centered cubic (fcc) short-range orders in normal and undercooled liquid of aluminum. In terms of OF-AIMD simulations, Anta et al. [138] calculated the ionic and electronic structure of liquid aluminum near the melting point using 115 atoms, and González et al. [137] described the liquid static structure as well as dynamic properties of aluminum at 943 K and 1323 K with 500 atoms. Although the system size of AIMD simulation is limited to a few hundred atoms compared with the thousands of classical MD, the calculated static and dynamic properties of liquid aluminum showed a satisfactory agreement with the experimental data. Recently, by using AIMD, Jakse and Bryk [176] studied the structure and dynamics of liquid Al with pressure along the melting line-up to 300 GPa. They found that the liquid Al undergoes uniform compression with pressure associated with a competition of the existing icosahedral local order with bcc ordering above 200 GPa. Dispersion of collective excitations indicates the presence of two non-propagative branches of transverse modes in the second pseudo-Brillouin zone. Under pressure, the second high-frequency branch manifests as the second peak position in transverse current correlation functions, while it corresponds to a smeared-out high-frequency shoulder at ambient pressure. The peak locations in vibrational density of states are closely related with the two transverse collective excitations and their linear evolution with density.

3.2 Titanium (Ti) and Zirconium (Zr)

Titanium and its alloys are widely used in aerospace, marine, military, industrial processes, medical prostheses, dental instruments and implants, sporting goods, and other areas, due to their excellent mechanical properties, high strength-to-density ratio, and strong corrosion resistance. Accurate measurements of the thermophysical properties of liquid titanium and understanding of its structure are very important to optimize existing or to design new Ti-based materials with better performance. However, because of experimental difficulties arising from its high melting point (1662 °C) and chemical reactivity, only a few works have been reported on the structure of liquid titanium which has nearly empty d-bands.

The structure factor and PCF of liquid titanium were first obtained in 1975 by Waseda and Tamaki [177] using the XRD technique. A quite symmetrical main peak was observed in structure factor with the peak position $q_1 = 2.45$ Å^{-1}, which remained unchanged with increasing temperature from 1700 to 1850 °C, except a slight decrease in amplitude. Thirty years later, Lee et al. [17] performed another XRD measurement in conjunction with electrostatically levitation technique to investigate the local structure of liquid titanium at temperatures above and below its melting point. Their measured structure factors wholly shifted toward to the high q region compared to those of Waseda [177], with the principle peak located at

$q_1 = 2.65$ Å^{-1}. In addition, a significant shoulder on the right q side of the second oscillation was observed, approximately at $q_{2s} = 5.09$ Å^{-1}, which is even more intense than the second peak locating at $q_2 = 4.66$ Å^{-1}. Although similar shoulder was also reported in other liquid transition metals, like iron [9], cobalt [11], and nickel [9], its intensity was lower than the second peak itself. Moreover, with undercooling, the shape and relative intensity between the second peak and shoulder changes were less than those observed for liquid nickel. Figures 6.8a and 6.11d show the comparison of structure factors for liquid titanium and nickel by using two different levitation (electrostatic levitation vs electromagnetic levitation) and diffraction (X-ray vs neutron) techniques [9, 17] as well as the traditional X-ray measurements by Waseda et al. [177], respectively. Following the same analysis approach of Schenk et al. [9, 10], they found the icosahedral clusters must be distorted for the best fit of the experimental data for liquid titanium. They explained

Fig. 6.11 Structure factors obtained from the combination of neutron diffraction and electromagnetic levitation techniques for liquid (**a**) iron and (**b**) nickel at different temperatures above and below their melting points, together with (**c**) supercooled nickel at a temperature $T = 1435$ K. Circles in (**c**) represent experimental data, lines give the results of simulations assuming bcc, fcc, icosahedral, and dodecahedral short-range order, respectively. (Reproduced from Ref. [9], with permission @2002 by the American Physical Society). (**d**) Comparison of the static structure factor of liquid nickel at two thermodynamic states above and below their liquidus melting points. (Reproduced from Ref. [17], with permission @2004 by the American Physical Society)
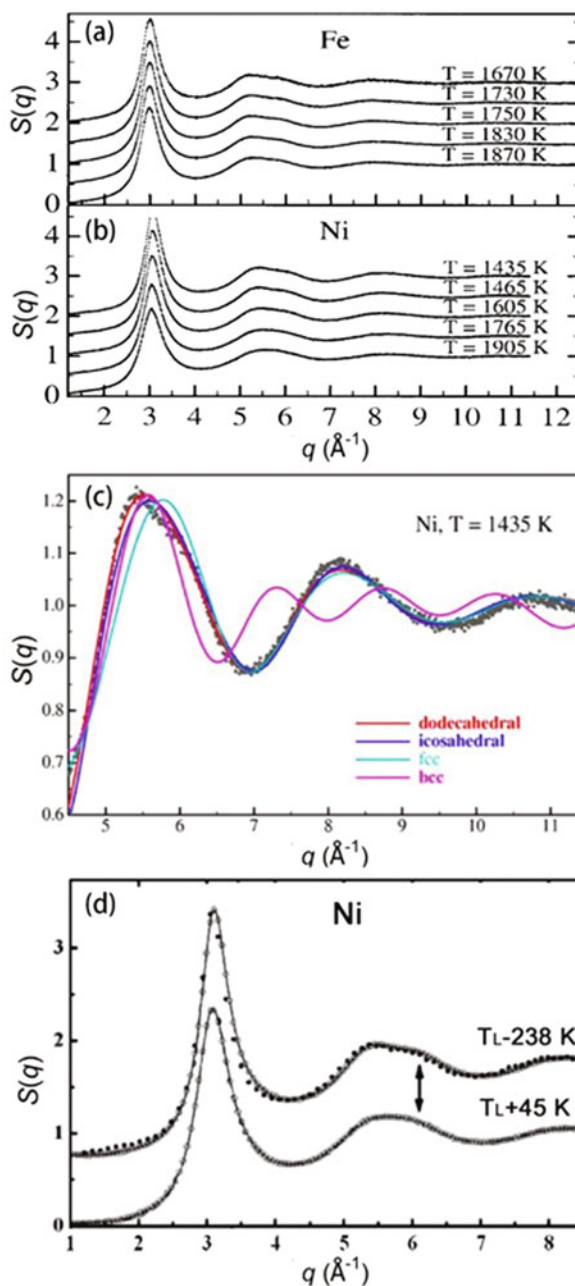
that this distortion of icosahedral cluster results from some angular dependence of the atomic potential in early transition metals, like titanium due to s-d hybridization effects. More recently, Holland-Moritz et al. [12] have conducted neutron diffraction

experiment combined with electromagnetic levitation technique to explore the SRO of stable and undercooled liquid titanium, but they did not observed the peculiar shape of the second peak in structure factor; instead, it is fairly symmetrical with the maximum occurring at $q_2 = 4.9$ Å^{-1}, smaller than 5.1 Å^{-1} reported by Lee et al. [17]. Also by simulating the structure factor in large q regime using the assumption that the melt contains one dominant cluster [9], they found that the measured structure factor of liquid titanium can be well described under the assumption that undistorted icosahedral SRO prevailed in the liquid and even a better fit was achieved by assuming the presence of larger polytetrahedral clusters, such as dodecahedra. For the two different conclusions drawn, it is clear that further studies are strongly required as their current discussion is based on available experimental data of their own.

Some theoretical works have also been conducted to provide more information about the liquid structure of titanium. For example, Kim and Kelton [26] used reverse Monto Carlo method to simulate Lee's experimental data of liquid titanium, nickel, and zirconium and made a comparison of their local structures. Their calculated results indicated that the icosahedral short-range order in undercooled liquid titanium is more distorted than in liquid zirconium and nickel. Recent ab initio cluster studies performed by Lee [178, 179] also support a distorted shape of icosahedron in titanium and revealed that such distortion is caused by the strong interaction between surface atoms but not associated with the core atom. Moreover, the distortion becomes more severe by adding atoms onto the surface of titanium icosahedral clusters resulting in shorter bond lengths among surface atoms, while no change was observed in the case of nickel cluster. Consequently, the constructed distorted 15 atom-containing abundant short bonds give a better description of experimental structure factor of liquid titanium than by the simple 13-atom icosahedra, particularly reproducing the reversed symmetry of the second oscillation. More recently, del Rio et al. [56] performed another AIMD to investigate the static and dynamic properties of liquid titanium near its melting temperature. Their calculated structure factor resembled well with the Lee's experimental data, including a pronounced shoulder in the second peak. From a detailed common neighbor analysis (CNA), they pointed out that the liquid titanium was dominated by the fivefold structures, supporting the existence of icosahedral short-range order, and these icosahedral clusters were somewhat distorted as compared to the ideal icosahedral one.

Zirconium, as one of important alloying elements, has the similar physical and chemical properties with titanium. Due to its high melting temperature ($T_m = 2125$ K), good resistance to corrosion and heat, high hardness and strength, zirconium, and its alloys have been widely used in high-temperature applications, such as nuclear reactor, space, and aeronautic industries [180–182]. The liquid structure of zirconium was first studied by Waseda and Ohtani [183] who performed XRD experiment to obtain the structure factor and PCF at 2173 K. The structure factor displays a very symmetrical main peak with its maximum locating at $q_1 = 2.32$ Å^{-1}. Analogous to titanium, the new measured neutron structure factor by Schenk et al. [9] shifted toward the high q side with the first maximum of about 2.42 Å^{-1}, compared to earlier

data [183], and accompanied by a shoulder on the high q side of the second peak in Fig. 6.8b. Subsequently, Jakse et al. [21, 127] further investigated the short-range order in the liquid zirconium and its evolution upon undercooling by applying a series of AIMD simulations. In addition to discovering the prevalence of complex icosahedron-type atomic packing than the simple 13-atom icosahedral one in stable and undercooled zirconium, they also revealed a gradually strengthening competition between the large polytetrahedral short-range order and the bcc-type order upon undercooling. The presence of both icosahedral character and bcc-type short-range order in the liquid zirconium was also supported by Wu et al. [184] using the same simulation scheme and by Kim and Kelton [26] based on a reverse Monte Carlo analysis of high-energy XRD data as well as by Gheribi [185] and Su et al. [77] who both adopted classical MD simulations. Besides, Su et al. [77] also explored the relationship between the local structure and viscosity of stable and undercooled liquid zirconium. They found at high temperature, high potential energy allows more low-coordinated clusters to survive in the liquid zirconium. Meanwhile their spatial correlations are weak, making the liquid high mobility and low viscosity. With decreasing temperature, the high-coordinated clusters and their strong spatial correlation increase, resulting in the increase of the local stability and viscosity. From the MD results, they also observed a liquid-to-liquid crossover in temperature-dependent internal energy, the nearest neighboring coordination number, and certain short-range order, like <0,3,6,4> indexed clusters.

Oxygen as an impurity (from a few to a few thousands ppm) presents in all metallic liquids, which affects physical properties of metallic liquids. Here we present one example, oxygen in Zr liquid effect on viscosity [77]. The oxygen concentration of the investigated Zr sample was indirectly determined in each cycle by the temperature width of the allotropic phase transformation of Zr above $T=1137$ K. Figure 6.9a exhibits a reproduced Zr-O phase diagram [186] in which the heating of Zr-O above 1137 K leads to an allotropic phase transformation from the hexagonal α-Zr to the cubic β-Zr. The temperature gap between the lower border of β-Zr and the upper border of the α-Zr can be roughly used to determine the oxygen concentration. From a typical temperature-time diagram in Fig. 6.9b, the α-Zr to β-Zr transition is clearly visible, and the ΔT is about 92 K, corresponding to the oxygen concentration of about 1.71 at.% in the Zr-O phase diagram. By this way, the averaged oxygen concentration in the liquid Zr during the investigation is about 1.2 ± 0.5 at.%. The black squares in Fig. 6.9c illustrate the temperature-dependent viscosity of undercooled liquid Zr (with 1.2 ± 0.5 at.% oxygen) measured in the EML experiments.

The black solid line represents a fit with the Vogel-Fulcher-Tammann (VFT) equation [187]:

$$\eta = \eta_0 \exp\left(\frac{T_0 D^*}{T - T_0}\right)$$
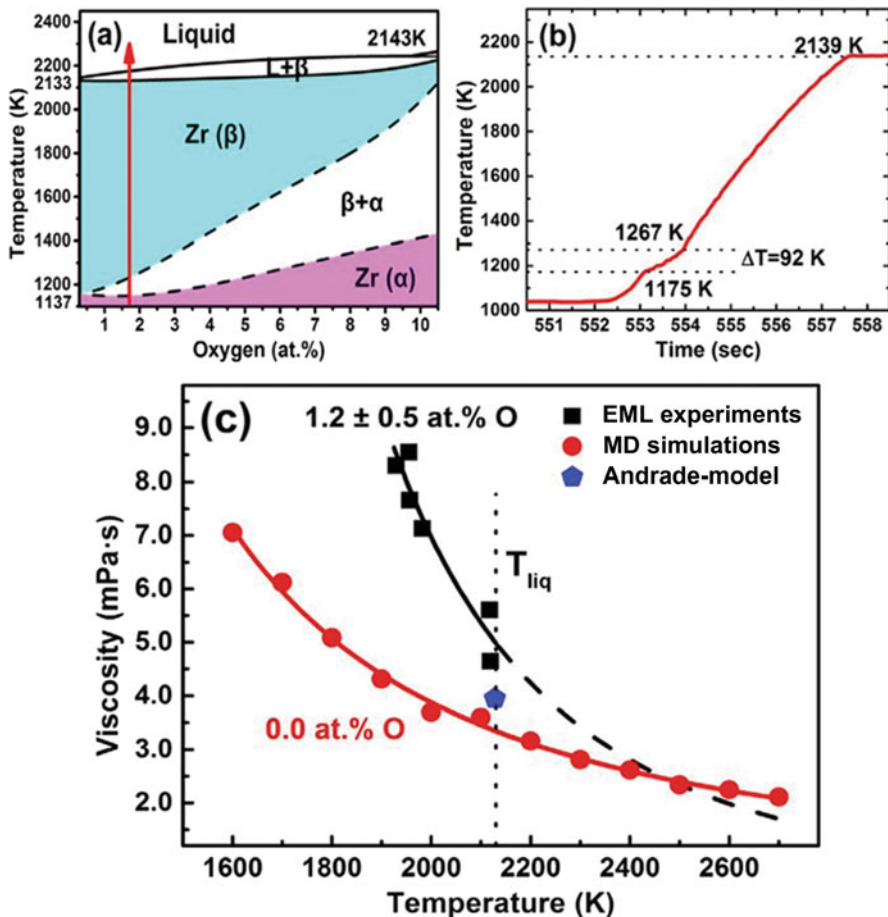
Fig. 6.9 (**a**) The reproduced Zr-O phase diagram. (**b**) A typical temperature-time diagram for one measurement where the α-Zr to β-Zr transition is clearly visible with the ΔT of about 92 K. (**c**) The viscosity of stable and undercooled liquid Zr (1.2 ± 0.5 at.% oxygen) measured by EML experiments (black squares), modeled viscosity of pure Zr at liquidus temperature by the Andrade model (blue pentagon), and MD simulations (red circles) [77]

where η_0 is the viscosity at infinity temperature and T_0 is the VFT temperature, while D^* represents the fragility index of a liquid. η_0, T_0, and D^* are used as fit parameters to be 0.034 mPa s, 59.49 K, and 173.56, respectively. The viscosity obtained by EML could be well fitted by the VFT equation, and the black dash line represents the viscosity extrapolation up to 2700 K. It is found that the viscosity at liquidus temperature is about 5 mPa s. Paradis et al. [188] and Paradis and Rhim [189] also obtained the viscosity at liquidus temperature of 4.74 and 4.83 mPa s, respectively, with the oscillation drop method in an ESL device for a sample with 0.2 at.% oxygen, which agree well with the value obtained by the ISS-EML here. The

viscosity of pure Zr in the temperature range from 2700 to 1600 K obtained by MD simulations is shown in Fig. 6.9c by red circles, together with the VFT fit. η_0, T_0, and D^* are found to be 0.38 mPa s, 68.84 K, and 65.45, respectively. In addition, the viscosity of liquid Zr calculated with the Andrade model [190] (Fig. 6.9c by blue pentagon) is in close agreement with the simulated values at the liquidus temperature. It is known that the Andrade model typically deviates from the experimental values by about $\pm17\%$ [190]. However, the viscosity obtained from EML experiments is higher than that from MD simulations at liquidus temperature by about 44%. This can be explained by the oxygen present in the Zr liquid for experiments. MD simulations can ensure an absolute oxygen-free situation, while the measurements in reality suffer from the presence of even small amounts of oxygen. Recently Ohishi et al. [191] measured the viscosities of Zr-O liquids for two compositions, $Zr_{0.9}O_{0.1}$ and $Zr_{0.8}O_{0.2}$, and found those viscosity values higher than the ones measured in our investigation with 1.2 ± 0.5 at.% oxygen. This result also supports the conclusion that oxygen dissolved in liquid Zr increases the viscosity.

The viscosity of liquid is sensitive to the local atomic packing structure. Although it is difficult to correlate local structural evolution with the dynamical behavior of liquid by in situ experiments, MD simulations help establish this relationship on the atomic scale. Su et al. [77] proposed that the internal energy is an important parameter to reflect the local structural change in a liquid. The red circles in Fig. 6.10a show the internal energy as a function of temperature obtained from MD calculations. It is found that with the decrease of temperature, the internal energy deviates from linearity at about 2000 K, indicating that a local structural change might occur when the stable liquid Zr is cooled into the undercooled liquid state. Interestingly, the viscosity obtained by MD simulations (Fig. 6.9c) also shows an accelerated increase when the temperature is below 2000 K. At high temperature, the mobile atoms with high potential energy (PE) are usually unstable and easy to move, which could be an effective parameter to describe the variation of viscosity. Figure 6.10b displays the ΔPE ($\Delta PE = PE_{atom} - PE_{system}$) of atoms around a central atom at each temperature. The negative peaks of the ΔPE curves in the r range of about 2.98–3.82 Å correspond to the first peak of $g(r)$ curves. It is no doubt that the stable atoms are likely to gather in the first shell of a central atom. The inset in Fig. 6.10b depicts the local magnification of the first peaks on the ΔPE curves. It is found that the decrease of interatomic distance raises the ΔPE rapidly, and the first peaks become lower and the peak positions shift to the large r side upon cooling, indicating that the local atomic packing structures of liquid Zr become more stable with a decrease of the temperature. Firstly, we can evaluate the evolution of the fraction of mobile atoms, F (%), and the results are presented in a y-logarithmic plot shown in Fig. 6.10c for six selected temperatures. Two aspects can be deduced as following: (1) No matter which ΔPE cutoff, the fraction of mobile atoms decreases with the decrease of the temperature, indicating the increase of the stability of local atomic packing structure upon cooling. (2) The $\ln(F)$ is linearly dependent on the ΔPE for all six temperatures. Hence, one can define the fraction of mobile atoms, F (%), as a function of ΔPE using the equation
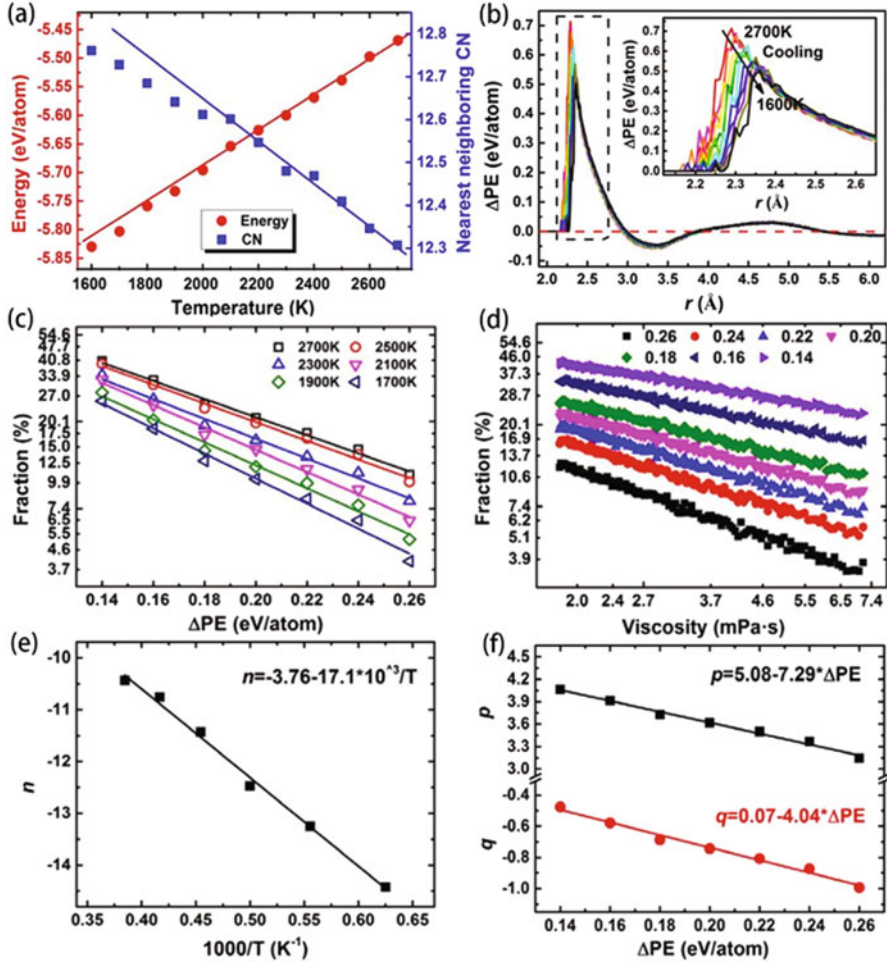
Fig. 6.10 (**a**) The red circles represent the internal energy of stable and undercooled liquid Zr as a function of temperature, while the blue squares show the temperature-dependent nearest neighboring coordination numbers (CNs). (**b**) The ΔPE of atoms around a centered atom within the *r* range of 6.2 Å at various temperatures upon cooling. The inset depicts the local magnification of the first peaks of the ΔPE curves. (**c**) The fraction of mobile atoms, *F* (%), versus ΔPE at six selected temperatures in a y-logarithmic plot. (**d**) The relationship between the fraction of mobile atoms, *F* (%), and the viscosity at seven different ΔPE cutoffs in a double-logarithmic plot. (**e**) The slopes, *n*, of the linear fitting curves in (**a**) as a function of temperature. (**f**) The intercepts, *p*, and the slopes, *q*, of the linear fitting curves in (**d**) as a function of temperature. (Reproduced from Ref. [77], with permission @2019 by Elsevier)

$$\ln (F) = c + n\Delta PE \qquad (6.14)$$

By the linear fitting, *c* is found to be about 5.166 ± 0.062, while the slope, *n*, is a temperature-dependent parameter which can be expressed as $n = -3.76 - 17.1 \times$

$10^3/T$ in Fig. 6.10e. Figure 6.10d shows the relationship between the fraction of the mobile atoms, $F(\%)$, and the viscosity, η, with different ΔPE cutoffs. Interestingly, the $\ln(F)$ also possesses a linear relationship with the $\ln(\eta)$, which can be expressed as

$$\ln(F) = p + q\ln(\eta) \qquad (6.15)$$

where the intercept, p, and the slope, q, are two ΔPE-dependent parameters. As shown in Fig. 6.10f, these two parameters can be expressed as $p = 5.08–7.29 \times \Delta$PE and $q = 0.07–4.04 \times \Delta$PE. Combining Eq. (6.15) with Eq. (6.16), the following equation can be deduced as

$$\ln(\eta) = \frac{0.086 + (3.53 - 17100/T)\Delta PE}{0.07 - 4.04\Delta PE} \qquad (6.16)$$

The temperature-dependent viscosity depends on the potential energy, ΔPE. At high temperature, the high ΔPE results in an unstable system, in which more low-coordinated clusters could be likely to survive in the pure Zr liquid, meanwhile their spatial correlations are weak, making the liquid high mobility and low viscosity. With the decrease of temperature, the fraction of the mobile atoms reduces, resulting in the increase of high-coordinated clusters and their spatial correlations. When pure Zr liquid is further cooled into the undercooled liquid state at 2000 K, the decrease of internal energy (Fig. 6.10a) and the sudden increase of icos-like SRO and bcc-like SRO raise the local stability and viscosity of system. In addition, if considering the oxygen additions of about 1.2 ± 0.5 at.%, it can be found that although the simulated and experimental viscosities could match well in the high-temperature region, they widely diverge in the low-temperature region (Fig. 6.9c). Due to the lack of a reliable EMA potential for the Zr-O system, it is difficult for us to perform MD simulations for Zr-O liquid to reveal the mechanism of the effect of oxygen on increasing the values of viscosity. However, other reported works of metal-metalloid systems in the high-temperature ranges might give us some enlightenments. In general, for the metallic melts containing metalloid elements with small radii, such as P, B, and C, the local atomic packing structures around these small metalloid atoms usually exhibit two characteristics: (1) the metalloid atoms show avoidance with each other, and (2) their local atomic packing structures exist strong chemical orders, resulting in preferring to form low-coordinated clusters, such as <0,3,6,0> or <0,2,8,0>, during the whole investigated temperature ranges. Thus, in the Zr-O liquid with small amount of oxygen, it is most likely to be that O central atoms are all surrounded by the Zr atoms to form the low-coordinated clusters during the whole temperature range from 2700 to 1600 K. In the high-temperature region, the Zr-O liquid is unstable with high ΔPE, in which both Zr- and O-centered atomic packings prefer to be low-coordinated clusters with weak spatial correlations. In this case, high mobility and weak spatial correlations make the oxygen effect on viscosity a bit weak. However, with the decrease of temperature, Zr-centered atomic packings trend to form high- coordinated clusters with strong spatial correlations.

Meanwhile, O-centered low-coordinated clusters could fill the spaces left by the Zr-centered high-coordinated clusters, making the atomic packings much denser than that of pure Zr liquid without oxygen. Consequently, Zr-O liquid could become more stable, and the atoms in low-temperature liquid could be much more difficult to diffuse, making the wide divergence between simulated and experimental viscosities in the low-temperature region.

3.3   Iron (Fe), Cobalt (Co), and Nickel (Ni)

Iron, belonging to the middle of the 3d transition series of the elemental periodic table, is a most abundant metal on earth, forming much of earth's outer and inner core. Therefore, the studies of liquid iron are of importance for both material scientists and geophysicists. Experimental data on the structure, transport, and thermodynamic properties of liquid iron are rare due to practical difficulties arising from the extreme conditions required to melt iron (~1808 K at ambient pressure). The static structure factor of liquid iron near its triple point at ambient pressure was determined by using neutron [9, 192] and XRD techniques [193, 194]. The measured $S(q)$ displays a symmetric main peak located at $q \approx 2.98$ Å^{-1}, similar to that in noble metals. Nevertheless, a small shoulder on the right-hand side of the second oscillation was observed, which becomes more pronounced with decreasing temperature. This characteristic feature of the second oscillation in structure factor has also been experimentally observed in other pure liquid metals and alloys, such as pure metals Ni [9, 10, 17], Co [11], Ti [12, 17], and Zr [9, 10]; melts of binary alloys Co-Pd [13] and Ti-Fe [14]; as well as melts forming quasi-crystalline or polytetrahedral phases, such as Al-(Fe/Co) [15] and Al-(Cu/Fe)-Co [10, 16]. Figure 6.11a, b shows that the shoulder appears in all structure factors of liquid iron and nickel measured by Schenk et al. [9] using neutron diffraction and electromagnetic levitation techniques in the stable regime and undercooled liquids. To understand this particular feature, they further applied some different geometries of local clusters, e.g., bcc, fcc, hcp, icosahedron, and dodecahedron, to individually simulate the structure factor for large q values. The method assumes that aggregates of one specific structure prevail in the liquid which do not interact with each other. Figure 6.11c shows one example of fitting results for undercooled nickel at $T = 1435$ K. For a SRO of bcc or fcc/hcp type, no reasonable description of the measured structure factor is achieved, while a significantly good fit can be obtained under the assumption that the liquid is dominated by isolated icosahedral clusters, in particular, reproducing the large oscillation at about 5.5 Å^{-1} and a characteristic shoulder on the right-hand side of this oscillation. When they applied a larger dodecahedral cluster, that is, a high-order icosahedral cluster consisting of 33 atoms, to perform the simulation, the best fit was obtained. Their results indicated that the icosahedral short-range order, including larger polytetrahedral aggregates (such as dodecahedra) rather than simple icosahedra of 13 atoms, prevails in the undercooled liquids of Fe and Ni.

Vocadlo et al. [195] were the first to use AIMD method to study the static structure and viscosity of liquid iron under earth's core conditions. Ganesh and Widom [27] used AIMD simulation to examine the short-range order in liquid and undercooled liquid Fe and Fe-based alloys. They found that the degree of icosahedral short-range order in undercooled liquid depends on the room temperature crystalline structure, where bcc metals such as Fe and W contain more icosahedral order than fcc metal Cu. Moreover, the addition of small B atoms and large Zr atoms could control the degree of geometric frustration of icosahedral order. Later, Marqués et al. [196] and Molla et al. [141] investigated the static structure and the dynamic properties of liquid iron near its melting point, by using KS-AIMD and OF-AIMD methods, respectively, both showing good agreement with the available experimental data. They also stressed that in order to achieve a good description of the static structure and dynamic properties of liquid iron it was necessary to consider the existence of atomic magnetic moments, even though it leads to wrong magnetic properties.

More recently, Ren et al. [197] performed classical MD simulations to investigate the temperature dependence of local structural change in liquid Fe, Fe-P, and Fe-Ni alloys by using the EAM potential and examined the relationship between the structural and dynamic properties with the glass-forming ability. The Voronoi polyhedron analysis showed that strong competition between the icosahedron-like clusters (including full icosahedron indexed as <0,0,12,0> and its deformed forms <0,1,10,3> and <0,1,10,2>) and bcc-like clusters (including <0,3,6,4>, <0,3,6,5>, <0,2,8,4>, and <0,4,4,6>) in liquids during cooling determined the final crystallization or amorphous solid structure. Alloying with P and Ni promoted the formation of icosahedron-like clusters with lower dynamic properties, and increased the dynamic heterogeneity, thereby inhibiting crystallization in undercooled liquid alloys. Li et al. [198] used MD method to simulate the nucleation process of undercooled liquid iron by virtue of Sutton-Chen potential and discussed the roles of structure and density fluctuations on nucleation. The statistical analysis showed that the pre-nucleus and nucleus are a mixture of bcc and hcp structures and their birth and growth are accompanied with aggregating and disaggregating process.

The structure factor and PCF of liquid cobalt were also measured by using XRD technique [193, 199, 200] at several temperatures within the range $1515\,°C \leq T \leq 1650\,°C$. Within the temperature region, the shape and peak position of diffraction patterns remained almost unchanged with the symmetrical main peak locating at $q_1 = 3.02\,\text{Å}^{-1}$. The increase of temperature leads to a slight decrease of coordination number. By combining the containerless processing technique of electromagnetic levitation with energy-dispersive XRD, Holland-Moritz et al. [11] investigated the local structure of stable and undercooled liquid cobalt. The structure factor also displays a clear shoulder on the right-hand side of the second maximum, indicating the presence of icosahedra in the liquid cobalt at temperatures above and below the melting point. Although many interatomic potentials of liquid cobalt have been developed, most of them focused on the description of static structure factor, thermodynamic properties, and electronic structures near the melting point, and no theoretical studies on the local structure of liquid cobalt and its structural evolution

with temperature have been reported yet. For example, on the basis of the tight-binging scalar cluster Bethe lattice method (SCBLM)-derived interatomic pair potentials, Do Phuong et al. [201] calculated the structure factor of 3d liquid transition metals near their melting points, which showed good agreement with the experiments. They particularly emphasized the key role of sp-d hybridization in the interatomic interactions on the liquid structure of transition metals. Bhuiyan et al. [202] presented a systematic study on the static structure and thermodynamic properties of 3d, 4d, and 5d liquid transition metals near their melting points based on the embedded-atom method (EAM)-derived effective pair potentials in conjunction with the variational modified hypernetted-chain (VMHNC) theory of liquids. Their computed results exhibit good qualitative agreement with the available experiments, except for the early 3d transition metals Sc, Ti, and V, whose structure factor shifts either toward the left or right compared to the experiments. Recently, Han et al. [203] used MD simulation with two different EAM potentials to calculate the thermodynamic properties of liquid cobalt, including density, specific heat, and self-diffusion coefficient, at temperatures above and below the melting point. Their results indicated that although both EAM potentials could produce a reasonable PCF, the accuracy of thermophysical properties of liquid cobalt predicted by Pasianot's EAM model [204] based on an hcp structure is better than that of Stoop's EAM model [205] in the framework of a fcc structure.

The liquid structure of nickel was first measured by Waseda et al. [193, 206] who used both neutron and XRD methods to obtain the structure factor and PCF near the melting point ($T_m = 1453$ °C), from which the interatomic distance and coordination number were evaluated as 2.54 Å and 11.7, respectively. With increasing temperature from 1500 to 1650 °C, the position and shape of the structure factor remained essentially unchanged, showing a symmetry main peak with its maximum at the position of $q = 3.1$ Å^{-1}. Later, by using the same experimental techniques, Johnson et al. [207] and Eder et al. [208] also obtained the structural factor of liquid nickel at 1600 °C, which was in good agreement with the data of Waseda except for slight difference in the height of the main peak. Recently, Schenk et al. [9, 10] investigated the microstructure of the stable and undercooled liquid nickel by using the combination of electromagnetic levitation with neutron scattering techniques. Figure 6.11 shows a clear shoulder on the high q side of the second oscillation was observed for all measured structure factors, and it becomes more evident with increasing the degree of undercooling, indicating the prevalence of icosahedral-type SRO in the liquid nickel. The same conclusion was also inferred from XRD study of liquid nickel by Lee et al. [17] who measured the structure factor of the electrostatically levitated metallic liquid nickel. Later, the reverse Monte Carlo analysis performed by Kim and Kelton [26] also supported the existence of icosahedral short-range order in the liquid nickel and zirconium but the distorted icosahedral clusters in the liquid titanium. Meanwhile, Jakse and Pasturel [127, 209] carried out a series of AIMD simulations to examine the local structure and its evolution in liquid and undercooled liquid nickel. Their analysis results supported Schenk's finding that the liquids are characterized by the full and distorted icosahedral clusters. With decreasing temperature, the coordination number increases, and the undercooled liquids develop a

more complex polytetrahedral short-range order that contains more numerous Frank-Kaper polyhedra with a higher coordination number than the simple 13-atom icosahedron.

Other classical MD and AIMD studies were also performed to study the structure and properties of liquid nickel. For example, Alemany et al. [210, 211] performed MD simulations to compute the static structure factor, some thermodynamic and dynamic properties of liquid Ni, Pd, Pt, Cu, Ag, and Au near their melting points on the basis of the Voter and Chen (VC) version of the EAM. The simulated results of various liquid metals agreed satisfactorily with their available experimental data, except for the diffusion coefficient of liquid copper. They speculated that such discrepancy was mainly because the reported experimental diffusion coefficient of liquid copper was an overestimate. Later, Cherne et al. [212] examined a variety of liquid nickel properties, including melting point, structure factor, viscosity, and self-diffusion coefficient, predicted from two different EAM potentials as well as four variations of the modified EAM (MEAM) model. The results emerging from the comparison of different potentials indicated that although they all produced reasonable structure in consistent with experimental data, the potential proposed by Angelo et al. [213] underestimated the melting temperature, while MEAM Ni1 and MEAM Ni2 both given by Baskes [214] overestimated the long-distance correlations of liquid nickel, resulting in the significant difference in the calculated viscosity and self-diffusion coefficient with the other potentials. Based on the TB method, Posada-Amarillas et al. [215] carried out MD simulations to study the microstructure of liquid and glassy nickel by characterizing the local environment around each atomic pair that contributes to the first two peaks of the PCF. The common neighbor analysis showed that the local atomic structure of liquid nickel is dominated by icosahedral and distorted icosahedral structures, while the glassy nickel also contains a certain number of crystalline ordering. Similar results in liquid nickel were also reported by del Rio et al. [216] who used AIMD simulations to evaluate the static and dynamic properties near the melting point. Good agreement was achieved in static and dynamic structure factors between predicated results and experimental data. Ma et al. [217] also performed AIMD method to explore the local atomic structure of undercooled liquid nickel from which they confirmed the existence of icosahedral short-range order. Their statistical analysis indicated that the icosahedral cluster has the longest average lifetime although it is not the most abundant one. The Voronoi cluster indexed by <0,4,8,1> has the highest amount.

3.4 Copper (Cu) and CuZr Alloys

Di Cicco et al. [20] successfully applied the reverse Monte Carlo (RMC) method to simulate the X-ray absorption spectroscopy (XAS) data of liquid and undercooled liquid copper. Through the structural analysis in terms of the bond-orientational order parameter, $\widehat{W}_6$ cubic invariant, which is sensitive to the orientational
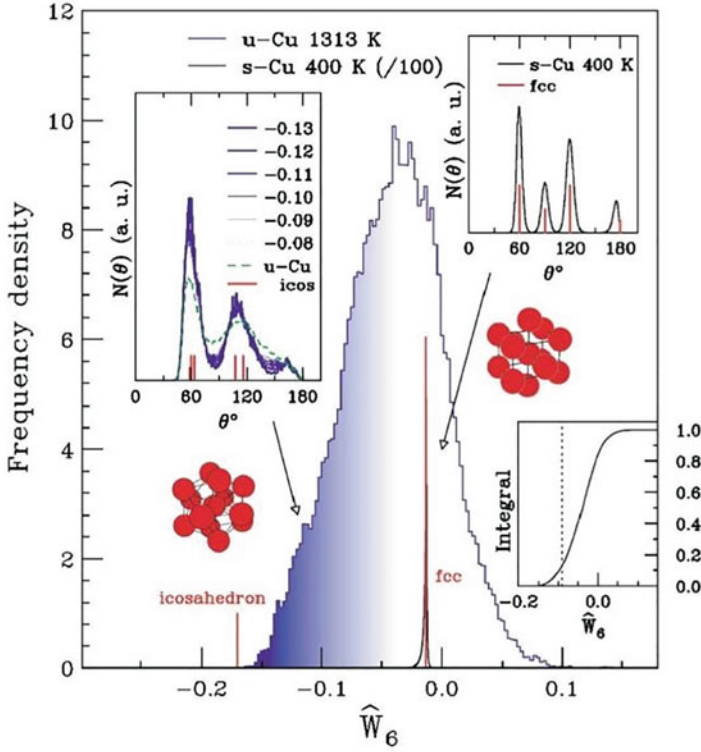
Fig. 6.12 Histogram of the frequency density of the $\hat{W}_6$ cubic invariant monitoring the local geometry around each atom in undercooled liquid copper. The histograms related to an isolated 13-atom fcc ($\hat{W}_6 = -0.01316$) and perfect icosahedral ($\hat{W}_6 = -0.1698$) structures are shown for comparison (scaled by a factor of 100). The $\hat{W}_6$ distribution is found to be very broad and includes a region (shaded area under the histogram) corresponding to distorted nearly icosahedral configurations as indicated by the typical angular distribution with peaks at 60° and 110° and a minimum at 90°(see the left inset). (Reproduced from Ref. [20], with permission @2003 by the American Physical Society)

symmetry, they found that the $\widehat{W}_6$ distribution is very broad and strongly asymmetric toward the negative values extending down to the ideal value of a perfect icosahedral cluster ($\widehat{W}_6 = -0.1698$) in Fig. 6.12. The bond-angle distribution also shows the structural characteristics of icosahedra. By integrating the $\widehat{W}_6$ distribution, they predicated the nearly icosahedral order to comprise up to 10% of all structural motifs in liquid copper. Subsequently, considerable theoretical simulations have supported this finding of abundant icosahedral SRO existed in liquid copper. For instance, Ganesh et al. [23] and Fang et al. [218] performed ab initio MD simulations to analyze the local structures of liquid and undercooled liquid copper, providing strong evidence for the presence of icosahedra. They also indicated that the degree of icosahedral ordering increased as temperature was dropped. Not only perfect but

also defective icosahedra were detected by Celino et al. [24] in liquid copper, who examined the role of defective icosahedra on the stability of undercooled copper by using the MD simulations based on tight-binding (TB) interatomic potential, which could reproduce the experimental structure factor over the entire range of wave vectors. They indicated that the defective icosahedra, embedded in a disordered matrix, could lower the overall energy and stabilize the undercooled liquid copper against crystallization, supporting Frank's hypothesis [4]. On the basis of TB-MD simulations, Winczewski et al. [219] recently used the combination of Voronoi tessellation and bond-orientational order parameters method to make a detailed analysis of the local structures of liquid copper according to their degree of similarity to the perfect icosahedron and examined their temperature dependence of evolution, lifetimes, and relative stability. Their results showed that the identified icosahedra and icosahedron-like polyhedra have longer lifetime and display a strong tendency toward clustering. Mo et al. also [220] used the largest standard cluster analysis to quantify all kinds of clusters in liquid copper through MD simulations and investigated the evolution of local atomic clusters in the rapid solidification process. They found that the liquid-to-solid phase transition of liquid copper experienced a series of intermediate stages, in accordance with Ostwald's rule that the metastable bcc structure was formed firstly and subsequently the most stable fcc phase became dominated. They also emphasized that the icosahedral ordering played an important role in stabilizing the undercooled liquid copper but also breeding the precursor of the metastable bcc clusters at the initial crystallization stage. Liquid copper solidification by MD simulations was also conducted by Liu et al. [221]. They found that the metastable hcp-type and stable fcc-type structures could coexist in the final configurations with all sorts of proportion and various forms controlled by the cooling rate. The slower cooling rate prefers the more stable structure.

Figure 6.13a shows representative structure factors obtained at several temperatures in the $Cu_{50}Zr_{50}$ glass and the liquid [222]. The metallic glass ribbons were not pre-annealed prior to the structural measurements so that structural relaxation could be studied during heating. The data in Fig. 6.13a, b were collected over several cycles of heating from room temperature to temperatures exceeding the glass transition temperature T_g. In the first cycle, the maximum temperature was slightly below T_g. Relaxation in the glass near the glass transition was marked by an increase in the height of the first peak in $S(q)$, $S(q_1)$, and a decrease in its full width at half maximum. After the relaxation that occurred during the initial cycle, the $S(q)$ measured in subsequent cycles was reversible as long as crystallization was avoided. The temperature profile (thermal processing program) for each cycle is shown in Fig. 6.13a. Due to the relatively narrow supercooled region for the $Cu_{50}Zr_{50}$ glass (the temperature region between the glass transition temperature and the crystallization temperature of the glass), the $S(q)$ could only be measured to ~20°C above T_g before devitrification occurred, which was marked by the appearance of noticeable polycrystalline diffraction rings in the diffraction pattern. Using the beamline electrostatic levitator (BESL), $S(q)$ for the liquid was obtained from 214 °C below the equilibrium melting temperature (T_m=940 °C, determined from differential thermal analysis measurements) to 125 °C above it. Figure 6.13c shows representative total pair correlation functions, $g(r)$s, calculated from the $S(q)$s in Fig. 6.13a. The first
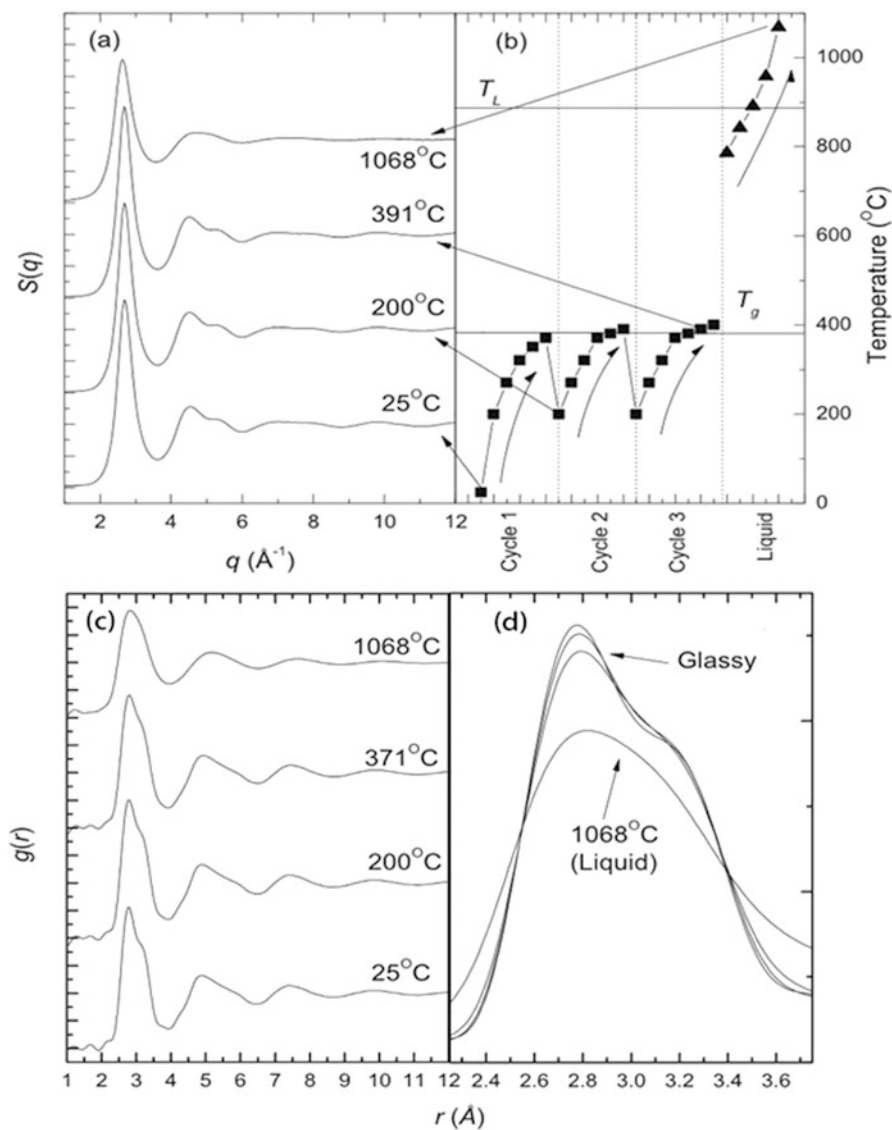
Fig. 6.13 (a) Representative measured structure factors $S(q)$ for $Cu_{50}Zr_{50}$ metallic glasses and liquids. (b) The temperature-time profile for the thermal processing program followed. (c) Pair correlation functions calculated from the structure factors in (a). (d) The first coordination shell for the $g(r)$s in (c), showing an asymmetry in the high-temperature liquid that is more pronounced in the glass. (Reproduced from Ref. [222], with permission @2013 by AIP)

peak in $g(r)$ (the first coordination shell) shows a marked asymmetry at all temperatures, which is characteristic of the Cu-Zr liquids and glasses. This asymmetry is far more pronounced in the glass. Within the Faber-Ziman (FZ) formalism [67], the total pair correlation function is composed of three partial pair correlation functions,

Fig. 6.14 (**a**) The maximum in the first peak in $S(q)$ ($S(q_1)$) in the glass and liquid as a function of temperature. Structural relaxation in the glass during the first heating cycle causes the observed increase in $S(q_1)$. This is not observed in subsequent cycles; $S(q_1)$ is fully reversible, signaling no further relaxation. When the liquid $S(q_1)$ data are extrapolated to T_g, they are significantly smaller (~13%) than the value for the fully relaxed glass. (**b**) Schematic illustration of how structural metrics such $S(q_1)$ and $g(r_1)$ change with temperature for (i) strong and (ii) fragile liquids (Reproduced from Ref. [222], with permission @2013 by AIP)
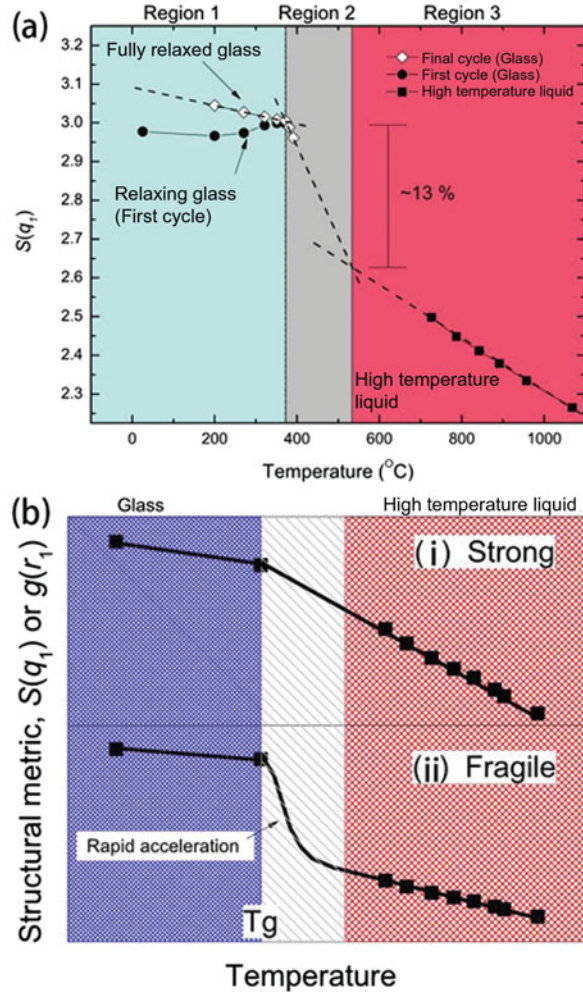
corresponding to Cu-Cu, Cu-Zr, and Zr-Zr in this alloy. Interestingly, the position of the maximum in the first peak decreases with increasing temperature, i.e., a negative temperature coefficient of expansion, in both the liquid and the glass. The dominant contribution to this peak comes from the Cu-Zr partial, which has a positive temperature coefficient, based on MD simulations [223]. The apparent negative temperature dependence observed in the position of the first peak in the total $g(r)$, then, is likely the result of a complicated interplay between the first peaks in the three partial pair correlation functions, which grow in height, sharpen in width, and shift in position as a function of temperature.

The temperature dependence of the first peak height of the total structure factor, $S(q_1)$, is shown in Fig. 6.14a. A significant increase in $S(q_1)$ is observed upon approaching the glass transition temperature when heating the as-quenched glass

from room temperature, consistent with structural relaxation. An approximately 3.5% increase in the first peak height in $S(q_1)$ is observed from the first and last cycles at a common temperature. The $S(q_1)$ obtained after the last cycle increases linearly with decreasing temperature (the dashed line is a linear fit to the data). Since the slow kinetics will not allow the structure of the glass to change significantly below T_g, the observed changes in $S(q)$ with temperature must be due to atomic vibrations, which can be described within the Debye theory [224]. Three distinct regions of behavior are observed in Fig. 6.14a for the growth of $S(q_1)$ with temperature, each of which is fit to a linear temperature dependence. The rate of change in $S(q_1)$ with respect to temperature, $dS(q_1)/dT$, for the glass at and below T_g (region 1) is -2.3×10^{-4}°C^{-1}; $dS(q1)/dT = -6.8 \times 10^{-4}$°C^{-1} in the liquid at high temperatures (region 3). The smaller rate of change in the glass is expected since there are no structural changes below T_g on laboratory time scales. What is unexpected, however, is that the extrapolated value for $S(q_1)$ in the liquid at T_g is much smaller than the measured value of $S(q_1)$ for the glass there. This suggests that in the $Cu_{50}Zr_{50}$ liquid, $dS(q_1)/dT$ accelerates in the supercooled liquid near T_g. This is confirmed from the measured value for $dS(q_1)/dT$ in the liquid just above T_g (region 2), which is -2.4×10^{3}°C^{-1}, much larger than the value for the high-temperature liquid. The maximum of the first peak in $g(r)$ as a function of temperature shows a similar discontinuity between the value for the glass and the value extrapolated from the high-temperature liquid to T_g, as is observed for $S(q_1)$ in Fig. 6.14a. This observed behavior is qualitatively different from that observed in the few previous experimental studies of bulk metallic glass (BMG) forming liquids and glasses [225, 226], which report no rapid acceleration of the static structure factor at or near T_g.

As mentioned earlier the temperature dependence of the viscosity of the liquid is often used to distinguish liquids with high glass-forming ability (GFA) within the concept of fragility [227]. Fragility has been linked with glass formation, where stronger liquids generally have a higher GFA than fragile ones. The Cu-Zr liquids not only have a lower GFA than the Pd- and Zr-based BMGs but are also more fragile liquids [228]. In addition to viscosity, other quantities, such as the specific heat and volume, also change more rapidly near T_g for fragile liquids than for stronger ones. When taken with previous data from strong liquids [229] and recent structural studies in fragile Ni-Nb- based liquids [230], the data presented here indicate that structural properties derived from the X-ray static structure factor have a fragility signature. Within the framework of fragility, the structural changes in strong liquids are expected to be more gradual than in fragile liquids, which would show significant structural changes only near the glass transition temperature (schematically illustrated in Fig. 6.14b).

Within the investigated temperature range of 1250–1425 K, the measured viscosity of $Cu_{50}Zr_{50}$ melt can be expressed by an Arrhenius law of $\eta(T) = \eta_0 \exp(E_A/k_B T)$ with $\eta_0 = (0.08 \pm 0.02)$ mPa·s and an activation energy $E_A = (0.58 \pm 0.03)$ eV in Fig. 6.15a [231]. The relatively small scatter of data, even when taken from rotating and non-rotating sample during thermal cycles, confirms that sample rotation had a negligible influence on the decay time [232]. A similar fit of the viscosity data taken in ground-based ESL experiments in the same temperature range [233]
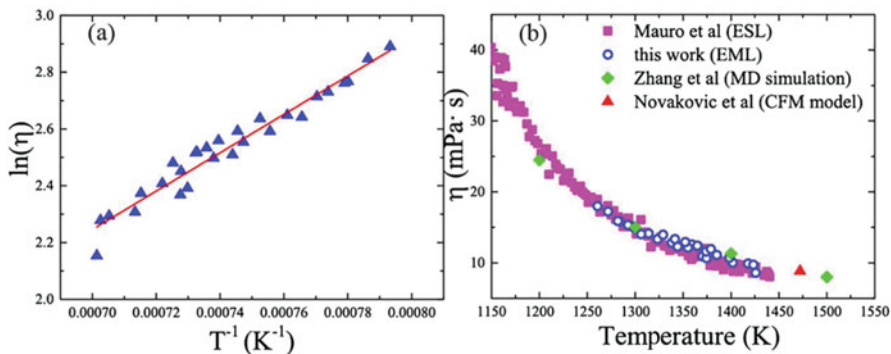
Fig. 6.15 (**a**) The measured temperature-dependent viscosities (triangles) of $Cu_{50}Zr_{50}$ melt follow an Arrhenius relation (straight line). (**b**) Comparison of viscosities of $Cu_{50}Zr_{50}$ melt from the present measurements (blue circle) with the ground-based ESL-studies [233] (purple squares), simulated MD results [234] (green diamond), and the value predicted by the CFM model at 1473 K [235] (red triangle)

give $\eta_0 = (0.028 \pm 0.01)$ mPa·s and $E_A = (0.65 \pm 0.02)$ eV, which are similar, but slightly different from that obtained from the ISS experiments. As shown in Fig. 6.15b, the two experimental data sets are also in reasonable agreement with the MD simulation data [234], as well as with the compound formation model (CFM) by Novakovic et al. [235]. Quantitative comparison of the viscosity data with the elemental melts using semi-empirical models is difficult. Due to the vastly different liquidus temperatures of the alloys from the elemental metals, their viscosities have been measured over different temperature regimes. The melting points of Zr (2124 K) and Cu (1357 K) are much higher than the melting point of $Cu_{50}Zr_{50}$ (1209 K). The available literature data for viscosity of Zr melt exist only for $T >$ 1800 K, which is far above the measured temperature range for $Cu_{50}Zr_{50}$ melt here. In addition, the existence of many intermetallic clusters in Cu-Zr melts [236], compared with the elemental melts, become problematic. As was shown experimentally by Holland-Moritz et al. [237], and also predicted by several MD simulations [234, 238], a variety of different aggregate structures exist in Cu-Zr melts. The classic MD simulations of Cu-Zr melts by Zhang et al. [234] predicted dynamic heterogeneity in the melts from the different packing of clusters. Icosahedrally packed clusters can form stiff, relatively immobile regions, while clusters with lower symmetry can lead to collective, string-like atomic movements.

Although the Arrhenius relationship between temperature and viscosity is known, the underlying mechanism still remains mysterious. Here, classic MD simulations are applied to reveal the structural evolution in $Cu_{50}Zr_{50}$ melt during cooling. Figure 6.16a–c show the evolution of five dominant Voronoi polyhedral (VP), of Zr-centered, Cu-centered, and all atoms during cooling, respectively. The fractions of Zr-centered <0,2,8,4>, <0,1,10,3>, and <0,1,10,4> VPs and Cu-centered <0,2,8,1>, <0,2,8,2>, and <0,0,12,0> VPs increase during cooling, indicating the increasing atomic packing order. Figure 6.16c shows that the evolution of total
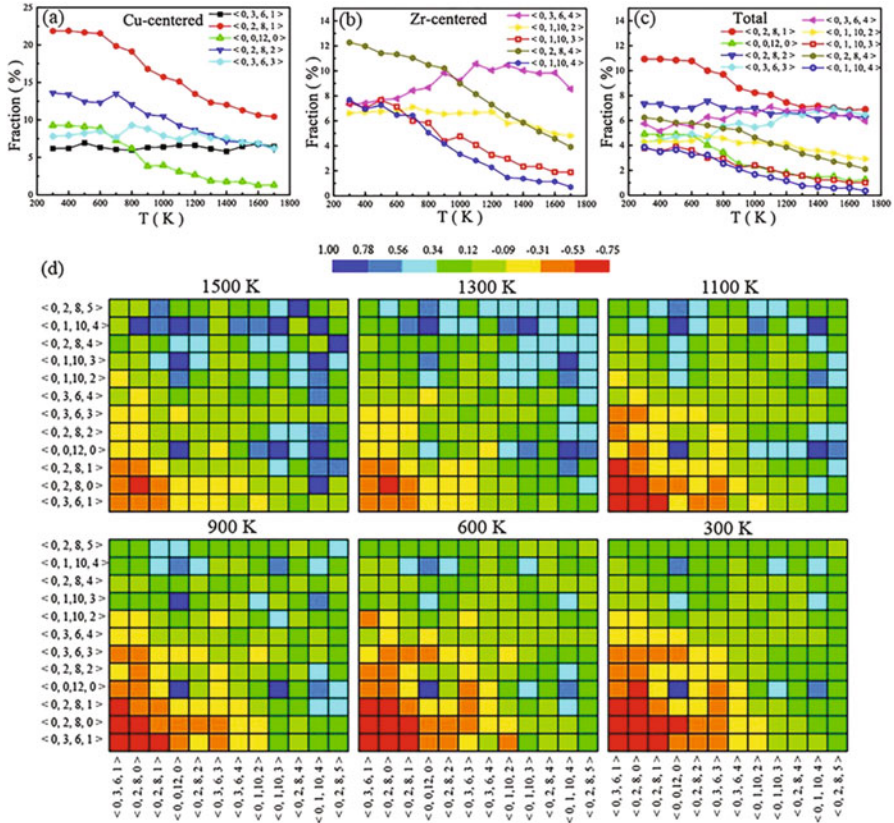
Fig. 6.16 Temperature-dependent evolution of the fractions of dominant VPs of (**a**) Cu-centered (**b**) Zr-centered, and (**c**) total atoms in $Cu_{50}Zr_{50}$ melt. (**d**) Connectivity of dominant VPs in $Cu_{50}Zr_{50}$ melt at 1500 K, 1300 K, 1100 K, 900 K, 600 K, and 300 K. (Reproduced from Ref. [231], with permission @2019 by Elsevier)

fractions of the dominant VPs exhibits different tendencies in four temperature regions, marked as T_1 (1700~1300 K), T_2 (1300~900 K), T_3 (900~600 K), and T_4 (600~300 K). Since the melting point, T_m and glass transition temperature, T_g, for $Cu_{50}Zr_{50}$ is 1205 K and ~900 K, respectively, T_1, T_2, T_3, and T_4 could be defined as liquid region, liquid-to-supercooled liquid region, glass transition region, and solid region, respectively. The fraction of <0,2,8,1>, <0,0,12,0>, <0,1,10,3>, and <0,1,10,4> obviously increases when decreasing temperature from T_1 to T_2, corresponding to the change from liquid state to supercooled liquid state. Interestingly, the viscosity also quickly increases when decreasing temperature from T_1 to T_2 in Fig. 6.15b, indicating the existence of possible correlation between atomic packing and viscosity. The spatial connectivity between VP i and j is defined according to the nearest correlation index $C_{ij} = P_{ij}/P_{ij0} - 1$ [100], where P_{ij} and P_{ij0} are the probability of VP i and j being the nearest neighbors in the MD configuration and random configuration, respectively. $C_{ij} < 0$ means that VPs i and

j tend to exclude with each other, vice versa. To further dig into the correlation between atomic packing and viscosity, we plot the connectivity of major VPs at various temperatures in Fig. 6.16d. The coordination number gradually increases from left to right and from down to up. Cu-centered VPs tend to exclude with each other and connect with Zr-centered VPs, showing closer packing among smaller atoms and big atoms in $Cu_{50}Zr_{50}$ melt. The increasing exclusion between Cu atoms during cooling indicates the increasing atomic order. Meanwhile, the exclusion between Cu atoms obviously increases with decreasing temperature from T_1 to T_2, which is also corresponding to the fast evolution of viscosity in Fig. 6.15. Thus, it is not unreasonable to conclude that both the fractions and their connectivity of major VPs are responsible for the evolution of viscosity in T_1 and T_2. However, the microscopic factor is still unclear, and even the reason for the evolution of VPs remains mysterious, i.e., what are the underlying origins for the evolution of viscosity, these VPs, and their connectivity?

From the dynamic point of view, viscosity is inversely related to the mobility of atoms, which should be linked with the stability of atoms. The atom stability could be quantified by the excess potential energy, $\Delta pe_i = pe_i - \overline{pe}$, where pe_i is the potential energy of atom *i* and $\overline{pe}$ is the average potential energy. A positive Δpe_i indicates that atom *i* is relatively unstable since it is in a higher energy state and vice versa. The average energy distribution curves are obtained by calculating the average Δpe as a function of radius distance from central atoms in Fig. 6.17a. Taking Cu-Cu coordination bonds as an example, there is a low-energy region (LER) in the middle of the distribution line, where $\Delta pe < 0$, indicating a relative stable atomic state. Δpe increases rapidly with decreasing interatomic distance, leaving a high-energy region (HER) in the left of LER. The energy distribution curves for Cu-Zr and Zr-Zr bonds are similar to that for the Cu-Cu bond, except that their LERs are in a bit farther region due to the larger radius for Zr atoms. The characteristics of energy distribution curves indicate that LER is an equilibrium region and HER is an unstable region. Therefore, by tracing the evolution of neighboring interatomic distance, one can observe the local atomic stability. Here, the atom is defined as closer neighboring atom (CNA) when its interatomic distance with another atom is shorter than the cutoff radius. The cutoff radius is defined as the interception between the cutoff *pe*, Δpe_c, and energy distribution curves as shown in Fig. 6.17a. For example, when $\Delta pe_c = 0.1$ eV at 1500 K, the cutoff radius is 2.14Å for Cu-Cu bond $\left(R_{Cu\text{-}Cu}^{0.1eV} = 2.14\text{Å}\right)$, 2.43Å for Cu-Zr bond $\left(R_{Cu\text{-}Zr}^{0.1eV} = 2.43\text{Å}\right)$, and 2.80 Å for Zr-Zr bond $\left(R_{Zr\text{-}Zr}^{0.1eV} = 2.8\text{Å}\right)$. The fraction of CNAs, *f*, which decreases with increasing Δpe_c and decreasing temperature as shown in Fig. 6.17b, could be an indicator for the local stability, i.e., the higher *f*, the higher local potential energy, and the more unstable of the local configuration. Interestingly, the evolution of CAN follows the fraction-energy-temperature (FET) function, which is $f = f_0 e^{-(19262/T+1.629)\Delta pe_c}$, where $f_0 = e^{4.787}$. It should be mentioned that *f* is actually a cumulative value according to the definition of CNA, e.g., $\left(R_{Cu\text{-}Cu}^{0.1eV} = 2.14\text{Å}\right) < \left(R_{Cu\text{-}Cu}^{0.04eV} = 2.27\text{Å}\right)$, therefore $CNA_{0.1eV}$ was included in $CNA_{0.4eV}$.
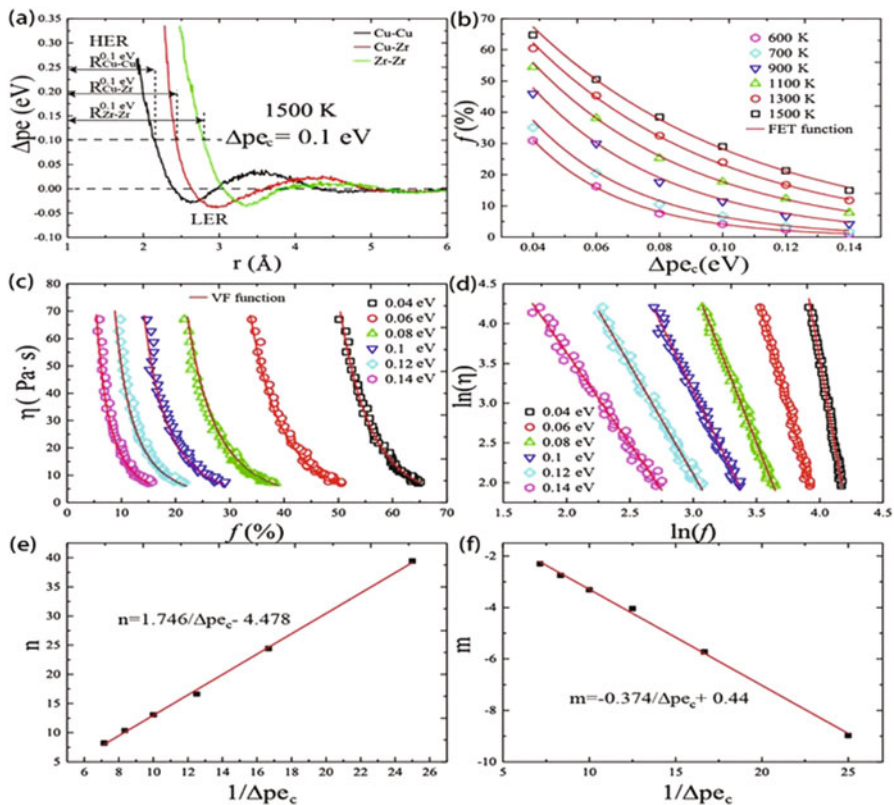
Fig. 6.17 (a) Energy distribution curves for Cu-Cu bond, Cu-Zr bond, and Zr-Zr bond in $Cu_{50}Zr_{50}$ melt, respectively. (b) Evolutions of the fractions of CNAs as a function of Δpe_c and temperature, together with the fitting of FET function of $f = f_0 e^{-(19262/T+1.629)\Delta pe_c}$, where $f_0 = e^{4.787}$. (c) The evolution of viscosity of $Cu_{50}Zr_{50}$ melt as a function of the fraction of CNAs, together with our fitting of VF function. (d) $\ln(\eta)$ as a function of $\ln(f)$, together with the linear fitting curves. (e) The intercept of the fitting line, n, in (d) as a function of $1/\Delta pe_c$, together with linear fitting curve. (f) The slope of the fitting line, m, in (d) as a function of $1/\Delta pe_c$, together with linear fitting curve. The linear relationship between $\ln(\eta)$ and $\ln(f)$ in (d) indicates the relationship of $\ln(\eta) = m\ln(f) + n$, where m and n are the slope and intercept of the linear fitting curve. (e) and (f) show $n = 1.746/\Delta pe_c - 4.478$ and $m = -0.374/\Delta pe_c + 0.440$, respectively. Finally, the VF function is expressed by $\eta = \exp^n f^m$, which is shown in (c). (Reproduced from Ref. [231], with permission @2019 by Elsevier)

Consequently, the sum of f is larger than unity. The expression of FET function reminds us of the Arrhenius law, since both are expressed in exponential form with temperature and energy factor in the exponential term. Figure 6.17c illustrates the evolution of viscosity as a function of f, together with our fitting of viscosity-fraction, VF, function, i.e., $\eta = \exp_n f_m$, where $n = 1.746/\Delta pe_c - 4.478$ and $m = -0.374/\Delta pe_c + 0.440$. The procedure to obtain the VF function could be referred in Fig. 6.17d–f and the corresponding caption. Viscosity increases with decreasing

the fraction of CNAs as illustrated by the VF function for all the cutoffs, Δpe, indicating the strong correlation between viscosity and CNAs. It should be mentioned that the viscosity data used in Fig. 6.17c are obtained from the previous Arrhenius fitting of the experiment data, $\eta(T) = 0.08\exp(0.58/k_{\mathrm{B}}T)$. The CNA model here describes the activation and restriction process of atoms, linking the evolution of atomic packing with viscosity. The LER is the equilibrium region for the coordination atoms and plays as a potential well. At high temperatures, atoms have enough energy to overcome the energy barrier and move in a large region, corresponding to high atomic mobility and low viscosity. During cooling, more atoms drop into the LER, corresponding to low atomic mobility and high viscosity. Besides, the CNA model is also helpful to understand the evolution of structure as shown in Fig. 6.16a–c. The existence of CNAs prevents the central atoms from connecting with more neighboring atoms and causes low coordination number. Therefore, the decreasing fraction of CNAs during cooling will cause the increase of high coordination VPs, which is consistent to the result in Fig. 6.16a–c that high coordination VPs, such as Zr-centered <0,2,8,4>, <0,1,10,3>, and <0,1,10,4> VPs and Cu-centered <0,2,8,1>, <0,2,8,2>, and <0,0,12,0>, gradually increase during cooling.

4   Summary and Outlook

In the past decades, numerous structural data of metallic liquids have been obtained through various experimental and theoretical methods. More and more evidences confirm the existence of short- and medium-range order in normal and supercooled liquids and even some unusual temperature-dependent phenomena. However, there are also many fundamental problems that remain unsolved. Here we give a brief summary and suggest several directions for further research:

1. Using advance synchrotron radiation XRD, X-ray absorption fine structure, neutron scattering, and containerless levitation technique, the structural characterization is the most effective method for experimental investigation of liquid structures. Liquid structural data of many pure metals confined near their melting point and obtained by a single diffraction method should be extended to a wide temperature and multi-techniques. It is necessary to expand the application of X-ray absorption fine structure in liquid, because it contains the most direct information of local atomic structure in the short range. It is always useful to record more high-quality temperature- dependent structural data for the study of the evolution of structures with temperature. For example, through the analysis of the PDF, it is found that as the temperature increases, the interatomic distance exhibits a general contraction, but the second- and higher-order peaks may show different changing trends for different systems. What is the underlying mechanism and how to correlate it to the macroscopic volume expansion behavior? Are there any general rules to predict the temperature dependences of the second- and higher-order peaks in PDF in metallic liquids?

2. Theoretical calculations are a powerful approach to complement the experiments, especially the classical MD simulations and ab initio molecular dynamic simulations, allowing us to construct the three-dimensional configurations at various thermodynamic states and explore the liquid structure and the related properties at the atomic scale. However, they have met limited success due to the absence of effective interatomic potentials or the finite system size effect and short time scale. Therefore, to give a better understanding of the structure and prediction of the various properties of a real liquid, it is necessary to develop more reliable potential functions and expand their scope of application that is not accessed in experiments, e.g., extreme high temperatures and high pressures. In addition, the current research on liquid structures are mostly carried out by a single or a combination of structural analysis methods on the special system, lacking a structural model that can describe all architectures in a unified manner. For example, the Voronoi tessellation has been commonly used to analyze the short-range order and their connection extending toward medium-range order in a certain liquid, but it may itself generate dozens or even hundreds of short- range cluster structures. A slight thermal disturbance will lead to the changes in the Voronoi index (local structure), to some extent which affects the analyses of structural evolution; therefore, it is difficult to establish the relationship between structure and properties. Finally, new advanced theories are welcome to be developed to effectively describe metallic liquids.

3. A large amount of experimental and theoretical results indicate that there exist abnormal structural changes in some metallic liquids, including liquid-to-liquid transition and liquid-to- liquid crossover. Among them, some liquids show a discontinuous change in density with temperature, while others exhibit continuous changes accompanied by several structural parameters deviating from the temperature-dependent linear relationship. How to understand the underlying physical origins of these two structural anomalies, whether it is a universal phenomenon in liquids, how to characterize the structural evolution, and how the liquid before and after the change affects the properties of quenched materials remain the fundamental questions. In addition, two dynamic anomalies, Arrhenius crossover and FTS transition, have been reported in some metallic glass-forming liquids. Many studies have revealed that the former is considered as the onset of cooperativity, while the latter is suggested as a general dynamic behavior, associated with the LLT. However, due to the complexity of the multicomponent system itself, it is still difficult to give an unambiguous explanation of these dynamic anomalies from the structural aspects using theoretical methods. In addition, the reported FTS transition always takes place in the supercooled liquids, also bringing great challenges to experiments. 4. The atomic dynamics in metallic liquids remains another promising issue, which could be not only closely related with the structural evolution of metallic liquids but also their most properties changing with external conditions, such as the temperature and pressure. The inelastic X-ray scattering and quasielastic neutron scattering are important experimental tools that can be used to measure the time-dependent atomic dynamics in metallic liquids. Meanwhile, the advanced MD simulations

can reproduce the normal vibration modes and vibrational density of states, which are fundamental for understanding of the dynamical excitations, and thermal transport properties of metallic liquids.

References

1. F. Zernike, J.A. Prins, Die Beugung von Röntgenstrahlen in Flüssigkeiten als Effekt der Molekülanordnung. Zeitschrift für Physik A Hadrons and nuclei **41**, 184–194 (1927)
2. P. Debye, H. Menke, The determination of the inner structure of liquids by X-ray means. Physik Z **31**, 797–798 (1930)
3. S.J.L. Billinge, M.G. Kanatzidis, Beyond crystallography: The study of disorder, nanocrystallinity and crystallographically challenged materials with pair distribution functions. Chem. Comm. **35**, 749–760 (2004)
4. F.C. Frank, Supercooling of liquids. Proc. R. Soc. Lond. A Math. Phys. Sci. **215**, 43–46 (1952)
5. D. Turnbull, Formation of crystal nuclei in liquid metals. J. Appl. Phys. **21**, 1022–1028 (1950)
6. P.J. Steinhardt, D.R. Nelson, M. Ronchetti, Bond-orientational order in liquids and glasses. Phys. Rev. B. **28**, 784–805 (1983)
7. H. Jónsson, H.C. Andersen, Icosahedral ordering in the Lennard-Jones liquid and glass. Phys. Rev. Lett. **60**, 2295–2298 (1988)
8. H. Reichert, O. Klein, H. Dosch, M. Denk, V. Honkimäki, T. Lippmann, et al., Observation of five- fold local symmetry in liquid lead. Nature **408**, 839–841 (2000)
9. T. Schenk, D. Holland-Moritz, V. Simonet, R. Bellissent, D.M. Herlach, Icosahedral short-range order in deeply undercooled metallic melts. Phys. Rev. Lett. **89**, 075507 (2002)
10. D. Holland-Moritz, T. Schenk, V. Simonet, R. Bellissent, P. Convert, T. Hansen, et al., Short-range order in undercooled metallic liquids. Mater. Sci. Eng. A. **375**, 98–103 (2004)
11. D. Holland-Moritz, T. Schenk, R. Bellissent, V. Simonet, K. Funakoshi, J.M. Merino, et al., Short- range order in undercooled Co melts. J. Non-Cryst. Solids. **312–314**, 47–51 (2002)
12. D. Holland-Moritz, O. Heinen, R. Bellissent, T. Schenk, Short-range order of stable and undercooled liquid titanium. Mater. Sci. Eng. A. **449**, 42–45 (2007)
13. D. Holland-Moritz, T. Schenk, V. Simonet, R. Bellissent, D.M. Herlach, Short-range order in metastable $Co_{75}Pd_{25}$ melts. J. Metastable Nanocryst. Mater. **24-25**, 305–310 (2005)
14. D. Holland-Moritz, O. Heinen, R. Bellissent, T. Schenk, D.M. Herlach, Short-range order of liquid Ti72.3Fe27.7 investigated by a combination of neutron scattering and X-ray diffraction. Int. J. Mater. Res. **97**, 948–953 (2006)
15. D. Holland-Moritz, T. Schenk, V. Simonet, R. Bellissent, P. Convert, T. Hansen, Short-range order in undercooled melts forming quasicrystals and approximants. J. Alloy. Compd. **342**, 77–81 (2002)
16. T. Schenk, V. Simonet, D. Holland-Moritz, R. Bellissent, T. Hansen, P. Convert, et al., Temperature dependence of the chemical short-range order in undercooled and stable Al-Fe-Co liquids. Europhys. Lett. **65**, 34–40 (2004)
17. G.W. Lee, A.K. Gangopadhyay, K.F. Kelton, R.W. Hyers, T.J. Rathz, J.R. Rogers, et al., Difference in icosahedral short-range order in early and late transition metal liquids. Phys. Rev. Lett. **93**, 037802 (2004)
18. F.C. Frank, Supercooling of liquids. Proc. R. Soc. A. **215**, 43–46 (1952)

19. K.F. Kelton, G.W. Lee, A.K. Gangopadhyay, R.W. Hyers, T.J. Rathz, J.R. Rogers, et al., First x-ray scattering studies on electrostatically levitated metallic liquids: Demonstrated influence of local icosahedral order on the nucleation barrier. Phys. Rev. Lett. **90**, 195504 (2003)
20. A. Di Cicco, A. Trapananti, S. Faggioni, A. Filipponi, Is there icosahedral ordering in liquid and undercooled metals? Phys. Rev. Lett. **91**, 135505 (2003)
21. N. Jakse, A. Pasturel, Local order of liquid and supercooled zirconium by ab initio molecular dynamics. Phys. Rev. Lett. **91**, 195501 (2003)
22. N. Jakse, A. Pasturel, Molecular-dynamics study of liquid nickel above and below the melting point. J. Chem. Phys. **123**, 244512 (2005)
23. P. Ganesh, M. Widom, Signature of nearly icosahedral structures in liquid and supercooled liquid copper. Phys. Rev. B. **74**, 134205 (2006)
24. M. Celino, V. Rosato, A. Di Cicco, A. Trapananti, C. Massobrio, Role of defective icosahedra in undercooled copper. Phys. Rev. B. **75**, 174210 (2007)
25. A. Hirata, T. Morino, Y. Hirotsu, K. Itoh, T. Fukunaga, Local atomic structure analysis of Zr-Ni and Zr-Cu metallic glasses using electron diffraction. Mater. Trans. **48**, 1299–1303 (2007)
26. T.H. Kim, K.F. Kelton, Structural study of supercooled liquid transition metals. J. Chem. Phys. **126**, 054513 (2007)
27. P. Ganesh, M. Widom, Ab initio simulations of geometrical frustration in supercooled liquid Fe and Fe-based metallic glass. Phys. Rev. B. **77**, 014205 (2008)
28. N. Jakse, A. Pasturel, Local order and dynamic properties of liquid and undercooled Cu_xZr_{1-x} alloys by ab initio molecular dynamics. Phys. Rev. B. **78**, 214204 (2008)
29. N.A. Mauro, W. Fu, J.C. Bendert, Y.Q. Cheng, E. Ma, K.F. Kelton, Local atomic structure in equilibrium and supercooled liquid $Zr_{75.5}Pd_{24.5}$. J. Chem. Phys. **137**, 044501 (2012)
30. N. Jakse, T.L.T. Nguyen, A. Pasturel, Local order and dynamic properties of liquid and undercooled $Cu_{55}Hf_{45}$ and $Cu_{62}Hf_{38}$ alloys by ab initio molecular dynamics. J. Appl. Phys. **114**, 063514 (2013)
31. A.D. Cicco, F. Iesari, S. De Panfilis, M. Celino, S. Giusepponi, A. Filipponi, Local fivefold symmetry in liquid and undercooled Ni probed by x-ray absorption spectroscopy and computer simulations. Phys. Rev. B. **89**, 060102 (2014)
32. J. Ding, Y.-Q. Cheng, E. Ma, Full icosahedra dominate local order in $Cu_{64}Zr_{34}$ metallic glass and supercooled liquid. Acta Mater. **69**, 343–354 (2014)
33. A. Murin, I. Shabanova, Comparative study of local atomic structure of liquid and supercooled Cu, Ni, and Au. Surf. Interface Anal. **46**, 869–872 (2014)
34. N. Jakse, O. Le Bacq, A. Pasturel, Prediction of the local structure of liquid and supercooled tantalum. Phys. Rev. B. **70**, 174203 (2004)
35. M.Z. Li, H.L. Peng, Y.C. Hu, F.X. Li, H.P. Zhang, W.H. Wang, Five-fold local symmetry in metallic liquids and glasses. Chin. Phys. B. **26**, 016104 (2017)
36. Y.Q. Cheng, H.W. Sheng, E. Ma, Relationship between structure, dynamics, and mechanical properties in metallic glass-forming alloys. Phys. Rev. B. **78**, 014207 (2008)
37. D. Holland-Moritz, S. Stüber, H. Hartmann, T. Unruh, T. Hansen, A. Meyer, Structure and dynamics of liquid $Ni_{36}Zr_{64}$ studied by neutron scattering. Phys. Rev. B. **79**, 064204 (2009)
38. L. Huang, C.Z. Wang, K.M. Ho, Structure and dynamics of liquid $Ni_{36}Zr_{64}$ by ab initio molecular dynamics. Phys. Rev. B. **83**, 184103 (2011)
39. J. Ding, Y. Cheng, E. Ma, Charge-transfer-enhanced prism-type local order in amorphous $Mg_{65}Cu_{25}Y_{10}$: Short-to-medium-range structural evolution underlying liquid fragility and heat capacity. Acta Mater. **61**, 3130–3140 (2013)
40. Y.Q. Cheng, E. Ma, Atomic-level structure and structure–property relationship in metallic glasses. Prog. Mater. Sci. **56**, 379–473 (2011)
41. D.B. Miracle, A structural model for metallic glasses. Nat. Mater. **3**, 697–702 (2004)
42. H.W. Sheng, W.K. Luo, F.M. Alamgir, J.M. Bai, E. Ma, Atomic packing and short-to-medium- range order in metallic glasses. Nature **439**, 419–425 (2006)
43. K.N. Lad, N. Jakse, A. Pasturel, Signatures of fragile-to-strong transition in a binary metallic glass-forming liquid. J. Chem. Phys. **136**, 104509 (2012)

44. X.W. Fang, C.Z. Wang, S.G. Hao, M.J. Kramer, Y.X. Yao, M.I. Mendelev, et al., Spatially resolved distribution function and the medium-range order in metallic liquid and glass. Sci. Rep. **1**, 194 (2011)

45. J. Kang, J. Zhu, S.H. Wei, E. Schwegler, Y.H. Kim, Persistent medium-range order and anomalous liquid properties of $Al_{1-x}Cu_x$ alloys. Phys. Rev. Lett. **108**, 115901 (2012)

46. J.Y. Qin, X.F. Bian, S.I. Sliusarenko, W.M. Wang, Pre-peak in the structure factor of liquid Al-Fe alloy. J. Phys. Condens. Matter. **10**, 1211–1218 (1998)

47. S.K. Das, J. Horbach, M.M. Koza, S. Mavila Chatoth, A. Meyer, Influence of chemical short-range order on atomic diffusion in Al–Ni melts. Appl. Phys. Lett. **86**, 011918 (2005)

48. J. Brillo, A. Bytchkov, I. Egry, L. Hennet, G. Mathiak, I. Pozdnyakova, et al., Local structure in liquid binary Al–Cu and Al–Ni alloys. J. Non-Cryst. Solids. **352**, 4008–4012 (2006)

49. O.S. Roik, O.V. Samsonnikov, V.P. Kazimirov, V.E. Sokolskii, Short and medium-range order in liquid binary Al–Ni and Al–Co alloys. J. Mol. Liq. **145**, 129–134 (2009)

50. O.S. Roik, O.V. Samsonnikov, V.P. Kazimirov, V.E. Sokolskii, S.M. Galushko, Medium-range order in Al-based liquid binary alloys. J. Mol. Liq. **151**, 42–49 (2010)

51. L. Zhang, Y.H. Wu, X.F. Bian, H. Li, W.M. Wang, J.G. Li, et al., Origin of the prepeak in the structure factors of liquid and amorphous Al-Fe-Ce alloys. J. Phys. Condens Matter. **11**, 7959–7969 (1999)

52. N.A. Mauro, V. Wessels, J.C. Bendert, S. Klein, A.K. Gangopadhyay, M.J. Kramer, et al., Short- and medium-range order in $Zr_{80}Pt_{20}$ liquids. Phys. Rev. B. **83**, 184109 (2011)

53. J.D. Wicks, R.L. McGreevy, RMC: modelling neutron diffraction, X-ray diffraction and EXAFS data simultaneously for amorphous materials. J. Non-Cryst. Solids. **192–193**, 23–27 (1995)

54. C.J. Benmore, A review of high-energy X-ray diffraction from glasses and liquids. ISRN Mater. Sci. **2012**, 1–19 (2012)

55. H.E. Fischer, A.C. Barnes, P.S. Salmon, Neutron and x-ray diffraction studies of liquids and glasses. Rep. Prog. Phys. **69**, 233–299 (2006)

56. B.G. del Rio, O. Rodriguez, L.E. González, D.J. González, First principles determination of static, dynamic and electronic properties of liquid Ti near melting. Comput. Mater. Sci. **139**, 243–251 (2017)

57. B.H. Toby, T. Egami, Accuracy of pair distribution function analysis applied to crystalline and non-crystalline materials. Acta Cryst. **48**, 336–346 (1992)

58. V.P. Kazimirov, S.Y. Smyk, Sokol'skii VÉ., Termination effect in X-ray diffraction studies of disordered systems. Crystallogr. Rep. **45**, 6–9 (2000)

59. C. EaN, Y. Greenberg, E. Yahel, B. Beuneu, G. Makov, What is the structure of liquid Bismuth? J. Phys. Conf. Ser. **340**, 012079 (2012)

60. Y. Waseda, *The Structure of Non-crystalline Materials: Liquids and Amorphous Solids* (McGraw-Hill International Book Co., New York/London, 1980)

61. J.L. Finney, Random packings and the structure of simple liquids. I. The geometry of random close packing. Proc. R. Soc. A Math. Phys. Eng. Sci. **319**, 479–493 (1970)

62. Q. Yu, X.D. Wang, H.B. Lou, Q.P. Cao, J.Z. Jiang, Atomic packing in Fe-based metallic glasses. Acta Mater. **102**, 116–124 (2016)

63. H. Lou, X. Wang, Q. Cao, D. Zhang, J. Zhang, T. Hu, et al., Negative expansions of interatomic distances in metallic melts. Proc. Natl. Acad. Sci. USA **110**, 10068–10072 (2013)

64. L.H. Xiong, H.B. Lou, X.D. Wang, T.T. Debela, Q.P. Cao, D.X. Zhang, et al., Evolution of local atomic structure during solidification of Al2Au liquid: An ab initio study. Acta Mater. **68**, 1–8 (2014)

65. Y. Su, X.D. Wang, Q. Yu, Q.P. Cao, U. Ruett, D.X. Zhang, et al., Temperature dependent structural evolution in liquid $Ag_{50}Ga_{50}$ alloy. J. Phys. Condens. Matter. **30**, 015402 (2018)

66. W.B. Zhang, X.D. Wang, Q.P. Cao, D.X. Zhang, H.J. Fecht, J.Z. Jiang, Structure and dynamical properties of liquid $Ni_{64}Zr_{36}$ and $Ni_{65}Hf_{35}$ alloys: An ab initio molecular dynamics study. J. Phys. Condens Matter. **30**, 365401 (2018)

67. T.E. Faber, J.M. Ziman, A theory of the electrical properties of liquid metals. Philos. Mag. **11**, 153–173 (1965)
68. N.W. Ashcroft, D.C. Langreth, Structure of binary liquid mixtures. J. Phys. Rev. **156**, 685–692 (1967)
69. A.B. Bhatia, D.E. Thornton, Structural aspects of the electrical resistivity of binary alloys. Phys. Rev. B. **2**, 3004–3012 (1970)
70. Y. Waseda, *Novel Application of Anomalous (Resonance) X-ray Scattering for Structural Characterization of Disordered Materials* (Springer, Berlin/Heidelberg, 1984)
71. Y. Waseda, K. Sugiyama, E. Matsubara, K. Harada, Partial structural functions of GeO_2 glass determined by the anomalous X-ray-scattering data coupled with neutron-diffraction. Mater. Trans. Jim. **31**, 421–424 (1990)
72. S. Hosokawa, J.F. Bérar, N. Boudet, S. Kohara, J. Stellhorn, W.C. Pilgrim, et al., A combination of anomalous x-ray scattering and neutron diffraction for structural characterizations of $Zr_{63}Ni_{25}Al_{12}$ metallic glass. J. Phys. Conf. Ser. **502**, 012023 (2014)
73. A.C. Barnes, S.B. Lague, P.S. Salmon, H.E. Fischer, A determination of the structure of liquid using neutron diffraction and isotopic substitution. J. Phys. Condens. Matter. **9**, 6159–6173 (1997)
74. P.S. Salmon, I. Petri, P.H.K. Jong, P. Verkerk, H.E. Fischer, W.S. Howells, Structure of liquid lithium. J. Phys. Condens. Matter. **16**, 195–222 (2004)
75. S. Krishnan, D.L. Price, X-ray diffraction from levitated liquids. J. Phys. Condens. Matter. **12**, R145–RR76 (2000)
76. L.H. Xiong, H. Yoo, H.B. Lou, X.D. Wang, Q.P. Cao, D.X. Zhang, et al., Evolution of atomic structure in $Al_{75}Cu_{25}$ liquid from experimental and ab initio molecular dynamics simulation studies. J. Phys. Condens. Matter. **27**, 035102 (2015)
77. Y. Su, M. Mohr, R.K. Wunderlich, X. Wang, Q. Cao, D. Zhang, et al., The relationship between viscosity and local structure in liquid zirconium via electromagnetic levitation and molecular dynamics simulations. J. Mol. Liq. **298**, 111992 (2019)
78. L. Fonda, Multiple-scattering theory of X-ray absorption: A review. J. Phys. Condens. Matter. **4**, 8269–8302 (1992)
79. J.J. Rehr, R.C. Albers, Theoretical approaches to x-ray absorption fine structure. Rev. Mod. Phys. **72**, 621–654 (2000)
80. B. Ravel, M. Newville, Athena, artemis, hephaestus: Data analysis for X-ray absorption spectroscopy using IFEFFIT. J. Synchrotron Radiat. **12**, 537–541 (2005)
81. E.A. Stern, P. Livns, Z. Zhang, Thermal vibration and melting from a local perspective. Phys. Rev. B. **43**, 8850–8860 (1991)
82. S. Wei, H. Oyanagi, W. Liu, T. Hu, S. Yin, G. Bian, Local structure of liquid gallium studied by X-ray absorption fine structure. J. Non-Cryst. Solids. **275**, 160–168 (2000)
83. Y. Su, X. Wang, P. An, J. Zhang, T. Hu, Y. Ren, et al., Temperature-dependent structural evolution in $Au_{44}Ga_{56}$ liquid eutectic alloy. J. Phys. Chem. C. **123**, 25209–25219 (2019)
84. J.A. Barker, D. Henderson, Theories of liquids. Annu. Rev. Phys. Chem. **23**, 439–484 (1972)
85. J.-P. Hansen, I.R. McDonald, Chapter 2 – Statistical mechanics, in *Theory of Simple Liquids*, ed. by J.-P. Hansen, I. R. McDonald, 3rd edn., (Academic, Burlington, 2006), pp. 11–45
86. C. Caccamo, Integral equation theory description of phase equilibria in classical fluids. Phys. Rep-Rev. Sec. Phys. Lett. **274**, 1–105 (1996)
87. J.A. Barker, D. Henderson, Perturbation theory and equation of state for fluids: The square-well potential. J. Chem. Phys. **47**, 2856–2861 (1967)
88. J.A. Barker, D. Henderson, Perturbation theory and equation of state for fluids. II. A successful theory of liquids. J. Chem. Phys. **47**, 4714–4721 (1967)
89. J.D. Weeks, D. Chandler, H.C. Andersen, Perturbation theory of the thermodynamic properties of simple liquids. J. Chem. Phys. **55**, 5422–5423 (1971)
90. H.C. Andersen, D. Chandler, J.D. Weeks, Roles of repulsive and attractive forces in liquids: The optimized random phase approximation. J. Chem. Phys. **56**, 3812–3823 (1972)

91. J.K. Percus, G.J. Yevick, Analysis of classical statistical mechanics by means of collective coordinates. Phys. Rev. **110**, 1–13 (1958)

92. J.L. Lebowitz, J.K. Percus, Mean spherical model for lattice gases with extended hard cores and continuum fluids. Phys. Rev. **144**, 251–258 (1966)

93. W.G. Madden, S.A. Rice, The mean spherical approximation and effective pair potentials in liquids. J. Chem. Phys. **72**, 4208–4215 (1980)

94. T. Morita, Theory of classical fluids: Hyper-netted chain approximation III. Prog. Theor. Phys. **23**, 829–845 (1960)

95. G. Zerah, J.P. Hansen, Self-consistent integral equations for fluid pair distribution functions: Another attempt. J. Chem. Phys. **84**, 2336–2343 (1986)

96. Y. Rosenfeld, N.W. Ashcroft, Theory of simple classical fluids: Universality in the short-range structure. Phys. Rev. A. **20**, 1208–1235 (1979)

97. R.L. McGreevy, Reverse Monte Carlo modelling. J. Phys. Condens. Matter. **13**, 877–913 (2001)

98. M.A. Howe, R.L. McGreevy, L. Pusztai, I. Borzsák, Determination of three body correlations in simple liquids by RMC modelling of diffraction data. II. Elemental liquids. Phys. Chem. Liq. **25**, 205–241 (2006)

99. O.F. Yagafarov, Y. Katayama, V.V. Brazhkin, A.G. Lyapin, H. Saitoh, Energy dispersive x-ray diffraction and reverse Monte Carlo structural study of liquid gallium under pressure. Phys. Rev. B. **86**, 174103 (2012)

100. M. Li, C.Z. Wang, S.G. Hao, M.J. Kramer, K.M. Ho, Structural heterogeneity and medium-range order in Zr_xCu_{100-x} metallic glasses. Phys. Rev. B. **80**, 184201 (2009)

101. R. Car, M. Parrinello, Unified approach for molecular dynamics and density-functional theory. Phys. Rev. Lett. **55**, 2471–2474 (1985)

102. A. Rahman, Liquid structure and self-diffusion. J. Chem. Phys. **137**, 2585–2592 (1966)

103. A.R. Leach, *Molecular Modelling: Principles and Applications* (Prentice Hall, 2001)

104. K. Binder, J. Horbach, W. Kob, W. Paul, F. Varnik, Molecular dynamics simulations. J. Phys. Condens. Matter. **16**, S429–SS53 (2004)

105. M.P. Allen, D.J. Tildesley, *Computer Simulation of Liquids* (Oxford University Press, 2017)

106. W.C. Swope, H.C. Andersen, 10(6)-particle molecular-dynamics study of homogeneous nucleation of crystals in a supercooled atomic liquid. Phys. Rev. B. **41**, 7042–7054 (1990)

107. W. Kob, Computer simulations of supercooled liquids and glasses. J. Phys. Condens. Matter. **11**, R85–R115 (1999)

108. N.W. Ashcroft, J. Lekner, Structure and resistivity of liquid metals. Phys. Rev. **145**, 83–90 (1966)

109. J.P. Hansen, I.R. McDonald, *Theory of Simple Liquids* (Academic, London, 1986)

110. J. Hafner, G. Kahl, The structure of the elements in the liquid state. J. Phys. F. Met. Phys. **14**, 2259–2278 (1984)

111. J.F. Wax, N. Jakse, J.L. Bretonnet, Comparative study of structure determination schemes: Application to liquid alkali metals. Phys. Rev. B. **55**, 12099–12107 (1997)

112. G. Jacucci, M.L. Klein, R. Taylor, The static structure factor of liquid Li. Solid State Commun. **19**, 657–659 (1976)

113. J.M. Gonzalez Miranda, V. Torra, The effect of the Born-Mayer core on the properties of liquid lithium and sodium at their melting points. Phys. Lett. A. **103**, 126–128 (1984)

114. J.M.G. Miranda, A molecular dynamics study of liquid potassium at 340K. J. Phys. F. Met. Phys. **16**, 1–10 (1986)

115. J. Hafner, W. Jank, Structural and electronic properties of the liquid polyvalent elements. III. The trivalent elements. Phys. Rev. B. **42**, 11530–11539 (1990)

116. M.M.G. Alemany, J. Casas, C. Rey, L.E. González, L.J. Gallego, Dynamic properties of liquid alkaline-earth metals. Phys. Rev. E. **56**, 6818–6828 (1997)

117. J.F. Wax, R. Albaki, J.L. Bretonnet, Structural and dynamical properties of liquid alkaline-earth metals near the melting point. Phys. Rev. B. **62**, 14818–14827 (2000)

118. M.S. Daw, S.M. Foiles, M.I. Baskes, The embedded-atom method: A review of theory and applications. Mater. Sci. Rep. **9**, 251–310 (1993)
119. F. Ducastelle, Modules élastiques des métaux de transition. J. Phys. **31**, 1055–1062 (1970)
120. F. Ercolessi, E. Tosatti, M. Parrinello, Au (100) surface reconstruction. Phys. Rev. Lett. **57**, 719–722 (1986)
121. K.W. Jacobsen, J.K. Norskov, M.J. Puska, Interatomic interactions in the effective-medium theory. Phys. Rev. B. **35**, 7423–7442 (1987)
122. D.K. Belashchenko, Computer simulation of liquid metals. Uspekhi Fizicheskih Nauk. **183**, 1281–1322 (2013)
123. W. Kohn, L.J. Sham, Self-consistent equations including exchange and correlation effects. Phys. Rev. **140**, A1133–A11A8 (1965)
124. M. Born, J.R. Oppenheimer, Zur Quantentheorie der Molekeln. Annalen der Physik. **389**, 457–484 (1927)
125. S.R. Bickham, O. Pfaffenzeller, L.A. Collins, J.D. Kress, D. Hohl, Ab initiomolecular dynamics of expanded liquid sodium. Phys. Rev. B. **58**, R11813–R118R6 (1998)
126. M.M.G. Alemany, L.J. Gallego, D.J. González, Kohn-Sham ab initio molecular dynamics study of liquid Al near melting. Phys. Rev. B. **70**, 134206 (2004)
127. N. Jakse, O.L. Bacq, A. Pasturel, Short-range order of liquid and undercooled metals: Ab initio molecular dynamics study. J. Non-Cryst. Solids. **353**, 3684–3688 (2007)
128. A. Pasturel, E.S. Tasci, M.H.F. Sluiter, N. Jakse, Structural and dynamic evolution in liquid Au-Si eutectic alloy by ab initio molecular dynamics. Phys. Rev. B. **81**, 140202 (2010)
129. F.S. Ke, G.Q. Yue, B. Shen, F. Dong, S.Y. Wang, Y.X. Zheng, et al., Bergman-type medium-range order in rapidly quenched $Ag_{0.74}Ge_{0.26}$ eutectic alloy studied by ab initio molecular dynamics simulation. Acta Mater. **80**, 498–504 (2014)
130. B.G. del Rio, L.E. González, Structure and dynamics of liquid Zn: An analysis of ab-initio simulations. EPJ Web Conf. **151**, 03004 (2017)
131. J. Qiao, L. Zhang, X. Hui, J. Lin, Kinetic and thermodynamic properties of liquid zinc: An ab initio molecular dynamics study. Comput. Mater. Sci. **141**, 180–184 (2018)
132. P. Hohenberg, W. Kohn, Inhomogeneous electron gas. Phys. Rev. **136**, B864–BB71 (1964)
133. Y.A. Wang, E.A. Carter, Orbital-free kinetic-energy density functional theory, in *Theoretical Methods in Condensed Phase Chemistry*, ed. by S. D. Schwartz, (Springer, Dordrecht, 2002), pp. 117–184
134. M. Chen, J.R. Vella, A.Z. Panagiotopoulos, P.G. Debenedetti, F.H. Stillinger, E.A. Carter, Liquid Li structure and dynamics: A comparison between OFDFT and second nearest-neighbor embedded-atom method. AIChE J. **61**, 2841–2853 (2015)
135. B.G. del Rio, J.M. Dieterich, E.A. Carter, Globally-optimized local pseudopotentials for (orbital-free) density functional theory simulations of liquids and solids. J. Chem. Theor. Comput. **13**, 3684–3695 (2017)
136. S. Gómez, L.E. González, D.J. González, M.J. Stott, S.M. DalgiçS, Orbital free ab initio molecular dynamics study of expanded liquid Cs. J. Non-Cryst. Solids. **250–252**, 163–167 (1999)
137. D.J. González, L.E. González, J.M. López, M.J. Stott, Dynamical properties of liquid Al near melting: An orbital-free molecular dynamics study. Phys. Rev B. **65**, 184201 (2002)
138. J.A. Anta, B.J. Jesson, P.A. Madden, Ion-electron correlations in liquid metals from orbital free ab initio molecular dynamics. Phys. Rev. B. **58**, 6124–6132 (1998)
139. S. Sengul, D.J. Gonzalez, L.E. Gonzalez, Structural and dynamical properties of liquid Mg. An orbital-free molecular dynamics study. J. Phys. Condens. Matter. **21**, 115106 (2009)
140. M.R. Molla, A.Z. Ziauddin Ahmed, H. Sarker, G.M. Bhuiyan, M.R. Amin, L.E. González, et al., Static and dynamic properties of liquid Zn, Cd and Hg divalent metals: An orbital free ab initio molecular dynamics study. J. Non-Cryst. Solids. **406**, 45–53 (2014)
141. M.R. Molla, A.Z.Z. Ahmed, M.A. Hossain, G.M. Bhuiyan, M.M. Rahman, Static and dynamic properties of liquid Fe: An OF-AIMD simulation study. Phys. B. Condens. Matter. **567**, 129–137 (2019)

142. G.M. Bhuiyan, L.E. González, D.J. González, Orbital free ab initio molecular dynamics simulation study of some static and dynamic properties of liquid noble metals. Condens. Matter. Phys. **15**, 33604 (2012)

143. V. Heine, D. Weaire, Pseudopotential theory of cohesion and structure. Solid State Phys. **24**, 249–463 (1970)

144. J. Hafner, V. Heine, The crystal structures of the elements: Pseudopotential theory revisited. J. Phys. F. Met. Phys. **13**, 2479–2501 (1983)

145. J. Hafner, G. Kahl, The structure of the elements in the liquid state. J. Phys. F Metal Phys. **14**, 2259–2278 (1984)

146. W. Jank, J. Hafner, Structural and electronic properties of the liquid polyvalent elements. II. The divalent elements. Phys. Rev. B. **42**, 6926–6938 (1990)

147. W. Jank, J. Hafner, Structural and electronic properties of the liquid polyvalent elements: The group-IV elements Si, Ge, Sn, and Pb. Phys. Rev. B. **41**, 1497–1515 (1990)

148. J. Hafner, W. Jank, Structural and electronic properties of the liquid polyvalent elements. IV. The pentavalent semimetals and trends across the periodic table. Phys. Rev. B. **45**, 2739–2749 (1992)

149. del R, Pascual, Rodriguez, González, González., First principles determination of some static and dynamic properties of the liquid 3d transition metals near melting. Condens. Matter. Phys. **23**, 23606 (2020)

150. T. Si, M. Inui, S. Tamaki, K. Maruyama, Y. Waseda, Electron-ion correlation in liquid magnesium. J. Phys. Soc. Jpn. **63**, 1794–1802 (1994)

151. S. Tahara, H. Fujii, Y. Yokota, Y. Kawakita, S. Kohara, T. Si, Structure and electron–ion correlation in liquid Mg. Phys. B. Condens. Matter. **385-386**, 219–221 (2006)

152. L.E. González, A. Meyer, M.P. Iñiguez, D.J. González, M. Silbert, Liquid structure of the alkaline-earth metals. Phys. Rev. E. **47**, 4120–4129 (1993)

153. K.H. Seok, Thermodynamics and pair structures of liquid alkali and alkaline-earth metals from the perturbative hypernetted-chain equation. Phys. Rev. B. **60**, 6362–6371 (1999)

154. C. Fiolhais, J.P. Perdew, S.Q. Armster, J.M. MacLaren, M. Brajczewska, Erratum: Dominant density parameters and local pseudopotentials for simple metals. Phys. Rev. B. **53**, 13193 (1996)

155. G.A. de Wijs, G. Pastore, A. Selloni, W. van der Lugt, Electron-ion correlation in liquid metals from first principles: Liquid Mg and liquid Bi. Phys. Rev. Lett. **75**, 4480–4483 (1995)

156. Y. Kawakita, S. Hosokawa, T. Enosaki, K. Ohshima, S. Takeda, W.-C. Pilgrim, et al., Coherent dynamic scattering law of divalent liquid Mg. J. Phys. Soc. Jpn. **72**, 1603–1606 (2003)

157. T.T. Debela, X.D. Wang, Q.P. Cao, D.X. Zhang, J-J. Zhu, J.Z. Jiang, Phase selection during solidification of liquid magnesium via ab initio molecular dynamics simulations. J Appl Phys **117**, 114905 (2015)

158. C. Gamertsfelder, Atomic distributions in liquid elements. J. Chem. Phys. **9**, 450–457 (1941)

159. P.J. Black, J.A. Cundall, The structures of liquid mercury and liquid aluminum. Acta Crystallogr. **19**, 807–814 (1965)

160. R.R. Fessler, R. Kaplow, B.L. Averbach, Pair correlations in liquid and solid aluminum. Phys. Rev. **150**, 34–43 (1966)

161. Y. Waseda, K. Suzuki, Structure factor and atomic distribution in liquid metals by X-ray diffraction. Phys. Status Solid B. **49**, 339–347 (1972)

162. J.M. Stallard, C.M. Davis, Liquid-aluminum structure factor by neutron diffraction. Phys. Rev. A. **8**, 368–376 (1973)

163. N.A. Mauro, J.C. Bendert, A.J. Vogt, J.M. Gewin, K.F. Kelton, High energy x-ray scattering studies of the local order in liquid Al. J. Chem. Phys. **135**, 044502 (2011)

164. VahvaselkäKS., X-ray diffraction analysis of liquid Hg, Sn, Zn, Al and Cu. Phys. Scripta **18**, 266–274 (1978)

165. R.V.G. Rao, A.K.K. Murthy, Mean spherical model and structure factor of liquid mercury and aluminium. Phys. Stat. Sol. **66**, 703–707 (1974)

166. I. Ebbsio, T. Kinell, I. Waller, The dynamical structure factor for liquid aluminium. J. Phys. C. Solid. Stat. Phys. **13**, 1865–1885 (1980)
167. L. Hui, W. Guanghou, Z. Jijun, B. Xiufang, Cluster structure and dynamics of liquid aluminum under cooling conditions. J. Chem. Phys. **116**, 10809–10815 (2002)
168. B. Shen, C.Y. Liu, Y. Jia, G.Q. Yue, F.S. Ke, H.B. Zhao, et al., Molecular dynamics simulation studies of structural and dynamical properties of rapidly quenched Al. J. Non-Cryst. Solids. **383**, 13–20 (2014)
169. Z.Y. Hou, K.J. Dong, Z.A. Tian, R.S. Liu, Z. Wang, J.G. Wang, Cooling rate dependence of solidification for liquid aluminium: A large-scale molecular dynamics simulation study. Phys. Chem. Chem. Phys. **18**, 17461–17469 (2016)
170. Y. Jiang, J. Luo, Y. Wu, The validation and preference among different EAM potentials to describe the solid–liquid transition of aluminum. Model Simul. Mater. Sci. Eng. **25**, 045012 (2017)
171. M.I. Mendelev, M.J. Kramer, C.A. Becker, M. Asta, Analysis of semi-empirical interatomic potentials appropriate for simulation of crystalline and liquid Al and Cu. Philos Mag. **88**, 1723–1750 (2008)
172. J.B. Sturgeon, B.B. Laird, Adjusting the melting point of a model system via Gibbs-Duhem integration: Application to a model of aluminum. Phys. Rev. B. **62**, 14720–14727 (2000)
173. J.M. Winey, A. Kubota, Y.M. Gupta, Thermodynamic approach to determine accurate potentials for molecular dynamics simulations: Thermoelastic response of aluminum. Model Simul. Mater. Sci. Eng. **18**, 029801 (2010)
174. X.W. Zhou, R.A. Johnson, H.N.G. Wadley, Misfit-energy-increasing dislocations in vapor-deposited CoFe/NiFe multilayers. Phys. Rev. B. **69**, 144113 (2004)
175. X.W. Fang, C.Z. Wang, Y.X. Yao, Z.J. Ding, K.M. Ho, Competition between FCC and icosahedral short-range orders in pure and samarium-doped liquid aluminum from first principles. Phys. Rev. B. **83**, 224203 (2011)
176. N. Jakse, T. Bryk, Pressure evolution of transverse collective excitations in liquid Al along the melting line. J Chem Phys. **151**, 034506 (2019)
177. Y. Waseua, S. Tamake, Structure and effective interionic potential of liquid titanium. Phys. Stat. Sol. **71**, 665–670 (1975)
178. B. Lee, G.W. Lee, Comparative study of Ti and Ni clusters from first principles. J. Chem. Phys. **127**, 164316 (2007)
179. B. Lee, G.W. Lee, Local structure of liquid Ti: Ab initio molecular dynamics study. J. Chem. Phys. **129**, 024711 (2008)
180. T.R.G. Kutty, K. Ravi, C. Ganguly, Studies on hot hardness of Zr and its alloys for nuclear reactors. J. Nucl. Mater. **265**, 91–99 (1999)
181. H.-G. Kim, Evaluation of the corrosion and Oxide microstructural characteristics of pure Zr and the Zr-1.5Nb Alloy. Met. Mater-Int. **14**, 83–89 (2008)
182. D. Guo, M. Li, Y. Shi, Z. Zhang, H. Zhang, X. Liu, et al., High strength and ductility in multimodal-structured Zr. Mater. Design. **34**, 275–278 (2012)
183. Y. Waseda, M. Ohtani, Structure and effective interionic potential of liquid palladium, platinum and zirconium. Z Physik B **21**, 229–234 (1975)
184. S. Wu, X.W. Fang, S.Y. Wang, C.Z. Wang, Y.X. Yao, K.M. Ho, et al., Fluctuation between icosahedral and body-centered-cube short-range orders in undercooled Zr liquid. J. Appl. Phys. **110**, 103518 (2011)
185. A.E. Gheribi, Molecular dynamics study of stable and undercooled liquid zirconium based on MEAM interatomic potential. Mater. Chem. Phys. **116**, 489–496 (2009)
186. R.J. Ackermann, S.P. Garg, E.G. Rauh, High-temperature phase-diagram for system Zr-O. J. Am. Ceram. Soc. **60**, 341–345 (1977)
187. C.A. Angell, Formation of glasses from liquids and biopolymers. Science **267**, 1924–1935 (1995)

188. P.F. Paradis, T. Ishikawa, S. Yoda, Non-contact measurements of surface tension and viscosity of niobium, zirconium, and titanium using an electrostatic levitation furnace. Int. J. Thermophys. **23**, 825–842 (2002)
189. P.F. Paradis, W.K. Rhim, Thermophysical properties of zirconium at high temperature. J. Mater. Res. **14**, 3713–3719 (1999)
190. T. Iida, R.I.L. Guthrie, *The Thermophysical Properties of Metallic Liquids* (Oxford University Press, New York, 2015)
191. Y. Ohishi, T. Kondo, T. Ishikawa, J.T. Okada, Y. Watanabe, H. Muta, et al., Thermophysical properties of Zr-O liquid alloys measured by electrostatic levitation. Int. J. Microgravity S. **35**, 350105 (2018)
192. Y. Waseda, K. Suzuki, Atomic distribution and magnetic moment in liquid iron by neutron diffraction. Phys. Stat. Sol. **39**, 669–678 (1970)
193. Y. Waseda, M. Ohtani, Static structure of liquid noble and transition metals by X-ray diffraction. Phys. Stat. Sol. **62**, 535–546 (1974)
194. M. Inui, K. Maruyama, Y. Kajihara, M. Nakada, Icosahedral ordering in liquid iron studied via x-ray scattering and Monte Carlo simulations. Phys. Rev. B. **80**, 180201 (2009)
195. L. Vocadlo, G.A. de Wijs, G. Kresse, M. Gillan, G.D. Price, First principles calculations on crystalline and liquid iron at Earth's core conditions. Faraday Discuss. **106**, 205–217 (1997)
196. M. Marqués, L.E. González, D.J. González, Ab initio study of the structure and dynamics of bulk liquid Fe. Phys. Rev. B. **92**, 134203 (2015)
197. N. Ren, B. Shang, P. Guan, L. Hu, General structural and dynamic characteristics beneficial to glass-forming ability of Fe-based glass-forming liquids. J Non-Cryst. Solids. **481**, 116–122 (2018)
198. R. Li, Y. Wu, J. Xiao, The nucleation process and the roles of structure and density fluctuations in supercooled liquid Fe. J. Chem. Phys. **140**, 034503 (2014)
199. Y. Waseda, S. Tamaki, The structures of 3d-transition metals in the liquid state. Philos. Mag. **32**, 273–281 (1975)
200. VahvaselkäKS., Structure investigation and pair potentials for liquid Fe, Co and Ni by X- rays. Phys. Scripta. **24**, 59–64 (1981)
201. L. Do Phuong, A. Pasturel, D.N. Manh, Effect of s-d hybridization on interatomic pair potentials of the 3d liquid transition metals. J. Phys. Condens. Matter. **5**, 1901–1918 (1993)
202. G.M. Bhuiyan, M. Silbert, M.J. Stott, Structure and thermodynamic properties of liquid transition metals: An embedded-atom-method approach. Phys. Rev. B. **53**, 636–645 (1996)
203. X.J. Han, J.Z. Wang, M. Chen, Z.Y. Guo, Molecular dynamics simulation of thermophysical properties of undercooled liquid cobalt. J. Phys. Condens. Matter. **16**, 2565–2574 (2004)
204. R. Pasianot, E.J. Savino, Embedded-atom-method interatomic potentials for HCP metals. Phys. Rev. B. **45**, 12704–12710 (1992)
205. D.L. Tönsing, P.M. Stoop, J.H. van der Merwe, The formation of misfit dislocations by climb in pseudomorphic monolayers. Surf. Sci. **277**, 193–206 (1992)
206. Y. Waseda, K. Suzuki, S. Tamaki, S. Takeuchi, Neutron diffraction study of nickel in the liquid state. Phys. Stat .Sol **39**, 181–188 (1970)
207. M.W. Johnson, N.H. March, B. McCoy, S.K. Mitra, D.I. Page, R.C. Perrin, Structure and effective pair interaction in liquid nickel. Philos. Mag. **33**, 203–206 (1976)
208. O.J. Eder, B. Kunsch, M. Suda, E. Erdpresser, H. Stiller, P. Weinzierl, The structure factor of liquid nickel at 1873K. J. Phys. F. Met. Phys. **9**, 1215–1222 (1979)
209. N. Jakse, A. Pasturel, Ab initio molecular dynamics simulations of local structure of supercooled Ni. J Chem. Phys. **120**, 6124–6127 (2004)
210. M.M.G. Alemany, M. Calleja, C. Rey, L.J. Gallego, J. Casas, L.E. González, A theoretical and computer simulation study of the static structure and thermodynamic properties of liquid transition metals using the embedded atom model. J. Non-Cryst. Solids. **250-252**, 53–58 (1999)

211. M.M.G. Alemany, L.J. Gallego, L.E. González, D.J. González, A molecular dynamics study of the transport coefficients of liquid transition and noble metals using effective pair potentials obtained from the embedded atom model. J. Chem. Phys. **113**, 10410–10411 (2000)

212. F.J. Cherne, M.I. Baskes, P.A. Deymier, Properties of liquid nickel: A critical comparison of EAM and MEAM calculations. Phys. Rev. B. **65**, 024209 (2001)

213. J.E. Angelo, N.R. Moody, M.I. Baskes, Trapping of hydrogen to lattice defects in nickel. Model. Simul. Mater. Sci. Eng. **3**, 289–307 (1995)

214. M.I. Baskes, Determination of modified embedded atom method parameters for nickel. Mater. Chem. Phys. **50**, 152–158 (1997)

215. A. Posada-Amarillas, I.L. Garzon, Microstructural analysis of simulated liquid and amorphous Ni. Phys. Rev. B. **53**, 8363–8368 (1996)

216. B.G. Del Rio, L.E. Gonzalez, D.J. Gonzalez, Ab initio study of several static and dynamic properties of bulk liquid Ni near melting. J. Chem. Phys. **146**, 034501 (2017)

217. J. Ma, Y. Dai, J. Zhang, Z. Zhang, J. Wang, B. Sun, Ab initio molecular dynamics study of the structure of undercooled Ni melt. J. Non-Cryst. Solids. **376**, 216–220 (2013)

218. H.Z. Fang, X. Hui, G.L. Chen, Z.K. Liu, Structural evolution of Cu during rapid quenching by ab initio molecular dynamics. Phys. Lett. A. **372**, 5831–5837 (2008)

219. S. Winczewski, J. Dziedzic, J. Rybicki, In-depth characterization of icosahedral ordering in liquid copper. Comput. Mater. Sci. **166**, 57–74 (2019)

220. Y.F. Mo, Z.A. Tian, R.S. Liu, Z.Y. Hou, C.C. Wang, Structural evolution during crystallization of rapidly super-cooled copper melt. J. Non-Cryst. Solids. **421**, 14–19 (2015)

221. C.S. Liu, J. Xia, Z.G. Zhu, D.Y. Sun, The cooling rate dependence of crystallization for liquid copper: A molecular dynamics study. J. Chem. Phys. **114**, 7506–7512 (2001)

222. N.A. Mauro, A.J. Vogt, M.L. Johnson, J.C. Bendert, K.F. Kelton, Anomalous structural evolution in $Cu_{50}Zr_{50}$ glass-forming liquids. Appl. Phys. Lett. **103**, 021904 (2013)

223. M.I. Mendelev, M.J. Kramer, R.T. Ott, D.J. Sordelet, M.F. Besser, A. Kreyssig, et al., Experimental and computer simulation determination of the structural changes occurring through the liquid-glass transition in Cu-Zr alloys. Philos. Mag. **90**, 3795–3815 (2010)

224. S. Sinha, P.L. Srivastava, R.N. Singh, Temperature-dependent structure and electrical transport in liquid-metals. J. Phys. Condens. Matter. **1**, 1695–1705 (1989)

225. N. Mattern, H. Hermann, S. Roth, J. Sakowski, M.P. Macht, P. Jovari, et al., Structural behavior of $Pd_{40}Cu_{30}Ni_{10}P_{20}$ bulk metallic glass below and above the glass transition. Appl. Phys. Lett. **82**, 2589–2591 (2003)

226. N. Mattern, J. Sakowski, U. Kuhn, H. Vinzelberg, K. Eckert, Structural behavior and glass transition of bulk metallic glasses. J. Non-Cryst. Solids. **345**, 758–761 (2004)

227. C.A. Angell, Perspective on the glass-transition. J. Phys. Chem. Solids. **49**, 863–871 (1988)

228. J.C. Bendert, K.F. Kelton, Correlation between kinetic strength, volumetric properties, and glass forming ability in metallic liquids. J Non-Cryst. Solids. **376**, 205–208 (2013)

229. S.K. Chung, D.B. Thiessen, W.K. Rhim, A noncontact measurement technique for the density and thermal expansion coefficient of solid and liquid materials. Rev. Sci. Instrum. **67**, 3175–3181 (1996)

230. N.A. Mauro, M.L. Johnson, J.C. Bendert, K.F. Kelton, Structural evolution in Ni-Nb and Ni-Nb-Ta liquids and glasses – A measure of liquid fragility? J Non-Cryst. Solids. **362**, 237–245 (2013)

231. L.Y. Chen, M. Mohr, R.K. Wunderlich, H.J. Fecht, X.D. Wang, Q.P. Cao, et al., Correlation of viscosity with atomic packing in $Cu_{50}Zr_{50}$ melt. J. Mol. Liq. **293**, 111544 (2019)

232. M. Mohr, R.K. Wunderlich, S. Koch, P.K. Galenko, A.K. Gangopadhyay, K.F. Kelton, et al., Surface tension and viscosity of $Cu_{50}Zr_{50}$ measured by the oscillating drop technique on board the international space station. Microgravity Sci. Tech. **31**, 177–184 (2019)

233. N.A. Mauro, M. Blodgett, M.L. Johnson, A.J. Vogt, K.F. Kelton, A structural signature of liquid fragility. Nat. Commun. **5**, 4616 (2014)

234. H. Zhang, C. Zhong, J.F. Douglas, X.D. Wang, Q.P. Cao, D.X. Zhang, et al., Role of string-like collective atomic motion on diffusion and structural relaxation in glass forming Cu-Zr alloys. J. Chem. Phys. **142**, 164506 (2015)
235. R. Novakovic, T. Tanaka, M.L. Muolo, J. Lee, A. Passerone, Bulk and surface properties of liquid Ag-X (X = Ti, Hf) compound forming alloys. Surf. Sci. **591**, 56–69 (2005)
236. C.P. Lee, M.J. Lyell, T.G. Wang, Viscous damping of the oscillations of a rotating simple drop. Phys. Fluids. **28**, 3187–3188 (1985)
237. D. Holland-Moritz, F. Yang, T. Kordel, S. Klein, F. Kargl, J. Gegner, et al., Does an icosahedral short-range order prevail in glass-forming Zr-Cu melts? Epl-Europhys. Lett. **100**, 56002 (2012)
238. S.G. Hao, C.Z. Wang, M.J. Kramer, K.M. Ho, Microscopic origin of slow dynamics at the good glass forming composition range in $Zr_{1-x}Cu_x$ metallic liquids. J. Appl. Phys. **107**, 053511 (2010)

Chapter 7
Theory of Nucleation and Glass Formation

Kenneth F. Kelton

1 Introduction

Almost all first-order phase transformations are initiated by a process of nucleation, where small regions with an order parameter characterizing the new phase stochastically form [1]. In addition to the fundamental interest in this process, nucleation is of extreme practical importance. An ability to control nucleation is central to grain refinement [2], glass formation [3, 4], and the production of glass ceramics [5]. In addition, nucleation control is essential in the pharmaceutical [6, 7] and food [8, 9] industries, and it can play a vital role in biological systems [10] and in medical diseases [11].

A central feature of nucleation processes is the existence of a nucleation barrier. This was first evident in a set of experiments by Fahrenheit, who noted that liquid water could be maintained in a supercooled state (i.e., below the melting temperature) for long periods of time without crystallizing [12]. Turnbull was the first to observe this in liquid metals and showed that the amount of supercooling can be quite large, up to one third of the melting temperature in liquid mercury, for example [13]. Such dramatic supercooling in a liquid metal was surprising given the similarity in the densities of metallic liquids and crystals and their similar coordination numbers. It is now recognized that all metallic liquids can be deeply undercooled, typically to approximately 20% of their liquidus temperatures [1].

Nucleation can be either homogeneous or heterogeneous. Homogeneous nucleation is the more fundamental of the two types, occurring randomly in space and time. Heterogeneous nucleation is more common, occurring at specific sites in the initial phase. Even though it is less common, studies of homogeneous nucleation are possible under the right conditions. This chapter will focus on homogeneous

K. F. Kelton (✉)
Washington University in St. Louis, St. Louis, MO, USA
e-mail: kfk@wustl.edu

nucleation, review some experimental data in liquids and glasses, and discuss models for nucleation. A discussion of heterogeneous nucleation can be found elsewhere [1]. Computer simulations are increasingly valuable for enabling a microscopic investigation of nucleation processes and will also be briefly discussed. Of particular interest for this book are studies of nucleation under microgravity conditions. A brief discussion of these for protein, colloidal, and metallic liquids is presented. Finally the role of nucleation in glass formation is very briefly described.

2 Nucleation Theories

The classical nucleation theory (CNT) is most commonly used to analyze nucleation data, but it has several shortcomings. The most important of these are discussed in this section and more advanced theories that address them are presented. But, first, we turn to a discussion of CNT and its development.

2.1 Classical Nucleation Theory (CNT)

The thermodynamic formulation of CNT is due to J. W. Gibbs [14]. Assuming that the nucleation barrier arises from the energy required to create an interface between the initial phase and a small cluster of the new phase, he showed that the minimum amount of work required to form a spherical cluster of n atoms of the new phase, $W(n)$, is

$$W(n) = n\Delta\mu + \kappa n^{2/3}\sigma, \tag{7.1}$$

where $\Delta\mu$ is the difference in chemical potential between the original and the final phase, σ is the interfacial free energy between the nucleating cluster and the original phase, κ is a geometrical factor equal to $(4\pi)^{1/3}(3\overline{v})^{2/3}$, and $\overline{v}$ is the molecular volume. The work can also be expressed in terms of the cluster radius, r:

$$W(r) = \frac{4}{3}\pi r^3 \Delta g + 4\pi r^2 \sigma, \tag{7.2}$$

where $\Delta g = \Delta\mu/\overline{v}$. The work of cluster formation as a function of cluster size, n, is shown in Fig. 7.1a. For small clusters, $W(n)$ increases with increasing size but goes through a maximum, $W(n^*) = W^*$, at a critical cluster size n^*, beyond which it decreases with increasing size. As indicated, clusters smaller than n^* are on average dissolving, and those larger than n^* are on average growing. Nucleation is dominated by the time required for clusters to diffuse (in cluster size space) through a critical region that is located $k_B T$ less than W^*, where k_B is the Boltzmann constant and T is the temperature in absolute units.
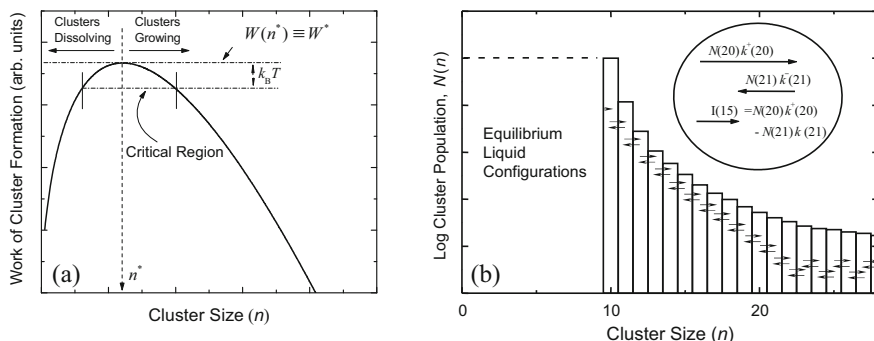
Fig. 7.1 (**a**) Work of cluster formation as a function of the number of molecules in the cluster, n, showing the critical size, n^*, and the critical region. (**b**) A histogram of the cluster population as a function of the number of molecules in a cluster, n. (Adapted from Ref. [1], copyright (2010), with permission from Elsevier)

The critical radius, r^*, is found by differentiating $W(r)$ with respect to the radius and setting that equal to zero, giving $r^* = 2\sigma/|\Delta g|$. The corresponding number of molecules in the critical cluster is $n^* = [32\pi/(3\overline{v})](\sigma/|\Delta g|)^3$. The critical work of cluster formation is obtained by substituting r^* into Eq. (7.2), giving

$$W^* = \frac{16\pi}{3} \frac{\sigma^3}{|\Delta g|^2} \tag{7.3}$$

Gibbs assumed that the nucleation rate is proportional to the probability of having a fluctuation that gives a cluster of the new phase containing n^* molecules, i.e., $\propto \exp{(-W^*/k_B T)}$. The computation of the proportionality constant requires a kinetic model that describes the rate that clusters evolve in size. Following an approach used in chemical kinetics, Volmer and Weber [15] assumed that this occurs by a series of bi-molecular reactions with single molecular attachment or detachment at each step, as illustrated in Fig. 7.1b. The nucleation rate is the flux past a given size and is in general time dependent:

$$I_{n,t} = N_{n,t} k_n^+ - N_{n+1,t} k_{n+1}^-. \tag{7.4}$$

Assuming, however, that the cluster distribution is time invariant, Becker and Döring [16] obtained an expression for the steady-state nucleation rate per mole:

$$I^{st} = k_{n*}^+ \left(\frac{|\Delta\mu|}{6\pi k_B T n^*} \right) N_A \exp\left(-\frac{W^*}{k_B T} \right) = k_{n*}^+ Z N_A \exp\left(-\frac{W^*}{k_B T} \right), \tag{7.5}$$

where N_A is Avogadro's number and Z is the Zeldovich factor. These equations were developed for gas condensation, for which k_{n*}^+ could be computed from molecular dynamics. Turnbull and Fischer were the first to apply them to nucleation from a

liquid by assuming that the kinetics of attachment were determined by the diffusion coefficient in the original phase [17], giving

$$I^s \;=\; \frac{24D(n^*)^{2/3}N_A}{\lambda^2}\; Z\,\exp\left(-\frac{W^*}{k_B T}\right) \;=\; A^*\exp\left(-\frac{W^*}{k_B T}\right). \qquad (7.6)$$

The development of CNT assumes that the interface between the nucleating cluster and the original liquid or glass phase is sharp. The first suggestion that this might not be correct came from experimental studies of the nucleation rate in liquid mercury [13], where the pre-factor measured from fits to the data was seven orders of magnitude larger than the value calculated from Eq. (7.6). These were brought into agreement by assuming that the interfacial free energy, σ_{ls}, increased with temperature. Since a free energy should decrease, not increase, with increasing temperature due to the entropy term, Turnbull argued that there must be a sizable entropy deficit due to ordering in the liquid in front of the advancing interface. This indicates that the interface is then diffuse, rather than sharp. As discussed next, more sophisticated theories of nucleation support this conclusion.

2.2   Density Functional Theory (DFT)

DFT is based on a position-dependent order parameter description of the original and nucleating phases. The density is a good order parameter for gas condensation, since the densities of the two phases are very different. However, an order parameter that takes account of local symmetry is a better one for a liquid/glass to crystal transition. The work of cluster formation is expressed as a functional (i.e., a function of a function) of the chosen order parameter. By setting the derivative of the work with respect to the order parameter equal to zero, the critical fluctuation of the order parameter is obtained. This is analogous to the critical size in CNT. A more in-depth discussion may be found elsewhere (Chapter 4 in Ref. [1]).

There have been many proposed DFT formulations of the work of cluster formation (see Chapter 4 in Ref. [1]). Gránásy tested these for nucleation in liquids [18] and glasses [19], finding that the semi-empirical density functional approximation (SDFA) fit the data best. This model is based on a single non-conserved structural order parameter, M, which is equal to 1 in the macroscopic crystal phase and zero in the liquid phase [20]. Two key predictions from this theory are as follows: (i) the interface is diffuse, not sharp, and (ii) the order parameter becomes much less than the expected value of 1, even in the center of the cluster, as the departure from equilibrium is increased (i.e., increased supercooling for crystallization from the liquid). These points are illustrated in Fig. 7.2a, for the order parameter as a function of scaled distance for three different scaled critical sizes, which correspond to three values of $\widetilde{\Delta}$, a scaled dimensionless free energy difference between the liquid and the solid.
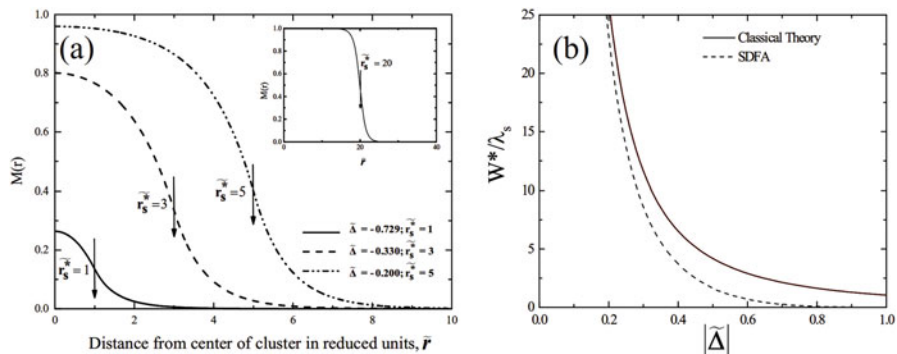
Fig. 7.2 (**a**) The order parameter, *M*, as a function of the scaled distance from the center of the cluster, measured in reduced units. (**b**) The scaled work of formation as a function of the scaled driving free energy. (Reprinted with permission from Ref. [20], copyright (1994), American Institute of Physics)

As for CNT, the values of $\widetilde{\Delta}$ become more negative, and the critical sizes decrease with increased departure from equilibrium, with the order parameter systematically decreasing in the center of the cluster. For large departures from equilibrium, the difference between the order parameter in the cluster and in the liquid is very small, indicating that the structural order in the liquid and the nucleating phase is similar. Close to equilibrium, shown in the inset, the order parameter is the same as for the macroscopic crystal, although it should be noted that the interface remains diffuse.

The predictions of the work of critical cluster formation behave similarly as a function of $\widetilde{\Delta}$. As shown in Fig. 7.2b, the critical work from the SDFA, scaled to the curvature of the free energy curve for the solid phase, (W^*/λ_s), approaches the value for that calculated from CNT for small magnitudes of $\widetilde{\Delta}$, i.e., close to equilibrium. The value from SDFA becomes less than the value from CNT with increasing magnitude of $\widetilde{\Delta}$, approaching zero at large departures from equilibrium.

2.3 Diffuse Interface Theory (DIT) of Nucleation

While density functional theories give quantitative predictions for the profile of the order parameter, their use for analyzing nucleation experimental data is not straightforward since many of the parameters needed are poorly known or not known at all. The diffuse interface theory (DIT) [21–23] offers a phenomenological thermodynamic approach that can be more readily used. In contrast with the CNT, the DIT explicitly assumes that the interface is diffuse, in agreement with predictions from DFT theories (Sect. 2.2) and computer simulations (Sect. 3). Based on the DFT studies, the profile of the Gibbs free energy should qualitatively have the form shown in Fig. 7.3a, with a maximum in the interfacial region.
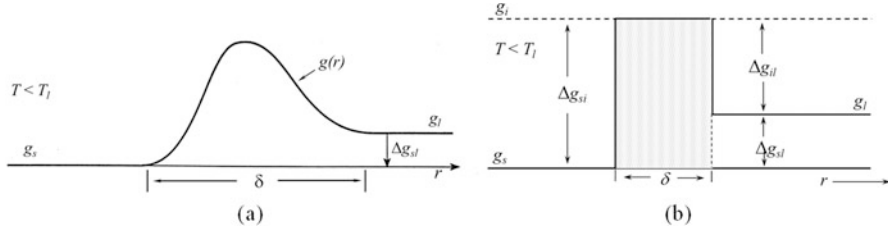
Fig. 7.3 (**a**) The qualitative profile of the Gibbs free energy density as a function of distance through the interfacial region. (**b**) The simplified profile assumed within the DIT. (Adapted from Ref. [21], copyright (1994), with permission from Elsevier)

As shown in Fig. 7.3b, within the DIT this profile can be approximated as a step function having a width δ, which corresponds to the width of the interface. The interfacial width reflects the difference between the profile of the enthalpy and the entropy on transitioning through the interface [24]. Assuming a spherical cluster, the work of cluster formation is

$$W = \int_0^\infty (\Delta h - T\Delta s) 4\pi r^2 dr \qquad (7.7)$$

where $\Delta h = N(r)[H(r) - H_1]$ and $\Delta s = N(r)[S(r) - S_1]$, $N(r)$ is the local molecular number density, and $H(r)$ and $S(r)$ are the molecular enthalpy and entropy; the subscript one refers to the parent phase. For clusters with a radius that is significantly larger than the interfacial width, $\delta \cong R_S - R_H$, where R_H and R_S are the midpoints of the enthalpy and entropy profiles on traversing through the interface. It follows that $\Delta h \cong \Delta h_0[1 - \theta(r - R_H)]$ and $\Delta s \cong \Delta s_0[1 - \theta(r - R_S)]$, where θ represents the step function approximation in Fig. 7.3b. The work of cluster formation is

$$W = \frac{4\pi}{3} \left(R_H^3 \Delta h_0 - R_S^3 T\Delta s_0 \right) \qquad (7.8)$$

and the area enclosed between the Δh and $T\Delta s$ curves is proportional to the interfacial free energy. Using $\delta \cong R_S - R_H$ and maximizing the work of cluster formation with respect to R_S, the critical size, R_S^*, and the critical work of cluster formation, W^*, can be obtained:

$$R_S^* = \frac{\delta\Delta h_0 + \delta\sqrt{\Delta h_0 T\Delta s_0}}{\Delta h_0 - T\Delta s_0} \quad \text{and} \quad W^* = -\frac{4\pi}{3}\delta^3 \Delta g_o \psi \qquad (7.9)$$

where $\Delta g_o = \Delta h_o - T\Delta s_o$, $\psi = 2(1 + q)\zeta^{-3} - (3 + 2q)\zeta^{-2} + \zeta^{-1}$, $q = (1 - \zeta)^{1/2}$, and $\zeta = \Delta g_o/\Delta h_o$. The critical work of formation can be written in a more compact form as [25]

$$W^* = -\frac{\frac{4\pi}{3}\delta^3 \Delta h_0 T \Delta s_0}{\Delta h_0 + T\Delta s_0 - 2\sqrt{\Delta h_0 T \Delta s_0}}. \tag{7.10}$$

A key result of the DIT model is the confirmation that a positive temperature dependence of the interfacial free energy indicates that the interface of the nucleating cluster is more ordered than the liquid or glass parent phase [21].

2.4 Composition Effects on Nucleation

The theories discussed in Sects. 2.1, 2.2, and 2.3 apply to nucleation processes in which the chemical compositions of the initial and final phases are the same. This is true for only a limited number of cases. If the diffusion rates are sufficiently fast in undercooled liquids, only interfacial processes need be considered. It is then reasonable to expect that the steady-state nucleation rate for a binary system (A, B) will be

$$I_{a,b}^s = A_{a,b}^* \exp\left(-\frac{W_{a,b}^*}{k_B T}\right), \tag{7.11}$$

where $W_{a,b}^*$ is the reversible work of formation of a cluster of critical size n^*, composed of a^* molecules of A and b^* molecules of B, and $A_{a,b}^*$ is the pre-factor. Assuming an effective interfacial free energy, σ, for a sharp interface between the nucleating cluster and the parent phase, $W_{a,\,b}$ is (approximately)

$$W_{a,b} = a\delta g_A + b\delta g_B + \zeta\sigma(a\bar{v}_A + b\bar{v}_B)^{2/3} \tag{7.12}$$

where δg_A and δg_B are the changes in the Gibbs free energy per atom for A and B, ζ is a geometric factor (which is $(36\pi)^{1/3}$ for spherical clusters), and $\bar{v}_A$ and are the molecular volumes of A and B atoms, respectively. Reiss showed [26] that the pre-factor, $A_{a,b}^*$ is a function of the composition of A and B in the liquid, their atomic mobility at the interface, and the two mutually orthogonal curvatures of $W_{a,b}$ at the saddle point, P and Q. Assuming that the forward and backward rate constants have a similar form to those in the CNT and that the cluster composition corresponds to the maximum driving free energy (corresponding to a saddle point in the free energy as a function of the cluster number and concentration), he obtained the following expression for the steady-state nucleation rate:

$$I^s = k_{a^*,b^*}^+ \sqrt{P/Q} N_{a^*,b^*}^{eq}, \tag{7.13}$$

where the equilibrium number of clusters at the critical size in terms of Avogadro's number of single molecules, N_A^0 and N_B^0, is [27]
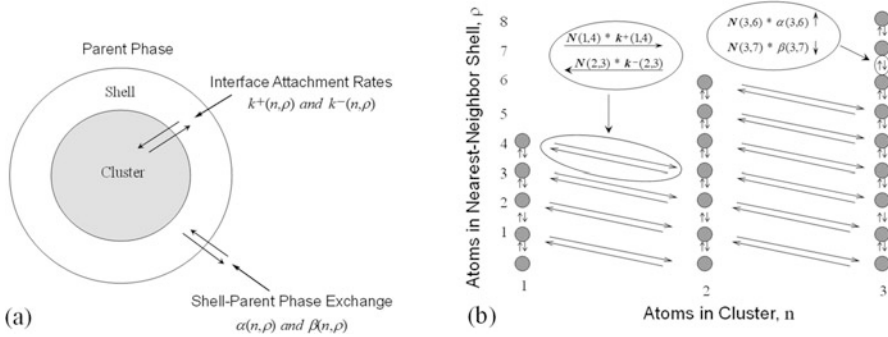
Fig. 7.4 (**a**) Schematic illustration of the fundamental features of the coupled-flux model, showing the interfacial fluxes and those between the shell and parent phase. (**b**) Schematic illustration of the kinetic processes in the coupled-flux model, shown here up to a cluster size of 3. Motion between the shell and the parent phase, changing the shell composition, occurs along the vertical axes, while interfacial attachment occurs along the horizontal and diagonal lines. The upper cutoff of the vertical axis corresponds to a complete filling of the shell region of a cluster of size n. (Adapted from Ref. [34], copyright (2000), with permission from Elsevier)

$$N_{a,b}^{\text{eq}} = \left(N_A^0\right)^{N_A^0/\left(N_A^0+N_B^0\right)} \left(N_B^0\right)^{N_B^0/\left(N_A^0+N_B^0\right)} \exp\left(-\frac{W_{a,b}}{k_{\text{B}}T}\right). \qquad (7.14)$$

The effect of chemical composition is reflected in changes in the driving free energy, interfacial free energy, and the atomic mobility. Several refined treatments have been offered to deal with shortcomings in Reiss development [28–30]. Wu offered the most complete solution for binary nucleation by mapping nucleation onto a one-component system [27]. His approach can also be extended to more than two component systems. A more detailed discussion of interface controlled multicomponent nucleation can be found elsewhere [1].

If the diffusion and interface kinetics are comparable, the stochastic fluxes for diffusion in cluster space and diffusion in the real space of the parent phase become coupled, which can have a strong influence on nucleation in cases like solid-state transformations, precipitation, and crystallization from the liquid phase, if stirring is minimized such as in a microgravity environment. To understand this, it is easiest to think about precipitation of a pure phase from solute atoms in a solution. Following an approach first suggested by Russell [31], the coupled fluxes can be treated by focusing attention on three regions: the cluster, the immediate neighborhood around the cluster, and the parent phase (Fig. 7.4a). The number of atoms in the cluster, n, and the number in the cluster neighborhood, ρ, must both be considered. Assuming that the number of atoms in the clusters and their nearest-neighbor shells occur by the gain or loss of a single atom at a time, the rate kinetics are described within a two-dimensional (n,ρ) space (Fig. 7.4b). Since only the nearest-neighbor shell is considered, the upper limit on ρ (p^m) increases with cluster size n, $p^m \approx 4n^{2/3}$, giving the staircase appearance in Fig. 7.4b.

The equilibrium cluster distribution in the coupled-flux model is

$$N(n,\rho) = N_o \exp\left(-\frac{W_n}{k_B T}\right) P\{\rho\}, \tag{7.15}$$

where N_o is the number of solute atoms per unit volume in the initial phase distributed among the number of possible sites (N_S), W_n is the work of cluster formation, and $P\{\rho\}$ is the probability for having ρ solute atoms in the nearest-neighbor shell around the cluster. For simplicity, the work of cluster formation is taken to be the same as in the classical theory. From Fig. 7.4b, the differential equation that describe the rate of change of the cluster distribution is

$$\begin{aligned}
\frac{\partial N(n,\rho,t)}{\partial t} &= \alpha(n,\rho-1)N(n,\rho-1,t) - [\alpha(n,\rho)+\beta(n,\rho)]N(n,\rho,t) \\
&+ \beta(n,\rho+1)N(n,\rho+1,t) + k^+(n-1,\rho+1)N(n-1,\rho+1,t) \\
&+ k^-(n+1,\rho-1)N(n+1,\rho-1,t) - [k^+(n,\rho)+k^-(n,\rho)]N(n,\rho,t).
\end{aligned} \tag{7.16}$$

This is a natural extension of the differential equation in CNT that describes cluster growth in size space. The interfacial attachment and detachment rates as well as the rates controlling the parent/shell exchanges are discussed in Chapter 5 of Ref. [1].

The steady-state nucleation rate obtained from a numerical solution of Eq. (7.16) as a function of the ratio of the effective long-range diffusion coefficient, ξD, to the effective diffusion coefficient governing interfacial attachment, D_i, is shown in Fig. 7.5. (The constant ξ is introduced to take proper account of the average diffusion distance for an atom to leave the shell and return to the parent phase. Its value is determined by setting the cluster growth rate for large clusters in coupled-flux nucleation equal to the known diffusive macroscopic growth rate.) For $\xi D < D_i$, the steady-state rate scales linearly with the ratio of rates. With increasing values of the ratio, the coupled-flux nucleation rate asymptotically approaches the CNT value (shown by the dashed line), reflecting the crossover from diffusion limited to interface-limited nucleation. Predictions from the coupled-flux model have been shown to be in much better agreement with nucleation data for oxygen precipitation in silicon than are CNT calculations [32], and they agree with the results from a kinetic Monte Carlo simulation [33].

3   Computer Modeling Studies of Nucleation

Computer models for nucleation are becoming increasingly more important for probing the underlying processes involved in nucleation. For example, Monte Carlo studies of Ising models have demonstrated the stochastic nature of nucleation [35]. Ising models have also been useful in studies of the pre-factor, A^*. Fits to the simulation data, for example, show that A^* is several orders of magnitude smaller than expected from CNT and is a strong function of cluster size [28, 36]. A more extended discussion of these early results can be found elsewhere [1].
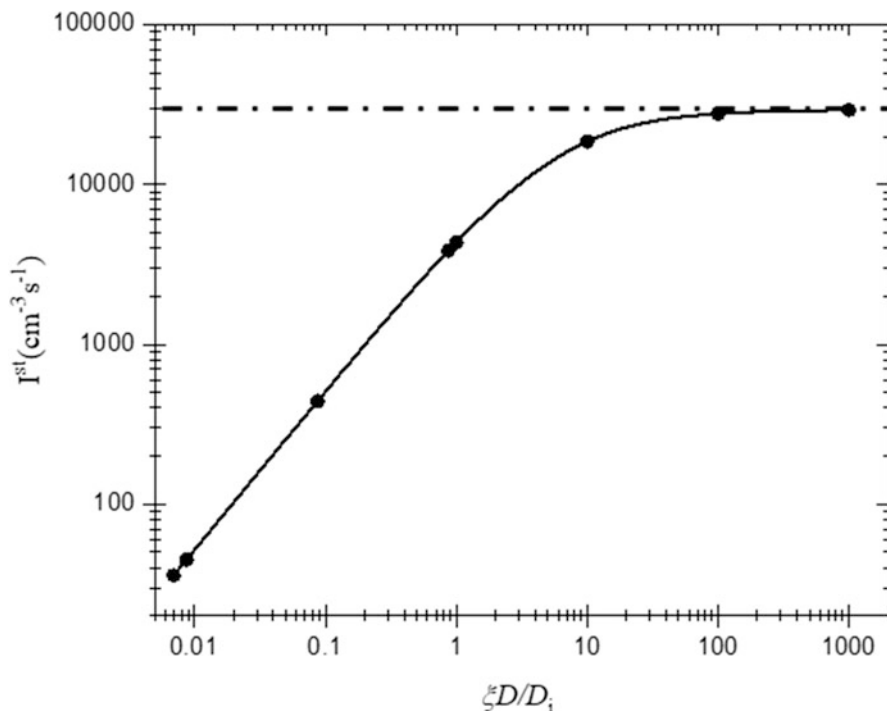
Fig. 7.5 The steady-state nucleation rate computed from the coupled-flux differential equations as a function of the ratio of the effective diffusion rate in the parent phase, ξD, to an effective diffusion rate governing interfacial attachment, D_i. The dashed line corresponds to the nucleation rate from CNT multiplied by $x^{2/3}$, where x is the atom fraction of solute ($x = N_o/N_S$). (Adapted from Ref. [34], copyright (2000), with permission from Elsevier)

Molecular dynamics (MD) studies have demonstrated the existence of a nucleation barrier [37] and have identified the critical sizes [38]. However, the ensemble sizes in these early simulations consisted of a few thousand to a few ten thousand atoms. Within the past decade, the increase in computer speed and the amount of accessible memory have greatly expanded the ensemble sizes, some now containing up to a billion atoms. The MD simulations have provided new insight into the validity of some of the key assumptions in the development of the CNT and have identified new features of nucleation that have not yet been incorporated into analytical models. Most of these are classical MD simulations, which use model potentials that may not capture all of the features of the actual atomic interactions and the structural development. First-principle (ab initio) calculations are not hindered by these problems, but the ensemble sizes that can be studied are very limited. Ab initio calculations are most useful for studies of small clusters of atoms, identifying structural and chemical ordering more accurately than classical MD studies.
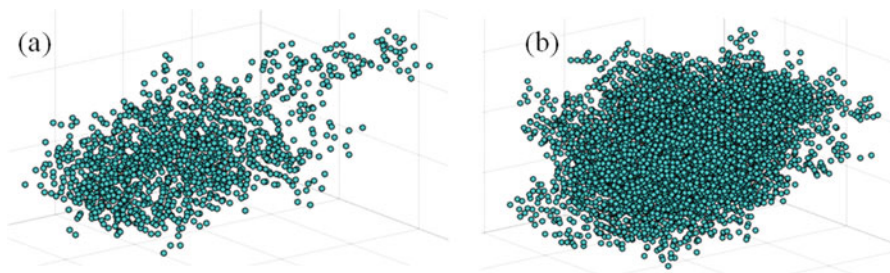
Fig. 7.6 (**a**) 1226 atom $Al_{20}Ni_{60}Zr_{20}$ bcc cluster at 1016 K. (**b**) 4330 atom $Al_{20}Ni_{60}Zr_{20}$ bcc cluster at 996 K

The properties of the nucleating clusters are critically important for developing a quantitative understanding of nucleation. Monte Carlo studies of a 100-atom cluster suggested that the clusters that formed in an Ar vapor are diffuse [39]. This is dramatically evident in recent MD calculations. Figure 7.6a shows a bcc crystal cluster of 1226 atoms that has nucleated in a supercooled liquid of $Al_{20}Ni_{60}Zr_{20}$, for an ensemble size of 1 million atoms [40]. The cluster is clearly not compact nor spherical, as assumed in the CNT, although it approximates this more closely as the cluster size increases (Fig. 7.6b). In all cases, however, the interface is diffuse. A study of a large number of clusters in the ensemble shows that both the density and the bcc order parameter decay on transitioning from the center of the cluster to the cluster boundary, in agreement with the density functional and diffuse interface models for nucleation discussed in Sect. 2.

As will be discussed in Sect. 4, experimental studies have confirmed Frank's hypothesis [41] that icosahedral short-range order (ISRO) develops in many supercooled transition metal alloy liquids and that this order couples to the nucleation barrier, making it more difficult to nucleate crystallographic phases. Ab initio MD studies have shown that the degree of ISRO is more prominent for bcc forming liquids and less so in fcc and hcp forming liquids, possibly because icosahedral disclination line defects are more easily incorporated into bcc environments [42]. While initially growing in the supercooled bcc forming liquid, the ISRO begins to decrease upon approaching the nucleation temperature, replaced by local bcc ordering [43, 44]. Regions of bcc ordering also appear in the initial nucleation of Zn and Pb, before crystallizing to the hcp or fcc structures, respectively [45]. All of the models discussed in Sect. 2 assume that nucleation can occur anywhere within the liquid. These MD results suggest that nucleation is more complicated than that. The results are in agreement with the proposed explanation of the experimental studies in $Ti_{39.5}Zr_{39.5}Ni_{21}$, i.e., that regions of order in the liquid catalyze the nucleation of the crystal phases [46]. They also suggest that nucleation is a coupled process, with orientational ordering occurring prior to density ordering, as was proposed by Tanaka and co-workers [47, 48]. An MD result indicates that chemical ordering can also catalyze nucleation [49], as predicted earlier [50]. The result that nuclei initially have a bcc orientational order before changing to the expected crystal
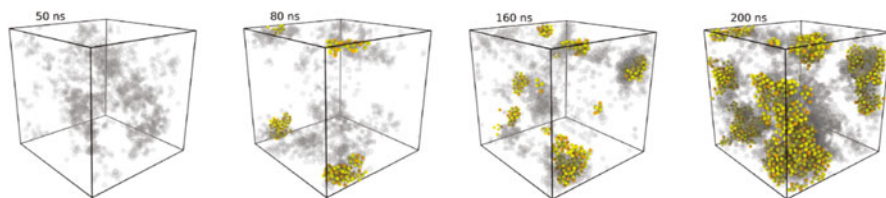
Fig. 7.7 The correlation between the slow regions of dynamical heterogeneities (gray regions) with the formation of crystal nuclei (colored spheres) for several times at 837 K. (Reprinted with permission from Ref. [53], copyright (2019), American Physical Society)

structure indicates that the nucleation pathway is more complicated than assumed; a similar case was recently identified in a silicate glass, where the first phase to nucleate had a chemical composition different from that of the crystallizing phase [51]. A billion atom MD simulation of pure Fe indicated that nucleation proceeds in two stages where satellite nuclei form in the region surrounding the initial nuclei [52]. This has not been reported in other MD simulations; however, so further investigation is called for to understand why this might be the case.

Recent MD studies also suggest an additional role for ISRO in the kinetics of nucleation in metallic liquids. Liquids are known to be characterized by heterogeneous structures and dynamics. Many MD calculations have shown that local regions with icosahedral order are also dynamically slow [54]. The development of these dynamical heterogeneities has been argued to underlie the breakdown of the Stokes-Einstein relation [55] and lead to the glass transition. As illustrated in Fig. 7.7, MD studies also suggest that these are the sites where nucleation preferentially occurs. The development of dynamically slow regions with local icosahedral order occurs after 20 ns at 837 K; subsequent nucleation and growth of the Cu_5Zr phase preferentially occur in these regions [56].

There have been a few studies of the agreement between the predicted nucleation rate and computer results, and the results have been varied. A study of the Lennard-Jones liquid, for example, found that nucleation proceeds along multiple pathways around the minimum free energy path and that in addition to size, the shape and structure of growing clusters play an important role [57], features that are not commensurate with CNT. However, a later study of liquid Al showed good agreement with CNT, particularly the time lag for nucleation [58]. A later MD study of nucleation in liquid Al found that the nucleation times followed a Poisson distribution, in agreement with the stochastic model for nucleation in CNT. They also found agreement to within one order of magnitude between the simulation results and CNT predictions, although this required using the pre-term and the interfacial free energy as fitting parameters [59]. A recent MD study of nucleation in a barium sulfide (BaS) liquid found agreement to within an order of magnitude with predictions from CNT, using only the interfacial free energy as a fitting parameter [60]. Similar results were obtained for nucleation in a $Ni_{50}Ti_{50}$ liquid [61]. So, despite the problems with CNT identified earlier, it seems that it remains a reasonable phenomenological framework

for describing homogeneous polymorphic nucleation, if the interfacial free energy is taken as a fitting parameter.

4 Ground-Based Studies of Nucleation in Metallic Liquids

The earliest attempts to study homogeneous nucleation in liquids used methods to isolate impurities that would cause heterogeneous nucleation (see Ref. [1], Chapter 7). The samples were dispersed into fine droplets either in a medium on or a surface so that some of the droplets would be free of impurities. The maximum supercooling observed was then attributed to homogeneous nucleation in those droplets.

Recently, levitation techniques have been developed that allow single macroscopic droplets to be repeatedly processed in a containerless environment. The most common of these are electromagnetic levitation and electrostatic levitation, which are discussed in Chaps. 3, 5, 8, 10, and 12 in this book. A statistical analysis of many measurements of the maximum supercooling from a single droplet in a containerless, high-vacuum environment can in principle allow studies of the type of nucleation (heterogeneous or homogeneous) and the different nucleation barriers for the nucleating phases. It is assumed that due to the rapid growth rates at high temperatures, one nucleation event leads to crystallization of the droplet, and the solidification is essentially adiabatic [62, 63]. The probability density for one nucleation event as a function of temperature at a constant cooling rate, Q, is [1, 64]

$$P(1;T) = \frac{I^{\text{st}}(T)V}{Q} \exp\left(-\frac{V}{Q} \int_{T_{\min}}^{T_{\ell}} I^{\text{st}}(T)\mathrm{d}T\right), \qquad (7.17)$$

where V is the volume of the droplet, I^{st} is the steady-state nucleation rate, T_{ℓ} is the liquidus temperature (the melting temperature for a pure liquid), and $T_{\min}$ is the maximum supercooling temperature. The shape of the distribution is sensitive to the temperature dependence of the nucleation pre-factor and the nucleation barrier. As the magnitude of the pre-factor increases, the distribution becomes narrower and less skewed toward lower temperatures (smaller third moment). The validity of the Skripov method was examined by measuring the supercooling distribution in zirconium liquid samples of three different purities [62] and by Monte Carlo calculations [63].

As discussed in the introduction, the ability to significantly supercool liquid metals, indicating the presence of a significant nucleation barrier, came as a surprise when it was first reported. Before Turnbull's studies of dispersed droplets, this had not been possible. Although he recognized that the failure of previous attempts to supercool was likely due to heterogeneous nucleation, this was not widely regarded as the reason. Instead, the similarity in the densities and coordination numbers of the
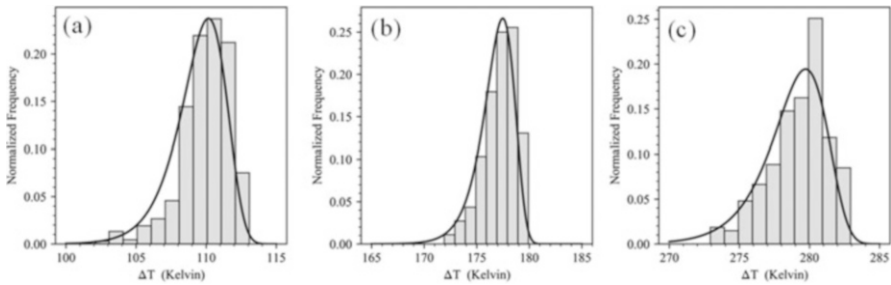
Fig. 7.8 (**a**) The histogram of maximum supercooling values for $Ti_{39.5}Zr_{39.5}Ni_{21}$, (**b**) $Ti_{40}Zr_{40}Ni_{30}$, and (**c**) $Zr_{80}Pt_{20}$. The solid line shows the fit to Eq. (7.17). (Reprinted with permission from Ref. [67] copyright (2019), American Institute of Physics)

Table 7.1 Fit values for nucleation parameters

Liquid	A^* $(m^3 s)^{-1}$	$W^*/k_B T$	σ (J/m^2)
$Ti_{39.5}Zr_{39.5}Ni_{21}$	2.74×10^{25}	37.18	0.057
$Ti_{40}Zr_{30}Ni_{30}$	4.85×10^{39}	70.54	0.114
$Zr_{80}Pt_{20}$	8.76×10^{45}	84.17	0.134

Data from Ref. [67]

liquids and corresponding crystal phases led many to believe that the phases have similar local atomic order and hence the nucleation barrier should be small. Frank proposed that the local structure of the liquid was dominated by icosahedral order, which like close-packed crystal phases has a coordination number of 12 and a similar density [41]. X-ray scattering studies have demonstrated that transition metal liquids do indeed contain a significant amount of icosahedral short-range order (ISRO) [65]. This order was linked to the nucleation barrier in a liquid that nucleated a metastable icosahedral quasicrystal phase [46], a non-translationally ordered phase with extended icosahedral order [66]. As a further investigation into this problem, the Skripov method was recently employed to analyze maximum supercooling data for metallic liquids that contain significant ISRO but nucleate different phases, some of which have ISRO and some do not [67]. The alloy liquids investigated were $Ti_{39.5}Zr_{39.5}Ni_{21}$, which nucleates the icosahedral quasicrystal; $Ti_{40}Zr_{40}Ni_{30}$, which forms the C14 Laves phase (a poly-tetrahedral crystal phase with local order similar to that of the icosahedral quasicrystal); and $Zr_{80}Pt_{20}$, which nucleates a phase mixture of Zr_5Pt_3 and βZr, both phases lacking icosahedral or poly-tetrahedral order. Several hundred supercooling studies were made for each of the three alloys. The resulting distributions and the fits to Eq. (7.17) are shown in Fig. 7.8. In all cases the fits were good, with *p*-values greater than 0.999.

The values for the nucleation pre-factor, A^*; the work of critical cluster formation, W^*; and the value for the interfacial free energy, σ, obtained from the fits are listed in Table 7.1. A^* increases with decreasing icosahedral local order of the nucleating crystal phases, as do the work of cluster formation and consequently the interfacial free energy. This is consistent with Frank's hypothesis. The smallest value for A^* in the quasicrystal-forming liquid suggests that the local regions of icosahedral order in

the liquid catalyze the nucleation of the ordered phase. This is consistent with the computer modeling studies shown in Fig. 7.7 and with conclusions from X-ray scattering studies [46]. It could also be consistent with a proposal by Tanaka that nucleation proceeds in stages instead of the one-step nucleation approach in the classical theory [68]. In that case, the small nucleating region first undergoes spatial ordering (to ISRO in this case) and then densifies. As already mentioned, these multiple pathways for nucleation is an emerging topic of considerable interest

5 Nucleation in Metallic and Silicate Glasses

Nucleation has been studied extensively in the silicate glasses. Understanding and controlling crystal nucleation is essential in glass formation and is also important in the production of glass ceramics with the desired properties. Both the nucleation and growth rates have peaks as a function of temperature, although the quantitative function is different for the two rates. The two peaks are often significantly separated in temperature in silicate glasses, which allows the nucleation rate to be accurately measured using a two-step annealing method, in which samples of the glass are first annealed for different times at a temperature, T_N, where the nucleation rate is high, but the growth rate is low to produce a population of small nuclei. These nuclei are then grown to visible size by heating at a higher temperature, T_G, where the growth rate is large, but the nucleation rate is small. For steady-state nucleation, the number of nuclei produced at T_N should be a linear function of the annealing time, so the slope of the line fit through the data will equal the steady-state nucleation rate. However, as shown in Fig. 7.9a for a barium silicate glass, the observed behavior is quite different. For long annealing time, the nucleation rate eventually reaches the steady-state rate, but at shorter times, the rate is smaller. The extrapolation of the straight line to the time axis gives the induction time, θ, which provides a measure of the relaxation time of the cluster distribution inherited from high temperature to the steady-state distribution at T_N. This is an example of time-dependent nucleation, which is best described by the following expression [69]:

$$I_{n*,t} = I^{st} \left[1 + 2 \sum_{m=1}^{\infty} (-1)^m \, \exp \left(-\frac{m^2 t}{\tau_K} \right) \right] \quad . \tag{7.18}$$

I^{st} is the steady-state nucleation rate. The Kashchiev transient time, τ_K, is related to the induction time, θ, by

$$\tau_K = -\frac{24 \, k_B \, T \, n^*}{\pi^2 \, k_{n*}^+ \, \delta\mu} \quad = \frac{6}{\pi^2} \, \theta. \tag{7.19}$$

Since θ scales inversely with k_{n*}^+, a more quantitative fit to glass nucleation data is possible than by using the diffusion coefficient or viscosity of the glass.
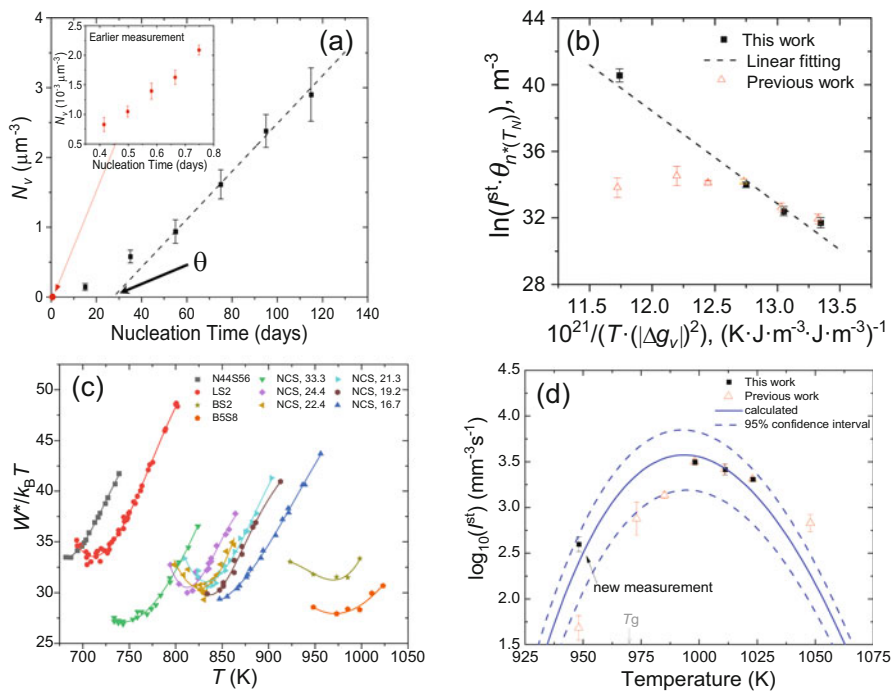
Fig. 7.9 (**a**) The number of nuclei per unit volume as a function of nucleation time at 948 K for a 5BaO·8SiO$_2$ glass; previously measured data [70] are shown in the inset. (**b**) A plot of ln($I^{st}\theta_{n*}$ $_{(TN)}$) vs. $1/(T|\Delta g_v|^2)$ for the 5BaO·8SiO$_2$ glass from the previously measured data [70] (red triangles) and the more recent data [71] (dark squares). The dashed line is the expected linear behavior. (**c**) The scaled nucleation barrier, $W^*/k_B T$, as a function of temperature for several silicate glasses, 44Na$_2$O·56SiO$_2$ (N44S56), Li$_2$O·2SiO$_2$ (LS2), BaO·2SiO$_2$ (BS2), 5BaO·8SiO$_2$ (B5S8), and xNa$_2$O·(50-x)CaO·50SiO$_2$ (NCS), where x values are 33.3, 24.4, 22.4, 21.3, 19.2, and 16.7 (see [71] for the data sources). The solid lines are guides to the eye. (**d**) The logarithm of the steady-state nucleation rate for a 5BaO·8SiO$_2$ glass. The CNT-predicted rate, based on fits to data obtained at temperatures higher than the peak temperature, is shown by the solid line. The previous data point (red triangle) at 948 K (corresponding to the inset in (**a**)) and the good agreement with the new data point at 948 K (black square). The dashed lines are the 95% confidence limits for the calculated curve. (From Ref. [71])

For over 40 years, it has been noted that below the peak nucleation temperature the measured nucleation rates in many silicate glasses lie below values expected from CNT. The CNT predicts that a plot of ln($I^{st}\theta_{n*(TN)}$) as a function of $1/(T|\Delta g_v|^2)$ (where $\theta_{n*(TN)}$ is the induction time measured for the critical size at the nucleation temperature and Δg_v is the driving free energy) should be linear when σ is a constant or when the relative change in σ as a function of temperature is smaller than the relative change in $|\Delta g_v|$. An example of this is shown in Fig. 7.9b for a BaO·2SiO$_2$ glass. The plot is linear at high temperatures but becomes increasingly nonlinear at low temperatures. Further, the scaled critical work of cluster formation, $W^*/k_B T$, derived from the data should decrease monotonically with decreasing temperature.

As shown in Fig. 7.9c, however, for many silicate glasses, W^*/k_BT plateaus and even begins to increase at low temperatures. All of these results suggest a failure of CNT at low temperatures, where the glass is far from equilibrium.

Many explanations have been advanced to explain this anomalous behavior [72–75]. However, because the function for the number of nuclei produced as a function of time is self-similar at different times, the failure could be an experimental artifact caused by insufficient annealing time at T_N to reach the steady state [76]. As an example, the inset in Fig. 7.9a shows data taken for approximately 1 day of annealing. After approximately one half of a day of annealing, the number of nuclei appears to increase linearly with time, suggesting that the steady-state rate has been reached. These data were used to compute the work of cluster formation for this glass that is shown in Fig. 7.9c [70]. However, as shown by the more recent data (black data points) in Fig. 7.9a, the data in the insert has clearly not reached the steady state. Using the new data from Fig. 7.9a, there is no longer an anomalous behavior in a plot of $\ln(I^{st}\theta_{n*(TN)})$ vs. $1/(T|\Delta g_v|^2$ (black data points in Fig. 7.9b) nor in the work of cluster formation [71]. Also, the steady-state nucleation data point at 748 K is now in good agreement with CNT predictions (Fig. 7.9d). Given the results for this glass, and the fact that all other silicate glasses show a similar anomalous behavior at low temperature, it is possible that all of the existing nucleation data for silicate glasses at temperatures below the peak are incorrect. As for the results discussed in Sect. 3, it appears that CNT remains quantitatively correct (but with a temperature-dependent interfacial free energy, consistent with a diffuse interface) even in cases where nucleation occurs far from equilibrium. Studies have also shown that the kinetic model of CNT appears to be quantitatively correct at these low temperatures [77, 78]. Therefore, if a breakdown of CNT does occur as suggested from the DFT calculations, it must be at even greater departures from equilibrium and may not be experimentally accessible.

Nucleation rate measurements in metallic glasses have been obtained from single-step annealing treatments [79] and from ultrafast heating and cooling studies [80, 81]. Two-step annealing studies are more difficult because of the overlap in the temperature ranges for nucleation and growth. The one result for the nucleation of an icosahedral phase in a $Zr_{59}Ti_3Cu_{20}Ni_8Al_{10}$ glass was consistent with predictions from CNT for time-dependent nucleation. Further, the interfacial free energy derived from the fit to that data was extremely small (0.01 ± 0.004 J/m^2), consistent with the observed icosahedral order in the glass.

6 Stirring Effects on Nucleation and Microgravity

On Earth, liquids are stirred by Marangoni and gravity-induced flow, which can mask some features of nucleation, such as the diffusion effects discussed in Sect. 2.4. Stirring effects are also important in the crystallization and aggregation of proteins [82] and industrial crystallization in the pharmaceutical industry [83]. To examine these effects, nucleation rate measurements have been made in stirred environments

on Earth and in the less stirred microgravity environment available on parabolic flights, the space shuttle, and most recently the International Space Station.

Most studies have been made for proteins [84] and colloids, with a smaller number of studies of inorganic liquids [85] [86]. The results are varied. Some studies have reported that shear flow decreases the nucleation rate [87], while others have found a considerable increase in the rate under stirring [88, 89]. One simulation of colloids with a screened repulsion suggest that the nucleation barrier increases as the square of the shear rate [90], and others offer evidence for a maximum nucleation rate with stirring [91, 92]. A recent extension of CNT gives good agreement with this disparate behavior. It accounts for the contribution of flow to the kinetics of interfacial attachment in the Volmer-Weber kinetic equations but also argues for a change in the work of cluster formation due to mechanical deformation of the nucleus due to the flow [93]. These two competing effects lead to a maximum in the nucleation rate and a quadratic dependence of the nucleation rate on stirring, in agreement with the simulation results. Studies in a microgravity environment allow the effect of stirring on the nucleation rate to be investigated. But, they also allow other features of the nucleation process that are otherwise masked by flow to be explored. Emerging key features are that nucleation involves a degree of self-organization that is dependent on geometric, kinetic, and structural factors and that it is described by multiple order parameters involving non-classical nucleation pathways. As already mentioned, similar results have resulted from studies of crystallization in silicate glasses.

There are fewer studies of the effect of stirring on metallic liquids. A study of nucleation in liquid Zr as a function of stirring in the MSL mission on Spacelab found no evidence of a change in the rate for flow rates between 5 and 43 cm/s, based on the maximum supercooling achieved prior to crystallization. Above 50 cm/s the supercooling was smaller, which was taken as evidence for cavitation-induced nucleation in the liquid [94]. The maximum supercooling of liquid $Al_{40}Ni_{60}$ was 70 K smaller in a microgravity environment than it was in ground-based experiments [95]. One possible explanation is that since a thin layer of Al_2O_3 forms on the surface of the Al, and since there is evidence that the liquid orders next to this layer [96, 97], the layer could catalyze nucleation, as in the case where the icosahedral ordering in liquid $Ti_{39.5}Zr_{39.5}Ni_{21}$ catalyzes the nucleation of a metastable icosahedral phase [46]. Significant stirring in the ground-based experiments may disturb this ordering, while it may persist under microgravity conditions. A recent study examined a coupling of nucleation events, measuring the delay time for a ferrite to austenite transition as a function of shear in a Fe-Cr-Ni stainless steel liquid [98]. Based on ground-based ESL and EML measurements and measurements in the microgravity environment of the ESA EML facility on the ISS, it was concluded that the observed delay time is due to a shear-enhanced retained driving free energy from the meta-stable ferrite phase. The coupled-flux model (Section 2.4) predicts that when the flow is reduced and long-range diffusion becomes dominant, the nucleation rate for phases with a different chemical concentration from that of the liquid should decrease. There is some experimental evidence for this in microgravity studies of the solidification of Al-Bi-Sn alloys [99]. A more recent study of a

$Zr_{57}Cu_{15.4}Ni_{12.6}Al_{10}Nb_5$ (Vit106), $Cu_{50}Zr_{50}$, and the quasicrystal-forming $Ti_{39.5}Zr_{39.5}Ni_{21}$ liquids showed that the maximum nucleation rate increased systematically with increased fluid flow in the liquids for Vit106, with compositional changes during crystallization, but stayed nearly unchanged for the other two, where the compositional changes were small [100]. To date, this is the best supporting evidence for the coupled-flux model for nucleation in the liquid; future studies on the ISS to improve the statistical significance of this result are planned.

7 Nucleation and Glass Formation

The key problem for glass formation is preventing significant nucleation and growth during the cooling of the liquid [101, 102]. For this reason, the earliest prediction for glass formation focused on liquid alloys with deep eutectics [101], since the temperature range over which nucleation could occur was small before the kinetics effectively froze out upon reaching the glass transition temperature. But in addition to the nucleation rate, the growth rate must also be considered. By combining these two rates, it becomes possible to determine the critical quenching rate for glass formation using a time-temperature-transformation (TTT) diagram, showing the times at a given temperature required to develop a certain volume fraction crystallization. A series of TTT diagrams fit to experimental data for Cu-Zr liquids of different compositions is shown in Fig. 7.10 [103]; the temperature is normalized to the liquidus temperature, T_l. The three diagrams show liquids of nearby concentration to the best glass-forming compositions, $Cu_{64}Zr_{36}$ (Fig. 7.10a), $Cu_{56}Zr_{44}$ (Fig. 7.10b), and $Cu_{50}Zr_{50}$ (Fig. 7.10c). If the cooling rate is sufficient to bypass the nose of the TTT curve, glass formation will result (shown schematically in Fig. 7.10b for illustration). The results of this study were that the effect of
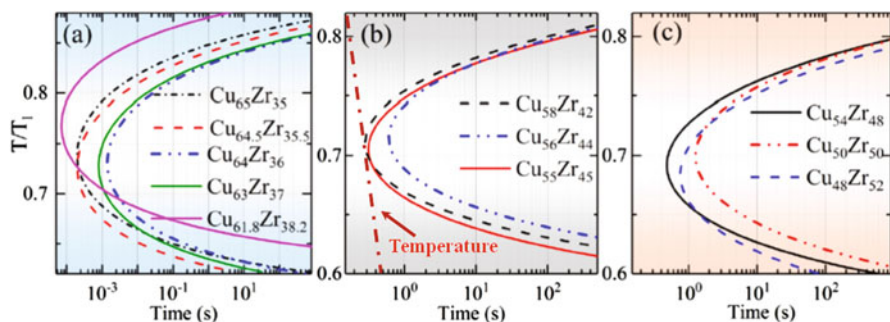
Fig. 7.10 The TTT diagrams for Cu-Zr alloys of different compositions normalized to the liquidus temperatures, T_l. Glass formation occurs if the temperature during cooling (illustrated by the solid dashed line in (**b**)) remains to the left of the nose of the TTT diagram. (Reprinted with permission from Ref. [103], copyright (2018), American Physical Society)

compositional change on glass-forming ability of the three best glasses differs, which had not been recognized before.

Recently, it has proven possible to do this in the microgravity environment of the ISS, constituting the first time that metallic glass production has been demonstrated in space [104]. Since metallic glasses are increasingly finding applications for specific needs, such as lubrication free gears for use in the cold environment of space [105], the ability to produce them in space or on other planets having a different gravitational environment could be very important.

Both nucleation and growth depend on the atomic mobility (generally estimated from the diffusion coefficient in the liquid) and the driving free energy. At high temperatures, the diffusion coefficient in the liquid can be related to the viscosity, using the Stokes-Einstein relation. The viscosity can be characterized by the fragility of the liquid [106], which is related to the temperature dependence of the viscosity in a normalized temperature plot (i.e., T/T_g where T_g is the glass transition temperature). Within the metallic glass community, fragility is often associated with glass formability [107], which is reasonable since glass formation hinges on avoiding crystal nucleation and growth. Stronger liquids are believed to be thermodynamically more stable than fragile ones and have larger viscosities at high temperatures, properties that will suppress the nucleation and growth of the crystal phases and make glass formation easier. However, there are exceptions to the link between fragility and glass-forming ability. Sorbitol and Salol, for example, are very fragile liquids that form glasses [108], and a recent study in metallic glasses showed that fragility alone did not give a good prediction of glass formability [109]; a better prediction was found there when using the fragility and reduced glass transition temperature. Using the fragility and glass transition temperature as a predictor of glass formability poses a problem, however, since the glass must first be prepared. A recent study found that these quantities can be calculated from properties of the high-temperature liquid, allowing a truly predictive model of glass formability from the perspective of nucleation and growth [110, 111].

8   Conclusions

In conclusion, there has been a recent resurgent interest and activity in the study of nucleation in liquid and glasses. There are new tools, such as containerless processing and the availability of the microgravity environment on the International Space Station, that are allowing nucleation to be probed more deeply. An increased computational power has led to more realistic simulations of nucleation processes. The results of these studies show that the thermodynamic model of the commonly used classical nucleation theory is inadequate for developing a quantitative understanding of the nucleation process. A key problem is that the interface between the nuclei of the new phase and the original phase is not sharp, but diffuse. However, there are now models that take this into account, and they are starting to be used to analyze nucleation data. Of greater consequence is the increasing realization that

nucleation involves multiple connected order parameters and that there can exist multiple nucleation pathways. The structure of the liquid or glass is also now seen to be important in the nucleation process. Clearly, a great deal more of study is needed to sort out these issues and to develop new models to treat them. Microgravity research has played and will continue to play an important role in deepening our understanding of nucleation processes.

References

1. K.F. Kelton, A.L. Greer, in *Nucleation in Condensed Matter – Applications in Materials and Biology*, Pergamon Materials Series, ed. by R. W. Cahn, 1st edn., (Elsevier, Amsterdam, 2010), p. 726
2. Z.L. Liu, Review of grain refinement of cast metals through inoculation: Theories and developments. Metall. Mater. Trans. A. Phys. Metall. Mater. Sci. **48A**, 4755–4776 (2017)
3. C.A. Angell, Glass formation and glass transition in supercooled liquids, with insights from study of related phenomena in crystals. J. Non-Cryst. Solids **354**, 4703–4712 (2008)
4. E.D. Zanotto, Glass crystallization research a 36-year retrospective. Part I, fundamental studies. Int. J. Appl. Glas. Sci. **4**, 105–116 (2013)
5. L.R. Pinckney, G.H. Beall, Microstructural evolution in some silicate glass-ceramics: A review. J. Am. Ceram. Soc. **91**, 773–779 (2008)
6. J.R. Cox, L.A. Ferris, V.R. Thalladi, Selective growth of a stable drug polymorph by suppressing the nucleation of corresponding metastable polymorphs. Ang. Chem. Int. Ed. **46**, 4333–4336 (2007)
7. S.D. Thakore, A. Sood, A.K. Bansal, Emerging role of primary heterogeneous nucleation in pharmaceutical crystallization. Drug Dev. Res. **81**, 3–22 (2020)
8. Y.S. You, T.Y. Kang, S.J. Jun, Control of ice nucleation for subzero food preservation. Food Eng. Rev. **13**, 15–35 (2021)
9. M.J.H. Akanda, M.R. Norazlina, F.S. Azzatul, S. Shaarani, H. Mamat, J.S. Lee, J. Norliza, A.H. Mansoor, J. Selamat, F. Khan, P. Matanjun, M.Z.I. Sarker, Hard fats improve the physicochemical and thermal properties of seed fats for applications in confectionery products. Food Rev. Int. **36**, 601–625 (2020)
10. K.B. Storey, J.M. Storey, Biochemical adaption for freezing tolerance in the Wood Frog, Rana Sylvatica. J. Comp. Physiol. B Biochem. Syst. Environ. Physiol. **155**, 29–36 (1984)
11. C. Cerini, S. Geider, B. Dussol, C. Hennequin, M. Daudon, S. Veesler, S. Nitsche, R. Boistelle, P. Berthezene, P. Dupuy, A. Vazi, Y. Berland, J.C. Dagorn, J.M. Verdier, Nucleation of calcium oxalate crystals by albumin: Involvement in the prevention of stone formation. Kidney Int. **55**, 1776–1786 (1999)
12. D.G. Fahrenheit, Experimenta et observationes de congelatione aquae in vacuo factae. Philos. Trans. R. Soc. **39**, 78–89 (1724)
13. D. Turnbull, Kinetics of solidification of supercooled liquid mercury droplets. J. Chem. Phys. **20**, 411–424 (1952)
14. J.W. Gibbs, *Scientific Papers*, vol I, II (Longmans Green, London, 1906)
15. M. Volmer, A. Weber, Keimbildung in übersättigten Gebilden. Z. Phys. Chem. **119**, 227–301 (1926)

16. R. Becker, W. Döring, Kinetic treatment of grain-formation in super-saturated vapours. Ann. Phys. **24**, 719–752 (1935)
17. D. Turnbull, J.C. Fisher, Rate of nucleation in condensed systems. J. Chem. Phys. **17**, 71–73 (1949)
18. L. Granasy, F. Igioi, Comparison of experiments and modern theories of crystal nucleation. J. Chem. Phys. **107**, 3634–3644 (1997)
19. L. Granasy, P.F. James, Nucleation in oxide glasses: comparison of theory and experiment. Proc. R. Soc. Lond. Ser. A (Math. Phys. Eng. Sci.) **454**, 1745 (1998)
20. C.K. Bagdassarian, D.W. Oxtoby, Crystal nucleation and growth from the undercooled liquid: A nonclassical piecewise parabolic free energy model. J. Chem. Phys. **100**, 2139–2148 (1994)
21. F. Spaepen, Homogeneous nucleation and the temperature dependence of the crystal-melt interfacial tension, in *Solid State Physics*, ed. by H. Ehrenreich, D. Turnbull, (Academic, New York, 1994), pp. 1–32
22. L. Gránásy, Diffuse interface theory of nucleation. J. Non-Cryst. Solids **162**, 301–303 (1993)
23. L. Granasy, Diffuse interface model of crystal nucleation. J. Non-Cryst. Solids **219**, 49–56 (1997)
24. L. Granasy, Diffuse interface approach to vapour condensation. Europhys. Lett. **24**, 121–126 (1993)
25. D. Van Hoesen, *Thermophysical Properties and Phase Transformations in Metallic Liquids and Silicate Glasses*. PhD thesis in Physics (Washington University in St. Louis, 2000)
26. H. Reiss, The kinetics of phase transitions in binary systems. J. Chem. Phys. **18**, 840–848 (1950)
27. D.T. Wu, Nucleation theory, in *Solid State Physics*, ed. by H. Ehrenreich, F. Spaepen, (Academic, Boston, 1997), pp. 37–187
28. K. Binder, D. Stauffer, Statistical theory of nucleation, condensation and coagulation. Adv. Phys. **25**, 343–396 (1976)
29. D. Stauffer, Kinetic theory of two-component ('heteromolecular') nucleation and condensation. J. Aerosol Sci. **7**, 319–333 (1976)
30. D.E. Temkin, V.V. Shevelev, On the theory of nucleation in two-component systems. J. Cryst. Growth **52**, 104–110 (1981)
31. K.C. Russell, Linked flux analysis of nucleation in condensed phases. Acta Metall. **16**, 761–769 (1968)
32. P.F. Wei, K.F. Kelton, R. Falster, Coupled-flux nucleation modeling of oxygen precipitation in silicon. J. Appl. Phys. **88**, 5062–5070 (2000)
33. H. Diao, R. Salazar, K.F. Kelton, L.D. Gelb, Impact of diffusion on concentration profiles around near-critical nuclei and implications for theories of nucleation and growth. Acta Mater. **56**, 2585–2591 (2008)
34. K.F. Kelton, Time-dependent nucleation in partitioning transformations. Acta Mater. **48**, 1967–1980 (2000)
35. S. Wonczak, R. Strey, D. Stauffer, Confirmation of classical nucleation theory by Monte Carlo simulations in the 3-dimensional Ising model at low temperature. J. Chem. Phys. **113**, 1976–1980 (2000)
36. V.A. Shneidman, K.A. Jackson, K.M. Beatty, On the applicability of the classical nucleation theory in an Ising system. J. Chem. Phys. **111**, 6932–6941 (1999)
37. W.C. Swope, H.C. Andersen, 106 particle molecular-dynamics studie of homogeneous nucleation of crystals in a supercooled atomic liquid. Phys. Rev. B **41**, 7042–7054 (1990)
38. J.K. Bording, J. Tafto, Molecular-dynamics simulation of growth of nanocrystals in an amorphous matrix. Phys. Rev. B **62**, 8098–8103 (2000)
39. J.K. Lee, J.A. Barker, F.F. Abraham, Theory and Monte-Carlo simulation of physical clusters in imperfect vapor. J. Chem. Phys. **58**, 3166–3180 (1973)
40. K. Dahlberg, A. Agrawal, R. Chang, Z. Nussinov, K.F. Kelton, private communication (2021)
41. F.C. Frank, A discussion on theory of liquids: Supercooling of liquids. Proc. R. Soc. Lond. Ser. A (Math. Phys. Eng. Sci.) **215**, 43–46 (1952)

42. P. Ganesh, M. Widom, *Ab initio* simulations of geometrical frustration in supercooled liquid Fe and Fe-based metallic glass. Phys. Rev. B. **77**, 014205 (2008)
43. T.T. Debela, X.D. Wang, Q.P. Cao, D.X. Zhang, J.Z. Jiang, The crystallization process of liquid vanadium studied by *ab initio* molecular dynamics. J. Phys. Condens. Matter **26**, 155101 (2014)
44. T.T. Debela, X.D. Wang, Q.P. Cao, Y.H. Lu, D.X. Zhang, H.-J. Fecht, H. Tanaka, J.Z. Jiang, Nucleation driven by orientational order in supercooled niobium as seen via ab initio molecular dynamics. Phys. Rev. B **89**, 104205 (2014)
45. T.T. Debela, X.D. Wang, Q.P. Cao, D.X. Zhang, J.Z. Jiang, Comparative study of crystallization process in metallic melts using ab initio molecular dynamics simulations. J. Phys. Condens. Matter **29**, 185401 (2017)
46. K.F. Kelton, G.W. Lee, A.K. Gangopadhyay, R.W. Hyers, T.J. Rathz, J.R. Rogers, M.B. Robinson, D.S. Robinson, First X-ray scattering studies on electrostatically levitated metallic liquids: demonstrated influence of local icosahedral order on the nucleation barrier. Phys. Rev. Lett. **90**, 195504 (2003)
47. T. Kawasaki, H. Tanaka, Formation of a crystal nucleation from liquid. Proc. Natl. Acad. Sci. U. S. A. **107**, 14036–14041 (2010)
48. J. Russo, H. Tanaka, The microscopic pathway tocrystallization in supercooled liquids. Sci. Rep. **2**, 505 (2012)
49. Z.G. Wang, C.H. Chen, S.V. Ketov, K. Akagi, A.A. Tsarkov, Y. Ikuhara, D.V. Louzguine-Luzgin, Local chemical ordering within the incubation period as a trigger for nanocrystasllization of a highly supercooled Ti-based liquid. Mater. Des. **156**, 504–513 (2018)
50. E. Cini, B. Vinet, P.J. Desre, A thermodynamic approach to homogeneous nucleation via fluctuations of concentration in binary liquid alloys. Phil. Mag. A **80**, 955–966 (2000)
51. M.E. McKenzie, B. Deng, D.C. Van Hoesen, X. Xia, D.E. Baker, A. Rezikyan, R.E. Youngman, K.F. Kelton, Nucleation pathways in barium silicate glasses. Sci. Rep. **11**, 69 (2021)
52. Y. Shibuta, S. Sakane, E. Miyoshi, S. Okita, T. Takaki, M. Ohno, Heterogeneity in homogeneous nucleation from billion-atom molecular dynamics simulation of solidification of pure metal. Nat. Commun. **8**, 10 (2017)
53. F. Puosi, A. Pasturel, Dynamic slowing-down and crystal nucleation in a supercooled metallic glass former induced by local icosahedral order. Phys Rev Mater **3**, 6 (2019)
54. Y.Q. Cheng, H.W. Sheng, E. Ma, Relationship between structure, dynamics, and mechanical properties in metallic glass-forming alloys. Phys. Rev. B **78**, 7 (2008)
55. L. Berthier, G. Biroli, Theoretical perspective on the glass transition and amorphous materials. Rev. Mod. Phys. **83**, 587–645 (2011)
56. F. Puosi, A. Pasturel, Nucleation kinetis in a supercooled metallic glass former. Acta Mater. **174**, 387–397 (2019)
57. D. Moroni, P.R. ten Wolde, P.G. Bolhuis, Interplay between structure and size in a critical crystal nucleus. Phys. Rev. Lett. **94**, 235703 (2005)
58. R.S. Aga, J.F. Morris, J.J. Hoyt, M. Mendelev, Quantitative parameter-free prediction of simulated crystal-nucleation times. Phys. Rev. Lett. **96**, 245701 (2006)
59. G.E. Norman, V.V. Pisarev, Molecular dynamics analysis of the crystallization of an overcooled aluminum melt. Russ. J. Phys. Chem. A **86**, 1447–1452 (2012)
60. S.C. Costa Pradoa, J.P. Rino, E.D. Zanotto, Successful test of the classical nucleation theory by molecular dynamic simulations of BaS. Comput. Mater. Sci. **161**, 99–106 (2019)
61. A.O. Tipeev, E.D. Zanotto, Nucleation kinetics in supercooled $Ni_{50}Ti_{50}$: Computer simulation data corroborate the validity of the Classical Nucleation Theory. Chem. Phys. Lett. **735**, 136749 (2019)
62. C.W. Morton, W.H. Hofmeister, R.J. Bayuzick, A.J. Rulison, J.L. Watkins, The kinetics of solid nucleation in zirconium. Acta Mater. **46**, 6033–6039 (1998)
63. W.H. Hofmeister, C.W. Morton, R.J. Bayuzick, Monte Carlo testing of the statistical analysis of nucleation data. Acta Mater. **46**, 1903–1908 (1998)

64. V. Skripov, Homogeneous nucleation in melts and amorphous films. Curr. Top. Mater. Sci. **2**, 327–378 (1977)

65. T. Schenk, D. Holland-Moritz, V. Simonet, R. Bellissent, D.M. Herlach, Icosahedral short-range order in deeply undercooled metallic melts. Phys. Rev. Lett. **89**, 075507 (2002)

66. D. Shechtman, I. Blech, D. Gratias, J.W. Cahn, Metallic phase with long-range orientational order and no translational symmetry. Phys. Rev. Lett. **53**, 1951 (1984)

67. M.E. Sellers, D.C. Van Hoesen, A.K. Gangopadhyay, K.F. Kelton, Maximum supercooling studies in $Ti_{39.5}Zr_{39.5}Ni_{21}$, $Ti_{40}Zr_{30}Ni_{30}$, and $Zr_{80}Pt_{20}$ liquids-Connecting liquid structure and the nucleation barrier. J. Chem. Phys. **150** (2019)

68. H. Tanaka, Bond orientational ordering in a metastable supercooled liquid: A shadow of crystallization and liquid-liquid transition. J. Stat. Mech. Theory Exp. **1–27** (2010)

69. D. Kashchiev, Solution of the non-steady state problem in nucleation kinetics. Surf. Sci. **14**, 209–220 (1969)

70. X. Xia, D.C. Van Hoesen, M.E. McKenzie, R.E. Youngman, O. Gulbiten, K.F. Kelton, Time-dependent nucleation rate measurements in $BaO\cdot2SiO_2$ and $5BaO\cdot8SiO_2$ glasses. J. Non-Cryst. Solids **525**, 119575 (2019)

71. X. Xia, D.C. Van Hoesen, M.E. McKenzie, R.E. Youngman, K.F. Kelton, Low-temperature nucleation anomaly in silicate glasses shown to be artifact in a $5BaO\cdot8SiO_2$ glass. Nat. Commun. **12**, 2026 (2021)

72. M.C. Weinberg, E.D. Zanotto, Re-examination of the temperature dependence of the classical nucleation rate: homogeneous crystal nucleation in glass. J. Non-Cryst. Solids **108**, 99–108 (1989)

73. A.S. Abyzov, V.M. Fokin, A.M. Rodrigues, E.D. Zanotto, J.W.P. Schmelzer, The effect of elastic stresses on the thermodynamic barrier for crystal nucleation. J. Non-Cryst. Solids **432**, 325–333 (2016)

74. V.M. Fokin, A.S. Abyzov, E.D. Zanotto, D.R. Cassar, A.M. Rodrigues, Crystal nucleation in glass-forming liquids: Variation of the size of the "structural units" with temperature. J. Non-Cryst. Solids **447**, 35–44 (2016)

75. A.S. Abyzov, V.M. Fokin, N.S. Yuritsyn, A.M. Rodrigues, J.W.P. Schmelzer, The effect of heterogeneous structure of glass-forming liquids on crystal nucleation. J. Non-Cryst. Solids **462**, 32–40 (2017)

76. D.R. Cassar, A.H. Serra, O. Peitl, E.D. Zanotto, Critical assessment of the alleged failure of the Classical Nucleation Theory at low temperatures. J. Non-Cryst. Solids **547**, 120297 (2020)

77. K.F. Kelton, A.L. Greer, Test of classical nucleation theory in a condensed system. Phys. Rev. **B38**, 10089–10092 (1988)

78. A.L. Greer, K.F. Kelton, Nucleation in lithium disilicate glass: A test of classical theory by quantitative modeling. J. Am. Ceram. Soc. **74**, 1015–1022 (1991)

79. M. Buchwitz, R. Adlwarth-Dieball, P.L. Ryder, Kinetics of the crystallization of amorphous Ti_2Ni. Acta Metall. Mater. **41**, 1885–1892 (1993)

80. F.X. Bai, J.H. Yao, Y.X. Wang, J. Pan, Y. Li, Crystallization kinetics of an Au-based metallic glass upon ultrafast heating and cooling. Scr. Mater. **132**, 58–62 (2017)

81. K. Kosiba, S. Scudino, R. Kobold, U. Kühn, A.L. Greer, J. Eckert, S. Pauly, Transient nucleation and microstructural design in flash-annealed bulk metallic glasses. Acta Mater. **127**, 416–425 (2017)

82. A. Penkova, W. Pan, F. Hodjaoglu, P.G. Vekilov, Nucleation of protein crystals under the influence of solution shear flow. Ann. N. Y. Acad. Sci. **1077**, 214–231 (2006)

83. J.A. Baird, D. Santiago-Quinonez, C. Rinaldi, L.S. Taylor, Role of viscosity in influencing the glass-forming ability of organic molecules from the undercooled melt state. Pharm. Res. **29**, 271–284 (2012)

84. A.A. Chernov, Protein crystals and their growth. J. Struct. Biol. **142**, 3–21 (2003)

85. M.R. Meier, L. Lei, A. Rinkenburger, J. Plank, Crystal growth of Ca3Al(OH)(6)·12H(2)O (2)·(SO4)(3)·2H(2)O (Ettringite) studied under microgravity conditions. J. Wuhan Univ. Technol. Mater. Sci. Ed. **35**, 893–899 (2020)

86. X.Y. Liu, K. Tsukamoto, M. Sorai, New kinetics of $CaCO_3$ nucleation and microgravity effect. Langmuir **16**, 5499–5502 (2000)

87. A. Tsuchida, E. Takyo, K. Taguchi, T. Okubo, Kinetic analyses of colloidal crystallization in shear flow. Colloid Polym. Sci. **282**, 1105–1110 (2004)

88. A. Penkova, W.C. Pan, F. Hodjaoglu, P.G. Vekilov, Nucleation of protein crystals under the influence of solution shear flow, in *Interdisciplinary Transport Phenomena in the Space Sciences*, ed. by S. S. Sadhal, (Wiley-Blackwell, Hoboken, 2006), pp. 214–231

89. C. Forsyth, P.A. Mulheran, C. Forsyth, M.D. Haw, I.S. Burns, J. Sefcik, Influence of controlled fluid shear on nucleation rates in glycine aqueous solutions. Cryst. Growth Des. **15**, 94–102 (2015)

90. R. Blaak, S. Auer, D. Frenkel, H. Lowen, Crystal nucleation of colloidal suspensions under shear. Phys. Rev. Lett. **93**, 068303 (2004)

91. A.V. Mokshin, B.N. Galimzyanov, J.L. Barrat, Extension of classical nucleation theory for uniformly sheared systems. Phys. Rev. E **87**, 062307 (2013)

92. D. Richard, T. Speck, The role of shear in crystallization kinetics: From suppression to enhancement. Sci. Rep. **5**, 7 (2015)

93. F. Mura, A. Zaccone, Effects of shear flow on phase nucleation and crystallization. Phys. Rev. E **93**, 11 (2016)

94. W.H. Hofmeister, R.J. Bayuzick, R. Hyers, G. Trapaga, Cavitation-induced nucleation of zirconium in low earth orbit. Appl. Phys. Lett. **74**, 2711–2713 (1999)

95. D.M. Herlach, S. Burggraf, P. Galenko, C.A. Gandin, A. Garcia-Escorial, H. Henein, C. Karrasch, A. Mullis, M. Rettenmayr, J. Valloton, Solidification of undercooled melts of Al-based alloys on Earth and in space. JOM **69**, 1303–1310 (2017)

96. S.H. Oh, Y. Kauffmann, C. Scheu, W.D. Kaplan, M. Ruhle, Ordered liquid aluminum at the interface with sapphire. Science **310**, 661–663 (2005)

97. A.L. Greer, Liquid metals: Supercool order. Nat. Mater. **5**, 13–14 (2006)

98. D.M. Matson, Retained free energy as a driving force for phase transformation during rapid solidification of stainless steel alloys in microgravity. npj Microgravity **4**, 6 (2018)

99. H.X. Jiang, S.X. Li, L.L. Zhang, J. He, J.Z. Zhao, Effect of microgravity on the solidification of aluminum-bismuth-tin immiscible alloys. npj Microgravity **5**, 9 (2019)

100. A.K. Gangopadhyay, M.E. Sellers, G.P. Bracker, D. Holland-Moritz, D.C. Van Hoesen, S. Koch, P.K. Galenko, A.K. Pauls, R.W. Hyers, K.F. Kelton, Demonstration of the effect of stirring on nucleation from experiments on the International Space station. npj Microgravity, **7**, 31 (2021)

101. D. Turnbull, Under what conditions can a glass be formed? Contemp. Phys. **10**, 473–488 (1969)

102. H. Fecht, W.L. Johnson, Thermodynamic properties and metastability of bulk metallic glasses. Mater. Sci. Eng. A-Struct. Mater. Prop. Microstruct. Process. **375**, 2–8 (2004)

103. S. Ganorkar, S. Lee, Y.H. Lee, T. Ishikawa, G.W. Lee, Origin of glass forming ability of Cu-Zr alloys: A link between compositional variation and stability of liquid and glass. Phys Rev Mater **2**, 115606 (2018)

104. M. Mohr, R.K. Wunderlich, D.C. Hofmann, H.J. Fecht, Thermophysical properties of liquid $Zr_{52.5}Cu_{17.9}Ni_{14.6}Al_{10}Ti_5$ – prospects for bulk metallic glass manufacturing in space. npj Microgravity **5**, 8 (2019)

105. https://www.space.com/34890-metallic-glass-ideal-for-space-mission-gears.html

106. C.A. Angell, *Strong and Fragile Liquids. in Relaxation in Complex Systems* (National Technical Information Service, U.S. Department of Commerce, Springfield, 1984)

107. R. Busch, E. Bakke, W.L. Johnson, Viscosity of the supercooled liquid and relaxation at the glass transition of the $Zr_{46.76}Ti_{8.25}Cu_{7.5}Ni_{10}Be_{27.5}$ bulk metallic glass forming alloy. Acta Mater. **46**, 4725–4732 (1998)

108. R. Böhmer, K.L. Ngai, C.A. Angell, D.J. Plazek, Nonexponential relaxations in strong and fragile glass formers. J. Chem. Phys. **99**, 4201–4209 (1993)
109. W.L. Johnson, J.H. Na, M.D. Demetriou, Quantifying the origin of metallic glass formation. Nat. Commun. **7**, 10313 (2016)
110. R. Dai, R. Ashcraft, A.K. Gangopadhyay, K.F. Kelton, Predicting metallic glass formation from properties of the high temperature liquid. J. Non-Cryst. Solids **525**, 119673 (2019)
111. R. Dai, A.K. Gangopadhyay, R.J. Chang, K.F. Kelton, A method to predict the glass transition temperature in metallic glasses from properties of the equilibrium liquid. Acta Mater. **172**, 1–5 (2019)

Part III
Ground Based Methods

Chapter 8
Ground-Based Electromagnetic Levitation (EML) for the Measurement of Thermophysical Properties

Jürgen Brillo

1 Introduction

Thermophysical properties of liquid melts are crucially important for process design, layout and optimization, as well as for a basic (academic) understanding of materials science [1]. The latter is essential for computer-aided materials design and materials optimization. The importance of the liquid phase becomes impressively clear in view of the fact that more than 70% of all materials are produced under direct involvement of the melt [2]. This includes, for instance, processes like casting, welding, soldering or melting in powder-based 3D laser printing [3].

On the other hand, and despite intensive research carried out and eminent progress made during the past 20 years, systematic data on liquid multicomponent melts are still sparse. This is owed to the high chemical reactivity of liquid metals and ionic liquids at elevated temperature. Thus, in standard container-based techniques, a specimen at high temperature pollutes and changes composition due to chemical reactions with the substrate or crucible material being in contact with. Consequently, this renders the investigation of such materials with conventional, container-based techniques a difficult task, often leading to erroneous results.

Containerless techniques offer an elegant way to bypass this problem [4–8]. They have become indispensable for the investigation of liquid metals and other high-temperature melts. Containerless techniques offer the additional advantage that liquids can deeply be undercooled and investigated in this otherwise inaccessible temperature range.

At the current point in time, the following levitation techniques are mainly used: aerodynamic levitation (ADL) [4–6], electrostatic levitation (ESL) [7], and

J. Brillo (✉)
Institut für Materialphysik im Weltraum, Deutsches Zentrum für Luft- und Raumfahrt (DLR), Köln, Germany
e-mail: juergen.brillo@dlr.de

electromagnetic levitation (EML) [8]. In ADL, the sample is levitated on a gas-stream. In ESL, the sample is electrically charged and positioned by the electrostatic forces in a static electrical field, whereas the strength of the latter needs to be controlled in order to keep the sample in a stable position. In ADL, as well as in ESL, heating of the sample is accomplished by an IR laser. In EML, the sample is positioned against gravity by Lorentz forces. Heating takes place inductively. While ADL has become the standard for the investigation of liquid oxides, ESL as a versatile and comparatively new platform is well suited for high-temperature refractory materials with low work function, so that thermionic emission prevents charge loss.

Among the levitation techniques, EML is the most popular and most stable technique for electrically conducting materials, such as metals and alloys. EML provides a containerless environment and, at the same time, inductive heating and melting.

In order to exploit this environment for the measurement of thermophysical properties, EML must be combined with contactless diagnostic tools for the corresponding measurements. It is obvious that the development and integration of these tools are the major challenges in this field. They are mostly based on optical methods (videometry, spectroscopy) or sometimes also on inductive methods.

Electromagnetic levitation is around since more than 70 years. The concept of EML, however, has first been proposed in a patent by Muck in 1923 [9], i.e. almost 100 years ago. Nearly 30 years later, in 1952, Westinghouse group proposed to use EML as a preparation technique with the idea to use it for the commercial production of extremely pure metals [10]. Although this expectation was not fulfilled, the enormous potential of EML as a measurement technique became obvious at the same time. Ten years later, in 1964, Rony and Fromm [11, 12] provided a detailed theory of electromagnetic levitation with an analysis of acting forces, heat absorption, coil geometry, field strengths and necessary frequency ranges. Furthermore, they discussed the applicability of EML to nearly all metals of the periodic table.

Ground-based thermophysical property measurements were then performed by a number of groups. As early examples, El-Mehairy [13] and Shiriashi [14] published first preliminary density data measured on a number of transition metals.

During the 1990s, Krishnan measured spectral emissivity and other optical properties for a number of liquid pure metals and alloys combining an electromagnetic levitator with an ellipsometer [15–18].

Brooks [19], Egry [20–23] and others successively enlarged the spectrum of properties that can be measured with ground-based EML [19]. A comprehensive overview on recent activities is given in the review by Brillo et al. [8] as well as in Ref. [3].

2 Method

When an electrically conducting material is placed in an alternating magnetic field, eddy currents are induced in it. On the one hand, interacting with the magnetic field, these eddy currents generate a Lorentz force F that can stably support the metal against gravity. Simultaneously, these eddy currents heat the sample leading finally to its melting.

Figure 8.1 shows a photograph of a typical EML setup. A liquid droplet levitates within a water-cooled coil (≈ 1 µH) to which a current of ca. 200 A is applied at a frequency of 200–300 kHz. The applied power, of which $\approx 98\%$ is dissipated to the cooling water of the coil, is roughly 2 kW or larger, depending on the type of generator used. As the top winding of the coil has opposite polarity, a spatially inhomogeneous magnetic field B is generated with a minimum of B^2 in its centre (see Fig. 8.1). The Lorentz force F acting on the sample is given by the following expression [10]:

$$F = -\frac{\nabla B^2}{\mu_0} \frac{4\pi}{3} r^3 Q(q) \tag{8.1}$$

In Eq. 8.1, μ_0 is the magnetic permeability, r is the radius of the sample with an assumed spherical shape and $q = r/\delta$ is the dimensionless quantity with $\delta = \sqrt{2/(\mu_0 \sigma \omega)}$ being the skin depth with μ_0 being the magnetic permeability in vacuum, ω being the frequency and σ denotes the electrical conductivity. In Eq. 8.1, the function $Q(q)$ takes the effect of the skin depth into account.

As a necessary condition for levitation, the vertical component of F, i.e. F_z, must compensate the weight of the sample. When ρ is the density of the sample, g its gravitational acceleration and V the volume, Eq. 8.1 becomes [10]
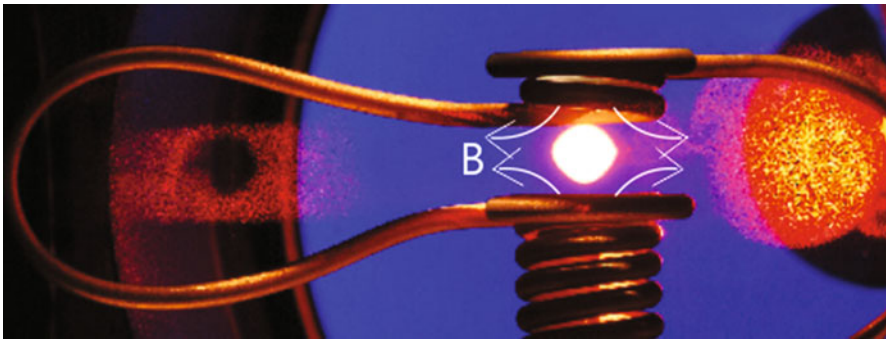
Fig. 8.1 Photograph of a levitated liquid Cu sample at ≈ 1600 K. The back light illumination is clearly visible on the right-hand side, as well as the shadow of the sample backscattered on the chamber window on the left-hand side. The magnetic field is illustrated by the white lines

Fig. 8.2 Functions $Q(q)$ (solid line) and $H(q)$ (dashed line) versus $q = R/\delta$. Low q-values correspond to low electrical conductivity and/or low frequency, while large values of q mean high frequency and high electrical conductivity
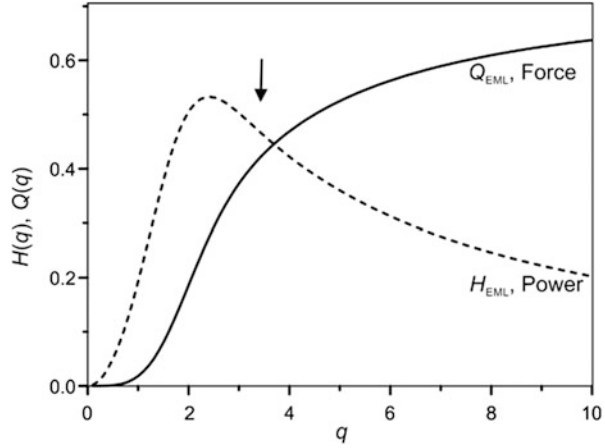
$$\rho g = -\frac{\nabla_z B^2}{\mu_0} Q(q) \tag{8.2}$$

From Eq. 8.2, one can read the factors governing the levitation process: In particular, it does not depend on the mass of the sample but on its density instead. Samples with a low density will thus be easier to levitate. The other main factor is $-\nabla B^2$ with which the force scales. In Eq. 8.1, it is always directed away from the field, i.e. towards the centre of the coil where B^2 is minimum. A restoring force thus exists for sample displacement, so that electromagnetic levitation is intrinsically stable and no active position control is needed.

As the sample has finite electrical conductivity, eddy currents induced inside experience ohmic losses leading to inductive heating. The corresponding heating power P is given by the following Eqation [10]:

$$P = \frac{B^2 \omega}{2\mu_0} \frac{4\pi}{3} r^3 H(q) \tag{8.3}$$

Here, $H(q)$ plays the same role as $Q(q)$ in Eq. 8.1. It takes the effect of the skin depth into account and may be interpreted as an effective efficiency factor for heating.

One can understand from the right side of Eq. 8.3 that P is proportional to the power density, $B^2\omega/(2\mu_0)$, and to the volume of the sample which is reduced by the factor $H(q)$ due to the skin effect. In ground-based electromagnetic levitation, heating and positioning are not decoupled. $Q(q)$ and $H(q)$ are given as analytical functions of q. They are plotted in Fig. 8.2.

Obviously, both functions are zero for $q = 0$. This situation corresponds to a perfect insulator or to $\omega = 0$. In both cases, currents cannot be induced, and neither positioning nor heating occurs. In the case of the other extreme, i.e. $q \to \infty$, $Q(q) > 0$ but $H(q) = 0$. So, for a perfect conductor, levitation takes place, but there is no

heating. Experimentally, it can sometimes be observed that very good electrical conductors, such as aluminum, copper or gold, levitate very stably, because the positioning force is high. However, their temperature rise may occur slowly making it difficult to reach the targeted temperature at all.

Between these extreme cases, the ratio between heating and positioning can be adjusted, within limits, by changing the frequency and the power of the electromagnetic field and the volume of the sample or by changing ∇B^2 through using coils of different geometry. As a compromise between heating and positioning, one would adjust the system around q-values of roughly 3.3 as marked in Fig. 8.2 by the vertical arrow.

In typical devices, the coil system is placed inside a high-vacuum chamber with a base pressure of 10^{-7} mbar. The chamber is evacuated prior to each experimental run in order to remove gaseous impurities such as adsorbed water, O_2, CO, CO_2, N_2, NO_x, hydrocarbons, and others. Levitation experiments are carried out under protecting atmospheres so that pronounced evaporation of sample material is suppressed or markedly reduced.

For this purpose, the chamber is backfilled with 500–900 mbar of Ar or He having purities of at least 6 N. In some cases, also admixtures of 5–8 vol.-% of H_2 are used, in order to reduce persistent oxygen impurities.

At the beginning of each experiment, the sample is placed on top of a vertical ceramic tube located inside the induction coil (see Fig. 8.1). Typical coil dimensions are 40×15 mm, while the sample radius is roughly 5 mm corresponding to a mass of 0.5–1.0 g. When the power is slowly increased, the sample begins to levitate, and the tube can be withdrawn. Depending on sample material and the available power, temperatures far above the respective melting points are accessible. Deep undercoolings of up to 300 K are also not unusual.

As in ground-based EML, positioning and heating are not decoupled, and a certain desired temperature is best adjusted by counter-cooling of the specimen. To this end, the sample is exposed to a weak laminar flow of the processing gas, i.e. Ar or He, admitted via one or several small nozzles. Often, the small ceramic tube is also used for that purpose.

The temperature T is measured using an infrared pyrometer aimed at the sample either from the top or from the side. As the normal spectral emissivity of the sample is not known in general, it is necessary to recalibrate the pyrometer signal T_P with respect to the known liquidus temperature T_L. For this purpose, Wien's law can be formulated once for the sample as an assumed black body with effective temperature T_P at wavelength λ:

$$L_B(T_P) = \frac{c_1}{\lambda^5 \exp\left(c_2/\lambda T_P\right)} \tag{8.4}$$

and once for the sample with real emissivity $\varepsilon(\lambda, T)$ and real temperature T:
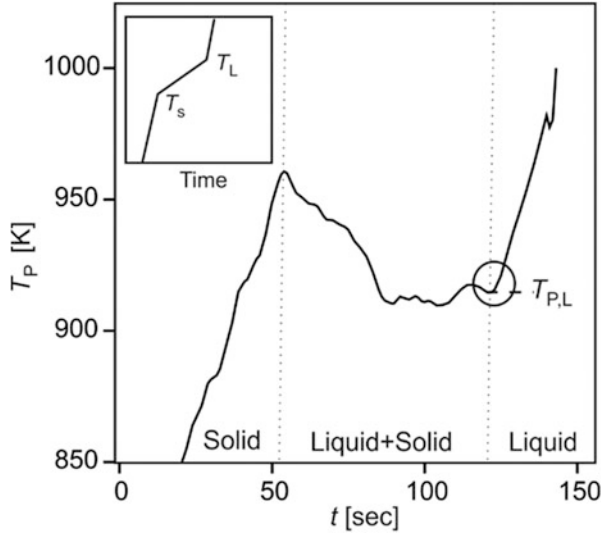
Fig. 8.3 Typical temperature record during melting. The output signal T_P is used to calibrate the pyrometer with respect to the known liquidus temperature T_L. $T_{P,L}$ is hereby the pyrometer signal at the liquidus point. When the sample begins to melt, the effective emissivity slightly decreases which, in this example, results in an apparent temperature drop. An ideal (simplified schematic) temperature-time profile with marked solidus (T_S) and liquidus (T_L) temperature is shown by the inset. The vertically dotted lines mark solidus and the liquidus

$$L(T) = \epsilon(\lambda, T)L_B(T) \tag{8.5}$$

In both equations, L and L_B are the radiance of the real sample and the black body, respectively. T_P is chosen such that Eqs. 8.4 and 8.5 are equal, i.e. $L_B(T_P) = \epsilon(\lambda,T) L_B(T)$. Moreover, if T_L is the liquidus temperature and $T_{P,L}$ is the temperature signal delivered by the pyrometer at this point, one may obtain $L_B(T_{P,L}) = \epsilon(\lambda,T_L)L_B(T_L)$. Under the assumption that $\epsilon(\lambda,T) = \epsilon(\lambda,T_L)$, i.e. that ϵ is constant over a sufficiently large temperature range, the following simple and well-known relation is derived from Eqs. 8.4 and 8.5 [15]:

$$\frac{1}{T} - \frac{1}{T_P} = \frac{1}{T_L} - \frac{1}{T_{P,L}} \tag{8.6}$$

In an experiment, T_P is measured by the pyrometer and is basically its output signal. When the sample absorbs power during heating, T_P rises, until melting sets in. At this point, some materials exhibit an apparent drop in temperature due the loss of surface roughness which results in a smaller emissivity. The situation is shown in Fig. 8.3.

Pure metals and congruently melting systems exhibit a plateau until the sample is fully molten. In alloys with a melting range, T_P would still keep rising during the melting process – eventually after the aforementioned initial drop – but with a much

smaller rate. When melting is completed, T_P rises fast again, and the liquidus point is identified by a sudden change in the steepness of the T_P-vs-time diagram where T_P equals $T_{P,L}$. The real liquidus temperature T_L is taken from literature or is determined from independent experiments (i.e. DTA). Knowing $T_{P,L}$ and T_L, Eq. 8.6 can be applied in order to determine T.

Equation 8.6 is based on the assumption that the emissivity is constant over the experimentally scanned temperature range. For most metals and alloys, this assumption is indeed a good approximation [15, 17].

Due to the induction coil's cylindrical symmetry, the shape of the sample deviates from that of a sphere [24, 25]. In fact, the resulting shape of the droplet is flat at the top and elongated at the bottom (see Fig. 8.1). This phenomenon can only partly be explained by the geometry of the magnetic field. It can be shown, in addition, that fluid flow inside the sample plays a key role in this context [26–28].

The (magneto-hydrodynamic) fluid flow is driven by the Lorentz force necessary to lift the sample against gravity. This flow is turbulent in ground-based EML experiments under the correct conditions [24–28]. A turbulent flow inside the sample might have some homogenizing effect on it, for instance, with respect to temperature and composition. However, under unfavourable conditions, it can sometimes cause heavy sample movements like vivid translational or surface oscillations or fast rotations around any axis [29, 30]. These instabilities are only limited by energy dissipation due to inner friction. They may become so intense that an accurate measurement is no longer possible.

The strong magnetic levitation field also leads to a strong damping of the surface oscillations. This and especially energy consumption by the turbulent flow prohibit the measurement of the viscosity under terrestrial conditions [31].

Electromagnetic levitation has also a number of advantages: It is intrinsically stable. Active position control is not needed. EML is tolerant to ambient conditions, and a large variety of different materials can be processed. The turbulent flow also excites spontaneous surface oscillations which is very convenient for surface tension measurements. The method allows access to high temperatures, broad temperature ranges, and deep undercoolings. It allows to process highly reactive materials and is, at the present point in time, still the most suitable and indicated technique for the investigation of electrically conductive materials, such as liquid metals, alloys or even semiconductors, such as Si or Ge [32].

3   Diagnostics

The main challenge with levitation techniques consists in development of suitable diagnostics for the contactless measurement of thermophysical properties. In this section a brief overview will be given on the portfolio of currently existing methods for measuring density, surface tension, electrical conductivity, emissivity, heat capacity and thermal conductivity of liquid metals and alloys.

3.1 Density

Density and thermal expansion are measured from the liquid sample by measuring
its volume. This is accomplished by illuminating the sample from one side and
recording shadow images on the other [33].

The light source is often an expanded laser, and the camera is equipped with a
polarizer and a band pass. The latter assures that only light from the laser is detected.
A lens and a pinhole ($\phi = 0.5$) act together as optical Fourier filters removing
scattered light and reflections (see Fig. 8.4).

The shadow graph principle becomes also obvious from Fig. 8.1, where the
expanded laser appears as a bright red circle on the right side. The shadow of the
sample is visible in the reflection of the beam at the chamber window on the left.

The images are analysed by an edge detection algorithm which locates the edge
curve, $R(\varphi)$. Here, R and φ are the radius and polar angle with respect to the drop
centre. In order to eliminate the influence of surface oscillations, the edge curve is
averaged over typically 1000 frames and fitted with Legendre polynomials of order
≤ 6 [33].

If it can be assumed that the averaged edge curve corresponds to a body which is
rotational symmetric with respect to the vertical axis, the volume of this body can be
calculated using the following integral [33, 34]:
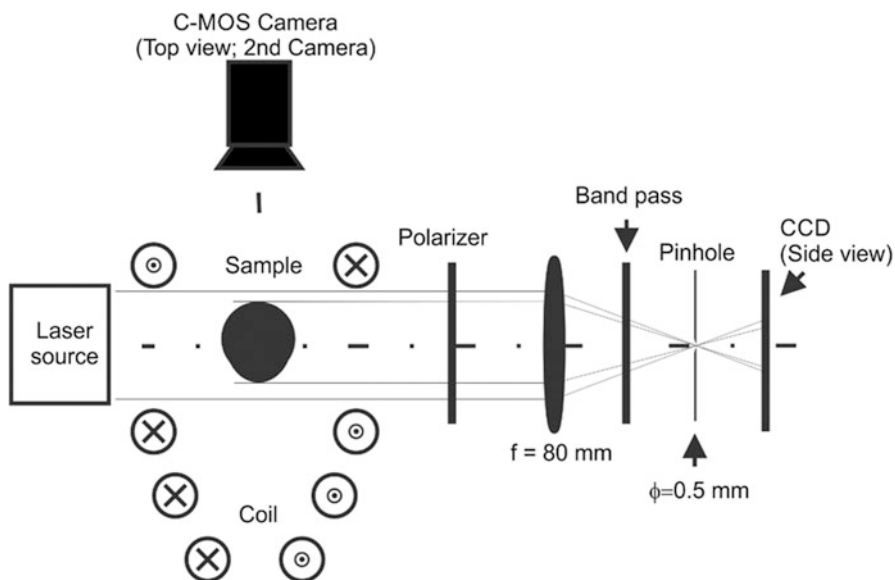
Fig. 8.4 Schematic diagram of the optical setup for density and surface tension measurement:
Density is measured by the side view camera and, if necessary, with an additional second camera in
top view position [34]. Surface tension is measured by the top view camera only

Fig. 8.5 Density of liquid Ti versus temperature (symbols) as measured in our facility. The solid line is a linear fit, and the dotted and the dashed lines correspond to data from Refs. [36, 37], respectively
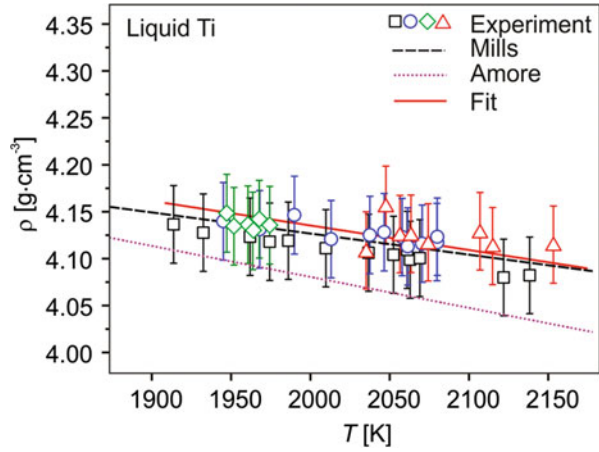
$$V_{p,\text{Circle}} = \frac{2}{3}\pi \int\limits_{0}^{\pi} \langle R(\varphi)\rangle^3 \sin(\varphi)d\varphi. \tag{8.7}$$

In Eq. 8.7, $V_{P,\text{Circle}}$ is the volume in pixel units. The subscript 'Circle' indicates that, on average, the cross section is circular. The pixel volume is related to the real volume of the sample V by a calibration procedure using bearing balls as described in reference [33].

The density, finally, is calculated from $\rho = M/V$, where M is the mass of the sample. The absolute experimental uncertainty in the density is $\Delta\rho/\rho = \pm 1\%$ [35]. The main contributions to this uncertainty originate from mass loss which must not be larger than 0.1%, and the calibration procedure, using the bearing balls.

As an example, Fig. 8.5 shows density data of pure liquid Ti [34]. The different symbols correspond to different samples and measurement runs. The overall temperature interval ranges from 1920 to 2150 K. In this example, undercooling was practically not observed. Over the temperature interval, the density ranges from 4.15 to 4.10 g/cm^3, whereas there is a linear dependency on temperature, and the slope is negative.

The method described here is based on the assumption that, averaged over time, the sample is symmetric with respect to the vertical axis. If this assumption is violated, the data become attached with large uncertainties. One typical problem in this context is sample rotation which leads to a permanent deformation of the sample. Another, yet avoidable, problem is static deformation due to misalignment of the coil. Fukuyama has tried to tackle these problems by superimposing a strong static magnetic field of several T on the levitation field [38]. As a result, nearly all fluid flow is suppressed, and the shape of the sample gets approximately spherical.

Another strategy has been reported by Brillo [34] who added a second camera directed at the sample from the top as shown in Fig. 8.4. With this camera, the shape of the sample's cross section is determined, and the data are corrected accordingly.

Fig. 8.6 Density data of liquid $Ni_{50}Ti_{50}$ versus temperature [34]. The sample is heavily rotating, and the axis-symmetry is severely violated. The hollow symbols represent results obtained under the assumption of axis-symmetry (Eq. 8.7). The solid symbols represent the same measurement but with an additional camera correcting for the missing axis-symmetry [34]. The dotted line corresponds to data measured by Zhou [39] using electrostatic levitation
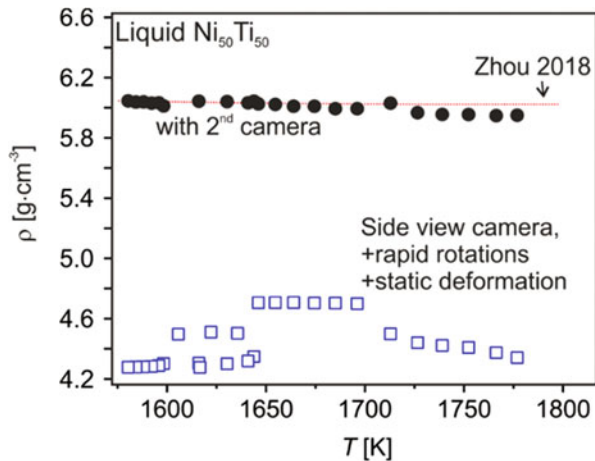
The result is shown in Fig. 8.6, where data measured on a heavily rotating $Ni_{50}Ti_{50}$ droplet are shown.

The strong rotations lead to deformation of the sample due to centrifugal forces. Without using the second camera, the hollow symbols are obtained. Obviously, the resulting data are wrong: They appear far too small, their scatter is far too large, there are apparent jumps in the density and positive as well as negative apparent slopes can be observed.

Applying the second camera method and correcting the results accordingly lead to the solid symbols in Fig. 8.6. These are in excellent agreement with corresponding literature values [34].

3.2 Surface Tension

Surface tension is measured using the oscillating drop technique [24]. Turbulent fluid flow inside the droplet generates self-excited oscillations around its equilibrium shape which can be described as normal modes by spherical harmonics $Y_{l,m}$. The indices l and m ($-l \leq m \leq +l$) are integers ('quantum numbers') that characterize each mode.

For $l \geq 2$, the modes correspond to surface oscillations, and the surface tension γ is obtained from the frequencies of these modes. The $l = 2$ mode is hereby the most pronounced one, and it is therefore of interest. In the case of $l = 2$, m can accept five different values, -2, -1, 0, $+1$, and $+2$. Under force-free conditions, i.e. under microgravity, the drop is spherical, and the mode is degenerate with respect to different values of m. Thus, only one frequency ω_R, the Rayleigh frequency, is visible in the spectrum, and the surface tension γ is proportional to ω_R^2. Thus, one

Fig. 8.7 Spectrum of an oscillating $Ag_{60}Cu_{40}$ droplet at 1440 K [41]. The solid line corresponds to the sum of two vertical radii (denoted by Ξ), and the dotted line corresponds to their difference (denoted by Δ). The arrows assign each peak to its respective value of m
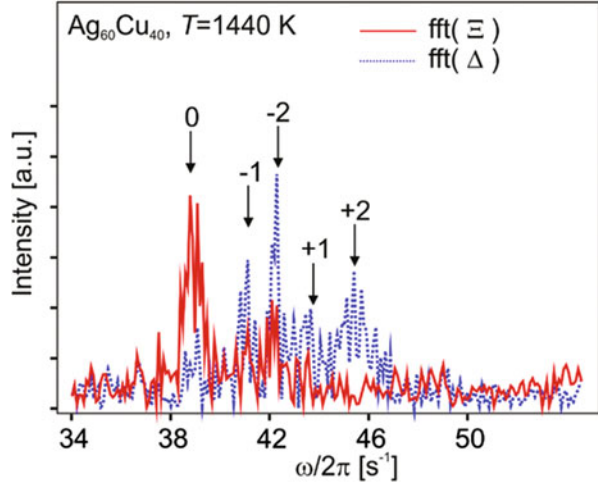
might compare the role of the surface tension for the surface oscillations to that of a spring constant for an oscillating spring [40].

In ground-based EML, the sample is no longer spherical and might also rotate weakly. As a result, the degeneracy is fully lifted with all five modes at distinct frequencies $\omega_{2,-2}, \ldots, \omega_{2,+2}$.

Knowing these frequencies, γ can be calculated using the sum rule of Cummings and Blackburn [24]:

$$\gamma = \frac{3M}{32\pi} \left[\frac{1}{5} \sum_{m=-2}^{+2} \omega_{2,m}^2 - 1.9\overline{\Omega_{tr}^2} - \frac{0.3}{\overline{\Omega_{tr}^2}} \left(\frac{g}{r} \right)^2 \right] \tag{8.8}$$

The first term inside the square brackets averages over the squares of all five frequencies $\omega_{l,m}$. The rest forms a correction term which accounts for the influence of the magnetic pressure. The latter is implicitly estimated from the mean quadratic translation frequency $\overline{\Omega_{tr}^2}$, whereas $\overline{\Omega_{tr}^2}$ is given as $\overline{\Omega_{tr}^2} = \frac{1}{3}\left(\omega_X^2 + \omega_Y^2 + \omega_Z^2 \right)$ with ω_x, ω_y, and ω_z being the translational frequencies in all spatial directions.

Typical setups for measuring the surface tension consist of a digital camera observing the sample from the top [3]. So, the second (i.e. top view) camera in Fig. 8.4 can be used for that purpose. The frame rate of the camera must at least be twice of that of the highest frequency in the spectrum. For typical EML samples with diameters of roughly 5 mm, $\omega_{l,m}/2\pi$ is in the range of typically 30–60 Hz so that 200 frames per second (fps) is a safe choice.

The camera records images of the sample, and an image processing algorithm extracts two vertical radii $r(t,0)$ and $r(t,\pi/2)$, as function of time t. For the analysis, their difference and sum are calculated, and their respective spectra, Δ and Ξ, are obtained from fast Fourier transformations (fft) [3] (see Fig. 8.7).

Fig. 8.8 Surface tension γ of liquid Ti versus (mono-atomic) oxygen bulk mole fraction x and/or the mole fraction y of TiO_2 compounds [42]. The solid line represents a model calculation based on Butler's model [42]
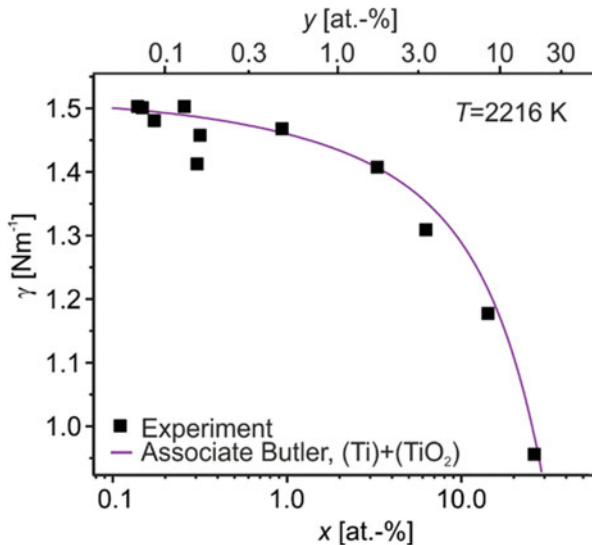
This way, the modes can be identified: The mode corresponding to $m = 0$ is symmetric with respect to the vertical axis, i.e. $r(t,0) = r(t,\pi/2)$. Hence, it appears as a peak in Ξ but not Δ. In contrast, the modes corresponding to $m = \pm 1$ obey $r(t,0) + r(t,\pi/2) = 0$; they appear as peaks in Δ but not in Ξ. The $m = \pm 2$ modes would appear in both spectra. Example spectra Ξ and Δ with assigned peaks are shown in Fig. 8.7 [41].

Figure 8.8 shows example data on liquid Ti at constant temperature [42]. Figure 8.8 shows example data on liquid Ti at constant temperature [42]. Different amounts of oxygen have been added to the sample in the form of TiO_2 particles. These would completely dissolve in the melt, whereas compound formation partly takes place. The figure shows how the surface tension decreases with increasing oxygen bulk concentration. Good agreement with a model calculation based on Butler's equation is found [42]. Because of the large solubility of oxygen in liquid titanium, the surface tension starts to decrease only when the oxygen concentration is already considerably large.

3.3 Self-Diffusion Coefficient

Self-diffusion coefficients can be measured by combining ground-based electromagnetic levitation with quasi-elastic neutron scattering (QNS) [43–47]. The experiments are performed at a high-intensity, high-resolution neutron source. If the wavelength of the primary neutrons is around 5 Å, the energy resolution would typically be 100 µeV. Incoherent scattering is dominant for wavenumbers q between 0.7 and 1.3 Å^{-1}. This is the quasi-elastic regime where the energy transfer $\hbar\omega$ is zero

and the width $2\,\Gamma$ of the elastic peak of the dynamic scattering factor $S(q, \omega)$ at $\hbar\omega = 0$ is proportional to q^2 and the self-diffusion coefficient D. The latter can thus be determined by the following relation [48]:

$$D = \frac{\Gamma}{\hbar q^2} \tag{8.9}$$

In Eq. 8.9, $\hbar$ is the Planck number divided by 2π. Compared to other methods, the accuracy of QNS is very high, and the data are suitable to serve as benchmark data.

When investigating alloys, it must be considered that the different elements contribute to the scattering process according to their individual cross sections. For the measurement on alloys, investigations are mostly done on materials where one element has a dominant cross section (like Cu, Ni, Ti, Co, etc.), and the others have very small ones, like Al. Alternatively, financially yet more expensive isotopes can also be used in order to selectively set the individual cross sections.

3.4   Electrical Conductivity

The electrical properties of the sample, in particular its impedance, contribute to the overall impedance of the levitation coil. This fact can be used in order to measure the electrical conductivity of the sample. Such measurements have been performed by Richardsen [49, 50] on Cu-Ni binary liquid alloys using ground-based electromagnetic levitation. In their setup, a small transformer, consisting of two concentric coils, is inserted into the actual levitation coil system. During the measurement, a current I_P through the primary coil of this transformer generates an alternating magnetic field $B_P \sim I_P$, and the voltage U_{ind} induced inside the sample drives an eddy current. The strength of the latter depends on the sample's electrical conductivity σ. The induced eddy current generates a secondary magnetic field B_S leading to an induced voltage U_S in the secondary coil. This can be summarized by the following equation [49–52]:

$$\frac{U_S}{I_P} e^{i\varphi} = Z_{\mathrm{coil}} + \Delta Z_{\mathrm{sample}}(\sigma, R, \alpha) \tag{8.10}$$

where φ is the phase difference between U_s and I_P, Z_{coil} is the impedance of the coil system and ΔZ denotes the impedance of the sample, i.e. the property of interest. In order to extract the latter, Z_{coil} is determined in an independent measurement without sample. ΔZ is given as explicit function of σ and the sample radius R via the physical model derived in Ref. [52]. It also depends on the mean deviation of sample from sphericity, which is expressed in Eq. 8.10 by the parameter α. The three unknown parameters, σ, R and α, can be determined from the two parts of ΔZ, i.e. the real and the imaginary one, if ΔZ is measured at high frequency ($\approx$1 MHz) and at comparatively low frequency ($\approx$10 kHz). In addition, a calibration experiment has to be

Fig. 8.9 Electrical
conductivity σ versus
temperature T. In the
undercooled range,
$T < 1500$ K, the data
(symbols) deviate from the
linear auxiliary line (dotted)
indicating the onset of
atomic ordering
processes [51]
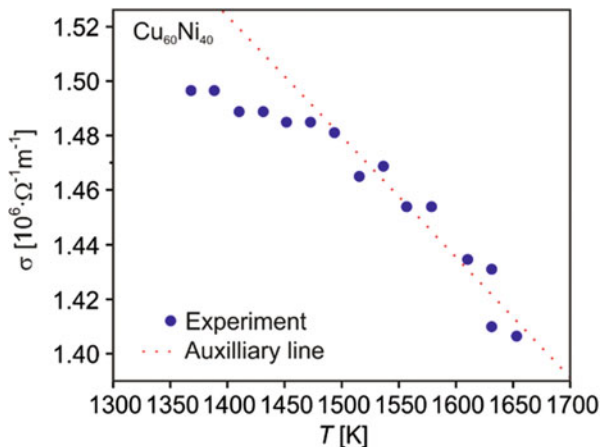
carried out using a spherical sample with well-defined radius and conductivity. In order to prevent interactions between the measurement and the strong levitation field, measurements are carried out only during a short time of 1 ms during which the levitation field is completely switched off [49, 50].

Figure 8.9 shows electrical conductivity data of a liquid $Cu_{60}Ni_{40}$ sample versus temperature [51]. It is worth to note that, at deep temperature, $T < 1500$ K, there is a deviation of σ from linearity towards smaller values. This can be interpreted as an indication for the beginning of demixing or other low-temperature ordering processes [51].

Measuring electrical conductivity in ground-based electromagnetic levitation is technically very ambitious, as many parameters, such as electrical conductivity and permittivity of the cooling water which is in contact with the measurement current, for example, need to be controlled precisely [49]. Hence, the method never became popular. In contrast, measuring electric conductivity, using basically the same principle, is straightforward under microgravity where the conditions are naturally well defined [53]. Here, the method is regularly applied.

3.5 Emissivity

Electric conductivity and normal spectral emissivity $\varepsilon(T,\lambda)$ are intimately related though their measurement principles are completely different. There are two major ways: how $\varepsilon(T,\lambda)$ can be measured containerless (a relative one where the sample radiance, measured by a spectrometer, is compared to the independently measured radiance of a quasi-black body under same the conditions [54, 55]), or $\varepsilon(T,\lambda)$ is determined from the complex refraction index $\underline{n}$ using ellipsometry or polarimetry [15–18].

Fig. 8.10 Spectral normal emissivity $\varepsilon(T,\lambda)$ of liquid Al-Ti alloys versus Al bulk mole fraction x_{Al}. The squares represent data measured with the relative method at 940 nm [56], and the circles have been obtained using the ellipsometer method at 633 nm [18]. $T = 1800$ K for both measurements
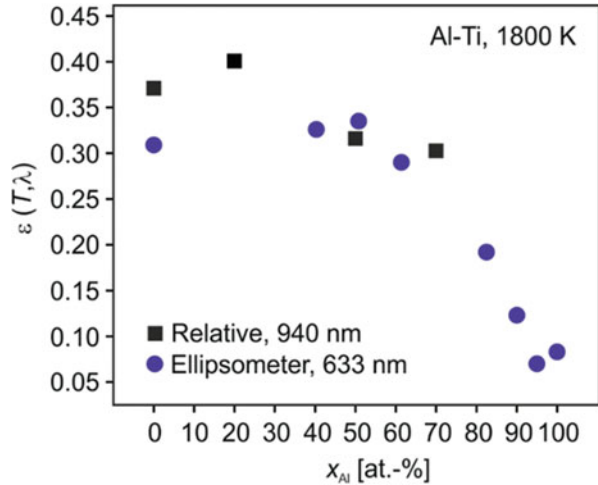
In the relative method, a suitable quasi-black body can be realized as a graphite container with a deep narrow bore. The graphite container contains liquid copper serving as a heat bath. The graphite and the copper are heated inductively by the levitation coil. When the copper melts, its melting plateau appears as a kink in the temperature profile so that the pyrometer can be recalibrated according to Eq. 8.6. The black body radiance then is measured by the spectrometer as function of wavelength and temperature, whereas the latter is determined by means of the pyrometer using.

The ellipsometer method has successfully been applied by the group of Krishnan [15–17] in different modifications. In a common setup, a linearly polarized laser beam of defined wavelength λ is shone under a certain angle at the sample's surface. The reflection is collected by the ellipsometer which basically determines two parameters, the phase difference between the component polarized in plane and the one polarized vertically to it as well as the angle about which the polarization plane has been rotated. From these parameters, the complex refraction index $\underline{n} = n + ik$ is obtained via solving Fresnel's equations, and $\varepsilon(T,\lambda)$ is obtained as follows assuming the validity of Kirchhoff's law [54–56]:

$$\varepsilon(T,\lambda) = 1 - \frac{(1-n)^2 + k^2}{(1+n)^2 + k^2} \tag{8.11}$$

Electromagnetically levitated samples usually tend to move considerably. They perform rotations and translations and sometimes travel out of the focus of any incident beam or optical sensor. In contrast to this, it is one big advantage that the ellipsometry method is completely insensitive with respect to such disturbances, as it involves the measurement of intensity ratios instead of absolute intensities. On the other hand, it is technical challenging, though not impossible [16], to vary the wavelength, and the scattering geometry is usually fixed.

As an example, Fig. 8.10 shows data on binary liquid AlTi alloys, measured in electromagnetic levitation once using the ellipsometry method [18] and once using the relative method [56].

3.6 Heat Capacity

In ground-based electromagnetic levitation experiments, heat capacity C_P as well as thermal conductivity can also be measured. This is accomplished by applying a variant of the modulation calorimetry technique which is based on the heat-flow model of Fecht [57, 58]. In this method, the heating power is periodically modulated at a frequency ω with comparatively small amplitude ΔP_ω. The total absorbed power P is then given by the following expression, where t is the time:

$$P(t) = P_0 + \Delta P_0 + \Delta P_\omega \cos{(\omega t)} \tag{8.12}$$

P_0 is hereby the equilibrium power, and ΔP_0 is the net increase of the absorbed power, due to the quadratic dependency of P on the induction current.

As a result of the modulation, the temperature also oscillates at the same frequency ω but with a phase lag $\Delta\phi$:

$$T(t) = T_0 + \Delta T_0 + \Delta T_\omega \cos{(\omega t - \Delta\phi)} \tag{8.13}$$

In Eq. (8.13), T_0 is the equilibrium temperature, ΔT_0 is the offset due to ΔP_0 and ΔT_ω is the oscillation amplitude. The heat capacity is obtained from the following relation, where M is the mass of the sample:

$$\Delta T_\omega = \frac{\Delta P_\omega}{\omega M C_P} \tag{8.14}$$

Using this method, heat capacity has been measured in ground-based EML by Guo [59] and by Fukuyama [60].

Guo estimated the absorbed power from the equilibrium temperature T_0, the Stefan-Boltzmann law, the dc component I_0 of the levitation current and its ac amplitude ΔI_ω. This involves knowledge of the total hemispherical emissivity. This way, data on liquid Ti and Zr were obtained [59].

In the experiment of Fukuyama [60], the power is modulated by means of an infra-red laser shown at the sample from the top. The *absorbed* power ΔP_ω is thus given by $\varepsilon(T,\lambda) A \Delta P_L$ if ΔP_L is amplitude of the *laser* power and A the surface area of the sample. Thus, Eq. 8.14 becomes

Fig. 8.11 $\omega\Delta T_\omega$ versus ω (triangles) and $\phi(\omega)$ versus ω (crosses) for a liquid Ti droplet processed at 2015 K using the laser oscillation calorimetry method [61]. The solid lines are fits of corresponding models. The maximum of $\omega\Delta T_\omega$ is clearly visible where $\phi \approx 90°$ and $\omega \approx 0.1$ rad·s^{-1}
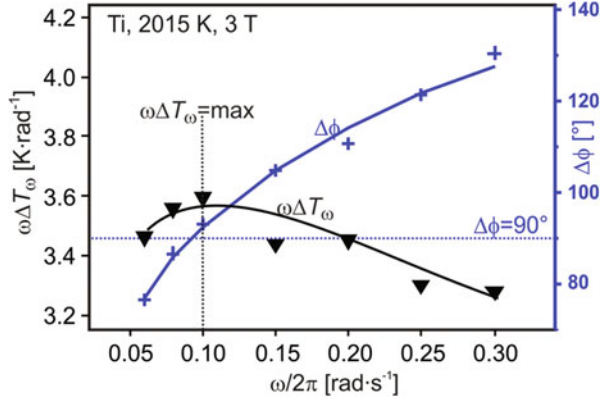
$$\Delta T_\omega = \frac{\varepsilon(T,\lambda)A \cdot \Delta P_L}{\omega M C_P} \tag{8.15}$$

In their experiment, the high-frequency magnetic levitation field is also superimposed by a strong static axial magnetic field of typically 2–20 T. The field is generated by a tunable superconducting magnet. It markedly suppresses almost all fluid flow inside the sample, and the latter is getting approximatively a spherical shape.

Equations 8.14 and 8.15 are valid if the time constant of heat conduction can be neglected compared to the time constant of radiative heat loss [57–60]. This condition is assured by a suitable choice of the modulation frequency ω. In fact, it is fulfilled when $\omega\Delta T_\omega$ becomes maximum as function of ω. This corresponds to a phase shift of $\phi \approx 90°$. Figure 8.11 shows an example $\omega\Delta T_\omega$-vs-$\Delta\phi$ curve for liquid Ti [61].

3.7   Thermal Conductivity

The laser modulation technique can also be used in order to measure thermal conductivity λ. However, the procedure is much more complicated. Its description is beyond the scope of this article. Detailed information is given in Ref. [62].

The principle of the measurement method is as follows: a model for the temperature distribution inside the sample is solved numerically and fitted to the experimentally obtained $\Delta\phi$ versus ω curves by adjusting the free parameters ε and λ. $\varepsilon = \varepsilon(T)$ hereby denotes the total hemispherical emissivity. This way, these parameters are obtained simultaneously as results.

4   Summary

In ground-based electromagnetic levitation, a spatially inhomogeneous magnetic field, alternating at a frequency of 300 kHz, induces eddy currents inside the sample. These eddy currents generate a Lorentz force which then leads to a stable positioning and levitation of the sample. Electromagnetic levitation is intrinsically stable. Positioning and heating are not decoupled. Temperature needs to be adjusted by counter-cooling in a laminar gas jet.

In order to determine density, side view shadowgraph images are recorded of the droplet by a camera. The volume is obtained from the edge profile by integration. Surface tension is obtained from the frequency spectrum of the droplet oscillations using the sum rule of Cummings and Blackburn. The latter takes the fact into account that, in contrast to the case of a force-free spherical droplet, five peaks are visible in the spectrum. If ground-based electromagnetic levitation is combined with quasi-elastic neutron scattering, self-diffusion coefficients can be determined, provided that the individual contributions of the elements to $S(q, \omega)$ can be identified. Electrical conductivity is determined from the impedance of the sample. The latter is measured by a transformer surrounding the levitating sample. Normal spectral emissivity is measured either by a relative method, comparing the radiance of the sample with the one of a quasi-black body or from the complex diffraction index determined by means of an ellipsometer. Heat capacity and thermal conductivity are determined by modulation calorimetry. This is partly achieved by combining the electromagnetic levitator with a superconducting magnet generating a static magnetic field of several Tesla suppressing fluid flows inside the sample.

Ground-based electromagnetic levitation is well suited for the measurement of density, surface tension, heat capacity and spectral normal emissivity. These measurements can successfully be done in the lab under normal conditions. Equally well, thermal conductivity and self-diffusion coefficient are measured routinely, but the required experimental effort is slightly larger. Self-diffusion measurements are also best done on earth. The measurement of electrical conductivity in ground-based EML, however, is 'ambitious' that the technique has not established itself as a standard technique. The ground-based measurement of viscosity is basically impossible in EML. Under microgravity, however, heat capacity, total hemispherical emissivity, surface tension, viscosity and electrical conductivity are routinely measured.

References

1. T. Iida, R.I.L. Guthrie, *The Thermophysical Properties of Metallic Liquids, Vol 1: Fundamentals* (Oxford University Press, Oxford, 2015)
2. M. Holtzer, R. Danko, S. Zymankowska-Kumon, Metalurgija **51**, 337 (2012)
3. J. Brillo, *Thermophysical Properties of Multicomponent Liquid Alloys* (de Gryuter, Berlin, 2016)

4. D. Langstaff, M. Gunn, G.N. Greaves, A. Marsing, F. Kargl, Rev. Sci. Instrum. **84**, 124901 (2013)
5. P.C. Nordine, R.M. Atkins, Rev. Sci. Instrum. **53**, 1456 (1982)
6. S. Krishnan et al., High Temp. Sci. **31**, 45 (1991)
7. P.F. Paradis, T. Ishikawa, G.-W. Lee, D. Holland-Moritz, J. Brillo, W.-K. Rhim, J.T. Okada, Mater. Sci. Eng. R **76**, 1–53 (2014)
8. J. Brillo, G. Lohöfer, F. Schmid-Hohagen, S. Schneider, I. Egry, Int. J. Mater. Prod. Technol. **26**, 247–272 (2006)
9. O. Muck, German Patent 422004, 30 Oct 1923
10. E.C. Okress, D.M. Wroughton, G. Comenetz, P.H. Brace, J.C.R. Kelly, J. Appl. Phys. **23**, 549–552 (1952)
11. S.-T. Rony, in Vacuum Metallurgy Conf. – Transactions, 7th Annual Vacuum Metallurgy Conference, Madison, 4–9 June 1964
12. E. Fromm, H. Jehn, Br. J. Appl. Phys. **16**, 653–663 (1965)
13. A.E. El-Mehairy, R.G. Ward, Trans. Met. Soc. AIME **227**, 1226–1228 (1963)
14. S.Y. Shiriashi, R.G. Ward, Can. Met. Quat. **3**, 117–122 (1964)
15. S. Krishnan, G.P. Hansen, R.H. Hauge, J.L. Margrave, High Temp. Sci. **29**, 17–52 (1990)
16. S. Krishnan, P.C. Nordine, J. Appl. Phys. **80**, 1735–1742 (1996)
17. S. Krishnan, Y. Yugawa, P.C. Nordine, Phys. Rev. B **55**, 8201 (1997)
18. S. Krishnan, C. Anderson, J.K. Weber, P. Nordine, W. Hofmeister, R. Bayuzick, Met. Mat. Trans. **A24**, 67–72 (1993)
19. R.F. Brooks, B. Monaghan, A.J. Barnicoat, A. McCabe, K.C. Mills, P.N. Quested, Int. J. Thermophys. **17**, 1151–1161 (1996)
20. I. Egry, S. Sauerland, Mat. Sci. Eng. A **178**, 73–76 (1994)
21. I. Egry, G. Lohöfer, G. Jacobs, Phys. Rev. Lett. **75**, 4043–4046 (1995)
22. I. Egry, S. Sauerland, G. Jacobs, High Temp.-High Press. **26**, 217–223 (1994)
23. R.A. Eichel, I. Egry, Z. Metallk. **90**, 371–375 (1999)
24. D.L. Cummings, D.A. Blackburn, J. Fluid Mech. **224**, 395 (1991)
25. S. Sauerland, PhD thesis, RWTH-Aachen, Aachen, Germany, 1993
26. R.W. Hyers, G. Trapaga, B. Abedian, Metall. Trans. B **34**, 29 (2003)
27. A.D. Sneyd, H.K. Moffatt, J. Fluid Mech. **117**, 45 (1982)
28. R.W. Hyers, Meas. Sci. Technol. **16**, 394 (2005)
29. J. Priede, G. Gerbeth, IEEE Trans. Magn. **36**, 349 (2000)
30. J. Priede, G. Gerbeth, IEEE Trans. Magn. **36**, 354 (2000)
31. S. Schneider, PhD thesis, RWTH-Aachen, Aachen, Germany, 2002
32. Y. Luo, B. Damaschke, S. Schneider, G. Lohöfer, N. Abrosimov, M. Czupalla, K. Samwer, NPJ Microgravity **2**, 1 (2016)
33. J. Brillo, I. Egry, Int. J. Thermophys. **24**, 1155 (2003)
34. J. Brillo, T. Schumacher, K. Kajikawa, Met. Mat. Trans. A **50**, 924–935 (2019)
35. J. Brillo, I. Egry, I. Ho, Int. J. Thermophys. **27**, 494 (2006)
36. S. Amore, S. Delsante, H. Kobatake, J. Brillo, J. Chem. Phys. **139**, 064504–064501 (2013)
37. K.C. Mills, *Recommended Values of Thermophysical Properties for Selected Commercial Alloys* (Woodhead Publishing Ltd, Cambridge, 2002)
38. M. Adachi, T. Aoyagi, A. Mizuno, M. Watanabe, H. Kobatake, H. Fukuyama, Int. J. Thermophys. **29**, 2006–2014 (2008)
39. P.F. Zhou, H.P. Wang, S.J. Wang, L. Hu, B. Wei, Metall. Mater. Trans. A **49A**, 5488–5496 (2018)
40. G. Lohöfer, Int. J. Thermophys. **41**, 29–42 (2020)
41. J. Brillo, G. Lauletta, L. Vaianella, E. Arato, D. Giuranno, R. Novakovic, E. Ricci, ISIJ Int. **54**, 2115–2119 (2014)
42. J. Brillo, J.J. Wessing, H. Kobatake, H. Fukuyama, High Temp.-High Press. **49**, 89–105 (2020)
43. A. Meyer, Phys. Rev. B **66**, 134205-1–134205-9 (2002)
44. A. Meyer, S. Stüber, D. Holland-Moritz, O. Heinen, T. Unruh, Phys. Rev. B **77**, 092201 (2008)

45. A.I. Pommrich, A. Meyer, D. Holland-Moritz, T. Unruh, Appl. Phys. Lett. **92**, 241922 (2008)
46. J. Horbach, R. Rozas, T. Unruh, A. Meyer, Phys. Rev. B **80**, 212203 (2009)
47. S. Stüber, D. Holland-Moritz, T. Unruh, A. Meyer, Phys. Rev. B **81**, 024204 (2010)
48. J.P. Boon, S. Yip, *Molecular Hydrodynamics* (McGraw-Hill, New York, 1980)
49. T. Richardsen, *Ein induktives Messverfahren zur Bestimmung der elektrischen Leitfähigkeit an unterkühlten Metallschmelzen* (Shaker, Aachen, 2001)
50. T. Richardsen, G. Lohöfer, Int. J. Thermophys. **20**, 1029 (1999)
51. G. Lohöfer, J. Brillo, I. Egry, Int. J. Thermophys. **25**, 1535–1550 (2004)
52. G. Lohöfer, Int. J. Eng. Sci. **32**, 107–117 (1994)
53. G. Lohöfer, Rev. Sci. Instrum. **89**, 124709 (2018)
54. R. Kurosawa, T. Inuo, Y. Baba, K. Sugioka, M. Kubo, T. Tsukada, H. Fukuyama, Meas. Sci. Technol. **24**, 015603-1–015603-7 (2013)
55. H. Kobatake, H. Khosroabadi, H. Fukuyama, Meas. Sci. Technol. **22**, 015102-1–015102-7 (2011)
56. J. Brillo, J.J. Wessing, H. Kobatake, H. Fukuyama, High Temp.-High Press. **48**, 423–438 (2019)
57. H.-J. Fecht, W.L. Johnson, Rev. Sci. Instrum. **62**, 1299–1303 (1991)
58. R.K. Wunderlich, H.-J. Fecht, Meas. Sci. Technol. **16**, 402–416 (2005)
59. B. Guo, G. Teodorescu, R.A. Overfelt, P.D. Jones, Int. J. Thermophys. **29**, 1997–2005 (2008)
60. H. Fukuyama, H. Kobatake, K. Takahashi, I. Minato, T. Tsukada, S. Awai, Meas. Sci. Technol. **18**, 2059 (2007)
61. J.J. Wessing, PhD thesis, RWTH-Aachen, Aachen, 2018
62. H. Fukuyama, Y. Waseda (eds.), *High-Temperature Measurements of Materials* (Springer, Berlin/Heidelberg, 2009)

Chapter 9
The Measurement of Density, Surface Tension, and Viscosity of Metallic Liquids by the Discharge Crucible Method

Quentin Champdoizeau and Hani Henein

1 Introduction

The development of an accurate database for the viscosity, the gas-liquid surface tension, and the density of metals and alloys is crucial in order to optimize high-temperature metallurgical processes affected by the values of these thermophysical properties. Atomization, welding, casting, and spray forming are examples of such applications [1]. Computer-based simulations use these properties as inputs to model and analyze the physics of these processes. For example, viscosity and surface tension are used to model convection and macro-segregation or the Marangoni effect [2, 3]. Numerous methods have been developed to measure the thermophysical properties of metallic liquids at high temperatures. For instance, density is also a property often required to build semi-empirical models based on dimensionless numbers and is measurable using pycnometric and dilatometric methods [4, 5]. Rotational, oscillating, or capillary methods can provide measurements of the viscosity of metallic liquids [6–9]. The surface tension can also be calculated at high temperatures using techniques such as the sessile drop, the maximum bubble pressure, the capillary rise, or the drop weight [10–14]. The accuracy of these methods is greatly limited by contamination from the atmosphere or the container at high temperatures due to the reactivity of the materials.

The levitated drop method, which uses electromagnetic levitation (EML-LD), is a containerless technique and the only one to provide a measurement of these three thermophysical properties with a single experimental run [15, 16]. The installation of an EML-LD apparatus on the International Space Station (ISS) provides ideal measurement conditions under micro-gravity and in an oxygen-free atmosphere

Q. Champdoizeau (✉) · H. Henein
Faculty of Engineering – Chemical and Materials Engineering Department,
University of Alberta, Edmonton, AB, Canada
e-mail: champdoi@ualberta.ca; hhenein@ualberta.ca

[17, 18]. The discharge crucible method (or DC method) appears as a terrestrial alternative to the ISS-EML-LD method to measure cost-effectively and simultaneously the density, surface tension, and viscosity of metals and alloys at high temperature. The method was developed and described for the first time by Roach and Henein at the University of Alberta in 2001 [19]. The technique measures these three properties for a metallic liquid at a given temperature with only one simple experimental run. During the experiment, the liquid drains by gravity through an orifice at the bottom of a crucible, and the evolution of the level of the fluid with time is measured. A nonlinear regression analysis is then conducted to determine the thermophysical properties of the liquid. The DC method has been used to measure the thermophysical properties of Al, Sn, Sb, and Zn and various alloys, such as AZ91D, Al-Cu, Al-Sn-Ag, Al-Zn, Al-Li-Zn, Sb-Sn, Sb-Sn-Zn, Pb-Sb, Al-Mg, Al-Mg-Zn, Ga-Sn, and Ga-Sn-Zn [19–30]. In this chapter, the general analysis and experimental procedure of the DC technique will be described, and some results obtained for pure aluminum, Al-Mg system, and AZ91D alloy will be presented. These sample results are selected to illustrate the applicability of the DC method to reactive metals and alloys as well as the ability to determine the effect of gas atmosphere on the gas-liquid surface tension of an alloy. Note that in this chapter the term surface tension will be used to refer to the gas-liquid surface tension.

2 The Discharge Crucible Method

2.1 The High-Temperature Apparatus

2.1.1 General Description

The DC method requires collecting data on the flow rate of the desired metallic liquid draining from a crucible at a specific temperature under gravity for analysis and calculation of the density, surface tension, and viscosity of the liquid. The experiments have to be conducted in a high-temperature apparatus. Detailed descriptions of various apparatus used to apply the DC method are available elsewhere [19, 23]. The experimental setup used in the Advanced Materials and Processing Laboratory (AMPL) of the University of Alberta will be described as an example (see Fig. 9.1). This setup consists of a sealed tower divided into two sections, the furnace and the collection. In the furnace unit, an induction furnace (8) is powering induction coils (9) to heat a graphite susceptor (2). The material is melted inside a crucible (1) of a non-reactive chosen material placed inside the graphite susceptor. The system is sitting on a water-cooled stainless steel plate with a drilled hole at the center to allow the melt to drain through and be collected in the collection unit. The temperature is monitored using a type C thermocouple (10) and a two-color pyrometer in case of failure of the thermocouple at high temperatures. In the collection unit, a vessel (13) is screwed on top of a load cell (12) to collect the melt. A stopper rod (11) is used to block the orifice and avoid any draining before reaching the desired
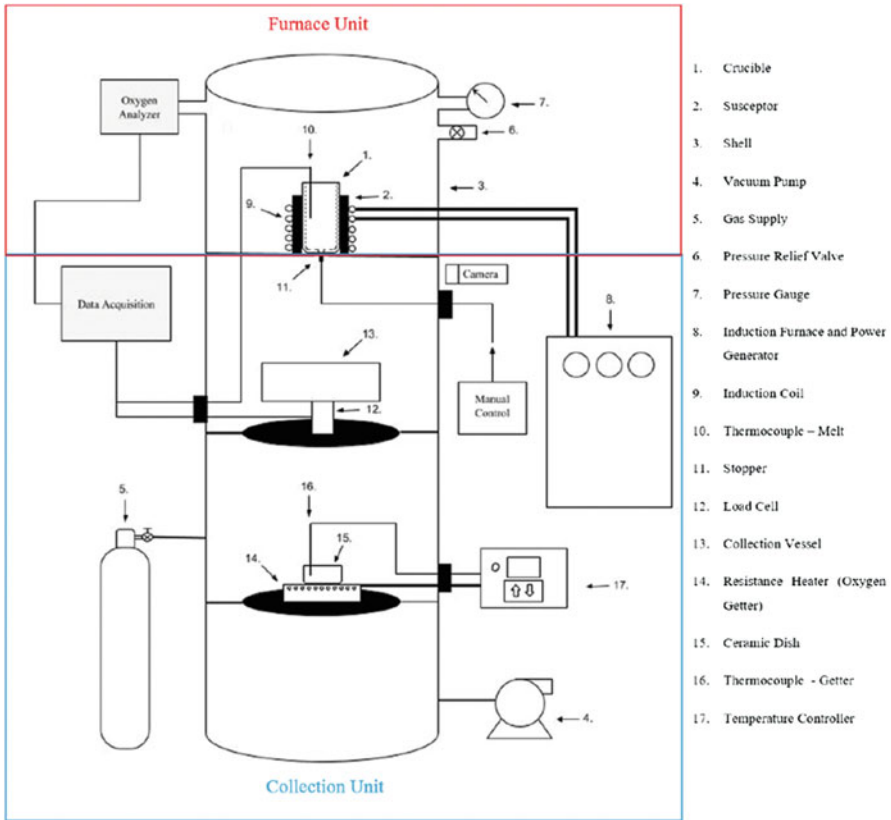
Fig. 9.1 Schematic of the experimental setup in AMPL. [23]

temperature. The oxygen getter (14) enables the experiments to be run under very low oxygen levels, e.g., 1. 10^{-8}ppm. A pump (4) is used to remove the oxygen before filling the tower with an inert gas (5), helium, or argon, to avoid oxidation.

2.1.2   Crucibles and Orifices

The choice of the crucible and the design of the drilled orifice are of crucial importance for the experiments. The crucible has to be non-reactive with the material to be melted at high temperatures, and the orifice design will influence greatly the flow rate of the fluid and the validity of the fluid mechanics model used for analysis and described in Sect. 2.2.1.

Clay graphite, for example, was used in DC experiments in [19, 21] as a suitable choice of crucible due to its ability to resist high temperatures and its non-reactivity with aluminum and magnesium alloys. These graphite crucibles were designed to be able to contain approximately 0.9 L of melt. A hole was drilled at the bottom of the
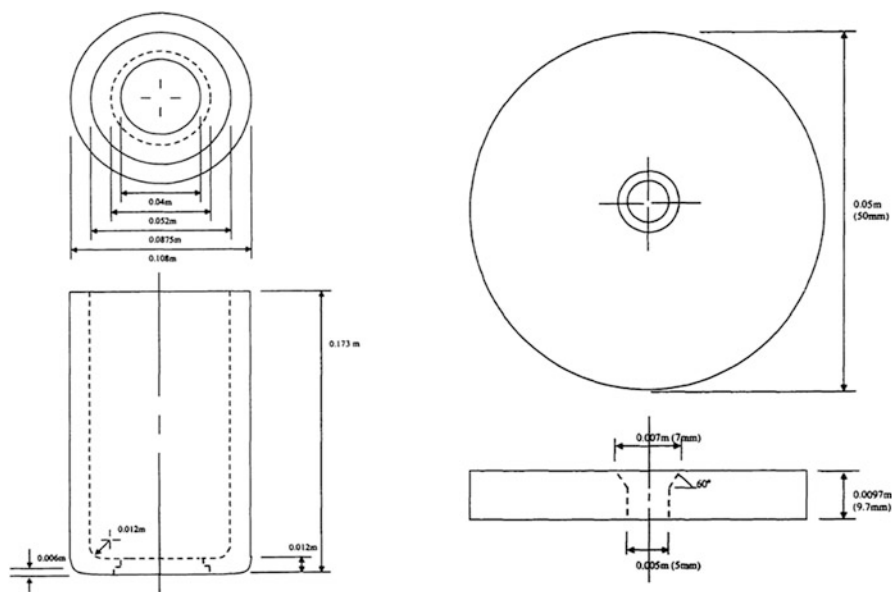
Fig. 9.2 Schematics of a clay graphite crucible and an orifice plate [19]

crucible with a depression to be able to cement a graphite orifice plate. A chamfered hole was also drilled through the plate to allow the melt to drain when desired. The dimensions of the chamfered hole were chosen to ensure a continuous jet was formed by the draining metallic liquid at the exit of the orifice. A schematic of the crucible and the orifice plate design is presented in Fig. 9.2. Different crucible and nozzle plate materials may be used such as alumina, boron nitride, or zirconium. The selection depends on the potential reactivity with the alloy to be tested and its structural integrity at test temperatures. The stopper rod shown in Fig. 9.1 is also made of the same materials as the crucible.

Once the desired oxygen atmosphere is attained, the alloy is melted. When the melt temperature has been attained and the temperature is stable, the stopper rod is removed, and the melt is allowed to drain onto the load cell. The weight gained on the load cell is recorded as a function of time, and the data is analyzed as described in the following section.

2.2 Principle of the DC Technique Analysis

2.2.1 Model Derivation

Detailed descriptions of the model used in the DC method are presented elsewhere [21–24]. The derivation presented here will consist of a brief overview. The
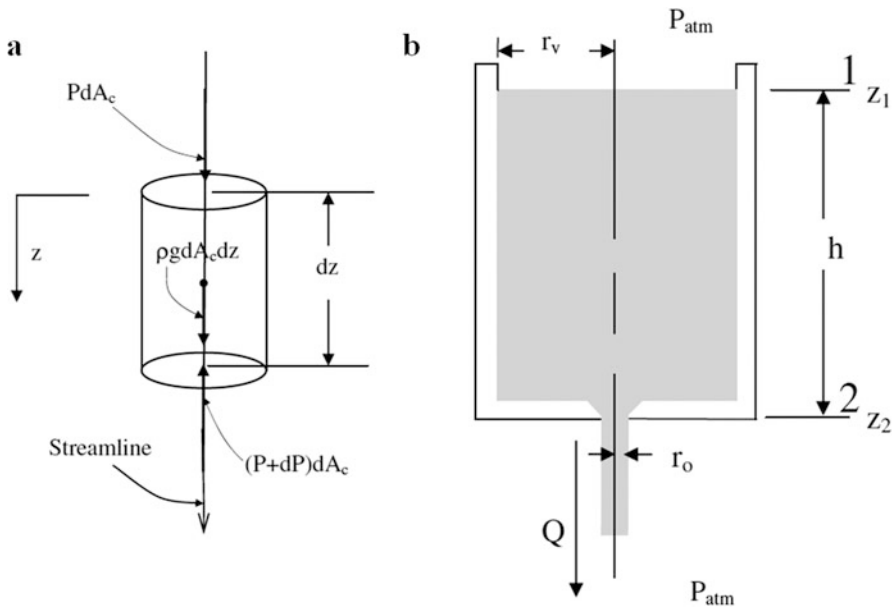
Fig. 9.3 Schematics of (**a**) infinitesimal cylindrical geometry and (**b**) draining vessel system with reference locations [21]

objective of this model is to predict the flow rate of the draining liquid as a function of the orifice dimensions, the thermophysical properties, and the level of the fluid. To achieve this objective, the Bernoulli equation for unsteady flow can be applied on a small cylindrical element as depicted in Fig. 9.3a [21]:

$$-\mathrm{d}P\mathrm{d}A_{\mathrm{c}} + \rho g \mathrm{d}A_{\mathrm{c}}\mathrm{d}z = \rho \mathrm{d}A_c\mathrm{d}z\left(u\frac{\partial u}{\partial z} + \frac{\partial u}{\partial t}\right), \tag{9.1}$$

with P the pressure, A_{c} the cross section, g the gravity constant, z the vertical coordinate, u the velocity, ρ the density, and t the time. In the case of a fluid draining from a vessel, Eq. 9.1 can be integrated between the top of the fluid and the exit of the orifice (locations 1 and 2 as shown in Fig. 9.3b are used as subscripts in the following) after dividing by $-\rho \mathrm{d}A_{\mathrm{c}}$ and rearranging terms the unsteady Bernoulli equation is given as

$$\frac{P_2 - P_1}{\rho} - g(z_2 - z_1) + \frac{u_2^2 - u_1^2}{2} = -(z_2 - z_1)\left(\frac{\partial u}{\partial t}\right). \tag{9.2}$$

The term $-(z_2 - z_1)\left(\frac{\partial u}{\partial t}\right)$ comes from the assumption that the evolution of the velocity with time is linear; thus the derivative is constant. This assumption was validated by Roach and Henein [19]. The velocity at point 1 in Eq. 9.2 can be written

as a function of the velocity at point 2 by conservation of the volumetric flow rate such as

$$u_1 = u_2 \left(\frac{r_0}{r_v}\right)^2, \tag{9.3}$$

with r_0 and r_v, respectively, the radius of the orifice and the radius of the crucible as shown in Fig. 9.3b. In practice, the crucibles are chosen such as $r_v \gg r_0$ which means the assumption $u_1 \ll u_2$ can be made, and thus the velocity at the top (point 1) can be neglected compared to the velocity at the exit of the orifice (point 2). Equation 9.2 can now be rearranged in terms of the velocity u_2 which gives

$$u_2 = \sqrt{2g\left(h - \frac{P_2 - P_1}{\rho g} - \frac{h}{g}\left(\frac{\partial u}{\partial t}\right)\right)} \tag{9.4}$$

as $(z_2 - z_1) = h$ in this situation. The term $\frac{h}{g}\left(\frac{\partial u}{\partial t}\right)$ is the acceleration of the head and can be neglected as shown in [19]. The pressure around points 1 and 2 in the surrounding is uniform and equal to the atmospheric pressure P_{atm}. However, the curvature of the interface will induce a pressure differential due to interfacial phenomena according to the Young-Laplace equation:

$$\Delta P = \sigma\left(\frac{1}{R_a} + \frac{1}{R_b}\right), \tag{9.5}$$

with σ the surface tension, ΔP the difference of pressure between the liquid and the gas across the interface, and R_a and R_b the principal radii of curvature of the interface. By convention, R_a and R_b are positive if the curvature is convex and negative if concave. At point 1, the interface can be considered planar, and thus the pressure difference negligible $P_1 \sim P_{atm}$. Assuming the jet at the exit to be cylindrical (no wetting), the principal radii of curvature can be approximated as

$$R_a = \infty, R_b = r_0. \tag{9.6}$$

The pressure differential at location 2 can then be written as

$$\Delta P_2 = \frac{\sigma}{r_0},$$
$$P_2 = P_{atm} + \frac{\sigma}{r_0}. \tag{9.7}$$

Neglecting $\frac{h}{g}\left(\frac{\partial u}{\partial t}\right)$ (quasi-steady-state assumption), approximating $P_1 \sim P_{atm}$ and injecting Eq. 9.7 into Eq. 9.4 gives
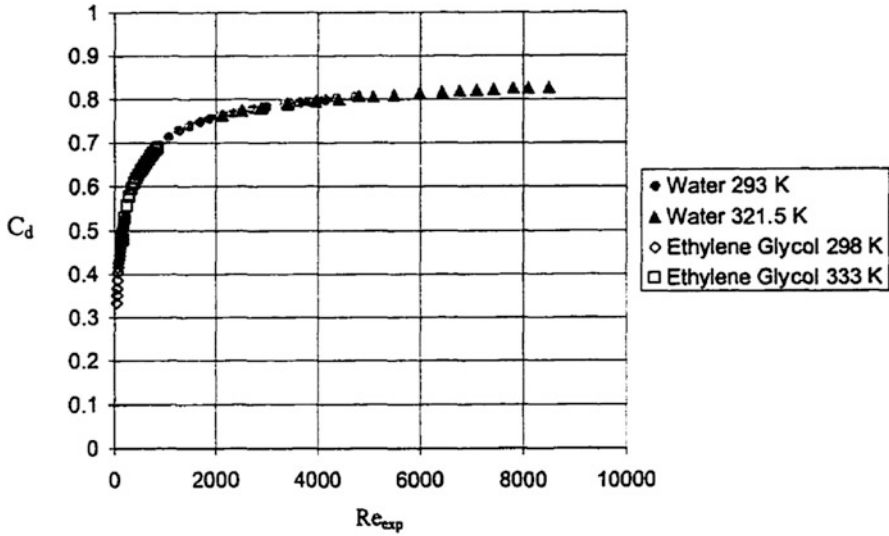
Fig. 9.4 Example of calibrated evolution of the discharge coefficient as a function of the Reynolds number [19]

$$u_2 = \sqrt{2g(h - \frac{\sigma}{\rho g \, r_0})}. \tag{9.8}$$

Equation 9.8 completely neglects the influence of viscosity on the flow so it is only valid for an inviscid draining. To characterize the friction losses in the orifice, the discharge coefficient C_d is defined as the ratio between the experimental velocity (or flow rate) and the theoretical velocity (or flow rate) and is introduced such as $C_d = \frac{u_{\text{exp}}}{u_{\text{theo}}}$. The discharge coefficient is a corrective coefficient on the velocity of the flow, bounded such as $C_d < 1$, and usually monotonously depending on the Reynolds number, R_e. The evolution of C_d as a function of R_e can be experimentally determined through low-temperature experiments with different fluids for each specific crucible and orifice design as shown in Fig. 9.4.

The velocity of the fluid exiting the orifice is then satisfying the implicit equation depending on the three thermophysical properties, namely, the density ρ, the surface tension σ, and the viscosity η as well as the level of fluid h and the geometry of the orifice (in particular the diameter d):

$$u_2 = C_d(R_e)\sqrt{2g\left(h - \frac{\sigma}{\rho g \, r_0}\right)},$$

$$R_e = \frac{\rho u_2 d}{\eta}. \tag{9.9}$$

Equation 9.9 can be rewritten in terms of the volumetric flow rate Q_{exp} as

$$Q_{\text{exp}} = \pi \, r_0^2 \, C_{\text{d}}(R_{\text{e}}) \sqrt{2g(h - \frac{\sigma}{\rho \, g \, r_0})}. \tag{9.10}$$

From Eq. 9.10 the level of fluid h can be isolated as this quantity is directly experimentally measurable for the analysis section of the DC method such as

$$h = \frac{1}{2g} \left(\frac{Q_{\text{exp}}}{\pi r_0^2 C_{\text{d}}(R_{\text{e}})} \right)^2 + \frac{\sigma}{\rho g r_0}. \tag{9.11}$$

The dimensionless form of Eq. 9.11 can be obtained by introducing the Froude (F_{r}) and the Bond number (B_{o}). The Froude number is a dimensionless number defined as the ratio between the inertia of the fluid and the potential gravitational energy such as

$$F_{\text{r}} = \frac{\left(\frac{Q_{\text{exp}}}{\pi \, r_0^2 \, C_{\text{d}}} \right)^2}{2 \, g \, h}. \tag{9.12}$$

The Bond number is also a dimensionless number describing the ratio of gravitational forces to capillary and surface tension forces:

$$B_{\text{o}} = \frac{\rho g r_0 h}{\sigma} = \frac{r_0 h}{\lambda_{\text{c}}^2}, \tag{9.13}$$

with λ_{c} the capillary length. Equation 9.10 can then be rewritten in terms of these two dimensionless numbers:

$$F_{\text{r}} + B_{\text{o}}^{-1} = 1. \tag{9.14}$$

Equation 9.14 shows that during the draining, the potential energy is partially dissipated and balanced in viscous losses (quantified in C_{d}) and surface tension forces, while the remaining gravitational energy is converted to inertia. Thus, the F_{r} and B_{o} numbers are balancing as the level of fluid is decreasing during the draining. As h is decreasing, B_{o} is decreasing and so F_{r} should follow to satisfy Eq. 9.14. This naturally means that the velocity should drop as the potential energy is declining until B_{o} reaches a value of 1 and the draining theoretically stops. The diameter of the orifice is to be selected carefully as it has a great impact on this balance of energy/forces during the draining. If the diameter is too large, B_{o} will also become large, and the surface tension will not contribute to the flow rate. On the contrary, if the diameter is too small, the surface tension forces will be too high, and the fluid might not flow or will drip which will invalidate Eq. 9.10 [19, 23].

Using the model for the flow rate given by Eq. 9.10, the DC method can be applied. After choosing an appropriate crucible material and orifice design, the equation giving the evolution of C_{d} as a function of R_{e} should be calibrated with low-temperature experiments. Afterward, high-temperature draining experiments

can be conducted for the desired metallic liquid at a certain temperature. During these experiments, the evolution of the flow rate and the level of the fluid are measured as a function of time. The theoretical evolution of the level of the fluid h can be calculated using Eq. 9.11 with only unknowns being the thermophysical properties, the density, the viscosity, and the surface tension. Through a nonlinear regression process and using initial guesses from the literature, the theoretical and experimental evolution of the level of fluid $h(t)$ are fitted to obtain the best-fit thermophysical properties. This mathematical solution is assumed to give the density, surface tension, and viscosity of the metallic liquid at the draining temperature within certain uncertainties.

2.2.2 Nonlinear Regression

The nonlinear regression process to fit the theoretical level of fluid given by Eq. 9.11 to the experimental signal can be conducted using any nonlinear regression algorithm. This analysis was described using the Gauss-Newton algorithm in [19, 23]. This section will then constitute a summary of these derivations. The objective of this nonlinear regression process is to minimize the sum of squares of the residuals between the theoretical and experimental signals, also called a nonlinear least-squares regression. In this case, the residuals r are defined as

$$r = h_{\exp} - f(Q_{\exp}, \beta), \tag{9.15}$$

with f the function giving the evolution of the theoretical level of fluid as a function of the experimental flow rate $Q_{\exp}$ and the vector of the thermophysical properties $\beta = (\rho, \sigma, \eta)$. The regression process consists of minimizing the L2 norm of the residuals such as

$$\min \left(\left\| r(h_{\exp}, Q_{\exp}, \beta) \right\|^2 \right). \tag{9.16}$$

The variables are the properties in β which are getting iterated by the algorithm until convergence is achieved. The iteration scheme is derived in [31] as

$$(\Delta\beta)_i = \left(J(\beta_i)^T J(\beta_i) \right)^{-1} J(\beta_i)^T r_i(\beta_i), \tag{9.17}$$

with $\Delta\beta = \beta_{i+1} - \beta_i$, the variation of the variables after iteration i and $J(\beta_i)$, the Jacobian of the function f. The other parameters such as the experimental evolution of the level of fluid, the flow rate, and the geometrical parameters are voluntarily omitted to simplify the formalism. The Gauss-Newton algorithm then iterates the variables using Eq. 9.17 until the desired convergence is reached. The computation, transposition, and inversion of the Jacobian are the most time-consuming steps of the algorithm. The Jacobian is defined as

$$J = (\begin{array}{ccc} \dfrac{\partial f(Q_{\exp})_1}{\partial \rho} & \dfrac{\partial f(Q_{\exp})_1}{\partial \sigma} & \dfrac{\partial f(Q_{\exp})_1}{\partial \eta} \\ \cdots & \cdots & \cdots \\ \dfrac{\partial f(Q_{\exp})_i}{\partial \rho} & \dfrac{\partial f(Q_{\exp})_i}{\partial \sigma} & \dfrac{\partial f(Q_{\exp})_i}{\partial \eta} \\ \cdots & \cdots & \cdots \\ \dfrac{\partial f(Q_{\exp})_n}{\partial \rho} & \dfrac{\partial f(Q_{\exp})_n}{\partial \sigma} & \dfrac{\partial f(Q_{\exp})_n}{\partial \eta} \end{array}), \qquad (9.18)$$

with n the number of points available in the data set. The partial derivatives of the Jacobian are, among others, depending on the chosen formulation for C_d. Detailed formulations of the partial derivatives were derived by Flood [23]. After convergence of the algorithm, the uncertainties on the results can be estimated using a propagation of error analysis.

2.2.3   Propagation of Error Analysis

The nonlinear regression process is subjected to statistical issues such as parameter evaporation or sloppiness that make the estimation of the statistical uncertainties on the best-fit thermophysical properties difficult [32]. The systematic errors on the measured density, surface tension, and viscosity can be, however, quantified using a propagation of error analysis [21, 24]. The measurement errors on the evolution of the head and the flow rate but also the formulation of C_d will have an impact on the systematic uncertainties of the thermoproperties such as

$$\delta\rho = \sqrt{\left(\frac{\partial\rho}{\partial h_{\exp}}\right)^2 \left(\delta h_{\exp}\right)^2 + \left(\frac{\partial\rho}{\partial Q_{\exp}}\right)^2 \left(\delta Q_{\exp}\right)^2 + \left(\frac{\partial\rho}{\partial C_d}\right)^2 \left(\delta C_d\right)^2},$$

$$\delta\sigma = \sqrt{\left(\frac{\partial\sigma}{\partial h_{\exp}}\right)^2 \left(\delta h_{\exp}\right)^2 + \left(\frac{\partial\sigma}{\partial Q_{\exp}}\right)^2 \left(\delta Q_{\exp}\right)^2 + \left(\frac{\partial\sigma}{\partial C_d}\right)^2 \left(\delta C_d\right)^2},$$

$$\delta\eta = \sqrt{\left(\frac{\partial\eta}{\partial h_{\exp}}\right)^2 \left(\delta h_{\exp}\right)^2 + \left(\frac{\partial\eta}{\partial Q_{\exp}}\right)^2 \left(\delta Q_{\exp}\right)^2 + \left(\frac{\partial\eta}{\partial a}\right)^2 (\delta a)^2 + \left(\frac{\partial\eta}{\partial b}\right)^2 (\delta b)^2},$$

$$(9.19)$$

with $\delta\rho$, $\delta\sigma$, and $\delta\eta$ the uncertainties on the density, surface tension, and viscosity, respectively. To estimate the partial derivative terms in Eq. 9.19, it is necessary to rewrite Eq. 9.10 in terms of each thermophysical property. The evolution of C_d as a function of R_e is complex but can be locally approximated as an affine function at high Reynolds number for the derivation of the viscosity terms ($C_d = aR_e + b$) [19]:

$$\rho = \frac{\sigma}{gr_o\left(h_{\exp} - \frac{1}{2g}\left(\frac{Q_{\exp}}{C_d\pi r_o^2}\right)^2\right)},$$

$$\sigma = \rho g r_o\left(h_{\exp} - \frac{1}{2g}\left(\frac{Q_{\exp}}{C_d\pi r_o^2}\right)^2\right), \tag{9.20}$$

$$\eta = \frac{2a\rho r_o Q_{exp}}{\frac{Q_{\exp}}{\sqrt{2g\left(h_{\exp} - \frac{\sigma}{\rho g r_o}\right)}} - \pi r_o^2 b}.$$

From Eq. 9.20 we can calculate the partial derivative terms of Eq. 9.19 for the density:

$$\frac{\partial \rho}{h_{\exp}} = -\frac{\rho^2 g r_o}{\sigma},$$

$$\frac{\partial \rho}{\partial Q_{\exp}} = \frac{\rho^2 Q_{\exp}}{C_d^2 \pi^2 r_o^3 \sigma}, \tag{9.21}$$

$$\frac{\partial \rho}{\partial C_d} = -\frac{\rho^2 Q_{exp}^2}{\sigma \pi^2 r_o^3 C_d^3}.$$

The partial derivative terms for the surface tension can be derived similarly:

$$\frac{\partial \sigma}{\partial h_{\text{exp}}} = \rho g r_{\text{o}},$$

$$\frac{\partial \sigma}{\partial Q_{\text{exp}}} = -\frac{\rho r_{\text{o}}}{C_d \pi r_{\text{o}}^2}\left(\frac{Q_{\text{exp}}}{C_d \pi r_{\text{o}}^2}\right), \tag{9.22}$$

$$\frac{\partial \sigma}{\partial C_{\text{d}}} = \frac{\rho r_{\text{o}}}{C_{\text{d}}}\left(\frac{Q_{\text{exp}}}{C_d \pi r_{\text{o}}^2}\right)^2.$$

Finally, the partial derivative terms for the viscosity are given by

$$\frac{\partial \eta}{\partial h_{\text{exp}}} = \frac{2 a \rho r_{\text{o}} g Q_{\text{exp}}^2}{\pi^2 r_{\text{o}}^4 (C_{\text{d}} - b)^2 \left(2gh\left(1 - \frac{\sigma}{\rho g r_{\text{o}} h_{\text{exp}}}\right)\right)^{\frac{3}{2}}},$$

$$\frac{\partial \eta}{\partial Q_{\text{exp}}} = -\frac{2 a \rho d}{\pi r_{\text{o}}(C_{\text{d}} - b)^2},$$

$$\frac{\partial \eta}{\partial a} = \frac{2 \rho r_{\text{o}} Q_{\text{exp}}}{\pi r_{\text{o}}^2 (C_{\text{d}} - b)}, \tag{9.23}$$

$$\frac{\partial \eta}{\partial b} = \frac{\pi r_{\text{o}} \eta^2}{2 a \rho Q_{\text{exp}}}.$$

The uncertainties on the head, the flow rate, C_{d}, and the polynomial fitting coefficients a and b can be estimated experimentally to calculate the approximate systematic uncertainties on the calculated density ρ, the surface tension σ, and the viscosity η of the melted material according to Eq. 9.19.

3   Results for Aluminum and Alloys

The DC method has been used to measure the thermophysical properties of a wide range of metals and alloys. The reader is referred to [19–30]. In this section, three systems will be discussed as application examples of the DC method, pure

aluminum, Al-Mg alloy, and magnesium alloy AZ91D. Pure aluminum and Al-Mg alloy were tested in an inert atmosphere, while AZ91D was evaluated to explore the effect of gas atmosphere on the alloy properties.

3.1 Pure Aluminum

The thermophysical properties of aluminum were measured at various temperatures by Roach and Henein [22] and by Gancarz et al. [30] using the DC method. The reader is referred to [30] for more details on the analysis and experimental procedure to obtain the density, surface tension, and viscosity of pure Al. In this section, the obtained results will be presented to demonstrate the applicability of the method for pure metallic liquids. The experiments were carried using a glove-box with a high-purity Ar atmosphere. The oxygen content was measured below 1 ppm during the experiments, and the purity of the Al was 99.999%. The results for the density are compared to the literature from [22, 33–35] and presented in Fig. 9.5.

The density measured in [30] is in very good agreement with the published data. In particular, the results are really close to the equation based on literature data proposed by Assael et al. [35] (<0.3%) and the measurements obtained by Roach and Henein [22] using the DC method with a different apparatus (<1%). The results for the surface tension are also compared to previous data [22, 36–43] and presented in Fig. 9.6.

The measurements made by Gancarz et al. [30] are very similar to results obtained in the presented literature (<1%). The difference with the values obtained in [22] is increasing with temperature while remaining relatively low (<2%). Mills and Su [36] and Pamies et al. [43] report a decrease in surface tension results for pure aluminum due to the surface oxidation. The results presented in [30] are then consistent with an oxygen-saturated surface of aluminum. The values obtained from [30] for the viscosity of pure Al are presented in Fig. 9.7 and compared to published data [33, 35, 44, 45].

The viscosity results fall also in reasonable agreement with the literature on the evolution of the viscosity of pure aluminum with temperature. Changes in the purity of the aluminum and the protective atmosphere could explain the small differences in the measurements. It should be noted that the results reported in [22, 23] (not presented in Fig. 9.7) for the viscosity of pure aluminum, using the DC method, are much lower than other reported values in the literature. This is attributed to the oxygen content in the atmosphere but also the impact of the wetting phenomenon on the model of the DC method.

Fig. 9.5 Results for the density of pure aluminum. (Adapted from Ref. [30])
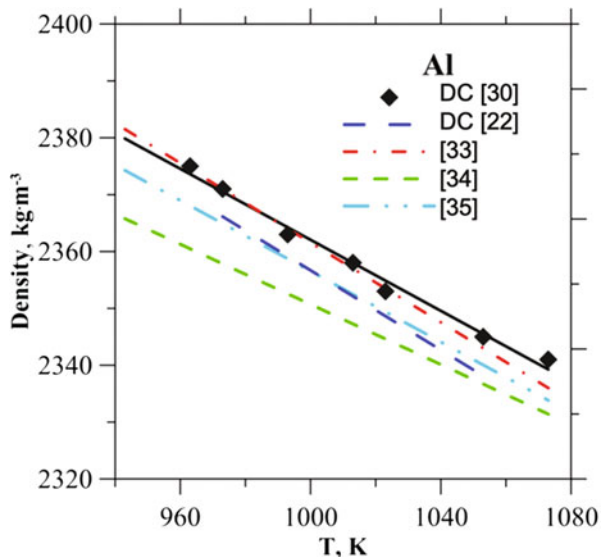
3.2 Al-Mg Alloy

The thermophysical properties of Al-Mg at a temperature of 973 K were also measured using a glove-box with a high-purity Ar atmosphere and presented as a function of the atomic concentration X_{MG} of magnesium in the alloy in [30]. The results for the density are specifically presented in Fig. 9.8 with published literature [33, 46, 47]. The ideal solution for the density ρ_{ideal} for an Al-Mg system is calculated from Eq. 9.24 [46]:

$$\rho_{ideal} = \frac{1}{\frac{\gamma_{Al}}{\rho_{Al}} + \frac{\gamma_{Mg}}{\rho_{Mg}}}, \tag{9.24}$$

with γ_{Al}, γ_{Mg}, ρ_{Al}, and ρ_{Mg} as the mass fractions and densities of the pure components Al and Mg at the temperature of 973 K taken from [34]. The model to calculate the density of the Al-Mg system proposed by Brillo and Egry [47] can be written as

$$\rho = \frac{X_{Al}m_{Al} + X_{Mg}m_{Mg}}{\frac{X_{Al}m_{Al}}{\rho_{Al}} + \frac{X_{Mg}m_{Mg}}{\rho_{Mg}} + V_E}, \tag{9.25}$$

with X_{Al}, X_{Mg}, m_{Al}, m_{Mg}, ρ_{Al}, and ρ_{Mg} corresponding to the atomic fractions, molar masses, and pure densities for Al and Mg, respectively. V_E is the excess volume which formulation is detailed in [47].

Fig. 9.6 Results for the surface tension of pure aluminum. (Adapted from Ref. [30])
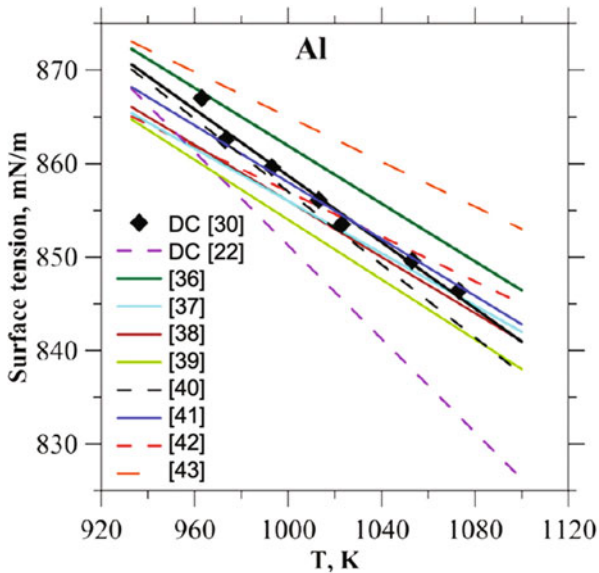
Fig. 9.7 Results for the viscosity of pure aluminum. (Adapted from Ref. [30])
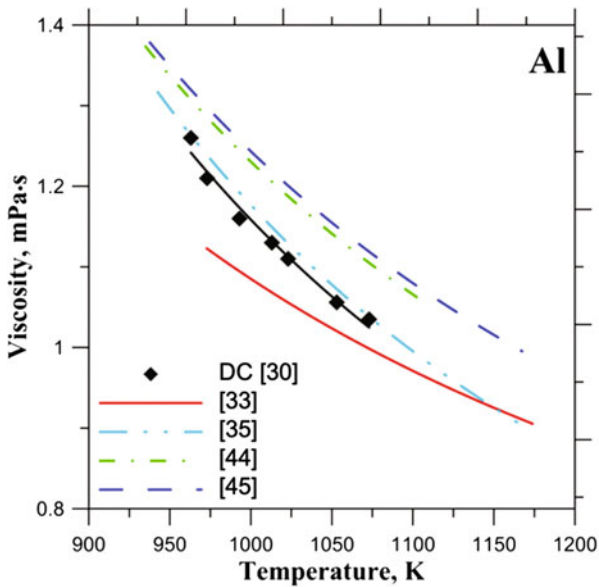
The results for the density measured with the DC method in [30] are in reasonable agreement with the literature presented. At low Mg content, the results are close to the ideal solution [46] but become lower than the Brillo model [47] with an increasing Mg content. The surface tension results for the Al-Mg system from [30] are presented in Fig. 9.9 and compared to the Butler ideal and non-ideal model [48]

Fig. 9.8 Results for the density of Al-Mg system. (Adapted from Ref. [30])
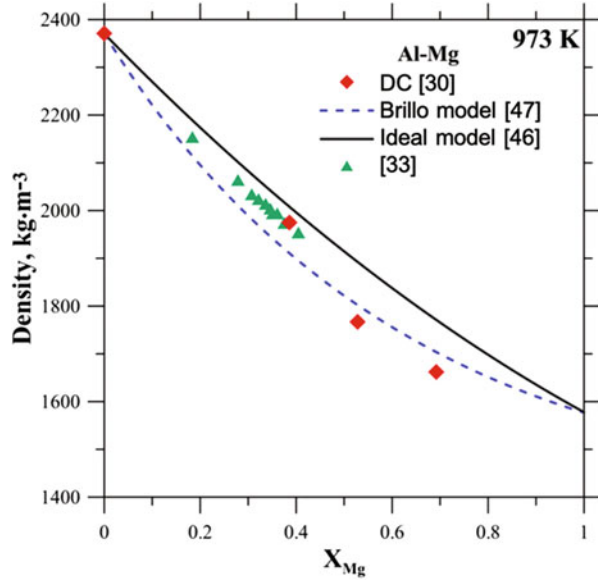
and experimental results obtained by Garcia-Cordovilla et al. [49] using the maximum bubble pressure method.

The measurements with the DC technique show very good agreement with the Butler model and [49] for low Mg content (<1%). Finally, the viscosity of the Al-Mg system measured with the DC method was compared to literature data [50–54] and several models [55–62] in Fig. 9.10. These models are presented in detail in [30].

There is an important discrepancy in the values for the viscosity of the Al-Mg system reported in the literature. The measurements obtained using the DC method [30] are, however, in good agreement with experimental results from [33, 50].

Overall, the DC method provided measurements in good agreement with the literature for the density, surface tension, and viscosity of the Al-Mg system and proved to be adequate to analyze the effect of alloying on the thermophysical properties of metallic liquids.

3.3   AZ91D Alloy: Effect of SF6

Alloy AZ91D is a widely used magnesium alloy usually processed under a protective partial SF6 atmosphere. This gas causes the surface layer of molten magnesium to form as a dense cohesive layer of solid MgO and MgF_2 protecting the melt from rapid oxidation and ignition [63]. However, the segregation of these elements at the surface leads to a significant drop in the surface tension. The DC method was applied by Roach and Henein [20] to measure the thermophysical properties of AZ91D alloy

Fig. 9.9 Results for the surface tension of Al-Mg system. (Adapted from Ref. [30])
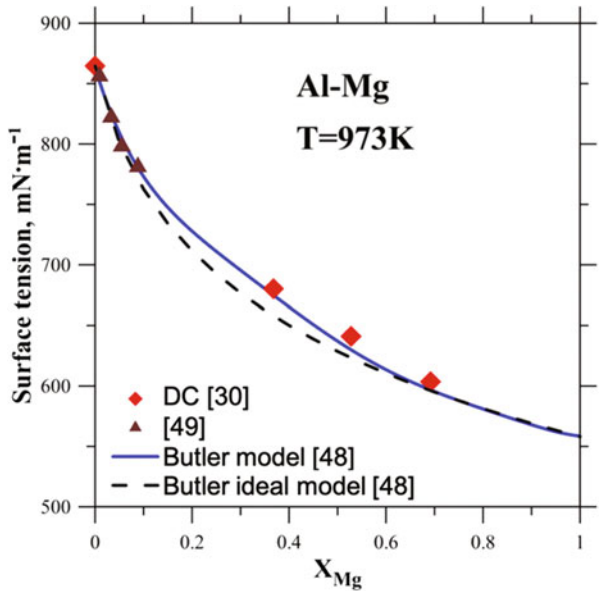
Fig. 9.10 Results for the viscosity of Al-Mg system. (Adapted from Ref. [30])
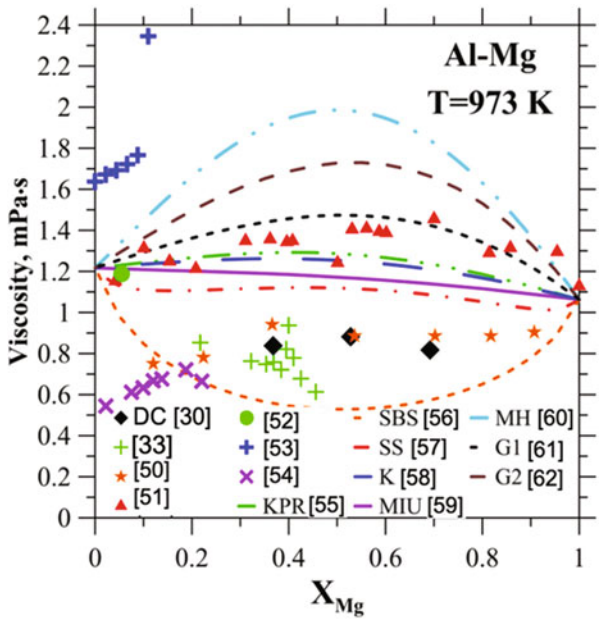
Fig. 9.11 Results for the
surface tension of AZ91D
under argon. (Adapted from
Ref. [20])
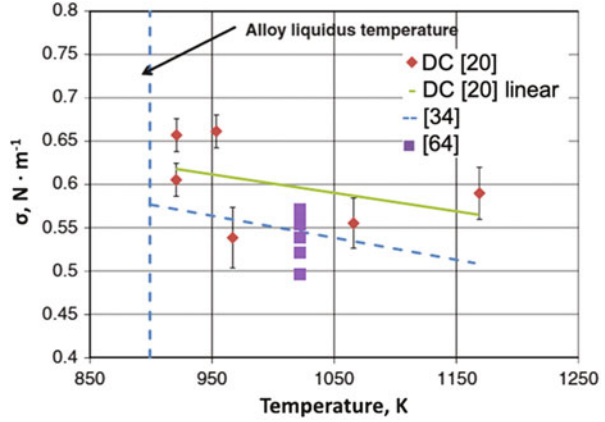
Fig. 9.12 Comparison of
surface tension
measurements for AZ91D
under argon and SF6.
(Adapted from Ref. [20])
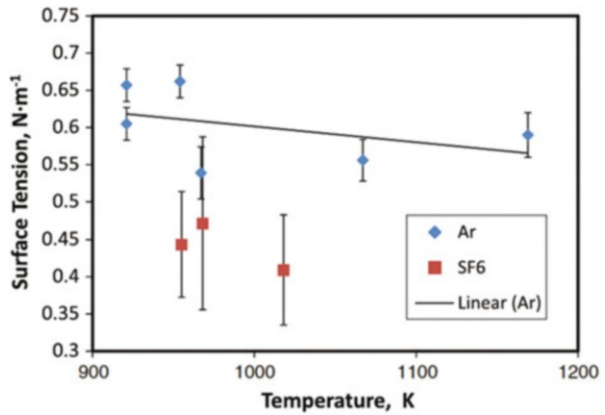
under argon and SF6 and study the influence of the gas on the surface tension. The measurements from this study made under the argon atmosphere are compared to published data for the surface tension of pure magnesium from [34, 64] in Fig. 9.11.

It appears that the AZ91D alloy has a surface tension superior to pure magnesium in the range of temperature measured. The surface tension of the alloy was also measured under an atmosphere of dry air premixed with 2% volume SF6 for comparison as shown in Fig. 9.12.

The change of atmosphere from argon to protective gas mixture with SF6 clearly had the effect of reducing the surface tension of AZ91D alloy by 10% approximately.

These results show the potential of the DC method in investigating the effect of atmosphere on the thermophysical properties of a metallic liquid. Overall, the discharge crucible method has been successfully applied to obtain the thermophysical properties of many metals and their alloys at different temperatures. These results have been validated by comparison to measurements reported in the

literature and to various theoretical models proposed to predict these properties [19–30]. As with many metallurgical processes, special care should be given to monitoring the oxygen content, the temperature, and the reactivity of the materials as they are factors impacting greatly the accuracy of the method. Moreover, issues such as the wetting of the liquid at the exit of the orifice or statistical divergence of the nonlinear regression process are arising due to the nature of the technique and still need to be understood to extend the applicability of the DC method to a wider range of metallic liquids [23].

References

1. A.J. Yule, J.J. Dunkley, *Atomization of Melts: For Powder Production and Spray Deposition* (Oxford University Press, Oxford, 1994)
2. J.J. Wessing, J. Brillo, Density, molar volume, and surface tension of liquid Al-Ti. Metall. Mater. Trans. A **48**(2), 868–882 (2017)
3. M. Schick, J. Brillo, I. Egry, B. Hallstedt, Viscosity of Al–Cu liquid alloys: Measurement and thermodynamic description. J. Mater. Sci. **47**(23), 8145–8152 (2012). https://doi.org/10.1007/s10853-012-6710-x
4. A.F. Crawley, D.R. Kiff, The density and viscosity of liquid antimony. Metall. Mater. Trans. B Process Metall. Mater. Process. Sci. **3**(1), 157–159 (1972)
5. Y. Sato, T. Nishizuka, K. Hara, T. Yamamura, Y. Waseda, Density measurement of molten silicon by a pycnometric method. Int. J. Thermophys. **21**(6), 1463–1471 (2000)
6. J. Cheng, J. Gröbner, N. Hort, K.U. Kainer, R. Schmid-Fetzer, Measurement and calculation of the viscosity of metals – A review of the current status and developing trends. Meas. Sci. Technol. **25**(6), 062001 (2014)
7. R.F. Brooks, A.T. Dinsdale, P.N. Quested, The measurement of viscosity of alloys – A review of methods, data and models. Meas. Sci. Technol. **16**(2), 354 (2005)
8. T. Iida, R.I. Guthrie, *The Physical Properties of Liquid Metals* (Clarendon Press, Oxford, 1988)
9. T. Iida, R.I. Guthrie, *The Thermophysical Properties of Metallic Liquids: Fundamentals* (Oxford University Press, Oxford, 2015)
10. Y. Matuyama, On the surface tension of molten metals and alloys. Sci. Rep. Tohoku Univ. **16**, 555–562 (1927)
11. D.N. Staicopolus, The computation of surface tension and of contact angle by the sessile-drop method. J. Colloid Sci. **17**(5), 439–447 (1962). https://doi.org/10.1016/0095-8522(62)90055-7
12. T.R. Hogness, The surface tensions and densities of liquid mercury, cadmium, zinc, lead, tin and bismuth. J. Am. Chem. Soc. **43**(7), 1621–1628 (1921)
13. T. Yoshikawa, Surface tensions of Fe–(30–40 mol%) Si–C Alloys at 1523–1723 K. Mater. Trans. **54**(10), 1968–1974 (2013)
14. B.J. Keene, Review of data for the surface tension of pure metals. Int. Mater. Rev. **38**(4), 157–192 (1993)
15. R.W. Hyers, Fluid flow effects in levitated droplets. Meas. Sci. Technol. **16**(2), 394 (2005)
16. P.-F. Paradis et al., Materials properties measurements and particle beam interactions studies using electrostatic levitation. Mater. Sci. Eng. R. Rep. **76**, 1–53 (2014). https://doi.org/10.1016/j.mser.2013.12.001
17. A. Diefenbach, S. Schneider, T. Volkmann, Experiment preparation and performance for the Electromagnetic Levitator (EML) onboard the International Space Station, in *Preparation of Space Experiments*, ed. by V. Pletser, (IntechOpen, 2020)

18. H.-J. Fecht, R. Wunderlich, E. Ricci, I. Egry, S. Seetharaman, L. Battezzati, The ThermoLab project: Thermophysical property measurements in space for industrial high temperature alloys. J. Jpn. Soc. Microgravity Appl. **27**(4), 190 (2010)
19. S. J. Roach, *Determination of the Physical Properties of Melts*. MSc Thesis, University of Alberta, Edmonton, Canada (2002)
20. S.J. Roach, H. Henein, Physical properties of AZ91D measured using the draining crucible method: Effect of SF 6. Int. J. Thermophys. **33**(3), 484–494 (2012)
21. S.J. Roach, H. Henein, A dynamic approach to determining the surface tension of a fluid. Can. Metall. Q. **42**(2), 175–186 (2003)
22. S.J. Roach, H. Henein, A new method to dynamically measure the surface tension, viscosity, and density of melts. Metall. Mater. Trans. B Process Metall. Mater. Process. Sci. **36**(5), 667–676 (2005)
23. P. Flood, in *Thermophysical Properties Measurement of Liquid Al and Al-Cu by the Discharge Crucible Method* (2020)
24. T. Gancarz, W. Gąsior, H. Henein, The discharge crucible method for making measurements of the physical properties of melts: An overview. Int. J. Thermophys. **35**(9–10), 1725–1748 (2014)
25. T. Gancarz, W. Gąsior, H. Henein, Physicochemical properties of Sb, Sn, Zn, and Sb–Sn system. Int. J. Thermophys. **34**(2), 250–266 (2013)
26. T. Gancarz, Z. Moser, W. Gąsior, J. Pstruś, H. Henein, A comparison of surface tension, viscosity, and density of Sn and Sn–Ag alloys using different measurement techniques. Int. J. Thermophys. **32**(6), 1210–1233 (2011)
27. M.E. Trybula, T. Gancarz, W. Gąsior, Density, surface tension and viscosity of liquid binary Al-Zn and ternary Al-Li-Zn alloys. Fluid Phase Equilib. **421**, 39–48 (2016). https://doi.org/10.1016/j.fluid.2016.03.013
28. A. Dobosz, T. Gancarz, Density, surface tension and viscosity of Ga-Sn eutectic based alloys with Zn additions. J. Mol. Liq. **264**, 600–606 (2018)
29. T. Gancarz, W. Gasior, Density, surface tension, and viscosity of liquid Pb–Sb alloys. J. Chem. Eng. Data **63**(5), 1471–1479 (2018)
30. T. Gancarz, J. Jourdan, W. Gasior, H. Henein, Physicochemical properties of Al, Al-Mg and Al-Mg-Zn alloys. J. Mol. Liq. **249**, 470–476 (2018). https://doi.org/10.1016/j.molliq.2017.11.061
31. A. Croeze, L. Pittman, W. Reynolds, Solving nonlinear least-squares problems with the Gauss-Newton and Levenberg-Marquardt methods. *Portable Doc. Format* (2012)
32. M.K. Transtrum, B.B. Machta, J.P. Sethna, Geometry of nonlinear least squares with applications to sloppy models and optimization. Phys. Rev. E **83**(3), 036701 (2011)
33. E. Gebhardt, K. Detering, Über die eigenschaften metallischer schmelzen. Die innere reibung eutektischer aluminiumlegierungen. Z. Met. **50**(7), 379–385 (1959)
34. W.F. Gale, T.C. Totemeier, *Smithells Metals Reference Book*, 8th edn. (Amsterdam/Boston/Heidelberg/London/New York/Oxford/Paris/San Diego/San Francisco/Singapore/Sydney/Tokyo, 2004)
35. M.J. Assael et al., Reference data for the density and viscosity of liquid aluminum and liquid iron. J. Phys. Chem. Ref. Data **35**(1), 285–300 (2006)
36. K.C. Mills, Y.C. Su, Review of surface tension data for metallic elements and alloys: Part 1–Pure metals. Int. Mater. Rev. **51**(6), 329–351 (2006)
37. Y.V. Naidich, V.N. Eremenko, Large drop method for determining the surface tension and density of molten metals at high temperatures. Fiz. Met. Metalloved. **11**(6), 883–888 (1961)
38. K. Mukai, Z. Li, M. Zeze, Fiz. Khim. Poverkl. Yavlenii vys. temp. 51, 1971. Mater. Trans. **43**(7), 1724–1731 (2002)
39. S.P. Yatsenko, V.I. Kononenko, A.L. Sukhman, Experimental studies of the temperature dependence of the surface tension and density of Sn, In, Al and Ga. High Temp. **10**(1), 55–59 (1972)
40. N. Eustathopoulos, J.C. Joud, P. Desre, J.M. Hicter, The wetting of carbon by aluminium and aluminium alloys. J. Mater. Sci. **9**(8), 1233–1242 (1974)

41. G. Lang, Effect of added elements on the surface tension of high-purity Al. Aluminium **50**(11), 731–734 (1974)
42. L. Goumiri, J.C. Joud, P. Desre, J.M. Hicter, Tensions superficielles d'alliages liquides binaires présentant un caractère dimmiscibilité: Al-Pb, Al-Bi, Al-Sn et Zn-Bi. Surf. Sci. **83**(2), 471–486 (1979)
43. A. Pamies, C.G. Cordovilla, E. Louis, The measurement of surface tension of liquid aluminium by means of the maximum bubble pressure method: The effect of surface oxidation. Scr. Metall. **18**(9), 869–872 (1984)
44. E. Rothwell, Precise determination of viscosity of liquid tin, lead, bismuth, and aluminium by an absolute method. J. Inst. Met. **90**(10), 389 (1962)
45. V.Z. Kisun'ko, I. Novokhatskii, Viscosity of secondary aluminum alloys with silicon, manganese, copper and magnesium.(Translation).(Retroactive Coverage). Sov. J. Non-Ferr. Met. **24**(1), 84–85 (1983)
46. T. Sak, M. Kucharski, Density of the copper-rich Cu-Pb-Fe alloys. Arch. Metall. Mater. **60**(3A), 1685–1692 (2015)
47. J. Brillo, I. Egry, Density and excess volume of liquid copper, nickel, iron, and their binary alloys. Z. Für Met. **95** (2004)
48. J.V. Butler, //Proc R Soc. 1932. V A135 **135**, 348 (1932)
49. C. Garcia-Cordovilla, E. Louis, A. Pamies, The surface tension of liquid pure aluminium and aluminium-magnesium alloy. J. Mater. Sci. **21**(8), 2787–2792 (1986)
50. W. Nozdryov, W. Smremouso, W. Tekuche, Russ. J. Phys. Chem. **53**, 1199–1202 (1979)
51. F. Lihl, E. Nachtigall, A. Schwaiger, Viscosity measurements on binary alloys of aluminium with silicon, zinc, copper, and magnesium. Z. Met. **59**(3), 213–219 (1968)
52. T. Sato, S. Munakata, Studies on the viscosity of molten metals and alloys.(III): The density of molten Sb-Sn and Sb-Pb alloys and the viscosity coefficients of molten Sb-Sn, Sb-Pb and Al-Cu alloys. Bull. Res. Inst. Miner. Dress. Metall. **11**(2), 183 (1956)
53. Y. Wang, Y. Wu, X. Bian, Composition dependence of viscosity for Al (1- x) Mg x (0≤ x≤ 0.10) alloys. Chin. Sci. Bull. **52**(11), 1441–1445 (2007)
54. W.R. Jones, W.L. Bartlett, The viscosity of aluminium and binary aluminium alloys. J. Inst. Met. **81** (1952)
55. L.Y. Kozlov, L.M. Romanov, N.N. Petrov, Predicting the viscosity of multicomponent metallic melts. Izv Vuzov Chernaya Met **3**, 7 (1983)
56. D. Sichen, J. Bygd'En, S. Seetharaman, A model for estimation of viscosities of complex metallic and ionic melts. Metall. Mater. Trans. B Process Metall. Mater. Process. Sci. **25**(4), 519–525 (1994)
57. S. Seetharaman, D. Sichen, Estimation of the viscosities of binary metallic melts using Gibbs energies of mixing. Metall. Mater. Trans. B Process Metall. Mater. Process. Sci. **25**(4), 589–595 (1994)
58. G. Kaptay, A new equation to estimate the concentration dependence of the viscosity of liquid metallic alloys from the heat of mixing data, in *Proceedings of microCAD 2003 International Conference* (2003), p. 23
59. Z. Morita, T. Iida, M. Ueda, The excess viscosity of liquid binary alloys. Liq. Met. **1976**, 600–606 (1977)
60. E.A. Moelwyn-Hughes, *Physical Chemistry, vols. 1 and 2* (Pergamon Press, Oxford, 1961)
61. W. Gąsior, Z. Moser, Modelowanie lepkości stopów metali analiza porównawcza. Pol. Metal. W Latach **2010**, 47–55 (2006)
62. W. Gąsior, Viscosity modeling of binary alloys: Comparative studies. Calphad **44**, 119–128 (2014)
63. S.P. Cashion, N.J. Ricketts, P.C. Hayes, The mechanism of protection of molten magnesium by cover gas mixtures containing sulphur hexafluoride. J. Light. Met. **2**(1), 43–47 (2002)
64. B.V. Patrov, I.A. Barannik, V.A. Polous, Interfacial tension between magnesium alloys and chloride-fluoride melts. J. Appl. Chem. USSR Engl. Transl. U. S. **57**(11) (1985)

Chapter 10
An Overview of Ground-Based Electrostatic Levitation

Michael P. SanSoucie

Electrostatic levitation (ESL) is a containerless processing method that uses Coulomb forces acting on an electrically charged sample to levitate it between two electrodes [1, 2]. The first electrostatic levitator for millimeter scale samples was developed by the NASA Jet Propulsion Laboratory (JPL) in the 1980s [3].

The electrostatic field is generated by six electrodes, which are positioned in pairs along three mutually orthogonal lines. Figure 10.1 is a schematic of a typical ESL electrode assembly. This geometry provides an unobstructed view of the sample of the levitated sample from all directions in the horizontal plane of the sample. Three of the six electrodes are grounded, and the other three electrodes are each connected to individual high-voltage DC-stable amplifiers.

The environment of the ESL chamber can either be high vacuum or gaseous provided that the gas can withstand the electric field. The breakdown voltage is the voltage necessary for an electric arc to form between two electrodes in a gas as a function of pressure and gap length. Arcing needs to be avoided, because it causes the sample to drop out of levitation and it can damage system hardware.

In 1842, Earnshaw [4, 5] proved that a charged body placed in an electric field cannot rest in stable equilibrium under the influence of electric forces alone.

For stable equilibrium, any small displacement of the body leads to restoring forces. Put another way, the potential $U(r)$ of the force vector $F = -\nabla U$ must have a local minimum at the equilibrium position [6].

A particle with charge q in an electric field, $E = \nabla \phi$, has the potential energy $U = q\phi$, where ϕ is the electrostatic potential.

If the particle is surrounded by a medium containing no space charge, then Maxwell's equations apply:

M. P. SanSoucie (✉)

Materials and Processes Laboratory, Metallic Materials & Processes Division (EM30), NASA Marshall Space Flight Center (MSFC), Huntsville, AL, USA
e-mail: michael.p.sansoucie@nasa.gov

Fig. 10.1 A schematic of an electrode assembly used to electrostatically levitate samples
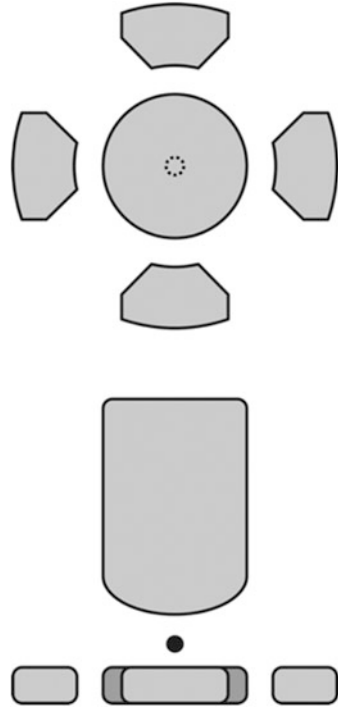
$$\nabla^2 \cdot \boldsymbol{E} = 0$$
$$\nabla \times \boldsymbol{E} = 0.$$

From these it can be shown that

$$\nabla^2 \phi = 0$$
$$\nabla^2 \boldsymbol{E}^2 \geqq 0$$

Because $\varepsilon \geqq \varepsilon_0$ (negative polarizabilities are never observed), it can be concluded that charged bodies exhibit the following:

$$\nabla^2 U \equiv U_{xx} + U_{yy} + U_{zz} = 0$$

and dielectric bodies exhibit the following:

$$\nabla^2 U \leqq 0$$
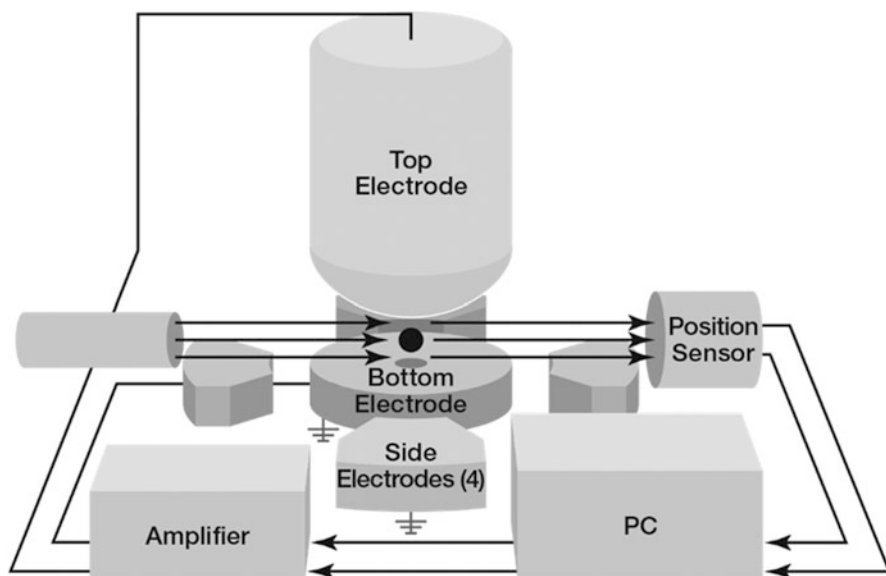
Fig. 10.2 Schematic of an electrostatic levitation control feedback loop

Therefore, at least one of the three curvatures (U_{xx}, U_{yy}, or U_{zz}) must be negative, and U cannot have an isolated minimum, which means that stable levitation by an electrostatic field in vacuum or air is not possible [6].

Since an electrostatic field does not have a three-dimensional potential minimum, an active control system is required to keep the specimen stationary. To maintain a user-entered set point, the specimen position is measured using two dual-axis position-sensitive detectors (PSDs) along with two collimated light sources, e.g., LED lights or laser beams. Each light source passes through the chamber, crosses at the center (sample position), and illuminates the PSDs. The sample casts a shadow on each PSD, which outputs the three-dimensional position of the sample. Control signals for the three axes are produced using a digital-to-analog converter card. Each control signal is connected to a high-voltage DC amplifier. Figure 10.2 is a schematic of the levitation control feedback loop just described.

Nearly all types of materials (metals, semiconductors, glasses, ceramics, aqueous solutions, and colloids) can be levitated by ESL, and samples are typically one to several millimeters in diameter. An advantage of ESL is that the sample positioning and heating are fully decoupled. Sample heating is achieved by a laser, and the sample temperature can be varied over a large range, from superheated to undercooled. A photo of a levitated sample during heating can be seen in Fig. 10.3.

Electrostatic levitation requires that the sample has and maintains an electrical charge. For metallic systems the sample is typically positively charged, and the top electrode is held at a negative potential. However, the sample rarely maintains its initial charge during experimentation. It often loses positive charge during heating, which necessitates recharging. A common technique for replenishing charge

Fig. 10.3 An
electrostatically levitated
sample during heating.
(Photo courtesy of NASA)
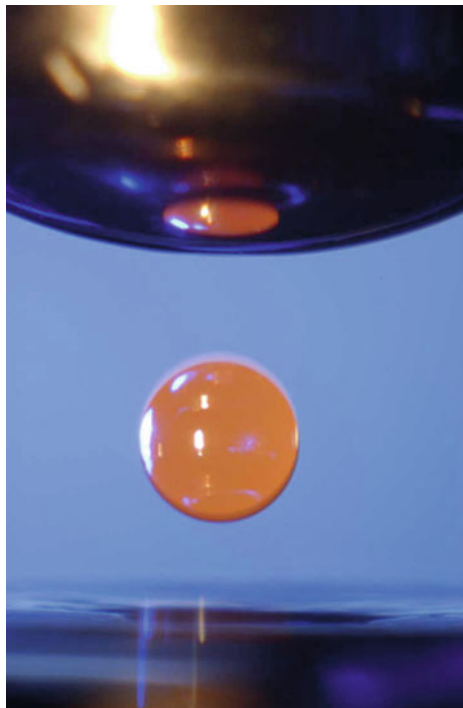
involves irradiating the sample with ultraviolet light, which causes it to eject electrons and become positively charged. The rate of charge loss tends to increase with increasing heating rate; therefore, the maximum heating rate is limited by the rate at which charge can be replenished.

Electrostatic levitation is a useful technique for the measurements of thermophysical properties, phase diagrams, and rates of nucleation and solidification, as well as the structure of undercooled liquids [7].

Surface tension is an important property for heat and mass transfer modeling of several industrial processes, including casting [8, 9], welding of metals [10], and additive manufacturing [11]. An isolated liquid drop that is free from external force will take on a spherical shape due to uniform surface tension [12]. If the drop undergoes a small amplitude axisymmetric oscillation, the surface tension of the drop determines the frequency of the oscillations according to Rayleigh's equation [13]:

$$\omega_\ell^2 = \frac{\ell(\ell-1)(\ell+2)\gamma}{\rho R_0^3}$$

where ω_ℓ is the angular frequency of oscillation mode *l*, for a droplet of surface tension γ, density ρ, and radius R_0. The viscosity μ of the droplet determines the damping time τ_ℓ of the oscillations, as determined by Lamb [14]:

$$\tau_\ell = \frac{\rho R_0^2}{(\ell - 1)(2\ell + 1)\mu}$$

Since the droplet is highly energized while levitated in an ESL, an additional term must be added to Rayleigh's equation to account for repulsion of the surface charges. For the mode $\ell = 2$, which is the fundamental mode for surface oscillations, Rayleigh's equation becomes [15]

$$\omega^2 = \frac{8\gamma}{\rho R_0^3} \left(1 - \frac{Q^2}{64\pi^2 R_0^3 \gamma \varepsilon_0} \right)$$

where Q is the net charge on the droplet and ε is the permittivity of the droplet. For liquid metals, $\varepsilon = \varepsilon_0$, where ε_0 is the permittivity of free space. The surface tension can be expressed as

$$\sigma = \frac{R_0^3 \rho}{8} \left(\omega^2 + \frac{Q^2}{8\pi^2 R_0^6 \rho \varepsilon_0} \right)$$

To perform the oscillation experiments with ESL, a variable frequency modulation is applied to the levitation field. The frequency is adjusted to match the natural frequency of the droplet, ω. When the excitation is stopped, the oscillations damp out, and the damping time τ determines the viscosity according to Lamb's equation. To measure the surface tension and viscosity of a levitated sample, the droplet's oscillations are recorded by a high-speed camera, typically at 1000 frames per second (fps) or greater, and a video analysis technique is performed on the data [16].

To perform density measurements with ESL, images of the backlit sample are taken with a video camera, typically at 30 fps, and analyzed by a computer to determine the volume of the sample under assumption of axisymmetry [17]. The images of the backlit sample are acquired by a digital camera and analyzed by a computer to determine the volume of the sample under assumption of axisymmetry. By massing the sample before and after, the calculated volume can be used to determine the sample density.

Electrostatic levitation is used for studies of nucleation [18] as well as glass formation due to its ability to process undercooled samples. Kelton et al. used ESL to determine the interfacial free energies for different combinations of crystal and liquid for alloys that form quasicrystals [19]. This research provided that the degree of icosahedral order in the undercooled liquid as determined by x-ray structural studies determined the nucleation rate of the solid [20].

The surface tension of molten metals is affected by even a small amount of adsorption of surface active elements such as oxygen [21]. The effects of oxygen partial pressure, p_{0_2}, are critical because it can exist as a gas phase.

Even a small adsorption of oxygen will cause a significant decrease in surface tension of molten metals because oxygen is a strong surfactant [22]. When performing surface tension measurements, oxidation of the samples may have an
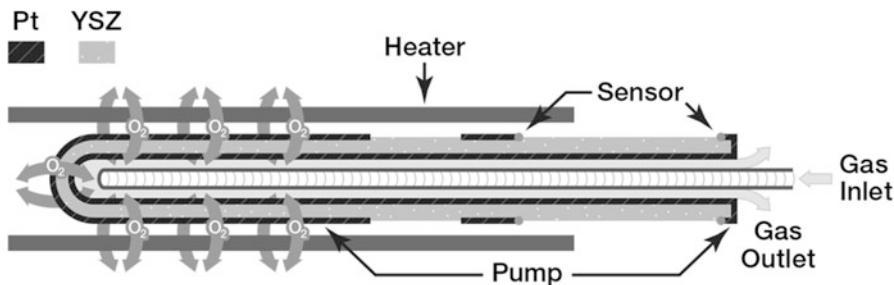
Fig. 10.4 Schematic of the oxygen ion pump and sensor

impact of 10–30% on the surface tension. It was shown that the p_{0_2} may need to be as low as 10^{-24} bar to avoid oxidation [23].

Many material processes are driven by high-temperature capillary phenomena. Examples include soldering and brazing, infiltration mechanisms in the fabrication of metal or ceramic matrix composites, and casting and solidification processes that influence the production of high-tech metals [24].

The electrostatic levitation laboratory at the National Aeronautics and Space Administration (NASA) Marshall Space Flight Center [25] has an oxygen partial pressure control system, which controls the p_{0_2} within approximately 10^9 to 10^{-28} bar. It consists of a potentiometric sensor, an oxygen ion pump, and a control unit.

The sensor and pump will be described below. The control unit consists of temperature controllers for the sensor and pump, PID-based current loop control for the ion pump, and a control algorithm.

The oxygen ion pump is based on a solid-state electrolyte, 8 mol% yttrium-stabilized zirconia (YSZ). The operating temperature of the pump must be high enough to enable the transport of O^{2-} through the electrolyte but low enough to suppress the electronic conduction as well as to maintain the long-term stability of the pump [23].

A schematic of the oxygen ion pump is shown in Fig. 10.4. The carrier gas is delivered to the pumping area, where oxygen is transferred through a solid-state electrolyte at 600 °C. The p_{0_2} is measured by an additional electrode that is on the same YSZ tube [26].

In the case of dominant ionic conductivity, the flux of oxygen is defined as

$$J_{O_2} = \frac{1}{4F}$$

where I and F are the electric current and Faraday constant, respectively. Assuming that the oxygen flow does not alter the total pressure, the p_{0_2} at the output of the pump depends on the electric current, total pressure, P_{tot}, and the initial oxygen partial pressure in the carrier gas, $p_{O_2}^0$ [23]:

$$p_{O_2} = p_{O_2}^0 + p_{\text{tot}} \left(\frac{J_{O_2}}{J_{\text{tot}}} \right)$$

The p_{0_2} is measured at the output of the pump using an additional small electrode. At the output, the electromotive force is measured and can be related to the p_{0_2} by the Nernst equation:

$$E_{\text{cell}} = \frac{RT}{4F} \ln \left(\frac{p_{O_2}}{p_{O_2}^{\text{ref}}} \right)$$

where R and T are the universal gas constant and the cell temperature, respectively. The oxygen partial pressure in the environment, $p_{O_2}^{\text{ref}}$, is assumed to be constant and equals 0.209 bar (3.03 psi). The error from considering $p_{O_2}^{\text{ref}}$ to be constant was found to be negligible [23].

The potentiometric sensor consists of a second YSZ tube at a different location in the chamber. The sensor is also operated at 600 °C. The combination of the ion pump and potentiometric sensor allows precise control of p_{O_2}.

The system described above was used to measure the effects of the oxygen partial pressure in the surrounding environment on surface tension of liquid nickel [27]. A similar system at the German Aerospace Center (DLR) was recently used to study the surface tension of liquid titanium samples under the influence of oxygen [28].

There are several electrostatic levitators throughout the World, some with very specialized capabilities.

Figure 10.5 is a photo of the NASA MSFC ESL laboratory, which has a technique for measuring creep deformation [29]. The ESL creep measurement takes advantage of the variation of stress within a rotating sphere to determine the stress dependence of the creep rate in a single test, rather than the many tests required with conventional methods.

Triggered nucleation has been successfully performed at the MSFC ESL laboratory. When a heterogeneous nucleation site is introduced to an undercooled sample, a rapid solidification occurs. This allows studies of solidification velocities and grain growth characteristics as a function of undercooling. A tungsten needle attached to a user controlled, motorized, linear translation vacuum feedthrough provides the nucleation point. This procedure has been used to study grain growth in triggered $Ni_{60}Nb_{40}$ samples [30].

The ESL system at Washington University in St. Louis is called the beamline electrostatic levitation (BESL) facility, and it was developed to perform in situ structural studies of stable and metastable solid and liquid phases over a wide temperature range under high vacuum using high-energy x-rays available from synchrotron sources [31, 32].

Dr. Kelton et al. [33] developed the Neutron Electrostatic Levitator (NESL), which takes advantage of the enhanced capabilities and increased neutron flux available at spallation neutron sources (SNSs). It currently resides at Oak Ridge
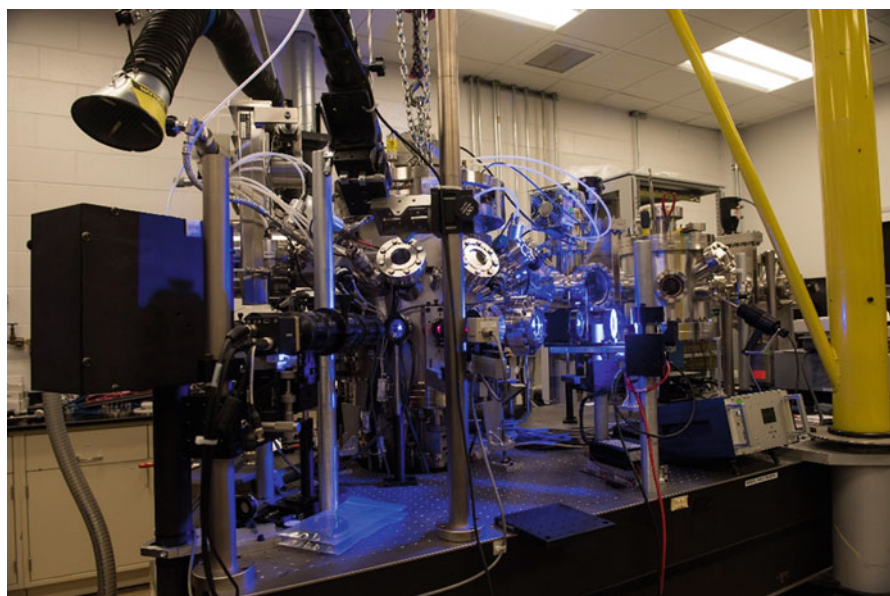
Fig. 10.5 NASA MSFC ESL lab's main levitation chamber

National Laboratory (ORNL), and it enables elastic and inelastic neutron scattering experiments on reactive metallic and other liquids in the equilibrium and supercooled temperature regime.

The Institute of Materials Physics in Space at the German Aerospace Center (DLR) in Cologne developed their electrostatic levitation facilities in the late 1990s. DLR developed a closed-loop sample position control algorithm, which controls the high voltages supplied to the electrodes on a millisecond timescale [34].

The Japan Aerospace Exploration Agency (JAXA) has done considerable investigation on oxide materials [35, 36] and even developed a hybrid electrostatic-aerodynamic levitation system for studies oxide materials [37].

The Korea Research Institute of Standards and Science (KRISS) has developed electrostatic levitation systems for the study of highly supersaturated solutions [38] and of colloidal crystallization [39].

In summary, electrostatic levitation enables thermophysical property measurements and the study of deeply undercooled melts and of high-temperature, highly reactive materials. Electrostatic levitation can be applied to both electrically insulating and electrically conducting specimens. There are several electrostatic levitation facilities throughout the World, each with unique capabilities.

However, electrostatic levitated samples have buoyancy-driven convection and sedimentation on Earth. This convective contamination negatively affects the fidelity of the property measurements done on Earth. In particular, nucleation and viscosity measurements necessitate quiescent conditions. Furthermore, it can be extremely

difficult to maintain an electrical charge on most oxide materials, which is required to maintain levitation.

These limitations necessitate levitation facilities in microgravity. For these reasons, and others, the European Space Agency (ESA) developed the International Space Station electromagnetic levitator (ISS-EML) [40], and the Japan Aerospace Exploration Agency (JAXA) developed the Electrostatic Levitation Furnace (ELF) [41]. Both of these facilities are currently in operation on the International Space Station (ISS). The ISS-EML provides an ideal platform to study conductive samples. The ELF enables the study of oxide samples, but it can also be used for metallic samples, just as with ground-based electrostatic levitation.

References

1. W.-K. Rhim, S.K. Chung, D. Barber, K.F. Man, G. Gutt, A. Rulison, R.E. Spjut, An electrostatic levitator for high-temperature containerless materials processing in 1-g. Rev. Sci. Instrum. **64**, 2961–2970 (1993). https://doi.org/10.1063/1.1144475
2. A.J. Rulison, J.L. Watkins, B. Zambrano, Electrostatic containerless processing system. Rev. Sci. Instrum. **68**(7), 2615 (1997)
3. W.K. Rhim, M. Collender, M.T. Hyson, W.T. Simms, D.D. Elleman, Development of an electrostatic positioner for space material processing. Rev. Sci. Instrum. **56**, 307–317 (1985). https://doi.org/10.1063/1.1138349
4. S. Earnshaw, On the nature of molecular forces that regulate the constitution of the luminiferous ether. Trans. Proc. Cambridge Philos. Soc. **7**, 97–112 (1842)
5. J.A. Cross, *Electrostatics: Principles, Problems, and Applications* (Adam Hilger, Bristol, 1987)
6. E.H. Brandt, Levitation in physics. Science **243**(4889), 349–355 (1989)
7. R.W. Hyers, J.R. Rogers, A review of electrostatic levitation for materials research. High Temp. Mater. Process. **27**(6), 461–474 (2008)
8. H.J. Fecht et al., Measurement of thermophysical properties of metallic melts for high quality castings, in *Space Technology and Applications International Forum*, ed. by M. S. El-Genk, (American Institute of Physics, Albuquerque, 2001)
9. D.M. Matson, R.W. Hyers, T. Volkmann, H.-J. Fecht, Phase selection in the mushy-zone: LODESTARS and ELFSTONE projects. J. Phys. Conf. Ser. **327**, 012009 (2011). https://doi.org/10.1088/1742-6596/327/1/012009
10. T. DebRoy, S.A. David, Physical processes in fusion welding. Rev. Mod. Phys. **67**(1), 85–112 (1995)
11. M. Mani et al., Measurement science needs for real-time control of additive manufacturing powder bed fusion processes. NIST Pubs., 1–17 (2015). https://doi.org/10.6028/NIST.IR.8036
12. W.-K. Rhim et al., Noncontact technique for measuring surface tension and viscosity of molten materials using high temperature electrostatic levitation. Rev. Sci. Instrum. **70**(6), 2796 (1999)
13. L. Rayleigh, On the capillary phenomena of jets. Proc. R. Soc. Lond. **29**, 71–97 (1879)
14. H. Lamb, On the oscillations of a viscous spheroid. Proc. Lond. Math. Soc. **13**(1), 51–66 (1881)
15. P.-F. Paradis, T. Ishikawa, N. Koike, Non-contact measurements of the surface tension and viscosity of molybdenum using an electrostatic levitation furnace. Int. J. Refract. Met. Hard Mater. **25**, 95–100 (2007)

16. R.W. Hyers et al., Surface tension and viscosity of quasicrystal-forming Ti–Zr–Ni alloys. Int. J. Thermophys. **25**(4), 1155–1162 (July 2004)
17. R.C. Bradshaw et al., Machine vision for high-precision volume measurement applied to levitated containerless material processing. Rev. Sci. Instrum. **76**(12), 5108–125108 (2005)
18. P.-F. Paradis et al., Materials properties measurements and particle beam interactions studies using electrostatic levitation. Mater. Sci. Eng. R **76**, 1–53 (2014)
19. K.F. Kelton et al., Studies of nucleation, growth, specific heat, and viscosity of undercooled melts of quasicrystals and polytetrahedral-phase-forming alloys, in *Proceedings of the NASA Microgravity Materials Science Conference 2000, Huntsville, AL, NASA/CP-2001-210827*, ed. by N. Ramachandran, N. Bennett, D. McCauley, K. Murphy, S. Poindexter, vol. 2, (2001), pp. 353–358
20. G.W. Lee et al., Local structure of equilibrium and supercooled Ti-Zr-Ni liquids. Phys. Rev. B Condens. Matter Mater. Phys. **77**, 184102 (2008)
21. S. Ozawa et al., Influence of oxygen partial pressure on surface tension and its temperature coefficient of molten iron. J. Appl. Phys. **109**, 014902 (2011)
22. S. Ozawa, Relationship of surface tension, oxygen partial pressure, and temperature for molten iron. Jpn. J. Appl. Phys. **50**(11), 11RD05 (2011)
23. M. Schulz et al., Oxygen partial pressure control for microgravity experiments. Solid State Ionics **225**, 332–336 (2012)
24. E. Arato et al., Surface oxidability of pure liquid metal and alloys. Appl. Surf. Sci. **258**, 2686–2690 (2012)
25. J.R. Rogers, M.P. SanSoucie, Containerless processing studies in the MSFC electrostatic levitator, in *50th AIAA Aerospace Sciences Meeting Including the New Horizons Forum and Aerospace Exposition 2012: Nashville, TN*, (2012)
26. M. Schulz, H. Fritze, C. Stenzel, Measurement and control of oxygen partial pressure at elevated temperatures, in *The 14th International Meeting on Chemical Sensors 2012: Nuremberg, Germany*, (2012)
27. M.P. SanSoucie et al., Effects of environmental oxygen content and dissolved oxygen on the surface tension and viscosity of liquid nickel. Int. J. Thermophys. **37**, 76 (2016)
28. J. Brillo, J. Wessing, H. Kobatake, H. Fukuyama, Surface tension of liquid Ti with adsorbed oxygen and its prediction. J. Mol. Liq. **290**, 111226 (2019)
29. J. Lee et al., Non-contact measurement of creep resistance of ultra-high-temperature materials. Mater. Sci. Eng. A **463**, 185–196 (2007)
30. T.J. Rathz et al., Triggered nucleation in Ni60Ni40 using an electrostatic levitator. J. Mater. Sci. Lett. **20**, 301–303 (2002)
31. A.K. Gangopadhyay, G.W. Lee, K.F. Kelton, J.R. Rogers, A.I. Goldman, D.S. Robinson, T.J. Rathz, R.W. Hyers, Beamline electrostatic levitator for in situ high energy x-ray diffraction studies of levitated solids and liquids. Rev. Sci. Instrum. **76**, 073901 (2005)
32. N.A. Mauro, K.F. Kelton, A highly modular beamline electrostatic levitation facility, optimized for in situ high-energy x-ray scattering studies of equilibrium and supercooled liquids. Rev. Sci. Instrum. **82**, 035114 (2011)
33. N.A. Mauro et al., Electrostatic levitation facility optimized for neutron diffraction studies of high temperature liquids at a spallation neutron source. Rev. Sci. Instrum. **87**, 013904 (2016)
34. T. Meister, H. Werner, G. Lohoefer, D.M. Herlach, H. Unbehauen, Gain-scheduled control of an electrostatic levitator. Control. Eng. Pract. **11**, 2 (2003). https://doi.org/10.1016/S0967-0661(02)00102-8
35. P.-F. Paradis, J. Yu, T. Ishikawa, T. Aoyama, S. Yoda, R. Weber, Contactless density measurement of superheated and undercooled liquid Y3Al5O12. J. Cryst. Growth **249**(3–4), 523–530 (2003). https://doi.org/10.1016/S0022-0248(02)02321-7
36. M.V. Kumar et al., Density measurement of glass and liquid CaAl2O4 using a pressurized electrostatic levitator. Meas. Sci. Technol. **25**, 085301 (2014)

37. P.-F. Paradis, T. Ishikawa, J. Yu, S. Yoda, Hybrid electrostatic–aerodynamic levitation furnace for the high-temperature processing of oxide materials on the ground. Rev. Sci. Instrum. **72**, 2811–2815 (2001)
38. S. Lee et al., Solution electrostatic levitator for measuring surface properties and bulk structures of an extremely supersaturated solution drop above metastable zone width limit. Rev. Sci. Instrum. **88**, 055101 (2017)
39. H. Hwang et al., Real-time monitoring of colloidal crystallization in electrostatically-levitated drops. Small **16**, 1907478 (2020). https://doi.org/10.1002/smll.201907478
40. I. Egry, A. Diefenbach, W. Dreier, J. Piller, Containerless processing in space – Thermophysical property measurements using electromagnetic levitation. Int. J. Thermophys. **22**, 2 (2001). https://doi.org/10.1023/A:1010753805462
41. T. Ishikawa, J.T. Okada, P.-F. Paradis, V.K. Marahalli, Towards microgravity experiments using the Electrostatic Levitation Furnace (ELF) in the International Space Station (ISS). Trans. Jpn. Soc. Aeronaut. Space. Sci. **12**, ISTS29 (2014). https://doi.org/10.2322/tastj.12.Th_15

Chapter 11
Levitation Research in Japan

**Masahito Watanabe, Shumpei Ozawa, Hiroyuki Fukuyama,
Takao Tsukada, and Taketoshi Hibiya**

1 Introduction

In this chapter, research activities of the Japanese team in the THERMOLAB-project are presented. The Japanese team has mainly performed thermophysical property measurements using an electromagnetic levitator (EML) on the ground to obtain reference data for materials science laboratory (MSL–EML) experiments in the International Space Station (ISS). Our typical experiments use static magnetic fields applied to EML, surface tension measurements by EML under controlled oxygen partial pressure, and viscosity measurements using the aerodynamic levitation (ADL) technique. The application of static fields on EML was developed by Fukuyama's group, surface tension measurements by EML under oxygen partial pressure (P_{O_2}) controlled conditions were mainly performed by Ozawa and Hibiya's group, and viscosity measurements by ADL were performed by Watanabe's group. In Sect. 2, we discuss the history of our research of thermophysical property measurements using the EML technique, including our motivation for joining the

M. Watanabe (✉)
Department of Physics, Gakushuin University, Toshima, Tokyo, Japan
e-mail: Masahito.Watanabe@gakushuin.ac.jp

S. Ozawa
Department of Advanced Materials Science and Engineering, Chiba Institute of Technology, Narashino, Chiba, Japan

H. Fukuyama
Institute of Multidisciplinary Research for Advanced Materials (IMRAM), Tohoku University, Sendai, Japan

T. Tsukada
Department of Chemical Engineering, Tohoku University, Sendai, Japan

T. Hibiya
Graduate School of System Design and Management, Keio University, Kanagawa, Japan

MSL–EML experiments. This history includes the reasons why we performed thermophysical property measurements on high-temperature liquids using EML. Next, our improvements in the measurement technique of thermophysical properties of high-temperature liquids by EML are described, and important results using these improvements are shown. The measured results include temperature dependence of surface tension of liquid Si under various Po_2 conditions and precise density measurements of molten alloys using static magnetic field applied to EML. Using static magnetic field applied to EML, emissivity and thermal conductivity of molten alloys were also measured. Viscosity at very high-temperature regions, compared with previous reported measurements, was obtained using the ADL technique.

2 Japanese Team History of Thermophysical Property Measurements of High-Temperature Liquids by EML

Our team began investigations into levitation for the measurement of thermophysical properties of high-temperature liquids in the 1980s. Initially, we focused on studies of thermophysical properties of liquid Si in order to understand melt flow of liquid Si during large-diameter Si crystal pulling. The purpose of this work was to help the Japanese semiconductor industry prosper. In 1984, the National Space Development Agency of Japan (NASDA) announced 34 space experiment subjects to be flown aboard a space shuttle operated by NASA, 22 and 12 of which were materials science and life science subjects, respectively. In 1986, the Ministry of International Trade and Industry of Japan established the Space Technology Corporation so that industries could join space experiments through the German Spacelab mission D2. Hibiya of NEC Fundamental Research Laboratories was assigned to be a manager of the third laboratory and proposed measurement of thermophysical properties of molten semiconductors, i.e., measurement of the thermal conductivity of the molten compound semiconductor InSb using a transient hot-wire method aboard the German sounding rocket TEXUS. In December 1988, Hibiya was invited to a review meeting organized by Walter of the ESA at DLR. At the same time, a scientist meeting was held at DLR for the preparation of electromagnetic levitation (EML) experiments using the TEMPUS facility on board the Spacelab IML-2 mission. The measurement of thermophysical properties of molten metallic materials using a containerless levitation technique was supposed to be done on this mission. Hibiya was encouraged to join this meeting of scientists and observed the breadboard model of the TEMPUS and learned a lot through detailed explanation by Egry. It has been noted that thermal conductivity of molten metallic melts cannot be directly measured by EML but can be estimated through measured electrical conductivity. Since we did not find appropriate container materials for handling molten semiconductors with high melting temperature and high reactivity, a containerless process was attractive for measuring thermophysical properties of molten semiconductors. In particular, surface tension measurements, which are easily affected by contamination from the

crucible material, were of interest. Fortunately, molten semiconductors show high electrical conductivity, which is a required condition for EML.

In 1990, NASA called for new experiment subjects to be carried out on the ISS. We proposed the "visualization of the Marangoni flow of molten silicon using an X-ray facility," which was accepted. This study was a basic research for silicon single crystal growth technology as the Marangoni flow controls the heat and mass transport process on the melt surface due to differences in surface tension. For this research, accurate values of surface tension and its temperature coefficient are required. In order to measure surface tension of molten silicon, a contamination-free condition was required. In 1994, Hibiya visited DLR and successfully measured the surface tension of molten silicon over a wide temperature range, including the undercooled condition, by a contamination-free process using an EML technique. The measurement atmosphere was 6N argon gas. B- and Sb-doped single crystal Si spheres were prepared to provide a sufficient amount of levitation power, because the resistivity of pure silicon is too high for EML. The surface tension and its temperature coefficient were determined to be 783.5×10^{-3} N/m and -0.65×10^{-3} N/m·K, respectively [1]. Egry and Hibiya discussed the possibility of EML for molten silicon under the microgravity condition. In May of 1994, this was attempted for the first time as an attachment to preparatory work of the IML-2 mission. This attempt was carried out under collaboration between DLR, MIT, NASA, and NEC and was presented in a poster session at the IXth European Symposium on Gravity-Dependence in Physical Sciences, Berlin, May 1995 [2]. Parallel to the Germany–Japan collaboration, Mukai and his group attempted to measure the oxygen partial pressure dependence of surface tension of molten silicon and its temperature coefficient using a sessile drop method. This was first published in Japanese [3] and then in English [4]. From 1900 to 1995, the Kimura Metamelt Project was involved in a basic research of silicon single crystal growth technology, including thermophysical property measurements in the molten state. Anomalous behavior of thermophysical properties of molten silicon was reported, i.e., density near the melting temperature shifted from linear behavior extrapolated from that at higher temperature. This was explained as the melt beginning to change its structure prior to solidification. However, as long as we measured density using EML, density of a melt changed linearly, including at the undercooled condition; there was no anomalous phenomenon [5]. After repeated discussions with German, Italian, and Japanese scientists, we prepared a "proposal application" in response to the international announcement of opportunities for microgravity research issued by NASA, ESA, and NASDA in 2000. The title of the project was "Investigations of thermophysical properties of liquid semiconductors in the melt and the undercooled state under microgravity conditions (SEMITHERM)" [6]. During the progress of the project, not only silicon but also the Si–Ge system was included. Investigation of the influence of oxygen partial pressure on thermophysical properties was a keyword for this project. Original members included Samwer (coordinator), Damaschke, Egry, Lohöfer, Ricci, Arato, Hibiya, Tsukada, von Ammon, and Fujiwara. The introduction and industrial relevance sections were prepared by Hibiya based on the Germany–Japan collaboration. Furthermore, papers were published and coauthored
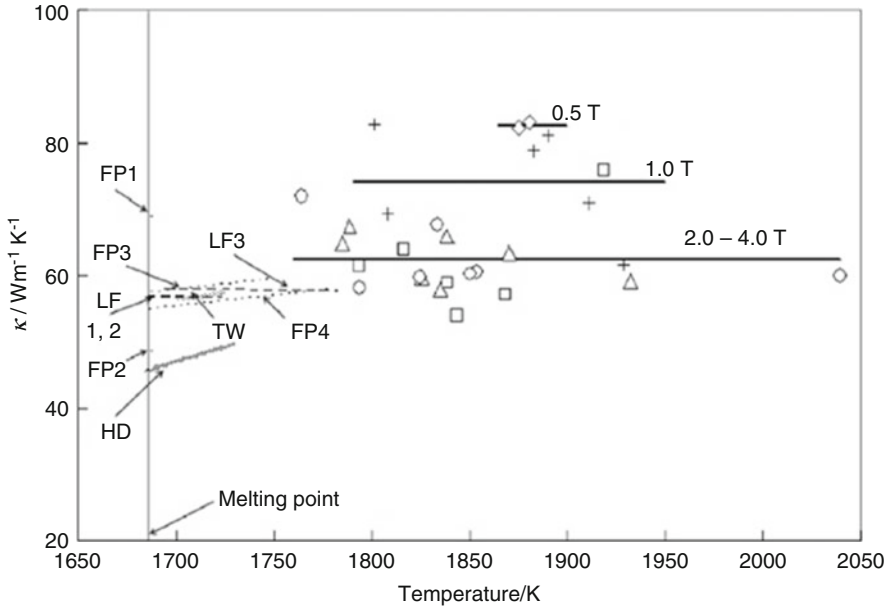
Fig. 11.1 Thermal conductivity of liquid silicon as a function of temperature in static magnetic fields of 0.5, 1.0, 2.0, 3.0, and 4.0 T. Results were obtained using several methods: the laser-flash method (LF1, LF2, and LF3), the hot disk method (HD), and the transient hot-wire method. Calculated κ assuming the Wiedemann–Franz law from electrical conductivity is given as FP1, FP2, FP3, and FP4 [10]

internationally as a result of the collaboration [7–9]. Part of this work is described in Sect. 3.

In Japan, Kobatake et al. from a group of Fukuyama and Tsukada successfully attempted the measurement of thermal conductivity of molten materials using EML, combined with a strong static magnetic field, which can suppress heat transfer to a great extent due to convection [10]. Although Fecht and Wunderlich have been engaged in research on thermal conductivity measurements of solid metallic materials [11, 12], their research was not applied to liquid materials. Thermal conductivity measurements of high-temperature melts are a successful extension of the EML technique through international collaboration. Figure 11.1 shows our first result of thermal conductivity measurements of molten silicon using a static magnetic field applied to the EML facility called Properties and Simulations Probed with Electromagnetic Containerless Technique (PROSPECT) [10]. The details of the works using PROSPECT are described in Sect. 4.

3 Surface Tension of High-Temperature Liquids Under Controlled Oxygen Partial Pressure Conditions

As described in Sect. 2, in Japan, scientists and engineers have been interested in the oxygen partial pressure (Po_2) dependence of surface tension for molten semiconductors, particularly molten silicon. Following the Ratto, Ricci, and Arato (RRA) model [13], Mukai proposed a necessary oxygen partial pressure control device equipped within a surface tension measurement system using EML [14]. From this suggestion, we developed a surface tension measurement facility under Po_2-controlled conditions using EML. Using this facility, we succeeded in measuring surface tension not only for molten silicon [15] but also for molten metals. At first, we obtained the surface tension affected by Po_2 for silver [16], iron [17], and nickel [18]. Measurements were also carried out in a controlled atmosphere under microgravity using parabolic flight [19]. Even in present day, although several scientists showed interest in the surface tension of molten silicon and tried to measure using a modern technique, scattered author-dependent data still remain. As long as the RAA model is employed, the temperature dependence of equilibrium constants for SiO and SiO$_2$ formation must be considered. However, this was ignored in previous work [15]. In the latest measurement, the temperature dependence of the equilibrium constants was considered [20].

3.1 *Po$_2$-Controlled Atmospheric Gas*

The surface tension measurement facilities under Po_2-controlled conditions using EML are based on a technique combining oxygen pump controlled atmospheric gas Po_2 with a gas transport system with thermal equilibrium conditions of the gas mixture. The oxygen pump and sensors made of yttria-stabilized zirconia are based on the Nernst equation; oxygen ions can be moved from the inside of the tube to the outside through the tube wall when a difference in electrical potentials is given between the tube walls. To measure the surface tension under a Po_2-controlled atmosphere, we confirmed Po_2 in atmospheric gas by the following processes. The oxygen pump and sensors were experimentally verified from the oxidation–reduction reaction of solid metals of copper, nickel, and iron. High-purity copper, nickel, and iron samples were heated up to 600 °C under nitrogen gas flow using a gold image furnace. The Po_2 of the gas was fixed above and below the equilibrium Po_2 for the reactions for formation of metal oxide (Cu$_2$O, NiO, and FeO) by the oxygen pump and sensors. The equilibrium oxygen partial pressure for formation of the metal oxide was theoretically calculated from its Gibbs energy at a given temperature. The difference between the set Po_2 and equilibrium oxygen partial pressure for formation of the metal oxide was carefully controlled within one order of magnitude by the oxygen pump and sensors. After heating the sample for several days, oxidation and reduction of the sample were evaluated by surface observation. As a

result, the P_{O_2} value indicated by the oxygen sensor corresponded well to the oxidation and reduction of the metallic samples. From these processes, it was confirmed that our oxygen sensors can detect the precise oxygen partial pressure of atmospheric gas within at least one order of magnitude of the true value. Moreover, on ground, gas convection is generated around the levitated liquid metal droplets. The gas convection would affect oxygen transport from gas to the liquid metal surface. If gas convection affects oxygen transport from gas to the liquid metal surface, the measured surface tension would depend on the conditions of gas convection. Therefore, we must examine the effect of gas convection around levitated droplets on surface tension measurements by comparing ground conditions to microgravity conditions. We must confirm the effect of gas convection around levitated droplets on the surface tension measurements in known P_{O_2} conditions from comparisons between ground and microgravity conditions. For these confirmation experiments, we performed EML experiments under microgravity conditions during parabolic flight. The results of the temperature dependence of surface tension in known P_{O_2} conditions under microgravity agreed well with measured data on the ground under the same P_{O_2} conditions. From these results, we confirmed that we can use the surface oscillation analysis EML droplet on ground for surface tension measurements under P_{O_2}-controlled conditions and without gas convection effects. These are important results for surface tension measurements under P_{O_2}-controlled conditions using MSL–EML in ISS in the near future.

3.2 Surface Tension Measurements Under P_{O_2}-Controlled Conditions

3.2.1 Molten Iron

Two types of Ar/He and Ar/He–5%H$_2$-mixed gases were introduced into the chamber to investigate the effect of P_{O_2} on the surface tension of molten iron [17]. Figure 11.2 shows the surface tension of molten iron measured under the flow condition of Ar/He gas and Ar/He–5%H$_2$ gas. Uncertainties for the measurement plot were calculated to $\pm2.3\%$. We successfully measured the surface tension of molten iron within a very wide temperature range of over 780 K, including the undercooling region, regardless of measurement atmosphere. The boomerang-shaped temperature dependence of surface tension was experimentally confirmed when P_{O_2} was fixed at 10^{-2} Pa under the flow condition of the Ar/He gas atmosphere. The surface tension increased, until about 2150 K, and then decreased as the sample temperature was raised. The pure surface tension of molten iron was deduced from the measurement data at a P_{O_2} of 10^{-2} Pa above 2150 K, which corresponded to the surface tension measured under Ar/He–5%H$_2$ gas above 2050 K. The temperature dependence of pure surface tension, σ^P, can be extrapolated from the negative temperature coefficient as follows:
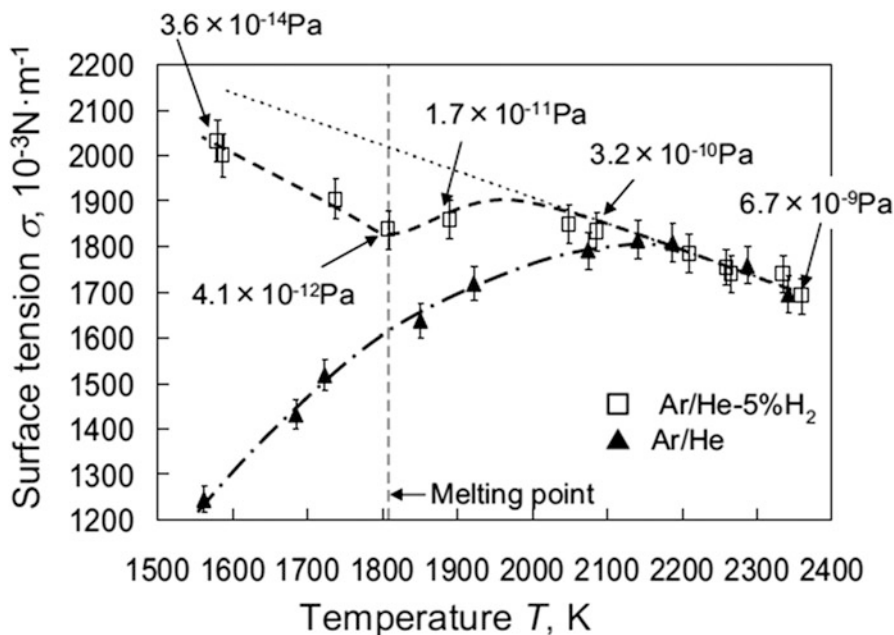
Fig. 11.2 Measurement results of surface tension for molten iron under the flow condition of mixed gases of Ar/He and Ar/He–5%H$_2$. The temperature dependence of the pure surface tension is extrapolated from the negative temperature coefficient of the surface tension measured under Ar/He gas atmosphere above 2150 K, as shown by the dotted line [17]

$$\sigma^P = 2017.6 - 0.579(T - 1808)\left[10^{-3}\text{Nm}^{-1}\right]. \tag{11.1}$$

The temperature dependence of the surface tension showed a kink at around 1850 K under the flow condition of Ar/He–5%H$_2$ gas. The surface tension decreased until 1810 K, and then it increased to approach to the pure value with increasing temperature. This anomalous temperature dependence of the surface tension was explained by competition between the temperature dependence of the P_{O_2} of H$_2$-containing gas and the oxygen adsorption equilibrium constant of the melt.

3.2.2 Molten Silver

The surface tension of molten silver was measured over a very wide temperature range of about 550 K and under a contamination-free condition from a container in consideration of the influence of oxygen adsorption from atmospheric gas [16, 21]. Figure 11.2 shows the temperature dependence of surface tension for molten silver. In Fig. 11.2, the influencer of P_{O_2} on the surface tension of molten silver is shown by oxygen activity (a_{O_2}), which is defined as the P_{O_2} of atmospheric gas relative to 1 atm (1.01235 Pa). Measurement results for 6N- and 5N-purity
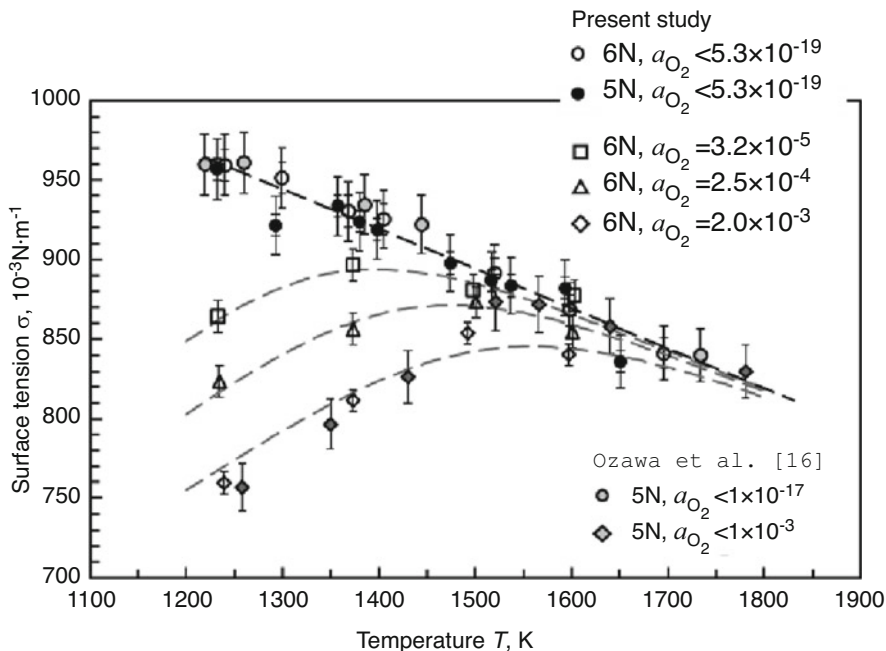
Fig. 11.3 Surface tension of molten silver measured under Ar/He mixture gas with a_{O2} values of 3.2×10^{-5}, 2.5×10^{-4}, and 2.0×10^{-3} with that measured under Ar-He–10vol.%H$_2$ gas ($a_{O2} < 5.3 \times 10^{-19}$). Also shown are the surface tension values measured under $a_{O2} < 1 \times 10^{-17}$ and $a_{O2} = 1 \times 10^{-5}$ in Refs. [16, 21]

samples [21] and the previous reported value for 5N-purity silver in ref. [16] are also shown. The boomerang-shaped temperature dependence of the surface tension is the same as that for molten iron and is explained by the temperature reliance of the equilibrium constant for the oxygen adsorption reaction; higher a_{O2} usually induces lower surface tension of molten metal owing to surface-active effects by oxygen adsorption at a comparatively low temperature. However, oxygen is desorbed from the melt surface with increasing temperature because of the decrease in the equilibrium constant of the oxygen adsorption reaction (k_{ad}). As a result, the surface tension of molten silver increases to approach to the surface tension of a pure state, free from oxygen adsorption, σ^P, at high temperature. From these results, the temperature dependence of σ^P can be described as follows:

$$\sigma^P = 961 - 0.25(T - 1234)\left[10^{-3}\text{N} \cdot \text{m}^{-1}\right]. \tag{11.2}$$

The intercept of Eq. (11.2) (961×10^{-3} N·m^{-1}) corresponds to the surface tension at the melting temperature of silver (1234 K) (Fig. 11.3).
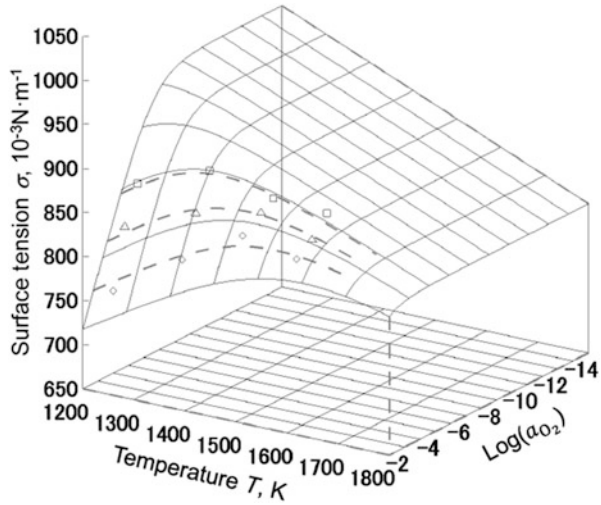
From the measured surface tension, the influence of Po_2 on surface tension of molten silver was described by the following Szyszkowski model [22] using oxygen activity (a_{O2}):

$$\sigma = \sigma^P - RT\Gamma_O^{\text{sat}}\ln(1 + k_{\text{ad}}\sqrt{a_{O_2}}), \tag{11.3}$$

where σ^{p} is the temperature dependence of the pure state value of surface tension, R is the gas constant, T is the temperature, Γ_O^{sat} is the excess amount of oxygen adsorption, and Γ_{ad} is the equilibrium constant for the oxygen adsorption reaction at the melt surface. The excess amount of oxygen adsorption at the surface of molten silver can be evaluated to be $\Gamma_O^{\text{sat}} = 4.71 \times 10^{-6}$ mol·m^{-2} for $a_{O2} > 10^{-5}$ from the surface tension plotted as a function of a_{O2} and by the slope of the fitting line using the Gibbs adsorption isotherm. Having deduced σ^p, Γ_O^{sat}, and $\ln k_{\text{ad}} = 27230T^{-1} - 14.742$ for molten silver, as thermodynamically mentioned, the surface tension of molten silver can be described as functions of temperature and oxygen activity using the following Szyszkowski model equation:

$$\sigma = 961 - 0.25(T - 1234) - 4.71$$
$$\times 10^{-6}RT \ln\left[1 + \exp\left(\frac{25203}{T} - 13.35\right)\sqrt{a_{O_2}}\right]\left[10^{-3}\text{Nm}^{-1}\right]. \tag{11.4}$$

The relationship between the surface tension, temperature, and oxygen activity for molten silver is depicted as a 3D graph using Eq. (11.4), as shown in Fig. 11.4, in which the boomerang-shaped temperature dependence of surface tension is prominently represented.

3.2.3 Molten Silicon

Surface tension of molten silicon was re-measured in an atmosphere with controlled Po_2. The Po_2 was measured at both the inlet and outlet positions using oxygen sensors so that the control method of oxygen partial pressure in the vicinity of the melt surface (effective Po_2) based on the RRA model could be validated [13]. The RAA model, based on a combination of thermodynamics and kinetics, was successfully applied to measure the surface tension of molten silicon. For the molten silicon case, the surface is easily oxidized; the equilibrium oxygen partial pressure for SiO_2 formation is 1.62×10^{-14} Pa. However, volatile oxide SiO is also formed as a result of simultaneous reaction; adsorbed oxygen can be removed from the surface. Therefore, a pure silicon surface appears even under a condition with high oxygen partial pressure, i.e., the equilibrium oxygen partial pressure for SiO formation of 1.98×10^3 Pa. In our studies, Po_2 was calculated using the inlet flow condition. From our recent measurements, the pure state value of surface tension for molten silicon, free of any oxygen adsorption, was $\sigma^P = 753 \times 10^{-3}$ N·m^{-1} at the melting temperature. This value was rather low compared with those measured previously under various oxygen partial pressures using a sessile drop method and a levitation technique [2, 3]. From the oxygen partial pressure dependence of surface tension, the saturation oxygen adsorption, Γ_O^{sat}, was calculated. According to the Szyszkowski model [22] in Eq. (11.4), the equilibrium constant for oxygen adsorption, k_{ad}, was obtained as a function of temperature; furthermore, an equilibrium constant of enthalpy change for adsorption was calculated using the van 't Hoff equation. From these calculations, the surface tension of molten silicon was described as functions of temperature, T, and a_{O2}, as was done for molten silver. From the results of the Szyszkowski model for surface tension, we illustrate the molten silicon surface tension T and a_{O2} dependence in Fig. 11.5 [20].

Fig. 11.5 Relationship between surface tension, temperature, and a_{O2} for molten silicon from experimental results using the Szyszkowski model [20]
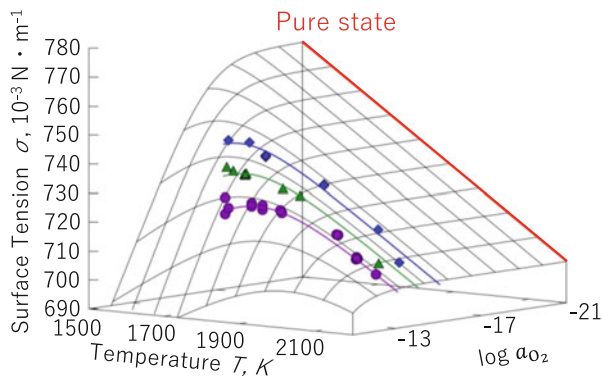
4   Development of Static Magnetic Field Applied to EML Facilities for Precise Density and Thermal Conductivity Measurements

In Sect. 2, abnormal behavior of molten silicon density at the melting temperature and observed using the Archimedean method in 1991 was disputed by EML measurements by extrapolating from the melting temperature to undercooled liquid states [2]. From our measurements, molten silicon density behavior in the undercooled state has been of interest in materials science. Angel suggested that molten silicon has maximum density in the undercooled state from molecular dynamic simulations [23]. We attempted to more precisely measure the density of molten silicon in the undercooled state for predictions [12]. For this purpose, we needed to suppress drop oscillations because they are the origin of increasing droplet volume deviation. To suppress drop oscillation, we apply a static magnetic field into the EML droplet, as reported by Yasuda's group in 1998 [24]. Moreover, by using a static magnetic field, the melt flow in an EML droplet is reduced by the Lorentz force. Using this technique, we can measure the thermal conductivity of high-temperature liquids without a container, without contact, and on the ground as proposed by Fecht and Wunderlich [11, 12]. In the following section, we describe our facilities for static magnetic field applied to EML named PROSPECT [25].

4.1   PROSPECT

On ground, we need a strong electromagnetic force to levitate liquid metal samples. In these conditions, a liquid metal drop has surface oscillations with large amplitude, and the droplet shape is largely deformed in the axisymmetric direction. If the droplet shape deforms in the axisymmetric direction, it is difficult to precisely obtain the volume of the sample droplet. For this reason, we tried to reduce drop shape deformation using the Lorentz force from the outer product of the electrical current density in the molten metal drop and the static magnetic field. First, Yasuda's group succeeded in applying a static magnetic field to an EML droplet and reduced both surface oscillations and asymmetrical drop shape modification [24]. Furthermore, the Lorentz force also acts to suppress melt flow in the molten metal drop, which is generated by the electromagnetic force from RF current in the levitation coils. The suppression of melt flow is intrinsically effective for measurements of the thermal conductivity of liquid. On the basis of these ideas, we developed facilities that focused on thermophysical property measurements of high-temperature liquid using static magnetic field applied to EML and named them PROSPECT [10, 25], as shown in Fig. 11.6 [26]. PROSPECT has an EML system that includes measurement and observation equipment with a superconducting magnet with a maximum magnetic field of 10 T. Moreover, PROSPECT has a semiconductor-laser heating system for modulation calorimetry for heat capacity and thermal conductivity
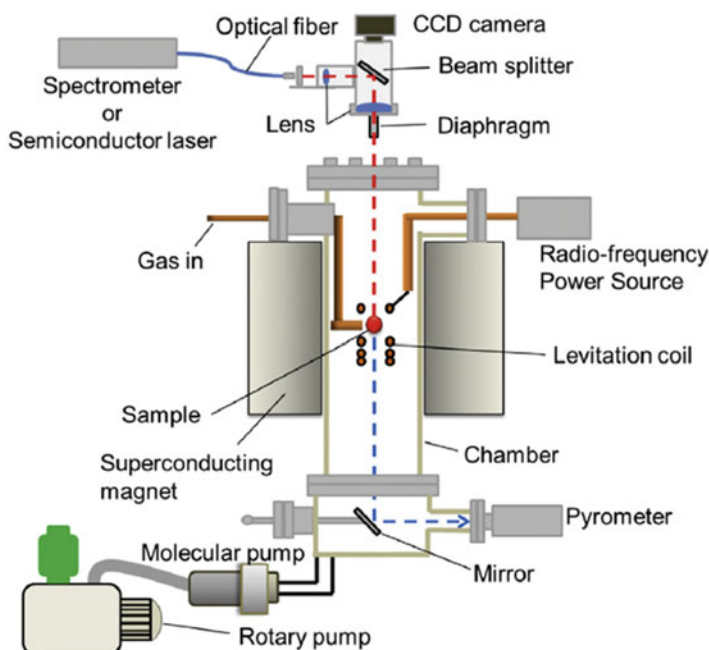
Fig. 11.6 Schematic diagram of PROSPECT [26]

measurements. Using PROSPECT, we precisely obtained the density, thermal conductivity, emissivity, and heat capacity of high-temperature molten metals by the suppression of both melt flow and surface oscillation using the Lorentz force from static magnetic fields. We first succeeded in measuring the density [27], hemispherical normal spectral emissivity [28], heat capacity, and thermal conductivity [7, 26] of molten silicon using PROSPECT. For molten silicon, we showed the sign of the density maximum in an undercooled state from direct density measurements using PROSPECT. The density maximum of molten Si is still a relevant subject in materials science. In the following section, our measurements of the thermophysical properties of molten alloys related to MSL–EML experiments are described. We focused on the density of binary alloy systems [26, 29] and the thermal conductivity of molten metals [30, 31].

4.2 Precise Density Measurements of High-Temperature Liquid Using PROSPECT

Using PROSPECT, we obtained the density of various binary molten alloys. Here, we show the results of density measurements of the Fe–Ni system [26] as an example of the effectiveness of using a static magnetic field in EML. The densities of liquid

Fig. 11.7 Temperature dependence of the density of liquid Fe–Ni. *MP* melting point, *LT* liquidus temperature of the Fe–Ni system; error bars show combined standard uncertainty [26]
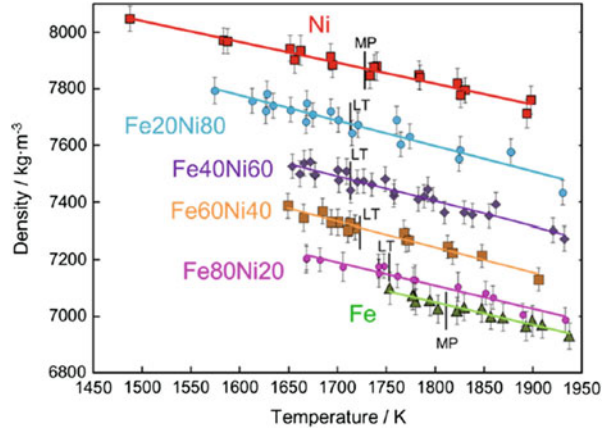
Fig. 11.8 Composition dependence of the density of liquid Fe–Ni at 1773 K; error bars show combined standard uncertainty [26]
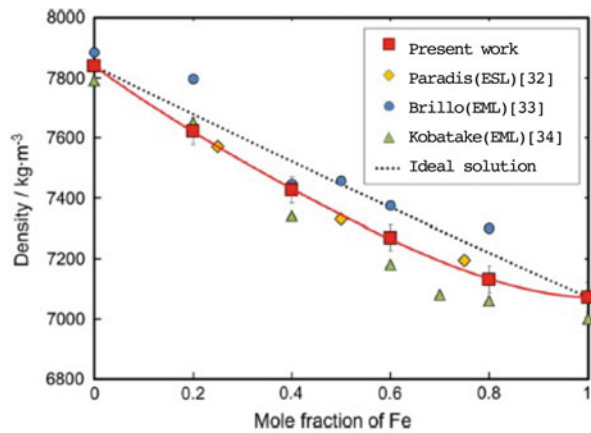
Fe–Ni alloys were measured accurately and within an expanded uncertainty, from 1.1% to 1.6%, using PROSPECT with a static magnetic field above 4 T. Densities were determined over a wide temperature range, including the supercooled region. The densities of all Fe–Ni alloys investigated vary linearly with temperature over the measurement range (Fig. 11.7). The temperature dependence of the densities of Fe–Ni melts are expressed as a linear function of temperature: $\rho = \rho_L + \kappa(T - T_L)$ where ρ_L is the density at the liquidus temperature (T_L) of the Fe–Ni system and κ is its temperature coefficient. From the density as a linear function of temperature, we were able to obtain density values at any temperature. Figure 11.8 shows the composition dependence of the density of Fe–Ni melts at 1773 K. The error bars in Figs. 11.6 and 11.7 present the combined standard uncertainty. For comparison, literature data [32, 33] are also plotted in Fig. 11.7. These data agree well with that obtained using electrostatic levitation (ESL) by Paradis [32]. Relatively large scatter exists between the two datasets obtained using the EML technique [31, 32]. This is attributed to the fact that the levitated liquid drop by ESL has no drop oscillation

without a time-dependent external force. However, the levitated liquid metal drop by EML without a static magnetic field generates drop oscillations by the EM force from the RF current in the coils. Therefore, the volume measurements of a liquid metal drop by EML without a static magnetic field include large uncertainty. From the comparisons, we confirmed the effectivity of a static magnetic field applied to EML for density measurements.

From the compositional dependence of density, excess volume from the ideal solution was obtained. The results were discussed within a thermodynamic framework using the relationship between excess volume and thermodynamic properties, such as the excess Gibbs energy and enthalpy of mixing. The excess volume is positively correlated with the excess Gibbs energy and enthalpy of mixing for various binary alloy systems [29]. Clarification of this relation by considering local liquid structures is an important subject for the future.

4.3 Thermal Conductivity Measurements of Molten Metals Using PROSPECT

The effect of applying a static magnetic field to an EML drop oscillation was explained in the previous section. The effect of a static magnetic field should suppress melt flow in an EML drop. If the melt flow is suppressed by a static magnetic field, we can measure thermal conductivity without melt flow contributions. Using PROSPECT, thermal conductivity was measured by noncontact laser modulation calorimetry [10, 25]. The top of the levitated sample was heated by a modulated laser at a power of $P_0(1 + \cos \omega t)$ with constant laser power (P_0) and angular frequency (ω). The temperature response was measured at the bottom of the sample using a pyrometer. The unsteady-state heat conduction equation for an axial symmetrical 2D spherical coordinate system (r, θ) is expressed as follows:

$$\rho C_P \frac{\partial T}{\partial t} = \kappa \left[\frac{1}{r^2} \left(r^2 \frac{\partial T}{\partial r} \right) + \frac{1}{r^2 \sin \theta} \frac{\partial}{\partial \theta} \left(\sin \theta \frac{\partial T}{\partial \theta} \right) \right] + Q(r, \theta), \qquad (11.5)$$

where, ρ is the density, C_P is the mass heat capacity at constant pressure, κ is the thermal conductivity, and $Q(r, \theta)$ is the heat generated by induction current. From solving Eq. (11.5) by applying suitable boundary conditions, the phase shift, $\Delta\phi$, from sine wave laser heating at the top of the drop to the responding sample temperature at the bottom of drop is obtained as follows:

$$\Delta\phi = \tan^{-1} \left(\frac{\Delta T_{ac}^{out}}{\Delta T_{ac}^{in}} \right), \qquad (11.6)$$

where $\Delta T_{ac}{}^{in}$ and $\Delta T_{ac}{}^{out}$ are the in-phase and out-of-phase components of the temperature amplitude, respectively. Thermal conductivity was determined by

curve fitting in Eq. (11.6) to measure the relationship between $\Delta\phi$ and ω. The modulated laser power irradiated at the top of the EML drop and the temperature response at the bottom of the EML drop was observed using a pyrometer. Example thermal conductivity measurements by modulation calorimetry are shown for molten Fe–Ni results in [30]. First, the effect of a static magnetic field on convection in the levitated sample droplet was studied. Figure 11.9 shows the static magnetic field dependence of the apparent thermal conductivity of a Fe–Ni melt with a Fe composition of 0.4 at 1750 K. The apparent thermal conductivity converged over 9 T within experimental uncertainty; thus, we considered that convection in the droplet was sufficiently suppressed by a static magnetic field greater than 9 T. On the basis of this result, the thermal conductivity of Fe–Ni melts was measured at a static magnetic field of 10 T. The effect of a static magnetic field on melt flow suppression depends on the electrical conductivity of the molten metal drop. From evaluation of convection and temperature gradient in EML droplets with a static magnetic field obtained by numerical simulation, magnetic fields of 10 and 7 T were sufficient to measure the true thermal conductivities of molten Fe and Ni, respectively. Thus, we conclude that a static magnetic field of 10 T is sufficient to obtain the true thermal conductivity of molten Fe–Ni.

From these procedures for thermal conductivity measurements with PROSPECT, the compositional dependence of thermal conductivity of molten Fe–Ne is shown in Fig. 11.9 with previously reported values. The reported values are estimated by the Wiedemann–Franz law from electrical resistivity measurements. From Fig. 11.9, the measured values of Fe–Ni alloys were larger than the values evaluated by the Wiedemann–Franz law, over the experimental uncertainty. From this result, heat propagation through atomic vibration in the Fe–Ni melts contribute to the thermal conductivity.

The examples discussed next show the results of thermal conductivity of molten transition metal elements. Using the same procedure for the thermal conductivity measurement of molten Fe–Ni, we obtained the thermal conductivity of transition
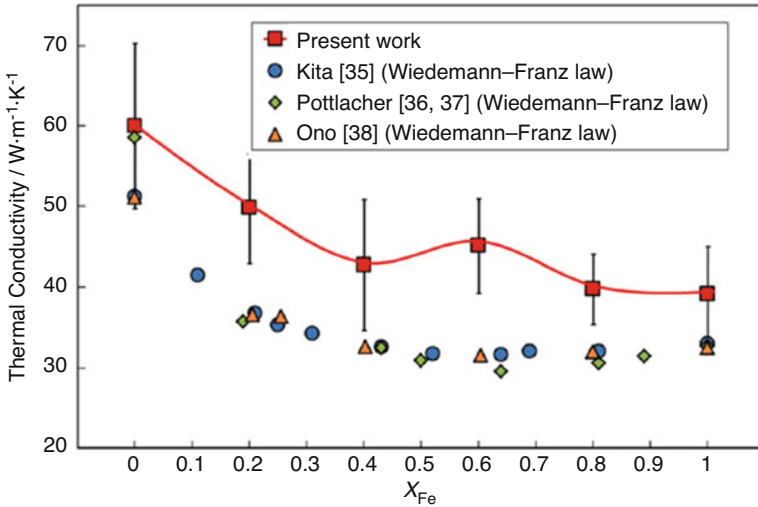
Fig. 11.10 Composition dependence of thermal conductivity of Fe–Ni melts at 1850 K [30]

metal elements Ti, Fe, Ni, and Pd [31]. The obtained thermal conductivity is discussed in regard to the electrical structure near the Fermi level [31]. On the basis of the Mott model, previous studies showed a correlation between thermal diffusivity and the reciprocal density of state at the Fermi level, $N(E_F)^{-1}$ [39]. The thermal diffusivities (α) were obtained by $\alpha = C_P \rho / \kappa$, where C_P is the heat capacity at constant pressure, ρ is the density, and κ is the thermal conductivity. These values were obtained from measurements using PROSPECT. A plot of α versus $N(E_F)^{-1}$ is shown in Fig. 11.10. From this figure, we found that α and $N(E_F)^{-1}$ have a good linear correlation, indicated by the solid line. Thus, α is proportional to $N(E_F)^{-1}$ for transition metals in a liquid state. From this result, we conclude that s-electrons carry the heat and that the mean free path of s-electrons increases with increasing $N(E_F)^{-1}$ for transition metals in liquid state, supporting the extended Mott model (Fig. 11.11).

5 Aerodynamic Levitation Technique for Measurements of Viscosity of Molten Oxides on Ground

Molten oxides are also important subjects for thermophysical property measurements. However, these materials cannot be levitated by EML because of their small electrical conductivity. We can apply ELS to levitate oxides; however, ESL cannot be applied to molten oxides because the composition of molten oxides is changed by vaporization in high-temperature regions and under high-vacuum conditions used on ground in ESL to avoid sparking of the gas atmosphere by high voltage. In contrast, the ADL technique can be applied for liquid sample levitation in a gas atmosphere

Fig. 11.11 Correlation between $N(E_F)^{-1}$ and thermal diffusivity of transition metals. Error bars show the expanded uncertainty ($k = 2$) [31]
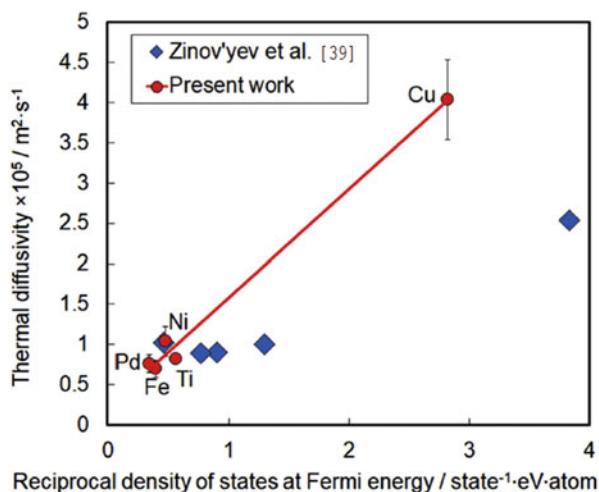
and can also generate surface oscillations when combined with an acoustical gas oscillation system. Langstaff et al. [40] of the DLR group first applied this idea in thermophysical property measurements of molten alumina. We also applied this idea to our ADL facility. We first confirmed the surface oscillation phenomenal of aerodynamically levitated droplets because thermophysical measurements require the fundamental oscillation mode of the natural surface oscillation of a droplet. An aerodynamically levitated droplet is affected by gas flow pressure, so the natural surface oscillation of an ADL droplet must be confirmed [41, 42]. Using this facility, we confirmed the fundamental oscillation mode of natural surface oscillation in an ADL droplet of molten Al_2O_3. Next, we applied this technique for viscosity measurements of molten oxides of the SiO_2–CaO–Al_2O_3 system [43].

5.1 ADL Setup and Density Measurements of Molten Oxides

ADL is fundamentally a simple method of floating samples by a gas-jet flow from conical nozzles, which achieves containerless conditions to maintain the sample position. For thermophysical property measurements, we installed a conical nozzle in a vacuum chamber with a sample changer system to maintain and control the atmospheric gas conditions [41, 42]. Our conical nozzle was separated into a nozzle surface part and a base part for supporting the nozzle surface parts. The materials for the nozzle surface part were selected to match the levitation sample to avoid reactions between samples and the nozzle surface during contact in the levitation process. Figure 11.12 shows a schematic illustration of our ADL system for the measurement of thermophysical properties of molten oxides. Spherical-shaped solid oxide samples with diameters of ~2 mm were levitated by gas-jet flow from the conical nozzle. Then, solid samples were melted under containerless conditions by
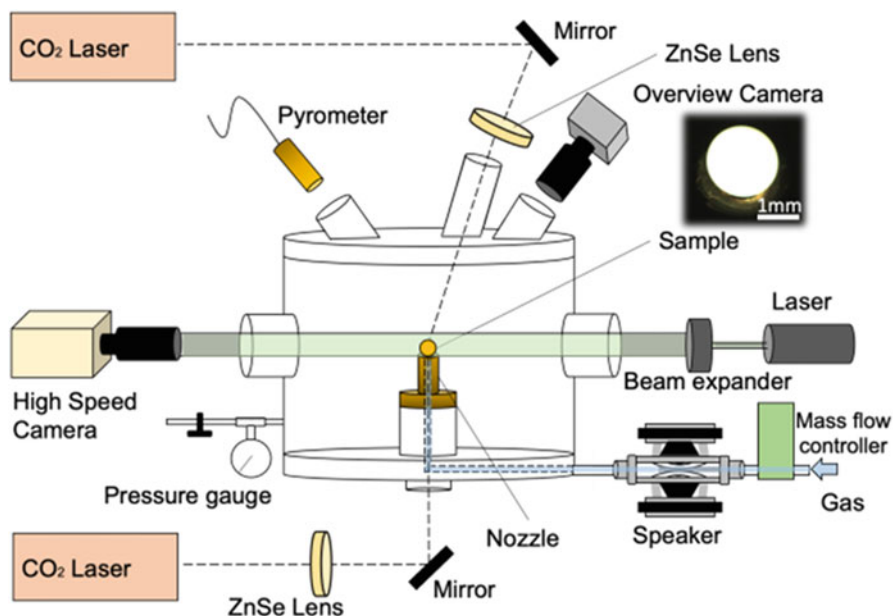
Fig. 11.12 Schematic diagram of the aerodynamic levitation system combined with acoustic oscillation generators

CO_2 laser irradiation. For the thermophysical property measurements, we applied CO_2 laser irradiation to the samples from both top and bottom to reduce the temperature gradient in the samples. The sample temperature was measured using a monochromatic pyrometer at a wavelength of 925 nm.

The measurement of molten oxides is challenging because of their emissivity, with only a few reports existing. Since the emissivity of molten oxides has rarely been reported, their correct temperature is unknown. Usually, temperature correction in a pyrometer uses the melting and liquidus temperature by recalescence, which is the temperature jump from energy release from the undercooled liquid phase to the crystalline phase during solidification in the cooling processes. However, many molten oxides are easily translated into glass phases from the undercooled liquid phase. In this case, we cannot use the melting and liquidus temperature for calibration. Thus, to overcome this problem, we proposed a calibration method for the temperature of molten oxide samples using a two-material contacting method [44]. Specifically, the base material (metal) has a known emissivity, and the sample with unknown emissivity (oxide) is melted simultaneously with the metal sample by EML. In this process, the molten oxide contacts the bottom of the metal sample because molten oxides exhibit no electrical conduction. Under the assumption that both samples have the same temperature, the difference in the radiation intensity between the metal and oxide can be obtained. Consequently, on the basis of this difference, the emissivity of the molten oxide can be determined. Using this method, we determined the emissivity of molten Al_2O_3 to be 0.8 at 925 nm. This value agrees

with previously reported values [45]. Using this method, we obtained the emissivity of molten oxides to calibrate their measured temperature using a single-wavelength pyrometer.

5.2 Density Measurements of Molten Oxides by ADL

The density of various compositions of molten SiO_2–CaO–Al_2O_3 with low SiO_2 content ($\leq$20 wt.%) was measured using the ADL system. Sample compositions of SiO_2–CaO–Al_2O_3 are listed in Table 11.1. The density, $\rho = M/V$, was obtained using the volume (V) calculated from the image and the mass (M) measured before floating. Specifically, the volume was obtained from the length of the sample in pixel units in the high-speed camera image. The sample length had an uncertainty of $\pm 5.3 \times 10^{-3}$ mm, which is the resolution limit of observation of the high-speed camera. The volume uncertainty was calculated by including the above uncertainty of the length. The mass of the samples was weighed three times per sample, the average was calculated, and the uncertainty was obtained from the distributions. Thus, the average uncertainty of the density measurements was $\pm 0.8\%$ for each measurement. Figure 11.13 shows density measurement results for slag oxide SiO_2–CaO–Al_2O_3 sample systems [41]. The density data of all the samples were measured in the temperature range of 800–2200 K. Significantly, the density values of the molten oxides of the SiO_2–CaO–Al_2O_3 system at high temperature were obtained for the first time. In the low-temperature range, our measured data are in good agreement with published data. The published density of slag-1 is 2.75×10^3 kg/m^3 at 1480 °C [46] and that of slag-2 is 2.73×10^3 kg/m^3 at 1600 °C [46]. Using the ADL system as a containerless technique, we could obtain the density data at high temperatures, over 2000 K, without the need for published data. These density data were obtained by free cooling in dried air conditions by laser power-off at the highest temperature. Therefore, all of the oxides changed from a supercooled liquid to a solid with an amorphous structure. Therefore, the density data shown in Fig. 11.13 include the liquid state and the solid state with an amorphous structure. In Fig. 11.13, for slag-1 and slag-4, the slope of the density changed with temperature at ~1500 K. This is

Table 11.1 Compositions of SiO_2–CaO–Al_2O_3 with low SiO_2 ($\leq$20 wt. %) content employed for the measurement of density, surface tension, and viscosity using the ADL technique

Slag no.	SiO_2	Al_2O_3	CaO	Liquidus temp. (K) (thermo-calc)	Solidus temp. (K) (thermo-calc)	Basicity $CaO/(SiO_2+Al_2O_3)$
1	10	40	50	1681	1614	1.00
2	10	35	55	1639	1613	1.22
3	10	30	60	1773	1637	1.50
4	14	36	50	1665	1616	1.00
5	10	44	46	1722	1620	0.85
6	20	30	50	1792	1668	1.00
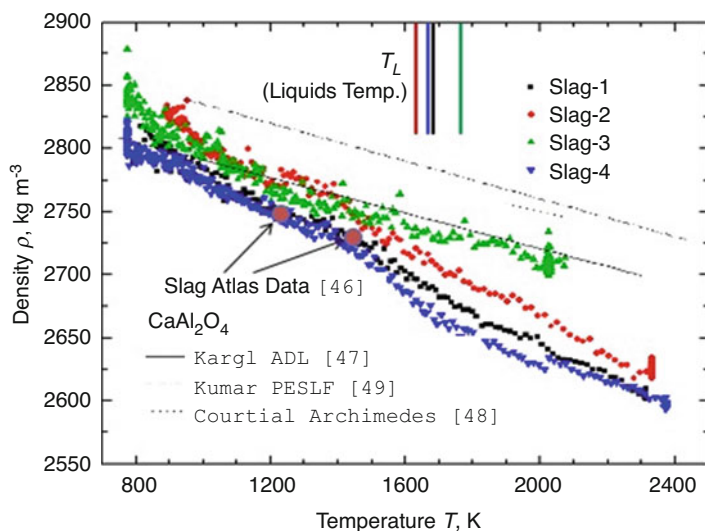
Fig. 11.13 Variations in the density of the molten SiO_2–CaO–Al_2O_3 system measured by ADL as a function of temperature for each composition. Comparison data of the density of molten $CaAl_2O_4$ measured using other methods is also plotted [39]

attributed to the fact that this temperature is the transition temperature from the supercooled liquid to the amorphous solid. However, we found that the transition temperature was at an even lower temperature of ~800 K by differential thermal analysis. Moreover, in the viscosity measurements, the temperature dependence did not show a change for slag-1 and slag-4. Therefore, for slag-1 and slag-4, the change in the slope of density with temperature at ~1500 K is due to another reason to be determined by future experiments. According to the present results, we determined the characteristic nature of the density of the SiO_2–CaO–Al_2O_3 system. In Fig. 11.12, the solid and dashed lines show previous results for molten $CaAl_2O_4$. In comparison with the density of $CaAl_2O_4$ [47, 48], the density of the SiO_2–CaO–Al_2O_3 system is relatively small. This means that the addition of SiO_2 expands the volume of the molten CaO–Al_2O_3 system [49]. From a structural viewpoint, the expansion of the volume by the addition of SiO_2 indicates that a large free volume space is created in the liquid. In future studies, the combination of our density measurement technique with structural analysis, X-ray, and neutron scattering should be a powerful tool for understanding the properties of molten oxides.

5.3 Viscosity Measurements of SiO_2–CaO–Al_2O_3 with Low SiO_2 Content

For the SiO_2–CaO–Al_2O_3 system with low SiO_2 content (≤ 20 wt.%), we successfully measured viscosity in a wide temperature range in combination with the rotating bob method (RBM) [43]. Using the ADL system, the low-viscosity region at high temperature was obtained, and the high-viscosity region at low temperature was obtained by RBM. According to these wide temperature range viscosity measurements, we can discuss the temperature dependence of the viscosity of the SiO_2–CaO–Al_2O_3 system with low SiO_2 content. The viscosity of the SiO_2–CaO–Al_2O_3 system with low SiO_2 content as a function of temperature determined using the ADL technique is shown in Fig. 11.14. For these viscosity measurements, the measurement uncertainty comes from the resolution of the camera and the accuracy of the weight measurement, similar to the surface tension measurement. The uncertainty of the viscosity is due to the uncertainty of the density, radius value, and decay time of the surface oscillation. The decay time was obtained from the variation in sample diameter with time. The camera recording rate was 1000 FPS, and the measurement of the decay time had an accuracy of 1.0×10^{-3} s. The combined average standard uncertainty was $\pm 1.2\%$ for each data point. The average uncertainty of the viscosity measurement using RBM is $\pm 0.8\%$ for each data point [43].
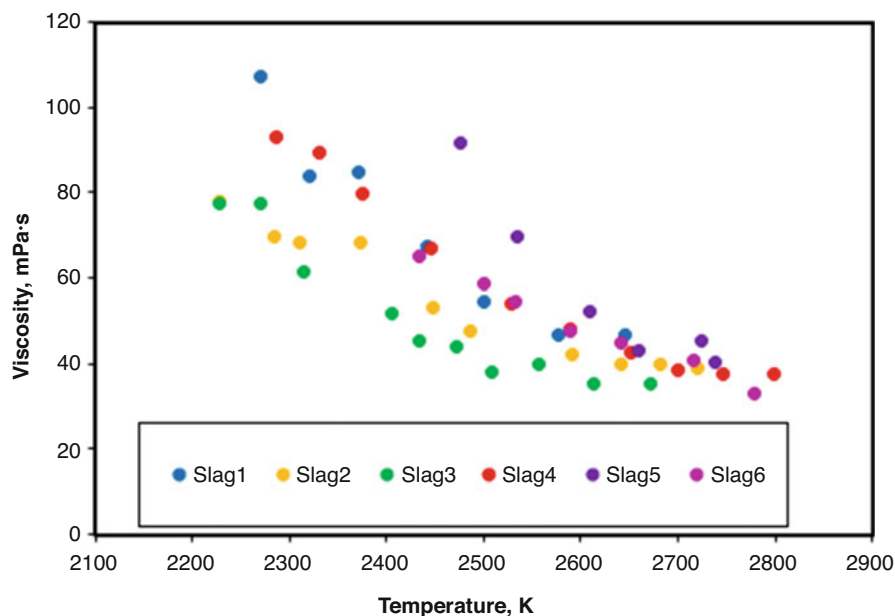
Fig. 11.14 Variations in the viscosity as a function of time measured using the ADL technique for each composition of the molten SiO_2–CaO–Al_2O_3 system
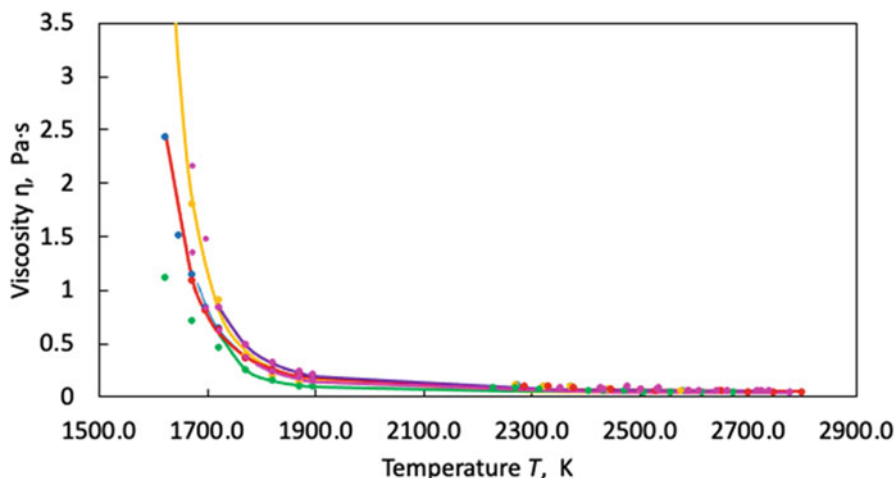
Fig. 11.15 Variation in viscosity in a wide temperature range for the molten SiO$_2$–CaO–Al$_2$O$_3$ system. In the high-temperature range (2200–2800 K), the viscosity was measured using the ADL technique, and in the low-temperature range (1650–1900 K), it was measured using the RBM [43]

The viscosity obtained using both methods was plotted as a function of temperature, as shown in Fig. 11.15. The fitting curves for each composition were obtained according to the temperature-dependent viscosity formula for the viscosity of glass transition liquids by Mauro et al. [50]:

$$\log_{10}\eta = \log_{10}\eta_\infty + \frac{\kappa}{T}\exp\left(\frac{C}{T}\right), \tag{11.7}$$

where η is the viscosity, T is the temperature, η_∞ is the fitting parameter that corresponds to the viscosity at infinite temperature, k is the fitting parameter related to the effective activation barrier and configurational entropy, and C is the fitting parameter related to the topological degrees of freedom per atom [51].

From the temperature dependence of viscosity obtained by both ADL and conventional RBM techniques, we confirmed that the ADL technique can be applied to measure the viscosity of molten oxide systems and can also cover a wide temperature range to measure the viscosity of molten oxide systems. Using our viscosity data, the compositional dependence of the viscosity of the SiO$_2$–CaO–Al$_2$O$_3$ system with low SiO$_2$ content was investigated [51]. According to the temperature dependence of the viscosity for each composition, we obtained the relationship between viscosity and SiO$_2$/Al$_2$O$_3$ ratio (mass ratio) with a constant amount of CaO as well as the relationship between viscosity and CaO/Al$_2$O$_3$ ratio (mass ratio) with a constant amount of SiO$_2$. In the case of a basicity of 1.0 for CaO/(Al$_2$O$_3$+SiO$_2$) and 50 wt.% of CaO, an increase in the SiO$_2$/Al$_2$O$_3$ ratio, the viscosity remained relatively constant. It can be concluded that Al$_2$O$_3$ and SiO$_2$ contribute to the viscosity, which indicates that the degree of the aluminosilicate

network is about the same in the present composition range. This implies that the viscosity mainly depends on the basicity of the slags and agrees with the existing SiO_2–CaO–Al_2O_3 ternary diagrams. On the contrary, the relation between the viscosity and CaO/Al_2O_3 ratio with 10 wt.% SiO_2 at different temperatures, in this relation, is not simple. CaO/Al_2O_3 = 1.25, 2.0, and 1.05 are consistent with the expected trend. In this study, the mole ratio of CaO/Al_2O_3 is higher than 1.0, and thus, Al_2O_3 should act as a network former, while CaO acts as a network modifier. Thus, the degree of polymerization decreases with an increase in the CaO/Al_2O_3 ratio. This implies that the viscosity should constantly decrease with an increase in the CaO/Al_2O_3 ratio owing to the depolymerization of the aluminosilicate network. However, in the case of CaO/Al_2O_3 = 1.57, the viscosity is increased. This cannot be explained only by the aluminosilicate network [52]. For this condition, we explain this phenomenon as follows. On the basis of short-range order idea theory, ions tend to rearrange themselves in liquid slag through strong ionic interactions and form compound-like clusters that resemble the structure of the primary precipitating solid phase. For the CaO–Al_2O_3 (10 wt.% of SiO_2) pseudo-binary phase diagram in the composition range of the present study, thermo-calc calculations showed the primary precipitating solid precipitates in the form of $CaO \cdot Al_2O_3$ (CA), $3CaO \cdot SiO_2$ (C3S), and $12CaO \cdot 7Al_2O_3$ (C12A7). For the case of CaO/Al_2O_3 = 1.57, the increase in viscosity is attributed to the formation of C12A7-like clusters. It was concluded that the total influence on the viscosity comes from the summation of both the influence of network depolymerization and the compound-like cluster formation of the primary solid phase.

Through this study, we confirmed that the ADL technique is a very useful tool for the measurement of the thermophysical properties of molten oxides. We have been obtaining the thermophysical properties of molten oxide along with our ISS experiments [53] using an electrostatic levitation furnace (ELF) [54, 55]. In the near future, we can compare the ADL results obtained in the lab with ELF results under microgravity with a small external force and no drop deformation conditions. On the basis of these comparisons, we will more precisely measure the thermophysical properties of molten oxides.

6   Conclusions

Thermophysical property measurements using EML on ground by the Japanese team in the THERMOLAB -project were reviewed. Surface tension measurements by EML under controlled oxygen partial pressure, the use of static magnetic field applied to EML for density and thermal conductivity measurements, and viscosity measurements using the ADL technique were presented. MSL–EML experiments have encouraged ground-based experiments for the determination of thermophysical properties. By this driving force, we have developed and improved measurement methods for precise thermophysical property measurements and have obtained

results for insightful scientific discussions. These are important results not only for MSL–EML experiments but also for materials research science and engineering.

References

1. M. Przyborowski, T. Hibiya, M. Eguchi, I. Egry, Surface tension measurement of molten silicon by the oscillating drop method using electromagnetic levitation. J. Cryst. Growth **151**, 60–65 (1995)
2. T. Hibiya, M. Eguchi, I. Egry, M. Przyborowsky, J. Szekely, Abstract of 9th European symposium on gravity-dependent Phenomena in Physical Sciences, Berlin, May 1995 (Poster Session)
3. Z. Niu, K. Mukai, Y. Shiraishi, T. Hibiya, K. Kakimoto, M. Koyama, Effect of oxygen and temperature on the surface tension of molten silicon. J. Jpn. Assoc. Cryst. Growth **24**(2), 31–40 (1997)
4. K. Mukai, Z. Yuan, K. Nogi, T. Hibiya, Effect of oxygen partial pressure on the surface tension of molten silicon and its temperature coefficient. ISIJ Int. **40**, S148–S152 (2000)
5. M. Langen, T. Hibiya, M. Eguchi, I. Egry, Measurement of the density and the thermal expansion coefficient of molten silicon using electromagnetic levitation. J. Cryst. Growth **186**, 550–556 (1998)
6. K. Samwer (Principal Investigator), Proposal to the international announcement of opportunity for microgravity research: SEMMITHERM. described in Ch.5.4 in this book in details.
7. T. Hibiya, I. Egry, Thermophysical property measurements of high temperature melts: Results from the development and utilization of space. Meas. Sci. Technol. **16**, 1–10 (2005)
8. I. Egry, E. Ricci, R. Novakovic, S. Ozawa, Surface tension of liquid metals and alloys—Recent developments. Adv. Colloid Interf. Sci. **159**, 198–212 (2010)
9. H. Kimura, M. Watanabe, K. Izumi, T. Hibiya, D. Holland-Moritz, T. Schenk, K.R. Bauchspieß, S. Schneider, I. Egry, K. Funakoshi, M. Hanfland, X-ray diffraction study of undercooled molten silicon. Appl. Phys. Lett. **78**, 604–606 (2001)
10. H. Kobatake, H. Fukuyama, I. Minato, T. Tsukada, S. Awaji, Noncontact measurement of thermal conductivity of liquid silicon in a static magnetic field. Appl. Phys. Lett. **90**, 094102-1–094102-3 (2007)
11. H.-J. Fecht, W.L. Johnson, A conceptual approach for noncontact calorimetry in space. Rev. Sci. Instrum. **62**, 1299–1303 (1991)
12. R.K. Wunderlich, H.-J. Fecht, Power modulation technique for noncontact high-temperature calorimetry. Appl. Phys. Lett. **62**, 3111–3113 (1993)
13. M. Ratto, E. Ricci, E. Arato, Mechanism of oxidation/deoxidation of liquid silicon: Theoretical analysis and interpretation of experimental surface tension data. J. Cryst. Growth **217**, 233–249 (2000)
14. K. Mukai, Z. Yuan, K. Nogi, T. Hibiya, Effect of the oxygen partial pressure on the surface tension of molten silicon and its temperature coefficient. ISIJ Int. **40**, 148 (2000)

15. T. Hibiya, K. Morohoshi, S. Ozawa, Oxygen partial pressure dependence of surface tension and its temperature coefficient for metallic melts: A discussion from the viewpoint of solubility and adsorption of oxygen. J. Mater. Sci. **45**, 1986–1992 (2010)

16. S. Ozawa, K. Morohoshi, T. Hibiya, H. Fukuyama, Influence of oxygen partial pressure on surface tension of molten silver. J. Appl. Phys. **107**, 014910 (2010)

17. S. Ozawa, S. Suzuki, T. Hibiya, H. Fukuyama, Influence of oxygen partial pressure on surface tension and its temperature coefficient of molten iron. J. Appl. Phys. **109**, 014902 (2010)

18. S. Ozawa, S. Takahashi, N. Watanabe, H. Fukuyama, Influence of oxygen adsorption on surface tension of molten nickel measured under reducing gas atmosphere. Int. J. Thermophysics **35**, 1705–1711 (2014)

19. S. Ozawa, N. Takenaga, T. Inoue, Y. Takei, T. Hibiya, A. Mizuno, M. Watanabe, Measurement of surface tension on molten metal under reducing gas atmosphere in microgravity condition during parabolic flight – Attempt to control oxygen partial pressure. Int. J. Microgravity Sci. Appl. **31**, 11–16 (2014)

20. S. Ozawa, Y. Nagasaka, M. Itakura, K. Sugisawa, Y. Seimiya, Influences of oxygen adsorption from atmosphere on surface tension of liquid silicon, J. Appl. Phys. **130**, 135101 (2021).

21. S. Ozawa, M. Nishimura, K. Kuribayashi, Surface tension of molten silver in consideration of oxygen adsorption measured by electromagnetic levitation. Int. J. Microgravity Sci. Appl. **35**, 23456 (2015)

22. B. von Szyszkowski, Experimental studies on capillary properties of aqueous solutions of fatty acids. Z. Phys. Chem. **64**, 385 (1908)

23. P.H. Poole, T. Grande, C.A. Angell, P.F. Mcmillan, Polymorphic phase transitions in liquids and glasses. Science **275**, 322 (1997)

24. H. Yasuda, I. Ohnaka, Y. Ninomiya, R. Ishii, S. Fujita, K. Kishio, Levitation of metallic melt by using the simultaneous imposition of the alternating and the static magnetic fields. J. Cryst. Growth **260**, 475–485 (2004)

25. H. Fukuyama, H. Kobatake, K. Takahashi, I. Minato, T. Tsukada, S. Awaji, Development of modulated laser calorimetry using a solid platinum sphere as a reference. Meas. Sci. Technol. **18**, 2059–2066 (2007)

26. M. Watanabe, M. Adachi, H. Fukuyama, Densities of Fe–Ni melts and thermodynamic correlations. J. Mater. Sci. **51**, 3303–3310 (2016)

27. A. Mizuno, H. Kawauchi, M. Tanno, K. Murai, H. Kobatake, H. Fukuyama, T. Tsukada, M. Watanabe, Concentration dependence of molar volume of binary Si alloys in liquid state. ISIJ Int. **54**, 2120–2124 (2014)

28. H. Kobatake, H. Khosroabadi, H. Fukuyama, Normal spectral emissivity of stable and undercooled liquid silicon using electromagnetic levitation in a dc magnetic field. Meas. Sci. Technol. **22**, 015102 (2011)

29. M. Watanabe, M. Adachi, M. Uchikoshi, H. Fukuyama, Densities of Pt-X (X: Fe, Co, Ni and Cu) binary melts and thermodynamic correlations. Fluid Phase Equilib. **515**, 112596 (2020)

30. M. Watanabe, M. Adachi, M. Uchikoshi, H. Fukuyama, Thermal conductivities of Fe-Ni melts measured by non-contact laser modulation calorimetry. Metall. Mater. Trans. A **50A**, 3295–3300 (2019)

31. M. Watanabe, M. Adachi, M. Uchikoshi, H. Fukuyama, Heat capacities and thermal conductivities of palladium and titanium melts and correlation between thermal diffusivity and density of states for transition metals in a liquid state. J. Mol. Liquids **324**, 115138 (2021)

32. P.-F. Paradis, T. Ishikawa, Y. Watanabe, J. Okada, Hybrid processing combining electrostatic levitation and laser heating: Application to terrestrial analogues of asteroid materials. Adv. Opt. Technol., 1–8 (2011)

33. K. Brillo, I. Egry, Density and excess volume of liquid copper, nickel, iron, and their binary alloys. Z. Metallkd. **95**, 691–697 (2004)

34. H. Kobatake, J. Brillo, Density and thermal expansion of Cr–Fe, Fe–Ni, and Cr–Ni binary liquid alloys. J. Mater. Sci. **48**, 4934–4941 (2013)

35. Y. Kita, Z. Morita, The electrical resistivity of liquid Fe-Ni, Fe-Co and Ni-Co alloys. J. Non-Cryst. Solids **61-62**, 1079–1084 (1984)

36. G. Pottlacher, Thermal conductivity of pulse-heated liquid metals at melting and in the liquid phase. J. Non-Cryst. Solids **250–252**, 177–181 (1999)

37. A. Seifter, G. Pottlacher, H. Jager, G. Groboth, E. Kaschnitz, Measurements of thermophysical properties of solid and liquid Fe-Ni alloys. Ber. Bunsenges. Phys. Chem. **102**, 1266–1271 (1998)

38. Y. Ono, T. Yagi, Electric resistivity of molten Fe-Ni and Fe-Co alloys. Trans. ISIJ **12**, 314–316 (1972)

39. V. Ye, V. Zinov'yev, F. Polev, S.G. Taluts, G.P. Zinovyeva, S.A. Ilinykh, Diffusivity and thermal conductivity of 3d-transition metals in solid and liquid states. Phys. Met. Metallogr. **61**, 85–92 (1986)

40. D. Langstaff, M. Gunn, G.N. Greaves, A. Marsing, F. Kargl, Aerodynamic levitator furnace for measuring thermophysical properties of refractory liquids. Rev. Sci. Instrum. Methods **84**, 124901 (2013)

41. K. Onodera, A. Nakamura, S. Hakamada, M. Watanabe, F. Kargl, Thermophysical property measurements of molten slag and welding flux by aerodynamic levitator, in *Proceedings of 10th international conference Molten Slags, Fluxes and Salts*, May, 2016, Seattle, U.S.A.

42. S. Hakamada, A. Nakamura, M. Watanabe, F. Kargl, Surface oscillation phenomena of aerodynamically levitated molten Al_2O_3. Int. J. Microgravity Sci. Appl. **34**, 340403 (2017)

43. D. Siafakas, T. Matsushita, S. Hakamada, K. Onodera, F. Kargl, A.E.W. Jarfors, M. Watanabe, Measurement of viscosity of SiO_2-CaO-Al_2O_3 Slag in wide temperature range by aerodynamic levitation and rotating bob methods and sources of systematic error. Int. J. Microgravity Sci. Appl. **35**, 350203 (2018)

44. S. Taguchi, S. Shimizu, H. Hasome, M. Watanabe, Spectral emissivity estimation molten oxides by two materials contacting method. Int. J. Microgravity Sci. Appl. in preraration.

45. P.-F. Paradis, T. Ishikawa, Y. Saita, S. Yoda, Non-contact Thermophysical property measurements of liquid and undercooled alumina. Jpn. J. Appl. Phys. **43**, 1496 (2004)

46. Data listed in the "SLAG ATRAS", 2nd Ed., Ed. By V. D. Eisenhüttenleute, and M. Alliber, Verlag Stahleisen GmbH (1995)

47. F. Kargl, C. Yuan, G.N. Greaves, Aerodynamic levitation: Thermophysical property measurements of liquid oxides. Int. J. Microgravity Sci. Appl. **32**, 320212 (2015)

48. P. Courtial, D.B. Dingwell, Nonlinear composition dependence of molar volume of melts in the CaO-Al_2O_3-SiO_2 system. Geochim. Cosmochim. Acta **59**, 3685 (1995)

49. M.V. Kumar, J.T. Okada, T. Ishikawa, P.-F. Paradis, Y. Watanabe, Density measurement of glass and liquid $CaAl_2O_4$ using a pressurized electrostatic levitator. Meas. Sci. Tech. **25**, 085301 (2014)

50. J.C. Mauro, Y. Yue, A.J. Ellison, P.K. Gupta, D.C. Allan, Viscosity of glass-forming liquids. PNAS **106**, 19780 (2009)

51. D. Siafakas, T. Matsushita, A.E.W. Jarfors, S. Hakamada, M. Watanabe, Viscosity of SiO_2–CaO–Al_2O_3 Slag with low silica – influence of CaO/Al_2O_3, SiO_2/Al_2O_3 ratio. ISIJ Int. **58**, 2180 (2018)

52. E. Turkdogan, P. Bills, A critical review of viscosity of CaO-MgO-Al_2O_3-SiO_2 melts. British Ceramic Soc. Bulletin **39**, 682 (1960)

53. M. Watanabe, K. Onodera, K. Tanaka, S. Taguchi, R. Serizawa, S. Hakamada, A. Nakamura, A. Mizuno, S. Ueno, T. Tsukada, H. Gotoh, T. Tanaka, H. Tamaru, T. Ishikawa, Interfacial phenomena and thermophysical properties of molten steel and oxides – fundamental research of steel processing using electrostatic levitation furnace (ELF). Int. J. Microgravity Sci. Appl. **33**, 330212 (2016)

54. H. Tamaru, T. Ishikawa, J.T. Okada, Y. Nakamura, H. Ohkuma, S. Yukizono, Y. Sakai, T. Takada, Overview of the electrostatic levitation furnace (ELF) for the international space station (ISS). Int. J. Microgravity Sci. Appl. **32**, 32104 (2015)

55. H. Tamaru, C. Koyama, H. Saruwatari, H. Nakamura, T. Ishikawa, T. Takada, Status of the electrostatic levitation furnace (ELF) in the ISS-KIBO. Microgravity Sci. Technol. **30**, 643–651 (2018)

Part IV
Thermophysical Property Measurement by Levitation

Chapter 12
Measurement of Thermophysical Properties Using the ISS-EML

Markus Mohr and Hans-Jörg Fecht

1 Introduction

The development and improvement of new materials are always linked to the creation and optimization of suitable manufacturing processes. Nowadays, industrial process development is strongly based on numerical simulations, in order to gain control over the solidification pathway. As a result, the final microstructure, defect density, residual stresses, porosity, and the mechanical performance of the produced parts can be predicted and optimized [1, 2]. For the development of new manufacturing processes, such as 3D printing, numerical simulations can also reduce the development time by avoiding a purely empirical, time-consuming, expensive search for the optimal process parameters. A prerequisite for developing useful, predictive computer models is the knowledge of precise thermophysical property data of the alloy in the solid and liquid phases [1, 2].

Conventional methods allow the measurement of some of the necessary data, especially for the solid phase. Determining metallic alloys' thermophysical properties in the liquid phase is either afflicted by significant uncertainties or even impossible to obtain with conventional container-based equipment.

The reason is the high chemical reactivity of molten metals, which leads to contaminations or container reactions that make the measurement of reliable thermophysical surface and bulk properties impossible. The solution is to use containerless methods, where the samples are investigated contactless.

Several levitation methods exist that allow containerless processing. The most relevant ones are aerodynamic levitation [3], electrostatic levitation [4], and electromagnetic levitation [1, 2, 5]. Ground-based levitation equipment needs to compensate for the large gravitational force on the samples. In the case of aerodynamic and

---

M. Mohr (✉) · H.-J. Fecht
Institute of Functional Nanosystems, Ulm University, Ulm, Germany
e-mail: markus.mohr@uni-ulm.de; hans.fecht@uni-ulm.de

electrostatic levitation, this becomes more and more challenging for samples of higher mass. One limitation of ground- and microgravity-based electromagnetic levitation is that only electrically conducting samples can be positioned. Nevertheless, the possibility of levitating bulk samples with the mass of a few grams and typical diameters of 6–8 mm, the good temperature homogeneity of the sample, and the sample position's intrinsic self-stabilization makes electromagnetic levitation a very versatile and reliable tool [6]. Furthermore, electromagnetic levitation allows to obtain high temperatures of up to 2200 °C.

Some thermophysical properties can principally be measured by ground-based electromagnetic levitation, such as the surface tension, density, and some more (see also Chap. 8, Part III, in this book). However, the large electromagnetic fields deform the molten droplet and generate turbulent fluid flows inside the sample [7]. This prevents the measurement of viscosity and complicates the measurement of other properties, such as surface tension. Furthermore, the strong positioning fields require the sample to be cooled convectively by high-purity gas like He or Ar.

These shortcomings of ground-based electromagnetic levitation can be overcome when the experiments are performed under reduced gravity conditions. In reduced gravity (microgravity), much smaller positioning forces are necessary, which drives only moderate fluid flows in the melt which are laminar over a wide parameter range. Additionally, the sample is of spherical shape, and if the processing time is long enough, no convective cooling is necessary. The spherical sample shape and the stable sample position also improves the measurement of temperature, density, and electrical resistivity. A laminar flow in the melt enables the measurement of viscosity. Moreover, the fluid flow conditions can be controlled by the heater field and thus allow to study the effects of fluid flow on solidification [8].

The electromagnetic levitation facility ISS-EML, operating onboard the International Space Station (ISS) in microgravity (μg), provides a perfect environment for the contactless measurement of different thermophysical properties of electrically conducting liquid samples. The ISS-EML facility uses a symmetric magnetic quadrupole field produced by two equal, parallel, and coaxial circular RF currents of the same strength but opposite directions. The resulting Lorentz forces confine the sample in the center of the coil (see Fig. 12.1). An additional, homogeneous RF magnetic dipole field is applied for efficient inductive heating and melting of the sample. This heating field is generated by two parallel and coaxial circular RF currents of the same strength flowing in the same direction.

Performed in the nearly force-free μg environment, this containerless technique has the advantage that the sample is confined to a very stable position between the coils. Secondly, the weak electromagnetic forces leave the spherical droplet undeformed and allow to reach low temperatures. The weak positioning forces also minimize the driving of fluid flow in the sample, thus allowing experiments under laminar fluid flow conditions. This way, electromagnetic levitation in microgravity is a good platform for applying contactless measurement methods to obtain different thermophysical properties in the liquid state.

The general experiment procedure is schematically depicted in Fig. 12.2.
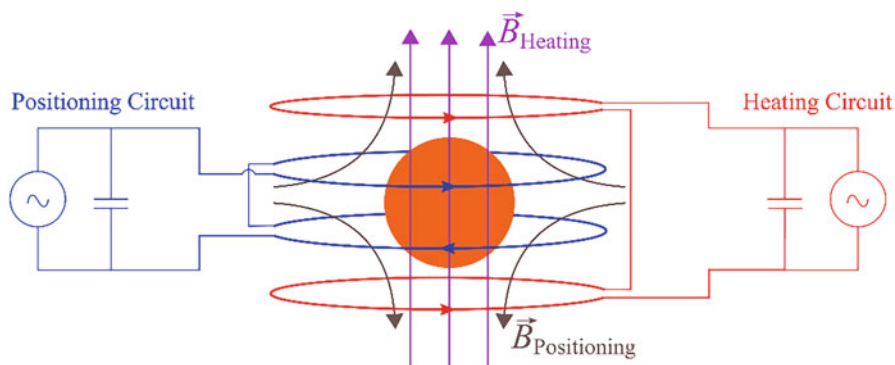
Fig. 12.1 Sketch of the electrical circuit of the ISS-EML facility, consisting of the positioning coil (blue), generating the positioning rf-field (brown), and the heating coil (red), generating a homogeneous heating rf-field (purple)
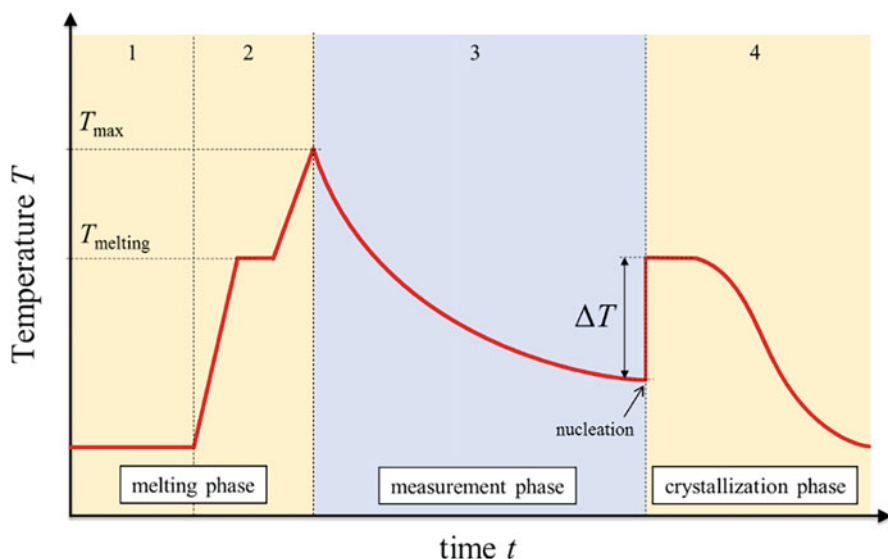
Fig. 12.2 Schematic drawing of the general experiment procedure, including the melting phase (1–2), the temperature-time range for measurements in the liquid state (3), and the crystallization phase with the onset of nucleation at undercooling ΔT (4)

The initial step is the positioning of the cold, solid sample in the center of the coils (1) in Fig. 12.2. The sample, when held in a stable position by the positioning field, is then heated by the heating field with heating rates of typically 100–500 K/s (2) in Fig. 12.2. The solid sample heats up in the solid phase, then melts at the melting point T_{melting}, and gets heated over the melting point until the desired maximum temperature T_{max}. At this point, the heating field is turned off and the sample cools freely (3), only held in place by the weak positioning forces of the positioning field.
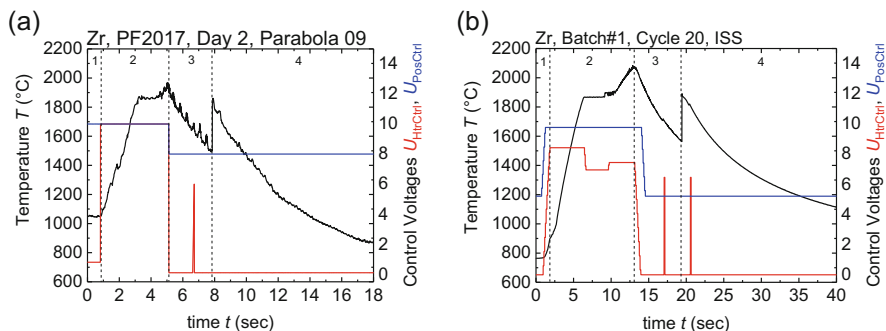
Fig. 12.3 Typical temperature-time diagram of zirconium. (**a**) Parabolic flight: The sample is cooled convectively by Helium (**b**) in the ISS-EML: The sample is processed in vacuum

The effective cooling rate depends on the experiment atmosphere (Vacuum, He, Ar) and the samples heat capacity and is typically between 1 and 10 K/s. During this phase of minimal external impact, the different experiments on the liquid sample are performed. Often, the sample can cool fast enough to reach temperatures below the equilibrium melting temperature, before solidification starts. The nucleation and growth of the solid, crystalline phase is accompanied by a steep temperature rise, called recalescence, which is a consequence of the liberation of the latent heat of transformation. In the last step (4), the sample finishes solidification and cools down.

Figure 12.3 shows process cycles for the determination of surface tension and viscosity of zirconium, performed in a parabolic flight (Fig. 12.3a) and in the ISS-EML (Fig. 12.3b). Due to the shorter microgravity time in the parabolic flight (~ 20 s), the sample was convectively cooled by He while it was processed in vacuum in the ISS-EML. In both cases, the process cycle consists of the same phases (1–4) as introduced in Fig. 12.2. The longer process times in the ISS-EML and the higher quality of the microgravity environment (remaining accelerations on ISS: about 10^{-5} to 10^{-6} g, on parabolic flight about 10^{-3} g) improve the sample positioning stability and hence also the temperature measurement by the pyrometer.

2 Surface Tension and Viscosity

The oscillating drop method is often used to measure surface tension and viscosity [8–10]. During the cooling phase, short heater pulses are applied to excite surface oscillations (see heater control voltage $U_{HtrCtrl}$ (red), Fig. 12.3). Subsequently, these oscillations of the droplet decay freely. The oscillation frequency of the droplet is determined by the surface tension of the liquid, while the damping time constant depends on the viscosity. To determine these two thermophysical properties (surface tension and viscosity), the motion of the surface is recorded by two high-speed cameras. The two cameras point toward the sample along the coil axis (axial camera)
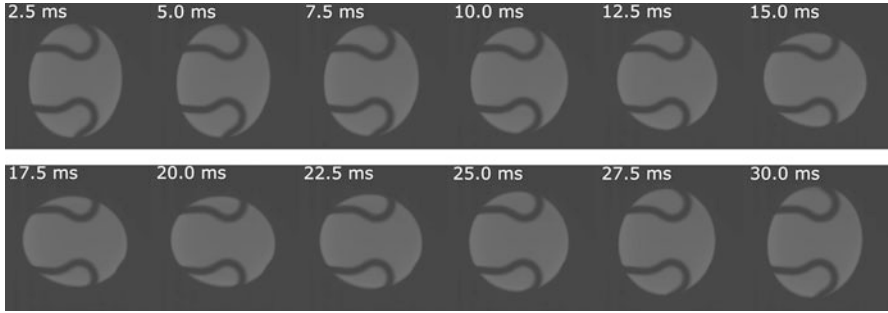
Fig. 12.4 Time series of high-speed camera images after surface oscillation excitation. The shadows on the sample originate from the wire cage around the sample that restricts the sample position in times when the positioning field is turned off

and perpendicular (radial camera) to it. Typical frame rates are between 150 and 400 Hz, which is more than double the observed oscillation frequencies between 20 and 50 Hz. For more technical details, see Chap. 3. In Fig. 12.4, a sequence of a 400 Hz video is shown, which is used to evaluate the oscillation frequency $f = \omega/2\pi$ and damping time constant τ. The time-dependent radius R of a liquid droplet can be described in spherical coordinates by

$$R(t, \vartheta, \varphi) = R_0 \left(1 + \varepsilon P_l^m(\vartheta) \cos{(m\varphi)} \cos{(\omega_{l,m}t)} e^{-t/\tau_{l,m}} \right) \tag{12.1}$$

where R_0 is the radius of the perfect sphere, ε is the amplitude of the oscillation, and P_l^m is an associated Legendre polynomial. The observed oscillations are typically dominated by the $l = 2$ mode, owing to the symmetry of the excitation. The oscillation modes ($l = 2$; $m = 0, \pm 1, \pm 2$) are degenerated under microgravity and assume all the same frequency. Figure 12.4 shows a series of images taken by the radial high-speed camera during the oscillation of the sample LEK94, Batch#1, directly after the surface oscillation excitation (more information on this sample can be found in Chap. 15). The $l = 2$ oscillation mode dominates the surface oscillations shown in Fig. 12.4.

Analyzing the recorded high-speed camera videos by appropriate edge detection algorithms [11], the time-dependent amplitude of the droplets surface shape oscillations $\delta(t) = R(t) - R_0$ can be obtained. The dominating surface oscillation frequency of mode $l = 2$, ω_2 is obtained either from a Fourier transformation or from fitting in time domain using an equation of the form

$$\delta_{(t)}/R_0 = \varepsilon \cdot \cos{(\omega_2 t + \varphi_0)} e^{-t/\tau_2} \tag{12.2}$$

which also reveals the damping time constant τ_2. Alternatively, the damping time constant can be found by fitting only the signal envelope by the exponential term in
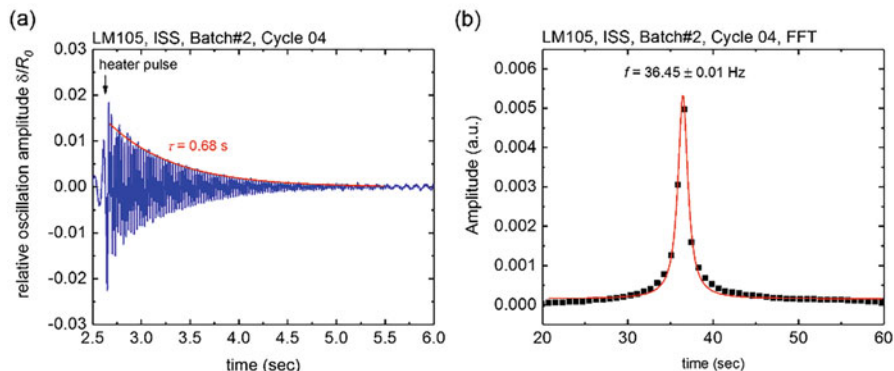
Fig. 12.5 (**a**) Relative oscillation amplitude as a function of time, together with a fit of the decay time constant. (**b**) Fourier transform of the oscillations in (**a**)

Eq. 12.2. Using the example of the liquid glass-forming LM105 droplet, Fig. 12.5a shows the data of its relative surface oscillation amplitude $\delta(t)/R_0$ derived from the high-speed video camera recordings. In Fig. 12.5b, the Fourier transform of $\delta(t)/R_0$ is displayed, showing one peak at a single frequency of $\omega/2\pi = 36.4$ Hz. This shows the excellent conditions present in the microgravity environment of the ISS.

Under the assumption of infinitely small oscillation amplitudes ε and negligible damping, Rayleigh derived the surface tension γ of a droplet as [12]

$$\omega_{l,m}^2 = l(l+2)(l-1)\frac{4\pi}{3}\frac{\gamma}{M} \tag{12.3}$$

with the sample mass M and l denoting the oscillation mode. Lamb derived later the relation between damping time constant $\tau_{l,m}$ and viscosity η of a droplet with low damping as [13]

$$\frac{1}{\tau_{l,m}} = (2l+1)(l-1)\frac{4\pi R_0}{3}\frac{\eta}{M} \tag{12.4}$$

Reid [14] and Chandrasekhar [15] extended this derivation to the case of droplets with large damping. Suryanarayana et al. [16] also used this derivation and presented a procedure to obtain surface tension and viscosity in the case of the viscous droplet. Lohöfer [17] simplified the derivations of Reid [14], Chandrasekhar [15], and Suryanarayana [16], obtaining two equations to determine surface tension and viscosity from the measured frequency $\omega_{l,m}$ and damping time $\tau_{l,m}$. The assumption of low damping is usually not strictly fulfilled. The traditional equations of Lamb (Eq. 12.4) can deviate for the strongly damped case (very viscous sample) by more than 10%. For this cases of strong damping, an improved expression for viscosity (for $l = 2$) was derived by Lofhöfer [17]

$$\frac{1}{\eta} = \frac{20\pi R}{3M} \tau_2 \left(1 - \left(\frac{18}{125} \frac{1}{\omega_2 \tau_2} \right)^{1/2} \right) \tag{12.5}$$

The measurement uncertainties for the surface tension consists only of the uncertainty of the measurement of the sample mass M and the uncertainty in determination of the oscillation frequency ω_2. The uncertainty of the surface oscillation frequency is determined by the frame rate, recording duration, etc. and is typically better than $\pm 0.25\%$. The measurement uncertainty of the mass is typically about $\pm 0.1\%$. The mass loss during processing is often negligible due to the relatively low surface to volume ratio of the 6–8 mm diameter samples. Hence, it is possible to obtain the surface tension with an accuracy of about $\pm 0.6\%$. This estimation is based on the assumption that the sample is free of adsorbents from the surrounding atmosphere.

The measurement uncertainty of the viscosity is determined by the measurement uncertainty of the sample average radius R, the mass M, and the damping time constant τ_2. In the widely undisturbed ISS-EML environment, the damping time constant can typically be obtained with an accuracy of $\pm 1\%$. The radius can be obtained with an accuracy of about $\pm 0.8\%$. This leads to a precision of the viscosity close to $\pm 2\%$. However, other effects that can further disturb the accuracy of the determination of the damping time constant, such as sample precession, are not considered in this estimation.

Another assumption, which is strictly not valid for real oscillating droplets, is the assumption of infinitely small oscillation amplitudes. It has been shown that the oscillation frequency decreases quadratically with increasing amplitude [18]. A methodology using a simple fitting procedure was developed by Xiao et al. [19]. However, it was shown that these nonlinear effects do not have a measurable influence on the damping time constant [20]. In the case of an additional sample rotation, the oscillation frequency is known to shift [21, 22]. For cases where the rotation axis is known, a method for correction for the frequency shift was demonstrated, using the oblate shape deformation of the sample [23].

3 Electrical Resistivity and Density

The temperature-dependent electrical resistivity of metallic melts has technological relevance for crystal growth under the influence of electromagnetic fields. Furthermore, the electrical resistivity depends on the scattering of electrons on the atoms in the liquid, as well as on the Fermi vector [24–27]. The radial distribution function of the liquid as well as the Fermi vector are influenced by the temperature [24–27]. Hence, temperature-dependent differences of the short-range order should be reflected by the temperature-dependent electrical resistivity. The electromagnetic heating field can serve as a noncontact diagnostic tool for the measurement of the electrical resistivity and the temperature-dependent density change of a liquid

droplet [28, 29]. The ISS-EML is equipped with a sample coupling electronics (SCE), which is utilized to measure the electrical resistivity of the processed sample. The SCE was developed by Georg Lohöfer (DLR Cologne) [30].

The basic effect used to determine the samples' electrical resistivity and density is the change of the coil's impedance that generates the electromagnetic heater field. The electromagnetic heater field induces eddy currents in the sample, which in turn generates another electromagnetic field. This field also induces a current in the primary coil [31, 32]. The sample can be viewed as an additional complex impedance [31, 32]. The measured impedance can be calculated for simple sample geometries, such as spherical samples [31, 32]. For a coil geometry that leads to a homogeneous field around the spherical sample, the sample impedance Z_s can be expressed as [30, 31]

$$Z_s(\omega_H, a, \rho) = c_c\, \omega_H\, a^3 \left(\frac{1}{q} - \frac{1}{q^2} + i\left(\frac{1}{q} - \frac{2}{3} \right) \right) \qquad (12.6)$$

where

$$q(\omega, a, \rho) = \frac{a}{\delta} = a\sqrt{\frac{\mu_0 \omega_H}{2\rho}} \qquad (12.7)$$

with the skin depth $\delta = \sqrt{2\rho/(\mu_0\omega_H)}$, where μ_0 is the magnetic vacuum permeability, a the sample radius, and ω_H the frequency of the coil current oscillation. This expression is an approximation, which is true under the circumstances realized in the ISS-EML and TEMPUS facilities, where $a/\delta \geq 3$. The heater field of the ISS-EML is generated by the coil arrangement connected to a 400 kHz rf power amplifier (see Fig. 12.1). In addition to the rf coil, a capacitor with capacitance C is connected in parallel to the heater coil (see Fig. 12.1). The total admittance Y_{tot} of the electrical heating circuit can hence be described as

$$Y_{tot} = \frac{I_0}{U_0} e^{-i\varphi} = 2i\omega_H C + \frac{2}{R_L + i\omega_H L + Z_s(\omega_H, a, \rho)/2} \qquad (12.8)$$

where L describes the coil inductance and R_L the coil resistance. To obtain the complex total admittance of the circuit, the sample coupling electronics (SCE) measures the current I_0, voltage U_0, as well as the phase angle φ between them. Measurements of I_0, U_0, and φ without a sample allow the determination of the circuit parameters R_L, L, and C. The coil constant c_c in Eq. 12.6 depends only on the coil geometry and can be calibrated by the measurement of a sample with well-known electrical resistivity, such as solid Zr. A more detailed description of the measurement principle is given in Ref. [30, 33].

In the experiment on a liquid $Si_{50}Ge_{50}$ performed in the ISS-EML facility [33], see Chap. 18 of this book, the electrical resistivity shows drastic departure from linear temperature dependency, which is attributed to structure formation in the melt.

In Chap. 20, the temperature-dependent resistivity was connected to the dynamics in the liquid melt. Another experiment, showing the merit of a precise temperature-dependent resistivity measurement in the undercooled state of a liquid, is that of Mohr et al. [34] (see Chap. 19).

4   Specific Heat

The temperature-dependent specific heat of the liquid phase is essential for modeling industrial solidification processes. Furthermore, the knowledge of specific heat in the solid and liquid phase enables the determination of the temperature-dependent thermodynamic driving force for solidification, crucially important for the development of new crystalline materials [35] or noncrystalline materials such as bulk metallic glasses [36, 37].

The heat capacity at constant pressure C_p is defined as the amount of heat dQ added to a substance to raise the temperature by dT while the pressure is kept constant. The heat capacity measurement in the liquid phase under container-based conditions is challenging, fraud with error, or in some cases even impossible due to the liquid melt's reactions with the container material. For this reason, the containerless measurement approach of the ISS-EML allows high-precision measurements of specific heat, free of systematic errors from container reactions and contaminations.

The exchange of heat of an object with its environment leads to a temperature change relative to the object's heat capacity. In order to apply container- and contactless measurement methods, relatively short relaxation times and, hence, short measurement times are favored. Typical adiabatic calorimeters have long relaxation times due to the insulation of the sample from the environment. The ac modulation technique for the measurement of thermophysical properties, first invented by Corbino 1910 [38], found its widest application in low-temperature heat capacity measurements [38, 39]. For the ac calorimetry method, the sample is in contact with a temperature reservoir and a heater. The heating power can be modulated, which leads to a modulated sample temperature [39]. For this method, the relaxation times can be relatively small, making it feasible for noncontact calorimetry [41].

The contact to the heat reservoir is given by the samples' heat loss by radiation and, in case of operation in inert gas atmosphere, additionally by the thermal transport in the surrounding gas [41]. The electromagnetic heater field transfers a heating power P_H into the sample, obtained from the heating coil current I_{coil} and a coupling factor $G_H(\rho_e, \omega_H, R)$. The coupling factor depends on the samples' specific electrical resistivity $\rho_e(T)$ and the radius of the sample $R(T)$ and the heaters' angular frequency ω_H. As a consequence of the changes in the sample's resistivity and radius, the em-coupling and hence the frequency ω_H is slightly varying as a function of the sample temperature. For considerations on the power dissipation in the sample, these variations are negligible. When the samples' radius R and resistivity

Fig. 12.6 Modulation
calorimetry cycle performed
in microgravity on board the
ISS. The sample is in the
liquid phase for about 9 min
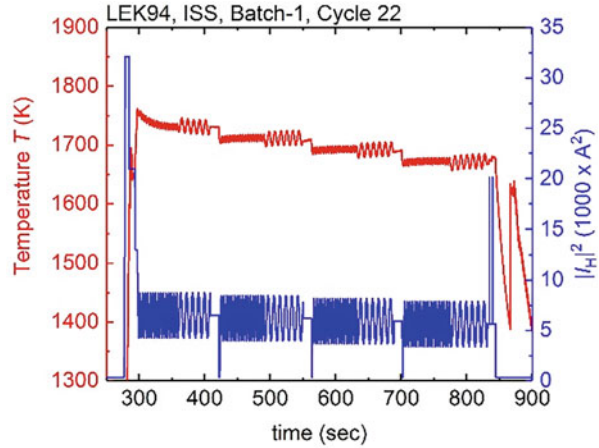
ρ_e are known as functions of temperature, the coupling factor $G_H(\rho_e(T), \omega_H, R(T))$ can be calculated by theoretical approaches, such as in Ref. [42] or [43], and suitable calibration with a known material. Since the assumption of perfect axial symmetry of the heating coils, made in [42], is not entirely fulfilled (feed lines to the coil), the deviation from the model presented in [42] is calibrated using ac calorimetry cycles performed on solid zirconium as a reference sample.

The most convenient way to modulate the heating power is by applying a power of the form

$$P_H(t) = P_{H0} + \Delta P_{av} + \Delta P_{mod} \sin(\omega_{mod} t + \varphi_0) \tag{12.9}$$

which requires a coil current of the following form [44, 45]

$$I_{coil}(t) = \sqrt{I_{H0}{}^2 + \Delta I_{coil}{}^2} \sin(\omega_{mod} t + \varphi_0). \tag{12.10}$$

The temperature response for a sinusoidal power modulation as given in Eq. 12.9 is [45]

$$T(t) = T_0 + \Delta T_{av}\left[1 - \exp\left(-t/\tau_{T,1}\right)\right] + \Delta T_{mod} \sin(\omega_{mod} t + \varphi_1) \tag{12.11}$$

where the term $\Delta T_{av}\left[1 - \exp\left(-t/\tau_{T,1}\right)\right]$ is the temperature response to the stepwise increase of the average heating power P_{H0} by ΔP_{av}. The relaxation time of this response is given by $\tau_{T,1}$. Furthermore, the last term is the response to the sinusoidal power modulation. The internal heat distribution is characterized by an internal relaxation time $\tau_{T,2}$, which furthermore leads to a phase shift $\varphi = \varphi_0 - \varphi_1$ between the temperature response and the heating power. Figure 12.6 shows a typical measurement cycle performed in the ISS-EML, where the sample is kept in the

liquid phase for several minutes. That way, the sample's heat capacity can be calculated by

$$C_p = \frac{\Delta P_{mod}}{\omega_{mod} \Delta T_{mod}} f(\omega_{mod}, \tau_{T,1}, \tau_{T,2}) \tag{12.12}$$

where f is a correction function taking the internal and external relaxation times into account. The time constant $\tau_{T,1}$ of the response to a stepwise power change is given by

$$\tau_{T,1} = \frac{C_p \cdot \Delta T_{av}}{\Delta P_{av}} \tag{12.13}$$

where C_p is the heat capacity of the sample. Equation 12.13 presents a second way to obtain C_p. But since the measurement of the amplitude of a sinusoidal temperature oscillation can be measured much more precisely than the absolute temperature rise ΔT_{av} and $\tau_{T, 1}$, the ac calorimetry method is preferred. If the stepwise change of average power ΔP_{av} and the resulting steps ΔT_{av} of the equilibrium temperature are small enough, the purely radiative heat loss in vacuum allows to describe the relaxation time as

$$\tau_{T,1} = \frac{C_p}{16\pi R^2 \varepsilon_{tot} \sigma_B T^3} \tag{12.14}$$

where ε_{tot} is the total hemispherical emissivity and σ_B the Stefan-Boltzmann constant. The cosine of the phase shift φ between the input power and temperature response can be described for small Biot numbers as [46]

$$\cos(\varphi) = \left(\frac{1}{\tau_{T,1} \tau_{T,2}} - \omega_{mod}^2 \right) \left[\left(\frac{1}{\tau_{T,1} \tau_{T,2}} - \omega_{mod}^2 \right)^2 + \left(\frac{1}{\tau_{T,1}} + \frac{1}{\tau_{T,2}} \right)^2 \omega_{mod}^2 \right]^{-\frac{1}{2}} \tag{12.15}$$

Knowing $\tau_{T, 1}$ and phase shift φ, the internal relaxation time $\tau_{T, 2}$ can be found numerically. For a sphere of radius R, the internal relaxation time can also be described as

$$\tau_{T,2} = \frac{3 C_p}{4\pi^3 \kappa R} \tag{12.16}$$

where κ denotes the effective thermal conductivity of the sample [41, 46]. Under the assumption that the fluid flow in the sample does not contribute to the thermal conduction, the thermal conductivity can be obtained using Eqs. 12.15 and 12.16. The application of magnetohydrodynamics simulations allows to extend the method for the measurement of the real thermal conductivity of the sample [47].

Fig. 12.7 Comparison of conventional DSC on a solid γ-Ti$_{48}$Al$_{48}$Nb$_2$Cr$_2$ sample and the ac calorimetry in the ISS-EML, performed for calibration/verification
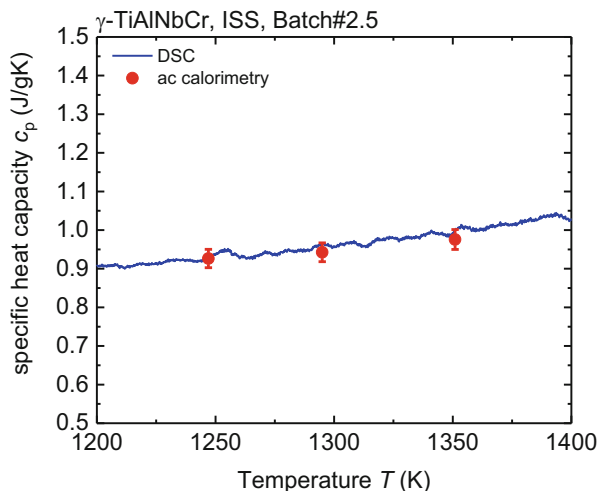
For metallic samples, the internal heat transport is typically much faster than the external heat loss [48]. It was shown that the sample's heat conductivity as well as the conductivity between the sample and the heat reservoir influence the temperature response [38, 40, 45]. That way, the temperature response is altered by a correction term $f(\omega_{mod}, \tau_{T,1}, \tau_{T,2})$ [39, 41]. This correction term is given as

$$f(\omega_{mod}, \tau_{T,1}, \tau_{T,2}) = \left(1 + \frac{1}{\omega_{mod}^2 \cdot \tau_{T,1}^2} + \omega_{mod}^2 \cdot \tau_{T,2}^2 + \frac{2K_b}{3K_s}\right)^{-1/2} \qquad (12.17)$$

where K_b and K_s are the thermal conductances between sample and reservoir and the sample's internal heat conductance. A proper parameter window for sample sizes, modulation frequency, etc., has been explored to either perform the experiment in or close to the adiabatic regime, for which the correction term becomes $f \approx 1$ and $\varphi \approx 90^\circ$ [41]. Much higher modulation frequencies are applied (see Fig. 12.6) to modulate in the nonadiabatic regime, thus allowing the analysis of the thermal conductivity. For the parameter range applied in most electromagnetic levitation studies shown in this book, the correction function's last term is small (<0.01). Simultaneously, the Biot number Bi $\sim \tau_{T,2}/\tau_{T,1}$ is often small (Bi << 1), under which circumstances the third term becomes negligible. Measurements of specific heat, obtained by this method, can be found in this book in Chaps. 15, 16, 17, and 19.

Further verification of the ac calorimetry method was done by applying the ac calorimetry method on a solid sample, which was also measured by conventional differential scanning calorimetry on ground. Figure 12.7 shows the comparison of the results for the specific heat c_P obtained by DSC measurements and by the ac calorimetry method, performed on solid γ-Ti$_{48}$Al$_{48}$Nb$_2$Cr$_2$. Within the measurement uncertainties, the obtained specific heat is identical for both methods.

The measurement uncertainty for the specific heat relies on the accurate determination of the temperature oscillation amplitude and the amplitude of the modulated power dissipation. The temperature can be measured with an accuracy of about ± 0.1 K, which translates to an accuracy of about $\pm 0.01\%$ to $\pm 0.005\%$. However, additional noise in the temperature data can be present due to precipitations on the sample surface or slight movements of the sample around the equilibrium position. The power dissipation, calculated from the electrical resistivity and coil geometry, is obtained with an accuracy mainly determined by the accuracy of the electrical measurement of the samples' resistivity and radius, which is possible about $\pm 0.05\%$ for the electrical resistivity. However, during the measurement, the sample is typically heated and as such is slightly distorted. The accuracy of the overall measurement is improved by the measurement of the sample diameter during measurement – leading to an effective sample diameter with an uncertainty in the order of the accuracy of the optical measurement method of about $\pm 0.05\%$. The sensitivity of the power dissipation to the sample resistivity is about 10^{-6} W/ ($\mu\Omega\cdot$cm) and about 10^{-3} W/mm for the sample radius. That way, the achievable accuracy of the specific heat can be estimated to be all better than $\pm 0.1\%$.

5   Total Hemispherical Emissivity

5.1   In Vacuum

In the simple case of a spherical, isothermal sample at temperature T_0, levitating freely in vacuum, the heat balance can be formulated as

$$C_{\mathrm{p}} \frac{\mathrm{d}T}{\mathrm{d}t} = P_0 - A\, \varepsilon_{\mathrm{tot}}\, \sigma_{\mathrm{B}}\, T_0{}^4 \qquad (12.18)$$

where $\varepsilon_{\mathrm{tot}}$ is the total hemispherical emissivity, σ_{B} the Stefan-Boltzmann constant, and P_0 the power input from an external heating source. In the steady-state case, $\mathrm{d}T/\mathrm{d}t = 0$ and the input power P_0 is equal to the radiated power $P_0 = A\, \varepsilon_{\mathrm{tot}}\, \sigma_{\mathrm{B}}\, T_0{}^4$. The increase of power input to $P_0 + \Delta P$ leads to a temperature rise to $T + \Delta T$. The solution of Eq. 12.18 is of the form $\Delta T(t) = \exp(-t/\tau_{\mathrm{T},1})$ with [41]

$$\tau_{\mathrm{T},1} = \frac{C_{\mathrm{p}}}{4\, A\, \varepsilon_{\mathrm{tot}}\, \sigma_{\mathrm{B}}\, T_0{}^3}. \qquad (12.19)$$

Typically, dedicated measurement cycles ("step cooling") in vacuum are used, where the heating power is reduced stepwise, while measuring the temperature transients. This way, a series of $\tau_{\mathrm{T},1}$ values are obtained as a function of temperature. The temperature-dependent total hemispherical emissivity can then be calculated with the help of Eq. 12.19.

The necessary quantities (heat capacity C_p, sample surface area A, and external relaxation time $\tau_{T,1}$) can be obtained with good accuracy (see above), which allows a precise measurement of the hemispherical emissivity with an accuracy typically better than $\pm 10\%$.

5.2 In Gas Atmosphere

Sometimes, it is not desired to perform long cycles in vacuum either due to a high evaporation rate of the sample (which inevitably adds to the layer of metal deposit on mirrors, reflectors, and the heating coil in the process chamber) or due to strong coupling of the sample to the positioning field, which could already heat the sample significantly in vacuum. Performing measurements in an inert gas atmosphere, such as in Ar or He, leads to lower evaporation onto mirrors and coil windings and a smaller impact of the positioner field on the sample temperature.

The fact that under microgravity buoyant convection does not occur in gas atmospheres simplifies the treatment of sample cooling in the presence of a gas atmosphere. Lohöfer and Schneider [49] described the gas cooling in the TEMPUS device in the case of free conductive cooling and in the case of forced gas convection. The application of the cooling model for conductive cooling in an atmosphere changes Eq. 12.19 to

$$C_p \frac{dT}{dt} = P_0 - A\,\varepsilon_{tot}\,\sigma_B\,T_0^{\,4} - P_{gas}(T) \tag{12.20}$$

where $P_{gas}(T)$ is the power loss into the gas. $P_{gas}(T)$ is given as [49]

$$P_{gas}(T) = \frac{4\pi R}{1 - R/b_g} \frac{\lambda_{0,g}}{\alpha_g + 1} \left(T^{\alpha_g+1} - (300\ \text{K})^{\alpha_g+1}\right) \tag{12.21}$$

with the heat conduction coefficients α_g and $\lambda_{0,g}$ and b_g depending on which kind of processing gas, Argon and/or Helium, is used. The model was verified in several parabolic flight campaigns using the TEMPUS device [49]. Since the coil geometry and sample holder geometry is similar in the ISS-EML device, the model can also be applied for the ISS-EML experiments. By the solution of Eq. 12.20 (in analogy to the solution of Eq. 12.18), we obtain the expression for the temperature relaxation time constant $\tau_{T,1}$ as

$$\tau_{T,1} = \frac{C_p}{4\,A\,\varepsilon_{tot}\,\sigma_B\,T^3 + \frac{4\pi R}{1-R/b_g}\,\lambda_{0,g}\,T^{\alpha_g}} \tag{12.22}$$

For verification, the same step cooling cycles were performed on solid zirconium in Ar and in vacuum. Figure 12.8a shows the verification measurement performed in
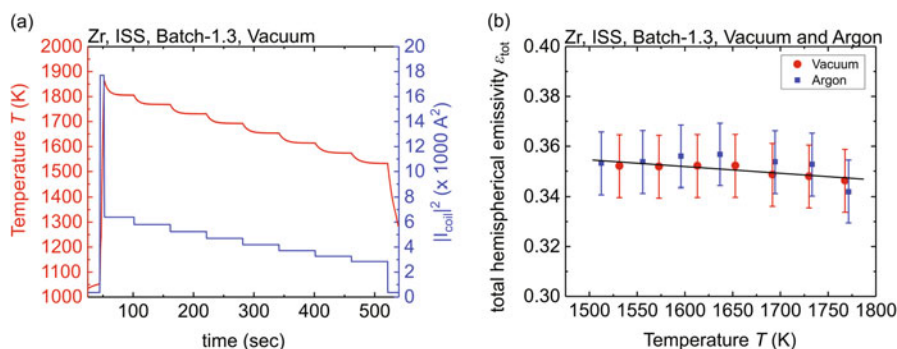
Fig. 12.8 (**a**) Step cooling cycle performed in vacuum on solid Zr. (**b**) Total hemispherical emissivity of Zr, measured in vacuum and in Argon atmosphere for calibration purposes

vacuum. Figure 12.8b shows the total hemispherical emissivity obtained for solid Zr between 1500 and 1800 K. The resulting total hemispherical emissivity, given in Fig. 12.8b, is identical for both measurement conditions, within the measurement uncertainty.

6 Conclusions

Many analytical methods to measure thermophysical properties of liquid droplets have been established and refined over the years. Several properties, such as the viscosity, can only be obtained using the presented methods while gravity is absent. In general, the experiments, such as the oscillating drop method, strongly benefit from the long-duration microgravity environment due to the higher stability of the sample position and consequently a higher achieved measurement precision. Furthermore, the electromagnetic levitator ISS-EML on board the International Space Station presents perfect conditions for experiments that require very long durations, such as the ac calorimetry.

References

1. H.-J. Fecht, R.K. Wunderlich, Fundamentals of liquid processing in low Earth orbit: From thermophysical properties to microstructure formation in metallic alloys. JOM **69**, 1261–1268 (2017). https://doi.org/10.1007/s11837-017-2417-4
2. M. Mohr, H.-J. Fecht, Investigating thermophysical properties under microgravity: A review. Adv. Eng. Mater. **23**, 2001223 (2021). https://doi.org/10.1002/adem.202001223
3. E. Trinh, Compact acoustic levitation device for studies in fluid dynamics and material science in the laboratory and microgravity. Rev. Sci. Instrum. **56** (1985)
4. P.-F. Paradis, W.-K. Rhim, Thermophysical properties of zirconium at high temperature. J. Mater. Res. **14**, 3713–3719 (1999). https://doi.org/10.1557/JMR.1999.0501

5. G. Lohöfer, P. Neuhaus, I. Egry, TEMPUS - a facility for measuring thermophysical properties of undercooled liquid metals. High. Temp. High. Press **23**, 333–342 (1991)

6. I. Egry, Structure and properties of molten metals, in *Treatise on Process Metallurgy*, (Elsevier, 2014), pp. 61–148

7. I. Egry, Properties, nucleation and growth of undercooled liquid metals: Results of the TEMPUS MSL-1 mission. J. Jpn. Soc. Microgravity. Appl. **15**, 215–224 (1998)

8. D.M. Matson, Retained free energy as a driving force for phase transformation during rapid solidification of stainless steel alloys in microgravity. npj Microgravity **4** (2018). https://doi.org/10.1038/s41526-018-0056-x

9. H. Fujii, T. Matsumoto, K. Nogi, Analysis of surface oscillation of droplet under microgravity for the determination of its surface tension. Acta Mater. **48**, 2933–2939 (2000). https://doi.org/10.1016/S1359-6454(00)00086-0

10. I. Egry, H. Giffard, S. Schneider, The oscillating drop technique revisited. Meas. Sci. Technol. **16**, 426–431 (2005)

11. S. Schneider, I. Egry, R. Wunderlich, et al., Evaluation of thermophysical data from electromagnetic levitation experiments with digital image processing. J. Jpn. Soc. Microgravity. Appl. **25**, 211–216 (2008)

12. F.R.S. Rayleigh, On the capillary phenomena of jets. Proc. R. Soc. **29**, 71–97 (1879)

13. H. Lamb, On the oscillations of a viscous spheroid. Proc. Lond. Math. Soc. **13** (1881)

14. W.H. Reid, The oscillations of a viscous liquid drop. Q. Appl. Math. **18**, 86–89 (1959)

15. S. Chandrasekhar, The oscillations of a viscous liquid globe. Proc. Lond. Math. Soc. **3–9**, 141–149 (1959)

16. P.V.R. Suryanarayana, Y. Bayazitoglu, Surface tension and viscosity from damped free oscillations of viscous droplets. Int. J. Thermophys. **12**, 137–151 (1991). https://doi.org/10.1007/BF00506127

17. G. Lohöfer, Viscosity measurement by the "oscillating drop method": The case of strongly damped oscillations. Int. J. Thermophys. **41**, 30 (2020). https://doi.org/10.1007/s10765-020-2608-z

18. J.A. Tsamopoulos, R.A. Brown, Nonlinear oscillations of inviscid drops and bubbles. J. Fluid Mech. **127**, 519–537 (1983)

19. X. Xiao, R.W. Hyers, R.K. Wunderlich, et al., Deformation induced frequency shifts of oscillating droplets during molten metal surface tension measurement. Appl. Phys. Lett. **113**, 11903 (2018). https://doi.org/10.1063/1.5039336

20. R.K. Wunderlich, M. Mohr, Non-linear effects in the oscillating drop method for viscosity measurements. High. Temp. Press **48**, 253–277 (2020). https://doi.org/10.32908/hthp.v48.648

21. F.H. Busse, Oscillations of a rotating liquid drop. J. Fluid Mech. **142**, 1–8 (1984). https://doi.org/10.1017/S0022112084000963

22. P. Annamalai, E. Trinh, T.G. Wang, Experimental study of the oscillations of a rotating drop. J. Fluid Mech. **158**, 317–327 (1985). https://doi.org/10.1017/S002211208500266X

23. M. Mohr, R.K.K. Wunderlich, S. Koch, et al., Surface tension and viscosity of Cu50Zr50 measured by the oscillating drop technique on board the International Space Station. Microgravity Sci. Technol. **31**, 177–184 (2019). https://doi.org/10.1007/s12217-019-9678-1

24. C.C. Bradley, T.E. Faber, E.G. Wilson, J.M. Ziman, A theory of the electrical properties of liquid metals II. Polyvalent metals. Philos. Mag. **7**, 865–887 (1962). https://doi.org/10.1080/14786436208212676

25. O. Dreirach, R. Evans, H.J. Guntherodt, H.U. Kunzi, A simple muffin tin model for the electrical resistivity of liquid noble and transition metals and their alloys. J. Phys. F Met. Phys. **2**, 709–725 (1972). https://doi.org/10.1088/0305-4608/2/4/015

26. H.J. Guntherodt, E. Hauser, H.U. Kunzi, et al., Negative temperature coefficients of electrical resistivity: The divalent liquid metals Eu, Yb and Ba. J. Phys. F Met. Phys. **6**, 1513–1522 (1976). https://doi.org/10.1088/0305-4608/6/8/011

27. G. Busch, H.J. Güntherodt, Hall-Koeffizient und spezifischer elektrischer Widerstand flüssiger Metallegierungen. Phys der Kondens Mater **6**, 325–362 (1967). https://doi.org/10.1007/BF02422512

28. G. Lohöfer, G. Pottlacher, Inductive measurement of thermophysical properties of electromagnetically levitated metallic melts. High. Temp. High. Press **40**, 237–248 (2011)

29. G. Lohöfer, Electrical resistivity measurement of liquid metals. Meas. Sci. Technol. **16**, 417–425 (2005). https://doi.org/10.1088/0957-0233/16/2/012

30. G. Lohöfer, High-resolution inductive measurement of electrical resistivity and density of electromagnetically levitated liquid metal droplets. Rev. Sci. Instrum. **89**, 124709 (2018). https://doi.org/10.1063/1.5065482

31. G. Lohöfer, Magnetization and impedance of an inductively coupled metal sphere. Int. J. Eng. Sci. **32**, 107–117 (1994). https://doi.org/10.1016/0020-7225(94)90153-8

32. G. Lohöfer, An electrically conducting sphere in a three-dimensional, alternating magnetic field. IMA J. Appl. Math. (Institute Math Its Appl) **68**, 1–21 (2003). https://doi.org/10.1093/imamat/68.1.1

33. Y. Luo, B. Damaschke, G. Lohöfer, K. Samwer, Thermophysical properties of a Si50Ge50 melt measured on board the International Space Station. npj Microgravity **6**, 10 (2020). https://doi.org/10.1038/s41526-020-0100-5

34. M. Mohr, R.K.K. Wunderlich, D.C.C. Hofmann, H.-J. Fecht, Thermophysical properties of liquid Zr52.5Cu17.9Ni14.6Al10Ti5—prospects for bulk metallic glass manufacturing in space. npj Microgravity **5**, 24 (2019). https://doi.org/10.1038/s41526-019-0084-1

35. M. Mohr, R. Wunderlich, Y. Dong, et al., Thermophysical properties of advanced Ni-based superalloys in the liquid state measured on board the International Space Station. Adv. Eng. Mater. **22**, 1901228 (2020). https://doi.org/10.1002/adem.201901228

36. S.C. Glade, R. Busch, D.S. Lee, et al., Thermodynamics of Cu47Ti34Zr11Ni8, Zr52.5Cu17.9Ni14.6Al10Ti5 and Zr57Cu15.4Ni12.6Al10Nb5 bulk metallic glass forming alloys. J. Appl. Phys. **87**, 7242–7248 (2000)

37. H.-J. Fecht, R.K. Wunderlich, S.C. Glade, W.L. Johnson, Thermophysical properties of bulk metallic glasses in the stable and undercooled liquid – A microgravity investigation. Materials Research Society Symposium – Proceedings (2001), pp. L4.5.1–L4.5.6

38. O.M. Corbino, Oscillazioni termiche delle lampade a filamento sottile percorse da correnti alternate, e conseguente effetto raddrizzatore per la presenza di armoniche pari. Nuovo. Cim. **19**, 75–84 (1910). https://doi.org/10.1007/BF02709856

39. P.F. Sullivan, G. Seidel, Steady-state, Ac-temperature calorimetry. Phys. Rev. **173**, 679–685 (1968). https://doi.org/10.1103/PhysRev.173.679

40. G.R. Stewart, Measurement of low-temperature specific heat. Rev. Sci. Instrum. **54**, 1–11 (1983). https://doi.org/10.1063/1.1137207

41. H.J. Fecht, W.L. Johnson, A conceptual approach for noncontact calorimetry in space. Rev. Sci. Instrum. **62**, 1299–1303 (1991). https://doi.org/10.1063/1.1142488

42. E. Fromm, H. Jehn, Electromagnetic forces and power absorption in levitation melting. Br. J. Appl. Phys. **16**, 653–663 (1965)

43. G. Lohöfer, Theory of an electromagnetically levitated metal sphere I: Absorbed power. SIAM J. Appl. Math. **49**, 567–581 (1989)

44. R.K. Wunderlich, H.-J. Fecht, Thermophysical property measurements by electromagnetic levitation methods under reduced gravity conditions. J. Jpn. Soc. Microgravity Appl. **20**, 192–205 (2003)

45. R.K. Wunderlich, H.-J. Fecht, R. Willnecker, Power modulation technique for noncontact high-temperature calorimetry. Appl. Phys. Lett. **62**, 3111–3113 (1993)

46. R.K. Wunderlich, H.-J. Fecht, Modulated electromagnetic induction calorimetry of reactive metallic liquids. Meas. Sci. Technol. **16**, 402–416 (2005)
47. X. Ye, *A Computational Study on Extension of Non-contact Modulation Calorimetry* (University of Massachusetts – Amherst, 2015)
48. R.K. Wunderlich, C. Ettl, H.-J. Fecht, in *Non-contact Electromagnetic Calorimetry of Metallic Glass Forming Alloys in Reduced Gravity* (European Space Agency, (Special Publication), ESA SP, 2000), pp. 537–544
49. G. Lohöfer, S. Schneider, Heat balance in levitation melting: Sample cooling by forced gas convection in Helium. High. Temp. High. Press **44**, 429–450 (2015)

Chapter 13
Modeling of Magnetohydrodynamic Flows in Electromagnetic Levitation

Gwendolyn P. Bracker and Robert W. Hyers

1 Overview

Electromagnetic levitation (EML) is widely used for a variety of investigations on nucleation, phase selection, and thermophysical properties, among others, on metals. The same electromagnetic forces that position the sample also drive internal flows. For some experiments, the objective is to minimize the flow. For others, the velocity, Reynolds number, or shear rate must be maintained below a particular threshold for critical phases of the experiment. Still, other experiments vary the flow over a wide range, using the flow as an independent variable and investigating the effects of the flow itself.

The internal flow of molten metal samples is difficult to directly observe due to the featureless and opaque nature of the surface. Additionally, molten metal samples require high temperatures and are highly reactive making the sample prone to contamination. While techniques exist to measure the flow of molten metal, these techniques require larger volumes of metal and conditions that are not present during levitation experiments. For EML, with only a few exceptions, the flow is characterized and quantified through modeling.

Prior work on flow effects in EML is reviewed elsewhere [1–4]. The methods used for modeling the flows are briefly summarized below, followed by some recent applications of the models.

G. P. Bracker · R. W. Hyers (✉)

Department of Mechanical and Industrial Engineering, University of Massachusetts, Amherst, MA, USA

e-mail: hyers@umass.edu

2 Modeling MHD Flow in EML

While the internal flow of the sample cannot be directly observed during the experiment, it can be calculated as a function of the applied electromagnetic field and the properties and dimensions of the sample. This is accomplished by evaluating the electromagnetic force field and the Navier-Stokes equations (Equation 13.1), using computational fluid dynamics (CFD) tools. For these experiments, the sample is discretized to solve Maxwell's equations (Equation 13.2) for locations inside the sample. The electromagnetic field is then interpolated to calculate the force on each element of the CFD mesh. To solve the internal flow of the sample, CFD software is used to analytically solve the Navier-Stokes equations with the force term added to account for the forces applied by the electromagnetic field.

Equation 13.1: Navier-Stokes Equations

$$\nabla \cdot \vec{V} = 0$$

$$\rho \frac{D\vec{V}}{Dt} = -\nabla p + \mu \nabla^2 \vec{V} + \rho \vec{F}$$

Equation 13.2: Maxwell's Equation, Magnetoquasistatic Form

$$\nabla \times \vec{E} = -\frac{\partial \vec{B}}{\partial t};$$

$$\nabla \times \vec{H} = \vec{J};$$

$$\nabla \cdot \vec{B} = 0$$

Equation 13.3: Reynolds Number

$$\mathrm{Re} = \frac{\rho u D}{\mu}$$

Equation 13.4: Magnetic Reynolds Number

$$\mathrm{Re}_{\mathrm{m}} = \frac{\tau_{\mathrm{m}}}{\tau_{\mathrm{conv}}} = \mu_0 \sigma_{\mathrm{el}} U_0 l_0$$

The magnetic Reynolds number (Equation 13.4) for EML droplets is much less than 1 [2], indicating that while the electromagnetic field and induced currents drive the flow in the liquid, the flow does not significantly perturb the electromagnetic field or induced currents. This one-way coupling means that the distribution of electromagnetic forces may be calculated only once, rather than being calculated at each time step or iteration, for steady-state conditions. For other conditions, including

simulations of droplet dynamics (e.g. [5]), changes in the shape of the drop require frequent updates to the calculated distribution of electromagnetic force. For these simulations, it is common to solve the flow and electromagnetic field simultaneously.

Another issue in the flow and associated modeling is turbulence. Depending on the sample and experimental conditions, the Reynolds number (Equation 13.3) of samples in EML ranges from much less than 1 to greater than 50,000. Experimental observations of a transition from laminar to turbulent flow in EML under well-characterized conditions were reported in [6], with models showing that the transitional Reynolds number was approximately 600. This result can be used to determine when to expect the flow to be laminar in experiments and is also often used to decide whether to use a turbulence model in calculations of the flow.

Different methods of modeling turbulent flow have been applied to EML calculations. Berry et al. [7] assessed several RANS-type turbulence models, concluding that the RNG k-ε model of [8] was the best of those considered. Bojarevics [9] prefers the k-ω model. For higher accuracy or further details of the flow, a direct numerical simulation of the turbulent flow (DNS) is needed. DNS has been applied to EML flows by Ai [10] and more recently by Shoji [11]. The latter simulation applied the DNS to determine the imposed DC magnetic field needed to cause a transition from turbulent to laminar flow in 1-g EML.

For many experiments, the required output of the model is not the full detailed flow field but only certain key parameters. Xiao et al. [12, 13] performed thousands of parametric simulations for flows in the ISS-EML for a range of sample properties and experimental parameters. They compiled these results to determine a polynomial fit for several key parameters, including maximum velocity, Reynolds number, and shear rate. As with all polynomial fits, the results are valid to the stated precision within the range of the input parameters but should be treated critically on extrapolation beyond these bounds. The polynomial fits allow quick estimation of the key parameters for many experiments.

3   Solidification Studies

EML experiments process samples in levitation, removing the interface between the melt and a container wall to reduce to opportunities for heterogeneous nucleation. This allows for solidification experiments to be conducted in the undercooled region of a melt. In EML experiments, undercoolings on the order of 200–300 °C are frequently observed. [14–16].

Microgravity EML has been used to study several different solidification phenomena including the formation of metastable phases [17, 18], coupled-flux nucleation [19, 20], and anomalous or dynamic nucleation [13, 15, 21]. These experiments require CFD modeling support to evaluate experimental parameters that are not
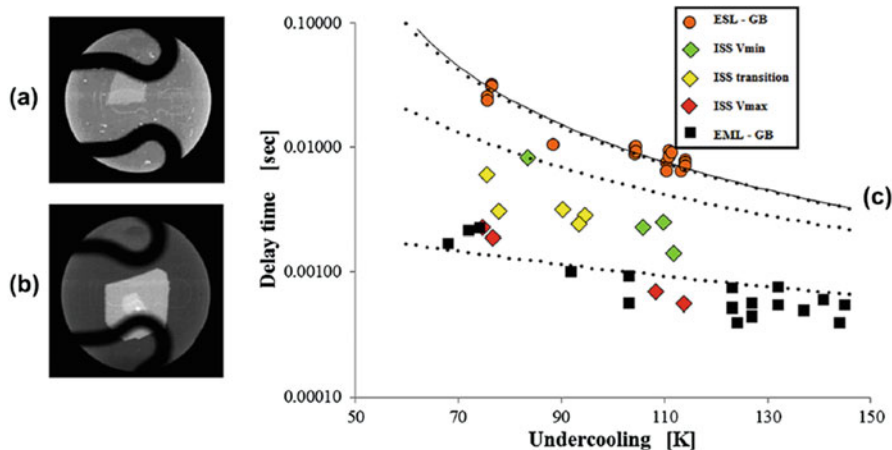
Fig. 13.1 Influence of convection on incubation time between nucleation of metastable phase and subsequent transformation to the stable phase in FeCr$_{20}$Ni$_{20}$: (**a**) Low stirring = long time, (**b**) high stirring = short time, and (**c**) relationship between delay and undercooling as a function of experimental conditions [22]

directly measurable. The mechanisms by which flow affects the nucleation and solidification differ in detail for each of these phenomena, so the modeling results needed differ accordingly.

In the first example, experiments on alloys that solidify by double recalescence show an effect of flow on the lifetime of the metastable phase. This lifetime is called "delay time," as it corresponds to the delay between primary and secondary recalescence. For the samples shown in Fig. 13.1, the delay time varies two orders of magnitude for the conditions shown [22]. These conditions span a range from almost zero flow (a few microns per second) (ESL-GB) to about 30 cm/s (EML-GB), with experimental conditions in ISS-EML spanning the range in between (Fig. 13.2) [22].

Matson [23] proposed that the fluid flow in the liquid affects the delay time through increasing the free energy of the new metastable solid, relative to its defect-free state. The resulting theory leads to a nondimensionalization of the delay time and driving free energy ("Dimensionless Driving Force"). As shown in Fig. 13.3, this formulation collapses the delay times to a single straight line for a wide range of Fe$_{(100-x-y)}$Cr$_x$Ni$_y$ compositions and convective conditions [23]. This figure also includes a wide range of undercoolings, which account for the distribution of similar symbols along the line.

The next example concerns the coupled-flux nucleation experiments described in [16, 20, 24]. In coupled-flux nucleation experiments, the probability of diffusion fields around subcritical nuclei interacting is of interest. This probability is a function of nonuniform flow fields in which subcritical nuclei on adjacent streamlines move at different velocities. For the diffusion fields to interact, the perpendicular distance between clusters must be smaller than that of the diffusion field, shown in Fig. 13.4.
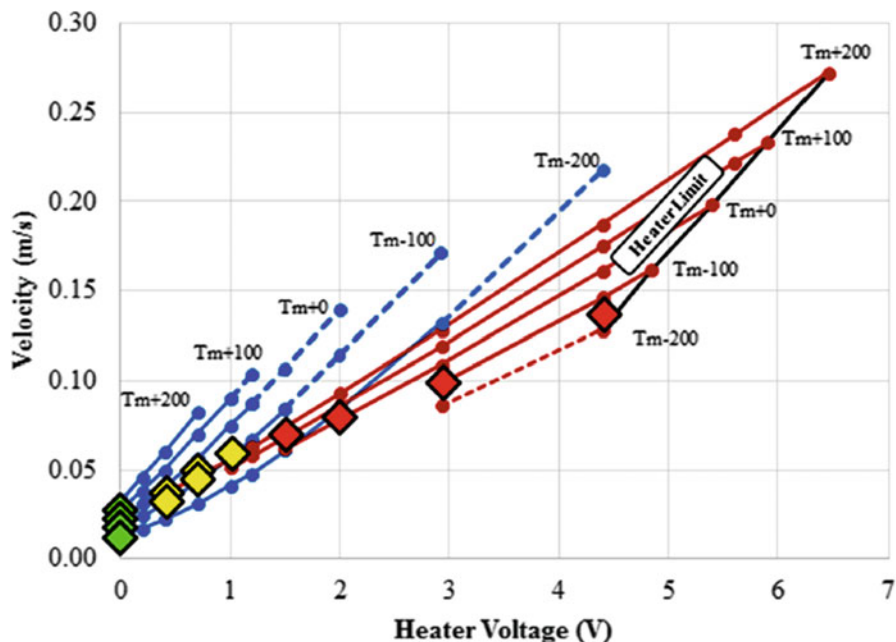
Fig. 13.2 Range of convection available in ISS-EML for different temperatures and control parameters for the sample in Fig. 13.1 [22]

The parameters of these experiments limit the shear-strain rate to ensure the diffusion fields around the nuclei do not interact.

The shear-strain rate contours are calculated using models of the electromagnetic force field applied to CFD simulations. In a positioner-dominated force field, the flow is driven into the sample near 45° from the axis of the sample where the EML forces are largest (Fig. 13.5). The shear-strain contours in Fig. 13.6 show that the largest shear-strain rates are located in places with large directional changes in the flow, such as where flow turns inward at the surface of the sample. Under heater-dominated conditions, the flow is driven into the sample along the equator of the sample and returns to the surface near the poles of the sample (Fig. 13.7). Heater-dominated flow can be seen in Fig. 13.8.

The last example concerns anomalous or dynamic nucleation in undercooled liquid metals. The kinetics of classical nucleation is such that even a small decrease in undercooling causes a very large decrease in the nucleation rate. For example, for a Zr sample that nucleates heterogeneously at 330 K undercooling, holding at 250 K undercooling reduces the nucleation rate by a factor of 3×10^{17}. This factor would change the nucleation time from, for example, 1 ms to 1 million years. It should be possible to hold the sample at modest undercooling for quite some time without nucleation.

However, it has been observed for Zr in vacuum that the maximum hold time is not years but a few minutes [15, 21]. Recent experiments [21] showed that in 18 out
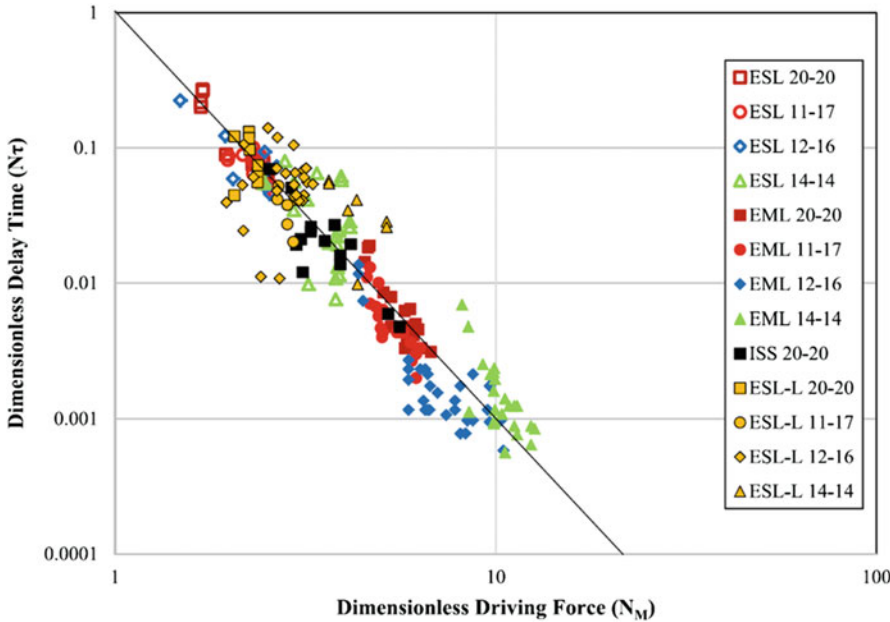
Fig. 13.3 Nondimensionalization of delay time vs. driving free energy for $Fe_{(100-x-y)}Cr_xNi_y$ samples in different conditions [23]. Open symbols represent no-flow conditions in ESL, and filled represent fully turbulent conditions in single-frequency EML. ISS laminar-transitional-turbulent flows (black) and laminar Marangoni flow ESL with laser on (yellow) are also included for comparison. The samples in Fig. 13.1 are presented here as "ESL 20-20," "ESL-L 20-20," "EML 20-20," and "ISS 20-20"

Fig. 13.4 Diffusion fields surrounding subcritical nuclei will interact in a time determined by the spacing and shear rate [20]
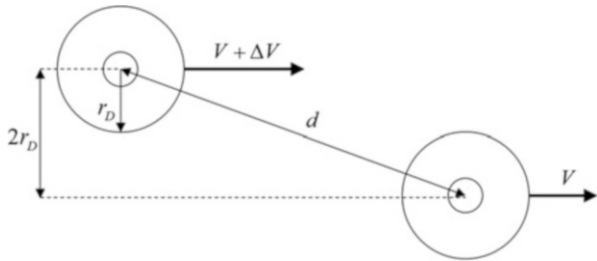
of 19 cycles, with isothermal holds at undercoolings between 47 and 287 K, the sample solidified in less than 600 s, even though on free cooling, the sample reached over 324 K undercooling before solidification. MHD calculations were performed to quantify the flow in the sample for each condition, to test the theory that the recirculating flow caused the nucleation of the solid by a cavitation mechanism. Homogeneous nucleation of bubbles was ruled out; however, excitation of existing defects in the liquid could not be ruled out. Any effect of variations in the flow over
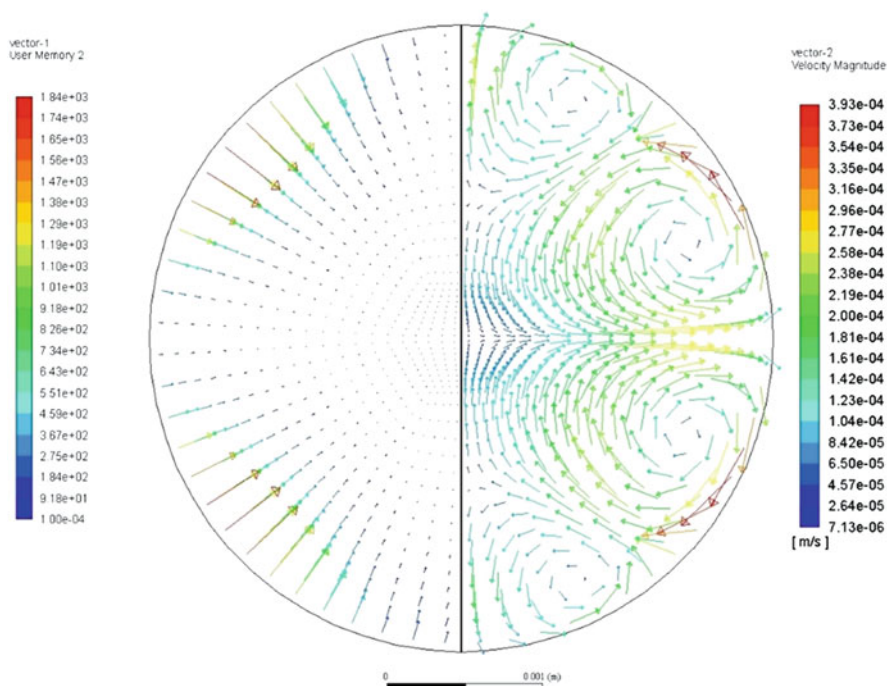
Fig. 13.5 (Left) Electromagnetic force and (right) resulting flow for $Ti_{39.5}Zr_{39.5}Ni_{21}$ sample under positioner-dominated flow conditions

the experimentally accessible range was overwhelmed by the variation in the time to nucleation [21].

4   Viscosity

Containerless processing provides an advantageous environment to study the fundamental thermophysical properties of a melt. In traditional processing, the high temperatures and reactivity of metal melts limit to options for a suitable contact surface that will not melt or react with the sample. Further, containerless processing removes the interface between the melt and its container reducing the risk of contamination and allowing access to the undercooled region of the melt due to the reduced opportunity for heterogeneous nucleation.

The oscillating drop method is used to measure the surface tension and viscosity of the melt. In oscillating drop experiments, a levitation sample is melted and held at the temperature of interest. Then EML forces are used to excite surface oscillations on the surface of the sample. The frequency and damping of the surface oscillations are observed and quantified using a high-speed camera. The surface tension and
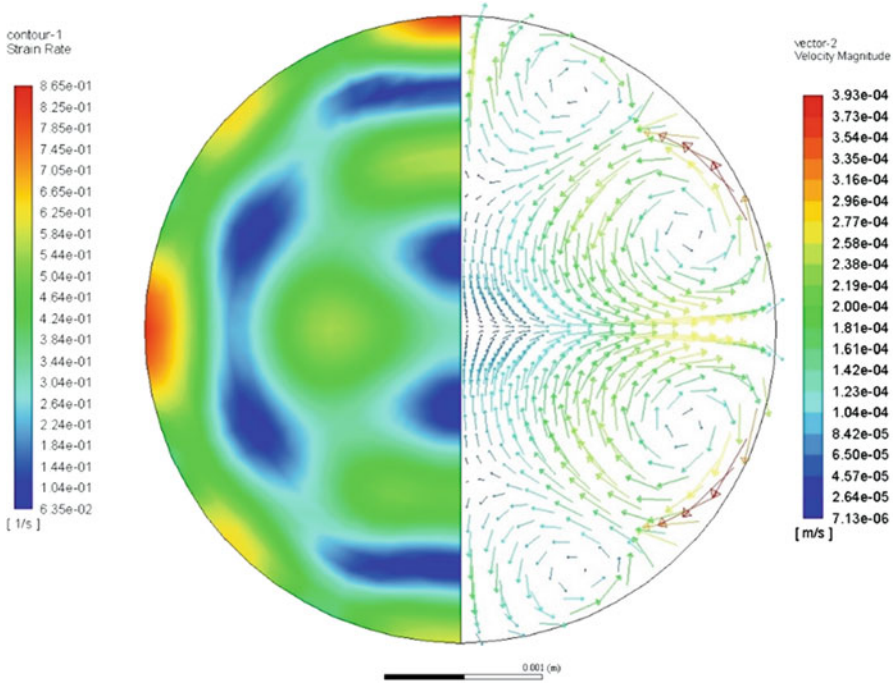
Fig. 13.6 Shear strain rate (left) and velocity (right) for TiZrNi sample under positioner-dominated flow conditions

viscosity of the melt are related to the frequency and damping of the oscillations using the given relations:

Equation 13.5: Rayleigh Equation Relates Oscillation Frequency to Surface Tension [25]

$$f_l = \left(\frac{l(l-1)(l+2)\gamma}{3\pi m} \right)^{1/2}$$

Equation 13.6: Lamb Equation Relates Damping Increment to Viscosity [26]

$$\tau_l = \frac{\rho R_0^2}{(l-1)(2l+1)\mu}$$

The oscillating drop experiments assume that the damping of the sample is controlled by only the redistribution of momentum by the viscosity of the melt. Experience shows that laminar MHD flows have a negligible effect on the damping of the oscillations. However, during turbulent flow, the turbulent eddies redistribute
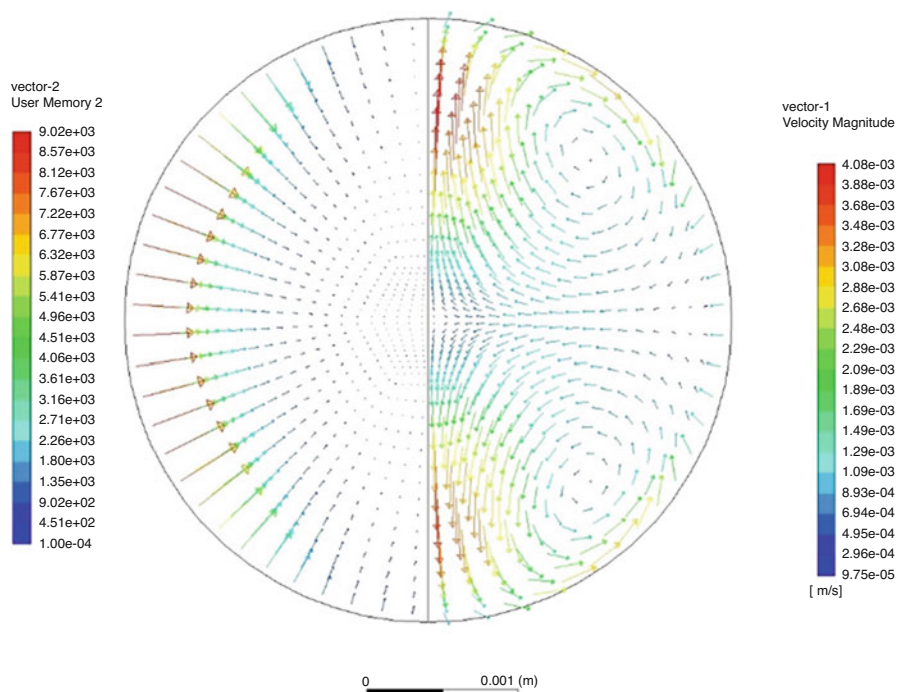
Fig. 13.7 (Left) Electromagnetic force and (right) resulting flow for TiZrNi sample under heater-dominated flow conditions

the momentum and provide additional damping. As a result, the observed oscillation damping does not correspond to the fundamental viscosity of the melt alone but reflects both the viscosity and turbulence in the sample. Therefore, Equations 13.5 and 13.6 assume the internal flow of the drop to be laminar. It is necessary to evaluate the flow prior to processing to ensure the accuracy of the measurements taken using the oscillating drop method.

Turbulent flow is more common in samples with higher electrical conductivity and lower viscosities. During EML experiments on gold samples and a gold-copper alloy samples, the observed damping corresponded to a viscosity nearly an order of magnitude higher than expected at the melting temperature [27]. Later experiments are planned for the ISS-EML facility to further investigate the thermophysical properties of gold. CFD calculations giving the flow and corresponding Reynolds Number for different experimental parameters, shown in Fig. 13.9, determined that any applied heater current results in turbulent flow [28].
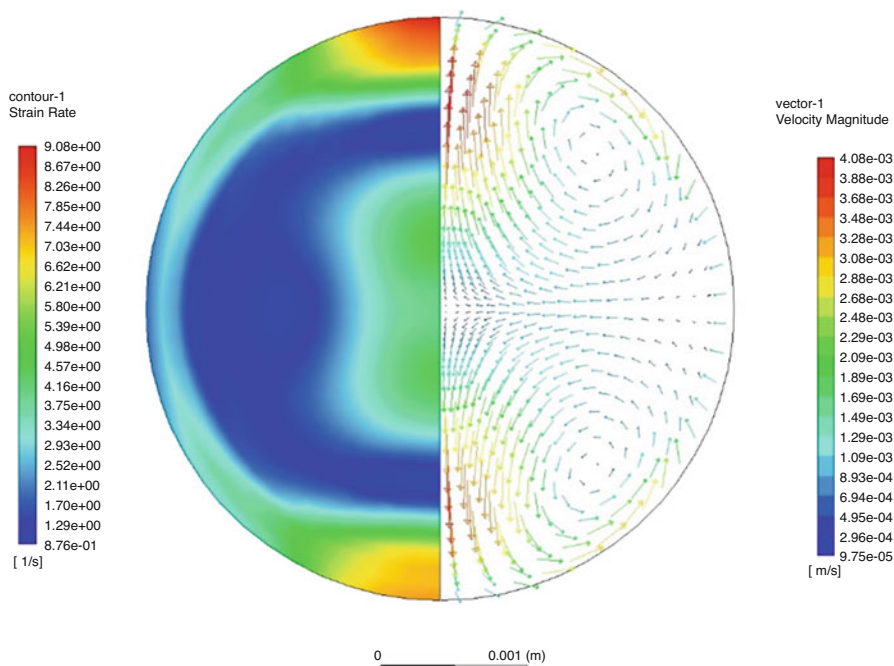
Fig. 13.8 Shear strain rate (left) and velocity (right) for TiZrNi sample under heater-dominated flow conditions

5 Thermal Conductivity

Thermal conductivity is a property with importance both to fundamental science and to applications in space exploration and aviation. Fundamentally, thermal conductivity is one property that characterizes a material's response to energy input. Changes in thermal conductivity reflect changes in the structure of the liquid. Better measurements will allow us to come closer to being able to predict thermal conductivity for new materials.

The key applications of thermal conductivity of liquid metals are in additive manufacturing, welding, and casting. Present methods for measuring thermal conductivity of liquid metals at high temperature are inadequate, particularly for reactive and undercooled metals.

Current modeling software is used in the casting industry to use the properties of the melt with mold geometry to predict the properties and structure of a cast part. Accurate measurements of thermal conductivity are critical to enable the modeling produce accurate results. In casting industries, models reduce waste when casting new parts. In addition, these models are the most likely path to producing parts by additive manufacturing with the repeatability, reliability, and certification needed for use in aerospace applications.
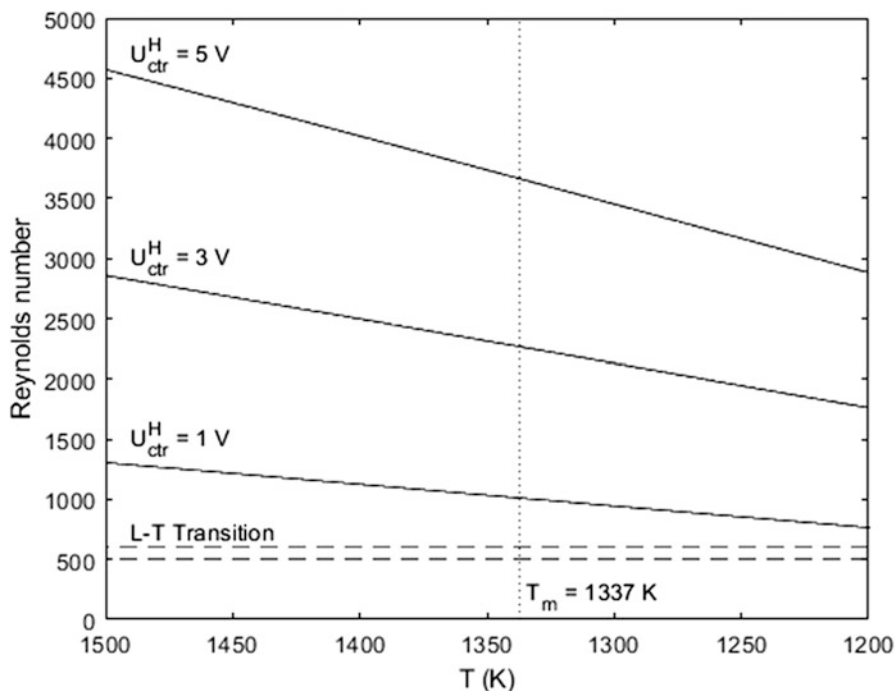
Fig. 13.9 Calculated Reynolds number vs. temperature for Au sample, various experimental parameters [28]. The sample is predicted to be turbulent for all of the accessible conditions

5.1   History and Principles of EML Modulation Calorimetry

Modulation calorimetry has been widely applied since the first theoretical work of Corbino in 1910 [29] and was first adapted to noncontact use in electromagnetic levitation (EML) by Fecht and Johnson with their 1991 paper [30] and extended by Wunderlich and Fecht [31]. This method was validated on solid niobium samples [32–34]. However, the large shape changes due to turbulent fluid flow from the strong positioning forces needed in 1 g prevented the application of this method to liquid samples in ground-based levitation.

EML modulation calorimetry was employed in microgravity on three Space Shuttle flights using TEMPUS: STS-65 IML-2, STS-83 MSL-1, and STS 97 MSL-1R. Measurements continue on the ISS-EML, including those described elsewhere in this volume [35]. Under microgravity conditions, the reduced stirring allowed stable, quiescent measurements on a range of samples, including pure metals and glass-forming alloys. These measurements confirmed the basic method for measuring specific heat while suggesting the possibility of measuring thermal conductivity if the effect of fluid flow could be accounted for appropriately [31, 36, 37].
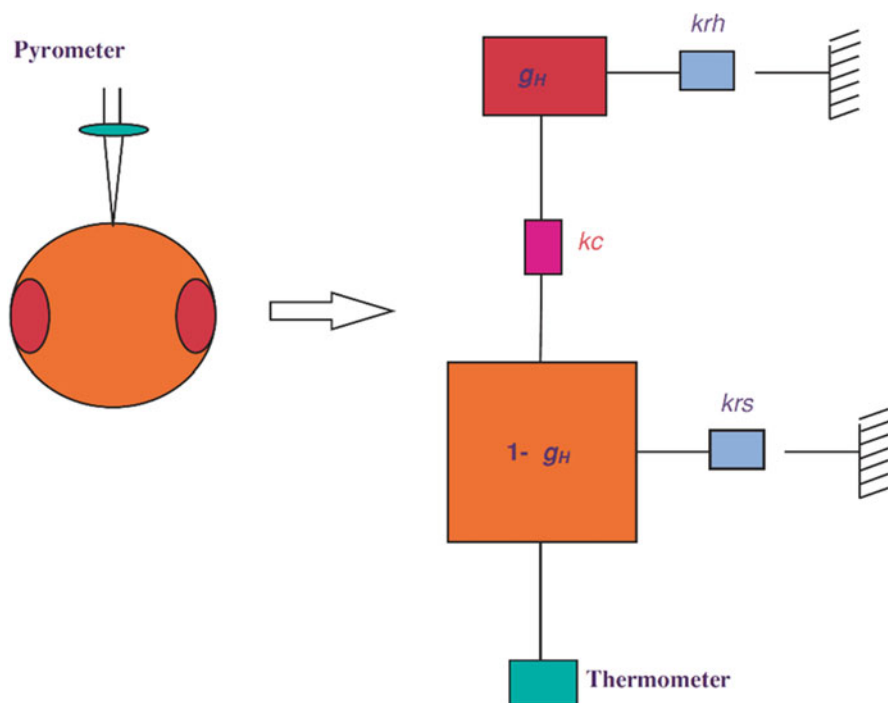
Fig. 13.10 Wunderlich's two-reservoir model of the internal heat flow in the sample in EML modulation calorimetry. g_H is the heated volume, and k_c is the conductive coupling between the two reservoirs [37]

The response of a sample to a sinusoidal heat input is a sinusoidal variation in temperature, with a phase lag determined by the properties of the sample. The principle of operation of EML modulation calorimetry is to use that phase lag to determine the specific heat of the sample. In order to relate the experimentally observed temperature response to the properties of the sample, Wunderlich [31] developed a simple two-reservoir model (Fig. 13.10) which captures the critical physics of this response.

When the sample is heated by an alternating electromagnetic field, the induced currents, and therefore the heating, are confined to a small region near the surface. The magnitude of the current falls exponentially with a characteristic distance called the skin depth. This distribution, shown in Fig. 13.11, was idealized as a "heated" and an "unheated" volume, connected by thermal conduction [31], as shown in Fig. 13.10. The volumes of the "heated" and "unheated" fractions, and the geometry factor in the conduction equation linking them, were determined empirically [31]. Since the coupling between the "heated" and "unheated" fractions is determined by the thermal conductivity of the sample, EML modulation calorimetry should be able to measure thermal conductivity as well.

Fig. 13.11 Calculated heating power distribution (left) and temperature distribution (right) for an FeCrNi alloy under isothermal holding simulation. The heating current is 135 A and positioning current is 150 A. The maximum temperature of the sample is 1543.7 K and the minimum 1539.9 K. The maximum difference in surface temperature is 1.38 K
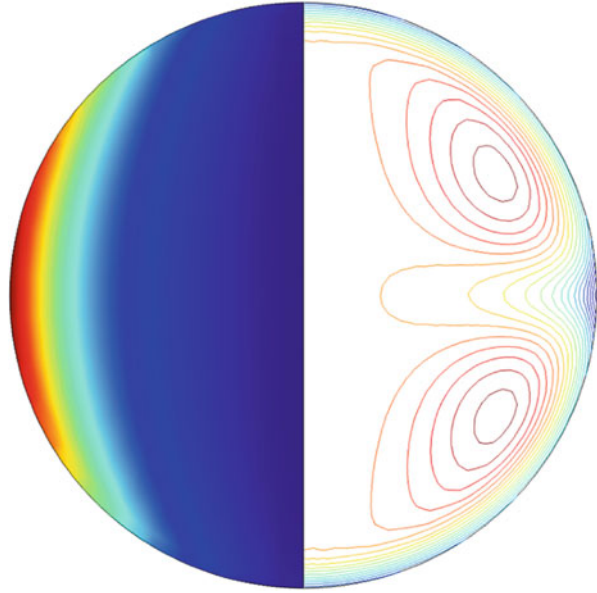
In this model, the thermal conductivity of the sample is related to the internal relaxation time τ_2 by Equation 13.7, where g_H is the "heated volume fraction" of the sample (see Fig. 13.10), γ is an empirical geometric factor, and δ is the electromagnetic skin depth.

Equation 13.7: Relationship Between Thermal Conductivity and Parameters in the Two-Reservoir Model [31]

$$k = \frac{C_p g_H (1 - g_H)}{4\pi(R - \gamma\delta)\tau_2}$$

5.2 Thermal Conductivity by EML Modulation Calorimetry

Modulating the power at a different frequency than the optimal one for measuring specific heat generates a phase shift that highlights the conductive coupling within the sample. For solid samples with purely conductive internal heat transfer, the simple model gives the thermal conductivity within a systematic error of about 10% [31].

This model uses only two regions to model the thermal response of the sample and so cannot resolve the actual distribution of temperature and heat input. Furthermore, this two-reservoir model does cannot consider motion of the liquid, even

though such convection is almost always a more important mechanism of heat transfer than conduction.

Even for highly viscous liquids like the glass-forming alloy $Zr_{65}Al_{7.5}Cu_{17.5}Ni_{10}$, with a viscosity of 0.27 Pa-s at 1024 K [30], Wunderlich reports his 2001 method for the thermal conductivity measurement gives errors of +81% and +112%, respectively, for the two temperatures he discusses. He attributed these errors to convection in the sample, which caused a faster relaxation of the thermal gradients than would be caused by the conduction alone, as was assumed in his model.

Etay et al. [38] also looked into the measurement of thermal conductivity. Their results confirmed a large effect of convection on the measurement of thermal conductivity but were not able to quantify the contribution or to provide a correction.

Successful noncontact measurements of thermal conductivity have been made in ground-based EML with a strong DC magnetic field imposed to damp convection [39]. This method does not require reduced gravity, nor is it available in reduced gravity to date. MHD models show that a field of the order 4T is required for the measurement of the thermal conductivity of Si [40].

5.3   Thermal Conductivity by EML Modulation Calorimetry Including Convective Effects

Ye [41] was able to quantify the effect of internal flow, using a finite element model with 6424 elements, vs. the two reservoirs of the analytical model. This high spatial resolution allows a physically accurate representation of the distribution of temperature and heating within the sample. The model was validated by comparison to experimental measurements that used a *solid* Nb sphere.

This model also includes the magnetohydrodynamic flow driven by the electromagnetic levitator. Through transient simulations of the response of the sample to different input parameters, Ye was able to determine the value of thermal conductivity for a wide range of convective conditions [41]. These simulations were used to build a correlation between the observed temperature response of the sample and the true thermal conductivity, for various combinations of sample size, heating, emissivity, and viscosity.

For the MSL-1 TEMPUS system, Ye determined [41]:

- For viscosity >1 Pa-s, the effect of convection is negligible, and the thermal conductivity as determined by the 2001 analysis of [31] is accurate, subject only to the systematic error of about 10% due to the simple model in this analysis. Note that only deeply undercooled glass-forming metals reach this viscosity.
- For 1 Pa-s > viscosity > 0.1 Pa-s, the error introduced by convective effects is comparable to the systematic error. The sample case outlined above lies in this range. This range is typical of moderately undercooled glass-forming and deeply undercooled quasicrystal-forming alloys.

- For 0.01 Pa-s > viscosity > 0.1 Pa-s, the measurement of thermal conductivity is dominated by the convective contribution. In this range, the numerical analysis of Ye is needed to determine any reasonable estimate of thermal conductivity. *Most industrial alloys have viscosities in the lower part of this range for the temperatures of interest for casting and additive manufacturing*.
- For viscosity <0.01 Pa-s, the measurement may be possible for particular conditions, but Ye does not draw conclusions about the general applicability of the method in this range. Recent advances in the precision and accuracy of the measurement of viscosity of liquid metals warrants revisiting this range of properties, where most of the pure elements reside.

Other parameters for further improvement of the precision and accuracy to explore include larger temperature perturbations and sample size effects.

6   Summary and Conclusion

Magnetohydrodynamic flow in electromagnetic levitation is an inherent feature of this method for liquid samples, as the flow is driven by the same forces that position the sample. Some experiments are conducted in reduced gravity to reduce the magnitude of the forces required. Even so, the flows affect many different types of experiments, whether the flow must be minimized, kept below a limit, or varied widely as an independent experimental parameter. Models of the MHD flow are the only practical method for evaluating the magnitude and distribution of the flow for almost all samples in EML. The MHD models enable a wide range of experiments that aim to improve practical knowledge and fundamental understanding of many different phenomena in liquid metals.

References

1. R.W. Hyers, Fluid flow effects in levitated droplets. Meas. Sci. Technol. **16**(2), 394–401 (2005). https://doi.org/10.1088/0957-0233/16/2/010
2. R. W. Hyers, in *Fluid Flow Effects in Electromagnetically Levitated Droplets*. Presented at the Proceedings of the Sohn international symposium on advanced processing of metals and materials: principles, technologies and industrial practice, San Diego (August 2006)
3. S.I. Bakhtiyarov, D.A. Siginer, *Electromagnetic Levitation Part I: Theoretical and Experimental Considerations* (2008), p. 14
4. L. Gao et al., Applications of electromagnetic levitation and development of mathematical models: A review of the last 15 years (2000 to 2015). Metall. Mater. Trans. B **47**(1), 537–547 (2016). https://doi.org/10.1007/s11663-015-0522-8

5. V. Bojarevics, R.W. Hyers, Levitated liquid dynamics in reduced gravity and gravity-compensating magnetic fields. JOM **64**(9), 1089–1096 (2012). https://doi.org/10.1007/s11837-012-0417-y

6. R.W. Hyers, G. Trapaga, B. Abedian, Laminar-turbulent transition in an electromagnetically levitated droplet. Metall. Mater. Trans. B **34**(1), 29–36 (2003). https://doi.org/10.1007/s11663-003-0052-7

7. S. Berry, R.W. Hyers, B. Abedian, L.M. Racz, Modeling of turbulent flow in electromagnetically levitated metal droplets. Metall. Mater. Trans. B **31**(1), 171–178 (2000). https://doi.org/10.1007/s11663-000-0142-8

8. V. Yakhot, S.A. Orszag, Renormalization group analysis of turbulence. I. Basic theory. J. Sci. Comput. **1**(1), 3–51 (1986). https://doi.org/10.1007/BF01061452

9. V. Bojarevics, K. Pericleous, Modelling electromagnetically levitated liquid droplet oscillations. ISIJ Int. **43**(6), 890–898 (2003). https://doi.org/10.2355/isijinternational.43.890

10. X. Ai, The instability analysis and direct numerical simulation of turbulent flows in electromagnetically levitated droplets (2004). [Online]. Available: https://research.libraries.wsu.edu:8443/xmlui/handle/2376/186. Accessed 20 May 2021

11. E. Shoji et al., Numerical simulation of laminar-turbulent transition in magnetohydrodynamic convection in an electromagnetically levitated molten droplet of Cu-Co alloys under a static magnetic field. Metall. Mater. Trans. B **52**(2), 896–902 (2021). https://doi.org/10.1007/s11663-021-02063-3

12. X. Xiao, J. Lee, R.W. Hyers, D.M. Matson, Numerical representations for flow velocity and shear rate inside electromagnetically levitated droplets in microgravity. Npj Microgravity **5**(1), Art. no. 1 (2019). https://doi.org/10.1038/s41526-019-0067-2

13. X. Xiao, R.W. Hyers, D.M. Matson, Surrogate model for convective flow inside electromagnetically levitated molten droplet using magnetohydrodynamic simulation and feature analysis. Int. J. Heat Mass Transf. **136**, 531–542 (2019). https://doi.org/10.1016/j.ijheatmasstransfer.2019.03.028

14. P. Galenko et al., Solidification kinetics of a Cu-Zr alloy: ground-based and microgravity experiments. IOP Conf. Ser. Mater. Sci. Eng. **192**, 012028 (2017). https://doi.org/10.1088/1757-899X/192/1/012028

15. W.H. Hofmeister, R.J. Bayuzick, R. Hyers, G. Trapaga, Cavitation-induced nucleation of zirconium in low earth orbit. Appl. Phys. Lett. **74**(18), 2711–2713 (1999). https://doi.org/10.1063/1.123945

16. A.K. Gangopadhyay et al., Demonstration of the effect of stirring on nucleation from experiments on the International Space Station using the ISS-EML facility. ArXiv210316439 Cond-Mat (2021). [Online]. Available: http://arxiv.org/abs/2103.16439. Accessed 14 May 2021

17. O. Shuleshova, W. Löser, D. Holland-Moritz, D. Herlach, J. Eckert, Solidification and melting of high temperature materials: In situ observations by synchrotron radiation. J. Mater. Sci. **47**(11), 4497–4513 (2012). https://doi.org/10.1007/s10853-011-6184-2

18. W. Loeser, O. Shuleshova, Nucleation and solidification kinetics of metastable phases in undercooled melts, in *Solidification of Containerless Undercooled Melts*, (Wiley-VCH Verlag GmbH & Co. KGaA, 2012)

19. P.F. Wei, K.F. Kelton, R. Falster, Coupled-flux nucleation modeling of oxygen precipitation in silicon. J. Appl. Phys. **88**(9), 5062–5070 (2000). https://doi.org/10.1063/1.1311309

20. R.W. Hyers, D.M. Matson, K.F. Kelton, J.R. Rogers, Convection in containerless processing. Ann. N. Y. Acad. Sci. **1027**(1), 474–494 (Nov. 2004). https://doi.org/10.1196/annals.1324.038

21. G.P. Bracker, S. Schneider, R. Wunderlich, H. Fecht, J. Zhao, R.W. Hyers, Confirmation of anomalous nucleation in zirconium. JOM **72**(9), 3140–3146 (2020). https://doi.org/10.1007/s11837-020-04257-7

22. D.M. Matson et al., Use of thermophysical properties to select and control convection during rapid solidification of steel alloys using electromagnetic levitation on the space station. JOM - J. Miner. Met. Mater. Soc. **69**, 1311–1318 (Aug. 2017). https://doi.org/10.1007/s11837-017-2396-5

23. D.M. Matson, Retained free energy as a driving force for phase transformation during rapid solidification of stainless steel alloys in microgravity. Npj Microgravity **4**(1), Art. no. 1 (2018). https://doi.org/10.1038/s41526-018-0056-x

24. A.K. Gangopadhyay, R.W. Hyers, K.F. Kelton, Nucleation and thermophysical properties of glass-forming liquids. JOM **64**(9), 1109–1117 (2012). https://doi.org/10.1007/s11837-012-0422-1

25. L. Rayleigh, *On the Capillary Phenomena of Jets* (Royal Society of London, 1879). [Online]. Available: http://archive.org/details/philtrans00740187. Accessed 7 May 2020

26. H. Lamb, On the oscillations of a viscous spheroid. Proc. Lond. Math. Soc. **s1-13**(1), 51–70 (1881). https://doi.org/10.1112/plms/s1-13.1.51

27. T. Tempus, Containerless processing in space: Recent results, in *Materials and Fluids Under Low Gravity*, (Berlin, Heidelberg, 1996), pp. 233–252. https://doi.org/10.1007/BFb0102523

28. G. Bracker et al., The effect of flow regime on surface oscillations during electromagnetic levitation experiments. High Temp.-High Press. **49**(1–2), 49–60 (2019)

29. E. Gmelin, Classical temperature-modulated calorimetry: A review. Thermochim. Acta **304–305**, 1–26 (1997). https://doi.org/10.1016/S0040-6031(97)00126-3

30. H.J. Fecht, W.L. Johnson, A conceptual approach for noncontact calorimetry in space. Rev. Sci. Instrum. **62**(5), 1299–1303 (1991). https://doi.org/10.1063/1.1142488

31. R.K. Wunderlich, C. Ettl, H.-J. Fecht, Specific heat and thermal transport measurements of reactive metallic alloys by noncontact calorimetry in reduced gravity. Int. J. Thermophys. **22**(2), 579–591 (2001). https://doi.org/10.1023/A:1010739318317

32. R.K. Wunderlich, H.-J. Fecht, Specific heat measurements by non-contact calorimetry. J. Non-Cryst. Solids **156–158**, 421–424 (1993). https://doi.org/10.1016/0022-3093(93)90210-O

33. R.K. Wunderlich, H.-J. Fecht, R. Willnecker, Power modulation technique for noncontact high-temperature calorimetry. Appl. Phys. Lett. **62**(24), 3111–3113 (1993). https://doi.org/10.1063/1.109626

34. H.-J. Fecht, R.K. Wunderlich, Development of containerless modulation calorimetry for specific heat measurements of undercooled melts. Mater. Sci. Eng. A **178**(1), 61–64 (1994). https://doi.org/10.1016/0921-5093(94)90519-3

35. M. Mohr, Thermophysical property measurements in the ISS-EML, in *Metallurgy in Space: Recent results from ISS (this volume)*, ed. by H.-J. Fecht

36. R. Wunderlich, D. Lee, W. Johnson, H.-J. Fecht, Noncontact modulation calorimetry of metallic liquids in low Earth orbit. Phys. Rev. B Condens. Matter. **55** (1997). https://doi.org/10.1103/PhysRevB.55.26

37. R.K. Wunderlich, H.-J. Fecht, Modulated electromagnetic induction calorimetry of reactive metallic liquids. Meas. Sci. Technol. **16**(2), 402–416 (2005). https://doi.org/10.1088/0957-0233/16/2/011

38. P. Schetelat, J. Etay, *Electromagnetic Stirring Effect on Thermal Conductivity of a Levitated Sample* (2008)

39. H. Kobatake, H. Fukuyama, I. Minato, T. Tsukada, S. Awaji, Noncontact measurement of thermal conductivity of liquid silicon in a static magnetic field. Appl. Phys. Lett. **90**(9), 094102 (2007). https://doi.org/10.1063/1.2710220

40. T. Tsukada, K. Sugioka, T. Tsutsumino, H. Fukuyama, H. Kobatake, Effect of static magnetic field on a thermal conductivity measurement of a molten droplet using an electromagnetic levitation technique. Int. J. Heat Mass Transf. **52**(21), 5152–5157 (2009). https://doi.org/10.1016/j.ijheatmasstransfer.2009.04.020

41. X. Ye, *A Computational Study on Extension of Non-contact Modulation Calorimetry* (University of Massachusetts Amherst). https://doi.org/10.7275/6757685.0

Chapter 14
Influence of Convection on Phase Selection

Douglas M. Matson

1 Introduction

Convection during solidification is often unavoidable. Processes such as welding involve significant field-induced melt-pool stirring. Conventional casting processes include inherent flow during mold-filling operations while continuous casting involves internal shrinkage-driven flow. It is desirable to understand how this flow influences phase selection on a local level to control properties and limit the formation of unwanted defect structures within a commercial product. Understanding the solidification path during competitive nucleation and growth of different crystal phases, with later transformation to the final microstructure during thermal treatment, is the goal for process modelers.

When processing molten metal alloys, the reactive nature of the melt can result in unwanted contamination due to reactions with crucible walls. During rapid solidification, undercooling of the melt results in the potential for a variety of nonequilibrium crystal structures to form. In order to study these phenomena, the influence of heterogeneous nucleation along the walls of the container must be eliminated. Levitation processing is used to process molten metals in a containerless fashion.

Previous chapters have discussed the broad range of conditions that are accessible using containerless levitation processing techniques. One of the prime differences between electrostatic levitation (ESL) and electromagnetic levitation (EML) is the level of melt stirring that is induced. Ground-based ESL methods decouple heating and levitation such that quiescent melt conditions may be achieved in a vacuum environment. Terrestrial EML methods require that large magnetic fields be employed to achieve levitation against gravity. Heating and levitation are coupled,

D. M. Matson (✉)
Department of Mechanical Engineering, Tufts University, Medford, MA, USA
e-mail: douglas.matson@tufts.edu

and cooling is only achieved by flowing gas across the sample surface. As discussed in the previous chapter on magnetohydrodynamic modelling (Chap. 13), significant convection results. In space, EML levitation and heating may be decoupled to a large degree since gravity is no longer a factor. The induced stirring is now a controlled experimental parameter with flows ranging from laminar to fully turbulent – thus accessing conditions between the extremes afforded by ground-based ESL and EML [1]. Testing may be accomplished in a vacuum to slow the cooling rate or in gas to reduce evaporation and thus limit compositional shifts due to differential evaporation of volatile alloy components [2].

Two international collaborations were assembled to leverage the unique environment afforded by microgravity testing in Low-earth Orbit (LEO) onboard the International Space Station (ISS) using the European Space Agency (ESA) electromagnetic levitation facility (ISS-EML) [3, 4]. One, as discussed in the next chapters, concentrated on measuring thermophysical properties to support quantification of the convection and melt shear present during space testing and the other to investigate phase selection during rapid solidification over a wide range of metal alloy systems. This chapter addresses evaluations supporting the latter of these two programs. We go to space not because the prime concern is microgravity solidification but rather because in space, we can access conditions where convection and melt shear are controllable, selectable experimental parameters during rapid solidification.

2   Alloy Selection

Commercially important iron-based alloys make up an extremely important segment of the world metal production capacity. The ternary FeCrNi system representing stainless steels has both pseudo-binary eutectic character when the ternary phase diagram is sectioned at constant Fe isopleths, and peritectic character when sectioned at constant solute ratio. This is seen in Fig. 14.1 where two solvent concentrations (72 wt% Fe and 60 wt% Fe) are displayed. The diagram presents dotted lines representing the metastable extensions from the equilibrium phase diagram to show how the metastable bcc delta phase and the stable fcc gamma phase would interact with the liquid if the other phase was suppressed, as could happen during nonequilibrium rapid solidification at high undercooling. The minimum undercooling that is required is the difference between stable and metastable liquidus temperatures ΔT_s as shown by the bold vertical lines at each composition in the figure. For the 72 wt% Fe isopleth, as the Cr content increases, the minimum undercooling decreases. Note that the 12-16 alloy and the 20-20 alloy have approximately the same minimum undercooling.
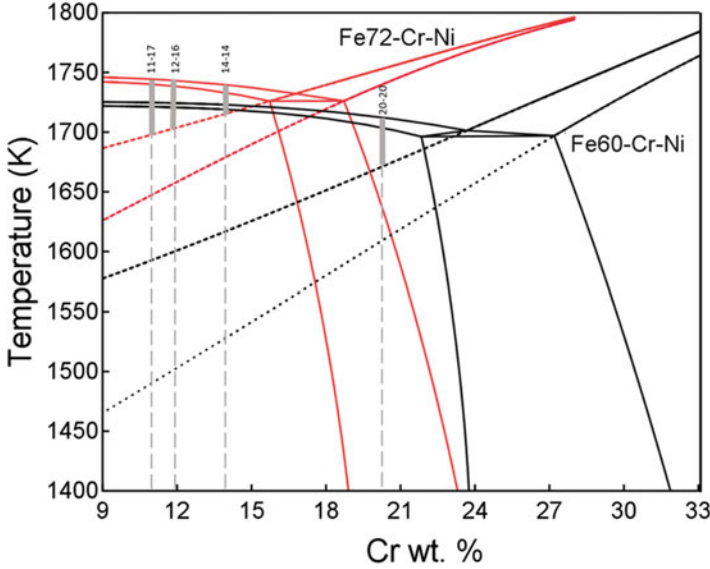
Fig. 14.1 Stainless steel alloys investigated using ground-based ESL, EML, and the ISS-EML facility under microgravity conditions

$$\Delta T_{\mathrm{s}} = T_{\mathrm{s}} - T_{\mathrm{m}} \tag{14.1}$$

During rapid solidification, the melt cools below the equilibrium stable phase liquidus to form a metastable liquid. If undercooled to a temperature below the metastable liquidus, solidification proceeds with formation of the metastable phase first, with an associated recalescence or temperature rise, and then a subsequent transformation at some later time to the stable phase, again with a new second associated recalescence. This is shown in Fig. 14.2 where the isothermal delay between the nucleation of the first and second phases is seen for two conditions. A long delay is observed at shallow undercoolings (condition 1), and a short delay is seen at deep undercoolings (condition 2). Note that both primary undercoolings are greater than the minimum undercooling required to access the metastable phase ΔT_{s}.

The duration of the isothermal hold is observed to be a weak function of undercooling and a strong function of melt convection as seen in Fig. 14.3 which shows the delay undercooling behavior for a series of ternary FeCrNi stainless steel alloys. Alloy composition is indicated by solute concentration in the form of Cr-Ni content in wt% (balance Fe). Each composition is given a different symbol, and open symbols represent no-flow condition during ground-based ESL testing while filled symbols represent turbulent flow conditions during ground-based EML testing. Crosses represent ISS-EML test results. At the time of this writing, only the 60Fe-20Cr-20Ni (20-20) alloy has been tested over a broad range of stirred conditions in
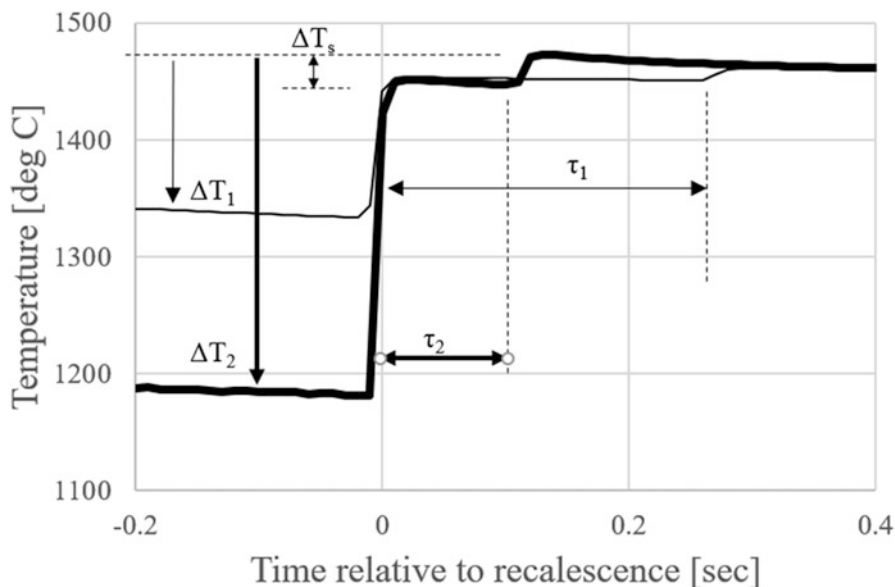
Fig. 14.2 Delay time behavior for shallow (1) and deep (2) undercoolings on a 72Fe-16Cr-12Ni (wt%) alloy during space levitation processing

space although the 72Fe-12Cr-16Ni (12-16) alloy has been manifested for additional future ISS-EML testing.

Several trends are apparent. First, as discussed earlier, as undercooling increases, the delay time becomes shorter for all alloys investigated. Second, ESL data with no induced stirring clusters at long delay times (top of the figure), while EML data with high stirring clusters at short delay times (bottom of the figure). Third, the space data, with variable intermediate stirring levels, clusters between these extremes. Careful evaluation of the space data shows that data taken under laminar flow conditions exhibits long delay times while data taken under turbulent flow conditions exhibit short times with transitional flow behavior distributed between [5]. Lastly, within the 72 wt% Fe isopleth, the delay times become longer as the Cr content increases. This final observation is consistent with the phase diagram presented in Fig. 14.1 where the thermodynamic driving force ΔT_s decreases with increasing Cr; with a lower driving force to promote nucleation of the second phase, we would anticipate longer delay times.
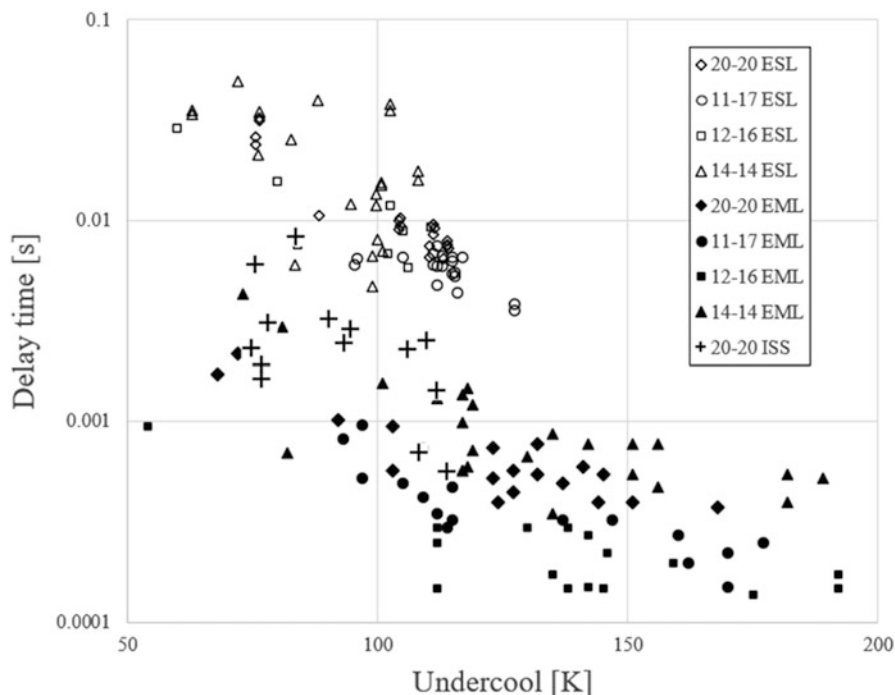
Fig. 14.3 Relating delay time to undercooling for several ternary compositions within the FeCrNi alloy family for quiescent conditions (ESL), turbulent conditions (EML), and a range of induced stirring between these extremes (ISS-EML)

3   Physical Model

For FeCrNi, if the sample is undercooled more than ΔT_s, to a temperature below the metastable phase liquidus, then it is possible to nucleate either metastable bcc δ-ferrite or stable fcc γ-austenite. Since the energy penalty associated with the surface-free energy of the bcc phase is much lower than that for the fcc phase, ferrite nucleates first [6]. Ferrite grows into the undercooled liquid raising the temperature of the sample to the metastable liquidus. After an isothermal incubation delay, stable phase nucleation occurs through heterogeneous nucleation of a dual spherical cap cluster [7] located along sub-grain boundaries within the metastable phase [8]. Subsequent growth of the stable phase occurs along the liquid/solid boundaries within the metastable mushy zone [9] and results in a second rise in temperature to the stable phase liquidus. This process is known as double recalescence. The transformation fully melts the metastable phase and results in a new, fragmented dendritic microstructure [10]. The location of the secondary nucleation site is often associated with the location of the primary site because that point has been solid longest, or it is associated with regions where convection and melt shear are highest [11].

Calculations show that the activation energy barrier for conversion from ferrite to austenite during the isothermal delay is rather large [6, 7] and that the energy associated with existence of a low-angle sub-grain tilt boundary is a significant factor in achieving interface potency. Since boundary misorientation relates to the concentration of defects, mainly as an aligned array of dislocations, this determines the surface energy of the low angle tilt boundary [12], the cluster wetting angle, and the cluster size [13].

Combining these observations with classical nucleation theory (CNT) [14] exposes an underlying contradiction. CNT adequately explains nucleation of the primary metastable phase from the melt. However, since during double recalescence the temperature is constant at the metastable liquidus T_s, it would be expected that the delay between first and second recalescence would be constant and independent of primary undercooling since the thermodynamic driving force that drives nucleation and subsequent transformation is defined as

$$\Delta G_s = \frac{\Delta H_s \, \Delta T_s}{T_s} \tag{14.2}$$

Under these conditions, the principle of microstructural reversibility [15] implies that the delay time τ is inversely related to the driving force ΔG_T raised to the fourth power [16] which is functionally in agreement with work proposed by Kantrowicz [17] and Kashchiev [18, 19]:

$$\tau = -\frac{\kappa \, k_B \, T_m}{\beta \left(\frac{\partial^2 \Delta G}{\partial n^2} \right)} = \frac{128 \, \pi \, k_B \, T_m \, \gamma^3 \, f(\theta)}{\beta \, \Delta G_T^4} \left(\frac{N_A}{\Omega} \right)^2 \tag{14.3}$$

Furthermore, since secondary nucleation occurs at grain boundaries within the metastable dendrites located inside the mushy zone, convection should not influence cluster formation. The mushy zone is composed of an array of fine dendrites surrounded by quiescent fluid, and any melt convection that was occurring prior to primary solidification has been effectively dampened out by the metastable array at the initiation of the delay period. According to CNT, prior melt shear accompanying this flow should not influence subsequent stable phase nucleation processes.

To resolve these two difficulties, the Retained Damage Model [20, 21] was proposed. This model is based on relating metastable growth conditions to that encountered during cold working of a metal. During cold working processes, defect energy is introduced into the solid phase to drive subsequent microstructural evolution such as recrystallization of the primary phase or transformation to new secondary phases. Alternately, if the initial solid is formed at slow growth rates when undercooling approaches zero, then a more perfect defect-free structure will form. The defect concentrations will also be lower in the absence of melt convection. These effects are commonly observed during growth associated with single crystal pulling operations. Deviation from idealized formation of "perfect" crystal structures

would be expected when undercooling is increased or when stirring of the melt is present.

Since tracking of the contribution by individual defect structures is difficult, a global approach is adopted where the energy contributed by various crystal defects, for example, vacancies, dislocations, or grain boundaries, is summed. Damage energy that is introduced during primary rapid solidification is subsequently retained in the metastable microstructure to promote later conversion to the stable phase. This retained damage is assumed to come from two sources: undercooling and melt shear. With this additional energy, the transformation from metastable to stable phase has a driving force ΔG_T that is the sum of three components: the first is ΔG_s from CNT and the phase diagram and the other two from retained damage energy where ΔG_m comes from undercooling and ΔG_c comes from melt convection.

$$\Delta G_T = \Delta G_s + \Delta G_m + \Delta G_c \qquad (14.4)$$

4   Influence of Undercooling

Damage-free energy from undercooling of the primary melt can be quantified based on the undercooling of the liquid below the metastable liquidus. Under these conditions, a limit exists where the maximum energy that could possibly be retained is equal to the driving force for primary recalescence ΔG_m based on the metastable undercooling ΔT_m defined by the metastable liquidus and the undercooled melt temperature T. If microstructural healing occurs during the incubation delay period, then this quantity should be reduced by a factor f_x with extreme values of zero if the defect structures were fully healed such that no retained damage contribution would exist to a value of one if all damage energy were retained.

$$\Delta T_m = T_m - T \qquad (14.5)$$

$$\Delta G_m = f_x \frac{\Delta H_m \, \Delta T_m}{T_m} \qquad (14.6)$$

Data taken from ground-based electrostatic levitation experiments is used to evaluate this factor. The analysis strategy is based on the observation that the first term in Eq. 14.4 is known from the equilibrium phase diagram based on parameters available from thermophysical property calculations for the stable phase, while the third term is zero because ESL experiments are run with zero-induced flow such that there will be no contribution from convection. The second term is only a function of the unknown healing factor, known thermophysical properties of the metastable phase and the primary melt temperature T. Thus, the experimentally determined undercooling defines a known driving force ΔG_T that is to be reduced by the healing

factor. This can be compared to a predicted driving force from Eq. 14.3 based on the observed experimental delay time. The ratio of these two values represents the unknown healing factor which, for the stainless steel alloys investigated as part of this study, was found to approach one, $f_x \rightarrow 1$, such that all damage energy was retained [16].

5 Influence of Melt Shear

As presented in the previous chapter, magnetohydrodynamic simulation is used to predict convection and melt shear within the molten droplet. The accessible range of flows can be evaluated as a function of alloy based on knowledge of the temperature dependence of thermophysical properties for the melt [5, 22]. As shown in the following chapters, these measurements can be conducted on the specific sample used in space at the time that the experiment is to be run over the range of temperatures that are observed for the thermal profile of any given melt cycle. Thus, dynamic changes in flow and melt shear can be evaluated as the test progresses. By developing a surrogate model that includes the influence of melt temperature on density, viscosity, and electrical conductivity over the range of values anticipated for any metallic system, the specific flow conditions during recalescence can be predicted [5, 23]. This can be accomplished for low-flow, rapid-cooling conditions where positioner control settings dominate [24] or high-stirring conditions where heater control settings dominate [25].

As done in the previous section, the unknown contribution to retained damage energy can be determined from experimental measurements of delay as a function of undercooling. Now with the known values of f_x, ΔG_s and ΔG_m, the only unknown in Eq. 14.4 is the final term, and the sum is again compared to the prediction from Eq. 14.3 to obtain the missing contribution from convection ΔG_c.

Since we have assumed that nucleation requires the existence of heterogeneous nucleation sites associated with low-angle tilt boundaries and that these boundaries form through development of an array of dislocations, it is logical to attempt to relate the damage energy to dislocation energy. From isotropic continuum elasticity theory, the Read-Shockley model [26] relates the strain fields surrounding dislocation cores to the number of dislocations required to impart the boundary misalignment angle. This energy is a linear function of angle and thus of dislocation concentration. Although it is unlikely for an alignment of dislocations to account for all damage, the form of the equation provides a guide for estimating the contribution from melt shear to retained damage energy. If we assume that the dislocation strain energy is proportional to the retained damage energy and that the dislocation concentration, and thus tilt angle, is proportional to melt shear $\dot{\gamma}$, an equation results relating melt shear to damage energy.
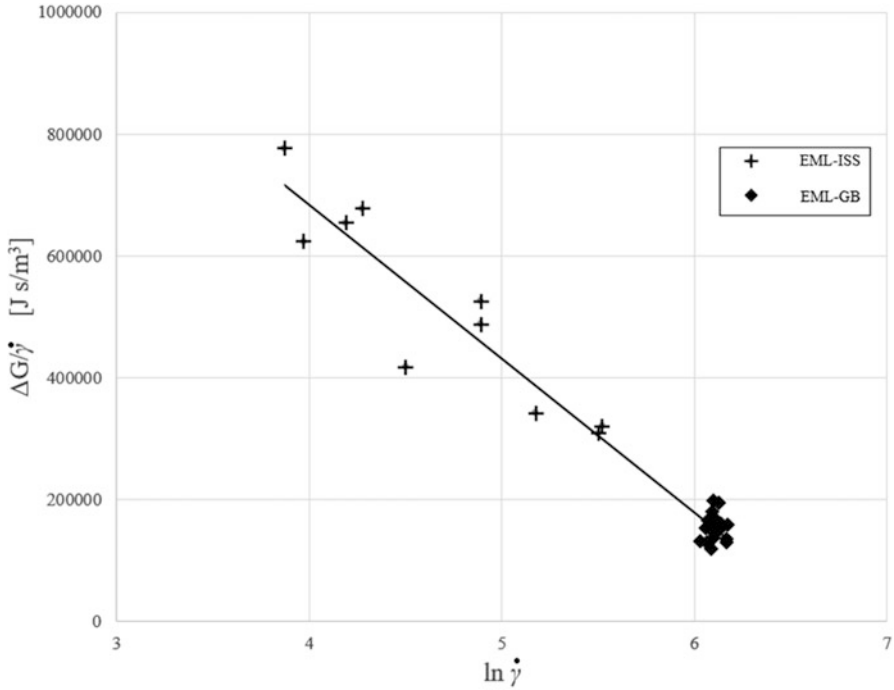
Fig. 14.4 Empirical evaluation of modified Read-Shockley parameters

$$\Delta G_c = f_x \quad \Delta_m \dot{\gamma} \left[\Delta_b / \Delta_m - \ln \dot{\gamma} \right] \tag{14.7}$$

Thus, a plot of the ratio of the retained energy and the shear rate as a function of the natural logarithm of shear rate will yield a straight line with slope Δ_m and intercept Δ_b. The ISS-EML data is used for this evaluation since the unique environment of microgravity in space allows for testing across a wide range of convective conditions with melt shear predicted by magnetohydrodynamic modeling. This treatment is shown in Fig. 14.4 for the space test results on the 20-20 steel alloy. Included are ground-based EML test results under high melt shear conditions. The resulting values for the empirical fit parameters are $\Delta_m = (2.52 \pm 0.012) \times 10^5$ Js/m^2 and $\Delta_b = (1.69 \pm 0.009) \times 10^6$ Js/m^2 such that prediction of delay time is uniquely defined with knowledge of the sample undercooling and melt shear. Note that in Eq. 14.3, there is only one adjustable parameter, representing the cluster atomic attachment rate β, which is defined from the experimental plot of delay versus undercooling.

This process is shown in Fig. 14.5 where model predictions are superimposed on test results such that the attachment rate may be identified. If we assume the attachment rate is proportional to the rate atoms impinge on a region of interest, for example, the growing subcritical cluster, then an appropriate value of β may be
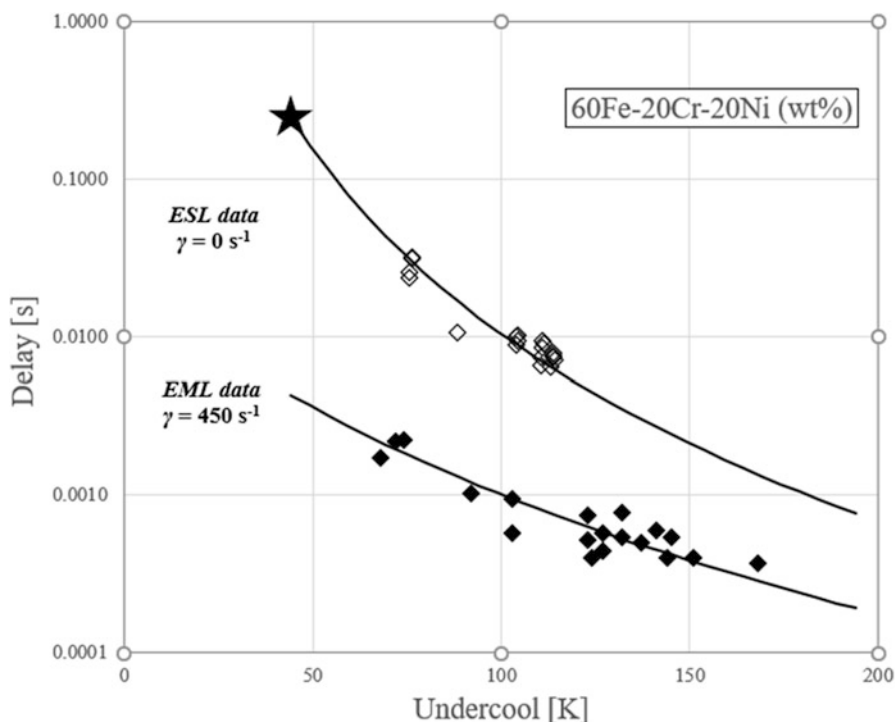
Fig. 14.5 Model predictions for ground-based ESL and EML testing

estimated based on the number of successful attachments per impingement (the success rate f_B is thus a number far smaller than one). In a related example, when solid state diffusivity is on the order of 10^{-11} m^2/s with atomic spacing of $a_o = 3 \times 10^{-10}$ m, the success rate is $f_B = 1 \times 10^{-5}$ successes per attempt assuming impingement is at the Debye frequency for iron and on the order of $\omega_D = 6 \times 10^{13}$ Hz. Kantrowitz [17] named this success rate the "accommodation coefficient for growth" and for water condensation calculated it to be on the order of $f_B = 5 \times 10^{-4}$. In the case of 20-20 stainless steel attachment, a success rate value of $f_B = 6.5 \times 10^{-7}$ or an attachment rate of $\beta = 4 \times 10^7$ atoms/sec provides the best fit to the data. If attachment is controlled by diffusion, then this corresponds to one successful attachment to the cluster every 17 diffusive impingements.

The star on the plot represents the longest delay time that is physically possible based on an evaluation of Eq. 14.3 with no convection and based on the estimation of the minimum free energy ΔG_s at the minimum undercooling to access the metastable phase ΔT_s.

Table 14.1 Properties specific to the FeCrNi alloy family

Property	Units	20-20 alloy	11-17 alloy	12-16 alloy	14-14 alloy
C_{Ni}	(wt% Ni)	20	17	16	14
ΔT_s	(K)	44.2	46.3	39.2	23.9
$T_{L,s}$	(K)	1713.0	1744.3	1743.1	1739.5
$T_{L,m}$	(K)	1668.8	1698.0	1703.8	1715.6
ΔH_s	(J/mol)	11235	12319	12152	11855
ΔH_m	(J/mol)	10629	11226	11009	10589
ΔG_R	(J/m^3)	3.87×10^7	4.36×10^7	3.65×10^7	2.17×10^7
τ_R	(s)	0.247	0.153	0.314	2.501

6   Characterizing Behavior with Dimensionless Quantities

In order to compare behavior across different alloy systems, a dimensionless approach was developed [20, 21]. It is based on alloy-specific values for the longest delay times and minimum free energy at minimum undercooling as described above; these quantities are taken as the reference values when defining two new dimensionless groups. Values for τ_R and ΔG_R are presented in Table 14.1 for the alloys in this chapter.

Dimensionless delay

$$N_\tau = \frac{\tau_{EXP}}{\tau_R} \qquad (14.8)$$

$$\tau_{EXP} \text{ measured delay}$$

$$\tau_R = \frac{128\,\pi\,k_B\,T_m\,\gamma^3\,f(\theta)}{\beta\,\Delta G_R{}^4}\left(\frac{N_A}{\Omega}\right)^2$$

Dimensionless driving force

$$N_M = \frac{\Delta G_T}{\Delta G_R} \qquad (14.9)$$

$$\Delta G_T = \Delta G_s + \Delta G_m + \Delta G_c$$

$$\Delta G_R = \Delta G_s$$

These quantities are independent of one another as they are each based on independently measured parameters – in one case, the experimentally observed delay time from high-speed video imaging and in the other case the melt undercooling from radiation pyrometry and melt stirring from the applied magnetic field.
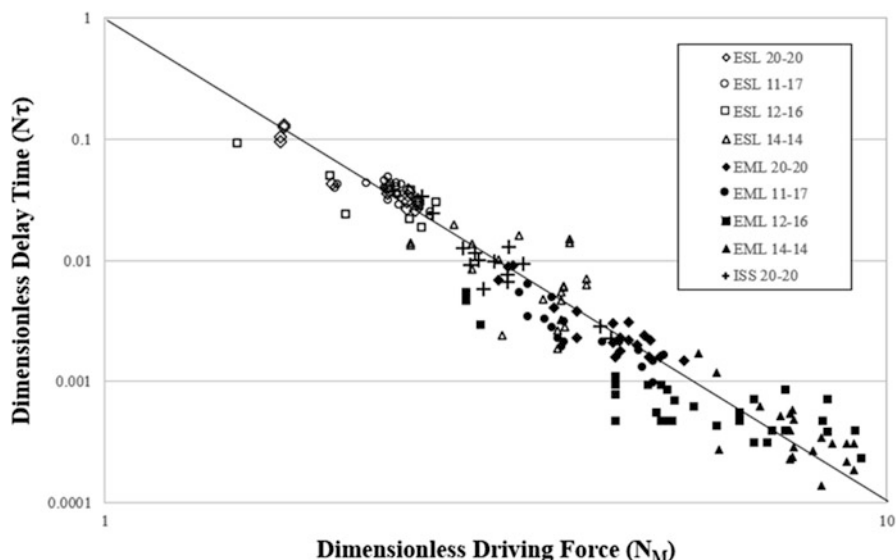
Fig. 14.6 Dimensionless presentation of results for a variety of FeCrNi alloys tested under the different flow conditions accessible using ESL, EML, and ISS-EML facilities

In order to evaluate the total driving force for any experiment, two things must be known beyond the thermophysical properties contained in Table I and the induced melt shear from magnetohydrodynamic modeling. An evaluation of the compositional dependence is needed for both the value for β and the empirical fit parameters from the modified Read-Shockley analysis. For the stainless steel alloy family, the variation of β appears to be rather small, and thus, this parameter is assumed to be a constant for all compositions. To evaluate the retained damage-free energy plot shown in Fig. 14.4 requires space testing which has not yet been accomplished for the other alloys. Thus, the 60 wt% Fe alloy parameters are used to estimate the behavior of the remaining 72 wt% Fe alloys.

Replotting the data from Fig. 14.3 in this new dimensionless format results in a linear fit on a log-log plot as shown in Fig. 14.6 where regression analysis shows the observed negative slope of 4.013 ± 0.023. This compares favorably to the theoretical value of negative 4.0 from Eq. 14.3 despite the required simplifications employed to estimate the composition invariant values of β and modified Read-Shockley parameters.

The new Retained Damage Model successfully predicts the relationship between undercooling and delay times across a wide range of compositions in ternary FeCrNi stainless steel alloys. The retained damage-free energy contribution from induced melt shear due to convection during primary recalescence influences the driving force for nucleation of the second phase and augments contributions from primary undercooling to reduce the transformation delay. A dimensionless treatment successfully demonstrates that theory and experiment show strong agreement.

Nomenclature

a_o	(m)	Lattice constant
C	(- -)	Fractional solute concentration (for bcc steel, this is Ni)
f_B	(- -)	Attachment success fraction
f_x	(- -)	Fraction of free energy retained
ΔG_c	(J/m^3)	Retained free energy from convection
ΔG_m	(J/m^3)	Retained free energy from undercooling
ΔG_R	(J/m^3)	Reference free energy
ΔG_s	(J/m^3)	Reference free energy relative to stable phase
ΔG_T	(J/m^3)	Total free energy
ΔH	(J/mol)	Enthalpy of fusion
k_B	(J/at·K)	Boltzmann constant
n	(at)	Number of atoms in a cluster
N_A	(at/mol)	Avogadro's number
N_M	(- -)	Dimensionless driving force ratio
N_τ	(- -)	Dimensionless delay time ratio
T	(K)	Undercooled melt temperature
T_m	(K)	Metastable phase liquidus
T_s	(K)	Stable phase liquidus
ΔT	(K)	Experimentally observed undercooling
β	(at/s)	Cluster atomic attachment rate
Δ_b	(J·s/m^2)	Empirical intercept constant relating shear and damage
Δ_m	(J·s/m^2)	Empirical slope constant relating shear and damage
$\dot{\gamma}$	(s^{-1})	Shear rate
τ	(s)	Calculated incubation delay
τ_R	(s)	Reference incubation delay
τ_{EXP}	(s)	Experimentally observed incubation delay
θ	(radian)	Heterogeneous nucleation wetting angle
θ	(radian)	Read-Shockley tilt grain boundary angle
κ	(- -)	Microstructural reversibility constant
Ω	(m^3/mol)	Atomic volume

Subscripts

M	Metastable phase
S	Stable phase

References

1. D.M. Matson, *Controlled Convection During Microgravity Solidification* (AIAA-2012-0592, 2012), pp. 1–5
2. J. Nawer, S. Gossé, D.M. Matson, Tracking evaporation during levitation processing of nickel-based superalloys on the ISS. JOM **72**(9), 3132–3139 (2020)
3. D.M. Matson, R.W. Hyers, T. Volkmann, H.-J. Fecht, Phase selection in the mushy zone: LODESTARS and ELFSTONE Programs. J. Phys. Conf. Ser. **327**(012009), 1–7 (2011)
4. D.M. Matson, Maximizing scientific return from shared facilities working in space: ESA's Investigator Working Group for the ISS-EML facility. Int. J. Microgravity Sci. Appl. **37**(3), 370301 1-4 (2020)
5. D.M. Matson, X. Xiao, J.E. Rodriguez, J. Lee, R.W. Hyers, O. Shuleshova, I. Kaban, S. Schneider, C. Karrasch, S. Burggraff, R. Wunderlich, H.-J. Fecht, Use of thermophysical properties to select and control convection during rapid solidification of steel alloys using electromagnetic levitation on the space station. JOM **69**(8), 1311–1318 (2017)
6. T. Koseki, M.C. Flemings, Solidification of undercooled Fe-Cr-Ni alloys: Part I. Thermal behavior. Metall. Mater. Trans. A **A26**(11), 2991–2999 (1995)
7. D.M. Matson, Chapter 10 – Nucleation within the mushy zone, in *Solidification of Container-less Undercooled Melts*, ed. by D. M. Herlach, D. M. Matson, (Wiley-VCH, Weinheim, 2012), pp. 213–238
8. D.M. Matson, A. Shokuhfar, J.W. Lum, M.C. Flemings, Imaging the double-recalescence behavior of undercooled Fe-Cr-Ni alloys using a high-speed video technique, in *Solidification Science and Processing*, ed. by I. Ohnaka, D. M. Stefanescu, (TMS Warrendale PA, 1996), pp. 19–26
9. J.E. Rodriguez, D.M. Matson, Lateral heat flux during Remelt growth into the mushy-zone. Acta Mater. **129**, 408–414 (2017)
10. A.B. Hanlon, D.M. Matson, R.W. Hyers, Microgravity experiments on the effect of internal flow on solidification of FeCrNi stainless steel. Ann. N. Y. Acad. Sci. **1077**, 33–48 (2006)
11. R. Venkatesh, R.W. Hyers, D.M. Matson, The influence of internal and external convection in the transformation behavior of Fe-Cr-Ni alloys, in *EPD Congress – 2004*, ed. by M. E. Schlesinger, (TMS Warrendale PA, 2004), pp. 337–344
12. M. Yoshiya, K. Nakajima, M. Watanabe, N. Ueshia, T. Nagira, H. Yasuda, Interface energies of hetero- and homo-phase boundaries and their impact on δ-γ massive-like phase transformations in carbon steel. Mater. Trans. **56**(9), 1461–1466 (2015)
13. D.M. Matson, X. Xiao, Identifying metastable interface potency limits during steel alloy transformations. Mater. Lett. **212**, 256–258 (2018)
14. D. Turnbull, Formation of crystal nuclei in liquid metals. J. Appl. Phys. **21**, 1022–1028 (1950)
15. J. Feder, K.C. Russell, J. Lothe, G.M. Pound, Homogeneous nucleation and growth of droplets in vapors. Adv. Phys. **15**(57), 111–178 (1966)
16. D.M. Matson, X. Xiao, S. Jeon, Optimization strategies for identifying the controlling mechanism for solid-state transformation in FeCrNi during rapid solidification. IOP Conf. Ser. Mater. Sci. Eng. **529**(012012), 1–7 (2019)
17. A. Kantrowitz, Nucleation in very rapid vapor expansions. J. Chem. Phys. **19**(9), 1097–1100 (1951)
18. D. Kashchiev, Solution of the non-steady state problem in nucleation kinetics. Surf. Sci. **14**(1), 209–220 (1969)
19. D. Kashchiev, Nucleation at existing cluster size distributions. Surf. Sci. **18**(2), 389–397 (1969)
20. D.M. Matson, Retained free energy as a driving force for phase transformation during rapid solidification of stainless-steel alloys in microgravity. npj Nat. Microgravity **4**(22), 1–6 (2018)
21. D.M. Matson, Influence of induced convection on transformation kinetics during rapid solidification of steel alloys: The Retained Damage Model. JOM **72**(11), 4109–4116 (2020)

22. J. Lee, X. Xiao, D.M. Matson, R.W. Hyers, Numerical prediction of the accessible convection range for an electromagnetically levitated $Fe_{50}Co_{50}$ droplet in space. Metall. Mater. Trans. B **46**(2), 199–207 (2015)
23. E.B. Baker, J. Nawer, X. Xiao, D.M. Matson, MHD surrogate model for control of convection in electromagnetically levitated molten metal droplets processed using the ISS-EML facility. npj Nat. Microgravity **6**(9), 1–9 (2020)
24. X. Xiao, R.W. Hyers, D.M. Matson, Surrogate model for convective flow inside electromagnetically levitated molten metal droplet using magnetohydrodynamic simulation and feature analysis. Int. J. Heat Mass Transf. **136**, 532–542 (2019)
25. X. Xiao, J. Lee, R.W. Hyers, D.M. Matson, Numerical representations for flow velocity and shear rate inside electromagnetically levitated droplets in microgravity. npj Nat. Microgravity **5**(7), 1–7 (2019)
26. W.T. Read, W. Shockley, Dislocation models of crystal grain boundaries. Phys. Rev. **78**(3), 275–289 (1950)

Chapter 15
Thermophysical Properties of Ni-Based Superalloys

Rada Novakovic, Donatella Giuranno, Markus Mohr, Jürgen Brillo, and Hans-Jörg Fecht

1 Introduction

Ni-based industrial superalloys are multicomponent systems often containing ten or more metallic elements, such as Cr, Co, Mo, Ta, Re, Ti, Hf, Nb, W, and Fe together with nonmetals C, B, Si, and P added as trace elements. In these complex systems, nonmetals either act as grain refiners or reduce grain defects and have a particular role in microstructural optimization, resulting in enhanced mechanical properties [1–3]. Some examples of Ni-based superalloys and their compositions are given in Table 15.1. The presence of the $AlNi_3$ intermetallic phase, known as the γ' phase, which exhibits a high degree of order at high temperatures, is a key to strengthening in binary Al-Ni [4] and multicomponent Ni-based alloys [5]. The outstanding high-temperature mechanical properties of Ni-based superalloys can be attributed to the coherency between their constituting phases γ (A1) matrix and γ' (L1$_2$) hardening precipitates (the L12 structure being an ordered state of the *fcc* (A1) lattice) and, together with good oxidation resistance, make these alloys suitable for extremely harsh environments [3, 6]. In recent years, there has been a growing interest in Ni-based superalloys because they exhibit a peculiar combination of high strength, toughness, and resistance to degradation in oxidizing and corrosive environments [7]. Ni-based superalloys are widely used in various fields such as turbine materials

R. Novakovic (✉) · D. Giuranno
Institute of Condensed Matter Chemistry and Technologies for Energy, National Research Council (CNR-ICMATE), Genoa, Italy
e-mail: rada.novakovic@ge.icmate.cnr.it

M. Mohr · H.-J. Fecht
Institute of Functional Nanosystems, Ulm University, Ulm, Germany

J. Brillo
Institut für Materialphysik im Weltraum, Deutsches Zentrum für Luft- und Raumfahrt (DLR), Köln, Germany

Table 15.1 Nominal compositions (wt %) of some Ni-based superalloys

Alloy	Ni	Cr	Co	Mo	W	Nb	Ti	Al	Ta	Re	Hf	Other elements	References
RENE 41	55.0	19.0	11.0	10.0	–	–	3.1	1.5	–	–	–	Fe < 0.3 B < 0.01 C = 0.09	[2]
RENE 88	56.4	16.0	13.0	4.0	4.0	0.7	3.7	2.1	–	–	–	B = 0.015 C = 0.03 Zr = 0.03 Bal = −0.025	[2]
Astroloy	56.5	15.0	15.0	5.25	–	–	3.5	4.4				Fe < 0.03 B = 0.03 C = 0.06 Zr = 0.06	[2]
CMSX-4	61.8	6.5	9.0	0.6	6.0		1.0	5.6	6.5	3.0	–	–	[9]
CMSX-4	60.31	6.4	9.6	0.61	6.4	–	1.02	5.61	6.5	2.9	0.1	Si = 0.4 Mn = 0.1 Fe = 0.042 Cu < 0.001 C = 0.0037	[42]
CMSX-4	60.3	6.4	9.6	0.61	6.4	–	1.02	5.6	6.5	2.9	–	Si = 0.4 C = 0.0037 Bal = 0.26	[56]
CMSX-4	61.7	6.5	9.0	0.6	6.0	–	1.0	5.6	6.5	3.0	0.1	–	[57]
CMSX-10	69.57	2.0	3.0	0.4	5.0	0.1	0.2	5.7	8.0	6.0	0.03	–	[37]
CMSX-10	69.70	2.0	3.0	0.4	5.0	0.1	0.2	5.7	8.0	6.0	0.03	Bal = −0.03	[57]
RENE N5	63.27	7.2	7.4	1.7	5.9	–	–	6.63	6.4	1.5	–	–	[54]
RENE N5	62.3	7.3	7.9	1.2	4.9	–	–	5.1	8.1	3.2	–		[56]
RENE N5	61.8	7.0	8.0	2.0	5.0	–	–	6.2	7.0	3.0	–	–	[9]
RENE 90	67.4	8.6	5.2	1.6	7.6	–	1.4	3.3	4.9	–	–	–	[54]
RENE 90	67.4	8.6	5.2	1.6	7.6	.	1.4	3.3	4.9	–	–	–	[56]

LEK-94	65.3	6.1	7.5	2.3	4.4	–	1.0	7.1	2.8	2.9	0.6	–	[37]
LEK-94	68.54	6.0	7.5	2.1	3.5	–	1.0	6.5	2.3	2.5	0.06	–	[58]
MC-2	64.3	8.0	5.0	2.2	8.0	–	1.5	5.0	6.0	–	–	–	[37]
MC-2	64.5	8.0	5.0	2.0	8.0		1.5	5.0	6.0	–	–	–	[9]
TMS-75	59.9	3.0	12.0	2.0	6.0	–	–	6.0	6.0	5.0	0.1	–	[59]
TMS-75	60.0	3.0	12.0	2.0	6.0	–	–	6.0	6.0	5.0	–		[9]
CM186LC	62.6	6.0	9.0	0.5	8.0	–	0.7	5.7	3.0	3.0	1.4	C = 0.07 Bal = 0.03	[57]
CM186LC	61.9	15.9	8.3	1.7	2.6	0.8	3.5	3.5	1.7	–	–	C = 0.1	[56]
IN718	52.5	19.0	1.0	3.1	–	5.2	0.9	0.5	–	–	–	Fe = 16.7 C = 0.08; Mn = 0.35; Bal = 0.67	[22]

for land-based power generation and aircraft propulsion working at high temperatures and high stress levels, automotive industries, fuel cell and hydrogen technology, catalytic chemistry, and protective coatings. Superalloys are also used in nuclear power and chemical processing plants, for production of the so-called supermetals, i.e., amorphous metal alloys such as thin sheets for electronic components with high ultimate strength to weight ratio, as construction materials for furnace parts and for biocompatible medical implants such as hip replacements [2, 8–11].

After 5000 years of technological advances, metal casting is more essential than ever, although, in the early 1970s, the emphasis turned toward powder metallurgy (P/M) [2, 12]. To produce materials with tailored properties, it is necessary to understand the relationships between the elements of the quadriade "*composition-processing-microstructure-properties*" and, based on it, to achieve a tailored microstructure associated with a unique combination of properties [13]. Accordingly, it is important to mention that slight differences in the composition of an industrial alloy, such as, for example, CMSX-4 (Table 15.1), will result in different property values. Design and development of Ni-based superalloys components involve different processing routes reported in [14–16], including the most advanced ones, such as additive manufacturing [17, 18]. The traditional liquid phase route, i.e., an investment casting process [1–3], is mainly used to produce Ni-based structural components. Model simulations that allow predicting the microstructural evolution during solidification can be helpful to evaluate the operating parameters relevant for the optimization of casting processes [19]. Therefore, the accuracy and reliability of the thermophysical property data, used as input to numerical simulations, are relevant for industry and basic science [20–22]. Among the thermophysical properties such as surface tension, viscosity, mass density, specific heat, total hemispherical emissivity, thermal conductivity, and electrical resistivity, *surface tension, density, and viscosity* of alloy melts are the key properties for the modelling of microstructure evolution during solidification [18, 23]. On the other hand, a comparison with a real system is the most reliable and preferred way to validate a simulation model. Therefore, surface tension and viscosity predictive models can be validated using corresponding experimental data obtained by accurate and precise measurements [24, 25].

In 1961, first measurements of the surface tension [26], density [26, 27], and viscosity [28] of liquid Ni and Al-Ni binary alloys using conventional techniques have been done. Several experiments have been carried out a few years later, with the same alloys and under the same or very similar operating conditions giving a good agreement among the corresponding datasets [29–31]. During the 90s, the experimental determination of thermophysical properties was extended to other Ni-based alloys [2, 32], and after the year 2000, complex Ni-based superalloys were investigated using advanced levitation methods [33–38]. There are considerable scientific and industrial interests in designing and developing novel metallic materials with a wide range of potential applications and relevant manufacturing methods [15]. At the same time, the fast progress of computer technologies contributed to developing more sophisticated numerical models, and containerless

measurement methods lead to more accurate results [20]. Measurements of high-temperature liquid metallic materials such as Ni-based and Ti-based industrial alloys and their thermophysical properties have become the subject of paramount research interest. In the last two decades, they have been widely investigated in the frameworks of the three international projects. Indeed, in August 2001, the ESA-MAP ThermoLab (Microgravity Application Program-Thermophysical Properties of Liquid Metallic Alloys for Modelling of Industrial Solidification Processes and Development of Advance Components and Products) project started with the aim to concentrate on specific experimental and theoretical aspects of thermophysical properties, including measurements in reduced gravity/microgravity conditions, thanks to containerless levitation processing [20, 21, 39]. Since 2009, the ESA-MAP ThermoProp (Microgravity Application Program-Thermophysical Properties of Liquid Metals for Industrial Process) project activities represent the continuation of the aforementioned project [40] extending the research to new classes of materials (bulk metallic glasses, steels, semiconductors, etc.) as well as performing short-time measurements on parabolic flights [34, 36] and long-duration microgravity experiments on board the International Space Station (ISS) [37]. In the framework of the two ESA MAP projects, the research activities were related to the study of thermophysical properties: from materials selection throughout the experiments design (measurement methods and experimental conditions) to the development of appropriate predictive models. Starting from conventional container-based followed by a quasi-containerless method and finally using advanced containerless processing techniques of hot melts on ground and under reduced gravity conditions, the thermophysical properties of liquid Ni-based alloys have been measured. Using theoretical models, the experimental data of surface tension, density, and viscosity [21, 34, 36, 37, 41, 42] were analyzed as it has been done in the case of Al-Ni melts [43]. In the framework of thermodynamics and statistical mechanics, many models describing the thermophysical properties of binary and ternary liquid alloys have been developed. However, until now, no theory exists which describes the surface tension and viscosity of multicomponent metallic alloys at high-temperature satisfactory [24, 44].

   Thermodynamic functions of mixing of Ni-based liquid alloys [45–49] indicate strong exothermic reactions in these complex compound forming systems, supported by CALPHAD (*Calculation of Phase Diagrams*)-type modelling [5, 50, 51]. Thermodynamic and thermophysical properties of Ni-based superalloys [52, 53] exhibit a close similarity with those of Al-Ni melts [4, 43]. Therefore, in this chapter, the surface tension, density, and viscosity experimental datasets of Ni-based liquid superalloys (Table 15.2), mainly obtained in the framework of the ThermoLab and ThermoProp ESA-MAP Projects [39, 40], have been analyzed with respect to their basic binary and/or ternary subsystems, using the corresponding models for such alloy systems. The surface tension and density data of Ni-based superalloys are mainly consistent with each other with respect to the Al-content in the alloys and are comparable to the property's value of Al-Ni alloys having the same Al-content [41, 54, 55]. To evaluate the surface tension, the Compound Formation Model (CFM), the Quasi Chemical Approximation (QCA) for regular solution, and Butler's

Table 15.2 Nominal and measured compositions (at %) of some Ni-based superalloys

Alloy	Ni	Al	Cr	Co	W	Mo	Ti	Ta	Re	Nb	Hf	Other elements	References
Nominal CMSX-4	62.07	12.58	7.45	9.86	2.11	0.38	1.29	2.17	0.94	–	0.1	1.05	[41, 42, 56, 57]
EDX	63.32	12.0	7.57	9.94	2.26	0.34	1.35	2.14	1.08	–	–	–	
Nominal CMSX-10	74.12	13.2	2.4	3.18	1.7	0.26	0.3	2.76	2.01	0.06	0.01	–	[36, 37, 55, 57]
EDX	71.2	13.5	2.6	5.7	2.2	–	–	2.9	1.9	–	–	–	
Nominal RENE N5	64.1	13.8	8.1	8.1	1.63	1.25	–	1.99	0.97	–	0.07	–	[54, 56]
EDX	63.62	14.5	8.3	7.4	1.99	1.3	–	2.22	0.67	–	–	–	
Nominal RENE 90	70.08	7.46	10.1	5.39	2.52	1.02	1.79	1.65	–	–	–	–	[54, 56]
EDX	65.31	11.12	9.66	5.52	3.48	1.26	1.71	1.94	–	·	–	–	
Nominal LEK-94	67.27	13.8	6.7	7.3	1.0	1.2	1.2	0.7	0.8	–	0.03	–	[36, 37, 55]
EDX	64.8	14.9	6.8	7.5	1.5	1.4	1.1	0.9	1.1	–	–	–	
Nominal MC-2	66.5	11.2	9.3	5.2	2.6	1.3	1.9	2.0	–	–	–	–	[37, 55]
EDX	65.2	11.3	9.6	5.2	3.3	1.4	1.7	2.3	–	–	–	–	
Nominal TMS-75	62.77	13.7	3.6	12.6	2.2	1.3	–	2.1	1.7	–	0.03	–	[55]
EDX	64.5	12.9	3.2	12.4	2.4	1.0	–	2.1	1.5	–	–	–	
Nominal IN718	53.9	1.1	21.6	1.0	–	1.9	1.1	–	–	1.7	–	Fe = 17.7	[22]
Nominal CM186LC	60.99	12.07	6.59	8.72	8.19	0.3	0.84	0.95	0.91	–	0.44	–	[57]

model were applied [24]. The thermophysical property values of Ni-based multicomponent alloys can also be approximated using the geometric models [52] representing Al-Ni-X (X = Cr, Co, Ta, Re) ternary alloys with the third major component after Ni and Al [55]. Preliminary analysis of the Al-Ni viscosity datasets [28, 30, 39, 40] in the framework of the models reported in [25, 44] identified the Iida-Morita model as the most appropriate. Subsequently, the viscosity data of Ni-based industrial alloys also is approximated using the model-predicted values of Al-Ni binary alloys with the same Al-content. In the following, all the experimental methods with a particular attention to the measurements in microgravity, predictive models, and their validity, as a part of Ni-based superalloys design, are discussed.

2   Experimental Methods: Surface Tension

Processing routes involving the liquid phase, such as casting, joining, crystal growth, liquid phase sintering, spraying, zone melting, and melt spinning are greatly influenced by the surface tension of the metallic liquid. Because a gradient in surface tension can drive Marangoni convection, which is often the dominant mass transport process in the abovementioned processing routes, it must be taken into account [24, 44]. The surface tension of metallic melts is very sensitive to impurities that segregate on the liquid surface, reducing its value significantly. Oxygen is the most surface-active element, followed by sulfur and carbon. For instance, only a few ppm of oxygen can significantly reduce the surface tension of metallic melts, by 30% and even more. This can be attributed to the high chemical reactivity of liquid metals at high temperatures, principally with oxygen present in the surrounding atmosphere and, in the case of container-based methods, the interfacial reactions between melt and substrate or container. To avoid or at least minimize these problems, evaluating the wetting behavior of the system of interest has been done, suggesting the appropriate measurement method or the possibility to limit chemical reactions (nonequilibrium measurements). In the case of extremely reactive melts, it is necessary to avoid or even suppress any possible reaction of the sample with the container material, and the application of containerless methods is recommended. Otherwise, a combined thermodynamic-kinetic study of the system under investigation can indicate the experimental conditions and the physical-chemical parameters (e.g., pressure, composition of the sample itself, composition of the gaseous and solid (support) environment, vapor pressure, etc.) aiming to achieve accurate and reliable surface tension data [20, 21, 24]. In the following, the measurement methods used to obtain the surface tension data of liquid Ni-based industrial superalloys (Table 15.2) are briefly described.

2.1 Container-Based Methods

2.1.1 Sessile Drop

The sessile drop (SD) is a drop shape method [60]. During the measurement, a liquid drop is placed on a flat, unwetted, solid support (Fig. 15.1a), and its profile image is acquired. The Laplace equation [61] describes the drop shape, and the surface tension is determined by the fitting of the experimental drop shape [62], as shown in Fig. 15.1b. The advantage of this method is a noninvasive character, and the best results are obtained for non-wetting systems [63], such as the metal/refractory systems. Numerical calculations and computer-aided imaging techniques allow the measurement of the drop shape with the highest possible precision. The recorded digital images of the drop are analyzed to obtain numerical data points of its contour. Based on an improved version of the Maze and Burnet algorithm [64, 65], dedicated software packages are adopted to obtain surface tension data in real time together with other experimental parameters. In order to obtain reliable surface tension data, some "standard criteria" both in the design of the apparatuses and in the procedures for the surface tension measurement at high temperatures should be taken into account, such as those described in [24].

2.1.2 Pinned Drop

When the contact angle between the liquid metal and the support/container material is greater than 90°, a variant of the sessile drop method, based on the concept of "*large drop*" (LD) [66] and called "pinned drop method," is recommended. In this case, the solid support is a special circular crucible with sharp edges (Fig. 15.1c). Equilibrium drop profile and its description by means of contour fitting are shown in Fig. 15.1b. The design of the edges of the crucible blocks the triple line at an

$$2 + \frac{\rho g b \, z}{\gamma} = \left[\frac{1}{(R/b)} + \frac{\sin\Phi}{(x/b)} \right]$$
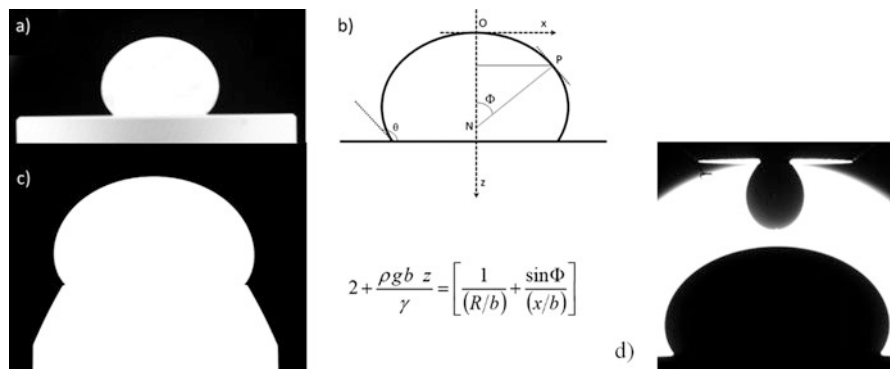
Fig. 15.1 Surface tension measurements by contact methods: (**a**) sessile and (**b**) large drops with (**c**) equilibrium drop profile described by fitting equation [62] (**d**) combined pendant/sessile drops

"*apparent*" contact angle that is much higher than the real one. A further advantage of the pinned drop method is that the axisymmetry of the drop can be imposed. More information and details can be found in [24].

2.1.3 Pendant/Sessile Drop

None of the container-based methods is appropriate to measure the surface tension of highly reactive metallic melts such as Ti-containing alloys with high melting temperatures. Recently, the method combining the pendant and sessile drops in one test has been assessed by an advanced experimental apparatus, designed for measurements up to 2400 K [24, 67]. In the combined pendant/sessile drop (PD/SD) procedure, the contact of a melt with either a capillary or a substrate is unavoidable, but the contact time is very short. Indeed, after reaching the required temperature, the flow of a melt through a capillary is very fast, the drop images are recorded, and after a few seconds, the droplets form the sessile drop deposited on the substrate, characterized by a high symmetry (Fig. 15.1d). The main advantage of this combined method compared with the pendant drop method is the absence of primary oxide film on the squeezed droplets [67].

2.2 Containerless Measurements

2.2.1 EML-Oscillating Drop on Ground (OD-EML^g)

By eliminating the contact of the melt with a container, there is no possibility of contamination with container material, which allows for measurements with higher precision. To this end, the containerless method of the oscillating drop (OD) is typically used [68–71]. The technique is described in detail in Chap. 8, Part III. Here, a brief summary will be given only. The electrically conducting sample is hereby levitated by an electromagnetic field, which inductively heats the latter and positions it against gravity due to Lorentz forces. The sample finally melts. Temperature is measured by a pyrometer. Self-induced surface oscillations are observed with a fast camera (200–400 Hz), and their spectrum is obtained. The surface tension is calculated from the five frequencies corresponding to the $l = 2$ Rayleigh oscillation mode using the sum rule of Cummings and Blackburn (see Eq. 8.8, Chap. 8, Part III).

2.2.2 Oscillating Drop Method in $\mu - g$ (OD-$EML^{\mu - g}$)

The oscillating drop method under microgravity allows the determination of surface tension and viscosity. While using the TEMPUS EML device in parabolic flights or the ISS-EML on board the International Space Station, the samples can be molten, overheated, and cooled down, and during the cooling period, the samples surface

Fig. 15.2 Typical
temperature-time diagram of
an oscillating drop cycle
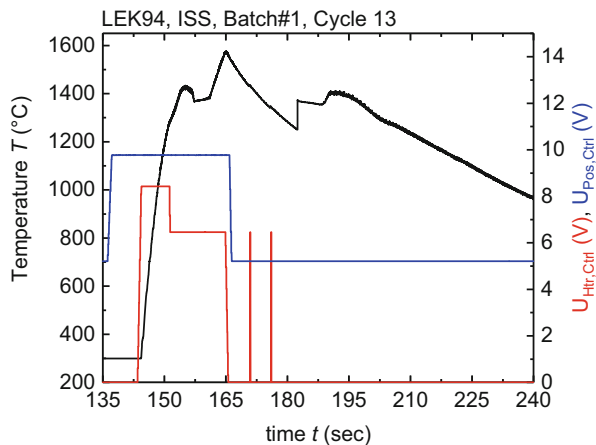
oscillations are excited using short pulses of the electromagnetic heater field. Thus, the sample is shortly squeezed and consequently starts oscillating. The oscillations are observed using high-speed cameras. Details for the ISS-EML can be found in Chap. 3, Part I. The analysis of these oscillations can obtain surface tension and viscosity. Figure 15.2 shows a typical temperature-time diagram recorded during a cycle designed for measurements using the oscillating drop method. Under microgravity conditions, the necessary positioning forces on the sample are strongly reduced (roughly by a factor of 1000). Furthermore, the positioning and heating of the sample are decoupled, which allows the access of larger temperature ranges and removes the necessity for counter-cooling of the sample. Most importantly, the liquid drop forms a spherical shape under microgravity. Together, this suffices to fulfill the assumption of a force-free spherical sample in Rayleigh's derivation [72]. As a result, the oscillation mode is not split, and consequently, under microgravity, the sub-modes $m = 0, \pm 1, \pm 2$ are degenerated, and only the Rayleigh mode is visible in the spectra as a single strong peak. After Rayleigh [72], the surface tension can be obtained from the observed oscillation frequency ω of the $l = 2$ mode [73, 74] for a nonviscous, force-free, spherical drop as

$$\sigma = \frac{3}{16\pi} M \omega^2 \tag{15.1}$$

Deviations from Rayleigh's theory are observed for strong sample rotations [75, 76], as well as for large oscillation amplitudes [77, 78] or very strong damping [38, 79, 80]. Further details are given in Chap. 12, Part IV.

3   Experimental Methods: Density

Since the mixing behavior of alloys and determination of the basic thermophysical properties of metallic liquids, such as molar volume, surface tension, and viscosity, depend on density, it is an indispensable fundamental property. Indeed, the density data are necessary for many practices, apparatuses, or devices involved in metallurgy as well as in a wide range of applications ranging from refining operations, slag/metal reactions, and physical separation of metallic liquids and overlaying slags. Furthermore, the simulation of solidification, as one of the most important steps for the Design of Materials and Processes involving the liquid phase, requires the knowledge of density data of metallic melts in order to predict volume changes at their melting temperatures [44]. Concerning the density of Ni-based liquid superalloys, due to experimental difficulties related to their high melting temperatures and strong reactivity, the number of datasets is still limited [39, 40]. The density values analyzed in this chapter have been obtained by the sessile or large drop container-based methods and by the containerless oscillating drop method in electromagnetic levitation on ground [81–83] and in microgravity conditions [37]. Further details can be found in Chap. 12, Part IV.

3.1   Sessile and Large Drop

Density measurements by the sessile or large drop/pinned method are carried out applying the same methodology as that used for the determination of the surface tension, described in Sects. 2.1.1 and 2.1.2. Indeed, the drop profile of the liquid drop is acquired by dedicated Labview software, which is used to obtain the surface tension value in real time. The output of particular parameters and quantities, such as drop volume, drop weight, *density*, shape factor, and contact angle, can also be obtained. The density of an alloy is calculated from the drop mass and volume measured at each temperature during the automatic acquisition procedure. The uncertainty in the density values is estimated to be <0.5%.

3.2   Density Measurement in EML – Oscillating Drop on Ground (OD-EML$^{\text{g}}$)

The setup for the containerless ground-based density measurement is described in detail in Chap. 8, Part III. Here, only a brief summary is given. *Density* is measured from the sample via its volume. The liquid levitated droplet is illuminated from one side by an expanded laser, and the shadow images are recorded by a camera on the other side; see Figs. 8.1 and 8.4 in Chap. 8. An edge detection algorithm locates the edge curve $R(\varphi)$ of the droplet shadow in each image and calculates its time average

$<R(\varphi)>$ from typically 1000 subsequent images. Here, R and φ are the radius and polar angle with respect to the drop center. The volume is then obtained from calculating an integral, Eq. 8.7 of Chap. 8, where it is assumed that the sample is symmetric with respect to its vertical axis.

3.3 Density Measurement in Oscillating Drop Method in $\mu - g$ (OD-EML$^{\mu - g}$)

The ISS-EML offers the possibility to obtain the sample radius, and hence for a known mass, the mass density as a function of temperature in a contactless, inductive manner. For this purpose, a dedicated measurement setup was developed and installed [32, 78]. Further details are given in Chap. 12 in Part IV. Under the correct measurement conditions, the method is able to achieve a precision of about ±0.05%. Another option is the measurement of the samples mass density by the optical images recorded by the high-speed cameras. During cooling, the samples are perfect spheres, since they are only influenced by weak positioning forces in the microgravity environment. The projected area A_s of the samples, recorded by the video cameras, can be used to obtain the sample volume V by

$$V = \frac{4}{3} \frac{A_s^{3/2}}{\sqrt{\pi}} \tag{15.2}$$

assuming the perfectly spherical symmetry. The mass density as a function of temperature is then given as $\rho(T) = M/V(T)$. Calibration of the image scaling was done by the measurement of a solid zirconium sample with precisely known diameter in comparison with literature data [79]. The measurement's accuracy depends on the quality of the edge detection algorithm, which contributed to an uncertainty of about ±0.5% on the sample radius. The mass was measured before the flight with an accuracy of ±0.1%. Mass loss during the experiment is not significantly influencing the accuracy. Overall, the optical method is able to give the sample density with an accuracy of about ±1.6%.

4 Experimental Methods: Viscosity

Viscosity is the thermophysical property related to a temperature-dependent transport process occurring in the melt due to the high mobility of its individual atoms. However, frictional forces set up by their nearest neighbors hamper the motions of atoms through a metallic melt. Viscosity can be considered a measure of the friction among atoms, and it plays an important role in understanding fluid behavior and problems related to the kinetics of reactions in materials processing. As it was

already mentioned for other thermophysical properties, the strong reactivity of metallic melts related to their high melting temperatures together with the lack of a rigorous model to calculate the viscosity are common reasons for data discrepancies [44]. In the case of Ni-based superalloys, the modelling of solidification also requires reliable viscosity data together with those of diffusion, surface tension, molar volume, and melting temperature to be used as input to numerical simulations.

4.1 Oscillation Viscosimetry

In ground-based experiments, the viscosity of high-temperature liquid metals is typically measured using an oscillating cup viscometer [35, 84]. A typical viscometer, like the one at DLR [85], consists of two parts: the furnace and the oscillation system. The heart of the latter is a torsional steel wire of 1300 mm in length and with a diameter of 0.228 mm. It is kept under isothermal conditions in order to maintain stable mechanical properties. A small mirror holder with a mirror is attached at the end of the wire in order to monitor the torsional angle. A tungsten (or molybdenum) rod is fixed to the mirror holder reaching inside the center of the furnace where it holds the crucible. The crucible (typical dimensions: height $= 100$ mm, inner diameter $= 15$ mm) contains the liquid sample; see Fig. 15.3. In order to measure the angle θ by which the wire is twisted, a laser is shone at the mirror, and the reflected beam is accepted by a position-sensitive detector. Experiments are done under $4 \cdot 10^4$ Pa Ar-atmosphere (99.999%) after prior evacuation to 10^{-4} Pa in order to remove gaseous impurities. In the setup used at DLR [85], the furnace is part of

Fig. 15.3 Schematic depiction of the oscillating cup viscometer used at DLR [85]. The crucible, placed inside the furnace, performs torsional oscillations excited by the motor. The pyrometer is directed at the crucible via an adjusted mirror
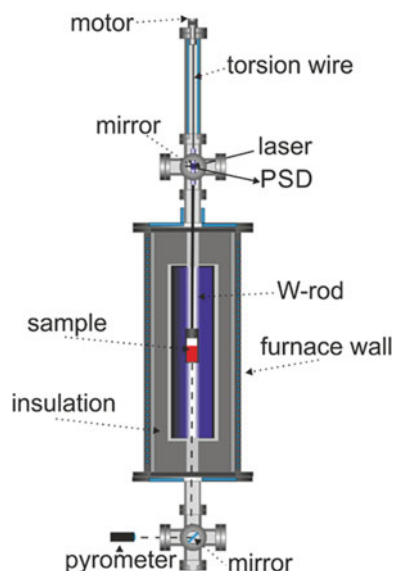
the vacuum system. It can reach temperatures of up to 2300 K. Sample temperature is measured by a pyrometer being directed at the bottom of the crucible.

In order to measure viscosity, torsional oscillations of the crucible are excited around the vertical axis, and θ is measured as a function of time. Due to the inner friction of the liquid, the oscillations are damped, and the viscosity η is obtained from the logarithmic decrement by solving the Roscoe equation [86, 87], which is a self-consistent equation that can only be solved numerically. Alternative analysis methods exist, like the one of Beckwith and Newell [88] or the one of Brockner [89]. From a systematic analysis of measured data, the absolute uncertainty of the method is estimated as $\Delta\eta/\eta \approx \pm 20\%$ [35].

4.2 Oscillating Drop Method in $\mu - g$ (OD-EML$^{\mu - g}$)

The oscillating drop method under microgravity allows the determination of surface tension and viscosity. Due to the small positioning forces required in microgravity, the positioning field does usually not contribute significantly to the heating of the sample, allowing it to reach deep undercooling. Furthermore, the positioning field does not drive considerable fluid flow, such that the fluid flow is in the laminar regime over a wide range of experimental parameters [90]. Surface oscillations of the sample, excited by short heater pulses, are damped due to the inner friction of the liquid. In the case of laminar flow, the damping of the droplets surface oscillations can be related to the viscosity of liquids. Lamb derived a relation between the viscosity η and the damping time constant τ. For the usually observed $l = 2$ oscillation mode, the viscosity η is related to the damping time constant τ as

$$\eta = \frac{3}{20\pi} \frac{M}{R} \frac{1}{\tau} \tag{15.3}$$

where M is the sample mass and R is the sample radius. Further details can be found in Chap. 12, Part IV. Using high-speed camera recordings and edge detection algorithms, several metrics for the sample shape deformations are obtained, such as the X- and Y-radius of the sample. Figure 15.4 shows the Y-radius of the sample LEK94, processed in Batch#1 on board the ISS, shortly after the second pulse (see Fig. 15.2). The oscillation amplitude is decreasing exponentially with a time constant τ. Further details of the method can be found in Chap. 12, Part IV.

5 Experimental Methods: Specific Heat

For the simulation of the industrial solidification processes, an important quantity is the temperature dependence of heat capacity of the material in the solid and liquid phase. The ac calorimetry is a containerless method developed for the measurement

Fig. 15.4 Exponential decay of the surface oscillation excited by the second heater pulse in Fig. 15.2

LEK94, ISS, Batch#1, Cycle 13, radial

$\tau = 1.6$ s
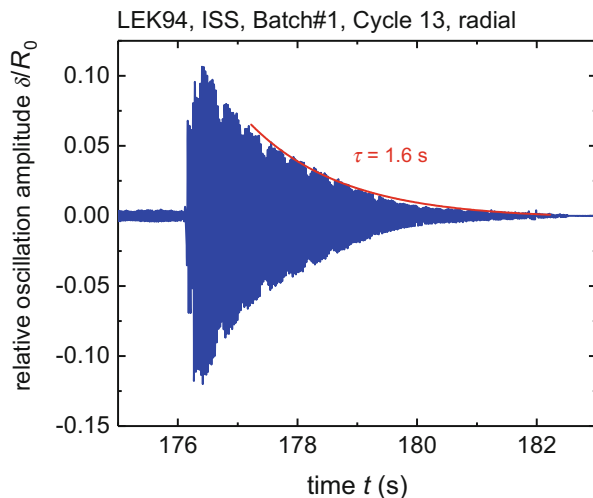
of heat capacity, emissivity, and, in principle, thermal conductivity [91]. The response of the sample to a sinusoidal modulation at a frequency ω_{mod} of the heating power is a sinusoidal modulation of amplitude ΔT_{mod} and of the same frequency. As proposed in [91], the samples heat capacity can be calculated by

$$C_p = \frac{\Delta P_{mod}}{\omega_{mod} \Delta T_{mod}} f \qquad (15.4)$$

where f is a correction function close to unity, which depends among other things on the modulation frequency ω_{mod}. By the right choice of ω_{mod}, the experiment takes place in adiabatic conditions, which leads to $f = 1$. Further information is given in Chap. 12, Part IV.

6   Models

The various experimental and theoretical information available for the thermophysical properties of liquid Ni-based industrial alloys are put together in order to give an understanding of the relationship between the experimental results and theoretical approaches. Indeed, the modelling of thermophysical properties provides useful data to complement experimental studies [76]. To this aim, over the last two decades, an innovative multidisciplinary scientific approach that combines synergistically advanced and dedicated measurement techniques, including the use of microgravity environment, with the properties modelling and simulation as a part of the product and process design has been applied [39, 40]. After summarizing the experimental techniques described briefly in the previous section and detailed in Chaps. 3, 4, and 12, the models developed in the framework of thermodynamics,

statistical mechanics, and hard sphere-like theory have been applied, and subsequently, the corresponding experimental datasets obtained by the abovementioned methods were used for their validation. Preliminary analysis of the thermodynamic and thermophysical properties data of various binary [92, 93] and ternary subsystems [54, 55] of multicomponent Ni-based systems indicates a close similarity between the last mentioned and the Al-Ni [37, 41, 43, 54, 55]. Therefore, in the following, the models predicting its thermophysical properties will be shortly described.

6.1 Surface Tension

The Compound Formation Model (CFM) is the most appropriate to describe the surface tension of strongly interacting compound forming systems such as, for example, liquid Al-Ni alloys [43]. Taking into account the energetic contribution and structure of an $A_\mu B_\nu$ (μ, ν are stoichiometric coefficients) energetically favored intermetallic compound, the CFM includes the effects of short-range ordering on the surface properties. To evaluate such effects on the surface tension of compound forming systems, the Quasi Chemical Approximation (QCA) for the regular solution or Butler's model has to be used together with the CFM. The difference between the surface tension values calculated by the CFM and those obtained by the QCA for regular solution (or by Butler's model) represents the contribution of short-range ordering to an increase in the surface tension. The CFM, QCA for the regular solution, Butler's, and perfect solution models are based on the concepts of a layered interfacial structure, which is often simplified to a monolayer. Assuming the reduced coordination of the surface phase as a factor of proportionality, the energetics of the *bulk* and *surface* phases are expressed in terms of the thermodynamic potentials. At the interface, the two phases are in equilibrium with each other. In this chapter, only the basic equations used for the data analysis (see Sect. 7) are given. Detailed mathematical formalisms of the CFM, QCA for the regular solution, Butler's, and perfect solution model can be found elsewhere [24, 52, 92–94].

6.1.1 Compound Formation Model (CFM)

In the framework of CFM, the functional form of the Gibbs free energy of mixing G_M is fitted to the experimental thermodynamic data (the enthalpy of mixing and activities of alloy components) to obtain four interaction energy parameters. Combining the energetic terms with the coordination number, melting temperatures, molar volumes, and reference surface tension data of pure components, the surface tension of compound forming melts can be calculated by

$$\sigma = \sigma_A + \frac{k_B T}{\alpha} \cdot \ln\left(\frac{c_A^s}{c_A}\right) + \frac{k_B T}{\alpha} \cdot \ln\left(\frac{\gamma_A^s}{\gamma_A}\right) \tag{15.5a}$$

$$\sigma = \sigma_B + \frac{k_B T}{\alpha} \cdot \ln\left(\frac{c_B^s}{c_B}\right) + \frac{k_B T}{\alpha} \cdot \ln\left(\frac{\gamma_B^s}{\gamma_B}\right) \tag{15.5b}$$

where k_B, α, σ_i, c_i, c_i^s, γ_i, γ_i^s ($i = A, B$) are the Boltzmann constant, mean surface area, surface tensions, compositions, activity coefficients of the pure components in the bulk, and the surface phase, respectively [24, 92, 93].

6.1.2 Quasi Chemical Approximation for Regular Solution (QCA)

Thermodynamic and surface properties of alloy systems with weak and moderate interactions among constituent atoms can be appropriately described by the first or Quasi Chemical Approximation (QCA) for regular solution [52]. This model can also be applied to calculate the surface properties of more complex liquid alloys, but a comparison between the predicted and experimental values indicates a large difference. It is still larger in the case of the alloy systems involving either strongly exothermic or endothermic reactions [24]. The QCA for the regular solution is characterized by one energy parameter ω that, using thermodynamic data, can be obtained together with its temperature dependence. In the framework of QCA, the surface tension is calculated by

$$\sigma = \sigma_A + \frac{k_B T (2 - pZ)}{2\alpha} \cdot \ln\left(\frac{c_A^s}{c_A}\right) + \frac{Z k_B T}{2\alpha}$$
$$\times \left[p \cdot \ln \frac{(\beta^s - 1 + 2c_A^s)(1 + \beta)}{(\beta - 1 + 2c_A)(1 + \beta^s)} - q \cdot \ln \frac{(\beta - 1 + 2c_A)}{(1 + \beta)c_A} \right] \tag{15.6a}$$

$$\sigma = \sigma_B + \frac{k_B T (2 - pZ)}{2\alpha} \cdot \ln\left(\frac{c_B^s}{c_B}\right) + \frac{Z k_B T}{2\alpha}$$
$$\times \left[p \cdot \ln \frac{(\beta^s - 1 + 2c_B^s)(1 + \beta)}{(\beta - 1 + 2c_B)(1 + \beta^s)} - q \cdot \ln \frac{(\beta - 1 + 2c_B)}{(1 + \beta)c_B} \right] \tag{15.6b}$$

where Z is the coordination number, β and β^s are auxiliary variables containing implicitly the order energy parameter ω, and c_i and c_i^s are compositions of component $i = A$, B in the bulk and surface phase, respectively. p and q are the surface coordination fractions defined as the fractions of the total number of nearest neighbors of an atom in its own layer and in the adjoining layer. Therefore, $p + q = 1$. For a closed-packed structure, the values of p and q parameters usually are taken as ½ and ¼, respectively [52, 92].

6.1.3   Butler's Model

Due to its simplicity, Butler's model is the most used to calculate the surface tension of liquid alloys, although it is, as the QCA for regular solution, appropriate for weakly/moderate interacting systems. Moreover, when both models are applied to weakly interacting systems, the surface tension isotherms overlap. Using the Butler's model, the surface tension can be calculated by

$$\sigma = \sigma_i + \frac{RT}{S_i} \ln\left(\frac{c_i^s}{c_i^b}\right) + \frac{1}{S_i}\left[G_i^{xs,s}\left(T, c_i^s\right) - G_i^{xs,b}\left(T, c_i^b\right)\right] \ (i = A, B) \qquad (15.7)$$

where R, S_i, c_i^b, c_i^s, $G_i^{xs,b}$, $G_i^{xs,s}$ are gas constant, surface area, composition, and partial excess Gibbs free energy of a component i in the bulk and surface phase, respectively. The last two mentioned are the functions of temperature and composition. From an energetic point of view, the partial excess Gibbs free energy $G_i^{xs,s}$ of the surface phase has the same functional form as that of $G_i^{xs,b}$ times a factor of the reduced coordination [24, 52].

6.1.4   Perfect Solution Model

Surface tension of alloys exhibiting the ideal behavior in the bulk and in the surface phase can be accounted for by the perfect solution model [94] as follows:

$$\exp\left(-\left(\frac{\sigma\overline{A}}{k_B T}\right)\right) = c_A \cdot \exp\left(-\left(\frac{\sigma_A\overline{A}}{k_B T}\right)\right) + c_B \cdot \exp\left(-\left(\frac{\sigma_B\overline{A}}{k_B T}\right)\right) \qquad (15.8)$$

where $\overline{A}$, c_A, c_B, σ_A, σ_B are the mean surface area, composition, and surface tension of alloy components, respectively. Otherwise, the difference between the most appropriate surface tension isotherm and that calculated by the perfect solution model can be used as an indicator of the interactions in an alloy system. Indeed, positive deviations of ideality is related to the systems of which the mixing thermodynamic properties deviate negatively from Raoult's law and vice versa [44].

6.2   Molar Volume

The molar volume of binary alloys is expressed by

$$V_{\text{Alloy}} = \frac{c_A M_A + c_B M_B}{\rho_{\text{Alloy}}} \qquad (15.9)$$

where M_A, M_B are the molar masses of components A and B and ρ_{Alloy} is the alloy density. The excess quantities are characteristics of real alloy systems [35, 44]. Therefore, the excess volume can be calculated by

$$V^E = V_A - V_{\text{ideal}} = \frac{c_A M_A + c_B M_B}{\rho_{\text{Alloy}}} - \left(\frac{c_A M_A}{\rho_A} + \frac{c_B M_B}{\rho_B} \right) \tag{15.10}$$

6.3 Viscosity

The scarcity and/or controversial trend of experimentally determined viscosity data is the main problems of developing and approving models for the viscosity of liquid binary alloys. There are many empirical and semiempirical viscosity models [35, 44], and after preliminary calculations, the model reported by Iida et al. [44, 95] seems to be the most appropriate to predict the viscosity of liquid Al-Ni alloys. Taking into account the mixing functions of a melt, Iida et al. [95] have developed the viscosity model that combines the energetics of a system in terms of thermodynamic and hard-sphere contributions. An extension of Iida's model [95] was proposed by Terzieff [96, 97]. According to that model, the relative viscosity of an alloy melt is expressed as the ratio of the excess viscosity and additive viscosity, in the form

$$\frac{\eta^{xs}}{\eta_{id}} = \alpha \cdot \frac{c_A c_B (\overline{\sigma_1} - \overline{\sigma_2})^2}{c_A \overline{\sigma}_1^2 - c_B \overline{\sigma}_2^2} + \beta \cdot \left[\left(1 + \frac{c_A c_B (m_1^{0.5} - m_2^{0.5})^2}{(c_A m_1^{0.5} - c_B m_2^{0.5})^2} \right) - 1 \right]$$
$$+ \gamma \cdot \frac{2H_{\text{mix}}}{RT} + \delta \cdot \frac{2 c_A c_B |V_1 - V_2|}{V_1 + V_2} \tag{15.11}$$

where H_{mix}, R, c_i, m_i, $\overline{\sigma}_i$, V_i ($i = A, B$) are the enthalpy of mixing, gas constant, atomic fraction, atomic mass, hard-sphere diameter, and molar volume of a component i, respectively. α, β, γ, and δ are statistical weights obtained by fitting to Eq. (5.13) a large number of experimental viscosity datasets at the equiatomic composition [96]. $\eta_{id} = c_A \eta_A + c_B \eta_B$ is the viscosity of the ideal mixture where η_1 and η_2 are the viscosities of the pure components.

Based on the standard relation $\eta(T) = \eta(T)_{id} + \eta(T)^{xs}$, the viscosity of binary melts can be expressed by

$$\eta(T) = \eta(T)_{id}(1 + \eta(T)^{xs}) \tag{15.12}$$

7   Data Analysis

Thermophysical property *data analysis* has a fundamental role in the theory and experimental determination aiming to assess more elaborated models and procedures. In general, such a goal is achieved for binary alloys and only partially attained for ternaries, while in the case of multicomponent alloy systems, until now, there is not a single appropriate theory describing their thermophysical properties in terms of mathematical models [22, 35, 44, 98]. Therefore, the thermophysical properties data of complex metallic melts such as Ni- and Ti-based alloys can be analyzed with respect to the dominant binary subsystem, i.e., the Al-Ni [34, 36, 37, 41, 54, 55] or the Al-Ti [67, 76, 100, 101], respectively. In some cases, taking into account the third main component of a multicomponent alloy, the data analysis is extended to the corresponding ternary subsystem [54, 55]. In both analyses, the effects of the minority components on the investigated alloy property are estimated quantifying their cumulative impact on it.

An important part of the thermophysical properties data analysis is the sources of errors that will explain why the experimental results deviate from the model-predicted values. Roughly, one can distinguish two types of errors, i.e., *systematic errors* and *random errors*. The first type is inherent in the measurement process and affects the accuracy of a measurement. Repeating the experiments, no matter how carefully, systematic errors cannot be eliminated. Random errors are related to the precision of instruments, purity of materials, and surrounding atmospheres that can be reduced but never with absolute certainty [102]. However, speaking about multicomponent industrial alloys including Ni-based superalloys, the discrepancies in the reported properties data, such as the compositions of CMSX-4, LEK94, RENE N5, etc., are listed in Table 15.1, and as a consequence, different values of their thermophysical properties can be observed [37, 41, 55, 56].

In the framework of the ThermoLab and ThermoProp ESA MAP Projects [39, 40] that have been dedicated to the measurements and modelling of the thermophysical properties of liquid alloys, for the evaluation of validity and reliability of the experimental data [34, 36, 37, 41, 42, 54–57, 98], the methodological twofold approach has been applied. Indeed, in order to discern potential sources of systematic measurement errors associated with different equipment and/or methods, each property has been measured in parallel by different techniques at different participating laboratories using the alloys of the same compositions (Table 15.2), and the results were compared including existing literature data. On the other side, the obtained experimental data were used to validate the property models, and the two aspects change in concert to modify one another, aiming to improve the reliability of data as well as to identify the recommended values [98]. The present results can be used as the input data for numerical simulation of all industrial processes that involve the presence of the liquid phase.

In the following, the experimental datasets on the thermophysical properties such as the surface tension, density, viscosity, specific heat, and heat of fusion of Ni-based industrial superalloys (Tables 15.3, 15.4, and 15.5) and the corresponding theoretical models have been analyzed.

Table 15.3 Parameters of the linear fits $\sigma = \sigma_0 - d\sigma/dT(T - T_L)$ to the experimental surface tension datasets for liquid Ni-based superalloys

Alloy	Liquidus temperature T_L,K	Surface tension σ_0 at T_L, Nm^{-1}	Temperature coefficient $d\sigma/dT$, 10^{-4}Nm^{-1}K^{-1}	Measurement temperature range,K	Method	Exp. error %	References
CMSX-4	1660	1.807	-2.9	1680–1840	SD	± 2	[57]
CMSX-4	1654	1.844	-2.5	1650–1780	PD	± 2	[41]
[a]CMSX-4	1654	1.773	-5.6	1650–1930	R	± 2	[41]
CMSX-4	1654	1.79 ± 0.05	-9.09	1662–1893	$PF:OD-EML$	± 2.7	[34]
CMSX-10	1702	1.758 ± 0.025	-4.7 ± 0.4	1715–1773	PD	<3	[55]
CMSX-10	1683	1.71 ± 0.02	-5.80	1575–1925	$PF:OD-EML$	<1	[36]
CMSX-10	1706 ± 5	1.698 ± 0.002	-1.438 ± 0.294	1575–1825	$OD\text{-}EML^{\mu-g}$	$<\pm1$	[37]
RENE N5	1658 ± 11	1.752	-6.7	1638–1773	PD	± 3	[54]
RENE 90	1641 ± 10	1.851	-5.2	1643–1738	PD	± 3	[54]
RENE 90	1641 ± 10	1.712 ± 0.003	-2.16 ± 0.26	1463–1793	$OD\text{-}EML^g$	2	[56]
LEK-94	1668	1.718 ± 0.040	-5.2 ± 0.4	1685–1773	PD	<3	[55]
LEK-94	1666	1.73 ± 0.02	-4.51	1575–1930	$PF:OD-EML$	<1	[36]
LEK-94	1666 ± 5	1.677 ± 0.001	-3.208 ± 0.165	1550–1850	$OD\text{-}EML^{\mu-g}$	$<\pm1$	[37]
MC-2	1661 ± 5	1.680 ± 0.002	-1.533 ± 0.206	1575–1850	$OD\text{-}EML^{\mu-g}$	$<\pm1$	[37]
MC-2	1651	1.838 ± 0.045	-5.1 ± 0.4	1653–1723	PD	<3	[55]
TMS-75	1702	1.805 ± 0.044	-4.9 ± 0.4	1683–1753	PD	<3	[55]

(continued)

Table 15.3 (continued)

Alloy	Liquidus temperature T_L,K	Surface tension σ_0 at T_L, Nm^{-1}	Temperature coefficient $d\sigma/dT$, 10^{-4}Nm^{-1}K^{-1}	Measurement temperature range,K	Method	Exp. error %	References
IN718	1609; 2000[b]	1.842	−1.1	1850–2100	OD-*EML^g*	±1	[22]

SD sessile drop, *PD* pinned drop, *OD* oscillating drop, *EML* electromagnetic levitation, *PF* parabolic flights, *R* recommended values obtained combining the results of different measurements. Superscripts: *g* – on ground, *μ-g* – microgravity

[a]Equation for linear fits proposed by the authors

[b]Temperature used to describe the surface tension

Table 15.4 Density parameters of the linear fits $\rho = \rho_0 - d\rho/dT(T - T_L)$ to the experimental density datasets for liquid Ni-based superalloys

Alloy	Liquidus temperature T_L, K	Density ρ_0 at T_L, g·cm^{-3}	Temperature coefficient $d\rho/dT$, 10^{-3}g·cm^{-1}K^{-1}	Measurement temperature/range, K	Method	Exp. error %	References
CMSX-4	1660	7.75	−0.824	1660–1890	MSDM	±0.88	[57]
CMSX-4	1660	7.72	−0.913	1660–1890	MSM	±0.48	[57]
[a]CMSX-4	1660	7.74	−0.869	1660–1890	R	–	[57]
CMSX-4	1654	7.88	−1.32	1654–1760	SD	±1.5	[41]
CMSX-4	1654	7.781	−0.41	1723–1843	LD-EML^g	±1.5	[41]
[a]CMSX-4	1654	7.876	−1.23	1654–1843	R	–	[41]
[a]CMSX-4	1653	7.754	−0.9	1653–1873	R	–	[98]
CM186LC	1654	7.76	−0.774	1654–1890	MSDM	±0.88	[57]
CM186LC	1654	7.74	−0.502	1654–1890	MSM	±0.48	[57]
CM186LC	1654	7.75	−0.638	1654–1890	R	–	[57]
CMSX-10	1676	8.08	−0.661	1676–1825	MSDM	±0.88	[57]
CMSX-10	1702	7.19 ± 0.03	−1.6	1715–1773	PD	±5	[55]
CMSX-10	1706 ± 5	8.21 ± 0.15	−0.535 ± 0.05	1525–1875	OD-$EML^{\mu - g}$	1.6	[37]
RENE N5	1658 ± 11	7.53	−1.6	1658–1773	PD	±3	[54]
RENE 90	1641 ± 10	8.01	−1.8	1658–1778	PD	±3	[54]
RENE 90	1641 ± 10	8.355	−1.14	1591–1866	LD-EML^g	–	[56]

(continued)

Table 15.4 (continued)

Alloy	Liquidus temperature T_L, K	Density ρ_0 at T_L, g·cm^{-3}	Temperature coefficient $d\rho/dT$, 10^{-3} g·cm^{-1}K^{-1}	Measurement temperature/range, K	Method	Exp. error %	References
MC-2	1661 ± 5	7.91 ± 0.15	−0.658 ± 0.05	1550–1875	OD-$EML^{\mu-g}$	1.6	[37]
MC-2	1651	7.56 ± 0.07	−1.3	1653–1723	PD	±5	[55]
LEK-94	1668	7.13 ± 0.06	−0.95	1685–1773	PD	±5	[55]
LEK-94	1666 ± 5	7.57 ± 0.15	−0.631 ± 0.05	1550–1875	OD-$EML^{\mu-g}$	1.6	[37]
TMS-75	1702	7.37 ± 0.07	−1.15	1683–1753	PD	±5	[55]
IN718	1609	7.4	−0.88	1609–1873	R	–	[98]

SD sessile drop, *PD* pinned drop method, *MSDM* modified sessile drop method, *MPM* modified pycnometric method, *LD* levitated drop, *OD* oscillating drop, *EML* electromagnetic levitation, *PF* parabolic flights, *R* recommended values obtained combining the results of different measurements. Superscripts: *g* – on ground, *μ–g* – microgravity

[a]Equation for linear fits proposed by the authors

Table 15.5 Parameters of the Arrhenius type (η_0, ΔE_A) or linear ($\eta(T_L)$, $d\eta/dT$) fits to the experimental viscosity datasets for liquid Ni-based superalloys

Alloy	Liquidus temp. T_L, K	Viscosity $\eta(T_L)$, mPa · s	Viscosity η_0, mPa · s	Activation energy ΔE_A, eV/atom	Measurement temperature/range, K	Method	Exp. error %	References
CMSX-4	1654	9.6 ± 1.2	0.31	0.42	1690–1835	$PF : OD - EML$	20–30	[34]
CMSX-4	1654	$\eta = 8.36 - 0.0182(T - 1654)$			1640–1800	OCV	± 9	[41]
LEK-94	1666	9.7 ± 1.4	0.63	0.36	1615–1865	$PF : OD - EML$	± 14	[36]
LEK-94	1666 ± 5	8.4	0.0128	0.930	1560–1785	$OD\text{-}EML^{\mu - g}$	1.9	[37]
CMSX-10	1683	7.7 ± 1.2	0.23	0.16	1600–1840	$PF : OD - EML$	± 15	[36]
CMSX-10	1706 ± 5	8.6	0.406	0.449	1600–1780	$OD\text{-}EML^{\mu - g}$	1.9	[37]
MC-2	1661 ± 5	11.9	0.001421	1.294	1575–1725	$OD\text{-}EML^{\mu - g}$	1.9	[37]
IN718	1609	–	0.196	5848[a]	1635–1780	OCV	–	[22]

OCV oscillating cup viscosimetry, *OD* oscillating drop, *EML* electromagnetic levitation, *PF* parabolic flights; Superscripts: μ–g – microgravity

[a] $\Delta E_A/T$ [J/mol]

7.1 Surface Tension Data

Surface tension of Ni-based superalloys (Table 15.3) has been measured using container-based [41, 54, 55, 57] and containerless [22, 34, 36, 37, 56] methods. The overall temperature range of measurements varies between the lowest liquidus temperature of 1463 K [56] and the maximum reported temperature of 2100 K [22]. Due to experimental difficulties related to high temperatures and reactivity of metallic melts with substrate/container materials, in the case of the containerless methods, significantly larger measurement intervals can be observed. Temperature dependence of the surface tension of the alloys investigated obeys a linear law with a negative surface tension temperature coefficient, indicating a decrease in the surface tension with the increasing temperature. For each Ni-based superalloy, the values of the liquidus temperature, measured by different experimental methods, are very close to each other and agree within experimental uncertainty. Depending on the measurement method, the experimental errors vary between 1% and 3% (Table 15.3).

7.1.1 Surface Tension Data and Container-Based Measurements

There are eight surface tension datasets of Ni-based superalloys obtained by the container-based measurements (Table 15.3), mainly by the pinned drop method (PD; see Sect. 2.1.2). Indeed, CMSX-4 [41], RENE-5 [54], RENE-90 [54], CMSX-10 [55], LEK-94 [55], MC-2 [55], and TMS [55] have been measured by the pinned drop method. Preliminary wetting tests of the materials and experimental conditions have indicated non-oriented monocrystalline alumina (sapphire) as the most suitable crucible material and reducing atmosphere of Ar-5 at%H_2 that was further reduced with Ta [41] or Zr [54, 55] getters ensuring close to the sample the oxygen partial pressure of less than 10^{-18} Pa. The surface tension of CMSX-4 has also been measured by the sessile drop (SD; Sect. 2.1.1) method [57] using the substrate of high-purity alumina (99.8%), under a purified Ar-atmosphere with an oxygen partial pressure of less than 10^{-13} Pa in the gas outlet.

7.1.2 Surface Tension Data and Containerless Measurements

The experimental difficulties related to high temperatures and high reactivity of alloy melts with substrate/container materials have been overcome by using containerless processing techniques, such as the oscillating drop method (*OD*) with electromagnetic levitation both on ground (OD-*EML^g*), and in microgravity experiments on parabolic flights (*PF*) or on board of sounding rockets (OD-*$EML^{\mu-g}$*) [35, 99]. As in the case of container-based methods, eight surface tension datasets were obtained using the containerless methods (Table 15.3). The surface tension of RENE-90 [56] and IN718 [22, 101] was measured over wide temperature ranges using

electromagnetic levitation and the oscillating drop technique on ground (OD-EML^g; see Sect. 2.2.1) in an atmosphere of Ar-5 at%H_2 and purified argon, respectively. Two types of surface tension measurements were performed in microgravity conditions using the oscillating drop method with electromagnetic levitation (OD-$EML^{\mu - g}$; see Sect. 2.2.2). Indeed, CMSX-4 [34], LEK-94 [36], and CMSX-10 [36] were measured on board a parabolic flight (*PF*), while datasets on LEK-94 [37], CMSX-10 [37], and MC-2 [37] were obtained on board of the International Space Station (ISS). The microgravity conditions ensure the measurements in the undercooled liquid phase [36, 37] and the largest temperature intervals varying between 300 and 350 K above the liquidus temperature of the alloys (Table 15.3).

7.1.3 Surface Tension Isotherms of Al-Ni Melts

The Al-Ni system was taken as the model system to analyze the surface tension of Ni-based industrial alloys. The surface properties of liquid Al-Ni alloys have been detailed in [43]. Taking into account that the Al-Ni system is compound forming, the Compound Formation Model (CFM) as the most appropriate, together with the quasi-chemical approximation for regular solution (QCA) and the perfect solution model, was used to calculate the surface tension isotherms of Al-Ni melts (Eqs. 15.5a, 15.5b, 15.6a, 15.6b, and 15.8; see Sect. 6.1). QCA for regular solution and Butler's model calculations give similar results. The calculations were performed for $T = 1800$ K using the thermodynamic data of the Al-Ni liquid phase [4, 103, 104], Al and Ni molar volumes [44], as well as the surface tension reference data of liquid Al [105] and Ni [106] as the input data. CFM calculations assumed the *AlNi* intermediate phase as energetically favored. The energetics of Al-Ni liquid alloys for $T = 1800$ K is described by four interaction energy parameters (in *RT* units), $g = 4.78$, $\omega_{12} = -3.8$, $\omega_{13} = -2.4$, and $\omega_{23} = -3.11$, while the prevalence of *AlNi* dimers, at least near the melting temperatures, characterizes the melt structures [43]. An irregularity of the CFM surface tension isotherm indicates pronounced short-range ordering in liquid Al-Ni alloys (Fig. 15.5a).

7.1.4 Ni-Based Superalloys: Analysis of Surface Tension Data

The surface tension data of CMSX-4 [34, 41, 57], RENE-5 [54], RENE-90 [54, 56], LEK-94 [36, 37, 55], MC-2 [37, 55], TMS [55], and IN718 [22] of Ni-based superalloys were analyzed with respect to the calculated surface tension isotherms of liquid Al-Ni binary system. To this aim, the surface tensions of Ni-based superalloys are shown in Fig. 15.5 with respect to the Al-content in each alloy. For the alloys investigated, Al-content is ranging between 7 and 14 at %, and therefore, in order to have a clear picture of their surface tension, the data are shown in an enlarged area for $86 < $ Ni (at %) < 93 (Fig. 15.5b). An exception represents IN718 with 1.1 Al (at %), shown in Fig. 15.5a.
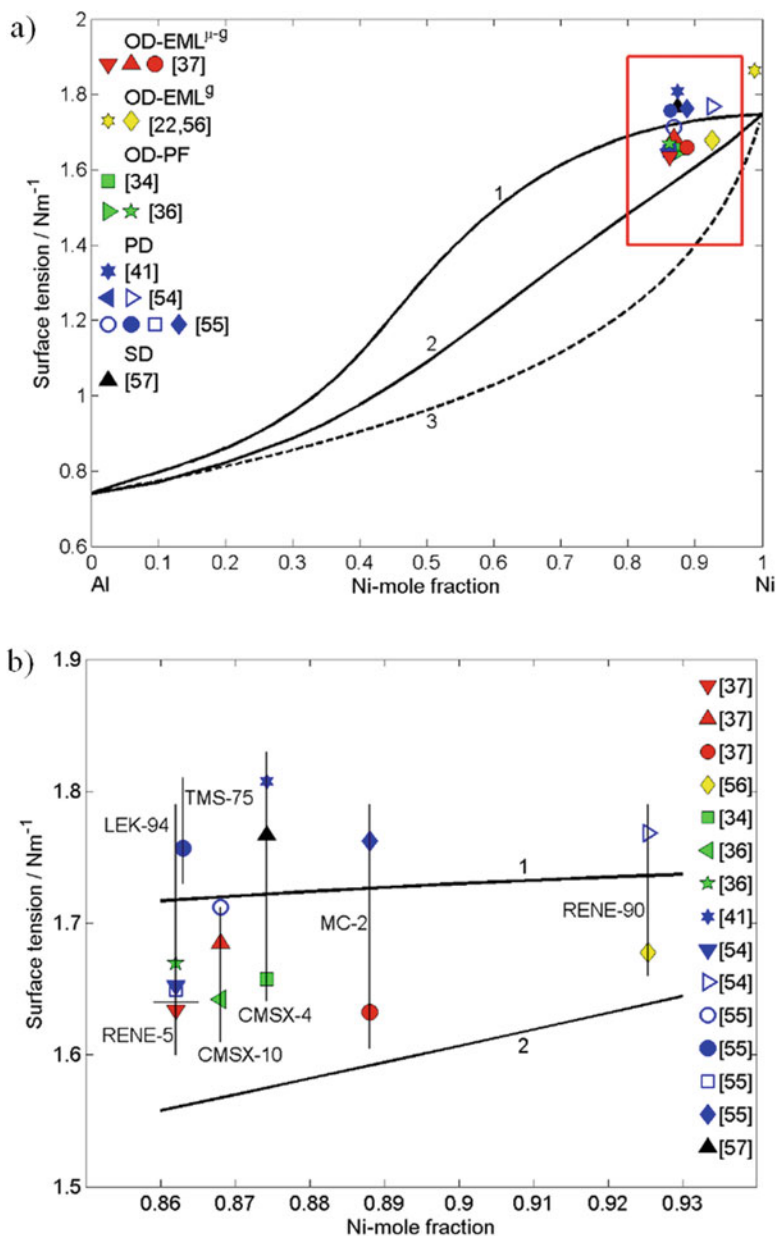
Fig. 15.5 (**a**) Surface tension experimental data [34, 36, 37, 41, 54–57] of liquid Ni-based superalloys. For comparison, the surface tension isotherms of Al-Ni alloys calculated for $T = 1800$ K are shown: 1 – CFM; 2 – QCA; 3 – perfect solution model. (**b**) An enlarged area of (**a**) with the respect to Al-content in Ni-based superalloys

The CFM, QCA for regular solution, and perfect (ideal) solution isotherms were calculated for $T = 1800$ K. To describe the surface tension of Al-Ni alloys, the CFM isotherm is the most appropriate [24, 43]. The effects of the minority alloying elements (transition and refractory metals) on the surface tension of Ni-based superalloys are comparable, at least to the first approximation, to that of liquid nickel itself. Therefore, for the calculations, the Ni-content was taken as the sum of the amount of Ni present in the alloy plus the minority alloying elements. Based on this, the surface tension data of each Ni-based alloy is compared to the corresponding Al-Ni calculated values. General agreement between the surface tension data of Ni-based alloys can be observed. For each alloy, at least the higher measured values of the surface tension are close or higher with respect to the CFM isotherm and may be considered more reliable. All other surface tension values are higher than the corresponding Al-Ni values calculated by the QCA. Decreasing Al-content in Al-Ni alloys, an increase in their surface tension is evident [43]. However, in the case of liquid Ni-based superalloys, this can be observed only for the surface tension data of RENE-90 [56] and IN718 [22], measured by the (OD-EML^g) in two different laboratories (Fig. 15.5a). On the contrary, within each of the surface tension datasets obtained by the same measurement method (Fig. 15.5b) such trend was not observed. The concomitant effects of surface oxidation, Al-vaporization, and segregation together with the presence of impurities in the alloy melts can explain what observed. Indeed, it is well known that the surface tension of metallic melts, such as Ni-based superalloys containing various reactive metals (Table 15.2), can be strongly affected by certain surface-active elements, mainly oxygen or/and sulfur [34, 54]. Concerning Ni-based superalloys, some effects of surfactants on their surface tensions are evident: Within the data of each alloy, the surface tensions at the melting temperatures differ up to 12%, and the surface tension temperature coefficients differ up to four times (Table 15.3).

The discrepancies between the surface tension experimental results (Fig. 15.5; Table 15.3) measured by the pinned [41, 54, 55] and sessile [57] drop methods and the two datasets obtained under microgravity conditions by PF- OD-EML^g [34, 36] and OD-EML^g on a board of ISS [37] containerless methods probably arise, as stated in [34, 41, 54], from differing amounts of oxygen present in the working atmospheres, from the determination of experimental temperature, as well as from different systematic errors of the compared measurements methods. A modification of the sample composition because of oxidation or Al-vaporization may have a strong influence on the measurements [41, 57]. In addition, SEM-EDS analysis performed on the Ni-based superalloys revealed the presence of highly reactive elements, such as Al, Re, Ta, and Ti, which have great influence on the surface tension values owing to their intrinsic reactivity in a gaseous environment as well as with common crucible materials.

Keeping in mind that the model-predicted values of the surface tension strongly depend on the choice of the surface tension reference data for pure components, one of the proposed strategies may be the recalculations of the Al-Ni surface tension isotherms within each measurement method, using the Al and Ni surface tension reference data obtained by that method (Table 15.3). Therefore, the higher accuracy

of model-predicted data could be obtained. Another strategy is the development of theoretical models that could describe the surface tension of multicomponent alloys properly.

7.2 Density Data

The density of liquid Ni-based superalloys (Table 15.4) has been measured by container-based [41, 54, 55, 57] and containerless [37, 41, 56] methods. The measurements were performed for the temperatures ranging between 1525 [37] and 1890 K [57]. As in the case of the surface tension, the largest measurement interval was observed for the data obtained by the containerless method [37]. The highest difference, up to 18%, is observed for CMSX-10 [37, 55, 57], while the CMSX-4 and CM186LC alloys exhibit the best agreement (Fig. 15.6). Indeed, the density data of four CMSX-4 alloys was determined by the three container-based methods and one containerless method, indicating a good agreement of the results within the experimental error, and are very close to the corresponding value recommended by Mills [98]. Density of all investigated liquid alloys can be described by a linear function with a negative temperature coefficient. The maximum experimental errors of $\pm 5\%$ was observed in [55].
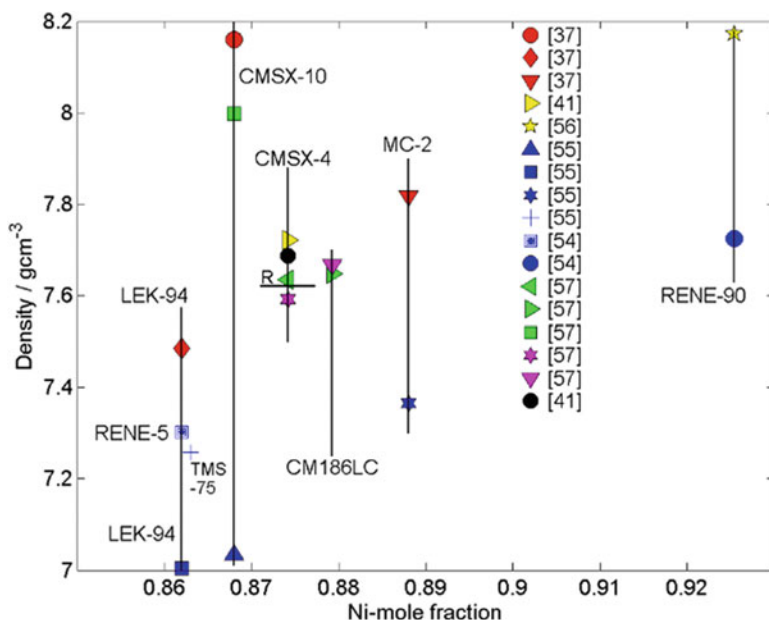
Fig. 15.6 Density experimental data [37, 41, 54–57] of liquid Ni-based superalloys measured at $T = 1800$ K and compared to the Al-Ni system with respect to Al-content in the superalloys (R – the recommended value [98])

7.2.1   Density Data and Container-Based Measurements

Density of twelve Ni-based liquid superalloys has been measured by the container-based methods. The sessile (SD) drop, pinned drop (PD; Sect. 3.1), modified sessile drop (MSDM), and modified pycnometric (MPM) methods were used to measure CMSX-4 [41, 57] alloy, while the last two methods were applied for the measurements of the CM186LC [57]. RENE-5 [54], RENE-90 [54], CMSX-10 [55], LEK-94 [55], MC-2 [55], and TMS [55] have been determined using the pinned drop method. Among the density data obtained by the pinned drop method, the largest measurement interval of 120 K and the undercooling of 19 K can be observed for RENE90 and TMS-75, respectively [54, 55]. The measurement errors vary between $\pm 0.48\%$ and $\pm 5\%$.

7.2.2   Density Data and Containerless Measurements

The density of liquid CMSX-10 [55], LEK-94 [55], and MC-2 [55] alloys was measured by the oscillating drop method (*OD*) with electromagnetic levitation on board of the ISS (OD-$EML^{\mu - g}$; Sect. 3.3) and assessed optically [37], while the data of RENE-90 [56] and CSMX-4 [41] were obtained by the same method with electromagnetic levitation on ground (OD-EML^g; Sect. 3.2). The microgravity conditions ensure the measurements in the undercooled liquid phase up to 350 K below the liquidus temperature as well as the larger measurement intervals varying between 325 and 350 K above the liquidus temperature of the alloys [37] (Table 15.4). The density data for CMSX-10, LEK-94, and MC-2, obtained by OD-$EML^{\mu - g}$ [37] and RENE-90 [56] measured by (OD-EML^g) shown in Fig. 15.6, are significantly higher with respect to the corresponding data obtained by the pinned drop method [54, 55].

7.2.3   Molar Volume Isotherms of Al-Ni Melts

Molar volume is often used in the theoretical treatment of metallic melts, for example, to display a steplike behavior on melting indicating a first-order transition or to link qualitatively the changes in volume with those in mixing thermodynamic functions and structural ordering on the short-range scale [44]. Indeed, negative deviation of the molar volume from ideality is typical for compound forming alloy systems, such as the Al-Ni. The density reference data of liquid Al [107], Ni [108], and Al-Ni alloys [109] were used to calculate the molar volume isotherm (Eqs. 15.9 and 15.10) for $T = 1800$ K. The molar volume isotherm of liquid Al-Ni alloys deviate negatively from the ideal mixture (Fig. 15.7a), indicating pronounced short-range ordering in the melts.
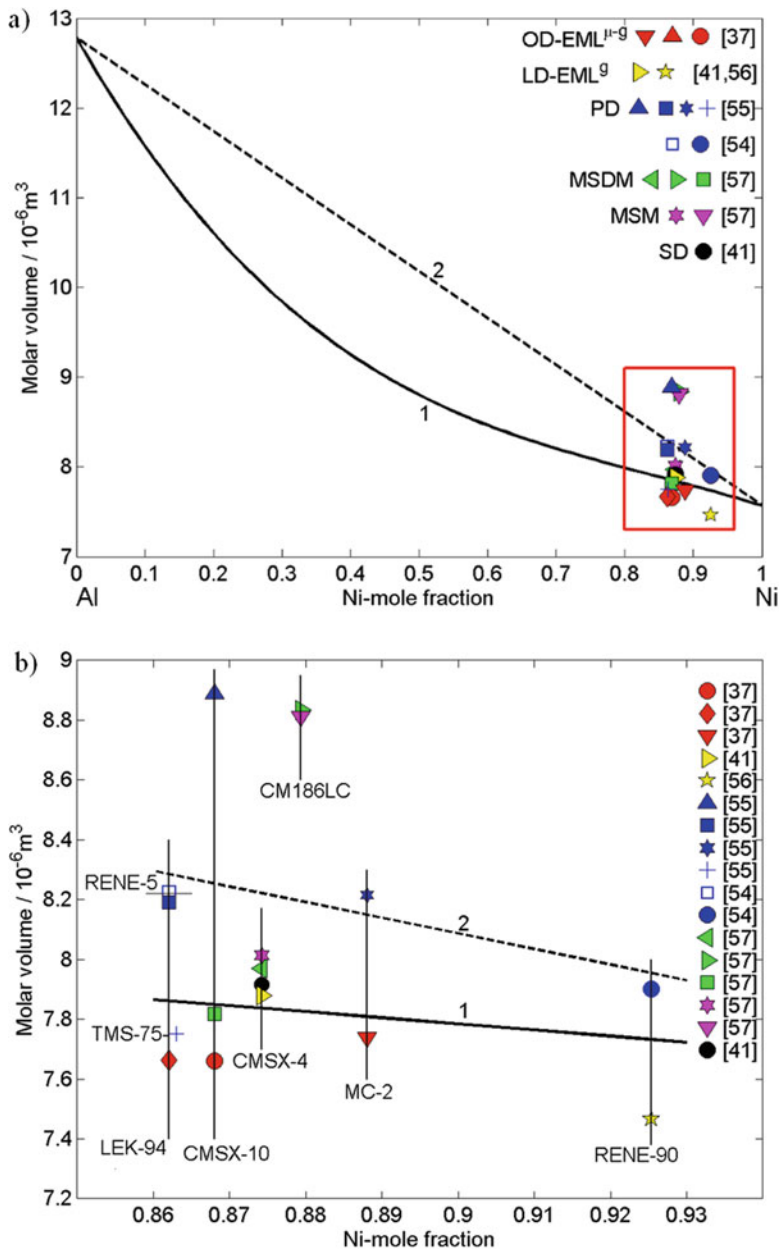
Fig. 15.7 (**a**) Molar volume data [37, 41, 54–57] of liquid Ni-based superalloys. For comparison, the molar volume isotherm of Al-Ni alloys calculated for T = 1800 K are shown: 1 – regular solution model; 2 – ideal solution model. (**b**) An enlarged area of (**a**) with respect to Al-content in Ni-based superalloys

7.2.4 Molar Volume Data

The density data of CMSX-4 [34, 41, 57], RENE-5 [54], RENE-90 [54, 56], LEK-94 [36, 37, 55], MC-2 [37, 55], TMS [55], and CM186LC [57] Ni-based superalloys (Table 15.4) were used to calculate their molar volume. Subsequently, the molar volume data of Ni-based superalloys were analyzed with respect to Al-content in each alloy with respect and compared to the molar volume isotherm of liquid Al-Ni binary system (Fig. 15.7a). For the alloys investigated, Al-content is ranging between 7 and 14 at %, and therefore, in order to have a clear picture of their molar volume, the data are shown in an enlarged area for $86 <$ Ni (at %) < 93 (Fig. 15.7b). The similarity of the thermodynamic mixing functions of liquid Al-Ni alloys and Ni-based superalloys, exhibiting negative deviations from the Raoult's law, suggests the same behavior of their molar volumes [44, 109]. Therefore, the molar volume values of Ni-based alloys lying below the ideal solution isotherm or, even better, below the regular solution isotherm can be considered as reliable. The best agreement exhibits the molar volume data calculated from the density data measured on board of the ISS (OD-$EML^{\mu - g}$) [37] and with electromagnetic levitation on ground (OD-EML^g) [56], while the data of CMSX-10 [55] and CM186LC [57] follow an opposite trend and may perhaps be less accurate.

7.3 Viscosity Data

Viscosity of Ni-based superalloys (Table 15.5) has been measured using container-based [22, 41] and containerless [34, 36, 37] methods. The overall temperature range of measurements varies from the lowest undercooling temperature of 1560 K [37] to the maximum temperature of 1865 K [36]. An Arrhenius behavior of the viscosity of Ni-based alloys [22, 34, 36, 37] can be observed, while for CMSX-4 [41], the temperature dependence of viscosity can be described by a linear equation with negative temperature coefficient. Depending on the measurement method, the experimental errors are in the range of 1.9–30% (Table 15.5).

7.3.1 Viscosity Data and Container-Based Measurements

The oscillating cup viscosimetry (OCV) is the container-based method (see Sect. 4.1) used to measure the viscosity of IN718 [22] and CMSX-4 [41]. For the last one, an undercooling of 15 K allowed the measurements at 1640 K, but due to a short temperature interval, an Arrhenius viscosity behavior was not observed. A comparison of the viscosity datasets reported in [41] shows that the IN718 dataset follows the same trend. However, a few years later, the new viscosity data of liquid IN718 [22] obtained by the measurements using the same apparatus obeys an Arrhenius-type equation (Table 15.5).

7.3.2   Viscosity Data and Containerless Measurements

The viscosity data of Ni-based superalloys were obtained in microgravity experiments (see Sect. 4.2) using the oscillating drop method with electromagnetic levitation (OD-$EML^{\mu - g}$) on parabolic flights (*PF*) [34, 35] and on board of the ISS [37]. The effect of O_2-content on the viscosity of CSMX-4 has been analyzed in terms of low and high oxygen-containing samples and the corresponding viscosity values [34]. Contrary to the surface tension, the presence of oxygen in an alloy melt increases its viscosity. The error of the individual viscosity values is estimated to be between 20% and 30%, while the error in the ratio of the low to high oxygen values is estimated as <10%. The viscosity of CMSX-10 and LEK-94 Ni-based superalloys was also measured by (OD-$EML^{\mu - g}$) on parabolic flights [36]. Viscosities of CSMX-4 [34], CMSX-10, and LEK-94 melts [36] obey to the Arrhenius behavior. The limited time of microgravity (about 20 s) per parabola limits the measurement precision and the type of measurements that can be performed. Long-duration microgravity experiments on the ISS (about 20 min) offer an improvement of accuracy and precision. Indeed, the viscosity measurement errors of about 1.9% for the viscosity data of CMSX-10, MC-2, and LEK-94 obtained on board of the ISS (OD-$EML^{\mu - g}$) are reported in [37]. The viscosity of the three alloys can be described by an Arrhenius-type equation (Table 15.5).

7.3.3   Viscosity Isotherm of Al-Ni Melts

The analysis of viscosity of liquid Ni-based alloys was done using the Al-Ni as the model system. Preliminary analysis of the viscosity models reported in [35, 44] indicated the model developed by Iida et al. [95] as the most appropriate to describe the viscosity of Al-Ni melts. Some improvements of the model [95] were done by Terzieff [96, 97], and therefore, to describe the viscosity of liquid Al-Ni alloys, the Terzieff model (Eqs. 15.11 and 15.12) was applied. Reference data for the viscosity of liquid Al [110] and Ni [111], the enthalpy of mixing of Al-Ni melts [103, 104], and the hard-sphere diameters of Al [112] and Ni [113] together with the atomic mass and molar volume of Al and Ni [44] were taken as the input data in the calculations of the viscosity isotherm for $T = 1800$ K (Eqs. 15.11 and 15.12; see Sect. 6.3). The reference datasets of the viscosity of liquid Al and Ni metals were measured by oscillating cup viscosimetry (OCV), and therefore, the data [22, 41] obtained by the same method are more representative when compared to the model-predicted values [24, 102].

7.3.4   Ni-Based Superalloys: Analysis of Viscosity Data

The viscosity data of CMSX-4 [34, 41], LEK-94 [36, 37], MC-2 [37], and IN718 [22] of Ni-based superalloys were analyzed with respect to the model-predicted viscosity of liquid Al-Ni binary system. To this aim, the viscosities of Ni-based superalloys are shown in Fig. 15.8 with respect to the Al-content in each alloy. For the alloys investigated, Al-content is ranging between 7 and 14 at %, and therefore, in order to have a clear picture of their viscosities, the data are shown in an enlarged area for 86 < Ni (at %) < 93 (Fig. 15.8b). An exception represents IN718 with 1.1 Al (at %), shown in Fig. 15.8a.

The viscosity isotherms were calculated for $T = 1800$ K using the Terzieff model [96, 97] and the ideal solution model. The effects of the minority alloying elements on the viscosity of Ni-based superalloys are comparable, at least to the first approximation, to that of liquid nickel itself. Therefore, as in the case of the surface tension, for the calculations, the Ni-content was taken as the sum of the amount of Ni present in the alloy plus the minority alloying elements. Based on this, the viscosity data of each Ni-based superalloy is compared to the corresponding Al-Ni calculated values. The transition and refractory components of Ni-based superalloys significantly increase their viscosities. For each Ni-based superalloy, its viscosity results higher than that of the Al-Ni alloy with the same Al-content; at least the higher measured values are above the Terzieff isotherm; accordingly, the experimental viscosity data [36, 37, 41] can be considered as reliable (Fig. 15.8b).

7.4   Specific Heat Capacity Data

Differential Scanning Microscopy (DSC) was used to measure the specific heat of CMSX-4 [42], LEK-94 [55], MC-2 [55], TMS-75 [55], and CMSX-10 [55] Ni-based superalloys for temperatures ranging between 1650 and 1813 K [55] or for singular temperatures within 1703–1813 K [42]. Measurement errors of up to 12% were observed. Specific heat capacity experimental data of CMSX-4 [42] differ 12.5% from the corresponding value recommended by Mills [98]. Recently, the specific heat (Sect. 5) of LEK-94, MC-2, and CMSX-10 of liquid Ni-based superalloys was measured for the first time by modulation calorimetry in the electromagnetic levitator (EML) on board of the ISS [37]. Measurements were performed with a typical duration of 15–20 min, for temperatures ranging between 1550 and 1800 K reaching an undercooling of 100 K. For the alloys investigated, linear temperature-dependent curves are characterized by very small temperature coefficients that can be neglected. For the measurements under microgravity conditions, an accuracy of about 1% was achieved [37]. A comparison between the specific heat capacity data [37, 55] indicates a good agreement (Table 15.6).
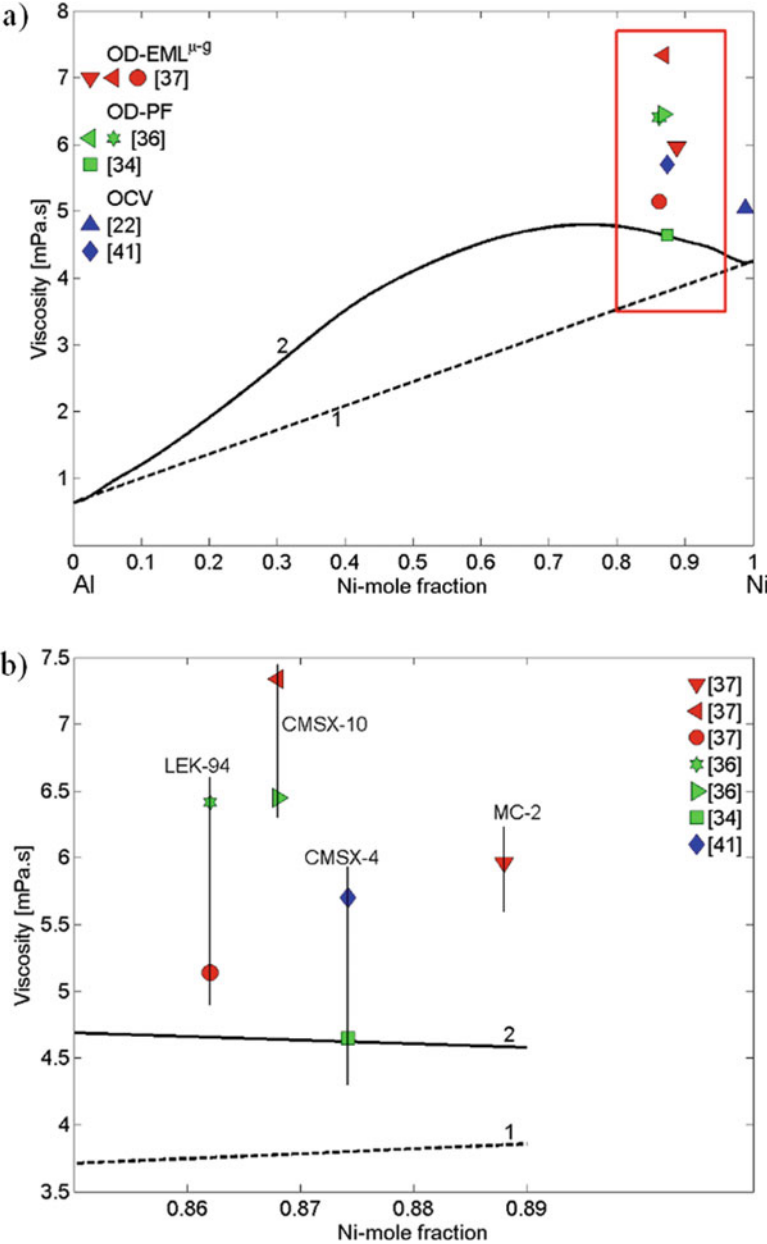
Fig. 15.8 (**a**) Viscosity experimental data [34, 36, 37, 41] of liquid Ni-based superalloys. For comparison, the viscosity isotherms of Al-Ni alloys calculated for $T = 1800$ K are shown: 1 – the ideal solution; 2 – Terzieff model. (**b**) An enlarged area of (**a**) with respect to Al-content in Ni-based superalloys

Table 15.6 Specific heat capacity experimental datasets for liquid Ni-based superalloys obtained by DSC (Differential Scanning Calorimetry), MC (Modulation Calorimetry) in EML (electromagnetic levitation)

Alloy	Al at %	Liquidus temp. T_L, K	Specific heat capacity C_p, J(gK)$^{-1}$		Measurement temperature range, K	Method	Exp. error %	References
TMS-75	13.7	1702 ± 2	0.6		1675–1710	DSC	±10	[55]
LEK-94	13.8	1668 ± 2	0.75		1650–1750	DSC	±10	[55]
LEK-94	13.8	1666 ± 5	0.749 ± 0.006		1550–1785	MC-*EML*$^{\mu-g}$	1.0	[37]
CMSX-10	13.2	1702 ± 4	0.7		1690–1730	DSC	±10	[55]
CMSX-10	13.2	1706 ± 5	0.71 ± 0.05		1650–1775	MC-*EML*$^{\mu-g}$	1.0	[37]
MC-2	11.2	1661 ± 5	0.67 ± 0.05		1630–1725	MC-*EML*$^{\mu-g}$	1.0	[37]
MC-2	11.2	1651 ± 6	0.7		1670–1730	DSC	±10	[55]
CMSX-4	12.58	1653	0.675[a]		1655–1773	R	–	[98]
CMSX-4	12.58	1654	1703/K	0.74	1703–1813	DSC	±12	[42]
			1723	0.78				
			1753	0.78				
			1773	0.77				
			1793	0.76				
			1813	0.75				

R recommended values obtained combining the results of different measurements. Superscripts: μ–*g* – microgravity

[a]Value proposed by the author

8   Summary

Thermophysical properties data of liquid Ni-based alloys are used as input data for numerical simulations of solidification as a step of all industrial processes that involve the presence of the liquid phase such as, for example, casting and joining. In particular, the production of big structural components/parts by casting and quality of the products depends on the microstructural evolution and possible formation of defects, which, on the other side, are directly related to numerical simulation of solidification. Surface tension, density/molar volume, viscosity, and specific heat capacity data of CMSX-4, CMSX-10, CM186LC, LEK-94, MC-2, TMS-75, RENE-5, RENE-90, and IN718 industrial Ni-based superalloys obtained by the container-based and containerless methods were analyzed. At high temperatures, due to the high reactivity of metallic melts with a substrate/crucible, the containerless methods represent an alternative for container-based methods. The most advanced containerless methods for the measurements of the thermophysical properties are those performed with EML on ISS. The experimental data obtained under microgravity conditions make possible accurate measurements at high temperatures; it can be performed over large temperature intervals with a significant temperature range of undercooling. The thermophysical properties data are used to validate the predictive models that in the case of multicomponent alloy systems are missing or inappropriate. Thermophysical properties data analyzed in this chapter can be used in materials and processes design.

References

1. M. Rappaz, M. Rettenmayr, Curr. Opin. Solid State Mater. Sci. **3**, 275–282 (1998)
2. D.U. Furrer, H.J. Fecht, JOM **51**, 14–17 (1999)
3. T.M. Pollock, S. Tin, J. Propuls. Power **22**(2), 361–374 (2006)
4. I. Ansara, N. Dupin, H.L. Lukas, B. Sundman, J. Alloys Compd. **247**(1–2), 20–30 (1997)
5. N. Dupin, I. Ansara, B. Sundman, Calphad **25**(2), 279–298 (2001)
6. J.S. Van Sluytman, T.M. Pollock, Acta Mater. **60**, 1771–1783 (2012)
7. S.-J. Park, S.-M. Seo, Y.-S. Yoo, H.-W. Jeong, H.J. Jang, Corros. Sci. **90**, 305–312 (2015)
8. A. Sato, A.C. Yeh, T. Kobayashi, T. Yokokawa, H. Harada, T. Murakumo, J.X. Zhang, Energy Mater. **2**, 19–25 (2007)
9. R.C. Reed, T. Tao, N. Warnken, Acta Mater. **57**, 5898–5913 (2009)
10. A. Sato, Y.-L. Chiu, R.C. Reed, Acta Mater. **59**(1), 225–240 (2011)
11. M. Xia, D. Gu, G. Yu, D. Dai, H. Chen, Q. Shi, Sci. Bull. **61**(13), 1013–1022 (2016)
12. G.H. Gessinger, M.J. Bomford, Int. Metall. Rev. **19**(1), 51–76 (1974)
13. M.F. Ashby, Y.J.M. Bréchet, D. Cebon, L. Salvo, Mater. Design **25**(1), 51–67 (2004)
14. J. Rösler, O. Näth, S. Jäger, F. Schmitz, D. Mukherji, Acta Mater. **53**, 1397–1406 (2005)
15. J.H. Weber, Y.E. Khalfalla, K.Y. Benyounis, *Nickel-Based Superalloys: Alloying Methods and Thermomechanical Processing BT-Reference Module in Materials Science and Materials Engineering* (Elsevier, 2016). https://doi.org/10.1016/B978-0-12-803581-8.03383-X
16. S. Sulzer, M. Hasselqvist, H. Murakami, P. Bagot, M. Moody, R. Reed, Metall. Mater. Trans. A **51A**, 4902 (2020)

17. P. Nandwana, A.M. Elliott, D. Siddel, A. Merriman, W.H. Peter, S.S. Babu, Curr. Opin. Solid State Mater. Sci. **21**(4), 207–218 (2017)
18. T. Keller, G. Lindwall, S. Ghosh, L. Ma, B.M. Lane, F. Zhang, U.R. Kattner, E.A. Lass, J.C. Heigel, Y. Idell, M.E. Williams, A.J. Allen, J.E. Guyer, L.E. Levine, Acta Mater. **139**(15), 244–253 (2017)
19. J.C. Wang, M. Osawa, T. Yokokawa, H. Harada, M. Enomoto, Comput. Mater. Sci. **39**(4), 871–879 (2007)
20. H.-J. Fecht, S. Schneider, R.K. Wunderlich, L. Battezzati, C. Papandrea, M. Palumbo, I. Egry, K. Mills, P. Quested, R. Brooks, D. Giuranno, R. Novakovic, A. Passerone, E. Ricci, S. Seetharaman, R. Aune, B. Vinet, J.-P. Garandet, Metallurgia Italiana **97**(3), 47–53 (2005)
21. H.-J. Fecht, High Temp. Mater. Proc. Spec. Issue **27**(6), 385–388 (2008)
22. P.N. Quested, R.F. Brooks, L. Chapman, R. Morell, Y. Youssef, K.C. Mills, Mater. Sci. Technol. **25**, 154–162 (2009)
23. N. Warnken, D. Mab, A. Drevermann, R.C. Reed, S.G. Fries, I. Steinbach, Acta Mater. **57**, 5862–5875 (2009)
24. I. Egry, E. Ricci, R. Novakovic, S. Ozawa, Adv. Colloid Interf. Sci. **159**, 198–212 (2010)
25. J. Brillo, E. Arato, D. Giuranno, H. Kobatake, C. Maran, R. Novakovic, E. Ricci, D. Rosello, High Tem.-High Press. **47**(5), 417–441 (2018)
26. V.N. Eremenko, V.I. Nizhenko, Y.V. Naidich, Izv. Akad. Nauk SSSR, Metallurgiya i Topivo **3**, 150–154 (1961)
27. V.N. Eremenko, Y.V. Naidich, Fiz. Met. Metalloved. **11**, 6–9 (1961)
28. A.A. Vertman, A.M. Samarin, Viscosity of liquid Ni-Al alloys. Izvest. Akad. Nauk SSSR: Metallurgya i topivo **2**, 59–160 (1961)
29. G.D. Ayushina, E.S. Levin, P.V. Gel'd, Russ. J. Phys. Chem. **43**(11), 1548–1551 (1969)
30. E.S. Levin, G.D. Ayushina, P.V. Gel'd, Izv. A.N. SSSR, Metaly **4**, 49 (1970)
31. E.S. Levin, G.D. Ayushina, Izv. Ural. Polytechn. Inst. **231**, 93–96 (1974)
32. G. Lohöfer, P. Neuhaus, I. Egry, High Temp. High Press. **23**, 333–342 (1991)
33. R. Aune, L. Battezzati, I. Egry, J. Etay, H.J. Fecht, D. Giuranno, R. Novakovic, A. Passerone, E. Ricci, F. Schmidt-Hohagen, S. Seetharaman, R. Wunderlich, Microgravity Sci. Technol. **XVIII**(3/4), 73–76 (2006)
34. K. Higuchi, H.-J. Fecht, R.K. Wunderlich, Adv. Eng. Mater. **9**(5), 349–354 (2007)
35. J. Brillo, *Thermophysical Properties of Multicomponent Liquid Alloys* (de Gryuter, Berlin, 2016)
36. R.K. Wunderlich, H.-J. Fecht, G. Lohöfer, Metall. Mater. Trans. A **B48**, 237–246 (2017)
37. M. Mohr, R. Wunderlich, Y. Dong, D. Furrer, H.-J. Fecht, Adv. Eng. Mater. **1901228**, 1–10 (2020)
38. G. Lohöfer, Int. J. Thermophys. **41**, 30 (2020)
39. Thermolab Final Report 2003, ESA MAP Contract Number AO-99-022
40. Thermoprop Final Report 2020, ESA MAP Contract Number AO-99-022/AO-2009-1020
41. E. Ricci, D. Giuranno, R. Novakovic, T. Matsushita, S. Seetharaman, R. Brooks, L. Chapman, P. Quested, Int. J. Thermophys. **28**(4), 1304–1321 (2007)
42. T. Matsushita, H.-J. Fecht, R.K. Wunderlich, I. Egry, S. Seetharaman, J. Chem. Eng. Data **54**, 2584–2592 (2009)
43. R. Novakovic, M. Mohr, D. Giuranno, E. Ricci, J. Brillo, R. Wunderlich, I. Egry, Y. Plevachuk, H.-J. Fecht, Microgravity Sci. Technol. **32**, 1049–1064 (2020)
44. T. Iida, R.I.L. Guthrie, *The Thermophysical Properties of Metallic Liquids, Vol 1: Fundamentals* (Oxford University Press, Oxford, 2015)
45. P. Saltykov, V.T. Witusiewicz, I. Arpshofen, O. Fabrichnaya, H.J. Seifert, F. Aldinger, Scand. J. Metall. **30**, 297–301 (2001)
46. P. Nash, H.N. Su, O. Kleppa, Trans. Nonferr. Met. Soc. **12**, 754–758 (2002)
47. T. Gheno, X.L. Liu, G. Lindwall, Z.-K. Liu, B. Gleeson, Sci. Technol. Adv. Mater. **16**, 055001 (2015)

48. P. Agraval, M. Turchanin, L. Dreval, A. Vodopyanova, J. Therm. Anal. Calorim. **128**, 1753–1763 (2017)
49. P. Agraval, L. Dreval, M. Turchanin, A. Storchak-Fedyuk, L. Artyukh, T. Velikanova, J. Chem. Thermodyn. **106**, 309–316 (2017)
50. N. Dupin, B. Sundman, Scand. J. Metall. **30**, 184–192 (2001)
51. X.L. Liu, G. Lindwall, T. Gheno, Z.K. Liu, Calphad **52**, 125–142 (2016)
52. C. Costa, S. Delsante, G. Borzone, D. Zivkovic, R. Novakovic, J. Chem. Thermodyn. **69**, 73–84 (2014)
53. K.C. Mills, Y.M. Youssef, Z. Li, Y. Su, ISIJ Int. **46**(5), 623–632 (2006)
54. D. Giuranno, S. Amore, R. Novakovic, E. Ricci, J. Mater. Sci. **50**, 3763–3771 (2015)
55. S. Amore, F. Valenza, D. Giuranno, R. Novakovic, G. Dalla Fontana, L. Battezzati, E. Ricci, J. Mater. Sci. **51**, 1680–1688 (2016)
56. L. Battezzati, D. Baldissin, High Temp. Mater. Proc. **27**(6), 423–428 (2008)
57. Z. Li, K.C. Mills, M. McLean, K. Mukai, Metall. Mater. Trans. A **36B**, 247–254 (2005)
58. I. Lopez-Galilea, S. Huth, S.G. Fries, N. Warnken, I. Steinbach, W. Theisen, Metall. Mater. Trans. A **43**(13), 5153–5164 (2012)
59. Y.L. Wang, X. Yu, N.L. Richards, M.C. Chaturvedi, Weldability of directionally solidified TMS-75 and TMD-103 superalloys, in *Superalloys 2004*, ed. by K. A. Green, H. H. Pollock, T. E. Howson, R. C. Reed, J. J. Schirra, (TMS (The Minerals, Metals & Materials Society), 2004), pp. 529–535
60. F. Padday, *Surface and Colloid Science* (Wiley-Interscience, New York, 1969)
61. R. Defay, *Thermodynamique de la tension superficielle* (Gauthier-Villars, Paris, 1971)
62. F. Bashforth, J. Adams, *An Attempt to Test the Theories of Capillary Action* (Cambridge University Press, Cambridge, 1883)
63. P. Kozakevitch, G. Urbain, Mém. Sci. Rev. Metall. **58**, 401, 517, 931 (1961)
64. C. Maze, G. Burnet, Surf. Sci. **13**(2), 451–470 (1969)
65. C. Maze, G. Burnet, Surf. Sci. **24**, 335–342 (1971)
66. Y.V. Naidich, The wettability of solids by liquid metals, in *Progress in Surface and Membrane Science*, ed. by D. A. Cadenhead, J. F. Danielli, (Academic, New York, 1981), pp. 353–484
67. R. Nowak, T. Lanata, N. Sobczak, E. Ricci, D. Giuranno, R. Novakovic, D. Holland-Moritz, I. Egry, J. Mater. Sci. **45**, 1993–2001 (2010)
68. I. Egry, J. Mater. Sci. **26**, 2997–3003 (1991)
69. I. Egry, H. Giffard, S. Schneider, Meas. Sci. Technol. **16**, 426–431 (2005)
70. J. Brillo, G. Lohöfer, F. Schmid-Hohagen, S. Schneider, I. Egry, Int. J. Mater. Prod. Technol. **26**, 247–273 (2006)
71. S. Amore, J. Brillo, I. Egry, R. Novakovic, Appl. Surf. Sci. **257**, 7739–7745 (2011)
72. L. Rayleigh, Proc. R. Soc. **29**, 71–97 (1879)
73. O.A. Basaran, J. Fluid Mech. **241**, 169–198 (1992)
74. F. Mashayek, N. Ashgriz, Phys. Fluids **10**, 1071–1082 (1998)
75. F.H. Busse, J. Fluid Mech. **142**, 1–8 (1984)
76. M. Mohr, R. Wunderlich, R. Novakovic, E. Ricci, H.-J. Fecht, Adv. Eng. Mater. **2000169**, 1–10 (2020)
77. J.A. Tsamopoulos, R.A. Brown, J. Fluid Mech. **127**, 519–537 (1983)
78. X. Xiao, R.W. Hyers, R.K. Wunderlich, H.-J. Fecht, D.M. Matson, Appl. Phys. Lett. **113**, 011903 (2018)
79. W.H. Reid, The oscillation of a viscous liquid drop. Q. Appl. Math. **18**, 86–89 (1960)
80. S. Chandrasekhar, *Hydrodynamic and Hydromagnetic Stability* (Dover Publications, New York, 1981)
81. S. Amore, S. Delsante, H. Kobatake, J. Brillo, J. Chem. Phys. **139**, 064504–064501 (2013)
82. G. Lohöfer, Rev. Sci. Instrum. **89**, 124709 (2018)
83. P.-F. Paradis, W.-K. Rhim, J. Mater. Res. **14**, 3713–3719 (1999)
84. S. Z. Beer (ed.), *Liquid Metals – Chemistry and Physics* (Marcel Dekker Inc, New York, 1997)
85. M. Kehr, W. Hoyer, I. Egry, Int. J. Thermophys. **29**, 1017–1025 (2007)

86. R. Roscoe, Proc. Phys. Soc. **72**, 576–584 (1958)
87. R.F. Brooks, A.P. Day, R.J.L. Andon, L.A. Chapman, K.C. Mills, P.N. Quested, High Temp. High Press. **33**, 73–82 (2001)
88. D.A. Beckwith, G.F. Newell, Appl. Surf. Sci. **8**, 450–465 (1957)
89. W. Brockner, K. Torklep, H.A. Oye, Ber. Bunsenges. Phys. Chem. **83**, 1–11 (1979)
90. X. Xiao, R.W. Hyers, D.M. Matson, Int. J. Heat Mass Transf. **136**, 531–542 (2019)
91. H.J. Fecht, W.L. Johnson, Rev. Sci. Instrum. **62**, 1299–1303 (1991)
92. R. Novakovic, T. Tanaka, Phys. B Condens. Matter **371**, 223–231 (2006)
93. R. Novakovic, J. Phys. Condens. Matter **23**, 235107 (2011)
94. G. Bernard, C.H.P. Lupis, Metall. Trans. A. **2**, 555–559 (1971)
95. T. Iida, M. Ueda, Z. Morita, Tetsu to Hagane **62**, 1169–1178 (1976)
96. P. Terzieff, J. Alloys Compd. **453**(1–2), 233–240 (2008)
97. P. Terzieff, Phys. B **404**, 2039–2044 (2009)
98. K.C. Mills, *Recommended Values of Thermophysical Properties for Selected Commercial Alloys* (Woodhead Publishing Ltd and ASM International, 2002)
99. M. Mohr, H.-J. Fecht, Adv. Eng. Mater. **23**(2001223), 1–15 (2021)
100. I. Egry, D. Holland-Moritz, R. Novakovic, E. Ricci, R. Wunderlich, N. Sobczak, Int. J. Thermophys. **31**, 949–965 (2010)
101. R.K. Wunderlich, U. Hecht, F. Hediger, H.-J. Fecht, Adv. Eng. Mater. **20**(1800346), 1–9 (2018)
102. Joint Committee for Guides in Metrology (JCGM/WG1), GUM 1995 with minor corrections, *evaluation of measurement data – Guide to the expression of uncertainty in measurement*, First edition September 2008, Corrected version 2010, pp. 1–120, JCGM 2008
103. V.M. Sandakov, Y.O. Esin, P.V. Geld, Zh. Fiz. Chim. **45**, 1798 (1971)
104. K.V. Grigorovitch, A.S. Krylov, Thermochim. Acta **314**, 255–263 (1998)
105. J. Brillo, G. Kolland, J. Mater. Sci. **51**, 4888–4901 (2016)
106. J. Brillo, I. Egry, J. Mater. Sci. **40**, 2213–2216 (2005)
107. J.J. Wessing, J. Brillo, Metall. Mater. Trans. A **48A**, 868–882 (2017)
108. D.H. Kobatake, J. Brillo, J. Mater. Sci. **48**, 4934–4941 (2013)
109. Y. Plevachuk, I. Egry, J. Brillo, D. Holland Moritz, I. Kaban, Int. J. Mater. Res. **98**, 107–111 (2007)
110. H. Kobatake, J. Schmitz, J. Brillo, J. Mater. Sci. **49**, 3541–3549 (2014)
111. H. Kobatake, J. Brillo, J. Mater. Sci. **48**, 6818–6824 (2013)
112. P. Protopapas, H.C. Andersent, N.A.D. Parlee, J. Chem. Phys. **59**(1), 15–25 (1973)
113. R.C. Gosh, M.R. Amin, A.Z. Ziauddin Ahmed, I.M. Syed, G.M. Bhuiyan, Appl. Surf. Sci. **258**, 5527–5532 (2012)

Chapter 16
Thermophysical Properties of Titanium Alloys

Markus Mohr, Rainer Wunderlich, and Hans-Jörg Fecht

1 Introduction

Titanium-based alloys are comprising high strength per weight ratio, high-temperature resistance, good corrosion resistance as well as ductility, and excellent biocompatibility [1–3]. Elemental titanium exhibits a hexagonal close-packed structure (α) that transforms to a body-centered cubic structure (β) above a temperature of 882 °C [4]. An important alloying element for titanium-based alloys is aluminum. At lower concentrations, aluminum is an α-stabilizing element, and for higher concentrations of Al, there exist several intermetallic Ti-Al phases, such as the γ-TiAl [4]. The Ti-Al phase diagram is shown in Fig. 16.1.

The α-β titanium alloy Ti64 (Ti90wt%-Al6wt%-V4wt%) is of particular interest for biomedical applications [2, 5], as well as for lightweight constructions and aerospace applications [1, 2, 6, 7]. The very commonly used titanium alloy Ti64 was developed in 1954 and formed the basis for a large group of α-β Ti-Al alloys [2, 7, 8].

Another class of alloys is developed around the γ-TiAl phase region, using Al-contents between 42 and 48 at% [4, 9]. One alloy of this class is the $Ti_{48}Al_{48}Nb_2Cr_2$ [10, 11]. As a heritage from the European FP6 research project IMPRESS [12], a similar alloy composition was processed in the electromagnetic levitator ISS-EML on board the international space station (ISS).

Several different fabrication routes exist for Ti-alloys that involve the liquid phase, such as casting, additive manufacturing, and injection molding. To gain control over the solidification process, simulations give valuable input for the process development and optimization, as well as for the prediction of microstructure and defect formation during the solidification process [13–17]. Such simulations

M. Mohr (✉) · R. Wunderlich · H.-J. Fecht
Institute of Functional Nanosystems, Ulm University, Ulm, Germany
e-mail: markus.mohr@uni-ulm.de
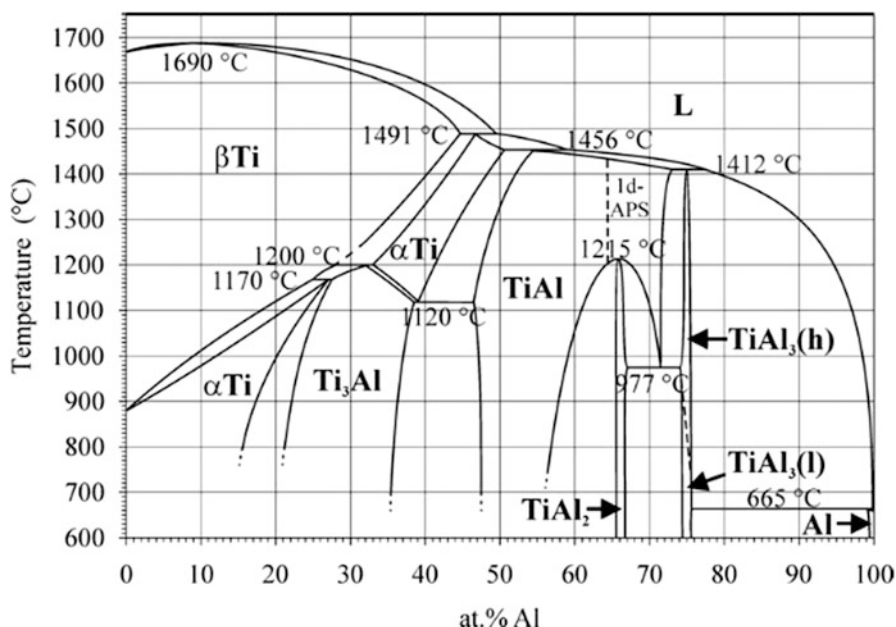
Fig. 16.1 The Ti-Al phase diagram (Schuster and Palm [13]). (Reprinted by permission from Springer Nature, *Journal of Phase Equilibria and Diffusion* [13], Copyright 2006)

require precise thermophysical property data of the involved solid and liquid phases. For the solid phase, such data can be obtained by conventional equipment. However, thermophysical property measurements of titanium alloys in the liquid phase are very unreliable or simply impossible due to the high melt reactivity. Thus, containerless approaches are necessary, such as electromagnetic levitation. While performing these experiments in microgravity, heating and positioning can be decoupled. Furthermore, the fluid flow in the liquid can be controlled to be laminar, which allows the measurement of, e.g., viscosity. Long-duration microgravity experiments allow to perform contactless measurements in thermodynamic equilibrium, which are necessary preconditions for methods such as ac calorimetry.

2   Investigated Materials

The alloy Ti-Al6wt%-V4wt% (Ti64) is a standard alloy for numerous automotive, aerospace, and biomedicine applications. However, the literature on the thermophysical properties of its liquid phase is scarce, and some values given in the literature are not in agreement with each other. In the Ti-Al system, also the γ-Ti-Al alloys have technical relevance. Several γ-Ti-Al alloys have been investigated by

containerless methods in microgravity, namely, γ-$Ti_{48}Al_{48}Nb_2Cr_2$, $Ti_{46}Al_{46}Nb_8$, and $Ti_{46}Al_{46}Ta_8$.

3   Experimental Methods

Due to the high reactivity of molten titanium with other materials [18], container-based methods are no choice for the precise measurement of thermophysical properties. By applying the oscillating drop method on ground-based electromagnetic levitators (1 g-EML), under short-term microgravity, using the TEMPUS device on board parabolic flights (PF), as well as by the electromagnetic levitator in the long-term microgravity environment of the board the international (ISS-EML), thermophysical property measurements of titanium-based alloys have been performed.

Short-time microgravity investigations in parabolic flights allow the measurement of some thermophysical properties. But only the long microgravity times on board the international space station ISS allow the precise measurement of properties that require the thermal equilibrium of the sample, such as the specific heat capacity of the liquid samples. The experimental methods used to obtain the thermophysical properties are described in Chap. 12.

4   Results

In the following, the results of thermophysical properties obtained in microgravity are given in detail.

4.1   Surface Tension

The surface tension of the α-β titanium alloy Ti64, as well as of several γ-Ti-Al alloys, was measured by different electromagnetic levitation facilities on ground and in microgravity.

The results of the surface tension can be expressed by a linear function of temperature, according to

$$\gamma(T) = \gamma_L + d\gamma/dT(T - T_{\text{liq}}) \tag{16.1}$$

where γ_L is the surface tension at the liquidus temperature T_{liq} and $d\gamma/dT$ is the temperature coefficient. Using linear regression, the measured surface tension data is

Fig. 16.2 Surface tension of Ti64 and Ti$_{48}$Al$_{48}$Nb$_2$Cr$_2$ measured on board the ISS
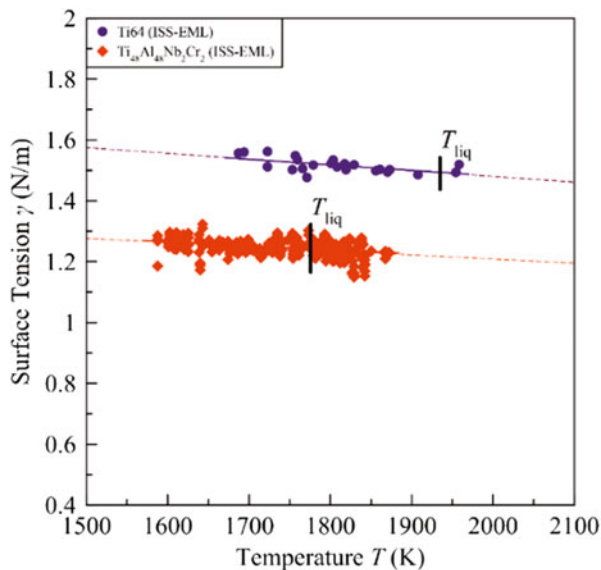
fitted by Eq. 16.1. Figure 16.2 shows the surface tension of Ti64 measured in the ISS-EML on board the ISS.

The clean, undisturbed conditions in the ISS-EML on board the ISS allowed the Ti64 sample and the γ-Ti$_{48}$Al$_{48}$Nb$_2$Cr$_2$ sample to reach high undercoolings of about 200 K. The measurement uncertainties of the surface tension are determined by the accuracy of the determination of the surface oscillation frequency. In the experimental conditions in microgravity, the $l = 2$ mode dominates, and the $m = 0, \pm1, \pm2$ oscillations are degenerate. Consequently, the oscillation frequency can typically be obtained with an uncertainty of about ±0.05 Hz. With a sample weight of (0.638 ± 0.005) g (Ti64) and (0.552 ± 0.005) g (γ-Ti$_{48}$Al$_{48}$Nb$_2$Cr$_2$), the measurement uncertainties of the single surface tension measurements are about 0.8%.

A comparison of the surface tension values of Ti64 measured by electromagnetic levitation techniques on the ground (1 g-EML) during several parabolic flights (PF) using the electromagnetic levitator TEMPUS, as well as the values obtained in the ISS-EML, is given in Table 16.1.

Figure 16.2 also shows the surface tension obtained for the γ-Ti-Al alloy Ti$_{48}$Al$_{48}$Nb$_2$Cr$_2$ measured in the ISS-EML. The obtained data is in good agreement with the data obtained in the TEMPUS device on board a parabolic flight [24].

Table 16.2 lists the surface tension of Ti$_{48}$Al$_{48}$Nb$_2$Cr$_2$ measured on board the ISS as well as a number of similar γ-Ti-Al alloys, measured on board of parabolic flights, as well as the surface tension data in a ground-based EML.

Table 16.1 Surface tension of Ti64

Composition	γ_L (N/m)	$d\gamma/dT$ (10^{-4} N m^{-1} K^{-1})	T_{liq} (K)	Temperature range (K)	Method	References
Ti64	1.49 ± 0.01	$-(1.9 \pm 0.5)$	1933	1675–1975	ISS-EML	[19]
Ti64	1.49	-4.1	1933	1775–2150	PF	[20]
Ti64	1.49	-4.0	1933	–	PF	[21]
Ti64	1.33	-1.9	1933	1800–2050	1 g-EML	[21]
Ti64	1.389 ± 0.090	-9.017	1933	1725–2075	1 g-EML	[22]
Ti64	1.38	-3.13	1933	1700–2250	1 g-EML	[23]

Table 16.2 Surface tension of γ-TiAl-based alloys

Composition	γ_L (N/m)	$d\gamma/dT$ (10^{-4} N m^{-1} K^{-1})	T_{liq} (K)	Temperature range (K)	Method	References
Ti$_{48}$Al$_{48}$Nb$_2$Cr$_2$	1.24 ± 0.01	$-(1.36 \pm 0.17)$	1780	1550–1900	ISS-EML	–
Ti$_{48}$Al$_{48}$Nb$_2$Cr$_2$	1.20 ± 0.03	$-(3.86 \pm 1.4)$	1775	1500–2000	PF	[24]
Ti$_{46}$Al$_{46}$Ta$_8$	1.21 ± 0.03	$-(2.69 \pm 0.70)$	1872	1600–2000	PF	[24]
Ti$_{46}$Al$_{46}$Ta$_8$	1.19 ± 0.09	$-(1.9 \pm 0.5)$	1890	1700–1900	1 g-EML	[25]
Ti$_{46}$Al$_{46}$Nb$_8$	1.19 ± 0.04	$-(3.42 \pm 1.00)$	1847	1650–2000	PF	[24]
Ti$_{46}$Al$_{46}$Nb$_8$	1.114 ± 0.05	$-(2.17 \pm 0.3)$	1842	1600–1950	1 g-EML	[25]

4.2 Viscosity

Another property that is important for the modeling of fluid flow of liquid Ti-Al alloys is viscosity. Figure 16.3 shows the viscosity of Ti64 and of $Ti_{48}Al_{48}Nb_2Cr_2$ measured in the ISS-EML on board the ISS. Viscosity data on further samples were obtained in parabolic flight campaigns [24].

In the temperature range of the investigations, the viscosity can be sufficiently well fitted by an Arrhenius-like equation:

$$\eta = \eta_0 \exp\left(E_A/k_B T\right) \tag{16.2}$$

where k_B is the Boltzmann constant and η_0 and E_A are characteristic parameters for each liquid. The parameter E_A is sometimes called the activation energy for viscous flow. The obtained parameters for the two liquid alloys are given in Table 16.3. In addition, the parameters obtained for three γ-Ti-Al using parabolic flight experiments [33] alloys are also given in Table 16.3 for comparison.

The measurement uncertainty of the viscosity measurement depends on the accuracy of measurement of the sample mass, the radius, and the damping time constant. In addition, laminar flow conditions must be present during the measurement. The flow conditions during the experiment can be predicted by magnetohydrodynamics simulations [26–28]. Using the model equations of a surrogate model [27], it was confirmed that only laminar flow is expected in the parameter range used for the viscosity measurements on Ti64 and γ-$Ti_{48}Al_{48}Nb_2Cr_2$ in the ISS-EML on board the ISS.

Fig. 16.3 Viscosity of Ti64 and γ-$Ti_{48}Al_{48}Nb_2Cr_2$ measured using the ISS-EML on board the ISS
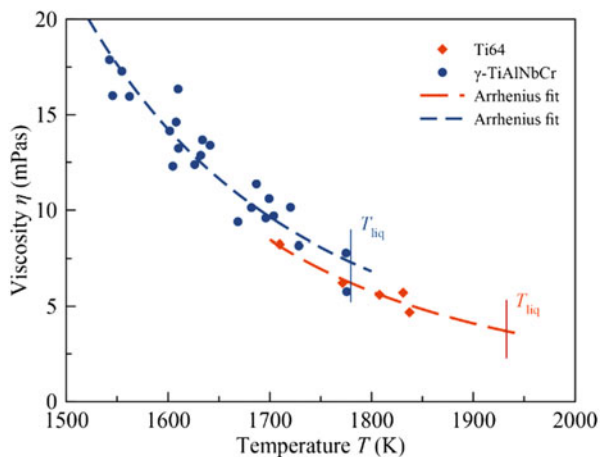
Table 16.3 Arrhenius parameters for Ti64 and γ-Ti$_{48}$Al$_{48}$Nb$_2$Cr$_2$

Composition	η_0 (mPa s)	E_A (eV)	T_{liq} (K)	$\eta(T_{\text{liq}})$ (mPa s)	Temperature range (K)	Method	References
Ti64	$(8.6 \pm 5.0) \cdot 10^{-3}$	1.01 ± 0.20	1933	3.7 ± 0.5	1700–1850	ISS-EML	[19]
Ti$_{48}$Al$_{48}$Nb$_2$Cr$_2$	$(19 \pm 10) \cdot 10^{-3}$	0.91 ± 0.08	1780	6.1 ± 0.2	1500–1800	ISS-EML	–
Ti$_{48}$Al$_{48}$Nb$_2$Cr$_2$	$3.95 \cdot 10^{-2}$	0.76 ± 0.05	1775	5.8 ± 0.4	1500–2000	PF	[33]
Ti$_{46}$Al$_{46}$Ta$_8$	$1.42 \cdot 10^{-2}$	0.99 ± 0.06	1872	6.9 ± 0.4	1600–1925	PF	[33]
Ti$_{46}$Al$_{46}$Nb$_8$	$4.88 \cdot 10^{-2}$	0.78 ± 0.06	1847	6.2 ± 0.4	–	PF	[33]

4.3 Electrical Resistivity

By the measurement of the inductive sample coupling introduced in Chap. 12, the electrical resistivity of the samples processed in the ISS-EML was obtained. Figure 16.4 shows the electrical resistivity of Ti64 and γ-Ti$_{48}$Al$_{48}$Nb$_2$Cr$_2$ as a function of temperature in the liquid and solid phase.

The rapid increase of the solid resistivity of Ti64 below about $T = 1100$ K is due to the $\beta \rightarrow \alpha$ phase transformation. The first recalescence event and the following transformation from the L + β to the α + β phase are recognizable by the discontinuities of resistivity during the cooling of the γ-Ti$_{48}$Al$_{48}$Nb$_2$Cr$_2$ alloy.

The electrical resistivity $\rho_{e,l}$ of Ti64 in the liquid state is expressed as

$$\rho_{e,l}(T) = \left\{(180.8 \pm 2.2) - (1.12 \pm 0.12) \cdot 10^{-2} \cdot T\right\} \, \mu\Omega \, \text{cm} \qquad (16.3)$$

and the resistivity of γ-Ti$_{48}$Al$_{48}$Nb$_2$Cr$_2$ in the liquid phase can be described by

$$\rho_{e,l}(T) = \left\{(248.7 \pm 0.6) - (3.13 \pm 0.04) \cdot 10^{-2} \cdot T\right\} \, \mu\Omega \, \text{cm} \qquad (16.4)$$

The uncertainties given in Eqs. 16.3 and 16.4 are the confidence interval of fitting for a confidence level of 95%. Additionally, there are systematic sources for measurement uncertainties given by the calibration of the measurement (Chap. 12). Random measurement errors that lead to the scatter of data are origin from small sample oscillations and small sample movements. The obtainable measurement uncertainty of the method itself is on the order of 0.05% [29].

Fig. 16.4 Electrical resistivity of Ti64 and γ-Ti$_{48}$Al$_{48}$Nb$_2$Cr$_2$ as a function of temperature
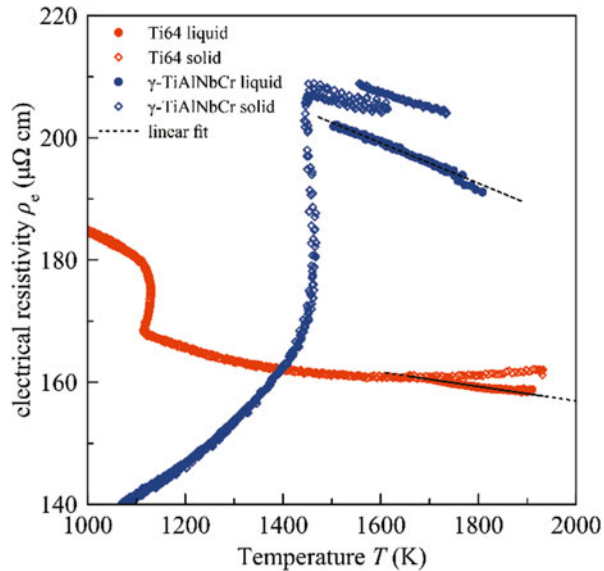
4.4 Mass Density

One crucial property for solidification is the temperature-dependent mass density and its change between the solid and liquid phase. Figure 16.5 presents the temperature-dependent mass density of Ti64 and γ-Ti$_{48}$Al$_{48}$Nb$_2$Cr$_2$, recorded during cooling using the inductive sample coupling measurement method (Chap. 12).

The slight discontinuity of the mass density of Ti64 around 1100 K is again signifying the $\beta \rightarrow \alpha$ phase transformation. For γ-Ti$_{48}$Al$_{48}$Nb$_2$Cr$_2$, at around 1450 K, a small discontinuity points toward the phase transformation from the hexagonal α phase into a mixture of α and γ phase. The first transformation from L + β toward the α phase cannot be recognized by a change in density.

The mass density of Ti64 in the solid phase in the temperature range of 1650–1900 K can be described by

$$\rho_{m,s} = \left\{ (4.163 \pm 0.003) - (0.145 \pm 0.001) \cdot 10^{-3} \left(T - T_{\text{liq}} \right) \right\} \text{ g cm}^{-3} \quad (16.5)$$

and in the liquid phase, the mass density can be described as

$$\rho_{m,l} = \left\{ (4.087 \pm 0.001) - (0.204 \pm 0.007) \cdot 10^{-3} \left(T - T_{\text{liq}} \right) \right\} \text{ g cm}^{-3} \quad (16.6)$$

This way, the increase of the mass density at the liquidus temperature due to the solidification is about 1.8%. For γ-Ti$_{48}$Al$_{48}$Nb$_2$Cr$_2$, the mass density in the solid phase between 1100 and 1400 K can be described as

Fig. 16.5 Mass density of Ti64 and γ-Ti$_{48}$Al$_{48}$Nb$_2$Cr$_2$ as a function of temperature
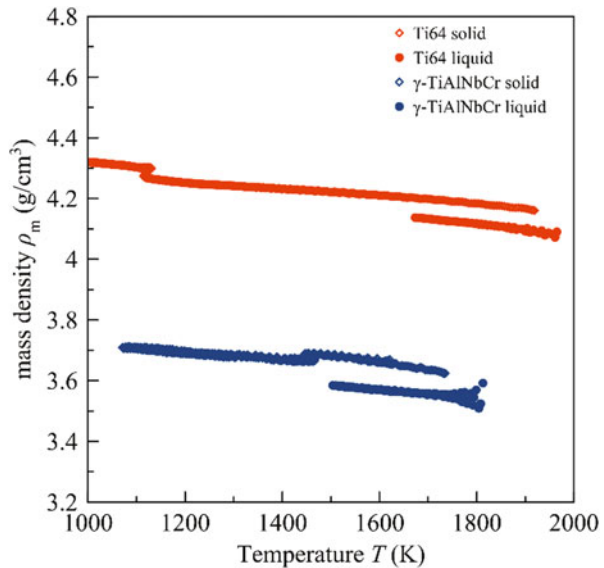
$$\rho_{m,s1} = \left\{(3.623 \pm 0.001) - (0.122 \pm 0.001) \cdot 10^{-3}(T - T_{\text{liq}})\right\} \text{ g cm}^{-3} \quad (16.7)$$

and in the temperature range between 1475 and 1700 K as

$$\rho_{m,s2} = \left\{(3.621 \pm 0.001) - (0.225 \pm 0.006) \cdot 10^{-3}(T - T_{\text{liq}})\right\} \text{ g cm}^{-3} \quad (16.8)$$

and in the liquid phase as

$$\rho_{m,l} = \left\{(3.545 \pm 0.001) - (0.138 \pm 0.008) \cdot 10^{-3}(T - T_{\text{liq}})\right\} \text{ g cm}^{-3} \quad (16.9)$$

Consequently, the mass density increases at the liquidus temperature during solidification by about 2.1%, which is larger than for the Ti64 alloy. The uncertainties given in Eqs. 16.7–16.9 are confidence intervals of the fitting, obtained for a confidence level of 95%. Systematic measurement errors, in addition to the measurement calibration (see also Chap. 12), are small residual sample deformations during the measurements. These were observed for the Ti64 sample to be below 0.3%, translating to an additional measurement uncertainty of only about 0.2%.

4.5   Thermal Conductivity

Under the assumption that the thermal conductivity is mainly carried by electrons, the thermal conductivity can be calculated using the Wiedemann-Franz Law. The domination of thermal conduction by electrons over all other mechanisms is a reasonable assumption for disordered systems such as liquids. The Wiedemann-Franz Law states that the thermal conductivity κ multiplied by the electrical resistivity ρ_e is equal to the Lorentz number L times the temperature T:

$$\kappa \cdot \rho_e = L \cdot T \quad (16.10)$$

The thermal conductivity obtained by application of the Wiedemann-Franz Law using the theoretical Lorentz number $L = 2.45 \cdot 10^{-8} \text{ W } \Omega \text{ K}^{-2}$ is given in Fig. 16.6.

4.6   Specific Heat

Figure 16.7 presents the specific heat capacity of Ti64 and γ-Ti$_{48}$Al$_{48}$Nb$_2$Cr$_2$, obtained containerless by the ac calorimetry method [30] using the ISS-EML on board the international space station (ISS).

The measurement uncertainties of the ac calorimetry method origin from the uncertainty of the measurement of the temperature oscillation amplitudes, which can be done with an accuracy of ± 0.1 K, as well as the uncertainty of the measurement of

Fig. 16.6 Thermal
conductivity of Ti64 and γ-
$Ti_{48}Al_{48}Nb_2Cr_2$, obtained
by the Wiedemann-
Franz Law
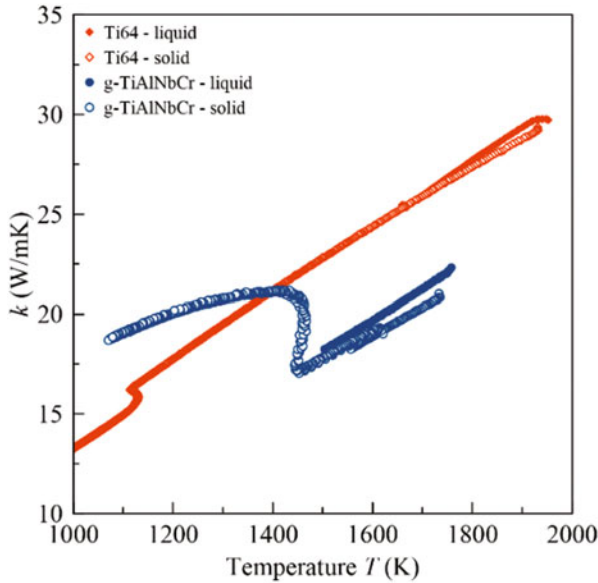
Fig. 16.7 Specific heat of
Ti64 in the solid and liquid
phase, as well as for γ-
$Ti_{48}Al_{48}Nb_2Cr_2$ in the
undercooled liquid state
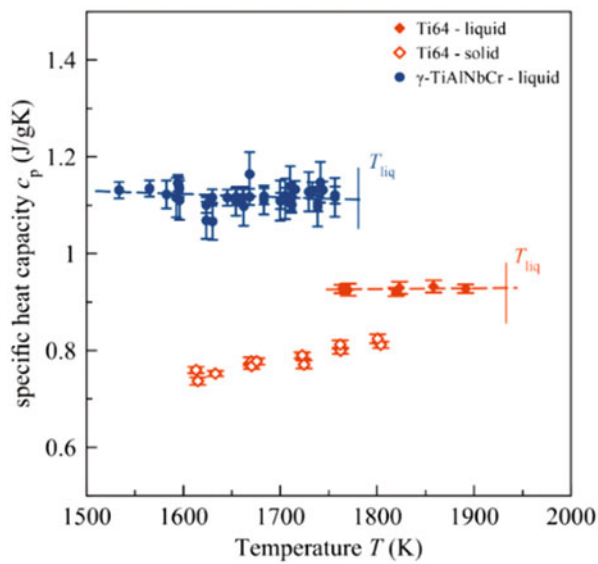
the sample mass, which can be done with an accuracy of ± 0.005 g. Another
contribution to the measurement uncertainty is the amplitude of the dissipated
power. The amplitude of power dissipation can be calculated using analytical
expressions [31] and calibrated by comparison with the power dissipation amplitude
measured on a solid Zr sample. On this basis, the measurement uncertainties given in
Fig. 16.7 are determined.

4.7   Total Hemispherical Emissivity

The cooling of molten metal is in many situations not only governed by the heat conduction to the environment but also due to heat radiation. Precise knowledge of the total hemispherical emissivity is needed to quantify the heat loss due to thermal radiation. Theoretical approximations have been developed over time to describe the total hemispherical emissivity of metal surfaces [32]. The theoretical estimation given by Parker and Abbott is based on the Drude free-electron model, under the assumption that the electronic relaxation time is negligibly small. After [32], the total hemispherical emissivity can be approximated by

$$\varepsilon_{\text{tot}} = 0.766 \times (\rho_e \ T)^{1/2} - (0.309 - 0.0889 \cdot \log (\rho_e \ T)) \cdot \rho_e \ T$$
$$- 0.0175 \cdot (\rho_e \ T)^{3/2} \tag{16.11}$$

This way, the electrical resistivity can be used to obtain theoretical values for the hemispherical emissivity. The total hemispherical emissivity of Ti64 and γ-Ti$_{48}$Al$_{48}$Nb$_2$Cr$_2$ is given in Fig. 16.8, together with the theoretical predictions by Eq. 16.11.

4.8   Postflight Investigations

The Ti64 sample, processed during Batch#1 in the ISS-EML, has already been returned to the ground. The microstructure of the sample that was solidified in space was investigated using standard grinding and polishing procedures, followed
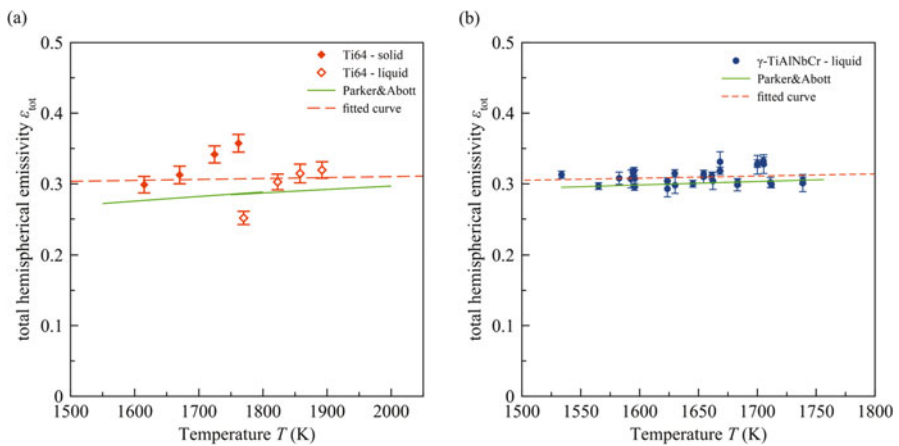
Fig. 16.8 Total hemispherical emissivity of (**a**) Ti64 in the solid and liquid phase and (**b**) γ-Ti$_{48}$Al$_{48}$Nb$_2$Cr$_2$ in the liquid phase
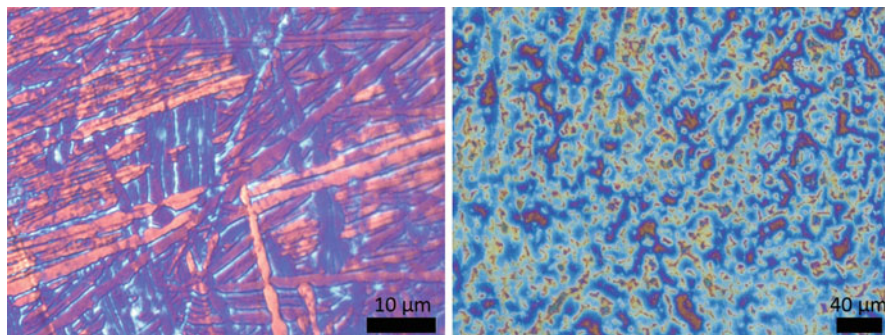
Fig. 16.9 (**a**) Ti64 sample solidified in microgravity – heat-tinted, showing with alpha colonies and alpha-beta eutectoid. (Courtesy of Prof. David Jarvis, HIPtec AS, Oslo, Norway). (**b**) Conventional Ti64 sample solidified on ground. (Courtesy of Prof. David Jarvis, HIPtec AS, Oslo, Norway)

by heat-tinting. The micrograph in Fig. 16.9 shows the heat-tinted sample cross-section at 200x magnification, with alpha colonies and alpha-beta eutectoid.

The large undercooling and the quiescent fluid flow conditions during solidification in microgravity show significantly different microstructures from conventionally solidified material.

5   Discussion

The obtained surface tension of Ti64 in the ISS-EML [19] is higher than the values obtained in other studies using 1 g-EML [21–23]. On the other hand, the surface tension obtained in other microgravity experiments [20, 21] is consistent with the values obtained in the ISS-EML [19].

The surface tension of the γ-Ti-Al alloys presented in Table 16.2 is between 1.11 and 1.24 N/m at the respective liquidus temperature. The agreement between PF and 1 g-EML is better for the $Ti_{46}Al_{46}Ta_8$ than for the $Ti_{46}Al_{46}Nb_8$ alloy. The surface tension obtained for the $Ti_{48}Al_{48}Nb_2Cr_2$ alloy measured in the ISS-EML and in the parabolic flight is close to be within the measurement uncertainty. The obtained surface tensions for the industrial Ti-Al-alloys can be compared to the surface tension of the binary Ti-Al system.

As shown in early parabolic flight experiments, the oxygen content of the Ti64-samples, as well as of the gas atmosphere, has an impact on the surface tension and viscosity [20]. This was also investigated in detail by ground-based levitation experiments, confirming that an increasing amount of oxygen in the sample is reducing the surface tension of titanium [33]. That way, a higher surface tension value for Ti64 compared to the other literature values might indicate a cleaner gas environment and a higher sample purity.

In Fig. 16.10, the experimental data of the surface tension obtained in the ISS-EML is compared to the surface tension measured in a ground-based EML on
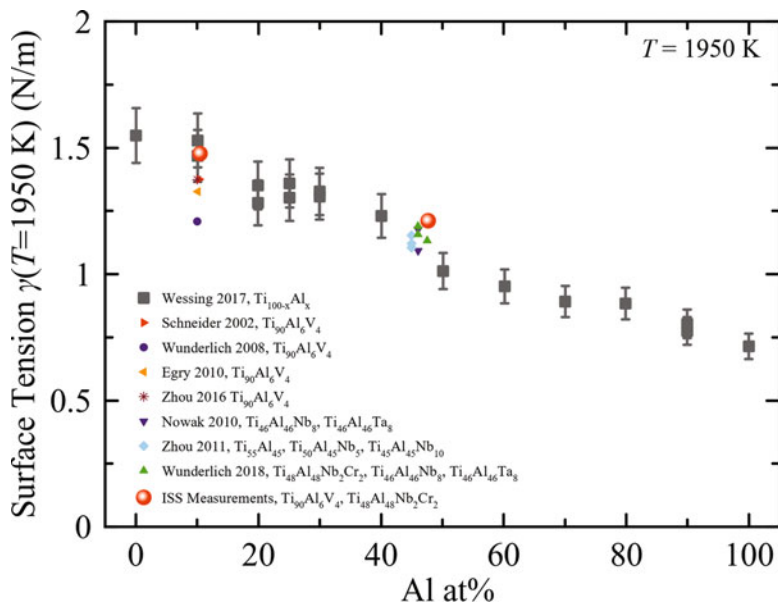
Fig. 16.10 Surface tension γ of Ti-Al alloys dependent on the atomic Al concentration at 1950 K. Binary $Ti_{100-x}Al_x$ alloy by Wessing et al. [34]. Ti64 alloys by Schneider et al. [22], Wunderlich et al. [20], Egry et al. [21], and Zhou et al. [23]. Industrial γ-Ti-Al compositions by Nowak et al. [25], Zhou et al. [35], Wunderlich et al. [24], and on board the ISS [19]

several Ti-Al compositions, as well as to literature values of the surface tension of industrial Ti-Al-based alloy compositions.

The viscosity determined for γ-$Ti_{48}Al_{48}Nb_2Cr_2$ on board the ISS is comparing well with the measurements performed during parabolic flights. For Ti-alloys, the literature data on viscosity is very scarce. The early parabolic flight results obtained at two temperatures by Wunderlich et al. [20] are in reasonably good agreement with the more precise data measured on board the ISS. Also, the viscosities of the γ-$Ti_{48}Al_{48}Nb_2Cr_2$ obtained in a parabolic flight and on board the ISS are in relatively good agreement.

While, to the best of our knowledge, there is no literature data for the electrical resistivity of γ-$Ti_{48}Al_{48}Nb_2Cr_2$, there have been other studies on the electrical resistivity of Ti64-alloy. Our measurements in the solid phase are lower than the values in Refs. [36, 37]. The resistivity in the solid state is always a function of the actual microstructure, which depends on the thermal history, which can explain differences in the literature. The measurements in the liquid phase, however, are in good agreement with the values presented in [38].

The mass density of the liquid Ti64 and γ-$Ti_{48}Al_{48}Nb_2Cr_2$ measured by the ISS-EML is higher (about 4% for Ti64 and about 8% for γ-$Ti_{48}Al_{48}Nb_2Cr_2$) than the mass density of the pure binary Ti-Al alloys (see Wessing et al. [34]), which can be explained by the additions of some heavy alloy components (V, Nb, Cr). The measured mass density of Ti64 in the solid phase is close to handbook values [39],

while the measurements obtained in the ISS-EML are about 28–32% higher than the liquid density given in the same handbook [39]. However, the mass density in the liquid phase obtained for Ti64 by Li et al. [40] is close to the values obtained in the ISS-EML. To the best of our knowledge, there are no literature values for the mass density of γ-Ti$_{48}$Al$_{48}$Nb$_2$Cr$_2$ in the liquid phase.

The thermal conductivities measured for Ti64 are similar to those of Boivineau et al. [38], which were also obtained under the assumption of the Wiedemann-Franz Law. Our measurement data in the liquid phase is, however, lower ($\kappa = 29.8$ W/mK, $T = 1933$ K) than reported for thermal diffusivity measurements ($\kappa = 33.3$ W/mK, $T = 1919$ K) [39].

The specific heat capacity for liquid Ti64 is given by Mills [39], to be 0.83 J/gK (38.79 J/mol K), which is about 10% smaller than the values obtained in the ISS-EML of (0.93 ± 0.02) J/gK (or (43.34 ± 1.00) J/mol K). The specific heat capacity obtained by Kaschnitz et al. [37] is, within the measurement uncertainties, in good agreement with our data. But it is noteworthy that the ISS-EML measurements have extended the available specific heat data for Ti64 by about 200 K into the undercooled liquid phase, which is not possible with container-based or subsecond pulse-heating measurement systems on earth. The specific heat of liquid γ-Ti$_{48}$Al$_{48}$Nb$_2$Cr$_2$ is similar to a measurement obtained for Ti-44Al-8Nb-1B in pulse-heating experiments [41] and much higher than values obtained in drop calorimetry experiments for the Ti50Al50 composition [42].

The total hemispherical emissivity is a quantity that is rather difficult to obtain by any other methods than by the ac modulation calorimetry on levitating droplets. The theoretical predictions by Eq. 16.11 seem to generally underestimate the measured values (see also [43]). The reason could be that the assumptions made in [32] for the electron transport model (a Drude free-electron model, with negligibly short electronic relaxation times) do not strictly hold for the investigated metallic liquids. Further information on the details of short- and medium-range order, as well as scattering mechanisms in the liquid alloy, could help to improve the theoretical prediction of the total hemispherical emissivity.

6 Conclusion

The thermophysical properties of several alpha-beta and gamma-Ti-Al alloys were successfully measured in parabolic flight campaigns, as well as on board the international space station.

The long experiment times in microgravity available on board the international space station allowed the precise measurement of thermophysical properties, such as surface tension and viscosity, including the specific heat capacity and total hemispherical emissivity in the stable and undercooled liquid phase.

References

1. R.R. Boyer, An overview on the use of titanium in the aerospace industry. Mater. Sci. Eng. A **213**, 103–114 (1996)
2. K. Wang, The use of titanium for medical applications in the USA. Mater. Sci. Eng. A **213**, 134–137 (1996)
3. I. Gurrappa, Characterization of titanium alloy Ti-6Al-4V for chemical, marine and industrial applications. Mater. Charact. **51**, 131–139 (2003). https://doi.org/10.1016/j.matchar.2003.10.006
4. M. Peters, J. Hemptenmacher, J. Kumpfert, C. Leyens, Structure and properties of titanium and titanium alloys, in *Titanium and Titanium Alloys*, ed. by C. Leyens, M. Peters, (2003), pp. 1–58
5. M. Long, H.J. Rack, Titanium alloys in total joint replacement – A materials science perspective. Biomaterials **19**, 1621–1639 (1998). https://doi.org/10.1002/acp.2350080606
6. P. Singh, H. Pungota, N.S. Kalsi, On the characteristics of titanium alloys for the aircraft applications. Mater. Today Proc. **4**, 8971–8982 (2017). https://doi.org/10.1016/j.matpr.2017.07.249
7. S. Liu, Y.C. Shin, Additive manufacturing of Ti6Al4V alloy: A review. Mater. Des. **164**, 107552 (2019). https://doi.org/10.1016/j.matdes.2018.107552
8. C. Chunxiang, H. Baomin, Z. Lichen, L. Shuangjin, Titanium alloy production technology, market prospects and industry development. Mater. Des. **32**, 1684–1691 (2011). https://doi.org/10.1016/j.matdes.2010.09.011
9. X. Wu, Review of alloy and process development of TiAl alloys. Intermetallics **14**, 1114–1122 (2006). https://doi.org/10.1016/j.intermet.2005.10.019
10. P. Bartolotta, J. Barrett, T. Kelly, R. Smashey, Use of cast Ti-48Al-2Cr-2Nb in jet engines. JOM **49**, 48–51 (1997). https://doi.org/10.1007/bf02914685
11. F. Appel, M. Oehring, Gamma-titanium aluminide alloys: Alloy design and properties, in *Titanium and Titanium Alloys*, ed. by C. Leyens, M. Peters, (Wiley-VCH Gmbh & Co. KGaA, 2003), pp. 89–152
12. D.J. Jarvis, D. Voss, IMPRESS integrated project – An overview paper. Mater. Sci. Eng. A **413–414**, 583–591 (2005). https://doi.org/10.1016/j.msea.2005.09.066
13. J.C. Schuster, M. Palm, Reassessment of the binary aluminum-titanium phase diagram. J. Phase Equilib. Diffus. **27**, 255–277 (2006). https://doi.org/10.1361/154770306X109809
14. H. Wang, G. Djambazov, K.A. Pericleous, et al., Modelling the tilt-casting process for the tranquil filling of titanium alloy turbine blades, in *Proceedings from the 12th International Conference on Modeling of Casting, Welding, and Advanced Solidification Processes*, (2009), pp. 53–60
15. H. Wang, G. Djambazov, K. Pericleous, et al., Numerical modelling of tilt casting process for γ-TiAl alloys. Int. J Cast. Met. Res. **25**, 65–74 (2012). https://doi.org/10.1179/1743133611Y.0000000024

16. N.J. Humphreys, D. McBride, D.M. Shevchenko, et al., Modelling and validation: Casting of Al and TiAl alloys in gravity and centrifugal casting processes. Appl. Math. Model. **37**, 7633–7643 (2013). https://doi.org/10.1016/j.apm.2013.03.030

17. Y. Jia, S. Xiao, J. Tian, et al., Modeling of TiAl alloy grating by investment casting. Metals (Basel) **5**, 2328–2339 (2015). https://doi.org/10.3390/met5042328

18. R.L. Saha, K.T. Jacob, Casting of titanium and its alloys. Def. Sci. J. **36**, 121–141 (1986). https://doi.org/10.14429/dsj.36.5967

19. M. Mohr, R. Wunderlich, R. Novakovic, et al., Precise measurements of thermophysical properties of liquid Ti–6Al–4V (Ti64) alloy on board the International Space Station. Adv. Eng. Mater. **2000169** (2020). https://doi.org/10.1002/adem.202000169

20. R.K. Wunderlich, Surface tension and viscosity of industrial Ti-alloys measured by the oscillating drop method on board parabolic flights. High Temp. Mater. Process. **27**, 401–412 (2008)

21. I. Egry, D. Holland-Moritz, R. Novakovic, et al., Thermophysical properties of liquid AlTi-based alloys. Int. J. Thermophys. **31**, 949–965 (2010). https://doi.org/10.1007/s10765-010-0704-1

22. S. Schneider, I. Egry, I. Seyhan, Measurement of the surface tension of undercooled liquid Ti 90Al6V4 by the oscillating drop technique. Int. J. Thermophys. **23**, 1241–1248 (2002). https://doi.org/10.1023/A:1019896321431

23. K. Zhou, B. Wei, Determination of the thermophysical properties of liquid and solid Ti–6Al–4V alloy. Appl. Phys. A Mater. Sci. Process. **122**, 1–5 (2016). https://doi.org/10.1007/s00339-016-9783-6

24. R.K. Wunderlich, U. Hecht, F. Hediger, H.J. Fecht, Surface tension, viscosity, and selected thermophysical properties of Ti48Al48Nb2Cr2, Ti46Al46Nb8, and Ti46Al46Ta8 from microgravity experiments. Adv. Eng. Mater. **20**, 1800346 (2018). https://doi.org/10.1002/adem.201800346

25. R. Nowak, T. Lanata, N. Sobczak, et al., Surface tension of γ-TiAl-based alloys. J. Mater. Sci. **45**, 1993–2001 (2010). https://doi.org/10.1007/s10853-009-4061-z

26. R.W. Hyers, D.M. Matson, K.F. Kelton, J.R. Rogers, Convection in containerless processing. Ann. N. Y. Acad. Sci. **1027**, 474–494 (2004). https://doi.org/10.1196/annals.1324.038

27. X. Xiao, R.W. Hyers, D.M. Matson, Surrogate model for convective flow inside electromagnetically levitated molten droplet using magnetohydrodynamic simulation and feature analysis. Int. J. Heat Mass Transf. **136**, 531–542 (2019). https://doi.org/10.1016/j.ijheatmasstransfer.2019.03.028

28. X. Xiao, J. Lee, R.W. Hyers, D.M. Matson, Numerical representations for flow velocity and shear rate inside electromagnetically levitated droplets in microgravity. npj Microgravity **5**, 7 (2019). https://doi.org/10.1038/s41526-019-0067-2

29. G. Lohöfer, High-resolution inductive measurement of electrical resistivity and density of electromagnetically levitated liquid metal droplets. Rev. Sci. Instrum. **89**, 124709 (2018). https://doi.org/10.1063/1.5065482

30. H.J. Fecht, W.L. Johnson, A conceptual approach for noncontact calorimetry in space. Rev. Sci. Instrum. **62**, 1299–1303 (1991). https://doi.org/10.1063/1.1142488

31. E. Fromm, H. Jehn, Electromagnetic forces and power absorption in levitation melting. Br. J. Appl. Phys. **16**, 653–663 (1965)

32. W.J. Parker, G.L. Abbott, Theoretical and experimental studies of the total emittance of metals, in *Symposium on Thermal Radiation of Solids, NASA SP-55*, ed. by S. Katzoff, (1964), pp. 11–28

33. J. Brillo, J. Wessing, H. Kobatake, H. Fukuyama, Surface tension of liquid ti with adsorbed oxygen and a simple associate model for its prediction. High Temp. High Press. **49**, 89–105 (2020). https://doi.org/10.32908/hthp.v49.849

34. J.J. Wessing, J. Brillo, Density, molar volume, and surface tension of liquid Al-Ti. Metall. Mater. Trans. A Phys. Metall. Mater. Sci. **48**, 868–882 (2017). https://doi.org/10.1007/s11661-016-3886-8

35. K. Zhou, H.P. Wang, J. Chang, B. Wei, Surface tension measurement of metastable liquid Ti-Al-Nb alloys. Appl. Phys. A Mater. Sci. Process. **105**, 211–214 (2011). https://doi.org/10.1007/s00339-011-6491-0

36. N.D. Milošević, I. Aleksic, Thermophysical properties of solid phase Ti-6Al-4V alloy over a wide temperature range. Int. J. Mater. Res. **103**, 707–714 (2012)

37. E. Kaschnitz, P. Reiter, J.L. McClure, Thermophysical properties of solid and liquid 90Ti-6Al-4V in the temperature range from 1400 to 2300 K measured by millisecond and microsecond pulse-heating techniques. Int. J. Thermophys. **23**, 267–275 (2002). https://doi.org/10.1023/A:1013925715428

38. M. Boivineau, C. Cagran, D. Doytier, et al., Thermophysical properties of solid and liquid Ti-6Al-4V (TA6V) alloy. Int. J. Thermophys. **27**, 507–529 (2006)

39. K.C. Mills, *Recommended Values of Thermophysical Properties for Selected Commercial Alloys* (Woodhead Publishing Limited, 2002)

40. J.J.Z. Li, W.L. Johnson, W.K. Rhim, Thermal expansion of liquid Ti-6AI-4V measured by electrostatic levitation. Appl. Phys. Lett. **89**, 1–2 (2006). https://doi.org/10.1063/1.2349840

41. C. Cagran, B. Wilthan, G. Pottlacher, et al., Thermophysical properties of a Ti-44%Al-8%Nb-1%B alloy in the solid and molten states. Intermetallics **11**, 1327–1334 (2003). https://doi.org/10.1016/S0966-9795(03)00175-4

42. K. Zhou, H.P. Wang, J. Chang, B. Wei, Specific heat measurement of stable and metastable liquid Ti-Al alloys. Appl. Phys. A Mater. Sci. Process. **103**, 135–137 (2011). https://doi.org/10.1007/s00339-010-6168-0

43. M. Mohr, D.C. Hofmann, H.-J.J. Fecht, Thermophysical properties of an Fe57.75Ni19.25Mo10C5B8 glass-forming alloy measured in microgravity. Adv. Eng. Mater. **2001143**, 1–8 (2020). https://doi.org/10.1002/adem.202001143

Chapter 17
Thermophysical Properties of Steels

Seshadri Seetharaman, Livio Battezzati, Markus Mohr, and Hans-Jörg Fecht

1 Introduction

Steel forms an important component of static as well as dynamic construction materials. The former includes buildings for living, industrial complexes, bridges, etc., while the latter encompass lorries, trucks, cars, and other types of vehicles. Today, the industrialized society is built out of steel which is illustrated by the enormous amounts of steel produced worldwide. In 2012, the annual global steel production amounted to 1.5 billion tons, a quantity corresponding to approximately five times the weight of the living global human population. The steel utilization is an index of the degree of industrialization. This has been shown historically in, for example, Europe, North America, Australia, and Japan, where the industrialization was marked by the huge amounts of steel consumed. A similar transition is apparent even in the case of BRIC (Brazil, Russia, India, and China) countries, with a corresponding increase in the steel production. The world steel production in the year 2017 is presented in Fig. 17.1 [1].

In a study performed by the Swedish Steel Producers Association, supported by Swedish Foundation for Strategic Environmental Research (Mistra), viz., the Steel Eco-Cycle program [2], ten different case studies have been performed on steel construction, where conventional steel has been replaced by high-strength steels (as,

S. Seetharaman (✉)
Royal Inst. Technol, Stockholm, Sweden
e-mail: raman@kth.se

L. Battezzati
Dipartimento di Chimica, Università di Torino, Torino, Italy
e-mail: livio.battezzati@unito.it

M. Mohr · H.-J. Fecht
Institute of Functional Nanosystems, Ulm University, Ulm, Germany
e-mail: markus.mohr@uni-ulm.de; hans.fecht@uni-ulm.de

377

Crude steel production
World total: 1689 million tonnes
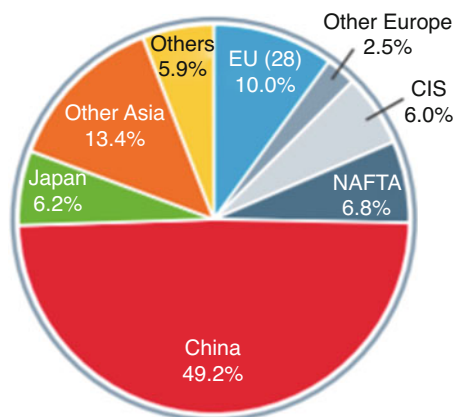
for example, TRIP (Transformation Induced Plasticity) and TWIP (TWinning Induced Plasticity). With stronger and more resilient steel, weight reductions of between 20 and 40% could be obtained. Lighter vehicles with the new steel grades lead to significant fuel savings corresponding to $-28,000$ GWh and reduced CO_2 emissions corresponding to -7300 ktonnes.

Modelling of casting of steels needs very reliable thermophysical data. It has long been felt that reliable information regarding the thermophysical properties of many metallic systems in the liquid phase is lacking. This is particularly true of liquid iron alloys. The reliability of the data is seriously affected by impurities in steel. Properties such as surface tension are impacted by oxygen impurity, which is surface-active. Further, during the modelling of the casting processes, it is important to delineate the effect of the gravitational forces. Thus, measurements of thermophysical properties of steels at high temperatures need to be carried out under microgravity environment. The results obtained need to be compared with those generated by conventional methods under terrestrial conditions so that the effect of gravity is well understood as industrial processes are carried out under 1 g. These unique measurements were carried out as a part of the ThermoLab/ThermoProp projects under the sponsorship of European Space Agency (ESA). The present paper summarizes the results obtained in the case of industrial steel samples. It combines classical thermoanalytical methods such as high-temperature DSC and the X-ray sessile drop method for surface tension measurements with containerless methods based on electromagnetic levitation in ground-based laboratory and under reduced gravity conditions. In the present contribution, an overview of the ThermoLab activities for Fe-alloys is presented. Five different alloys were investigated as part of the ThermoLab program [3]. The high alloy steel grade was supplied by Sandvik Materials Technology, Sweden, and low alloy grade alloy by CORUS, IJmuiden, Holland. Furthermore, in preparation for future measurements on the ISS-EML, a Fe-Si steel alloy and a prototype, low-alloyed boron

steel (Fe-10ppmC-50ppmB) from TATA Steel Europe, IJmuiden, Holland, were investigated in two parabolic flight campaigns. On board the international space station, the thermophysical properties of a generic stainless steel (Fe-21Cr-19Ni) were measured. The alloy suppliers are members of the industrial user group of the project.

2   Experimental

2.1   Characterization of As-Received Samples

2.1.1   SANDVIK Steel Sample

Sample composition was determined by the EDX microanalysis (Table 17.1)[3]. The target metals for the analysis were four characteristic elements, viz., Fe, Cr, Ni, and Mo. An average analysis over large areas of the samples was carried out with regard to both white-ferrite part as well as gray-austenite part. The EDX microanalyses in all the three cases agree with the nominal composition Fe 61.62%, C 0.03%, Cr 25%, Ni 7%, Mo 4%, Mn 1.2%, Si 0.8%, N 0.3%, P 0.035%, and S:0.015% (in mass %); mass % Fe, Cr, Ni, and Mo nominal 64 25 7 4, respectively; on large areas (average) $64 \pm 1\ 27 \pm 2\ 6 \pm 1\ 3 \pm 1$; white-ferrite (average) $63 \pm 1\ 28 \pm 1\ 6 \pm 2\ 3 \pm 1$; and gray-austenite (average) $64 \pm 1\ 25 \pm 2\ 8 \pm 1\ 3 \pm 1$.

   The Cr concentration is higher in the white-ferrite area, as expected due to its ferritic character. Analogously, the Ni concentration is higher in the gray-austenite area, as expected in view of its austenitic character. The XRD analysis of the as-received alloy has been performed in order to confirm the ferrite and austenite phases (Fig. 17.2).

   The computed phase diagram of the Sandvik steel sample is given in Fig. 17.3.

   It can be seen that the material contains bcc + fcc + σ phases, where the fcc + bcc phases are stable between 1171 K and solidus temperature, which is 1615 K. Thus, the σ phase (FeCr) is stable in the interval between room temperature and 1218 K. The liquidus temperature is 1717 K.

2.1.2   CORUS Steel Sample

The manganese steel sample received from CORUS was a low-oxygen eutectoid steel. The composition of the alloy was received from CORUS as Fe – 0.71% C, 0.35% Si, 1.09% Mn, 0.011% P, 0.02% S, 0.0044% N, and 0.0008% O (in mass%).

Table 17.1 Composition of as-received SANDVIK steel sample

Mass %	Fe	Cr	Ni	Mo
Nominal	64	25	7	4
On large areas (average)	64 ± 1	27 ± 2	6 ± 1	3 ± 1
White-ferrite (average)	63 ± 1	28 ± 1	6 ± 2	3 ± 1
Gray-austenite (average)	64 ± 1	25 ± 1	8 ± 1	3 ± 1
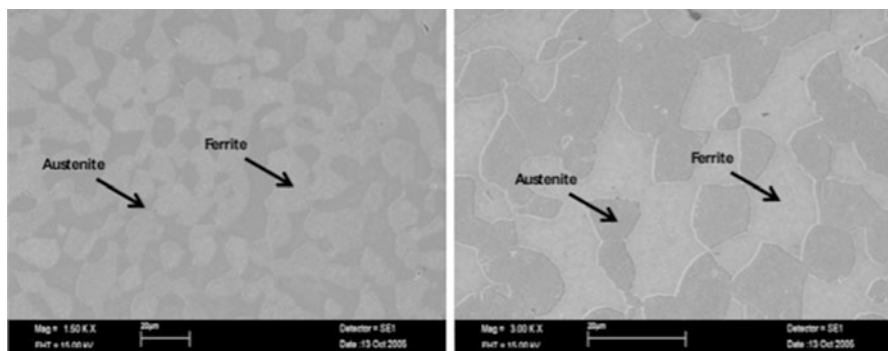
Fig. 17.2 Microstructure of the as-received Sandvik steel sample
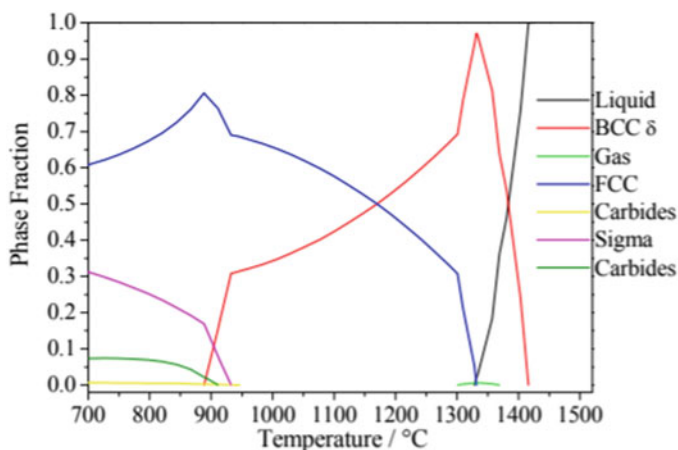
Fig. 17.3 The computed phases in the SANDVIK steel sample [3]. (Reproduced under the terms of the CC BY-NC-ND 3.0 license [3]. Copyright 2011, DeGruyter)

The microstructure of the as-received sample is presented in Fig. 17.4. The zones corresponding to pearlite and small amount of ferrite are noticeable.

Thermo-Calc computation of the CORUS sample showed that the material consisted of BCC phase below 954 K as presented in Fig. 17.5. Both BCC and FCC phases appear in the temperature range 954–1026 K, while, at higher temperatures, FCC phase is the stable phase below the solidus temperature of 1638 K. The liquidus temperature was indicated as 1746 K.

2.1.3 Fe-Si Alloy Sample

The composition of the received material of Fe-10wt%Si (Fe-18.1at%Si) was confirmed by EDX measurements. Iron-silicon alloys up to about 3–6wt%Si content are typical soft magnetic alloys for applications in electrical power transformers,

Fig. 17.4 The microstructure of the as-received sample from CORUS [3]. (Reproduced under the terms of the CC BY-NC-ND 3.0 license [3]. Copyright 2011, DeGruyter)
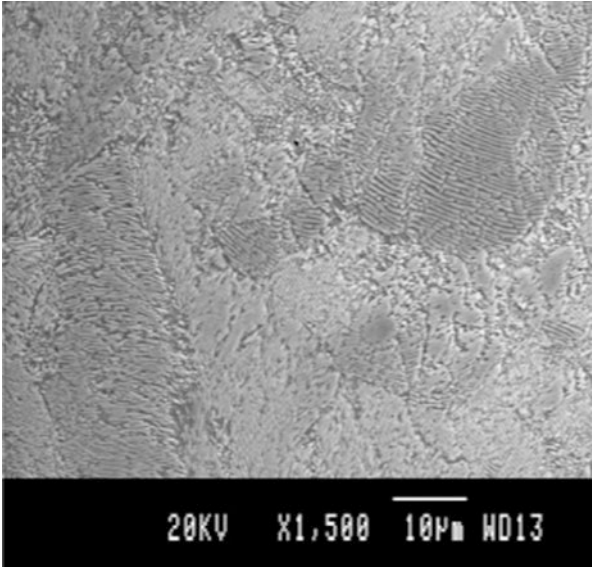
Fig. 17.5 Phase diagram of the CORUS sample as computed by Thermo-Calc. (Reproduced under the terms of the CC BY-NC-ND 3.0 license [3]. Copyright 2011, DeGruyter)
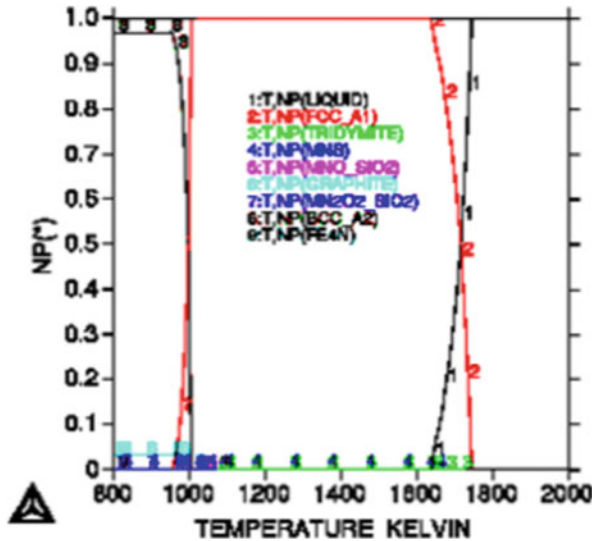
motors, and generators. Higher Si contents increase the electrical resistivity, which reduces eddy current losses. The downside of a high silicon concentration is the increased brittleness, which is a challenge for the traditional production route.

2.1.4 Fe-10ppmC-50ppmB sample

The prototype three-component boron steel Fe-10ppmC-50ppmB is a representative of a new-generation of steels where carbon is replaced with boron to achieve better

material properties. One challenge of the industrial production of this system is the rather unknown or unreliable thermophysical data. The possibility of a metatectic reaction in the system, where the segregation of boron leads to partial remelting of the material during cooling, brings new challenges for the industrial process development.

2.1.5   Fe-21Cr-19Ni sample

The generic stainless steel Fe-21Cr-19Ni was prepared from the elemental materials, molten and cast into spheres of 6.5 mm diameter by suction casting in an arc melter. The sample composition was confirmed by EDX measurements during the sample preparation.

2.2   *Differential Scanning Calorimetry*

Thermal analysis was performed with a High Temperature Differential Scanning Calorimeter (MultiHTC DSC) of Setaram, France. The calorimeter cell is made of an alumina tube, and the sample is contained in an alumina pan which is inserted into the cell housing covered with an alumina lid. The sample is covered with alumina powder to prevent it from sticking to the crucible walls. The reference cell is symmetrically placed in the tube. It is added only with alumina powder. The sensor for the sample and reference cell is a thermopile, and the instrumental output is a temperature difference. The cell is evacuated and purged several times before measuring under flowing helium filtered to remove residual oxygen and water vapor. The standard thermal cycle was as follows. Heating was provided by a graphite furnace kept under flowing Ar. The specimen was heated from room temperature to 893 K at the rate of 15 K min^{-1} and kept at this temperature for 30 min. Then it was heated at the rate of 10 K min^{-1} above the melting or liquidus point and kept at this temperature for 30 min. Finally, it was cooled at the rate of -10 K min^{-1} to 893 K and kept at this temperature for 30 min. For the various samples, one or more cycles have been performed. Experiments were also performed at the rates of 0.1, 0.5, 2, and 5 K min^{-1}. The DTA cell was first calibrated for the temperature and the heat flow by recording the melting temperature and heat of fusion of various pure metal samples (Al, Ag, Au, Cu, Ni) at the rates of 2, 5, and 10 K min^{-1}. The frequency of sampling of the data points was one point every 1 to 3 s according to the heating or cooling rate for a total of 4800 point per file. The temperature calibration was further checked by measuring the Curie point of pure Fe samples both on heating and cooling at various rates, and the time constant for temperature equilibration between the sample and reference cells was checked by melting a sample of pure Au at various rates (Fig. 17.6).

— Crucible

— Thermopile

— Alumina tube

— Graphite furnace
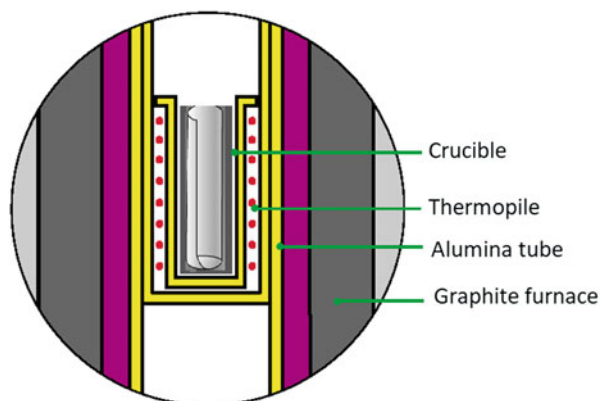
2.3 Thermal Diffusivity and Thermal Conductivity

The thermal diffusivity measurements were carried out on a Laser-Flash unit (model TC-7000H/MELT) supplied by Sinku-Riko, Japan. The maximum temperature at which the measurements can be carried out is 1873 K. A schematic diagram of the apparatus is presented in Fig. 17.7.

The sample temperature was measured using a Pt-13%Rh/Pt (R-type) thermo-couple positioned in an alumina tube and placed closed to the sample holder. In the present arrangement, the top side of a small disc of material is subjected to a laser radiation pulse irradiated with a laser, which provides an instantaneous energy pulse. The laser energy is absorbed on the top surface of the sample and gets converted to heat energy. The thermal energy is conducted through the sample. The temperature rise at the back surface of the sample is monitored using an infrared detector. A plot of the back surface temperature against time is plotted in Fig. 17.8. The magnitude of the temperature rise and the amount of laser energy are not required for a thermal diffusivity determination, but only the shape of the curve, which is used in the analysis. The time required for the rear surface to reach half of the maximum temperature rise is denoted as $t_{1/2}$. Depending on the specimen and the thermal diffusivity value, $t_{1/2}$ can range from a few milliseconds to a few seconds. The thermal diffusivity can be expressed as $\alpha = \frac{1.37}{\pi^2} \frac{L^2}{t_{1/2}}$, where L is the sample thickness.

For liquid metals, the sample is sandwiched between two sapphire crucibles to get an accurate thickness as shown in Fig. 17.9a. It is to be noted that the crucibles are transparent to the laser beam. In the case of molten mold flux, the three-layered cell arrangement was employed. The three layers are composed of the liquid sample having the form of a thin film, sandwiched between two platinum crucibles. The laser pulse is exposed on the top surface of the upper, and the temperature rise on the rear surface of the lower crucible is monitored as a function of time. The experiment is repeated by varying the sample thickness. Figure 17.9b shows the schematic of the three-layered arrangement.

Fig. 17.7 Laser-Flash unit
schematic diagram

Nd-Glass Laser

Quartz
Window

Gas Outlet

High Temperature
Furnace

Control Module &
Computer

Sample

Thermocouple

Protective Tube

To Vacuum
Pump

Gas Inlet

Gold-Plated
Mirror

IR Detector

Micrometer Screw
Gauge

Diaphragm
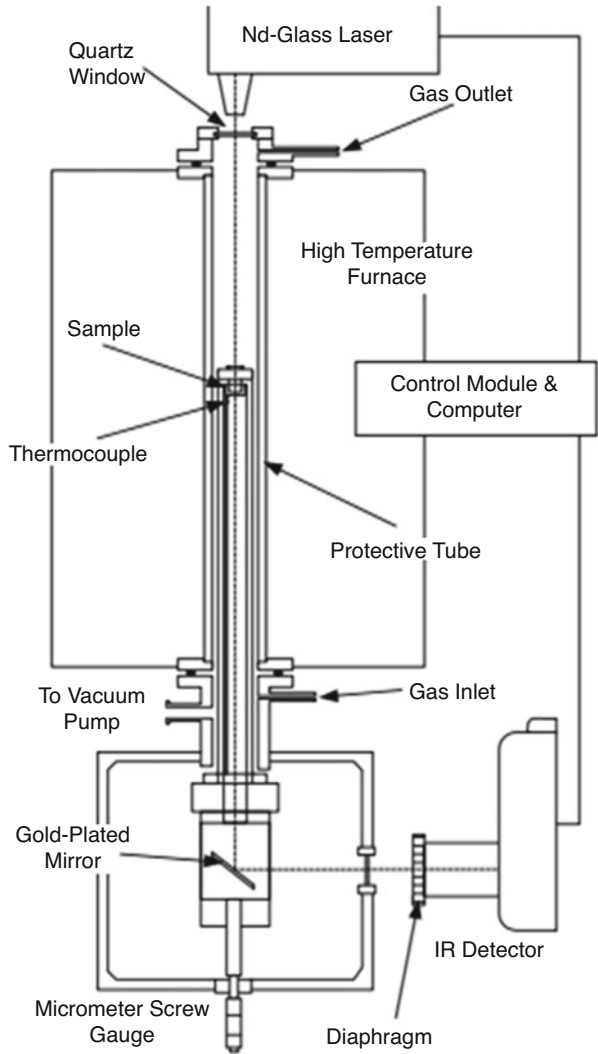
Fig. 17.8 The recorded
temperature history at the
rare surface of a specimen
calculated by instrument

T/T_{max}

1.0

0.5

0

0   $t_{1/2}$ time / s
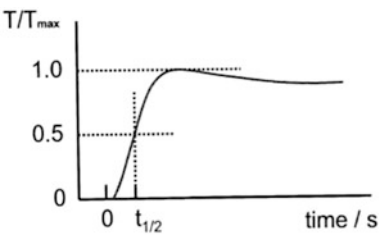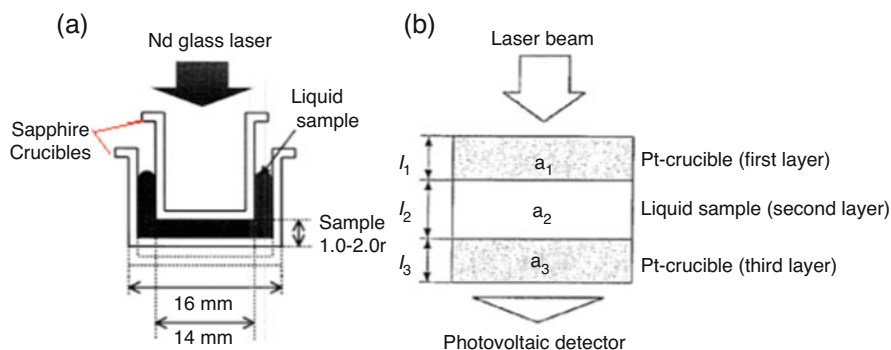
Fig. 17.9 (**a**) Sample arrangement during liquid alloy thermal diffusivity measurement. (**b**) Schematic diagram showing the three-layered cell arrangement in the case of oxide melts
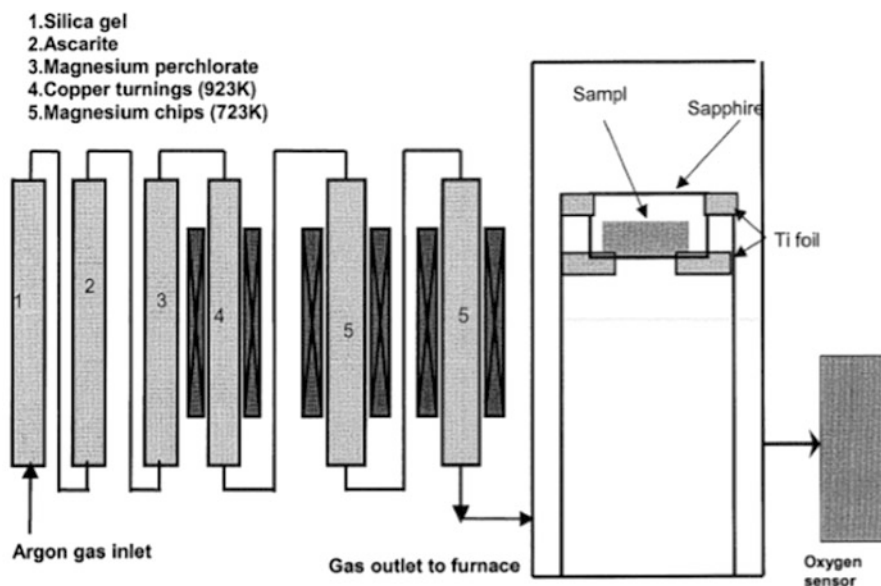
Fig. 17.10 The gas-cleaning system

The measurements at high temperatures are carried out in an inert atmosphere in order to prevent chemical reactions. The impurity levels in the commercial argon gas had to be brought down significantly, especially with respect to the oxygen potential. In order to lower the impurity levels, the argon gas was subjected to a number of purification steps. The gas-cleaning system used in the present work is schematically presented in Fig. 17.10. The moisture impurity in the argon gas was removed by passing the gas successively through silica gel as well as Mg $(ClO_4)_2$. To remove traces of CO_2 in the gas, a column of Ascarite was introduced in the gas-cleaning system. The gas was passed through columns of copper and magnesium turnings

kept at 923 K and 723 K, respectively. The final partial pressure of oxygen in the argon cleaned in this way was found by using a ZrO_2-MgO oxygen sensor to be less than 10^{-18} atm.

2.4 Surface Tension and Density

2.4.1 X-Ray Sessile Drop Method

The X-ray unit that enabled the measurements of surface tension is presented in Fig. 17.11. This consisted of a Philips BV-26 imaging system with an X-ray source of 40–105 kV. The focal spot of the X-rays could be varied between 0.6 and 1.5 mm. The imaging system consisted of a CCD camera, equipped with digital noise reduction. The unit could capture images in real time and had a storage capacity of 34 images. A schematic diagram of the method is shown in Fig. 17.12.

The recording system had an IBM-PC with a video card capable of handling 12 pictures per second. The graphic system had a resolution of 575 X 900 matrix. The system could store up to 192 images and a video memory of 32 images.

The furnace for the measurements was supplied by Thermal Technology Inc. (model 1000–3500-FP20). This was equipped with graphite heating elements with an effect of 20 kVA, capable of attaining a maximum temperature of 2573 K. The

Fig. 17.11 The X-ray imaging unit

Fig. 17.12 A schematic diagram of the principle of the X-ray sessile drop method
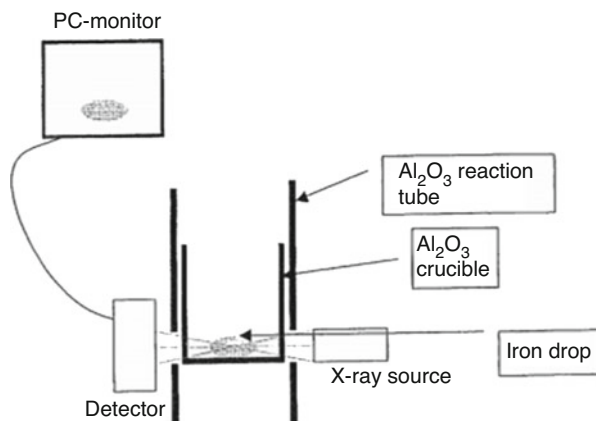
furnace was controlled by a Raytek single-color optical pyrometer. Two quartz windows of 40 mm diameter were provided on either side of the outer jacket for the X-rays. The reaction tube was made of recrystallized alumina, fitted inside with appropriate radiation shields so that the even temperature zone was about 100 mm in the central part of the tube. A gas-cleaning system similar to the one described earlier provided the inert atmosphere protecting the samples.

2.5 Microgravity Experiments

The microgravity experiments were performed using an electromagnetic levitation (EML) device on board the international space station for the Fe-21Cr-19Ni stainless steel sample. For the other steels, the microgravity experiments were performed using the EML (TEMPUS) on board a parabolic flight airplane [5]. From the experimentalists point of view, both EML devices are technically rather similar. The ISS-EML is described in detail in Chap. 3, and details on the TEMPUS EML can be found in Ref. [5]. The TEMPUS device on board the parabolic flight airplane of NoveSpace (www.airzerog.com) consists of a process and a sample chamber which are connected to a vacuum pump system and a gas circulation unit. The sample is heated and positioned by radio frequency (rf-) electromagnetic fields. A dipole field for heating and a quadrupole field for positioning are superimposed using a single coil system operating at frequencies of 330 kHz (heating) and 170 kHz (positioning). The process chamber is equipped with two high-speed cameras. The axial camera is additionally equipped with an optical pyrometer with a measurement range between 300 and 2100 °C. A second camera is mounted in radial direction. In addition, in the TEMPUS facility, the sample coupling electronics is used to measure the current, voltage, phase shift, and frequency of the rf-heating voltage with high accuracy and a data rate of 400 Hz. That way, the changed sample coupling due to

(a)   (b)
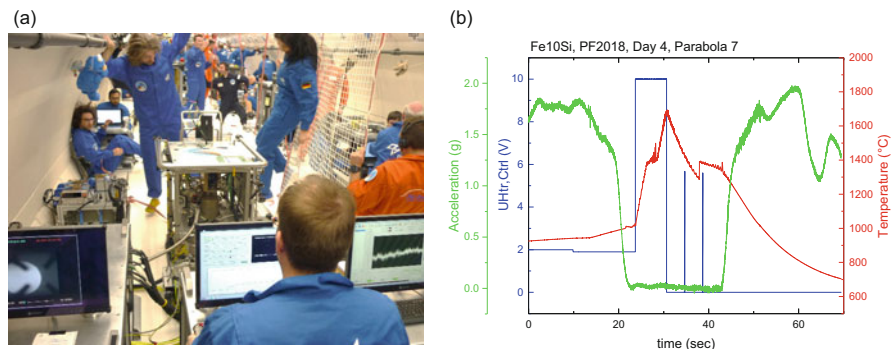
Fig. 17.13 (**a**) TEMPUS facility operated during a parabolic flight. (**b**) Typical temperature-time diagram recorded during a parabola

the varying sample diameter during oscillations can be measured and used to determine surface tension and viscosity.

The sample chamber is mounted below the process chamber and contains the six samples to be processed during one flight day (usually 30 parabolas per flight day). The samples are contained in a sample holder with either a metallic wire cage structure or a ceramic cup on top of a SiN pedestal.

Figure 17.13a shows the TEMPUS facility operated during a parabolic flight. Figure 17.13b shows a typical temperature-time diagram recorded during a single parabola. As seen in Fig. 17.13b, parabolic flights offer about 20 s of reduced gravity, which is sufficient for most alloys to heat the sample until melting, overheat the melt, and cool it down until solidification. The cooling period is the time span where the heater is turned off, and therefore, only minimal forces act on the sample. Hence, short heater pulses can be applied to initiate surface oscillations. The oscillation frequency is measured in order to obtain the surface tension, and the damping time constant of the surface oscillations is used to obtain the viscosity of the sample.

The surface tension σ is evaluated from the surface oscillation frequency ν_R and the sample mass M according to

$$\sigma = \frac{3}{8}\pi \ \nu_R^2 M \qquad (17.1)$$

The viscosity is determined by the damping time constant of the surface oscillations following

$$\eta = \frac{3}{20\pi} \ \frac{M}{R}\tau^{-1} \qquad (17.2)$$

where R is the sample radius. For more details, we refer to the Chap. 12.

3 Results and Discussion

The results of the various measurements are presented in this section.

3.1 Heat Capacity

3.1.1 SANDVIK Sample

DSC measurements have been carried out at three different heating rates for the SANDVIK steel sample. Figure 17.14 shows the DSC results on heating and cooling at different rates, respectively. On heating, the DSC traces present the first small endothermic signal possibly related to carbides dissolution. The second small peak is related to γ-δ transformation and possible nitrogen loss from the alloy, and the last peak is related to the melting of steel. On cooling, only one peak, which is related to solidification, has been found. The temperature of solidus and liquidus and the enthalpy of fusion and solidification are summarized in Table 17.2. Since nitrogen gas is lost during heating, the steel composition changes during the measurement. The melting temperature changes are related to the heating rate in that the lower heating rate is seen to lead to the higher melting temperature, most probably due to the escape of nitrogen from the alloy to the gas phase over a longer time.
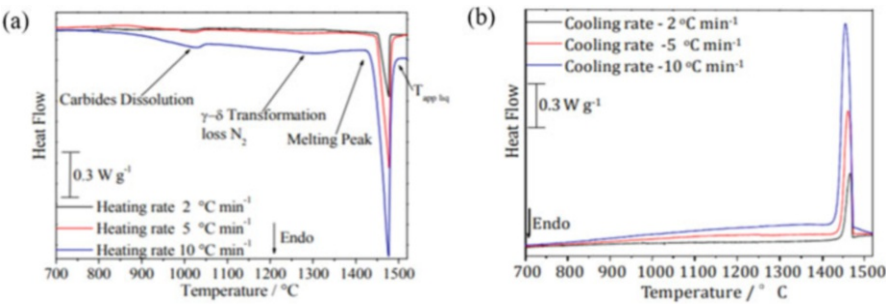
Fig. 17.14 DSC curve of SANDVIK steel sample. (**a**) Heating mode and (**b**) cooling mode. (Reproduced under the terms of the CC BY-NC-ND 3.0 license [3]. Copyright 2011, DeGruyter)

Table 17.2 DSC results of the SANDVIK sample

Heating rate (°C/min)	$T_{melt,onset}$ (°C)	$T_{app, liquidus}$ (°C)	T_{und} (°C)	ΔH Melting (J/g)	ΔH solidification (J/g)
10	1443	1482	1473	203	211
5	1449	1482	1473	199	193
2	1452	1479	1472	198	191
0[a]		1479 ± 2			

[a]Extrapolated value
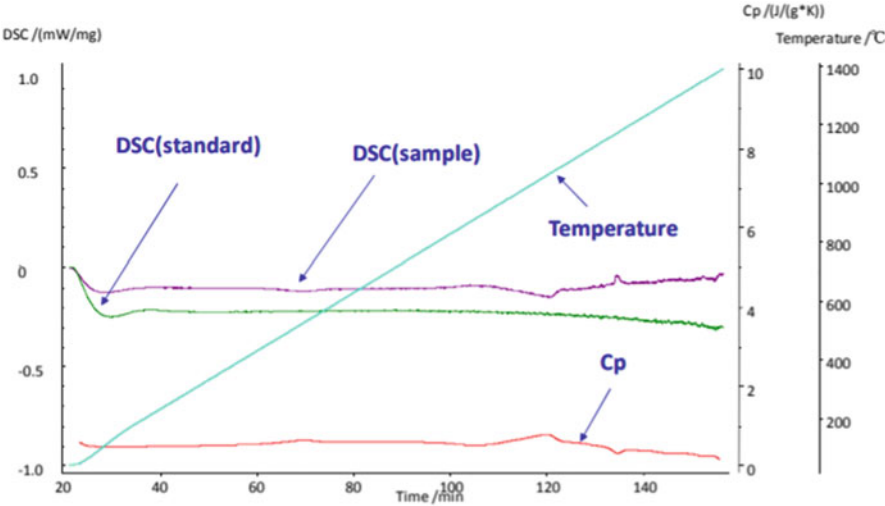
Fig. 17.15 Heat capacity of the SANDVIK steel sample

Table 17.3 DSC results of CORUS steel sample

Sample	Heating rate (°C/min)	Sample mass (mg)	$T_{melt,onset}$ (°C)	$T_{app, liquidus}$ (°C)	T_{und} (°C)	ΔH on heating (J/g)
1	2	190	1391	1496	1507	248
2	5	233	1386	1496	1498	267
3	5	211	1384	1496	1496	255
Average value			1387 ± 4	1496		257 ± 10 (UTORINO) 272 ± 12 (ULM)

Table 17.4 C_p values obtained from DSC results

	C_p (J/K/mol) 950 K	C_p (J/K/mol) 1100 K	C_p (J/K/mol) 1250 K
Low-alloyed steel	48	33	33
Heating	40 ± 3	31 ± 3	41 ± 5
Cooling	36 ± 4	34 ± 3	41 ± 5

The heat capacity values obtained by the DSC measurements are shown in Fig. 17.15.

3.1.2 CORUS Sample

The DSC measurement results for the CORUS sample are presented in Tables 17.3 and 17.4. A study on the comparability of the DSC measurements performed in different devices was performed using the CORUS sample. To this end, measurements were performed also at Ulm University in a NETZSCH High-Temperature
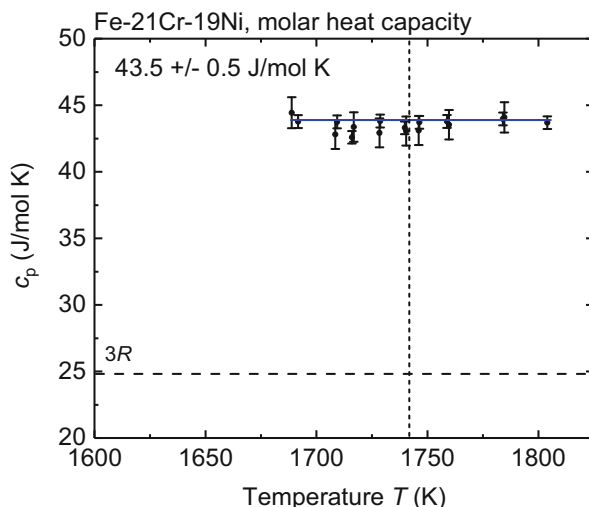
DSC. As shown in Table 17.3, the obtained melting enthalpy at Università di Torino and at Ulm University agree within the measurement uncertainties.

A common phenomenon encountered was the overheating and undercooling of the eutectoid transformation temperature. The undercooling leads to primary α precipitation followed by the eutectoid. The enthalpy associated with the eutectoid transformation is consistent with that of Fe-C alloys. The higher value found on cooling is due to transformation occurring in the undercooling regime.

3.1.3 Fe-21Cr-19Ni

As a benchmark reference experiment, the specific heat capacity of the generic Fe-21Cr-19Ni was measured in the stable and undercooled liquid phase in the ISS-EML, using the ac calorimetry method (see Chap. 12). The obtained measurement data is rather independent of temperature and is 43.5 J/K/mol as shown in Fig. 17.16.

This result is in general agreement with the specific heat capacity of other Fe-Cr-Ni compositions [7]. Theoretical predictions of the specific heat of Fe-Cr-Ni alloys is still difficult due to the unclear value of the specific heat of liquid Cr [7]. Further, Fe-Cr-Ni compositions are going to be measured in the future on board the ISS, which will enable a better theoretical description of the Fe-Cr-Ni system.

3.2 Thermal Diffusivity and Thermal Conductivity

3.2.1 SANDVIK Steel Sample

The temperature dependency of the thermal diffusivity of stainless steel sample is presented in Fig. 17.17. The phases that are expected to be present are also shown in
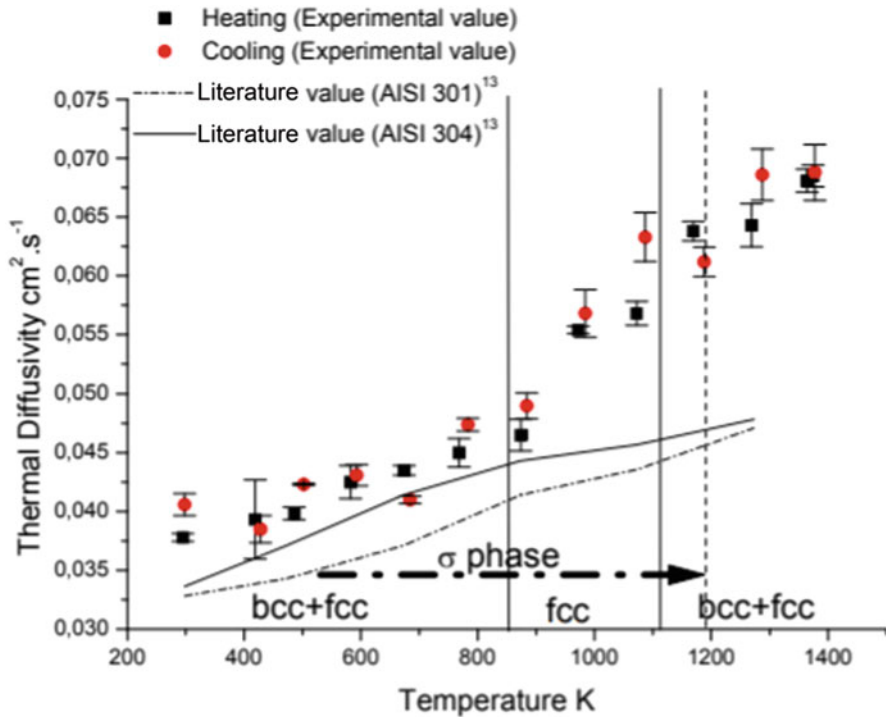
Fig. 17.17 Thermal diffusivity of the SANDVIK steel sample as a function of temperature. (Reproduced under the terms of the CC BY-NC-ND 3.0 license [3]. Copyright 2011, DeGruyter)

the figure. Thermal diffusivity is observed to be nearly constant up to about 700 K above which the value increases with increasing temperature. It is to be noted that AISI 301 and AISI 304 austenitic stainless steels show similar trends. It may be surmised in the case of 25Cr-6Ni stainless steel that the higher thermal diffusivity, as compared to that of austenitic stainless steel, may be attributed to the presence of bcc phase. The bcc phase also contributes to the increase in the slope above 950 K. It is also seen that there is no hysteresis between the heating and cooling cycles indicating the negligible effect of the σ phase on the thermal diffusivity in the experimental temperature range.

The thermal conductivity of the alloys, investigated in the present work, could be calculated from experimental thermal diffusivities using the values of the specific heat and density according to the formula

$$k = \alpha \, C_{\mathrm{p}} \, \rho \tag{17.3}$$

where "k" is the thermal conductivity, "α" the thermal diffusivity, "C_{p}" the heat capacity, and "ρ" the density. The heat capacity values of the alloys investigated in this have been taken from the publication of Mills [8]. The thermal conductivities calculated from the present results using the literature values of C_{p} and ρ are
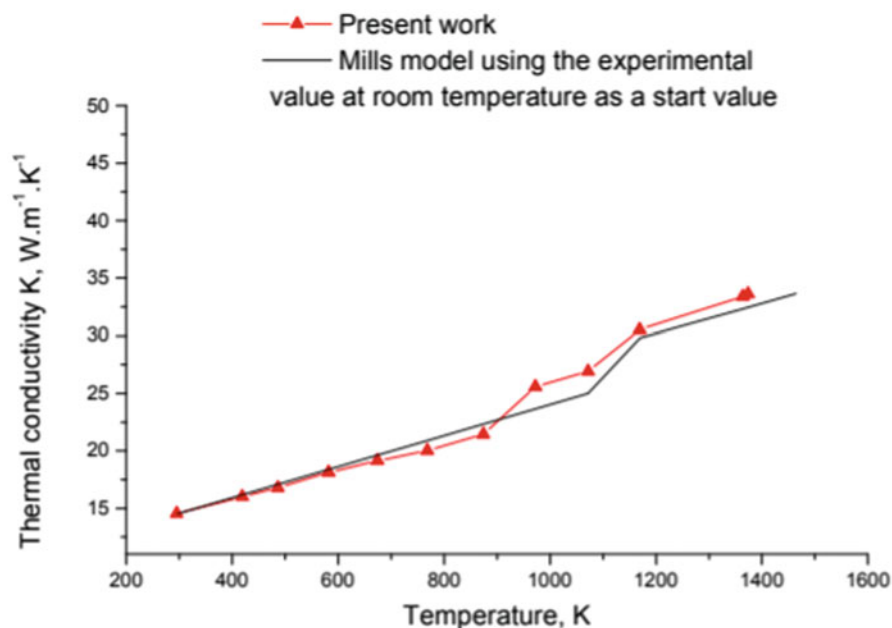
Fig. 17.18 Thermal conductivity of stainless steel sample from SANDVIK. (Reproduced under the terms of the CC BY-NC-ND 3.0 license [3]. Copyright 2011, DeGruyter)

presented in Fig. 17.17. In order to use Eq. 17.3, it is necessary to incorporate the values for the thermal conductivity at room temperature. In the present calculations, the results obtained at room temperature were used. The results obtained agree well with those estimated by a model proposed by Mills [8] as can be seen in Fig. 17.18.

3.2.2 CORUS Steel Sample

The thermal diffusivity values obtained in the present measurements in the case of plain carbon steel from CORUS steel are presented as a function of temperature in Fig. 17.19. It is seen in this figure that the thermal diffusivity decreases with increasing temperature up to 954 K, which may be attributed to a ferromagnetic transition. At 970 K corresponding to the Curie temperature, a minimum in the thermal diffusivity values is observed. Above 1026 K, an increase in the value is also seen corresponding to the fcc region. The trend is somewhat similar to that of Armco iron which has negligible amount of carbon.

As in the case of the SANDVIK steel sample, the thermal conductivity values were calculated and are compared with those estimated using the model by Mills [8]. The results are presented in Fig. 17.20.
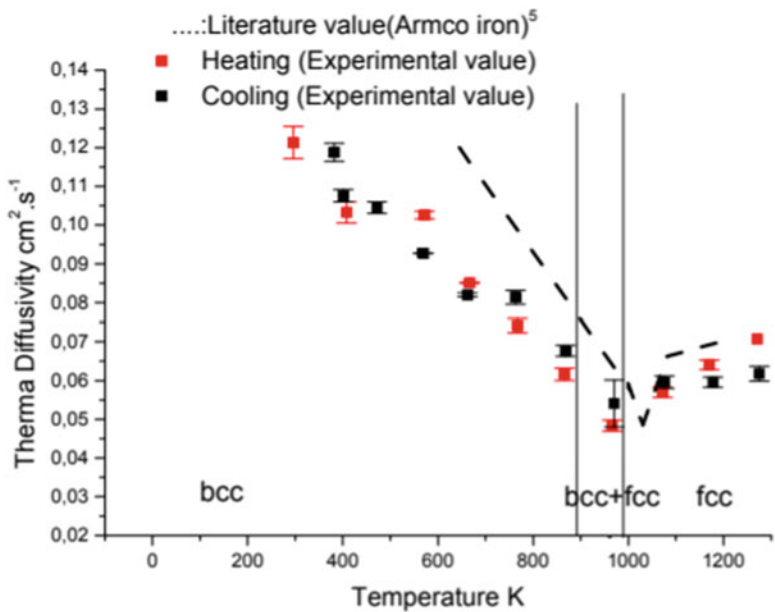
Fig. 17.19 The thermal diffusivity of CORUS steel sample. (Reproduced under the terms of the CC BY-NC-ND 3.0 license [3]. Copyright 2011, DeGruyter)
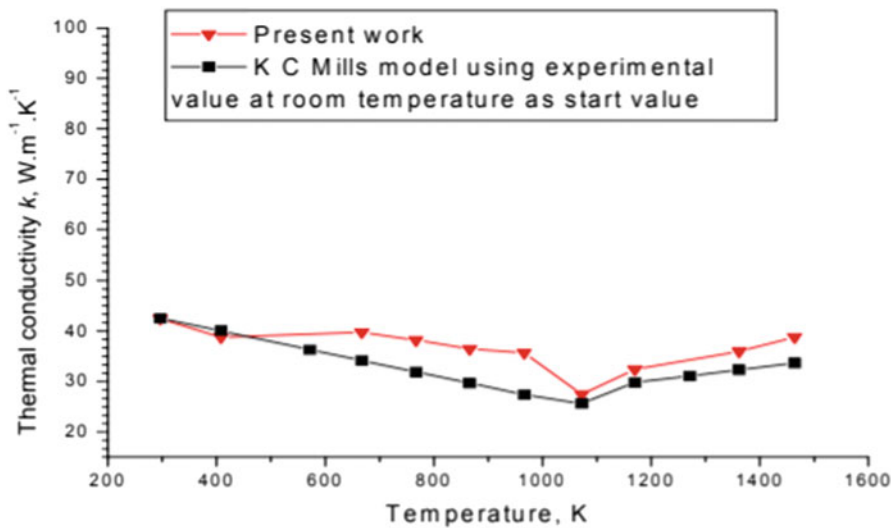
Fig. 17.20 The thermal conductivity of CORUS steel sample. (Reproduced under the terms of the CC BY-NC-ND 3.0 license [3]. Copyright 2011, DeGruyter)

3.3   Surface Tension

The surface tension of both the SANDVIK steel and the CORUS steel samples were measured by the oscillating drop method during parabolic flights. These measurements were complemented by electromagnetic levitation (EML) as well as sessile drop methods. Surface tension data of Fe-10Si and Fe-10ppmC-50ppmB were only obtained during parabolic flights.

3.3.1   SANDVIK Steel Sample

The results obtained in the case of SANDVIK steel by the oscillating drop method in 0 g using the TEMPUS device on board a parabolic flight have a negative temperature coefficient, as presented in Fig. 17.21. The linear fitting of the results can be represented as

$$\sigma(T) = 1.757 - 9.04 \cdot 10^{-4} \, (T - 1680 \, \text{K}) \, \text{N/m} \qquad (17.4)$$

In addition to the parabolic flight experiments, measurements of surface tension by the oscillating drop method in an electromagnetic levitation (EML) device as well as by the X-ray sessile drop method have been performed in ground-based laboratories. The results obtained by the 1 g-EML method are also shown in Fig. 17.21 and can be described by following equation:

Fig. 17.21 Surface tension values for SANDVIK steel obtained by EML method in microgravity measurements (0 g), on board a parabolic flight, and in ground-based measurements (1 g)
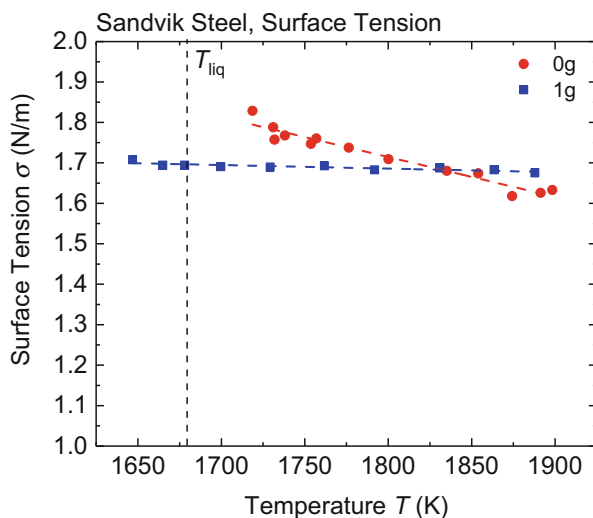
Table 17.5 Results of the
sessile drop measurements of
surface tension and density

Temperature (K)	Surface tension (N/m)	Density (kg/m³)
1750	1.656	$7.04 \cdot 10^3$
1783	1.586	$6.99 \cdot 10^3$

Fig. 17.22 Surface tension
values for CORUS steel
obtained by EML method in
microgravity measurements
(0 g), on board a parabolic
flight, and in ground-based
measurements (1 g)
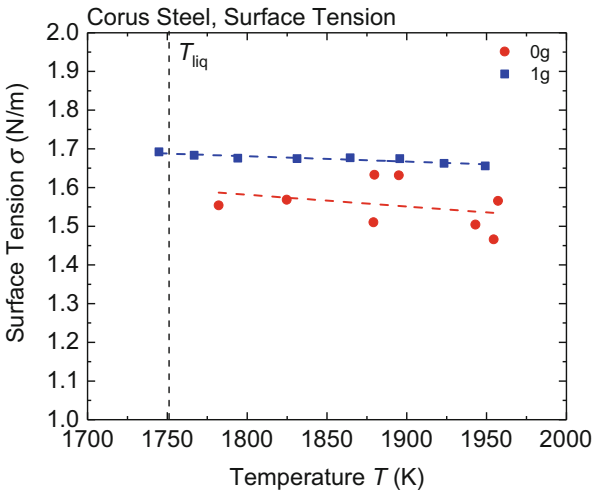
$$\sigma(T) = 1.697 - 0.8890 \cdot 10^{-4} \, (T - 1680 \, K) \, N/m \qquad (17.5)$$

Results of the corroborative measurements by the X-ray sessile drop method are
presented in Table 17.5 together with the density values.

3.3.2 CORUS Steel Sample

The parabolic flights have been employed for the surface tension measurement of
Corus steel sample as well. The results indicating negative temperature coefficient
are shown in Fig. 17.22.

$$\sigma(T) = 1.61 - 4.47 \cdot 10^{-4} \, (T - 1752) \, N/m \qquad (17.6)$$

In addition to the parabolic flight experiments, the surface tension was measured
by the 1 g-EML method as well. The results from the 1 g-EML measurement are also
shown in Fig. 17.22, and it was found that the surface tension can be described by
following equation:

$$\sigma(T) = 1.687 - 1.367 \cdot 10^{-4} \, (T - 1752) \, N/m \qquad (17.7)$$

3.3.3 Fe-10wt%Si Steel Sample

The surface tension was measured in five parabolas using the inductive and optical method to detect the surface oscillations. Using the combined data of all parabolas, the temperature dependence of the surface tension can be described as

$$\sigma(T) = (1.704 \pm 0.004) - (3.59 \pm 0.32) \cdot 10^{-4} \, (T - 1640 \, \text{K})$$

and is hence relatively similar to other steels, such as the SANDVIK steel or the CORUS low-alloyed steel.

3.3.4 Fe-10ppmC-50ppmB Steel Alloy

Surface-active species such as Boron have the potential to greatly influence the surface tension of the liquid boron steel. Figure 17.23 shows the surface tension data of Fe-10ppmC-50ppmB measured in the parabolic flight in 2020. The temperature-dependent surface tension is found to be

$$\sigma(T) = 1.65 - 4.32 \cdot 10^{-5} \, (T - 1818 \, \text{K})$$

It can be recognized that the obtained surface tension of about 1.64 N/m at the liquidus temperature of 1818 K is much smaller than the literature values obtained for pure liquid iron at its melting temperature, which is given in literature as 2.03 N/m [9] and 1.93 N/m [10]. Model calculations to describe the influence of boron on the surface tension of iron are ongoing. More precise results are also expected in the future, when the alloy is processed in the ISS-EML on board the ISS in the coming years.

Fig. 17.23 Surface tension of Fe-10ppmC-50ppmB obtained in one parabola
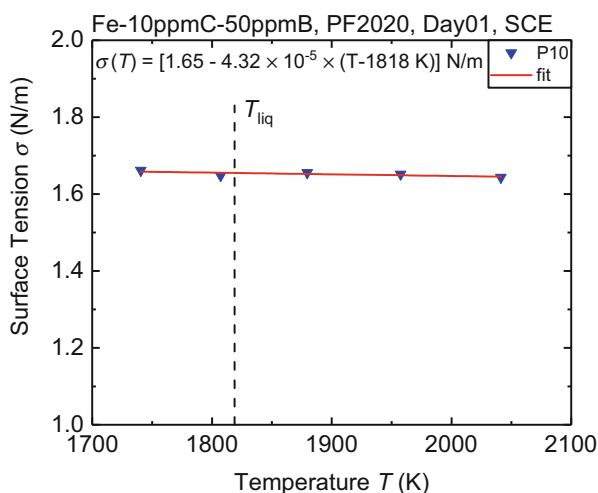
Fig. 17.24 Surface tension of Fe-21Cr-19Ni obtained in three cycles on board the ISS
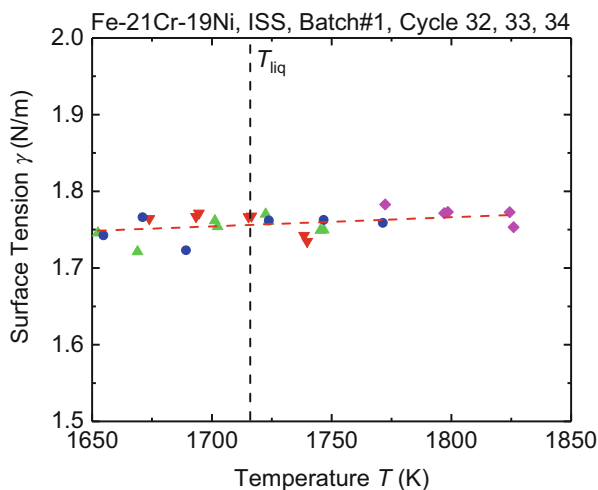
3.3.5 Fe-21Cr-19Ni

The surface tension found for the Fe-21Cr-19Ni sample processed on board the ISS in Batch#1 is shown in Fig. 17.24. As can be clearly seen, the temperature dependence has positive sign. This effect might be attributed to some surface-active species, such as oxygen, unintentionally adsorbed during the previous processing cycles.

This demonstrates clearly the importance for a very low oxygen partial pressure while surface properties of liquid Fe-based alloys are investigated. Future experiments will hence be performed while using an oxygen sensor and control system, as presented in Chap. 3.

3.4 Viscosity

In view of the turbulence of the liquid during EML measurements and consequent experimental errors, the viscosity measurements could only be carried out under microgravity conditions. In this case, spherical-shaped oscillating samples are formed during the experiment due to reduced force on the sample. This enables the identification of the single oscillating frequency with reasonable precision. In agreement with magnetohydrodynamics simulations, the observed damping of the oscillations is purely given by the dynamic viscosity [11].

Figure 17.25 presents the viscosity data of the Sandvik Cr-Ni steel obtained under microgravity conditions as a function of temperature. The liquidus temperature was obtained as $T_{liq} = 1745$ K. The viscosity of the CORUS steel sample obtained by the oscillating drop method under microgravity conditions is also presented in Fig. 17.25. It is seen that the viscosity of the Sandvik steel is relatively high, compared to that of pure iron [12] which can be attributed to the presence of Cr and Ni.

Fig. 17.25 Viscosity of the Sandvik and Corus steel samples obtained in microgravity measurements, together with literature values of pure liquid iron [12]
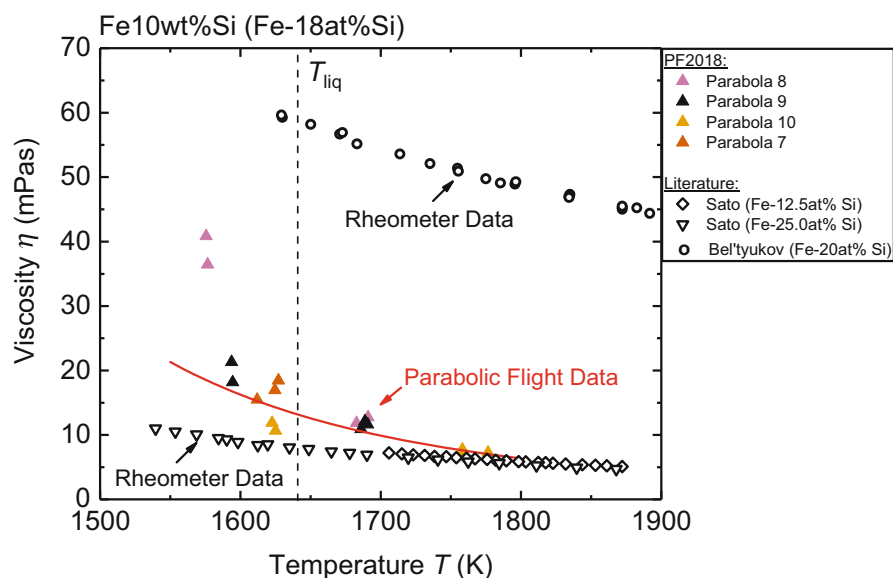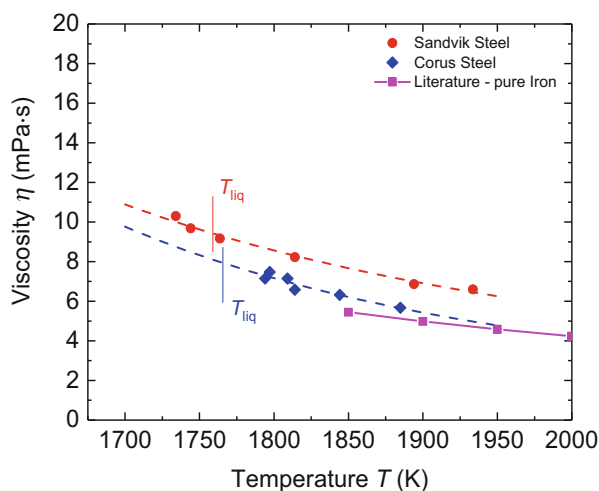
Fig. 17.26 Viscosity of Fe-10wt%Si, measured under microgravity in the parabolic flight campaign 2018, together with literature data of similar compositions

3.4.1 Fe-10wt%Si Steel Sample

The viscosity measured for Fe-10wt%Si (Fe-18at%Si) in the electromagnetic levitation facility TEMPUS, during a parabolic flight, is shown in Fig. 17.26 together with literature data from Bel'tyukov et al. [13] and Sato [14] for similar compositions.

The viscosity values obtained by Bel'tyukov et al. [13] using a viscometer, for a similar composition, are substantially higher than the values obtained by Sato [14] and in the TEMPUS EML. In the stable liquid phase, the viscosity measured in the EML is relatively close to the literature values obtained by Sato [14] in an oscillating viscometer while they significantly increase in the undercooled liquid range. This could be explained by the formation of small crystallites, such as nitrides. However, further studies of the microstructure and phase composition on the returned flight sample, like those already performed on low-alloyed steels [15], are still ongoing.

4   Summary

The present chapter summarizes the results on the thermophysical properties of several steel samples, one high-alloyed steel from SANDVIK, Sweden, the other from CORUS, Netherlands, as well as a Fe-10Si, a prototype boron steel and a generic stainless steel. The various physical properties measured are correlated with the phase changes in the system, as computed by Thermo-Calc. The measurements were carried out in ground-based European laboratories complemented by measurements under microgravity conditions on board parabolic flights and on board the ISS. The mutual compatibility of the data shows that it is very advantageous to measure the properties both under microgravity and terrestrial conditions and compare them so that the reliability of the data can be ascertained and uncertainties due to gravitational forces, as, for example, turbulence caused on the sample in EML measurements under 1 g conditions, are avoided. The reliable data obtained in this work as part of the ThermoLab project is considered to be extremely useful to European steel industry in their models for casting.

References

1. World Steel Association, *World Steel in Figures 2018* (World Steel Assoc, 2018) https://www.worldsteel.org/en/dam/jcr:f9359dff-9546-4d6b-bed0-996201185b12/World+Steel+in+Figures+2018.pdf

2. Swedish Steel Producers Association, The Steel Eco-Cycle – Environmental Research Programme – Closing the loop in the manufacture and use of steel in society (2013)

3. T. Matsushita, S. Seetharaman, Thermolab project: Results on thermophysical properties data of iron alloys. High. Temp. Mater. Process **27**, 413–422 (2008)

4. C. Papandrea, L. Battezzati, A study of the α ↔ γ transformation in pure iron: Rate variations revealed by means of thermal analysis. Philos. Mag. **87**, 1601–1618 (2007). https://doi.org/10.1080/14786430601080260
5. G. Lohöfer, P. Neuhaus, I. Egry, TEMPUS – a facility for measuring thermophysical properties of undercooled liquid metals. High Temp – High Press **23**, 333–342 (1991)
6. M. Mohr, H.J. Fecht, Investigating thermophysical properties under microgravity: A review. Adv. Eng. Mater. **23** (2021). https://doi.org/10.1002/adem.202001223
7. M. Rösner-Kuhn, D.M. Matson, K. Drewes, et al., Enthalpies and heat capacities of liquid Fe-Cr-Ni alloys with the focus on pure liquid chromium. Thermochim. Acta **314**, 123–129 (1998). https://doi.org/10.1016/S0040-6031(97)00460-7
8. K.C. Mills, *Recommended Values of Thermophysical Properties for Selected Commercial Alloys* (Woodhead Publishing Limited, 2002)
9. S. Ozawa, S. Takahashi, S. Suzuki, et al., Relationship of surface tension, oxygen partial pressure, and temperature for molten iron. Jpn. J. Appl. Phys. **50** (2011). https://doi.org/10.1143/JJAP.50.11RD05
10. K. Morohoshi, M. Uchikoshi, M. Isshiki, H. Fukuyama, Surface tension of liquid iron as functions of oxygen activity and temperature. ISIJ Int. **51**, 1580–1586 (2011). https://doi.org/10.2355/isijinternational.51.1580
11. X. Xiao, R.W. Hyers, D.M. Matson, Surrogate model for convective flow inside electromagnetically levitated molten droplet using magnetohydrodynamic simulation and feature analysis. Int. J. Heat Mass Transf. **136**, 531–542 (2019). https://doi.org/10.1016/j.ijheatmasstransfer.2019.03.028
12. M.J. Assael, K. Kakosimos, R.M. Banish, et al., Reference data for the density and viscosity of liquid aluminum and liquid iron. J. Phys. Chem. Ref. Data **35**, 285 (2006). https://doi.org/10.1063/1.2149380
13. A.L. Bel'tyukov, V.I. Lad'yanov, A.I. Shishmarin, Viscosity of Fe-Si melts with silicon content up to 45 at %. High Temp. **52**, 185–191 (2014). https://doi.org/10.1134/S0018151X14010040
14. Y. Sato, Representation of the viscosity of molten alloy as a function of the composition and temperature. Jpn. J. Appl. Phys. **50**, 11RD01 (2011). https://doi.org/10.1143/JJAP.50.11RD01
15. B. Bandi, B. Santillana, W. Tiekink, et al., 2D automated SEM and 3D X-ray computed tomography study on inclusion analysis of steels. Ironmak. Steelmak. **47**, 47–50 (2020). https://doi.org/10.1080/03019233.2019.1652437

Chapter 18
Thermophysical Properties of Semiconductors

Yuansu Luo, Bernd Damaschke, Georg Lohöfer, and Konrad Samwer

1 Introduction

The EML facility described in detail in Chap. 3 is actually designed for metallic samples. The processing of semiconductors is therefore a big challenge, because this kind of materials possesses a low electrical conductivity. The laser preheating, which was applied in earlier parabola flight experiments based on the TEMPUS-EML facility [1], is not available in ISS-EML. To overcome this difficulty, we introduced highly doped semiconductors Ge, $Si_{25}Ge_{75}$, and $Si_{50}Ge_{50}$ and processed them recently on board the ISS.

The work has been performed in the framework of the ESA project "SEMITHERM" ("Investigations of thermophysical properties of liquid semiconductors in the melt and the undercooled state under microgravity conditions," ESA-AO-2000-068). The goals of the project include the precision measurements of the density, thermal expansion, surface tension, viscosity, and electrical resistivity of the liquid Ge and alloys $Si_{1-x}Ge_x$ ($x = 0.75, 0.5,$ and 0.25). Due to the strong reactivity of the high-temperature melts, the experiments need to be performed without contact under low-gravity conditions. The Electromagnetic Levitator (ISS-EML) on board of the International Space Station (ISS) is the instrument of choice.

In this chapter, we give an overview over our experiments with semiconductors in ISS-EML. Data from the sample $Si_{50}Ge_{50}$ have already been published in NPJ Microgravity [2] and were taken here for comparison.

Y. Luo · B. Damaschke (✉) · K. Samwer
I. Physikalisches Institut, Georg-August-Universität Göttingen, Göttingen, Germany
e-mail: bdamasc1@gwdg.de

G. Lohöfer
Institut für Materialphysik im Weltraum, Deutsches Zentrum für Luft- und Raumfahrt (DLR), Köln, Germany

2   Sample Preparation, Characterization, and Ground Tests

The samples used are spherical with a diameter of 8 mm, which is the maximal allowed size for samples in the ISS-EML, due to the design of coils. The usage of large spheres is advantageous not only for a sufficient electromagnetic levitation force for relatively low electric conducting samples but also for precision measurements of the droplet size for the evaluation of thermal expansion data. Table 18.1 summarizes the information about the samples used for ISS experiments, including dopant concentration, electrical conductivity (σ), solidus/liquidus temperatures T_s/T_l, and density (ρ).

Here, Ge doped with Sb (donator, n-type) is commercially available, while the $Si_{1-x}Ge_x$ crystals with dopant B (acceptor, p-type) were grown by means of Czochralski technique in the group of N. Abrosimov at the Institute for Crystal Growth in Berlin [3]. A composition gradient along the crystal growth direction is unavoidable due to component segregations. The segregation coefficient for Ge was found to be 0.2 at.%mm^{-1} for $Si_{25}Ge_{75}$ and $Si_{75}Ge_{25}$, and 0.5 at.%mm^{-1} for $Si_{50}Ge_{50}$, corresponding to an uniaxial chemical inhomogeneity of ± 0.8 at.% and ± 2.0 at.%, respectively, for 8 mm spherical samples. The small chemical inhomogeneity does not influence a multicycle processing in ISS-EML.

The dopant concentration of about 10^{19} atoms cm^{-3} for Ge and about 10^{20} atoms cm^{-3} for the alloys corresponds to an electrical conductivity σ in the range of 10^3 Ω^{-1}cm^{-1} at 300 K. Due to the semiconducting behavior, the conductivity of the solid samples rises with T and jumps up to about 10^4 Ω^{-1}cm^{-1} [2] upon melting according to the semiconductor-metal phase transition. Taking frequencies of the heating field (400 kHz) and the positioning field (150 kHz), the skin depths $\delta = \sqrt{2/\sigma\omega\mu}$ (with the angular frequency ω and the magnetic permeability μ) of the eddy currents induced in spherical samples (8 mm) can be estimated to be about 2–3 mm for the solid and 0.8–1.2 mm for the liquid. The large δ (solid) implies a fast heating, while the small δ (liquid) benefits a stable positioning.

Relevant ground tests were made in advance by MUSC (Microgravity User Support Center) at DLR, Cologne, Germany, to obtain relevant parameters, such as spectral emissivity ε for the pyrometer, sample coil coupling efficiency as a measure for the heating capabilities of the doped semiconductors in ISS-EML, as well as the evaporation rate of the melts regarding the limits of dust generation. The spectral emissivity measured for the liquid state was 0.19 for Ge, 0.21 for $Si_{25}Ge_{75}$, and 0.22 for $Si_{50}Ge_{50}$, being about twice smaller than that measured for the solid state (not shown in Table 18.1). The coupling efficiency in the solid state was found to be strong enough for fast heating. In the liquid state, the samples are metallic and the coupling becomes enhanced by a factor of about 5.

In addition, the elements Si and Ge show—similar to water—a density anomaly near T_l [4]. The phenomenon is already reflected in the density values of the samples listed in Table 18.1. A liquid-liquid phase transformation due to a change of the coordination number of the nearest neighbor atoms in deeply undercooled Si melts has been predicted by Angell et al. [5].

Table 18.1 Summary of sample data (including dopant concentration, solidus/liquidus temperatures T_s/T_l, electrical conductivity σ, spectral emissivity ε, density ρ, values of overheating and undercooling, as well as cooling rates (in 350 mbar Ar) of the melts)

Samples (dopant) (atoms/cm³)	T_s/T_l (K)	Mass of samples (g)	Axial/radial camera (Hz)	Density ρ (gcm⁻³) at RT/T_l	$\sigma(\Omega^{-1}\text{cm}^{-1})$ at RT	Mean overheat (K)	ε (liquid)	Mean (max.) undercooling (K)	Cooling rate (K s⁻¹)
Ge(Sb) $n = 1.0 \times 10^{19}$	1211	1.447	50/200	5.34/5.57	1.0×10^3	430	0.19	65 (81)	4.9
Si₂₅Ge₇₅(B) $p = 1.5 \times 10^{20}$	1283/1423	1.180	50/400	4.73/5.07	1.3×10^3	340	0.21	20 (25)	13.3
Si₅₀Ge₅₀(B) $p = 1.9 \times 10^{20}$	1388/1548	1.066	150/400	3.95/4.23	1.7×10^3	370	0.22	165 (245)	12.3
[a]**Si₇₅Ge₂₅**(B) $p = 1.65 \times 10^{20}$	1533/1623	0.850	150/400	3.15/–	1.4×10^3	390	0.18	143 (245)	27.5

[a]Recently processed on board the ISS in batch #3

3   ISS Experiments in Detail

Before the transport to ISS, the samples were cleaned with acetone and ethanol in ultrasound bath and integrated in a special transport container, which was pumped down to 10^{-7} mbar and filled then with 600 mbar Ar. The end inspection was carried out in air, and thus, the sample surface is unavoidably covered with a natural thin passivation oxide layer, which prevented the sample from further oxidation.

For each semiconductor sample, 11 melting cycles were planned. A cycle consists of heating to a maximal temperature T_{max} and cooling down below T_s, as shown in Fig. 18.1a. At T_{max}, the heater control voltage U_H was set to 0 and the positioner control voltage U_P decreased accordingly from 9 V to 6 V. During the cooling phase, most measurements were executed in argon gas atmosphere (350 mbar). Here, the Ar gas is necessary not only for effective cooling of the sample but also for a reduction of the evaporation rate (mass loss) of overheated melts. A mass loss of about
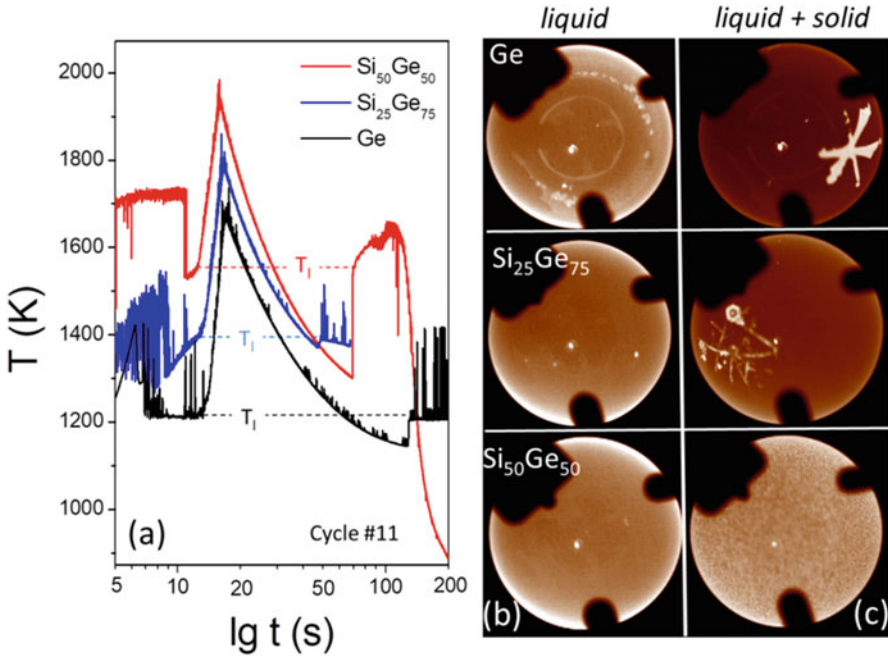
Fig. 18.1 (**a**) Time-temperature profiles (from cycle #11) of Ge (black), $Si_{25}Ge_{75}$ (blue), and $Si_{50}Ge_{50}$ (red) with dashed lines indicating their melting point T_l. (**b**) Axial images recorded at high T (liquid) showing a few residual oxide particles on the surface of the Ge and $Si_{25}Ge_{75}$ droplets. (**c**) Relevant images at beginning of the solidification (liquid + solid) exhibiting strongly heterogeneous nucleation for Ge and $Si_{25}Ge_{75}$ and more homogeneous nucleation for $Si_{50}Ge_{50}$ corresponding to small (black and blue) and large (red) undercooling degrees as shown in (**a**). (Note, the bright spot near the image center comes from pyrometer). (Data for $Si_{50}Ge_{50}$ are taken from Ref. [2])

0.1–0.2 mg per cycle was estimated from the evaporation experiments performed by MUSC.

The surface tension γ and viscosity η of the melt can be determined by the oscillating drop technique (for details, especially the situation with turbulent flow, see "viscosity of the droplet"). For this purpose, several cycles were performed with short pulses of the heating field (triangular pulses 6 or 8 V, 0.05 s) at different temperatures T. The pulse squeezes the drop into an elongated shape along the heating field and results in damped surface oscillations until the sample is back to its equilibrium spherical shape. The exponential decay constant λ of the oscillation amplitude gives the viscosity η of the melt, $\eta = \frac{3M}{20\pi\, r_0}\,\lambda$ with the mass M and the radius r_0 of the sample, while the resonance frequency ν can be used for the calculation of the surface tension $\gamma = \frac{3\pi M}{8}\,\nu^2$.

The droplet oscillations were monitored by the axial and radial video cameras. Different camera speeds (cf. Table 18.1) were set depending upon the melting point T_1 of the samples. For Ge (low T_1), for example, the emission of the droplet near T_1 may be dark, and therefore, the speed of axial and radial cameras was set down to 50 Hz and 200 Hz, respectively. The images were analyzed with respect to the above-described oscillating drop method using a dedicated software "TeVi" (SEA Datentechnik GmbH), which detects the droplet edges from the image contrast. The edge curve is fitted with a polynomial of degree 9 [6] and yields areas, radii, and semiaxes of the droplet. From these data also the thermal expansion coefficients β of the sample could be determined.

4   Melting, Cooling, Undercooling, and Solidification Behavior

Doped semiconductors Ge, $Si_{25}Ge_{75}$, and $Si_{50}Ge_{50}$ each with 11 melting and cooling cycles (always the same sample) were successfully processed on board the ISS. Achieved overheats in liquid state are 430 K for Ge, 340 K for $Si_{25}Ge_{75}$, and 370 K for $Si_{50}Ge_{50}$ in average. As an example, Fig. 18.1a reveals their time-temperature plots $T(t)$ of cycle #11 measured by the radiation pyrometer. The sample temperatures T given here were calibrated using Wien's law: $1/T = 1/T_p + (1/T_1 - 1/T_{lp})$ with T_p the pyrometer signal and T_{lp} the pyrometer signal at the liquidus temperature T_1.

As can be seen, in the beginning of the cycles, the temperature reading of the solid samples rises quickly and reaches a plateau corresponding to the solidus temperature T_s, where the sample starts to melt. The $T(t)$-profiles approaching T_s show no significant disturbances, indicating that in spite of a low electrical conductivity, the highly doped semiconductors could be well positioned in the ISS-EML facility. Because of the lower emissivity of the liquid (due to the semiconductor-metal transition, the emissivity changes drastically in the melting process), the temperature reading $T(t)$ drops down during melting and subsequently reaches a minimum, which corresponds to the actual liquidus temperature T_1. The large fluctuation (ΔT

≈ 200 K) of $T(t)$-profiles in the two-phase region arises from the different spectral emissivity ε of the solid and the liquid read by the pyrometer depending on the actual spot, while the small fluctuation ($\Delta T \approx 50$ K) may be due to changes in view factor caused by movement of the sample.

Upon melting, the samples become metallic so that the force applied by the electromagnetic levitation field on droplets grows and improves their positioning stability. As a consequence, $T(t)$-profiles in the liquid state appear very smooth. The low-T_1 sample Ge exhibits a much lower cooling rate and thus a longer cooling phase in comparison with $Si_{25}Ge_{75}$ and $Si_{25}Ge_{75}$ (cf. Fig. 18.1a and Table 18.1). At the end of the liquid phase, where T is usually below T_1 (undercooling), the $T(t)$ profiles rise abruptly up to T_1 (dashed lines in Fig. 18.1a) due to the exothermic nature of the crystallization (not in glassy case).

More interestingly, the red curve in Fig. 18.1a measured for $Si_{50}Ge_{50}$ reveals a large undercooling of about 245 K, associated with the disappearance of surface oxide impurities at high T as discussed below. As one of the advantages of the contactless processing in ISS-EML, the observation of a large undercooling of melts is actually expected. A small undercooling degree was observed however for Ge and $Si_{25}Ge_{75}$, which is attributed to residual oxide phases on the droplet surface.

Figures 18.1b, 18.2b–e, and 18.3b–d show images of Ge, $Si_{25}Ge_{75}$, and $Si_{50}Ge_{50}$ droplets recorded by axial and radial cameras at different T in the liquid state. A few residual oxide particles on the surface of the Ge and $Si_{25}Ge_{75}$ droplets are visible even at T_{max} and become slightly more due to precipitation with decreasing T (cf. Fig. 18.2b–e) in contrast to the $Si_{50}Ge_{50}$ droplet. The residual oxide impurities on the droplet surface serve as additional nuclei for solidification. Figure 18.1c gives relevant images captured at the beginning of solidification (liquid + solid), being dark and bright depending on T_1 of the samples. One can see a strongly heterogeneous nucleation for the droplets Ge and $Si_{25}Ge_{75}$ while the surface of $Si_{50}Ge_{50}$ remains quite smooth. The phenomenon mirrors the quantity of the observed undercooling degrees mentioned above.

For the sample $Si_{25}Ge_{75}$, the strongly heterogeneous nucleation was followed by a dendritic growth (Fig.18.1c, middle) and component segregations. The initially crystalized phase was found to be Si rich (~95 at.%). For pure Ge, the nuclei grew, forming single crystals (diamond lattice) with sixfold symmetry (Fig. 18.1c, upper), i.e., the most dense atomic plans (111). Because of a lower barrier height in the free energy, the heterogeneous nucleation is in general more common than homogeneous nucleation.

For the sample $Si_{50}Ge_{50}$, the rather "homogeneous" nucleation occurs actually for the first time in cycle #6, where the undercooling degree jumps up with no observable dendrite structure. The cycle #1–#5 delivered an undercooling of about 45 ± 10 K only, followed with a heterogeneous nucleation similar to that observed for $Si_{25}Ge_{75}$. The undercooling rises then gradually from 155 K for cycle #6 to 245 K for cycle #11. The results can be attributed to a gradual volatilization of surficial oxide impurities at T_{max} (~1973 K), which is close to the melting point (1986 K) of SiO_2 [7]. In addition, silicon monoxide (SiO) may gradually form at
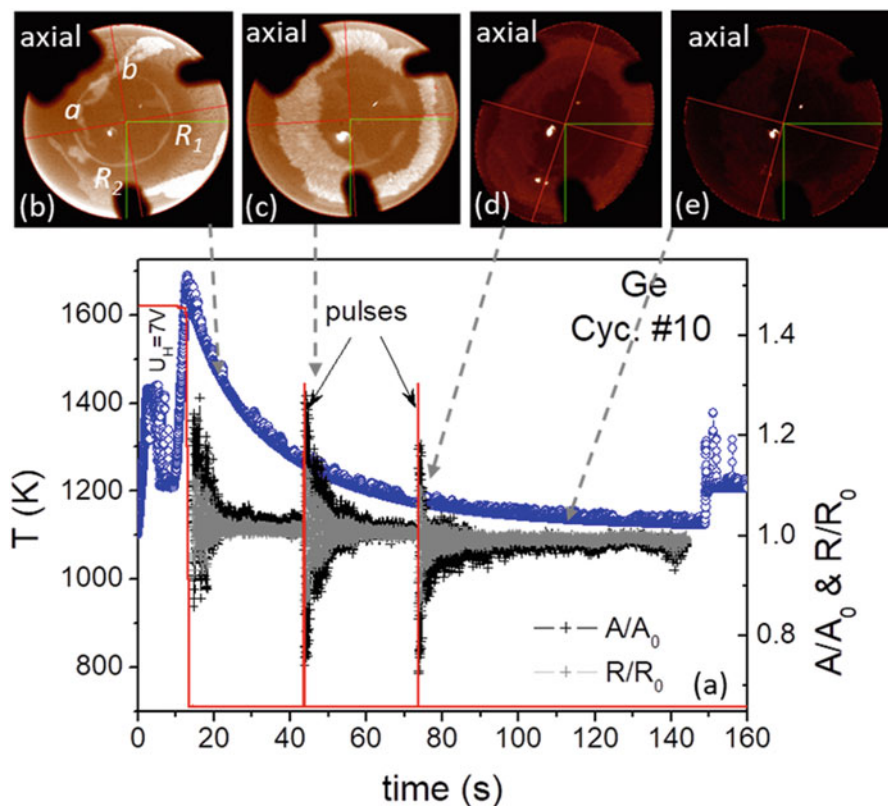
Fig. 18.2 (**a**) Time profiles of cycle #10 measured for Ge with temperature (blue circles), voltage U_H (red line) controlling the electromagnetic heating field with two short pulses used for exciting droplet oscillations, as well as normalized areas A/A_0 (black) and radii R/R_0 (gray). Relevant axial images of the droplet captured between heating-off and the 1st pulse (**b**), at the 1st and 2nd pulses (**c, d**), and far away from the 2nd pulse (**d**), respectively, including semiaxes a, b (red), horizontal and vertical radii R_1, R_2 (green), as well as areas A surrounded by edge curves

high T via a decomposition reaction, $SiO_2+Si \rightleftharpoons 2\ SiO$. It is volatile and can evaporate away by sublimation [8].

The maximum temperature T_{max} reached for $Si_{25}Ge_{75}$ (Fig. 18.1a) is about 1873 K and is too low to fully resolve the surficial oxide phase. The 11 cycles show a small and almost constant undercooling (20 ± 5 K).
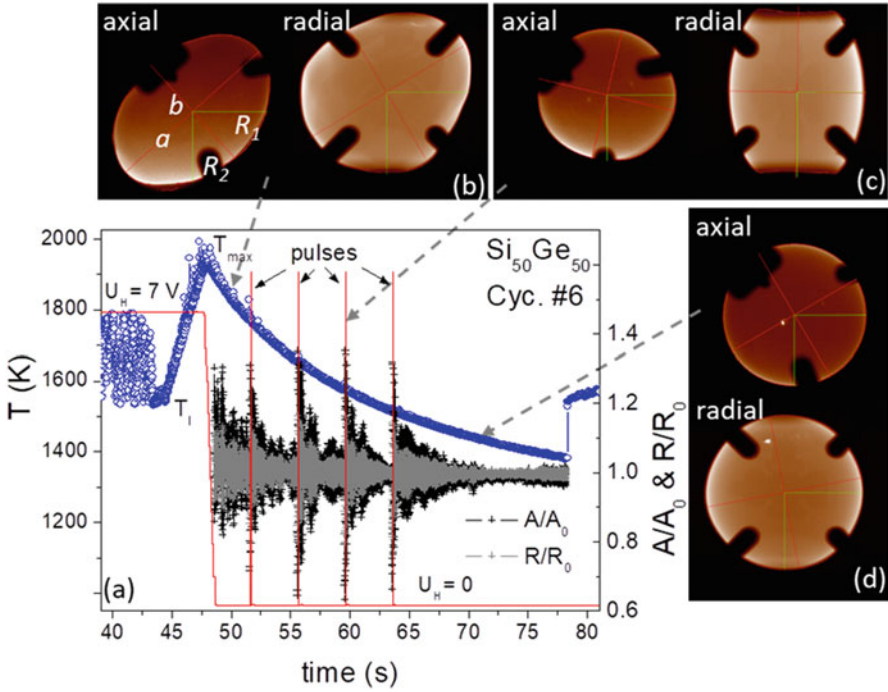
Fig. 18.3 (**a**) Time profiles of cycle #6 measured for $Si_{50}Ge_{50}$ with temperature (blue circles), voltage U_H (red line) controlling the electromagnetic heating field with four short pulses used for exciting droplet oscillations, as well as normalized areas A/A_0 (black) and radii R/R_0 (gray). Relevant axial and radial images of the droplet captured between heating-off and the 1st pulse (**b**), at the 3rd pulse (**c**), and far away from the 4th pulse (**d**), respectively, involving elliptical semiaxes a, b (red), horizontal and vertical radii R_1, R_2 (green), as well as areas A surrounded by edge curves. (Reproduced under the terms of the CC BY 4.0 license [2]. Copyright 2020, Springer Nature)

5 Oscillating Drop Method and Evaluations

Figures 18.2b–e and 18.3b–d show typical axial and radial images measured for Ge and $Si_{50}Ge_{50}$ at different points indicated in relevant $T(t)$-plots given in Figs. 18.2a and 18.3a, respectively. The Ge droplet became very dark for T below T_l. The shadowlike artifacts stem from parts of the sample holder, and their areas have been excluded in the edge fitting procedure. The digital procedure yields data of areas A and lengths of horizontal and vertical radii R_1 and R_2 as well as elliptical semiaxes, a and b, as a function of time and temperatures for evaluation of thermophysical properties via the oscillating drop method.

To minimize the scattering of data, we introduced an average radius R calculated from R_1, R_2, a, b, and r_{eff}, where r_{eff} is an effective radius extracted from the area $A = \pi r_{eff}^2$. The normalized areas A/A_0 and radii R/R_0 with A_0 and R_0 denoted as their mean values are plotted in Figs. 18.2a and 18.3a, showing damped oscillations

caused by switching off the electromagnetic heating field, which also squeezes the droplet, and short voltage pulses.

As illustrated in Fig. 18.3c, the short pulse (8 V, 0.05 s) squeezes the drop into a more elongated shape along the perpendicular axis. The cross section viewed from the top in axial direction correspondingly becomes smaller and in radial direction looked incomplete due to a hiding effect of the electromagnetic coil (its winding distance is 8 mm). The uniaxially deformed droplet relaxes to its equilibrium spherical shape, giving rise to surface oscillations. A similar behavior appears at T_{max} by turning off the heating. In this case, the uniaxial deformation is however much stronger than that induced by short pulses, giving rise to rotation of the droplet around an arbitrary axis with a period of about 1 Hz (see Fig. 18.3a). The overlap between rotation and oscillation makes the droplet temporarily aspherical (Figs. 18.2c, d, and 18.3b, c) and leads to extra scattering of the experimental data. Only for long times after the heating-off or pulses, the droplet becomes quiet and well spherical, as shown in Figs. 18.2e and 18.3d. For this case, all length data a, b, R_1, and R_2 are nearly identical and the scattering becomes smaller. The pulse height used for Ge was set down to 6 V to reduce the uniaxial deformation.

6   Viscosity of the Droplet

Typical oscillations of levitated Ge and Si-Ge droplets excited at different T by switching the heater off at T_{max} and by heating pulses are presented as a function of the time t in Figs. 18.2a, 18.3a, and 18.4a, c, e. The amplitude decays exponentially with t and approaches then the mean value A_0 (or R_0). The behavior can be fitted by $f = f_0 \pm \Delta f \cdot e^{-\lambda t}$; here, f/f_0 can be A/A_0 or R/R_0, and Δf is their maximal amplitude. The fit provides the envelope of the oscillation as plotted in Fig. 18.4a, c, e (red dashed lines) and yields a decay factor λ, which in the case of laminar flow can be referred as the magnitude of the viscosity, i.e., $\eta = \kappa \lambda$ [9]. Here, $\kappa = \frac{3M}{20\pi\, r_0}$ with the radius $r_0 = 4$ mm and the mass M of the droplets. In the case of the semiconductor samples discussed here, the fluid flow is turbulent and the model is not strictly applicable. Instead, we have evaluated the decay factor λ; for details, see the discussion below.

The red dashed lines in Fig. 18.4a demonstrate the envelopes fitted with exponential function of $e^{-\lambda t}$ from the oscillation data obtained from cycle #5 (axial) for Ge. The given oscillations were excited by four short pulses at 1658, 1553, 1473, and 1418 K with decay factors λ found to be in the order of 0.30 s^{-1}. Because of the small interval (4 s) between two pulses, the oscillations induced by the 1st, 2nd, and 3rd pulses decay not completely before the next pulse started (see also Fig. 18.3a). This makes the fitting more difficult; additionally, a rotation of the droplet creates a parasitic oscillation of about 1 Hz (near the pulses) and disturbs the direct observation of the decay behavior. Therefore, the fitting procedure is delicate and not all pulses could be fitted well. Fig. 18.4c, e show the fits of the oscillation data obtained
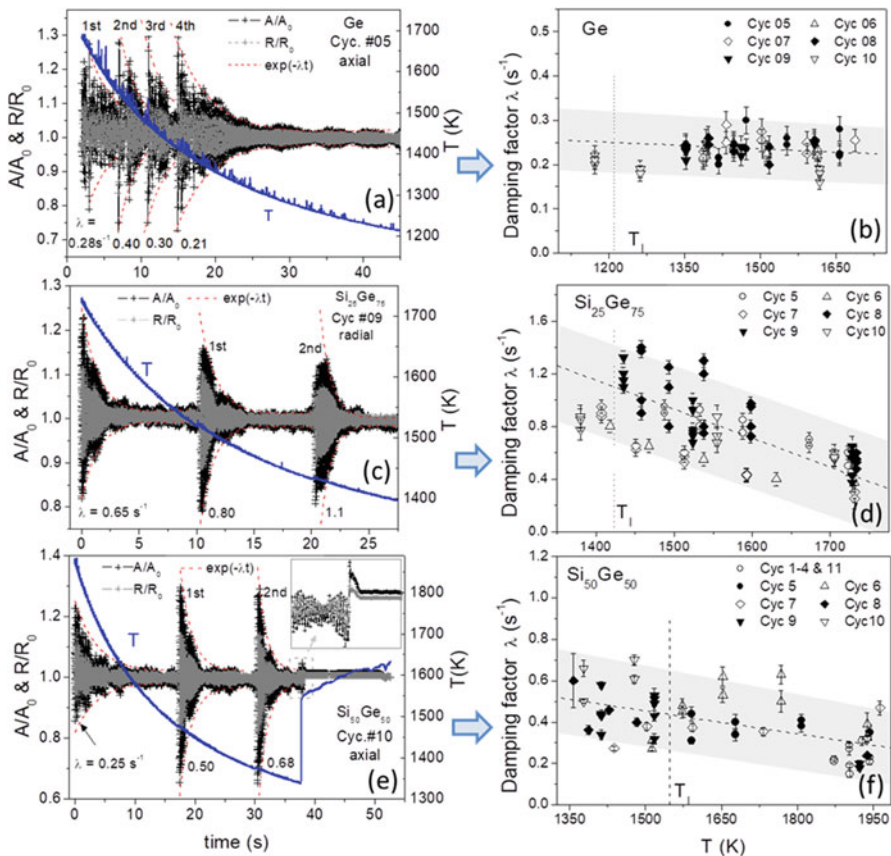
Fig. 18.4 (**a**), (**c**), and (**e**): $T(t)$ profiles (blue) measured for Ge (cycle #5, axial), $Si_{25}Ge_{75}$ (cycle #9, radial), and $Si_{50}Ge_{50}$ (cycle #10, axial) with normalized areas A/A_0 (black) and radii R/R_0 (gray) revealing oscillations excited by heating-off and short pulses (marked here by 1st, 2nd, and 3rd...), respectively, and decayed with t in an exponential function $e^{-\lambda t}$ (red dashed lines), as well as abrupt changes (inset in e) occurring upon solidification regarding the density anomaly mentioned [6]. (**b**), (**d**), and (**f**): Damping factors λ of the oscillations measured for relevant samples from pulse cycles. Note, here different λ-scales indicate different T dependence. The gray background indicates the scattering of ± 0.1–0.3 s^{-1}. The week T dependence is probably due to the influence of the turbulent flow. (Data for $Si_{50}Ge_{50}$ are taken from Ref. [2])

from the alloy droplets $Si_{25}Ge_{75}$ (radial, cycle #9) and $Si_{50}Ge_{50}$ (axial, cycle #10). The oscillations shown here were caused by heating-off and two short pulses (interval ~10 s). The impact from the rotation is visible as well. As indicated in Fig. 18.4e, for $Si_{50}Ge_{50}$, two pulses are located below T_l, but the oscillation behavior is similar to that observed above T_l.

Figure 18.4b, d, f gather the damping factors λ of the oscillating droplets Ge, $Si_{25}Ge_{75}$, and $Si_{50}Ge_{50}$ at different T from data of pulse cycles. They are weakly temperature dependent and do not show an Arrhenius-type behavior [10]. For

comparison, we drew schematically dashed lines in Fig. 18.4b, d, f, which present mean values and can be expressed by a fitting function $\lambda = \lambda_0 - \alpha \cdot 10^{-4}(T - T_l)$ with λ_0 denoted as damping factor at the liquidus temperature and α as the slope. We found thereby $\lambda_0 = 0.25$, 1.1, and 0.5 (s^{-1}) and $\alpha = 0.5$, 22, and 3.5 $(K^{-1}s^{-1})$ for Ge, $Si_{25}Ge_{75}$, and $Si_{50}Ge_{50}$, respectively. The results might suggest an alloying effect, i.e., the damping (near T_l) of the pure Ge is lower than that of two alloys. Accordingly, the temperature dependence of the damping is less pronounced for Ge $(\alpha = 0.5)$ in comparison with the two alloys $(\alpha = 22$ and 3.5). The slope α observed for $Si_{25}Ge_{75}$ is about six times larger than that for $Si_{50}Ge_{50}$. The phenomenon implies that, on the one hand, the alloying effect is possibly nonlinear with Si content in Ge and, on the other hand, an additional influence from the residual oxide phase on the surface may be possible as discussed above.

For a discussion of the viscosity data measured here by the oscillating drop method, the fluid flow in the droplets plays a crucial role. In EML facility, even a low positioning field (here 6 V) could lead to turbulent flow in a low viscosity droplet and therefore to an enhanced damping [11]. Qualitatively, the turbulent behavior can be observed by the movements of oxide particles, which exist on the surface (for $Si_{50}Ge_{50}$ in the first five cycles). Particles of about 50–100 μm in size could be tracked in video images. They circulate or move chaotically on the droplet surface with maximum observed velocities V of about 0.12 m s^{-1}. The Reynolds number R_e, which is defined as the ratio of inertial force $\frac{\rho V^2}{L}$ to viscous force $\frac{\eta V}{L^2}$ (ρ is the density of the droplet and L its characteristic dimension), i.e., $R_e = \frac{\rho V L}{\eta}$ [12], can be estimated to be $R_e \geq 4800$, taking $\rho = 5.0$ g cm^{-3} (for Ge and two alloys in average), $L = 8$ mm (diameter of the sample), and the viscosity η assumed to be $\leq$ 1 mPa·s as measured in experiments with an electrostatic levitator (ESL) [11, 13, 14]. Moreover, a detailed fluid flow modeling was made for the Ge droplet in the group of R. W. Hyers, Univ. of Massachusetts, and resulted in even higher Reynolds numbers of about 6500–70000 [15].

A further indication of the turbulent flow is the dynamical behavior of the droplet surface, showing self-excited oscillations during the whole cooling phase, as can be seen in Figs. 18.2, 18.3, and 18.4.

These findings lead to the conclusion that the measured damping factor λ may be dominated by the levitation force-induced fluid flow, and as a result, the relevant viscosity may deviate from the molecular viscosity measured in other experiments on earth. The argumentation is supported by the smaller value of $\eta < 1$ mPa·s measured for similar samples in an ESL [13, 14].

In addition, the molecular viscosity η may be estimated roughly by its relation to the surface tension γ as suggested by Egry et al. [16, 17], namely, $\frac{\gamma}{\eta} = 0.94\sqrt{\frac{RT}{W}}$, where R is the molar gas constant (8.314 J mol^{-1}K^{-1}) and W the molecular weight. In principle, this form provides an opportunity to separate the temperature dependence of the damping into turbulent and laminar flow. Though the form is valid strictly only for pure elements and simple metallic liquids, we have taken it for estimating the order of magnitude of the molecular viscosity. For example, for
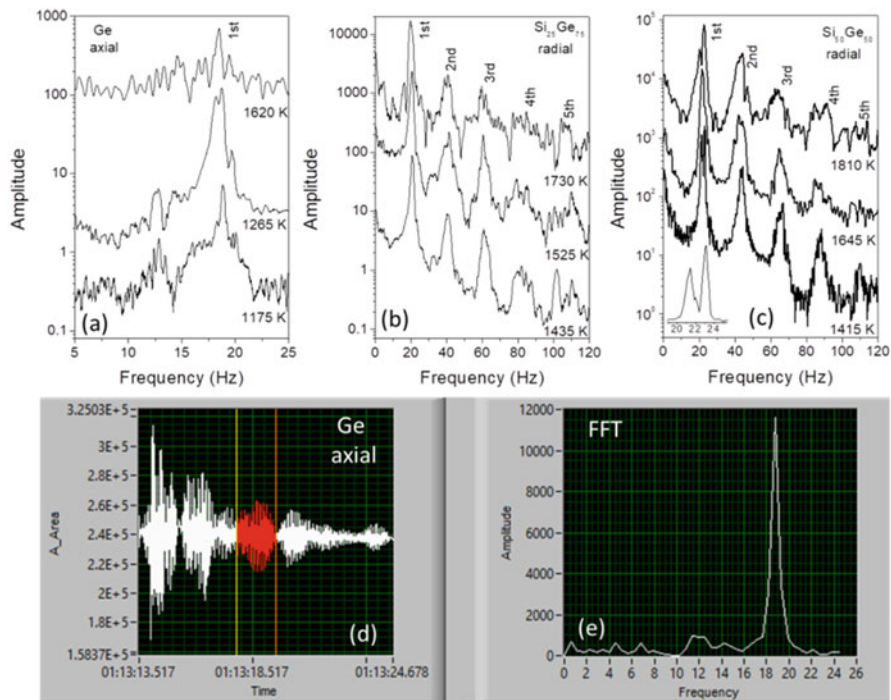
Fig. 18.5 (**a**), (**b**), and (**c**) Frequency spectra obtained from oscillations of the droplets Ge, $Si_{25}Ge_{75}$, and $Si_{50}Ge_{50}$ induced at different T. Inset in (**c**), splitting of the resonance peak arising from droplet rotations. (**d**) and (**e**) Time-segmental FFTs of oscillation data to minimize the impact from parasitic oscillations. (Data for $Si_{50}Ge_{50}$ are taken from Ref. [2])

$Si_{50}Ge_{50}$, with $W = 50.35$ g mol^{-1} and $\gamma = 0.6$ N m^{-1} measured near T_1 (cf. Fig. 18.6c), we get a value η of about 1.2 mPa·s supporting the discussion above.

7 Surface Tension of the Droplet

To determinate the surface tension γ of the droplets, the frequency spectra were deduced from the relevant oscillation data by means of fast Fourier transform (FFT). Figure 18.5a–c exhibit FFT frequency spectra obtained from oscillations of the droplets Ge, $Si_{25}Ge_{75}$, and $Si_{50}Ge_{50}$ excited by heating-off and short pulses at different temperatures. The occurrence of resonance peaks of the 1st order at about $\nu = 18$, 20, and 22 Hz can be seen, respectively, including higher harmonic peaks. The difference of the 1st peak positions partly mirrors the different masses M of the samples. The maximum frequency of FFT spectra shown in Fig. 18.5a–c depends on camera speeds. It is therefore smaller (~25 Hz) in Fig. 18.5a due to the usage of the low-speed axial camera (cf. Table 18.1).

Fig. 18.6 Surface tensions γ measured at different temperatures for Ge (**a**), Si$_{25}$Ge$_{75}$ (**b**), and Si$_{50}$Ge$_{50}$ (**c**), dashed lines drawn in view of the average. The lower values indicated by arrows (in **a**, **c** only for the cycle #9 and in **c** for cycle #6) are associated with highly deformed droplets at beginning of excited oscillations. (Data for Si$_{50}$Ge$_{50}$ are taken from Ref. [2])
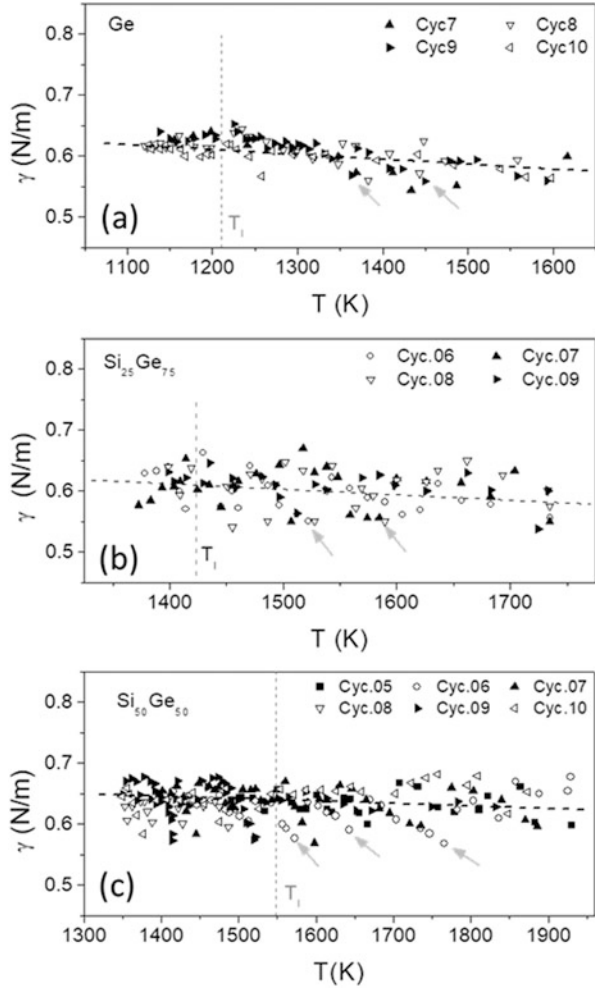
For each sample, temperature dependences are here visible, i.e., the resonance peaks are shifted slightly toward higher frequency for decreasing temperature. Since $\gamma = \frac{3\pi M}{8}\nu^2$ [9], this result implies an increase of γ for decreasing temperature.

Parasitic oscillations arising essentially from the droplet rotation (~1 Hz) are overlapped with the surface oscillation, leading to a splitting of the resonance peaks (also see the inset in Fig. 18.5c) and have to be taken into account by the evaluation of the resonance frequency. To minimize the impact from the parasitic oscillations, we have to operate the FFTs segmentally, as demonstrated in Fig. 18.5d. By means of a careful division, a segmentation of data yields a frequency spectrum with a single, nearly symmetrical resonance peak (Fig. 18.5e). A series of γ values as function of the temperature were extracted in this manner and are plotted versus T in Fig. 18.6a–c, where dashed lines are drawn in view of the average. The linear

T dependence can be approximately written as $\gamma = \gamma_0 - \xi \cdot 10^{-5}(T - T_1)$ with γ_0 as the value at the melting point and ξ as the slope. We got $\gamma_0 \approx 0.61$ N/m, $\xi \approx 8$ N/m·K for Ge, $\gamma_0 \approx 0.61$ N/m, $\xi \approx 9$ N/m·K for $Si_{25}Ge_{75}$, and $\gamma_0 \approx 0.65$ N/m, $\xi \approx 4$ N/m·K for $Si_{50}Ge_{50}$, respectively. Note, the slope ξ of $Si_{25}Ge_{75}$ is here slightly larger than that of $Si_{50}Ge_{50}$ by a factor of about two, being dissimilar to the relevant slopes of λ versus T given in Fig. 18.4d, f, different by a factor of about 6. This remarkable observation may be caused by a surface effect, but this interpretation has to be confirmed by additional measurements in the future.

In addition to errors caused by splitting or asymmetrical behavior of the resonance peak due to droplet rotation, the deformation (δ) of the droplet may give rise to a frequency shift, $\frac{\Delta \nu}{\nu} = p_1 \delta + p_2 \delta^2$, as recently investigated by Xiao et al. [18]. Here, the constant p_1 and p_2 are negative and the frequency shifts thus toward lower values. This nonlinear behavior is also visible here and even pronounced at the beginning of excited oscillations as indicated by arrows in Fig. 18.6. The deformation amplitude δ of the molten Ge, $Si_{25}Ge_{75}$, and $Si_{50}Ge_{50}$ can be estimated from the R/R_0 data shown in Figs. 18.2a, 18.3a, and 18.4a, c, e. It is about 15% at the beginning of the excited oscillations and decreases rapidly with t. After 1–2 s, δ becomes below 10%. Though it is slightly above the limit ($\delta = 7\%$) reported in Ref. [18], the equation mentioned above for the surface tension is only approximately valid.

The measured surface tension is comparable to published data in the literature. In previous parabola flight experiments with undoped Si-Ge samples [19] and doped Si-Ge samples with rich Ge-content [6], the values and the temperature dependences are similar. Measurements with an ESL also lie in the same range [14]. Experiments with the pendant drop method on earth show similar values [20].

8   Thermal Expansion

Figure 18.7a, b show normalized values of A/A_0 and R/R_0 obtained from the droplets of Ge (cycle #1) and $Si_{25}Ge_{75}$ (cycle #9), respectively. To optimize the accuracy of the thermal expansion data, largely scattered data beyond $\pm 10\%$ deformation arising from strong deformations of the droplets during the heating-off and short pulse period (about 1–2 s) were removed. Figure 18.7c shows the data obtained from the deeply undercooled droplet $Si_{50}Ge_{50}$ (cycle #11 with no pulse), showing very low scattering of 1 ± 0.02 much smaller than those given in Fig. 18.7a, b.

Linear fitting of these data yields coefficients $\beta_A = A^{-1}dA/dT$ (A = area) and $\beta_R = R^{-1}dR/dT$ (R = radius) of area and linear thermal expansion in given temperature ranges. The error values in brackets shown in Fig. 18.7a–c give the uncertainty of the linear fit. As expected, β_A is found here to be nearly equal to $2\beta_R$. It should be mentioned that the β values given in the plots are taken from different T-ranges, but in general, they become higher at higher temperatures. For example, the deeply undercooled droplet $Si_{50}Ge_{50}$ reveals the lowest coefficients ($\beta_A = 4.25 \times 10^{-5}$ K^{-1}
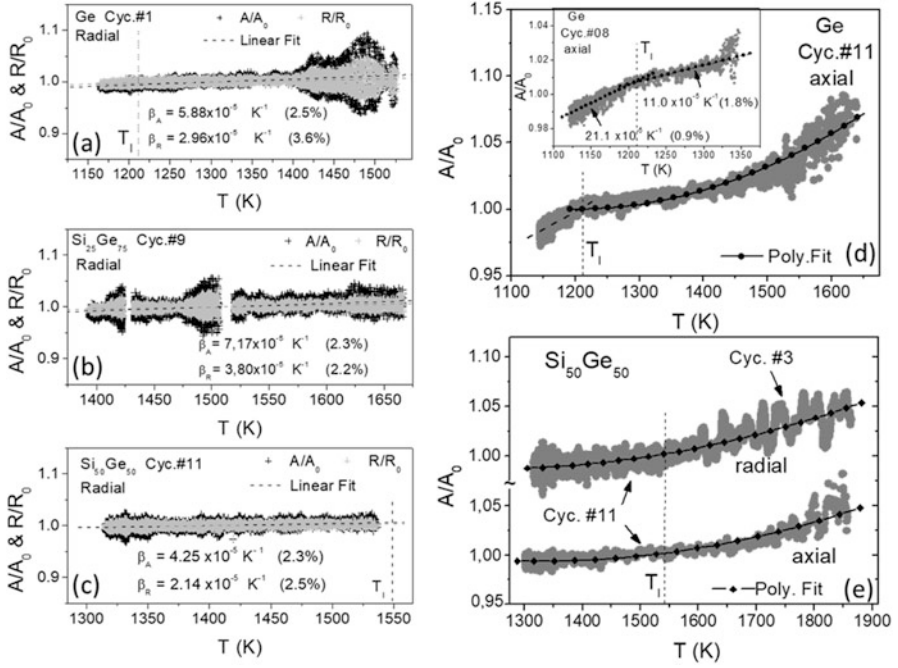
Fig. 18.7 (**a**), (**b**), and (**c**) Normalized radial areas A/A_0 and radii R/R_0 as a function of T measured for Ge (cycle #1), $Si_{25}Ge_{75}$ (cycle #9), and $Si_{50}Ge_{50}$ (cycle #11), linear fits give coefficients of the thermal expansion β_A (area) and β_R (radius) in given T ranges. (**d**) Axial data of Ge from cycles #11 and #8 (inset) and (**e**) axial and radial data of $Si_{50}Ge_{50}$ from cycles #3 and #11, showing a nonlinear behavior, which can be approximately fitted by a 2nd-order polynomial. As a special feature, the droplet Ge shows a nearly twice larger slope below T_l. (Data for $Si_{50}Ge_{50}$ are taken from Ref. [2])

and $\beta_R = 2.14 \times 10^{-5}$ K^{-1}) as given in Fig. 18.7c, being much lower than those ($\beta_A = 10.0 \times 10^{-5}$ K^{-1} and $\beta_R = 4.9 \times 10^{-5}$ K^{-1}) obtained from the same sample but highly overheated run from 1550 to 1875 K. The result suggests a nonlinear thermal expansion of the liquid.

To show this in more detail, Fig. 18.7d, e exhibit relevant axial/radial video data measured for the droplets Ge and $Si_{50}Ge_{50}$, covering both overheating and undercooling temperature ranges. Note that in Fig. 18.7e, the radial data of cycle #11 is combined here with the radial data of cycle #3, due to the limited data storage capacities on board the ISS and thus a restricted length (≤ 30 s) of radial image video data (400 Hz). In addition, to minimize the scattering, smoothing of the data were done by adjacent averaging. A nonlinear behavior of the droplet sizes with T is apparent and can approximately be fitted here by a 2nd-degree polynomial R/R_0 $(T) = \alpha_R + \beta_{R0}(T - T_l) + \beta_R'(T-T_l)^2$ or $A/A_0 = \alpha_A + \beta_{A0}(T - T_l) + \beta_A'(T - T_l)^2$ with constants $\alpha_{R,\ A}$ close to 1. Differential operation of the equation yields thermal expansion coefficients as a linear function of T, namely, $\beta_{R,\ A} = \beta_{R,\ A0} + 2\beta_{R,\ A}'(T - T_l)$ where $\beta_{R,\ A0} \approx 10^{-5}$ K^{-1} as initial value at T_l and $2\beta_{R,\ A}' \approx 10^{-7}$ K^{-2} as the slope.

With the help of the equation, the β_R value near the liquidus temperature T_l can be evaluated. Averaging over all cycles, for example, we get a mean β_R of about 3.15×10^{-5} K^{-1} for Si$_{50}$Ge$_{50}$. For Si$_{25}$Ge$_{75}$, which showed a small undercooling (~20 K), the mean values of β_A and β_R were found to be about 6.35×10^{-5} K^{-1} and 3.20×10^{-5} K^{-1}, respectively.

More interestingly, a special feature was observed for pure Ge, namely, below T_l, the droplet decreases in size with decreased T nearly twice faster than above T_l, as can be followed in Fig. 18.7d or inset. For this situation, we had to fit the data ($T > T_l$), and obtained mean thermal expansion coefficients of overheated Ge melt, $\beta_A = 5.94 \times 10^{-5}$ K^{-1} and $\beta_R = 3.10 \times 10^{-5}$ K^{-1} for the range of 1211–1525 K. Similar results were obtained earlier from parabola flight experiments [4, 19].

The change in slope of A/A_0 in the insert of Fig. 18.7d by a factor of two increasing with lower temperatures is very uncommon if compared to a liquid-crystal or liquid-glass transition. Normally, the thermal expansion coefficient decreases at lower temperatures. We also note that we observe this strong increase of the slope from $11.0 \cdot 10^{-5}$ K^{-1} to $21.1 \cdot 10^{-5}$ K^{-1} not in the Si$_{50}$Ge$_{50}$ alloy (see Fig. 18.7e). A change in the thermal expansion coefficient is most likely coupled to a change in the interatomic potential [21, 22]. This means that the phase transition observed in the liquid could be also reflected in the thermal expansion coefficient here. Further experiments and simulations are necessary to verify this observation.

Nonlinear temperature dependence of the thermal expansion of the melts of Si and Ge was also observed by a thermometric method by Glazov and Shcelikov about 20 years ago [23]. They discussed this behavior in terms of a decrease in the strength of interatomic bonds with increasing temperature. The experimental results are comparable with the behavior of the Ge and SiGe alloy droplets investigated here in the ISS-EML.

In addition, Kulkarni et al. performed ab initio MD simulations of Ge melts [24]. They argue that at lower temperatures, the structure factor shows a pronounced shoulder on the high k-side of the principal peak, which vanishes for high temperatures consistent with experimental scattering data in the literature. The coordination number increases with increasing temperature. This behavior of the structure factor is accompanied by an angle distribution function showing some tetrahedral arrangements at lower temperatures as well [25].

Following Kulkarni et al., our interpretation of the temperature dependence of the volume of the Si-Ge melt states that at very high temperatures, the melt behaves like a simple metallic melt where a linear thermal expansion is expected. With decreasing temperature, covalent, tetrahedral structure elements (small range order) begin to form, and therefore, the specific volume deviates from that of a simple liquid, which is characterized by a simple two-body interatomic potential with linear thermal expansion, leading to the observed nonlinear temperature dependence.

In addition, the solidification of the melt is accompanied by an abrupt increase in A/A_0 and R/R_0 as illustrated in the inset of Fig. 18.4d. The phenomenon can be partly contributed to the volume expansion due to T rise, and partly to the volume anomaly of the substances Si and Ge, whose density in the solid state is lower than that in liquid [4].

9 Electrical Resistivity

The EML levitation facility operating on board the ISS in microgravity (μg) provides a perfect environment for the contactless, inductive measurement of the electrical resistivity of well conducting liquid samples. By application of alternating magnetic fields of high frequency, electromagnetic levitation may stably position and heat conducting samples without external contact by inductive means only. For the handling of the droplets, the EML electromagnetic levitation facility uses a symmetric magnetic quadrupole field produced by two equal, parallel, and coaxial circular RF currents of the same strength but opposite directions to confine the sample against residual disturbances in μg in the center of the coil; see Fig. 18.8.

For an efficient inductive heating and melting of the sample, it applies an additional, widely homogeneous RF magnetic dipole field, generated by two parallel and coaxial circular RF currents of the same strength in the same directions. This "heating field" is simultaneously used as inductive measurement probe.

The almost forceless μg environment provides the advantage that (1) the measurement sample is confined at a fixed place in the coils; (2) the weak applied electromagnetic forces keep the droplet almost spherical and minimize driving turbulent fluid flow in it, which otherwise would result in oscillations of the droplet surface; and (3) the absence of gravity enables a mirror symmetric coil arrangement, which avoids mutual inductive interaction between the electrical heating (measurement) and positioning circuit. The immediate measurement quantity in the present case is the (complex) electrical impedance of the heating circuit $\widetilde{Z}_{tot} = U_0/I_0 e^{i\varphi}$ composed of the amplitude of the RF circuit voltage U_0, the circuit current I_0, and the phase shift φ between both. These three quantities are precisely detected and stored with a data rate of 10 Hz by a dedicated measurement electronics (SCE). After a separate calibration measurement without sample, which yields the impedance of the empty circuit $\widetilde{Z}_{circ}$, the measurement quantity $\widetilde{Z}_{tot}$ enables the determination of
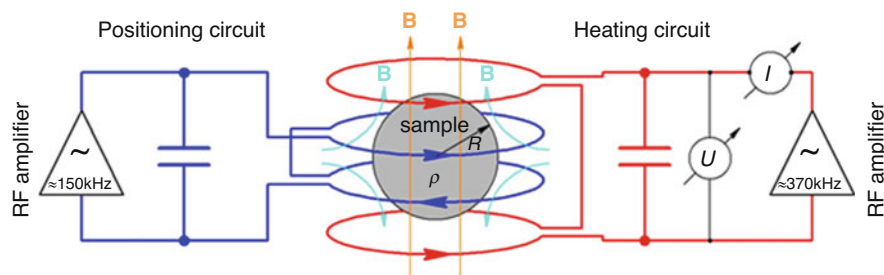
Fig. 18.8 Schematic sketch of the electrical oscillating circuit arrangement of the ISS-EML facility composed of the positioning coil (blue) generating an alternating (≈150 kHz) magnetic quadrupole field (light blue arrows) and the heating coil (red) generating an alternating (≈370 kHz), homogeneous magnetic dipole field (orange arrows). The electrical heating circuit contains an electronic for the precise measurement of the circuit voltage U, current I, and of the phase shift φ between both quantities
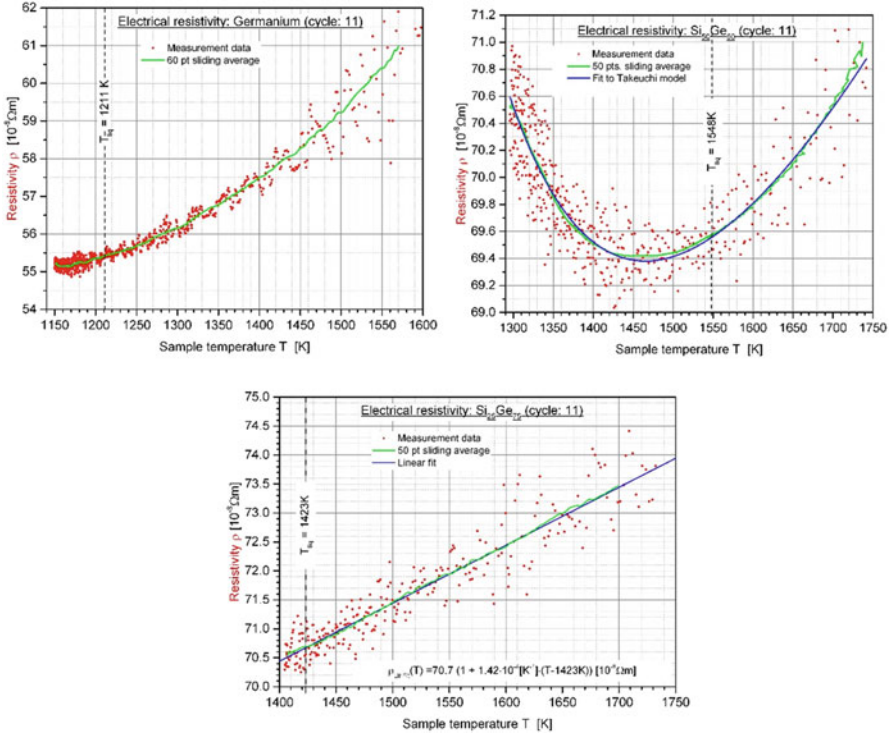
Fig. 18.9 Inductively measured electrical resistivity data (red dots) of liquid germanium, liquid $Si_{50}Ge_{50}$, and liquid $Si_{25}Ge_{75}$ in dependence of the sample temperature above and below the liquidus temperature in the undercooled state. Added are also the sliding averages of the data (green line) and the respective fitted physical models (blue line). (Data for $Si_{50}Ge_{50}$ are taken from Ref. [2])

$\widetilde{Z}_s(R, \rho)$, the contribution to the total impedance from the inductively coupled sample alone. For the simple, clear, and well-defined condition of a spherical sample in a homogeneous magnetic field, provided by the microgravity environment, the physical model derived in [26] allows finally to relate the electrical resistivity $\rho(T)$ and thermal expansion $R(T)$ independently from each other to the real and the imaginary part of $\widetilde{Z}_s(R, \rho)$. A detailed description of the actual levitation and measurement principle is given in Ref. [27].

Within the frame of the "SEMITHERM" project, the temperature-dependent electrical resistivities $\rho(T)$ of liquid germanium and of the two liquid semiconductor alloys $Si_{50}Ge_{50}$ and $Si_{25}Ge_{75}$ have been measured in the EML facility. Levitation and measurement are possible because of the metallic properties of semiconductors in the liquid state. The measurements are performed during the cooling phase of the liquid samples (see Fig. 18.1a) where the magnetic heating field and thus the magnetic forces on the droplets are lowest. The results are collected in Fig. 18.9.

The temperature-dependent electrical resistivity $\rho(T)$ is a sensitive indicator for structural changes in the melt. Generally, the electrical resistivity in liquid metals results from the scattering of the conduction electrons at the disordered metal ions. Accordingly, the decline of the temperature-dependent density fluctuations in the melt with decreasing temperature results in the usually observed linear decrease of ρ [28], a behavior which is shown by the liquid $Si_{25}Ge_{75}$ alloy in the whole measured temperature range; see Fig. 18.9.

In liquid electrically conducting alloys, a formation of compact structures (clusters) with decreasing temperature, due to chemical short-range ordering processes of the components, may result in an increase of the scattering cross section for the electrons and thus of the electrical resistivity [28]. Consequently, an onset of clustering phenomena in a liquid alloy may lead to a deviation of $\rho(T)$ from the typical linear temperature dependence. The lower the temperature of the melt is, the more pronounced this effect should show up. Such a deviation is clearly shown in Fig. 18.9 by both of the other two melts but especially by the present liquid $Si_{50}Ge_{50}$ sample due to its extreme deep undercooling.

Assuming that the $Si_{50}Ge_{50}$ melt can be considered as a regular solution with a positive heat of mixing $W > 0$, meaning that external heat is necessary to keep the liquid alloy components mixed, the unusual temperature behavior of the electrical resistivity can be described by the physical model of Takeuchi and Endo [29]:

$$\rho(x_{Si}, x_{Ge}, T) = \rho_0(x_{Si}, x_{Ge}) + \rho_1(x_{Si}, x_{Ge}) \cdot T + \rho_2(x_{Si}, x_{Ge}) \frac{2x_{Si}x_{Ge}W/RT}{1 - 2x_{Si}x_{Ge}W/RT}$$

where x_{si} and x_{Ge} denote the concentrations of the Si and Ge components (presently $x_{si} = x_{Ge} = 1/2$) and where $\rho_0(x_{si}, x_{Ge})$, $\rho_1(x_{si}, x_{Ge})$, and $\rho_2(x_{si}, x_{Ge})$ are temperature-independent constants. Corresponding to the conventional resistivity model, the above equation contains a constant term and a term which is linearly dependent on the temperature T and dominates for high temperatures. The last term finally considers the increase of the electrical resistivity with decreasing temperature due to the assumed increasing structural evolution of the deeply undercooled $Si_{50}Ge_{50}$ melt by tetrahedral order formation of the Si component. A weighted fit to the measured data points with $\rho_0^{Si,Ge} = 3.5 \times 10^{-5} \Omega$ cm , $\rho_1^{Si,Ge} = 2.2 \times 10^{-8} \Omega$ cm K^{-1}, $\rho_2^{Si,Ge} = 1.6 \times 10^{-5} \Omega$ cm, and $W^{Si, Ge} = 12$ KJ mol^{-1}, which covers the sliding average of the data points fairly well, is shown in Fig. 18.9 in the diagram of $Si_{50}Ge_{50}$. The electrical resistivity data support the interpretation of a structural phase transition in the liquid as discussed in the framework of the thermal expansion measurements.

10 Conclusion

In this work, we report about experiments in the ISS-EML for measurements of the thermophysical properties of highly doped semiconductors Ge, $Si_{25}Ge_{75}$, and $Si_{50}Ge_{50}$. Especially, thermal expansion, surface tension, and damping of the surface oscillations have been investigated.

For the thermal expansion of the melt, we found a nonlinear behavior of the volume as a function of temperature. The findings can be interpreted in terms of a structural change in the melt as a function of temperature. For high temperatures, the melt behaves like a simple metallic fluid with linear thermal expansion. With decreasing temperature, covalent, tetrahedral structure elements (small range order) begin to form, and therefore, the specific volume deviates from that of a simple liquid, which is characterized by a simple two-body interatomic potential with linear thermal expansion, leading to the observed nonlinear temperature dependence.

The surface tension was evaluated using surface oscillations (oscillating drop technique), which were determined with a fast Fourier analysis. The data are in the range of 0.6–0.7 N/m, comparable to previous experiments on parabola flights or in the earth lab and are nearly temperature independent.

The surface oscillations are exponentially damped. For melts showing a laminar flow behavior, the molecular viscosity can be calculated from the damping constant. In our case, however, the flow is turbulent and the damping is related to the flow field of the droplet. The turbulent flow stems from the strong coupling to the positioner field, which is supported by simulations performed in the group of R. Hyers, Univ. of Massachusetts, Amherst. The turbulent behavior could also be observed experimentally by the chaotic movement of small oxide islands on the surface.

The electric resistance of the droplets could be measured inductively by a technique developed by G. Lohöfer, DLR Cologne (sample coupling electronics). For the sample $Si_{50}Ge_{50}$, the resistance as a function of temperature shows a distinct minimum in the undercooled range. For higher temperatures, the resistance increases as expected for simple metallic melts, whereas in the undercooled range, the resistance increases with decreasing temperature. This result supports the interpretation of the thermal expansion data that at lower temperatures, structural changes occur.

In summary, the results of the ISS experiments are very promising, especially the structural changes in the undercooled melt. The data support strongly the idea of a structural phase transition in these melts. Future activities including simulation (R. Maass and P. Derlet) will take a clearer look on the phenomena.

References

1. 25th DLR Parabolic flight campaign, 20th–31st October 2014, Practical and Technical Information, *DI-2014-ed1-en, Novespace, Bordeaux-Mérignac, Mars 2014*. See also: www.novespace.com

2. Y. Luo, B. Damaschke, G. Lohöfer, K. Samwer, Thermophysical properties of a Si50Ge50 melt measured on board the International Space Station. npj Microgravity **6**, 10 (2020) http://creativecommons.org/licenses/by/4.0/

3. N.V. Abrosimov, S.N. Rossolenko, W. Thieme, A. Gerhardt, W. Schröder, Czochralski growth of Si- and Ge-rich SiGe single crystals. J. Cryst. Growth **174**, 182–186 (1997)

4. Y. Luo et al., Contactless processing of SiGe-melts in EML under reduced gravity. npj Microgravity **2**, 1–9 (2016)

5. C.A. Angell, S.S. Borick, Comment on 'Structure of supercooled liquid silicon'. J. Phys. Condens. Matter **11**, 8163–8166 (1999)

6. D. Keren, C. Gotsman, Fitting curves and surfaces with constrained implicit polynomials. IEEE Trans. Pattern Anal. Mach. Intell. **21**(1), 31–41 (1999)

7. W. M. Haynes (ed.), *CRC Handbook of Chemistry and Physics*, 92nd edn. (CRC Press, Boca Raton, 2011) ISBN 1439855110

8. E. Wiberg, N. Wiberg, A.F. Holleman, *Inorganic Chemistry* (Academic/De Gruyter, San Diego/New York/Berlin, 2001) ISBN 0-12-352651-5

9. I. Egry, G. Lohöfer, I. Seyhan, S. Schneider, B. Feuerbacher, Viscosity of eutectic Pd78Cu6Si16 measured by the oscillating drop technique in microgravity. Appl. Phys. Lett. **73**, 462–463 (1998)

10. T. Iwashita, D.M. Nicholson, T. Egami, Elementary excitations and crossover phenomenon in liquids. Phys. Rev. Lett. **110**, 205504 (2013)

11. R.W. Hyers, Fluid flow effects in levitated droplets. Meas. Sci. Technol. **16**, 394–401 (2005)

12. O. Reynolds, An experimental Investigation of the circumstances, which determine whether the motion of water shall be direct or sinuous, and of the law of resistance in parallel channels. Philos. Trans. R. Soc. Lond. **174**, 935–982 (1883)

13. Z. Zhou, S. Mukherjee, W.K. Rhim, Measurement of thermophysical properties of molten silicon using an upgraded electrostatic levitator. J. Cryst. Growth **257**, 350–358 (2003)

14. J.J.Z. Li, W.K. Rhim, C.P. Kim, K. Samwer, W.L. Johnson, Evidence for a liquid–liquid phase transition in metallic fluids observed by electrostatic levitation. Acta Mater. **59**, 2166–2171 (2011)

15. G. Bracker et al., *Reported on the 12th International Workshop on Subsecond Thermophysics* (IWSSTP 2019), hold June 3–6, 2019, Cologne, Germany

16. I. Egry, On the relation between surface tension and viscosity for liquid metals. Scripta Met. Mat. **26**, 1349 (1992)

17. J. Brillo, *Thermophysical Properties of Multicomponent Liquid Alloys, De Gruyter Oldenbourg* (Walter de Gruyter GmbH, Berlin/Boston, 2016)

18. X. Xiao, R.W. Hyers, R.K. Wunderlich, H.J. Fecht, D.M. Matson, Deformation induced frequency shifts of oscillating droplets during molten metal surface tension measurement. Appl. Phys. Lett. **113**, 011903 (2018)

19. S.M. Chathoth, B. Damaschke, K. Samwer, S. Schneider, Thermophysical properties of Si, Ge, and Si–Ge alloy melts measured under microgravity. Appl. Phys. Lett. **93**(1–3), 071902 (2008)

20. E. Ricci et al., Surface tension and density of Si-Ge melts. J. Chem. Phys. **140**, 214704 (2014)

21. D.S. Sanditor, A criterion for the glass-liquid transition. J. Non-Cryst. Solids **385**(148) (2014)

22. V.A. Drebushchak, A.I. Turkin, Relationship between heat capacity and thermal expansion derived from the Lennard–Jones potential. J. Therm. Anal. Calorim. **65**, 745–753 (2001)
23. O.V. Glazov, M.D. Shchelikov, Volume changes during melting and heating of silicon and germanium melts. High Temp. **38**, 405–412 (2000)
24. R.V. Kulkarni, W.G. Aulbur, D. Stroud, Ab initio molecular-dynamics study of the structural and transport properties of liquid germanium. Phys. Rev. B **55**, 6896 (1997)
25. S.M. Chathoth, B. Damaschke, T. Unruh, K. Samwer, Influence of structural changes on diffusion in liquid germanium. Appl. Phys. Lett. **94**, 221906 (2009)
26. G. Lohöfer, Magnetization and impedance of an inductively coupled metal sphere. Int. J. Eng. Sci. **32**, 107–117 (1994)
27. G. Lohöfer, High-resolution inductive measurement of electrical resistivity and density of electromagnetically levitated liquid metal droplets. Rev. Sci. Instrum. **89**, 124709 (2018)
28. S. Takeuchi, H. Endo, The electrical resistivity of the metals in the molten state. Trans. JIM **3**, 30–35 (1962)
29. S. Takeuchi, H. Endo, Theoretical and experimental studies on the resistivity of molten alloys. Trans. JIM **3**, 35–41 (1962)

Chapter 19
Thermophysical Properties of Bulk Metallic Glasses

Markus Mohr, Yue Dong, Douglas C. Hofmann, Antonia Neels, Alex Dommann, William L. Johnson, and Hans-Jörg Fecht

1 Introduction

When a liquid is cooled down fast enough, crystallization can be avoided, and an amorphous solid, a glass, can be formed. For a better understanding of this process, the knowledge of the temperature-dependent properties of the formed glass, as well as the temperature-dependent properties of the glass-forming liquid, are necessary [1–3]. To properly describe glass formation, also the understanding of crystal nucleation and growth is important (see, e.g., Chap. 7). Even though the present understanding of the crystal nucleation is still limited, the classical nucleation theory may be used to describe a temperature-dependent steady-state nucleation rate $J(T)$ as [4].

$$J(T) = \frac{A}{\eta(T)} \exp\left(-\frac{16\pi\sigma_i^3}{3k_BT\Delta G_V^{lx}(T)^2}\right) \quad (19.1)$$

M. Mohr (✉) · Y. Dong · H.-J. Fecht
Institute of Functional Nanosystems, Ulm University, Ulm, Germany
e-mail: markus.mohr@uni-ulm.de; hans.fecht@uni-ulm.de

D. C. Hofmann
Materials Development and Manufacturing Technology Group, NASA Jet Propulsion Laboratory/California Institute of Technology, Pasadena, CA, USA

A. Neels · A. Dommann
Center for X-Ray Analytics, Empa Swiss Federal Laboratories for Materials Science and Technology, Dübendorf, Switzerland

W. L. Johnson
Keck Engineering Laboratories, California Institute of Technology, Pasadena, CA, USA

where $\eta(T)$ is the viscosity, σ_i is the interface energy between liquid and nucleated crystalline solid phase, and ΔG_V^{lx} is the difference between the Gibbs free energy in the undercooled liquid and the nucleating crystalline phase. The quantities that enter Eq. 19.1 are typically scarce, tend to scatter strongly in the literature, or are completely unknown.

Furthermore, the data of thermophysical quantities, such as viscosity and specific heat, which enter Eq. 19.1, are usually not available over a large temperature range. One of the reasons is of technical nature since, e.g., the viscosity of a material varies by as much as 17 orders of magnitude between the liquid and solid glassy phase. Hence, a combination of different techniques in the low- and high-temperature range is needed. While conventional, container-based methods can be applied in the low-temperature regime (around the glass transition temperature, T_g), in the high-temperature range, the container walls can render the measurements erroneous. The generally high reactivity of liquid metals leads to reactions with containers and contaminations that disturb the precise measurement of thermophysical properties. Furthermore, the container walls present a source for heterogeneous nucleation, which disturbs investigations of the undercooled liquid state. Hence, containerless methods for the measurement of thermophysical quantities are preferred, especially for the high-temperature range when bulk metallic glass-forming liquids are investigated.

Proceeding from the discovery of metallic glasses on a laboratory scale [5], further glass-forming alloys containing metals, metalloids, and nonmetals have been investigated [3–5]. Bulk metallic glasses were mostly based on the early and late transition metals [9], while in recent years, new, more lightweight compositions have been developed [10]. Bulk metallic glasses lack crystalline order and interfaces, such as phase or grain boundaries. This gives rise to a number of outstanding properties when compared to their crystalline counterparts. A general characteristic of metallic glasses is their high strength, making them the material class with an exceptionally large ability to store elastic energy. Several strategies to improve the weakness of metallic glasses, their inherent tensile brittleness, have already shown promising results, leading to damage-tolerant glasses with high strength and toughness [11–13].

Iron-based metallic glasses have been known for a long time, finding their first uses in amorphous foils for electric transformers [14]. Fe-based glasses are still the lowest-cost form of amorphous metals. The high corrosion and wear resistance make Fe-based metallic glasses attractive for industrial applications [15]. While the excellent magnetic properties of, e.g., Fe-based metallic glasses have enabled a number of applications, their mechanical properties have yet to be fully exploited in real-world applications. The small critical casting thickness has limited their application to anticorrosion, anti-wear, or thermal-barrier coatings, applied by, e.g., spray coating [15, 16] or laser cladding [17, 18]. In more recent times, efforts have been made to develop Fe-based glass compositions with improved ductility and glass-forming ability [19–21]. These have the potential to increase their application potential and outperform other materials as structural and wear-resistive materials [22–

24]. Additive manufacturing of Fe-based metallic glasses using powder bed fusion (PBF), thermal spray additive manufacturing (TSAM), and direct energy deposition (DED) was already demonstrated for a FeCrMoCB glass-forming composition [25, 26]. A similar Fe-based glass former $Fe_{57.75}Ni_{19.25}Mo_{10}C_5B_8$ was investigated in this work, supplying the needed thermophysical property data to develop a 3D-printing process for this alloy.

The large casting thicknesses of Zr-based metallic glasses (e.g., between 5 and 10 cm for $Zr_{41}Ti_{14}Cu_{12.5}Ni_{10}Be_{22.5}$ [27]) make them attractive for industrial applications and feasible for industrial processes, such as injection molding or additive manufacturing [8–10, 28]. In order to avoid the toxic material Be, a number of Be-free alternatives with high glass-forming ability in the Zr-Cu-Ni-Al-X system were developed in the past years, such as X = Ti (LM105) [29] or X = Nb (Vit106a or Vit106) [30, 31]. The Zr-based metallic glass Vit106 was, e.g., used in the solar wind collector of NASA's Genesis mission, where it was one of the few samples that survived the unintended crash-landing of the satellite in the Utah desert in 2004 [32]. The amorphous structure of the alloy causes not only its high toughness but also allows the uniform etching of the sample. This was exploited to detect the collected compositions from the solar wind [32]. Despite the generally high glass-forming ability and fracture toughness of Zr-based glasses, the effect of processing on these properties needs to be well understood for successful commercialization [32]. The property data obtained from microgravity experiments can make an important contribution to this aim.

Another case of interest is the Cu_{100-x}-Zr_x binary alloy system since metallic glasses can be formed in this binary alloy in a rather wide composition range of $x = 25$-60at% [33]. It was reported that for the $Cu_{50}Zr_{50}$ composition, rods with up to 2 mm diameter could be cast [34], while only small additions of Al could increase the glass-forming ability furthermore [35]. Consequently, the Cu_{100-x}-Zr_x binary alloy system is a base for many Zr-Cu-based and Zr-Cu-Al-based metallic glass alloys. The simple composition of $Cu_{50}Zr_{50}$ and the existence of reliable potentials necessary for molecular dynamics simulations allow the comparison of measured thermophysical properties with those derived from molecular dynamics simulations. A glass former based on the $Cu_{50}Zr_{50}$ composition ($Cu_{43}Zr_{43}Al_7Be_7$) was successfully used to manufacture a metallic glass gear by a new low-cost manufacturing method, which allowed casting of net-shaped macroscale gears. The BMG gear outperformed the high-performance steel Vascomax C300 (which is used on the Mars rover "Curiosity") by exhibiting a 60% improvement of wear resistance [36].

Pd-based and Pt-based metallic glasses are known for their good glass-forming ability [6–8, 37]. Having a large supercooled liquid region between the glass transition temperature T_g and the crystallization temperature T_x of up to 100 °C, they possess good formability [38]. For the Pd-based and Pt-based metallic glass formers $Pd_{43}Ni_{10}Cu_{27}P_{20}$ and $Pt_{57.3}Cu_{14.6}Ni_{5.3}P_{22.8}$, continuous casting using semi-industrial equipment has been demonstrated [38]. These casting processes were accompanied by casting simulations, which require the knowledge of thermophysical properties, such as viscosity, specific heat, mass density, thermal conductivity, etc., in order to obtain meaningful results [38].

2   Experimental Methods

Containerless processing can avoid heterogeneous nucleation on the container walls, as well as reactions with container material. Even though the melting point of metallic glasses is often low, the reactivity of the liquid phase is still high, especially for the investigated Fe- and Zr-based glass alloys. Experiments on the Pd-based glass former $Pd_{43}Cu_{27}Ni_{10}P_{20}$ were conducted in the electromagnetic levitation facility TEMPUS on board parabolic flights. The Zr-based metallic glass former LM105 ($Zr_{52.5}Cu_{17.9}Ni_{14.6}Al_{10}Ti_5$) and Vit106a ($Zr_{58.5}Cu_{15.6}Ni_{12.8}Al_{10.3}Nb_{2.8}$) and the Fe-based metallic glass FeNiMoCB ($Fe_{57.75}Ni_{19.25}Mo_{10}C_5B_8$) were investigated under long-duration microgravity conditions in the electromagnetic levitator ISS-EML on board the international space station (ISS). The TEMPUS facility is similar to the ISS-EML from a technical point of view. More details on the TEMPUS facility can be found in Ref. [39]. Experimental details about the ISS-EML can be found in Chap. 3, and details on the applied methods can be found in Chap. 12.

3   Microgravity Measurement of the Thermophysical Properties of Bulk Metallic Glasses

Thermophysical properties of five bulk metallic glasses in the stable and undercooled liquid phase were obtained in microgravity. These properties can be divided into surface-related properties, such as surface tension, and bulk-related properties, such as heat capacity and transport properties. In the following, the results are shown and compared.

3.1   Surface Tension

Figure 19.1 shows the surface tension of the investigated bulk metallic glass formers.

The surface tension of the Fe-based glass former FeNiMoCB shows a boomerang-like shape. The measurements were performed both in the TEMPUS facility in an inert gas atmosphere and in vacuum in the ISS-EML. Since the oxygen partial pressure during both measurements was not known, it is not yet conclusive if oxygen adsorption or if surface-active species of the alloy, such as Boron, are responsible for the observed behavior [40]. The surface tension at the liquidus temperature ($T_{liq} = 1505 \pm 4$ K) was found to be 1.68 ± 0.04 N/m.

As seen in Fig. 19.1, the surface tension of the Zr-based metallic glasses is rather similar. For LM105, the surface tension is given as [3].

Fig. 19.1 Surface tension of FeNiMoCB, Vit106a, LM105, $Cu_{50}Zr_{50}$, and PdCuNiP measured containerless under microgravity
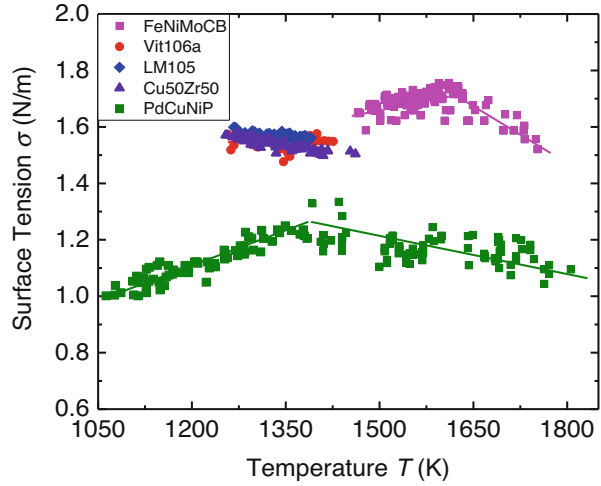
$$\sigma(T) = (1.612 \pm 0.008) - (1.72 \pm 0.31) \times 10^{-4} \times (T - 1091 \text{ K}) \qquad (19.2)$$

while for the binary $Cu_{50}Zr_{50}$, the surface tension is found to be [41].

$$\sigma(T) = (1.58 \pm 0.01) - (3.1 \pm 0.6) \times 10^{-4} \times (T - 1209 \text{ K}) \qquad (19.3)$$

The surface tension for $Pd_{43}Cu_{27}Ni_{10}P_{20}$ was investigated in a temperature range of about 750 K in the stable liquid phase. Also, for $Pd_{43}Cu_{27}Ni_{10}P_{20}$, it shows a boomerang-like shape [42], of which oxygen, as well as phosphorus as surface-active species, could be responsible. For temperatures above 1400 K, the surface tension of $Pd_{43}Cu_{27}Ni_{10}P_{20}$ can be described as

$$\sigma(T) = (1.53 \pm 0.09) - (4.28 \pm 0.67) \times 10^{-4} \times (T - 827 \text{ K}) \qquad (19.4)$$

3.2   Viscosity

The viscosity is an important property for the fabrication of bulk metallic glass parts by different production routes. The temperature-dependent viscosity of a liquid gives a manifestation of the change of the liquid's kinetics during cooling, which plays an important role in the glass formation. Glass-forming melts can be classified into fragile and strong liquids, depending on the steepness of viscosity change around the glass transition temperature T_g. According to the classical definition, the fragility index m is defined as

Fig. 19.2 Viscosity of FeNiMoCB, Vit106a, LM105, Cu$_{50}$Zr$_{50}$, and PdCuNiP as a function of temperature, measured in the ISS-EML, as well as the TEMPUS facility
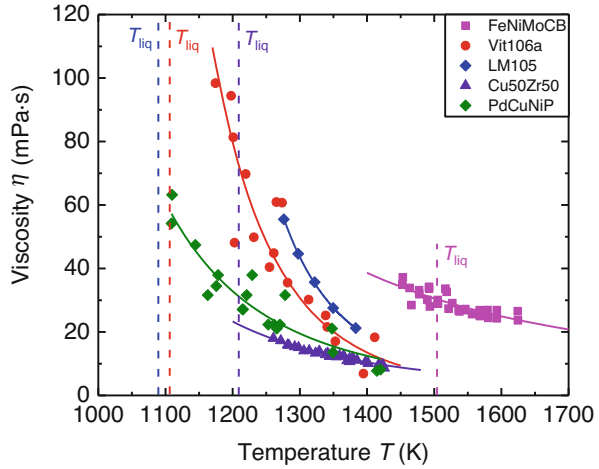
$$m = \left. \frac{d \ln(\eta)}{d(T_g/T)} \right|_{T=T_g} \tag{19.5}$$

High values of the fragility index m imply a steep rise in viscosity, indicating a fragile melt that shows non-Arrhenius behavior and an increase of the activation energy for viscous flow on decreasing temperature. Low values of m indicate a stronger liquid with a moderate temperature dependence of viscosity around the glass transition temperature. The viscosity of strong glasses follows an Arrhenius-like behavior with nearly constant activation energy for viscous flow over the whole temperature range. The change in viscosity as a function of temperature represents the change in the kinetics in the liquid and, hence, is important for the understanding of the changes in close- and midrange order in the liquid metals during cooling. This makes it especially important to measure the viscosity not only in the temperature range around the glass transition, which is experimentally easily accessible, but also in the stable and undercooled liquid phase.

The viscosity of the different glass formers investigated on board the international space station and during several parabolic flight campaigns is shown in Fig. 19.2. With the exception of the Fe-based metallic glass, the viscosity of the investigated glass formers was determined in the stable liquid phase, which is not easy to access by other methods due to the high melt reactivity of the investigated glasses.

3.3 Specific Heat

The relevance of the specific heat of bulk metallic glass formers in the liquid state is given by the need for simulations of industrial solidification processes. The heat flow

Fig. 19.3 Molar heat capacity as a function of temperature for FeNiMoCB, Vit106a, LM105, and $Cu_{50}Zr_{50}$ measured by the ac calorimetry method using the ISS-EML on board the ISS
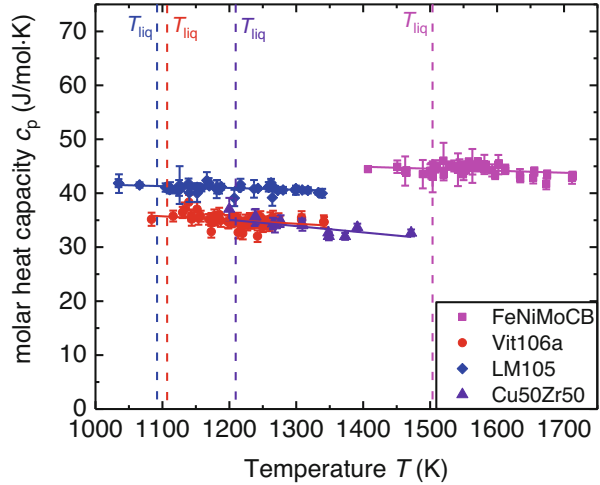
in these processes needs to be numerically predicted to allow for process optimizations in order to achieve the desired cooling rate. Furthermore, the specific heat can be used together with other thermodynamic quantities to describe ΔG_V^{lx}, the Gibbs free energy difference between the crystalline solid and liquid phase, required for models of nucleation.

The molar heat capacity in the liquid phase has been investigated for four bulk metallic glasses on board the ISS, as shown in Fig. 19.3. The precise data was obtained using the ac calorimetry method [43] (see Chap. 12).

Generally, a slight decrease in specific heat with increasing temperature is found in the temperature range just above the melting point of the alloys. The Fe-based metallic glass shows a higher molar heat capacity than the Zr-based metallic glasses.

3.4   Total Hemispherical Emissivity

Using the ac calorimetry method, the total hemispherical emissivity can be obtained independently from the specific heat capacity. Hence, the total hemispherical emissivity in the liquid phase for the four metallic glasses was determined. No strong temperature dependence was found. The total hemispherical emissivity ε_{tot} at the liquidus temperature for the examined compositions is given in Table 19.1.

The ε_{tot} of FeNiMoCB is found to have an average value of 0.30 ± 0.01, which is higher than predicted by a theoretical approach by Parker and Abbott [44], as shown in Fig. 19.4. The theoretical prediction of ε_{tot} considers a Drude free-electron model under the assumption of negligibly small electronic relaxation times. Thus, the details of the band structure and scattering mechanisms are not considered in detail by the model, which could explain the difference between measurement and theory.

Table 19.1 Total hemispherical emissivity at the liquidus temperature

Alloy	Liquidus temperature T_{liq} (K)	Total hemispherical emissivity ε_{tot} at T_{liq}
FeNiMoCB	1505	0.30 ± 0.01
Vit106a	1106	0.20 ± 0.02
LM105	1091	0.26 ± 0.01
$Cu_{50}Zr_{50}$	1209	0.25 ± 0.03
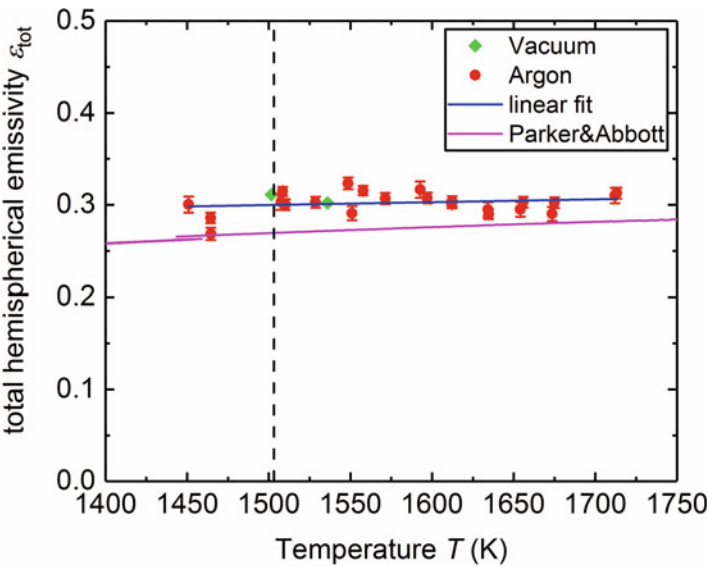
Fig. 19.4 Measured linearly fitted total hemispherical emissivity of FeNiMoCB as well as the theoretical prediction from the electric conductivity using the model of Parker and Abbott [44]. (Reproduced under the terms of the CC BY 4.0 license [40]. Copyright 2020, Wiley-VCH)

3.5 Vitrification Under Microgravity

3.5.1 Vitrification During a Parabolic Flight

Containerless processing removes the container walls as a source for heterogeneous nucleation. Hence, deep undercooling and the vitrification of the suspended liquid alloy sample become possible when the cooling rate is high enough. The vitrification of samples under microgravity, where controlled fluid flow conditions prevail, could also give further insights into the influence of fluid flow on nucleation and crystallization, or vitrification.

One example of successful vitrification of a bulk metallic glass during processing in microgravity is the Pd-based metallic glass $Pd_{43}Cu_{27}Ni_{10}P_{20}$ that repeatedly vitrified at the end of the microgravity phase. Figure 19.5a shows the temperature-time diagram (red) measured for $Pd_{43}Cu_{27}Ni_{10}P_{20}$ during the last parabola performed in the parabolic flight campaign. In blue, the heater control voltage is
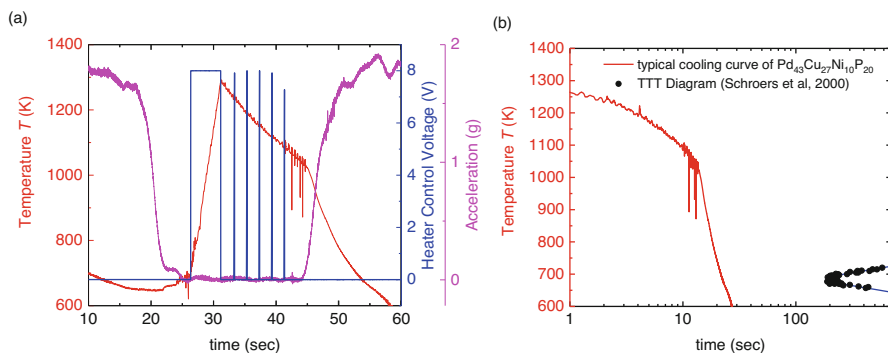
Fig. 19.5 (**a**) Temperature-time diagram during the last parabola of PdCuNiP (red), together with the heater control voltage (blue) and the acceleration on the sample (pink). (**b**) Temperature variation during cooling (red). For comparison, the temperature-time-transformation diagram measured by Schroers et al. [45] is shown. (Reproduced under the terms of the CC BY 4.0 license [42]. Copyright 2019, Springer Nature)

shown, which is at maximum during the heating and melting phase, while it is turned down during the cooling phase. The short heater pulses are used to initiate surface oscillations for the determination of surface tension and viscosity. Figure 19.5b shows the cooling curve (after the heater is turned off), together with the temperature-time-transformation diagram measured by Schroers et al. [45].

The absence of any recalescence signal indicates that the sample has solidified in a fully amorphous state. The increased cooling rate, starting at about 15 s after the heater is turned off, originates from the contact of the sample with the sample holder at the end of the parabola. It can be recognized that the cooling rate has been high enough to bypass the nose of the TTT diagram to prevent crystallization of the sample.

Together with the phase change from liquid to solid, a reduction in sample volume is typically witnessed, which can cause pores and voids in the sample. Absorption X-ray CT images were recorded in order to perform a volumetric reconstruction of the molten and vitrified metallic glass sample. Figure 19.6a shows the volumetric reconstruction of the sample. The nonspherical shape is a result of the contact of the sample with the sample holder at the end of the microgravity phase. Figure 19.6b shows an absorption X-ray CT image (slice) of the vitrified sample. The slice that is shown in Fig. 19.6b confirms the absence of any kind of internal crystalline feature. Reflection-based X-ray diffraction analyses have been performed on the samples retrieved from the parabolic flight campaigns. The resulting diffraction patterns that were recorded at different points on the sample are shown in Fig. 19.6c. The diffraction patterns confirm the glassy nature of the sample.
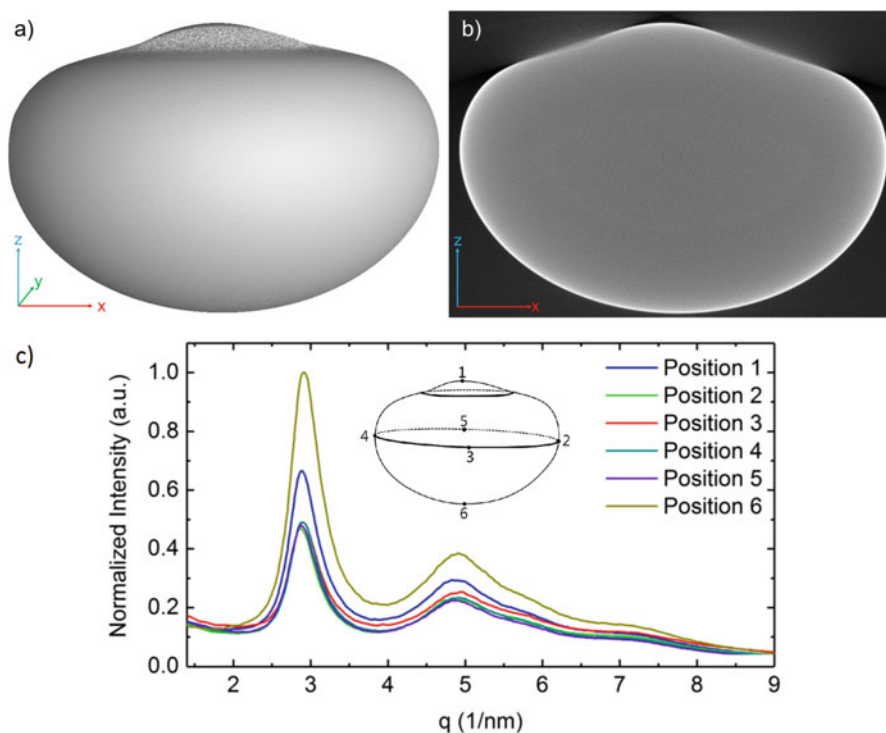
Fig. 19.6 (**a**) Three-dimensional volumetric reconstruction of the sample of an X-ray CT scan. (**b**) An exemplaric slice of the X-ray CT scan. (**c**) Diffraction patterns obtained after the parabolic flight. The inset shows a sketch of the vitrified sample shape. (Reproduced under the terms of the CC BY 4.0 license [42]. Copyright 2019, Springer Nature)

3.5.2 First Metallic Glass Made in Space

The electromagnetic levitator ISS-EML on board the international space station (ISS) offers the choice of processing in vacuum, in an argon, and in a helium atmosphere so that different cooling rates can be achieved. The cooling rate in He is the highest due to its higher thermal conductivity.

Figure 19.7a shows typical temperature-time diagrams for the 6.5-mm-diameter sphere of the alloy LM105, recorded during melting and free cooling in the three different atmospheres. As can be seen, the sample was molten, overheated, and cooled freely by radiative and conductive heat loss in the various process environments. During the processing of LM105 in helium, an average cooling rate of about 8 K/s was achieved, which is similar to the reported critical cooling rate for LM105 (~ 10 K/s [46]). Figure 19.7a shows a cycle performed in a helium atmosphere, where no recalescence is observed. This means that the sample solidified as a glass. Hence, this was the first production of a metallic glass sphere in space!
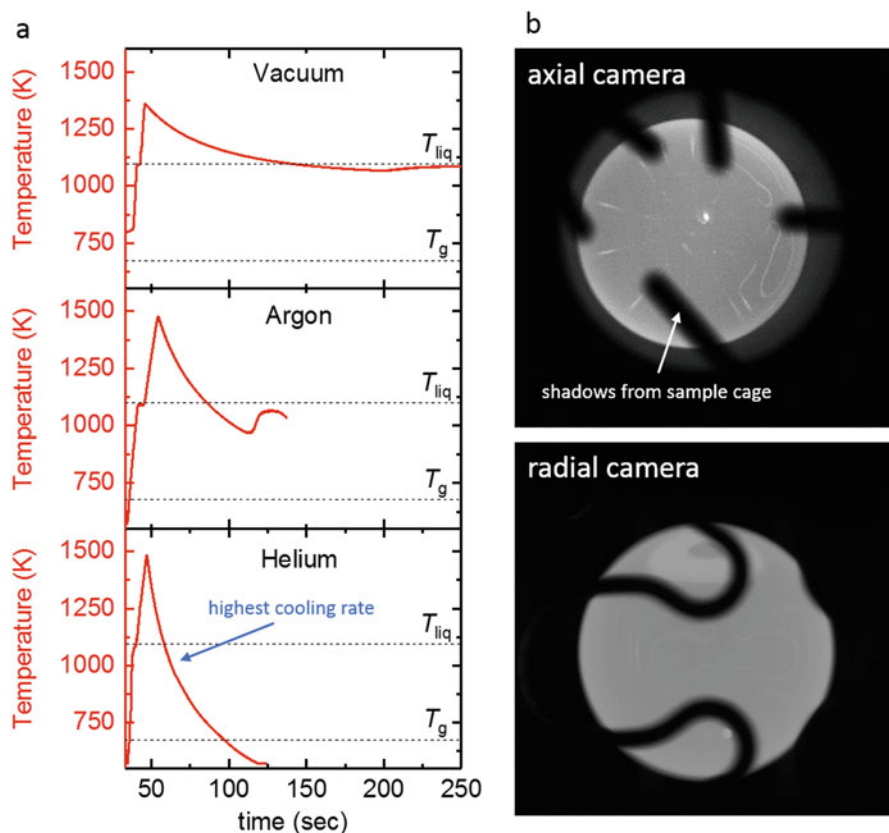
Fig. 19.7 (**a**) Containerless processing cycles of LM105 in the ISS-EML under different atmospheres. (**b**) Camera images of the liquid sample during cooling. The shadows on the sample originate from the (non-touching) sample cage. (Reproduced under the terms of the CC BY 4.0 license [3]. Copyright 2019, Springer Nature)

Figure 19.7b shows the axial and radial camera images taken during the cooling process, showing a perfectly spherical sample. Using image processing algorithms on the recorded high-speed video images, it could be shown that the residual sample elongation is only about 25 µm away from a perfect 6.5 mm sphere [3].

During the processing of the 6.5-mm-diameter sphere of LM105 in the He atmosphere, it was witnessed in four consecutive melt cycles that the sample solidified without the occurrence of a recalescence event.

While Fig. 19.8a shows a typical temperature-time diagram, when the sample was vitrified during cooling, Fig. 19.8c shows the recorded temperature-time diagram recorded while the sample crystallized under similar processing parameters during cooling. During sample cooling, the inductive measurement of the sample electrical resistivity was performed, and consequently, Fig. 19.8b, d show the electrical resistivity as a function of temperature. The discontinuity of the electrical resistivity
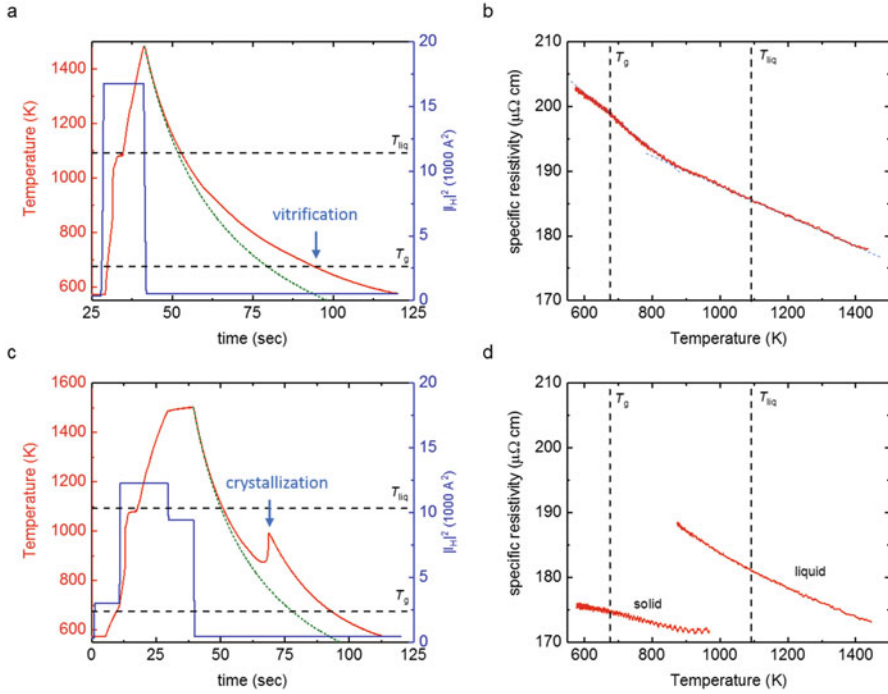
Fig. 19.8 (**a**) Temperature-time diagram recorded during vitrification of the sample. (**b**) The corresponding electrical resistivity as a function of temperature. (**c**) Temperature-time diagram recorded during crystallization of the sample, showing clear recalescence. (**d**) The corresponding electrical resistivity during crystallization, having a clear discontinuity proofing crystallization. (Reproduced under the terms of the CC BY 4.0 license [3]. Copyright 2019, Springer Nature)

that can be seen in Fig. 19.8d is a clear sign of crystallization of the sample, while the complete absence of any discontinuity in Fig. 19.8b is a clear proof for the full vitrification of the sample.

By using a surrogate model for convective flow inside the levitated droplet [47], the Reynolds number in the droplet during cooling can be approximated to below $Re = 15$.

Figure 19.9 shows a typical cooling curve (Cycle 75), in comparison with the temperature-time-transformation (TTT) diagrams obtained on board the ISS-EML and by Lin et al. [29], who studied the undercooling and nucleation of LM105 as a function of the oxygen concentration of the alloy using a ground-based ESL. Compared to the ground-based ESL results, the cooling rate achieved on the ISS-EML in He atmosphere should not be sufficient to vitrify the sample. As Fig. 19.9 shows, the cooling curve of the ISS-EML sample passes through the TTT diagrams obtained on ground (even for the lowest oxygen impurity concentration of 250 ppm) without crystallization. A possible reason could be the slightly lower oxygen concentration in the ISS sample (the initial oxygen concentration of the sample was better than 150 ppm). Additionally, also the lower level of fluid flow
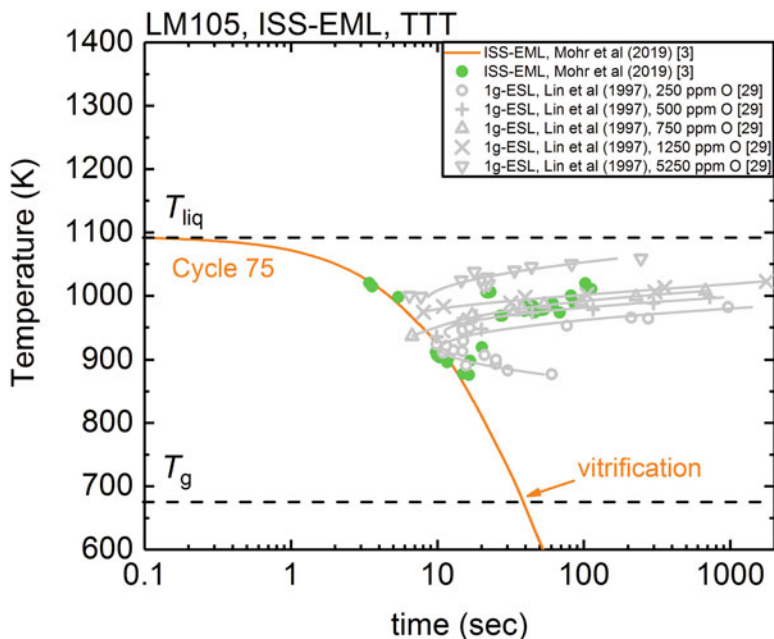
Fig. 19.9 Temperature-time-transformation diagram of LM105. A typical cooling curve (Cycle 75), during which the sample vitrified, together with ground-based ESL measurements of the TTT diagram of LM105 for different oxygen impurity levels [29]. The cooling curve of the ISS-EML sample passes through the TTT diagram without crystallization

in the melt, compared to the ground-based measurements in the ESL, could play a role for the improved glass-forming ability [3].

This first fabrication of a metallic glass sphere in space shows the feasibility of the production of metallic glass parts in space. This could support the manufacturing efforts already developed for the ISS.

We hope that these findings can inspire the design and development of manufacturing facilities for long-term exploration missions or on an extraterrestrial base, such as on the moon.

4 Discussion

The surface tension data reported in Fig. 19.1 shows that the surface tension of the Zr-based metallic glass formers is relatively similar, while that of the Pd-based metallic glass is much higher and the Fe-based metallic glass former shows a much lower one. This has important implications on the processing of these alloys. Furthermore, the surface tension of the Fe- and Pd-based glasses show a boomerang-like temperature dependence, which is usually attributed to surface-active species.
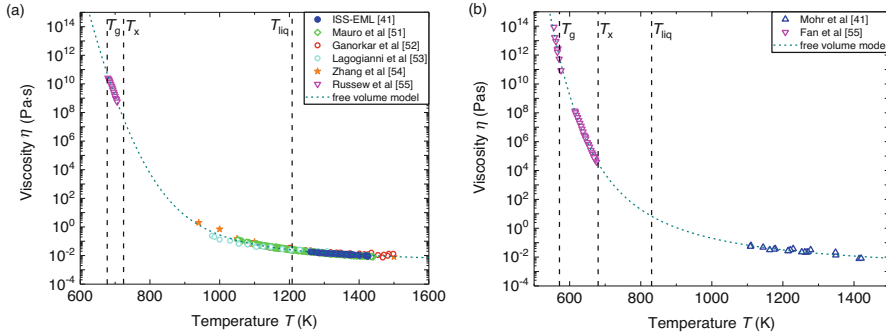
Fig. 19.10 (**a**) Viscosity of $Cu_{50}Zr_{50}$ measured on board the ISS [41], together with measurements in electrostatic levitation facilities [51–53], MD simulations [54], and measurements by dynamical mechanical analysis around T_g [55]. (**b**) Viscosity of $Pd_{43}Cu_{27}Ni_{10}P_{20}$ measured on board a parabolic flight [42], as well as by ground-based methods around T_g [56]

While effects of oxygen adsorption/desorption during the processing cannot be ruled out completely, the curve shape could also be an effect of the surface-active species contained in the liquid alloys. This could be boron for the Fe-based metallic glass or phosphorus in the case of the Pd-based glass. It is known that boron can lead to the reduction of the surface tension of steels [48]. Also, the influence of phosphorus on the surface tension of metallic liquids, such as steel, is well studied in literature [49]. Further studies to investigate this further, such as theoretical modeling of the surface tension, will be done in the future. The installation of an oxygen sensing and control system (OCS; see Chap. 3) will allow clarification of the role of residual oxygen atoms in the processing environment on the temperature dependence of the surface tension.

The viscosity data in the stable and undercooled liquid phase measured in space, together with data at the low temperatures around T_g, obtained by different container-based methods, such as three-point beam bending or parallel plate rheometry, can be combined to reveal the viscosity over a large temperature range. Such data is shown here for $Cu_{50}Zr_{50}$, a simple binary glass former, and for $Pd_{43}Cu_{27}Ni_{10}P_{20}$ in Fig. 19.10. The viscosities in the low- and high-temperature range could be fitted sufficiently well using the Cohen-Grest free volume model [50].

The viscosity of $Cu_{50}Zr_{50}$, measured on board the ISS [41], verified the results obtained by measurements using electrostatic levitation [51–53]. Furthermore, the relatively simple binary system allows molecular dynamics simulations, which revealed viscosities that are in agreement with the measured viscosity values [54, 57]. Furthermore, these simulations confirmed the existence of cooperatively rearranging regions, which suggests that modeling can help to gain further insights into the glass formation of simple alloy systems (Fig. 19.10a) [54, 57].

In a small temperature interval around the liquidus temperature, the fluidity (the inverse of the viscosity) can usually be described by an Arrhenius law:
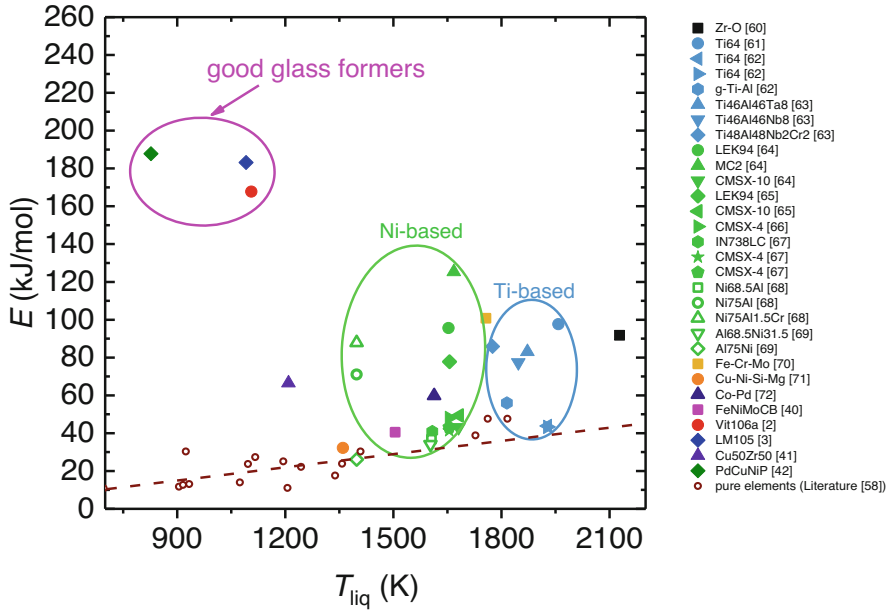
Fig. 19.11 Activation energy for viscous flow for Ni-based, Ti-based, and Zr-based metallic liquids, together with a number of glass-forming liquids as a function of their liquidus temperature. The viscosity of these metallic liquids were measured using an electromagnetic levitation device either on board a parabolic flight, on a TEXUS Sounding Rocket, on the Space Shuttle, or in the ISS-EML [2, 3, 40–42, 60–72]. The viscosities for the pure elements were taken from literature [58]

$$\frac{1}{\eta} = \frac{1}{\eta_0} \exp\left(-\frac{E}{k_B T}\right) \tag{19.6}$$

where η_0 is the theoretical infinite-temperature limit of viscosity, k_B is Boltzmann's constant, and E is the activation energy for viscous flow. Figure 19.11 shows the activation energy E for a number of pure elements [58], as well as for a number of industrial alloys and several glass-forming alloys. Hirai [59] showed that for metallic liquids, an empirical relationship exists between the activation energy E and the melting point of elemental metallic materials. This relationship is indicated by the dashed line in Fig. 19.11.

For the alloys studied in microgravity, the viscosity was typically measured in a temperature range between 50 K below the liquidus temperature until 100 K above the liquidus temperature. For the Zr- and Pd-based glass-forming alloys, the viscosity was measured at a temperature range far above the liquidus temperature (see Fig. 19.2). The fitting curves (see Fig. 19.10) of the free volume model were used in this case to obtain the activation energy E for these alloys around their liquidus temperature. It can be noted from Fig. 19.11 that the metallic glass formers have a generally lower T_{liq} compared to most of their elemental components since they are usually deep eutectic compositions. But it is striking that with the exceptions of the

Fig. 19.12 Viscosity of three metallic glasses shown in the Angell plot over a wide temperature range, using the combined data measured in microgravity [2, 3, 41, 42] and on ground [55, 56, 73, 74], together with literature data of SiO_2 and o-terphenyl [75]
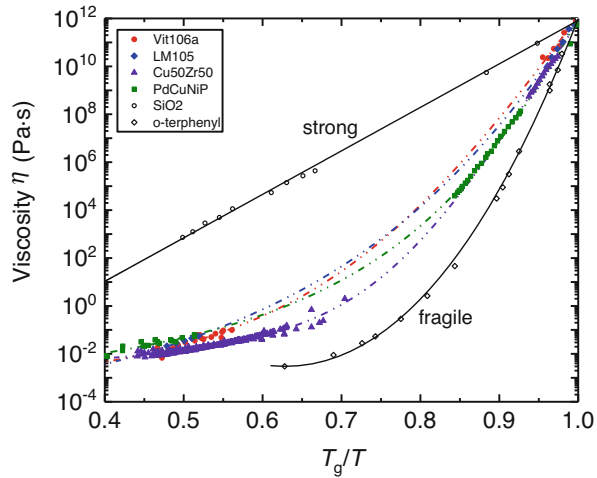
marginal glass formers $Cu_{50}Zr_{50}$ and FeNiMoCB, the activation energies for viscous flow, E, of the investigated metallic glasses are higher than those of the other alloys, indicating their generally high barrier toward viscous flow around the liquidus temperature. One reason might be their multielement compositions, consisting of elements with a negative enthalpy of mixing and large differences in atomic radii. Furthermore, for the investigated glass-forming alloys, the higher activation energy for viscous flow E coincides with a higher reduced glass temperature T_g/T_{liq}. This suggests that the activation energy E at the liquidus temperature can be an indicator for the glass-forming ability. In the low-temperature regime, close to T_g, the fragility m of the liquid is often used as an indicator for the glass-forming ability of a metallic glass former.

Figure 19.12 presents an Angell plot of the investigated glass formers. The figure shows literature values of ground-based viscosity measurements around T_g, as well as the viscosity values obtained for the stable liquid using containerless methods under microgravity.

Container-based measurements of the specific heat in the solid state are often possible by conventional differential scanning calorimetry. This way, the specific heat in the amorphous and crystalline state can be obtained. If crystallization can be avoided, the specific heat in the deeply undercooled liquid phase can be obtained the same way. However, the specific heat in the stable and high-temperature undercooled liquid state is only accessible by containerless measurement methods.

The ac calorimetry also allows the measurement of the total hemispherical emissivity of the liquid melts, which is a property important for the description of the radiative cooling of a liquid. Since the ac calorimetry is basically the only method that makes this quantity directly accessible, this data can now be compared with theoretic descriptions (see also Fig. 19.4). The theories developed to date cannot yet fully explain the measured values. Further improvements of the theoretical description of the hemispherical emissivity seem necessary.
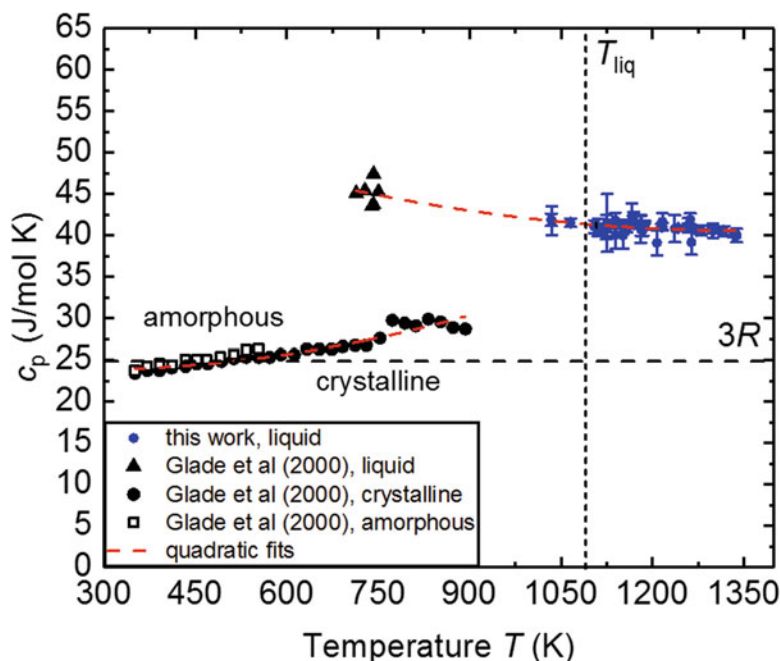
Fig. 19.13 Specific heat of LM105 in the liquid phase [3], in the solid phase, and in the undercooled liquid phase [46]. (Reproduced under the terms of the CC BY 4.0 license [3]. Copyright 2019, Springer Nature)

Figure 19.13 shows the specific heat of LM105 measured on ground and in space as an example (see also Fig. 19.3). The ground-based measurements by Glade et al. [46] in the amorphous and crystalline solid phase are complemented by measurements in the stable and undercooled liquid state measured by the containerless ac calorimetry method performed on board the ISS [3]. The combination of data obtained on ground and in space offers the possibility to calculate thermodynamic functions, such as the free energy difference ΔG^{lx} between the crystalline and liquid phase.

When the free energy difference ΔG^{lx} between the crystalline and liquid phase, as well as the viscosity, is known over a large temperature range, the temperature-time-transformation (TTT) diagram can be calculated. The prediction of TTT curves offers important guidelines for the development of manufacturing processes for bulk metallic glass parts. An example for the use of the calculated TTT diagram, together with numerical simulations of the solidification, was presented by Haag et al. [38] for the noble-metal-based metallic glasses $Pd_{43}Cu_{27}Ni_{10}P_{20}$ and for $Pt_{57.3}Cu_{14.6}Ni_{5.3}P_{22.8}$. The continuous casting machine and its simulation are shown in Fig. 19.14a, b. The produced rods are shown in Fig. 19.14c, showing typical shiny surfaces for the glassy Pd-based BMG rods.
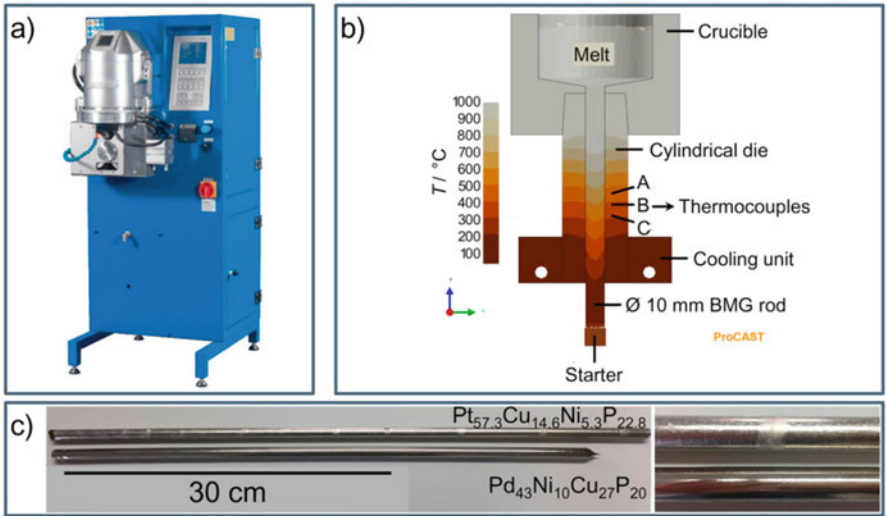
Fig. 19.14 Continuous casting of BMGs. (**a**) Continuous casting machine Indutherm CC 400. (**b**) Casting simulation using ProCAST software. (**c**) Rods with a length of >500 mm were reproducibly processes. (Reprinted from Ref. [38], Copyright 2018, with permission from Elsevier)
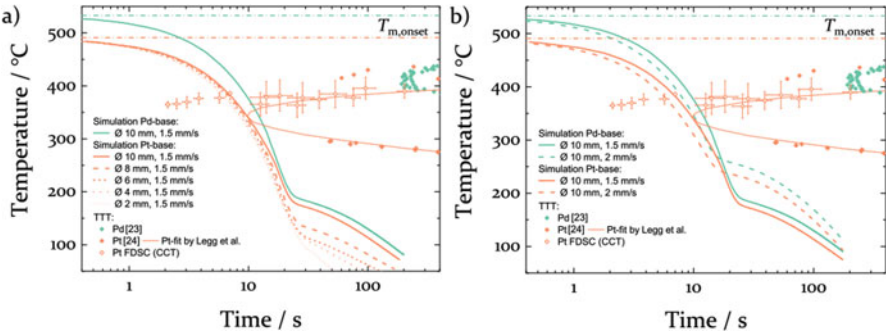
Fig. 19.15 Assessment of the glass-forming ability during vertical continuous casting of a Pd- and Pt-based bulk metallic glass alloy. (**a**) Cooling curves simulated for 1.5 mm/s pulling speed for rod diameters of 10 mm (Pd) and 2–10 mm (Pt), together with the TTT diagrams. The gap between the cooling curve and the crystallization nose is larger for $Pd_{43}Cu_{27}Ni_{10}P_{20}$ as for $Pt_{57.3}Cu_{14.6}Ni_{5.3}P_{22.8}$. (**b**) Simulation at higher pulling speeds (2 mm/s) have a pronounced effect on the cooling rate. (Reprinted from Ref. [38], Copyright 2018, with permission from Elsevier)

Figure 19.15 presents the assessment of the glass-forming ability during the vertical continuous casting with a pull speed of 1.5 mm/s (Fig. 19.15a) at different rod diameters (2–10 mm for Pt, 10 mm for Pd). These simulations were performed by Haag et al. [38].

The simulation shows clearly that the nose of the TTT diagram for the Pt-based glass is much closer to the cooling curve. Simulations of this kind can be used to find the optimal process conditions to obtain glassy rods.

5 Examples for Applications of Bulk Metallic Glasses

Bulk metallic glasses have prospects for their use in a number of applications. While some products have already become commercially available, other potential products have been demonstrated in the past and are on their way to commercialization. Here, some very promising applications of bulk metallic glasses are summarized.

Some devices, such as sensors and actuators, are depending on a number of compliant mechanisms. The performance of these devices is strongly dependent on the used material. Many polymers are not sufficient due to the limited temperature range of operation and their low strength [76]. Most metals are not appropriate due to the small elasticity and insufficient manufacturability of complex structures [76]. The outstanding mechanical properties of metallic glasses, especially their high fracture toughness and high elastic limit, can improve such compliant mechanisms. Furthermore, BMGs can be manufactured using low-cost methods like injection molding, known from polymer processing. In Ref. [76], several compliant mechanisms built by a Zr-based metallic glass were presented and successfully tested.

Some devices need to be operated under so-called harsh environmental conditions. Such conditions, which are quite unusual from a human perspective, are, e.g., low temperatures of about $-180\,^{\circ}\mathrm{C}$ and/or vacuum conditions. These conditions can be found on many exploration destinations in our solar system (e.g., the surface temperature of the earth's moon is between 95 and 390 K). Typically, the gears and gearboxes of the rovers used on the moon and Mars to date have to be heated in order to liquefy the gears' lubricants. The required power consumption can be enormous (e.g., for the Mars rover "Curiosity," 30% of the available power was used to heat the gear lubricant prior to its movements). Consequently, replacing the nitride maraging steel gears with materials that show low wear in the unlubricated state could lead to large power savings. A number of bulk metallic glasses have been tested for their wear loss [36], identifying Cu-Zr-BMG compositions with good wear resistance, superior to that of the currently used high-performance steel. Apart from these findings, another set of metallic glasses was investigated not only from a performance perspective but also from the commercialization perspective. A new casting process was developed and used for a number of Zr-based metallic glasses (also Vit106 and LM105) to produce strain wave gears [77].

The cost estimate showed that already for a production volume of 500 BMG flexspines, the costs per part would be lower than for a steel machined part. Furthermore, the produced BMG strain wave gears were successfully operated at 76 K with no liquid lubricant [77]. Figure 19.16a shows a cast and assembled BMG strain wave gear, while Fig. 19.16b shows the operation of the gearbox at 76 K.
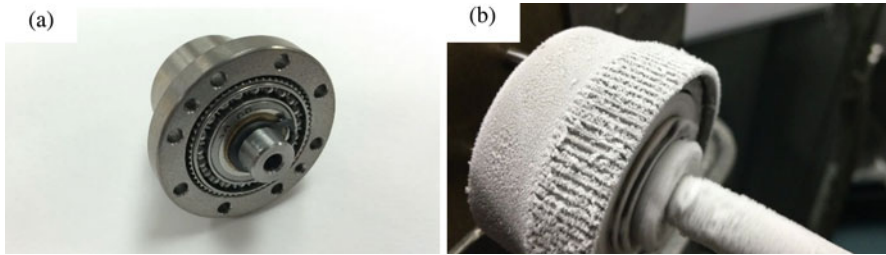
Fig. 19.16 (**a**) Casted BMG strain wave gear. (**b**) Unlubricated operation of the gearbox at 76 K. (Courtesy NASA/JPL)

Fig. 19.17 3D-Printed AMZ4 saw blade. (Courtesy NASA/JPL)
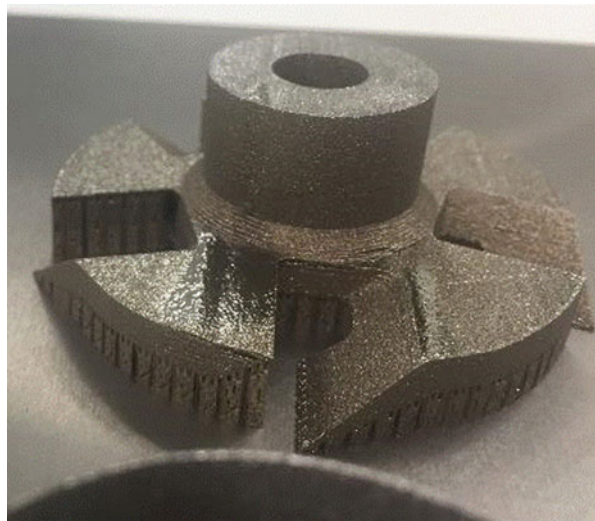
Additional cold temperature testing is ongoing to qualify the gears for use in future NASA missions.

Not only gears have to withstand extreme conditions, but also tools, such as saw blades, might be operated under extreme environmental conditions and used for very abrasive materials. An extreme example of this are saw blades that are used to cut into ice on cold planets or moons during exploration missions. In a recent study by NASA/JPL, a number of saw blades were additively manufactured by several materials, including the Zr-based metallic glass composition AMZ4 (Heraeus Additive Manufacturing, GmbH) [78]. The saw blades were tested on salt lick (as a regolith simulant). As a criterion for the cutting performance, the mechanical specific energy required to excavate a unit volume was measured during the cutting processes. The additively manufactured BMG saw blade performed better than the other conventional materials, such as A2 tool steel or Ti64. Figure 19.17 shows a 3D-printed AMZ4 cutting tool.

These examples show that nowadays, the production of BMG-based parts by different methods, such as casting, injection molding, and 3D printing, is feasible on an industrial scale. The insights in the thermophysical properties, such as heat capacity and viscosity, obtained by the microgravity experiments have led to significant improvements of the fabrication processes.

6   Conclusions

In this chapter, we summarized the measurements of thermophysical properties for a large number of metallic glass formers using containerless methods, including the newly developed Fe-based glass former FeNiMoCB; the Zr-based glass formers Vit106a; LM105, a Pt- and Pd-based glass former; and the prototype binary glass-former $Cu_{50}Zr_{50}$.

The obtained data, in combination with ground-based measurements, give access to the thermodynamic quantities relevant for the description of the glass formation or crystallization. Temperature-time-transformation curves obtained from these measured quantities give important guidance for the design of production processes. Bulk metallic glasses allow for a large number of different production methods such as casting, blow molding, injection molding, continuous casting, 3D printing, and many more. These processes enable different cooling rates and are usually designed such that the produced solid part is of a fully glassy nature. For this purpose, the thermophysical properties in the solid and liquid phases are important input parameters for numerical simulations of the production processes. The thermophysical properties for the investigated glass-forming alloys, relevant for the numerical simulation of production processes, were successfully measured.

An overview of the temperature dependence of the viscosity of a large number of elemental materials and alloys shows that good glass formers have a high activation energy E for viscous flow at the liquidus temperature, equivalent to a high energy barrier toward viscous flow.

By the successful vitrification of a 6.5 mm diameter sphere of LM105, the first metallic glass was fabricated in space! This proves the feasibility for in-space production of glassy alloys, e.g., during long-term space exploration missions.

References

1. H.J. Fecht, R.K. Wunderlich, Fundamentals of liquid processing in low earth orbit: From thermophysical properties to microstructure formation in metallic alloys. JOM **69**, 1261–1268 (2017). https://doi.org/10.1007/s11837-017-2417-4

2. M. Mohr, H.-J.J. Fecht, Investigating thermophysical properties under microgravity: A review. Adv. Eng. Mater. **23**, 2001223 (2021). https://doi.org/10.1002/adem.202001223

3. M. Mohr, R.K.K. Wunderlich, D.C.C. Hofmann, H.-J. Fecht, Thermophysical properties of liquid Zr52.5Cu17.9Ni14.6Al10Ti5 – Prospects for bulk metallic glass manufacturing in space. npj Microgravity **5**, 24 (2019). https://doi.org/10.1038/s41526-019-0084-1

4. K.F. Kelton, Crystal nucleation in liquids and glasses, in *Solid State Physics – Advances in Research and Applications*, (1991), pp. 75–177

5. W. Klement, R.H. Willens, P. Duwez, Non-crystalline structure in solidified gold-silicon alloys. Nature **187**, 869–870 (1960)

6. H.W. Kui, A.L. Greer, D. Turnbull, Formation of bulk metallic glass by fluxing. Appl. Phys. Lett. **45**, 615–616 (1984). https://doi.org/10.1063/1.95330

7. A.J. Drehman, A.L. Greer, D. Turnbull, Bulk formation of a metallic glass: Pd40Ni40P 20. Appl. Phys. Lett. **41**, 716–717 (1982). https://doi.org/10.1063/1.93645

8. H.S. Chen, Thermodynamic considerations on the formation and stability of metallic glasses. Acta Metall. **22**, 1505–1511 (1974). https://doi.org/10.1016/0001-6160(74)90112-6

9. A. Inoue, High strength bulk amorphous alloys with low critical cooling rates (overview). Mater. Trans. JIM **36**, 866–875 (1995). https://doi.org/10.2320/matertrans1989.36.866

10. J.Z. Jiang, D. Hofmann, D.J. Jarvis, H.J. Fecht, Low-density high-strength bulk metallic glasses and their composites: A review. Adv. Eng. Mater. **17**, 761–780 (2015). https://doi.org/10.1002/adem.201400252

11. M.D. Demetriou, M.E. Launey, G. Garrett, et al., A damage-tolerant glass. Nat. Mater. **10**, 123–128 (2011). https://doi.org/10.1038/nmat2930

12. Y. Dong, J.-Z. Jiang, H.-J. Fecht, Synthesis and mechanical properties of bulk metallic nanoglasses: A brief review. SDRP J. Nanotechnol. Mater. Sci. **2**, 106–120 (2019). https://doi.org/10.25177/JNMS.2.1.RA.560

13. H. Gleiter, Nanoglasses: A new kind of noncrystalline materials. Beilstein J. Nanotechnol. **4**, 517–533 (2013). https://doi.org/10.3762/bjnano.4.61

14. R. Roy, A.K. Majumdar, Thermomagnetic and transport properties of metglas 2605 SC and 2605. J. Magn. Magn. Mater. **25**, 83–89 (1981). https://doi.org/10.1016/0304-8853(81)90150-5

15. C. Suryanarayana, A. Inoue, Iron-based bulk metallic glasses. Int. Mater. Rev. **58**, 131–166 (2013). https://doi.org/10.1179/1743280412Y.0000000007

16. G.Y. Koga, A.M. Jorge Junior, V. Roche, et al., Production and corrosion resistance of thermally sprayed Fe-based amorphous coatings from mechanically milled feedstock powders. Metall. Mater. Trans. A Phys. Metall. Mater. Sci. **49**, 4860–4870 (2018). https://doi.org/10.1007/s11661-018-4785-y

17. T. Paul, S.H. Alavi, S. Biswas, S.P. Harimkar, Microstructure and wear behavior of laser clad multi-layered Fe-based amorphous coatings on steel substrates. Lasers Manuf. Mater. Process **2**, 231–241 (2015). https://doi.org/10.1007/s40516-015-0017-0

18. G. Telasang, J. Dutta Majumdar, G. Padmanabham, et al., Effect of laser parameters on microstructure and hardness of laser clad and tempered AISI H13 tool steel. Surf. Coat. Technol. **258**, 1108–1118 (2014). https://doi.org/10.1016/j.surfcoat.2014.07.023

19. A. Inoue, B.L. Shen, A.R. Yavari, A.L. Greer, Mechanical properties of Fe-based bulk glassy alloys in Fe-B-Si-Nb and Fe-Ga-P-C-B-Si systems. J. Mater. Res. **18**, 1487–1492 (2003). https://doi.org/10.1557/JMR.2003.0205

20. V. Ponnambalam, S.J. Poon, G.J. Shiflet, Fe-Mn-Cr-Mo-(Y,Ln)-C-B (Ln = Lanthanides) bulk metallic glasses as formable amorphous steel alloys. J. Mater. Res. **19**, 3046–3052 (2004). https://doi.org/10.1557/JMR.2004.0374

21. X.J. Gu, S.J. Poon, G.J. Shiflet, M. Widom, Mechanical properties, glass transition temperature, and bond enthalpy trends of high metalloid Fe-based bulk metallic glasses. Appl. Phys. Lett. **92**, 10–13 (2008). https://doi.org/10.1063/1.2917577

22. M.E. Launey, D.C. Hofmann, J.Y. Suh, et al., Fracture toughness and crack-resistance curve behavior in metallic glass-matrix composites. Appl. Phys. Lett. **94**, 31–33 (2009). https://doi.org/10.1063/1.3156026

23. D.C. Hofmann, J.Y. Suh, A. Wiest, et al., Designing metallic glass matrix composites with high toughness and tensile ductility. Nature **451**, 1085–1089 (2008). https://doi.org/10.1038/nature06598

24. P. Gargarella, A. Almeida, R. Vilar, et al., Formation of Fe-based glassy matrix composite coatings by laser processing. Surf. Coat. Technol. **240**, 336–343 (2014). https://doi.org/10.1016/j.surfcoat.2013.12.049

25. P. Bordeenithikasem, D.C. Hofmann, S. Firdosy, et al., Controlling microstructure of FeCrMoBC amorphous metal matrix composites via laser directed energy deposition. J. Alloys Compd. **157537** (2020). https://doi.org/10.1016/j.jallcom.2020.157537

26. D.C. Hofmann, P. Bordeenithikasem, A. Pate, et al., Developing processing parameters and characterizing microstructure and properties of an additively manufactured FeCrMoBC metallic glass forming alloy. Adv. Eng. Mater. **20**, 1–11 (2018). https://doi.org/10.1002/adem.201800433

27. A. Peker, W.L. Johnson, A highly processable metallic glass: Zr41.2Ti 13.8Cu12.5Ni10.0Be22.5. Appl. Phys. Lett. **63**, 2342–2344 (1993). https://doi.org/10.1063/1.110520

28. A. Wiest, J.S. Harmon, M.D. Demetriou, et al., Injection molding metallic glass. Scr. Mater. **60**, 160–163 (2009). https://doi.org/10.1016/j.scriptamat.2008.09.021

29. X.H. Lin, W.L. Johnson, W.K. Rhim, Effect of oxygen impurity on crystallization of an undercooled bulk glass forming Zr-Ti-Cu-Ni-Al alloy. Mater. Trans. JIM **38**, 473–477 (1997). https://doi.org/10.2320/matertrans1989.38.473

30. C.C. Hays, J. Schroers, U. Geyer, et al., Glass forming ability in the Zr-Nb-Ni-Cu-Al bulk metallic glasses. J. Metastable Nanocrystalline Mater. **8**, 103–108 (2000). https://doi.org/10.4028/www.scientific.net/JMNM.8.103

31. C.C. Hays, J. Schroers, W.L. Johnson, et al., Vitrification and determination of the crystallization time scales of the bulk-metallic-glass-forming liquid Zr58.5Nb2.8Cu15.6Ni12.8Al 10.3. Appl. Phys. Lett. **79**, 1605–1607 (2001). https://doi.org/10.1063/1.1398605

32. D.C. Hofmann, S.N. Roberts, Microgravity metal processing: From undercooled liquids to bulk metallic glasses. npj Microgravity **1**, 15003 (2015). https://doi.org/10.1038/npjmgrav.2015.3

33. W.H. Wang, J.J. Lewandowski, A.L. Greer, Understanding the glass-forming ability of Cu50Zr50 alloys in terms of a metastable eutectic. J. Mater. Res. **20**, 2307–2313 (2005). https://doi.org/10.1557/JMR.2005.0302

34. T. Mei-Bo, D.-Q. Zhao, M.-X. Pan, W.-H. Wang, Binary Cu–Zr bulk metallic glasses. Chin. Phys. Lett. **21**, 901–903 (2004)

35. P. Yu, H.Y. Bai, M.B. Tang, W.L. Wang, Excellent glass-forming ability in simple Cu50Zr 50-based alloys. J. Non-Cryst. Solids **351**, 1328–1332 (2005). https://doi.org/10.1016/j.jnoncrysol.2005.03.012

36. D.C. Hofmann, L.M. Andersen, J. Kolodziejska, et al., Optimizing bulk metallic glasses for robust, highly wear-resistant gears. Adv. Eng. Mater. **19**, 1600541 (2017). https://doi.org/10.1002/adem.201600541

37. A. Inoue, N. Nishiyama, T. Matsuda, Preparation of bulk glassy Pd40Ni10Cu30P20 alloy of 40 mm in diameter by water quenching. Mater. Trans. JIM. **37**, 181–184 (1996)

38. F. Haag, R. Sauget, G. Kurtuldu, et al., Assessing continuous casting of precious bulk metallic glasses. J. Non-Cryst. Solids **521**, 119120 (2019). https://doi.org/10.1016/j.jnoncrysol.2018.09.035

39. G. Lohöfer, P. Neuhaus, I. Egry, TEMPUS – A facility for measuring thermophysical properties of undercooled liquid metals. High Temp.-High Press. **23**, 333–342 (1991)

40. M. Mohr, D.C. Hofmann, H.-J.J. Fecht, Thermophysical properties of an Fe57.75Ni19.25Mo10C5B8 glass-forming alloy measured in microgravity. Adv. Eng. Mater. **2001143**, 1–8 (2020). https://doi.org/10.1002/adem.202001143

41. M. Mohr, R.K.K. Wunderlich, S. Koch, et al., Surface tension and viscosity of Cu50Zr50 measured by the oscillating drop technique on board the International Space Station. Microgravity Sci. Technol. **31**, 177–184 (2019). https://doi.org/10.1007/s12217-019-9678-1

42. M. Mohr, R.K. Wunderlich, K. Zweiacker, et al., Surface tension and viscosity of liquid Pd43Cu27Ni10P20 measured in a levitation device under microgravity. npj Microgravity **5**, 4 (2019). https://doi.org/10.1038/s41526-019-0065-4

43. H.J. Fecht, W.L. Johnson, A conceptual approach for noncontact calorimetry in space. Rev. Sci. Instrum. **62**, 1299–1303 (1991). https://doi.org/10.1063/1.1142488

44. W.J. Parker, G.L. Abbott, Theoretical and experimental studies of the total emittance of metals, in *Symposium on Thermal Radiation of Solids, NASA SP-55*, ed. by S. Katzoff, (1964), pp. 11–28

45. J. Schroers, W.L. Johnson, R. Busch, Crystallization kinetics of the bulk-glass-forming Pd43Ni10Cu27P20 melt. Appl. Phys. Lett. **77**, 1158–1160 (2000). https://doi.org/10.1063/1.1289033

46. S.C. Glade, R. Busch, D.S. Lee, et al., Thermodynamics of Cu47Ti34Zr11Ni8, Zr52.5Cu17.9Ni14.6Al10Ti5 and Zr57Cu15.4Ni12.6Al10Nb5 bulk metallic glass forming alloys. J. Appl. Phys. **87**, 7242–7248 (2000)

47. X. Xiao, R.W. Hyers, D.M. Matson, Surrogate model for convective flow inside electromagnetically levitated molten droplet using magnetohydrodynamic simulation and feature analysis. Int. J. Heat Mass Transf. **136**, 531–542 (2019). https://doi.org/10.1016/j.ijheatmasstransfer.2019.03.028

48. I. Korobeinikov, D. Chebykin, S. Seetharaman, O. Volkova, Effect of boron micro-alloying on the surface tension of liquid iron and steel alloys. Int. J. Thermophys. **41**, 1–14 (2020). https://doi.org/10.1007/s10765-020-02628-5

49. X.M. Xue, H.G. Jiang, Z.T. Sui, et al., Influence of phosphorus addition on the surface tension of liquid iron and segregation of phosphorus on the surface of Fe-P alloy. Metall. Mater. Trans. B Process Metall. Mater. Process. Sci. **27**, 71–79 (1996). https://doi.org/10.1007/BF02915079

50. M.H. Cohen, G.S. Grest, Liquid-glass transition, a free-volume approach. Phys. Rev. B **20**, 1077–1098 (1979). https://doi.org/10.1103/PhysRevB.20.1077

51. N.A. Mauro, M. Blodgett, M.L. Johnson, et al., A structural signature of liquid fragility. Nat. Commun. **5** (2014). https://doi.org/10.1038/ncomms5616

52. S. Ganorkar, Y.-H. Lee, S. Lee, et al., Unequal effect of thermodynamics and kinetics on glass forming ability of Cu–Zr alloys. AIP Adv. **10**, 045114 (2020). https://doi.org/10.1063/5.0002784

53. A.E. Lagogianni, J. Krausser, Z. Evenson, et al., Unifying interatomic potential, g (r), elasticity, viscosity, and fragility of metallic glasses: Analytical model, simulations, and experiments. J. Stat. Mech. Theory Exp. **2016** (2016). https://doi.org/10.1088/1742-5468/2016/08/084001

54. H. Zhang, C. Zhong, J.F. Douglas, et al., Role of string-like collective atomic motion on diffusion and structural relaxation in glass forming Cu-Zr alloys. J. Chem. Phys. **142**, 164506 (2015). https://doi.org/10.1063/1.4918807

55. K. Russew, L. Stojanova, S. Yankova, et al., Thermal behavior and melt fragility number of Cu100-x Zr x glassy alloys in terms of crystallization and viscous flow. J. Phys. Conf. Ser. **144**, 0–4 (2009). https://doi.org/10.1088/1742-6596/144/1/012094

56. G.J. Fan, H.J. Fecht, E.J. Lavernia, Viscous flow of the Pd43Ni10Cu27P 20 bulk metallic glass-forming liquid. Appl. Phys. Lett. **84**, 487–489 (2004). https://doi.org/10.1063/1.1644052

57. L.Y. Chen, M. Mohr, R.K. Wunderlich, et al., Correlation of viscosity with atomic packing in Cu50Zr50 melt. J. Mol. Liq. **293**, 111544 (2019). https://doi.org/10.1016/j.molliq.2019.111544

58. T. Iida, R.I.L. Guthrie, *The Thermophysical Properties of Metallic Liquids: Volume 1 – Fundamentals*, 1st edn. (Oxford University Press, 2015)

59. M. Hirai, Estimation of viscosities of liquid alloys. ISIJ Int. **33**, 251–258 (1986). https://doi.org/10.2355/isijinternational.33.251
60. Y. Su, M. Mohr, R.K. Wunderlich, et al., The relationship between viscosity and local structure in liquid zirconium via electromagnetic levitation and molecular dynamics simulations. J. Mol. Liq. **298**, 111992 (2020). https://doi.org/10.1016/j.molliq.2019.111992
61. M. Mohr, R. Wunderlich, R. Novakovic, et al., Precise measurements of thermophysical properties of liquid Ti–6Al–4V (Ti64) alloy on board the International Space Station. Adv. Eng. Mater. **2000169** (2020). https://doi.org/10.1002/adem.202000169
62. R.K. Wunderlich, Surface tension and viscosity of industrial Ti-alloys measured by the oscillating drop method on board parabolic flights. High Temp. Mater. Process. **27**, 401–412 (2008)
63. R.K. Wunderlich, U. Hecht, F. Hediger, H.J. Fecht, Surface tension, viscosity, and selected thermophysical properties of Ti48Al48Nb2Cr2, Ti46Al46Nb8, and Ti46Al46Ta8 from microgravity experiments. Adv. Eng. Mater. **20**, 1800346 (2018). https://doi.org/10.1002/adem.201800346
64. M. Mohr, R. Wunderlich, Y. Dong, et al., Thermophysical properties of advanced Ni-based superalloys in the liquid state measured on board the International Space Station. Adv. Eng. Mater. **22**, 1901228 (2020). https://doi.org/10.1002/adem.201901228
65. R.K. Wunderlich, H.-J.J. Fecht, G. Lohöfer, Surface tension and viscosity of the Ni-based superalloys LEK94 and CMSX-10 measured by the oscillating drop method on board a parabolic flight. Metall. Mater. Trans. B Process Metall. Mater. Process. Sci. **48**, 237–246 (2017). https://doi.org/10.1007/s11663-016-0847-y
66. K. Higuchi, H.-J. Fecht, R.K. Wunderlich, Surface tension and viscosity of the Ni-based superalloy CMSX-4 measured by the oscillating drop method in parabolic flight experiments. Adv. Eng. Mater. **9**, 349–354 (2007)
67. R. Aune, L. Battezzati, R. Brooks, et al., Surface tension and viscosity of industrial alloys from parabolic flight experiments – Results of the ThermoLab project. Microgravity Sci. Technol. **15**, 11–14 (2005)
68. R.K. Wunderlich, H.-J. Fecht, Surface tension and viscosity of NiAl catalytic precursor alloys from microgravity experiments. Int. J. Mater. Res. **102**, 1164–1173 (2011). https://doi.org/10.3139/146.110572
69. I. Egry, R. Brooks, D. Holland-Moritz, et al., Thermophysical properties of liquid Al-Ni alloys. High Temp.-High Press. **38**, 343–351 (2009)
70. R.K. Wunderlich, H.-J. Fecht, I. Egry, et al., Thermophysical properties of a Fe-Cr-Mo alloy in the solid and liquid phase. Steel Res. Int. **83**, 43–54 (2012). https://doi.org/10.1002/srin.201100156
71. E. Ricci, L. Battezzati, R. Brooks, et al., Thermophysical properties of Cu-based industrial alloys in the liquid phase. High Temp. -High Press. **38**, 43–61 (2009)
72. R.K. Wunderlich, H.-J. Fecht, Thermophysical property measurements by electromagnetic levitation methods under reduced gravity conditions. J. Jpn. Soc. Microgravity Appl. **20**, 192–205 (2003)
73. Z. Evenson, T. Schmitt, M. Nicola, et al., High temperature melt viscosity and fragile to strong transition in Zr–Cu–Ni–Al–Nb(Ti) and Cu47Ti34Zr11Ni8 bulk metallic glasses. Acta Mater. **60**, 4712–4719 (2012). https://doi.org/10.1016/j.actamat.2012.05.019
74. Z. Evenson, S. Raedersdorf, I. Gallino, R. Busch, Equilibrium viscosity of Zr-Cu-Ni-Al-Nb bulk metallic glasses. Scr. Mater. **63**, 573–576 (2010). https://doi.org/10.1016/j.scriptamat.2010.06.008

75. C.A. Angell, Formation of glasses from liquids and biopolymers. Science (80-) **267**, 1924–1935 (1995). https://doi.org/10.1126/science.267.5206.1924
76. E.R. Homer, M.B. Harris, S.A. Zirbel, et al., New methods for developing and manufacturing compliant mechanisms utilizing bulk metallic glass. Adv. Eng. Mater. **16**, 850–856 (2014). https://doi.org/10.1002/adem.201300566
77. D.C. Hofmann, R. Polit-Casillas, S.N. Roberts, et al., Castable bulk metallic glass strain wave gears: Towards decreasing the cost of high-performance robotics. Sci. Rep. **6**, 1–11 (2016). https://doi.org/10.1038/srep37773
78. D.C. Hofmann, P. Bordeenithikasem, L.P. Tosi, et al., Towards additively manufacturing excavating tools for future robotic space exploration. Eng. Rep. **2**, 1–12 (2020). https://doi.org/10.1002/eng2.12219

Chapter 20
Electrical Resistivity Measurements on the International Space Station for the Studies of Dynamics in Metallic Liquids

Anup K. Gangopadhyay and Kenneth F. Kelton

1 Introduction

If a liquid is cooled rapidly enough to bypass crystallization, it becomes frozen into an amorphous solid, i.e., a glass. Among the many fascinating properties of glass-forming liquids [1], the most scrutinized and least understood phenomenon is the evolution of the dynamic properties with temperature [2], which include the viscosity, diffusion coefficient, structural relaxation time, etc. Since numerous reviews [2–4] have been devoted to discussions of these properties, here, only some basic trends are discussed, focusing on the viscosity. This property changes by 12–14 orders of magnitude between the liquidus temperature, T_l, and the glass transition temperature, T_g.

The most widely used expression for the viscosity is the Vogel-Fulcher-Tammann (VFT) [5–7] equation, $\eta(T) = A \exp(DT_o/(T - T_o))$, where A, D, T_o are sample-dependent parameters. Originally proposed for polymeric liquids, this expression is inadequate for the metallic [8] and oxide [9] liquids. Several attempts have been made to unify the viscosities of diverse liquids [8–11] but with limited success. Angell proposed an important way to classify the liquids according to the change in viscosity while approaching T_g [12]. A parameter called fragility was introduced, which was defined in terms of the slope of the logarithm of the viscosity with respect to inverse temperature normalized to T_g, $m = d\log\eta/d(T/T_g)$ evaluated at T_g. Liquids for which the viscosity increases rapidly near T_g are called "fragile" and those with smaller slopes are called "strong." The VFT parameter, D, also reflects this property; however, in this case, a larger D represents a "strong" liquid. In contrast to the dynamical properties near T_g, much less attention has been paid to their evolution at high temperatures. Although known for a long time and observed

A. K. Gangopadhyay (✉) · K. F. Kelton
Washington University in St. Louis, St. Louis, MO, USA
e-mail: anup@wuphys.wustl.edu

in almost all types of liquids (metallic, molecular, oxides), the importance of a crossover temperature, T_A, at temperatures much above T_g, has not been widely recognized until recently. T_A is the temperature at which the high-temperature Arrhenius temperature dependence of viscosity, $\eta = \eta_o \exp(E/k_B T)$, starts to break down as the activation energy, E, becomes temperature dependent below T_A. Recent experimental and molecular dynamics simulation studies identified T_A as the temperature where cooperative dynamics sets in [8, 10, 13–15]. At higher temperatures, the atomic dynamical processes are uncorrelated; they become more and more cooperative as the temperature is lowered below T_A, causing the viscosity to increase rapidly. Mode coupling theory also postulates a transition at a temperature T_C [16]. However, that transition temperature is usually below T_l, while T_A is generally above T_l [8], at least in metallic liquids. It is important to emphasize that this crossover is in no way indicative of a phase transition. Therefore, associating this with a liquid-liquid transition as often proposed in the literature is misleading. In our view, this term should be reserved for cases where a change in coordination number occurs at a well-defined temperature. In contrast to a liquid-liquid transition, this crossover appears to be a generic behavior in most liquids. Another important characteristic of the liquids is the onset of dynamical heterogeneity [2, 17, 18] where the atomic dynamics in different parts of a liquid are different. It has not yet been settled whether the onset of the dynamical heterogeneity starts at T_A or T_C.

Experimentally, T_A can be measured from the viscosity. Other local probes, such as NMR, can also identify T_A [19]. We have recently demonstrated that a distinct change in the temperature coefficient of the electrical resistivity [20] occurs for $Cu_{50}Zr_{50}$ and $Zr_{64}Ni_{36}$ near T_A. Most surprisingly, the resistivity reaches a near saturation above T_A in a highly resistive state. This is entirely different from the usual resistivity saturation with small values observed near liquid helium temperature (4.2 K) in many crystalline and amorphous solids. The connection between T_A and electrical resistivity is entirely a new result, which opens up the possibility for studying the dynamics in liquids using this probe. The mechanism responsible for this unusual observation is still speculative; more in-depth studies on many different liquids are needed to understand this result. The experiments to be described here were possible because of the recently added experimental facility [21] on the International Space Station (ISS) for such measurements under microgravity using the electromagnetic levitation technique (EML). Before presenting those results, the necessary background and measurement techniques will be described in the next few sections.

2 Relevant Background

2.1 Temperature Dependence of Liquid Viscosity

The viscosities have been measured for a wide variety of liquids over many centuries. Terminal velocity measurements of a sphere falling through a liquid

column [22], torque measurements in rotating viscometers [23], and beam-bending experiments on highly viscous materials [24] are some of the experimental techniques generally used for such measurements. However, measurements of highly reactive materials, such as high-melting temperature metallic liquids, require more sophisticated experimental techniques, especially for the supercooled metastable liquids. Rapid crystallization below T_1 for liquids in containers makes such measurements impossible in most cases. Containerless measurement techniques, using electrostatic (ESL) [25], electromagnetic [26], aerodynamic [27], and aeroacoustic [28] levitation methods, have made such measurements possible. The absence of a container allows the liquid to be retained in the supercooled state for a sufficiently long time to make the measurements. This also eliminates the possibility of chemical reactions with the container material for reactive liquids. However, since aerodynamic and aeroacoustic levitation techniques require a gas environment, they are not suitable for most metallic liquids; small amount of impurities (parts per million) even in the most purified gases may catalyze crystallization. Therefore, the ESL and EML are the most suitable techniques for such measurements. Usually, surface oscillations are excited on levitated liquid drops and the decay constant of the oscillation amplitude, λ, is measured. λ and the viscosity, η, follow the relation [29]

$$\lambda = 20\pi\eta R_o/3m \tag{20.1}$$

where R_o and m are the radius and mass of the liquid drop. More details about this technique are provided in the literature [30] and also available in this book (Chap. 12).

The viscosities of a few metallic liquids measured by the ESL technique are shown for illustration in Fig. 20.1a. As mentioned earlier, the high temperature viscosity starts to deviate from an Arrhenius-type relationship below a characteristic temperature, T_A, which is marked by vertical arrows in the figure. Figure 20.1b shows the viscosities for a few oxide and molecular liquids to demonstrate that such behavior is not just confined to the metallic liquids; the data for the oxide and molecular liquids are taken from the literature [31–33]. Since the onset of T_A is not very well defined, an algorithm was developed by Ashcraft [34] to identify this temperature. In this method, the residual sums (R^2) between the measured and linear fits were tracked as the high temperature data points were selectively removed. The value of R^2 starts decreasing and reaches a minimum when all data above T_A are removed. The typical error in T_A determined by this method is about 2–5%.

2.2 Physical Interpretation of $\mathbf{T}_A$ from Molecular Dynamics Studies

The availability of fast computers has made molecular dynamics (MD) simulations a powerful tool for studying liquids. One advantage of MD studies is the ability to
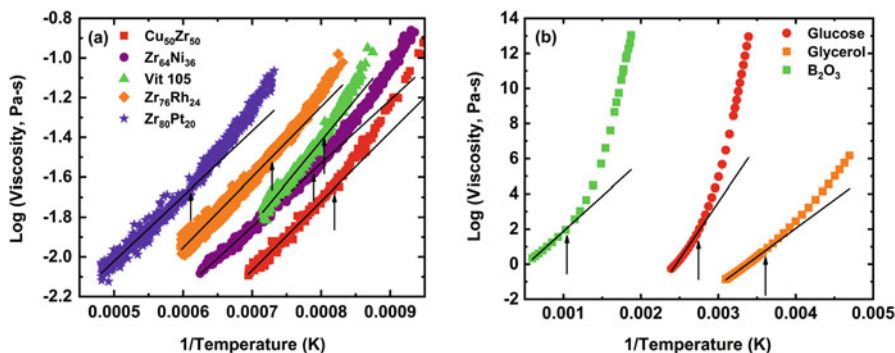
Fig. 20.1 The logarithm of the viscosity as a function of inverse temperature for a few metallic (**a**) and a few oxide and molecular liquids (**b**). The arrows identify the crossover temperatures, T_A. The data for the metallic liquids are from ESL experiments; the data for glucose [31], glycerol [32], and B_2O_3 [33] are taken from the literature

simulate the three-dimensional structure and dynamical behavior of liquids over a much wider temperature and pressure range than can be studied experimentally. Large vapor pressures at high temperatures and rapid crystallization of the supercooled liquids often limit the experimental data that can be obtained. Moreover, scattering experiments provide only two-dimensional snapshots of three-dimensional liquids, which handicap the ability to obtain detailed understanding of liquid structures. However, MD simulations also have many limitations. First and foremost, it is difficult to develop accurate interatomic potentials for multicomponent liquids. Second, the simulation times allowed by even the fastest computers are not sufficient to fully relax the liquid structure in the deeply supercooled and glassy states. Therefore, the MD data can be trusted only when the interatomic potentials are accurate and the simulation times are comparable to the structural relaxation times of the liquids. Naturally, then, the MD studies are most reliable at high temperatures (above and near T_1), which are of central interest in this discussion.

MD simulations are made for a large ensemble of atoms interacting via a model interaction potential. The ensemble size must be large enough (typically many tens of thousands to a million) so that the contributions of surface atoms are minimized and the properties of the bulk liquid can be simulated. While Newtonian dynamics is used in classical MD simulations, quantum or ab-initio MD studies use density functional theory to describe the interactions. Although more accurate, quantum MD simulations are restricted by the computational time to studies of only a few hundred atoms. The evolution of the atomic structure and dynamics [35], including spatial and dynamic heterogeneities [2, 17, 18], are monitored in MD studies.

MD simulations show the development of topologically and chemically ordered regions in liquids with decreasing temperature, which appear to percolate through the liquid at the glass transition temperature. An important question is at what

Fig. 20.2 The ratio τ_M/τ_{LC} as a function of T/T_A from MD simulations for ab initio and various embedded atom potentials for elemental Fe and two BMGs. The liquidus temperatures (T_l) are indicated. (Reprinted from Ref. [13], copyright (2013), American Physical Society)
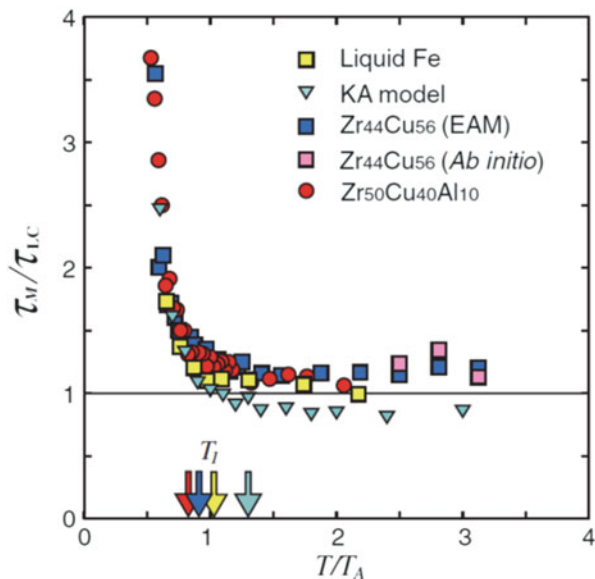
temperature the ordered regions start to form in a liquid. MD studies have shown that the atoms in the liquid associate and dissociate spontaneously. An investigation of the lifetime of these atomic bonds [13, 14] has been used to address this question in metallic liquids. At high temperatures, the atomic bonds between neighboring atoms are short-lived. If the time required to change the coordination number of a cluster of atoms by one atom (τ_{LC}) is too short, changes in the clusters cannot be communicated to neighboring clusters of atoms. Such fluctuations then occur independently in different atomic clusters. As the temperature is lowered, the fluctuations become sufficiently long lived so that they begin to influence nearby clusters, and the cluster dynamics become cooperative. This begins at a crossover temperature, T_A, which is characteristic of the particular liquid.

This structural cooperativity is reflected in the dynamical properties, such as the viscosity and diffusion coefficient. MD simulations for one ab-initio and a number of embedded atom potentials that represent a range of metallic liquids were studied to illustrate this point [13], focusing on the ratio of the average bond lifetime, τ_{LC}, and the Maxwell relaxation time, τ_M. The Maxwell relaxation time is defined as $\tau_M = \eta/G_\infty$, where G_∞ is the infinite frequency (instantaneous) shear modulus and η is the shear viscosity. In all of the cases considered, it was observed that the ratio τ_M/τ_{LC} remains constant above T_A (Fig. 20.2) and rises below that temperature. Since τ_{LC} is determined by the energy required to change the local coordination number, this result indicates that the activation energy for η is related to the bond energy and remains constant above T_A. This naturally explains the Arrhenius temperature dependence for the viscosity above T_A. As shown in Fig. 20.2, below T_A, τ_M increases faster than τ_{LC}, reflecting an increasing cooperativity in the dynamical behavior. With increasing cooperativity, the viscosity becomes super-Arrhenius with
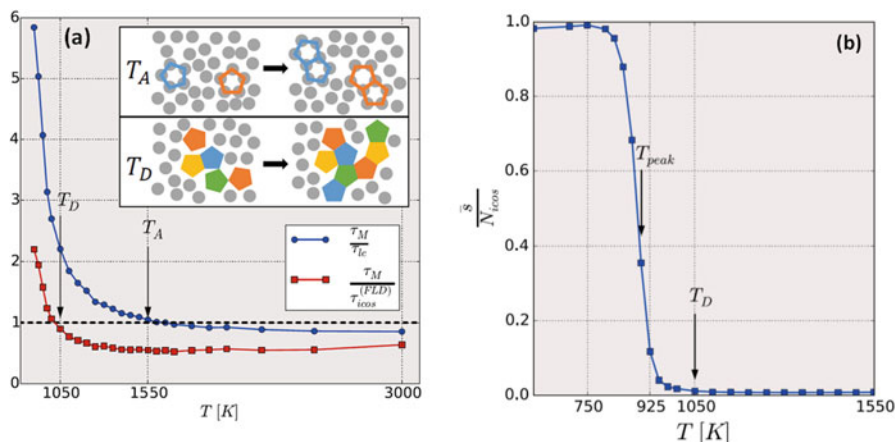
Fig. 20.3 (**a**) MD simulations for the ratio τ_M/τ_{LC} (blue circles) and $\tau_M/\tau_{icos}^{(FLD)}$ ($\tau_{icos}^{(FLD)}$ is the domain-connected icosahedron lifetime). Inset – schematic in 2D of the cooperative rearrangements that begin at T_A and T_D. (**b**) The fraction of the total number of icosahedra in a domain connected icosahedron. (Reprinted from Ref. [36] with permission: Taylor and Francis Ltd www.tandfonline.com)

an increasing activation energy with decreasing temperature. As mentioned earlier, the presence of a crossover temperature is a well-recognized experimental result. The MD results provide a local structural mechanism for the crossover. For most metallic liquids, T_A lies above T_l, although there are some exceptions. Interestingly, the reduced temperature, T_A/T_g, correlates well [14] with the fragility parameter, m, that was introduced by Angell [12]. The ratio is larger for the stronger liquids and smaller for the fragile ones, which is similar to the parameter D in the Vogel-Fulcher expression. The important point to note is that T_A signifies an important temperature below which cooperative dynamics sets in; this is related to structural ordering. This process is continued until the liquid freezes into a glassy solid. Therefore, T_A attains a special significance in the context of the glass transition.

A recent MD simulation considered the case of a binary $Cu_{64}Zr_{36}$ bulk glass-forming liquid [36] and observed a crossover from high-temperature Arrhenius behavior to super-Arrhenius behavior below T_A. The ratio τ_M/τ_{LC} is unity at high temperatures and grows dramatically upon decreasing the temperature below T_A (Fig. 20.3), as in the earlier study with model potentials [13]. The dominant structural motif in this liquid is icosahedral, which is consistent with a previous study [37]. Above T_A, this ordering is in the form of isolated icosahedral clusters. Below T_A, the clusters connect to form extended clusters (inset of Fig. 20.3a). Interestingly, another crossover temperature, T_D, was also identified (Fig. 20.3b) below T_A, which was not observed in the earlier MD study. This temperature was based on the ratio of the Maxwell relaxation time to the average time required for an icosahedral cluster, within a domain of interpenetrating icosahedra, to gain or lose a

vertex atom or otherwise distort its shape, $\tau_M/\tau_{i\ \cos}^{(FLD)}$. This ratio is smaller than unity at high temperatures, becomes one at T_D, and grows dramatically as the temperature is decreased. A very striking conclusion is that above T_D, the probability that a given cluster belongs to a network of clusters is small, while near T_D, this probability increases so that essentially all of the clusters are associated with domains. This transition is very gradual, occurring over more than 200 K. Therefore, it does not follow the trademark of a traditional (first-/second-order) phase transition. Irrespective of the type of the transition at T_D, the MD results indicate that the structural and dynamical processes that finally lead to glass transition possibly start at a much higher temperature, such as T_A.

2.3 Structural Signature for $\mathbf{T}_A$

As discussed in the previous section, since the onset of cooperativity has a structural origin, it is natural to expect that it should also be manifested in the liquid structural data. Experimentally, the structure factor in reciprocal space, $S(q, T)$, and the corresponding pair correlation function in real space, $g(r, T)$, are measured in the scattering experiments using x-rays or neutrons. As the liquid is cooled, the heights of the broad peaks of both functions increase and their widths decrease, indicating the development of more ordered structures. However, compared to the 12–14 orders of magnitude increase in the viscosity between T_l and T_g, the changes in $S(q, T)$ and $g(r, T)$ are small, only a few percent. Extensive studies by our group on metallic liquids have demonstrated that the rate of change of the first peak height and peak width of $S(q, T)$ and $g(r, T)$ correlate well with the fragility, indicating a connection between structure and dynamics [38, 39]. However, no detectable anomaly in those quantities was observed near T_A. Only recently, some indication for T_A was found in the second peak of $S(q, T)$ [40]. This is usually an overlap of two peaks, which can be separated by fitting to two Gaussian functions. The height of the low-q part of this peak showed a change in slope at a characteristic crossover temperature, T_S, as shown in Fig. 20.4.

The values of T_S in 10 binary and ternary liquids studied were observed to correlate well with the T_A values determined from the corresponding viscosity data, as shown in Fig. 20.5. However, since the magnitude of T_S was always 50–100 K lower than T_A, the structural connection between T_S and T_A was not firmly established. The difference may reflect less sensitivity in the scattering studies to the structural changes. An important point to note is that $S(q, T)$ represents an average property of all atoms in the liquid. It has been argued that the liquid dynamics are determined mostly by the most mobile subset of atoms [41, 42]. Therefore, the change in $S(q, T)$ near T_A may be determined by this subset of atoms, which may have a small contribution to the total $S(q, T)$. So the structural imprint of T_A on these average properties may be difficult to observe.
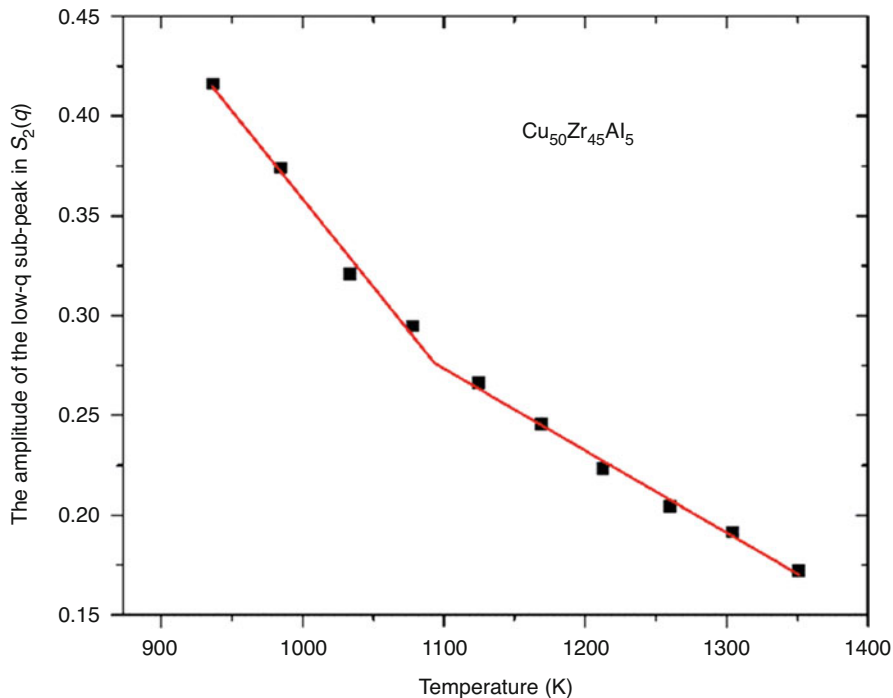
Fig. 20.4 The height of the low-q subpeak of the 2nd peak of $S(q, T)$ of $Cu_{50}Zr_{45}Al_5$ liquid as a function of temperature. The red line was determined from piecewise linear function fits to the data. A change in slope occurs near a characteristic temperature, $T_s = 1080$ K. (Reprinted from Ref. [40], copyright (2018), American Institute of Physics)

2.4 Electrical Resistivity of Solids and Liquids

The electrical resistivity, $\rho(T)$, is a fundamental property of every material. The two most relevant parameters that determine $\rho(T)$ are the charge carrier density and their scattering rates with various forms of excitations. Since in metals the conduction electron density is a weak function of temperature, the temperature dependence of resistivity is determined by the scattering rate of electrons and conversely by their mean free path. Due to the development of the quantum theory of solids [43] and the long-range periodicity of atoms in crystalline solids, the theories of charge conduction for the weakly correlated electrons in metals are fairly well developed. The theories for the strongly correlated electrons, however, are still at various stages of development [44]. At very low temperatures when the thermal excitations of all scattering modes become nearly frozen, the resistivity reaches near saturation. Called the "residual resistivity," this terminal property is determined by the concentrations of impurities and defects in the crystal. This property is routinely used to estimate the levels of impurities and imperfections in crystals [43]. As the temperature increases, various modes of thermal excitations, such as phonons (lattice vibration) and
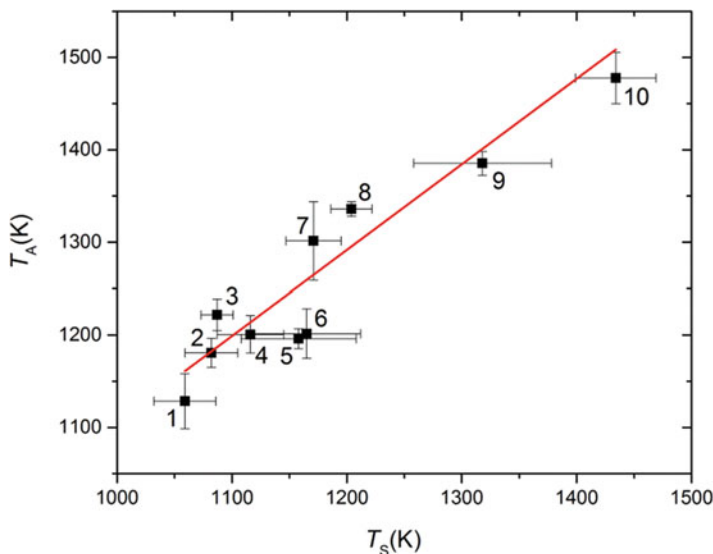
Fig. 20.5 The correlation between the crossover temperature (T_S) obtained from measurements of the growth in intensity of the low-q subpeak in $S_2(q, T)$ and that obtained from viscosity measurements (T_A). The alloy compositions corresponding to the numbers are $Cu_{46}Zr_{54}$ (1), $Cu_{50}Zr_{42.5}Ti_{7.5}$ (2), $Cu_{50}Zr_{45}A_5$ (3), $Cu_{50}Zr_{40}Ti_{10}$ (4), $Cu_{50}Zr_{50}$ (5), $Cu_{64}Zr_{36}$ (6), LM601 (7), Vit105 (8), $Zr_{56}Co_{28}Al_{16}$ (9), and $Zr_{82}Ir_{18}$ (10). (Reprinted from Ref. [40], copyright (2018), American Institute of Physics)

magnons (if magnetic) and even electrons, scatter the charge carriers. The temperature-dependent resistivity is then routinely used to study these excitations in crystalline solids. A metal may also undergo various types of phase transitions with increasing temperatures, including crystallographic [45], order-disorder [46], magnetic, and superconducting [43, 44] transitions. The electrical resistivity is routinely used to study these structural and electronic changes. This also applies to glasses, where the glass transition temperature, structural relaxation near T_g [47], and crystallization kinetics [48] are probed by electrical resistivity measurements.

The theoretical formulation of the electronic properties of disordered (crystallographic, chemical, magnetic, etc.) solids is more complicated than in crystalline ones. Extreme disorder [49] or strong electron-electron correlations [50] may cause the electron wave functions to become localized, producing a metal-insulator transition. Although understood at a fundamental level [51], many details of disordered metallic solids are still under development [44, 52, 53]. The theories for liquids are even less well developed. Liquids have no long-range spatial order. Instead, they have only short- and medium-range order, which does not extend beyond a few nearest neighbor atoms. Unlike glasses, the local order is not static but changes rapidly with time and temperature. These conditions make it difficult to develop quantitative theories for $\rho(T)$ in liquids. The discovery of metallic glasses in the early sixties [54] and bulk metallic glasses [55] in the early eighties of the last century

rejuvenated interest in this question. Since the disorder is frozen in glasses, it is somewhat easier to formulate a theory for $\rho(T)$ of glasses than for liquids. The experimental results from the electrical resistivity measurements before the advent of the bulk metallic glasses and their theoretical interpretation have been reviewed in several publications [56–58]. We are not aware of any recent review on this topic for the bulk metallic glasses. Here, we only discuss some unusual electrical properties of metallic glasses that are relevant for the present discussion.

As mentioned earlier, ordered crystalline metals reach a nearly saturated $\rho(T)$ of a few $\mu\Omega-\text{cm}$ at very low temperatures. In contrast, the low temperature $\rho(T)$ of metallic glasses are typically one to two orders of magnitude larger [57, 58]. The highly disordered state of atoms (both spatially and chemically) in metallic glasses is responsible for their high electrical resistivities. In stark contrast to crystalline solids, the temperature coefficient, $d\rho/dT$, for metallic glasses may be positive or negative depending on the magnitude of their electrical resistivity. Usually, alloys with $\rho > 150 \, \mu\Omega-\text{cm}$ show a negative value of $d\rho/dT$ [59], although there are exceptions [60]. One of the most influential theories for metallic liquids was developed by Ziman and coworkers [61, 62]. The resistivity was expressed in terms of an integral that contains the structure factor, $S(q)$ (partial $S(q)s$ for alloys), and the pseudopotential, $|V(q)|$ [61, 62], or the scattering matrix (t-matrix) [63, 64]. In both cases, the sign of $d\rho/dT$ arises due to the temperature dependence of the first peak height of $S(q)$ and its position with respect to the Fermi wave vector, k_f. When $2k_f$ lies on the higher q-side of the first peak of $S(q)$, $d\rho/dT$ becomes negative because of the decrease of $S(q_{2k_F})$ with increasing temperature. Since the higher q-side of the peak of $S(q, T)$ makes a much bigger contribution to this integral, the sign of $d\rho/dT$ is very sensitive to the position of $2k_f$ with respect to the peak position of $S(q, T)$.

Electrical resistivity measurements for metallic glasses have been mostly confined to near and below T_g [47, 48, 57, 58]. Fewer studies have been reported for the corresponding liquids; some examples are provided in refs. [65–69]. The temperature dependence of the resistivity may be only qualitatively explained by Faber-Ziman-type theories because of difficulties in estimating $2k_f$. Reliable experimental data for more metallic liquids at high temperatures are needed to develop more quantitative models. This was one motivation for the experiments that are described here. A second motivation is that since the resistivity is determined by the structure factor, and since electrons scatter more strongly from the structure than to x-rays or neutrons, the electrical resistivity might be sufficiently sensitive to detect the subtle structural changes at T_A. This was found to be the case.

3 Electrical Resistivity Measurement

The four-probe technique (with two current and two voltage leads connected to a sample) is the standard method for measuring the electrical resistivity of solids and liquids. The experimental results for the glasses at low temperatures, which will be

presented later, were obtained by using this method. However, chemical reaction with the current and voltage leads often cause problems for the high T_1 liquids. These may be eliminated by contactless methods, such as mutual inductance-type ac measurements [70, 71]. This consists of two coils, a primary one to generate a small ac magnetic field (a few Gauss) and a secondary coil wound on top of the primary near its center to pick up a signal from the sample. The ac magnetic field generates eddy currents on the surface of the sample, which interact with the applied field and change the mutual inductance between the coils. The mutual inductance is a complex quantity; the real part is related to the magnetic moment (susceptibility) and the imaginary part (dissipative loss due to electrical resistance) to the electrical resistivity. Such simple homebuilt devices are used in many laboratories around the world; commercial products are also available. Although this technique eliminates the need for attaching electrical leads, containers are still required.

To the best of our knowledge, the first noncontact containerless resistivity measurements on levitated Si and Ge liquids were made using an aerodynamic levitator [72]. The change in the inductance of a coil inside the chamber was measured when a levitated sample was inserted into it. However, as mentioned in §2.1, the aerodynamic levitation technique is not suitable for measurements on metallic liquids, especially in the supercooled state. The ESL was used to measure the electrical resistivity of liquid Al by Rhim et al. [73] using a different measurement technique. The electrical resistivity was determined from the torque experienced by a liquid sphere of Al under vacuum in a rotating magnetic field, which was produced by passing ac currents in four identical coils mounted on the positioning electrodes. This assembly acted like an asynchronous induction motor, where the coils acted as the stator and the sample as a rotor.

The ISS-EML facility uses the same principle as used in mutual inductance measurements but with a very different coil geometry [21]. Here, only the most essential aspects of this technique are discussed. As shown in Fig. 20.6, the EML consists of a pair of identical water-cooled Cu coils. Two separate circuits feed ac voltages into these coils. One is a positioner voltage from a power amplifier that feeds equal amounts of currents in the opposite directions into the upper and lower coils at 150 kHz. This produces a quadrupolar radio frequency magnetic field. A spherical, 6–8-mm-diameter sample is positioned by this field at the center of the coils where the field is minimum. Because of the microgravity environment, no force is necessary to levitate the sample; the quadrupolar field just maintains the sample in position. A separate power amplifier feeds currents in the same directions into the two coils at about 350–400 kHz to produce a dipolar field for heating the sample. Therefore, heating and positioning can be controlled independently, which is different from most of the ground-based EML instruments. The total complex admittance of the electrical heating circuit is given by [21, 74]:
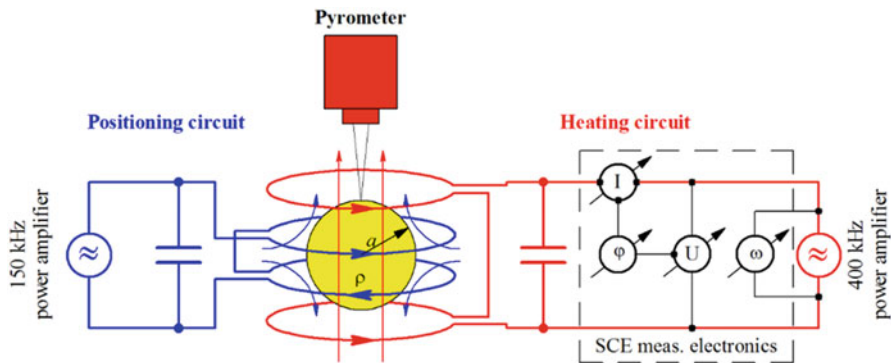
Fig. 20.6 The electrical circuit for resistivity measurements on the ISS-EML. Details are provided in the text. (Reprinted with permission from Ref. [20]. Copyright (2019) by the American Physical Society)

$$\widetilde{Y}_{\text{tot}} = 2i\omega C + \frac{2}{R_{\text{L}} + i\omega L + \widetilde{Z}_{\text{S}}(a,\rho)/2}, \tag{20.2}$$

where C is the capacitance of the condenser, L is the inductance, and R_{L} is the resistance of the coil; $\widetilde{Z}_{\text{S}}(a,\rho)$ is the complex impedance of the sample, which depends on the sample radius, a, and its electrical resistivity, ρ. The sample coupling electronics (SCE) unit in the EML facility on the ISS measures the amplitude of the RF current through the circuit, I_o, the voltage drop over the circuit, U_o, and the phase shift, φ, between the voltage and current and the frequency, ω. The total admittance of the circuit can then be obtained as

$$\widetilde{Y}_{\text{tot}} = \frac{I_0}{U_{\text{o}}} e^{-i\varphi}, \tag{20.3}$$

Without a sample, i.e., for $\widetilde{Z}_{\text{S}} = 0$, the circuit parameters C, L, and R_{L} can be obtained from Eq. (20.2). With these data, a subsequent measurement of $\widetilde{Y}_{\text{tot}}$ with a sample in the levitator yields the sample impedance, $\widetilde{Z}_{\text{S}}(a,\rho)$. For a spherical sample (as is the case for the liquid under microgravity) in a homogeneous RF magnetic field, the theoretical relation between $\widetilde{Z}_{\text{S}}(a,\rho)$, the sample radius, a, and the resistivity, ρ, has been calculated in refs. [21, 74]. The sample is first melted and heated to about 300–400 K above the melting temperature under high vacuum (10^{-8}Torr) or in inert gas atmosphere and then cooled with very small heater (0.1 V) and positioner (2–3 V) voltages so that shape distortions of the liquid droplet remain minimal. This allows the temperature-dependent sample radii to be determined from the video images of the levitated droplet using standard procedures [21, 75], which are required to estimate the electrical resistivity from the measured sample impedance.

4 Electrical Resistivity of $Cu_{50}Zr_{50}$ and $Zr_{64}Ni_{36}$ Liquids

Figure 20.7a, b show the measured electrical resistivity as a function of temperature for two alloys, $Zr_{64}Ni_{36}$ and $Cu_{50}Zr_{50}$, respectively, in the equilibrium and supercooled states. The former is a marginal glass former (critical thickness less than 100 microns) [76], and the latter forms a bulk metallic glass [77]. The T_L for these alloys are 1283 and 1222 K, respectively. The precision in the resistivity measurement is about 2%, 1% of which comes from the sample radius measurement. However, relative changes can be measured to approximately a 0.7% precision. The raw data are shown in the insets, and the 200-point adjacent smoothed data are shown in the main figures. Both alloys show negative temperature coefficients of resistivity, $d\rho/dT$; this is expected [59] since the magnitudes of the resistivities are large. This can be explained qualitatively by modified Ziman theory [62–64], using partial structure factors obtained from MD simulations (experimental $S(q, T)$ partials would need to be determined from neutron scattering experiments using isotopically enriched samples) and reasonable values of the Fermi wave vector (k_f) [supplemental in 20, 78]. The most interesting observation, however, is the saturation/near saturation of resistivity above T_A (shown by the shaded regions). This cannot be explained by the Ziman theory since the first peak of the total $S(q, T)$ and the partial structure factors continue to decrease above T_A, indicating that there should be a continuous decrease in resistivity, not a saturation.

An alternative explanation to the Faber-Ziman-type theories for the negative $d\rho/dT$ in glasses at low temperature was suggested a few decades ago [79, 80]. As mentioned in §2.4, electrons become localized in the presence of strong disorder,
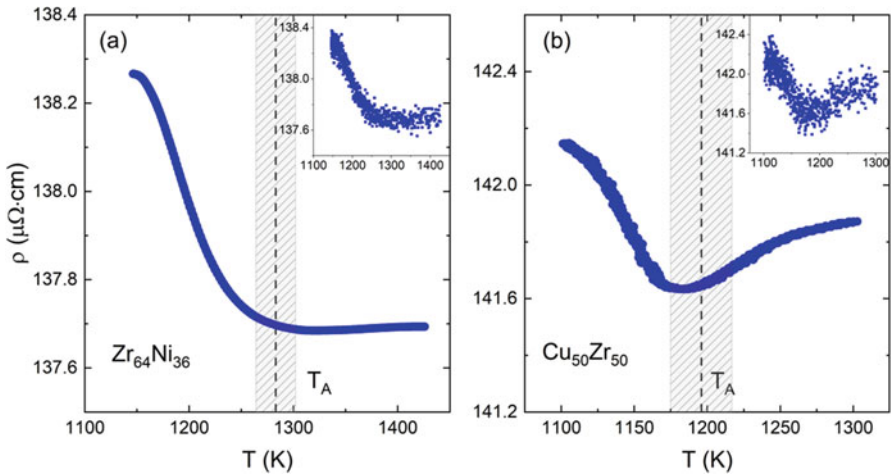
Fig. 20.7 The electrical resistivities of $Zr_{64}Ni_{36}$ (**a**) and $Cu_{50}Zr_{50}$ liquids. Both show negative temperature coefficients and near saturation above T_A (shaded regions). T_A was determined from viscosity measurements (Fig. 20.1). (The data are reprinted with permission from Ref. [20]. Copyright (2019) by the American Physical Society)

Fig. 20.8 The electrical
conductivities of $Zr_{64}Ni_{36}$
(**a**) and $Cu_{50}Zr_{50}$ increases
as $\sqrt{T}$ for the glasses. The
liquid data are the same as in
Fig. 20.7. T_A and the glass
transition temperature, T_g,
are marked by dashed
vertical lines. (The data are
reprinted with permission
from Ref. [20]. Copyright
(2019) by the American
Physical Society)
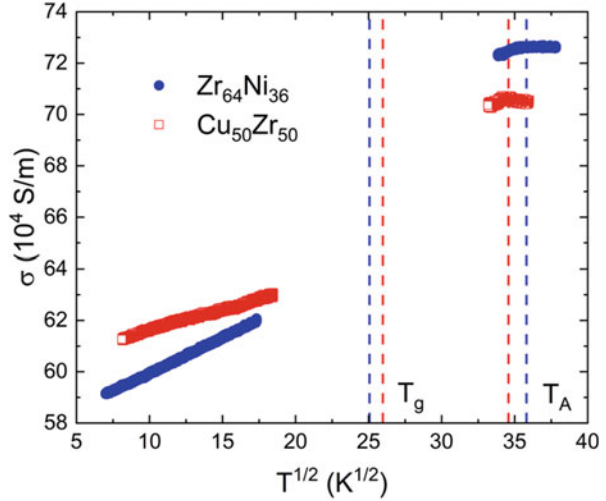
which is called Anderson localization. A similar concept of "weak localization" due
to chemical and structural disorder was introduced for the metallic glasses at low
temperatures [79, 80]. However, this differs from Anderson localization, where the
resistivity increases following a $T^{1/4}$ law [81] as the electrons start to hop from one
atomic site to another in an activated process. In the weak localization theories,
multiple inelastic scattering of electrons by phonons are coherent at low tempera-
tures. As the temperature increases, the loss of coherence in the scattering weakens
electron localization, and the electrical conductivity, $\sigma(T)$, increases (the resistivity
decreases) almost linearly at low temperatures and as $\sqrt{T}$ above the Debye temper-
ature, Θ_D [80]. This behavior has been observed at low temperatures in the $Cu_{50}Zr_{50}$
glass [80]. Figure 20.8 shows the electrical conductivity, $\sigma(T)$, for the two glasses at
low temperature, along with those of the liquids at high temperature. The data seem
to follow a $\sqrt{T}$ dependence for both glasses; however, because of the limited
temperature range, its functional relationship with temperature in the liquid is not
clear.

   Since no theory exists that predicts a saturation of the resistivity/conductivity in
liquids, a qualitative argument is provided [20]. T_g is usually defined as the temper-
ature where the structural relaxation time is about 100 s. As the temperature
increases, the relaxation time decreases sharply, in a similar fashion as the viscosity.
Since the electron scattering times are in the nano- to femtosecond ranges, such
structural changes in supercooled liquids above T_g appear static to the electrons.
Therefore, the increase in electrical conductivity above and below T_g should not be
entirely different. However, at higher temperatures, the short- and medium-range
order also starts to change rapidly. Since liquids cannot sustain shear, the normal
concept of phonons breaks down in liquids. However, the high-frequency (instan-
taneous) shear modulus remains finite, as was discussed in §2.2. Two things might
happen in the liquid with increasing temperature. First, the structural relaxation time

may become comparable to the electron scattering mean free time at higher temperatures. This may add an additional scattering mechanism for the electrons. If the structural relaxation time decreases faster than the electron scattering time, at some point again, the electrons cannot follow the structural changes, and this channel of scattering will become temperature independent. Second, as discussed in §2.2, the ratio of the Maxwell relaxation time, τ_M (which governs the structural relaxation time), and the time for adding/removing an atom from a cluster, τ_{LC}, becomes equal and temperature independent above T_A. Since such events of structural changes happen fast, this information cannot be conveyed to the nearest cluster. This inability to communicate is basically equivalent to the localization of the high-frequency phonons. As a result, electron scattering by the high-frequency phonons will also become temperature independent. Both of these mechanisms may contribute to a near saturation of the electron mean free path and, therefore, a saturation of the electrical conductivity/resistivity. Importantly, since this happens at T_A, these data provide the first direct experimental evidence for the connection between the local structure of the liquid and the liquid dynamics, which was predicted by the earlier MD simulations.

5   Conclusions

The work presented here demonstrates that the structural dynamics can be probed by electrical resistivity in equilibrium and supercooled liquids. It opens the possibility of using this technique to also probe other structural changes associated with liquid-liquid transitions, chemical clustering, phase separation, etc. The saturation of the resistivity is a novel observation that could only be obtained using the SCE unit in ISS-EML. Although demonstrated only for two alloy liquids, similar behavior was observed in $Ti_{39.3}Zr_{39.5}Ni_{21}$ and indicated in Vit106 ($Zr_{57}Cu_{15.4}Ni_{12.6}Al_{10}Nb_5$) liquids. However, since those liquids were processed in metallic cage sample holders on the ISS-EML, the results are somewhat uncertain; interaction of the metallic cage with the rf-field may have influenced those measurements. We are aware of only one other case where an indication of resistivity saturation in a high-temperature liquid was reported [69]. However, the reason for this was chemical phase separation in immiscible Cu-Co liquids. With large negative heats of mixing for $Zr_{64}Ni_{36}$ (-57 kJ/mol) and $Cu_{50}Zr_{50}$ (-34 kJ/mol) [82], this possibility can be ruled out for the present cases. Future experiments are planned on many more liquids using the ISS-EML facility to verify whether this is a common phenomenon in all liquids. If our postulate that this is associated with the crossover temperature is correct, it should be observed in almost all liquids.

are particularly indebted to the members of the Microgravity Users Support Center (MUSC) at the DLR, Köln, for their generous support in the planning and execution of the experiments.

References

1. M.H. Cohen, D. Turnbull, Composition requirements for glass formation in metallic and ionic systems. Nature **189**, 131–132 (1961). https://doi.org/10.1038/189131b0
2. L. Berthier, G. Biroli, Theoretical perspective on the glass transition and amorphous materials. Rev. Mod. Phys. **83**, 587–645 (2011). https://doi.org/10.1103/RevModPhys.83.587
3. T. Scopigno, G. Ruocco, Microscopic dynamics in liquid metals: The experimental point of view. Rev. Mod. Phys. **77**, 881–933 (2006). https://doi.org/10.1103/RevModPhys.77.881
4. C.P. Royall, S.R. Williams, The role of local structure in dynamical arrest. Phys. Rep. **560**, 1–75 (2015). https://doi.org/10.1016/j.physrep.2014.11.004
5. H. Vogel, Z. Phys. **22**, 645 (1921)
6. G.S. Fulcher, Analysis of recent measurements of the viscosity of glasses. J. Am. Ceram. Soc. **8**, 339 (1925). https://doi.org/10.1111/j.1151-2916.1925.tb16731
7. G. Tammann, W.Z. Hesse, The temperature dependence of viscosity of undercooled liquids. Anorg. Allgem. Chem. **156**, 245 (1926)
8. M.E. Blodgett, T. Egami, Z. Nussinov, K.F. Kelton, Proposal for universality in the viscosity of metallic liquids. Sci. Rep. **5**, 13837 (2015). https://doi.org/10.1038/srep13837
9. J.C. Mauro, Y. Yueb, A.Y. Ellisona, P.K. Gupta, D.C. Allan, Viscosity of glass-forming liquids. Proc. Natl. Acad. Sci. U. S. A. **24**, 19780–19784 (2009). https://doi.org/10.1073/pnas.0911705106.10
10. F. Mallamace, C. Branca, C. Corsaro, N. Leone, J. Spooren, S.-H. Chen, H.E. Stanley, Transport properties of glass-forming liquids suggest that dynamic crossover temperature is as important as the glass transition temperature. Proc. Natl. Acad. Sci. U. S. A. **107**, 22457–22462 (2010). https://doi.org/10.1073/pnas.1015340107
11. N.B. Weingartner, C. Pueblo, F.S. Nogueira, K.F. Kelton, Z. Nussinov, A phase space approach to supercooled liquids and a universal collapse of their viscosity. Front. Mater. **3**, 50 (2016). https://doi.org/10.3389/fmats.2016.00050
12. C.A. Angell, Strong and fragile liquids, in *Relaxations in Complex Systems*, ed. by K. L. Ngai, G. B. Wright, vol. 3, (U.S. GPO, Washington, DC, 1985)
13. T. Iwashita, D.M. Nicholson, T. Egami, Elementary excitations and crossover phenomenon in liquids. Phys. Rev. Lett. **110**, 205504 (2013). https://doi.org/10.1103/PhysRevLett.110.205504
14. A. Jaiswal, T. Egami, K.F. Kelton, K.S. Schweizer, Y. Zhang, Correlation between fragility and the arrhenius crossover phenomenon in metallic, molecular, and network liquids. Phys. Rev. Lett. **117**, 205701 (2016). https://doi.org/10.1103/PhysRevLett.117.205701
15. S. Sastry, P.G. Debenedetti, F.H. Stillinger, Signatures of distinct dynamical regimes in the energy landscape of a glass-forming liquid. Nature **393**, 554–557 (1998). https://doi.org/10.1038/31189
16. W. Götze, in *Liquids, Freezing and the Glass Transition*, ed. by J. P. Hansen, D. Levesque, J. Zinn-Justin, (North-Holland, 1991), p. 287
17. W. Kob, C. Donati, S.J. Plimpton, P.H. Poole, S.C. Glotzer, Dynamical heterogeneities in a supercooled Lennard-Jones liquid. Phys. Rev. Lett. **79**, 2827–2830 (1997). https://doi.org/10.1103/PhysRevLett.79.2827
18. J.P. Garrahan, D. Chandler, Geometrical explanation and scaling of dynamical heterogeneities in glass forming systems. Phys. Rev. Lett. **89**, 035704 (2002). https://doi.org/10.1103/PhysRevLett.89.035704

19. L. Li, J. Schroers, Y. Wu, Crossover of microscopic dynamics in metallic supercooled liquid observed by NMR. Phys. Rev. Lett. **91**, 265502 (2003). https://doi.org/10.1103/PhysRevLett.91.265502

20. D.C. Van Hoesen, A.K. Gangopadhyay, G. Lohöfer, M.E. Sellers, C.E. Pueblo, C. Koch, P.K. Galenko, K.F. Kelton, Resistivity saturation in metallic liquids above a dynamical crossover temperature observed in measurements aboard the International Space Station. Phys. Rev. Lett. **123**, 226601 (2019). https://doi.org/10.1103/PhysRevLett.123.226601

21. G. Lohöfer, High-resolution inductive measurement of electrical resistivity and density of electromagnetically levitated liquid metal droplets. Rev. Sci. Instrum. **89**, 124709 (2018). https://doi.org/10.1063/1.5065482

22. G.G. Stokes, On the effect of internal friction of fluids on the motion of pendulums. Trans. Cambr. Philos. Soc. **9**, 8–106 (1851)

23. W.P. Mason, M. Hill, Measurement of the viscosity and shear elasticity of liquids by means of a torsionally vibrating crystal. Trans. ASME. In. J. Lubr. Tech. **69**, 359–370 (1947)

24. H.E. Hagy, Experimental evaluation of beam-bending method of determining glass viscosities in the range 10^8 to 10^{15} Poises. J. Am. Ceram. Soc. **46**, 93–97 (1963). https://doi.org/10.1111/j.1151-2916.1963.tb11684.x

25. W.-K. Rhim, M. Collender, M.T. Hyson, W.T. Simms, D.D. Elleman, Development of an electrostatic positioner for space material processing. Rev. Sci. Instrum. **56**, 307–317 (1985). https://doi.org/10.1063/1.1138349

26. D.M. Herlach, R.F. Cochrane, I. Egry, H.-J. Fecht, A.L. Greer, Containerless processing in the study of metallic melts and their solidification. Int. Mater. Rev. **38**, 273–347 (1993). https://doi.org/10.1179/095066093790326267

27. P.C. Nordine, J.K.R. Weber, J.G. Abadie, Properties of high-temperature melts using levitation. Pure Appl. Chem. **72**(11), 2127–2136 (2000). https://doi.org/10.1351/pac200072112127

28. E.H. Trinh, Compact acoustic levitation device for studies in fluid dynamics and materials science in the laboratory and microgravity. Rev. Sci. Instrum. **56**, 2059–2065 (1985). https://doi.org/10.1063/1.1138419

29. J.W.S. Rayleigh, On the capillary phenomena of jets. Proc. R. Soc. Lond. **29**(196–199), 71–97 (1879). https://doi.org/10.1098/rspl.1879.0015

30. W.-K. Rhim, K. Ohsaka, P.-F. Paradis, R.E. Spjut, Noncontact technique for measuring surface tension and viscosity of molten materials using high temperature electrostatic levitation. Rev. Sci. Instrum. **70**, 2796–2801 (1999). https://doi.org/10.1063/1.1149797

31. G.S. Parks, L.E. Barton, M.E. Spaght, J.W. Richardson, The viscosity of undercooled liquid glucose. J. Appl. Phys. **5**, 193–199 (1934). https://doi.org/10.1063/1.1745251

32. K. Schröter, E. Donth, Viscosity and shear response at the dynamic glass transition of glycerol. J. Chem. Phys. **113**, 9101–9108 (2000). https://doi.org/10.1063/1.1319616

33. P.B. Macedo, A. Napolitano, Inadequacies of viscosity theories for B_2O_3. J. Chem. Phys. **49**, 1887–1895 (1968). https://doi.org/10.1063/1.1670321

34. R.A. Ashcraft, *Linking Structure and Dynamics in Metallic Liquids: A Combined Experimental and Molecular Dynamics Approach*. Ph.D. thesis, Washington University in St. Louis (2018)

35. Y.Q. Cheng, E. Ma, Atomic-level structure and structure-property relationship in metallic glasses. Prog. Mater. Sci. **56**, 379–473 (2011). https://doi.org/10.1016/j.pmatsci.2010.12.002

36. R. Soklaski, V. Tran, Z. Nussinov, K.F. Kelton, L. Yang, A locally preferred structure characterises all dynamical regimes of a supercooled liquid. Philos. Mag. **96**, 1212–1227 (2016). https://doi.org/10.1080/14786435.2016.1158427

37. J. Ding, Y.-Q. Cheng, E. Ma, Full icosahedra dominate local order in $Cu_{64}Zr_{36}$ metallic glass and supercooled liquid. Acta Mater. **69**, 343–354 (2014). https://doi.org/10.1016/j.actamat.2014.02.005

38. N.A. Mauro, M. Blodgett, M.L. Johnson, A.J. Vogt, K.F. Kelton, A structural signature of liquid fragility. Nat. Commun. **5**, 4616 (2014). https://doi.org/10.1038/ncomms5616

39. A.K. Gangopadhyay, C.E. Pueblo, R. Dai, M.L. Johnson, R. Ashcraft, D. Van Hoesen, M. Sellers, K.F. Kelton, Correlation of the fragility of metallic liquids with the high temperature

structure, volume, and cohesive energy. J. Chem. Phys. **146**, 154506 (2017). https://doi.org/10.1063/1.4981011

40. R. Dai, R. Ashcraft, K.F. Kelton, A possible structural signature of the onset of cooperativity in metallic liquids. J. Chem. Phys. **148**, 204502 (2018). https://doi.org/10.1063/1.5026801

41. S.S. Schoenholz, E.D. Cubuk, D.M. Sussman, E. Kaxiras, A.J. Liu, A structural approach to relaxation in glassy liquids. Nat. Phys. **12**, 469–472 (2016). https://doi.org/10.1038/NPHYS3644

42. J. Ding, Y.-Q. Cheng, H. Sheng, M. Asta, R.O. Ritchie, E. Ma, Universal structural parameter to quantitatively predict metallic glass properties. Nat. Commun. **7**, 13733 (2016). https://doi.org/10.1038/ncomms13733

43. N.W. Ashcroft, N.D. Mermin, *Solid State Physics* (Saunders College Publishing, New York, 1976) ISBN 0-03-083993-9. OCLC 934604

44. S. Sachdev, *Quantum Phase Transitions* (Cambridge University Press, New York, 1999)

45. A.W. McReynolds, Electrical observations of the austenite-martensite transformation in steel. J. Appl. Phys. **17**, 823 (1946). https://doi.org/10.1063/1.1707649

46. L.W. Shacklette, W.S. Williams, Influence of order-disorder transformations on the electrical resistivity of vanadium carbide. Phys. Rev. B **7**, 5041–5053 (1973). https://doi.org/10.1103/PhysRevB.7.5041

47. K.F. Kelton, F. Spaepen, Kinetics of structural relaxation in several metallic glasses observed by changes in electrical resistivity. Phys. Rev. B **30**, 5516–5524 (1984). https://doi.org/10.1103/PhysRevB.30.5516

48. A.K. Gangopadhyay, T.K. Croat, K.F. Kelton, The effect of phase separation on subsequent crystallization in Al88Gd6La2Ni4. Acta Metall. **48**, 4035–4043 (2000). https://doi.org/10.1016/S1359-6454(00)00196-8

49. P.W. Anderson, Absence of diffusion in certain random lattices. Phys. Rev. **109**, 1492–1505 (1958). https://doi.org/10.1103/PhysRev.109.1492

50. N.F. Mott, *Metal-Insulator Transitions* (Taylor and Francis, London, 1974), p. 23

51. P.A. Lee, T.V. Ramakrishnan, Disordered electronic systems. Rev. Mod. Phys. **57**, 287–337 (1985). https://doi.org/10.1103/RevModPhys.57.287

52. O. Gunnarsson, M. Calandra, J.E. Han, saturation of electrical resistivity. Rev. Mod. Phys. **75**, 1085–1099 (2003). https://doi.org/10.1103/RevModPhys.75.1085

53. R.A. Davison, K. Schalm, J. Zaanen, Holographic duality and the resistivity of strange metals. Phys. Rev. B **89**, 245116 (2014). https://doi.org/10.1103/PhysRevB.89.245116

54. W. Klement, R.H. Willens, P. Duwez, Non-crystalline structure in solidified gold–silicon alloys. Nature **187**, 869–870 (1960). https://doi.org/10.1038/187869b0

55. A.J. Drehman, A.L. Greer, D. Turnbull, Bulk formation of a metallic glass. Appl. Phys. Lett. **41**, 716–717 (1982). https://doi.org/10.1063/1.93645

56. U. Mizutani, Electronic structure of metallic glasses. Prog. Mater. Sci. **28**, 97–228 (1983). https://doi.org/10.1016/0079-6425(83)90001-4

57. M.A. Howson, B.L. Gallagher, The electron transport properties of metallic glasses. Phys. Rep. **170**, 265–324 (1988). https://doi.org/10.1016/0370-1573(88)90145-7

58. U. Mizutani, Electron transport in non-periodic metallic systems: Amorphous alloys and quasicrystals. Phys. Status Solidi B **176**, 9–30 (1993). https://doi.org/10.1002/pssb.2221760102

59. J.H. Mooij, Electrical conduction in concentrated disordered transition metal alloys. Phys Status Solidi A **17**, 521–530 (1973). https://doi.org/10.1002/pssa.2210170217

60. C.C. Tsuei, Nonuniversality of the Mooij correlation the temperature coefficient of electrical resistivity of disordered metals. Phys. Rev. Lett. **57**, 1943–1946 (1986). https://doi.org/10.1103/PhysRevLett.57.1943

61. J.M. Ziman, A theory of electrical properties of liquid metals: I The monovalent metals. Philos. Mag. **6**, 1013–1035 (1961)

62. T.E. Faber, *Introduction to the Theory of Liquid Metals* (Cambridge University Press, 1972)

63. R. Evans, D.A. Greenwood, P. Lloyd, Calculations of the transport properties of liquid transition metals. Phys. Lett. A **35**, 57–59 (1971). https://doi.org/10.1016/0375-9601(71)90543-3

64. O. Dreirach, R. Evans, H.-J. Guntherodt, H.-U. Kunzi, A simple muffin tin model for the electrical resistivity of liquid noble and transition metals and their alloys. J. Phys. F. Metal Phys. **2**, 709–725 (1972). https://doi.org/10.1088/0305-4608/2/4/015

65. T. Akasofu, S. Takeda, S. Tamaki, Compound forming effect in the electrical resistivity of liquid Pb-Te alloys. J. Phys. Soc. Jpn. **52**, 2485–2491 (1983)

66. J. Banhart, W. Pfeiler, J. Voitländer, Detection of short- and long-range order in Cu-Pt alloys. Phys. Rev. B **37**, 6027–6029 (1988). https://doi.org/10.1103/PhysRevB.37.6027

67. J.-G. Gasser, B. Kefif, Electrical resistivity of liquid nickel-lanthanum and ni-cerium alloys. Phys. Rev. B **41**, 2776–2783 (1990). https://doi.org/10.1103/PhysRevB.41.2776

68. T. Richardson, G. Lohöfer, I. Egry, Electrical resistivity of undercooled CuNi alloys. Int. J. Thermphys. **23**, 1207–1216 (2002). https://doi.org/10.1023/A:1019840203684

69. F. Guo, L. Ting, J. Qin, H. Zheng, X. Tian, Abnormal resistivity behavior of Cu-Ni and Cu-Co alloys in undercooled state. Physica B **407**, 4108–4113 (2012). https://doi.org/10.1016/j.physb.2012.06.024

70. Y. Kraftmakher, Eddy currents: Contactless measurement of electrical resistivity. Am. J. Phys. **68**, 375–379 (2000). https://doi.org/10.1119/1.19440

71. A.V. Rumyantseva, M.A. Nikishina, V.G. Kharyukov, A noncontact method for measuring the specific electrical resistance of metals in the high-temperature region. Instrum. Exp. Tech. **62**(3), 444–449 (2019)

72. J.E. Enderby, S. Ansell, S. Krishnan, D.L. Price, M.L. Saboungi, The electrical conductivity of levitated liquids. Appl. Phys. Lett. **71**, 116–119 (1997). https://doi.org/10.1063/1.119445

73. W.-K. Rhim, T. Ishikawa, Noncontact electrical resistivity measurement technique for molten metals. Rev. Sci. Instrum. **69**, 3628–3633 (1998). https://doi.org/10.1063/1.1149150

74. G. Lohöfer, Magnetization and impedance of an inductively coupled metal sphere. Int. J. Eng. Sci. **32**, 107–117 (1994). https://doi.org/10.1016/0020-7225(94)90153-8

75. W.-K. Rhim, S.K. Chung, D. Barber, K.F. Man, G. Gutt, A. Rulison, R.E. Spjutb, An electrostatic levitator for high-temperature containerless materials processing in l-g. Rev. Sci. Instrum. **64**, 2961–2970 (1993). https://doi.org/10.1063/1.1144475

76. K.H.J. Buschow, Short-range order and thermal stability in amorphous alloys. J. Phys. F. Met. Phys. **14**, 593–607 (1984) http://iopscience.iop.org/0305-4608/14/3/005

77. D. Wang, Y. Li, B.B. Sun, M.L. Sui, K. Lu, E. Ma, Bulk metallic glass formation in the binary Cu-Zr system. Appl. Phys. Lett. **84**, 4029–4031 (2004). https://doi.org/10.1063/1.1751219

78. D.C. Van Hoesen, *Thermophysical Properties and Phase Transformations in Metallic Liquids and Silicate Glasses*. Ph.D. thesis, Washington University in St. Louis (2020)

79. Y. Imry, Possible role of incipient anderson localization in the resistivities of highly disordered metals. Phys. Rev. Lett. **44**, 469–471 (1980). https://doi.org/10.1103/PhysRevLett.44.469

80. M.A. Howson, Incipient localisation and electron-electron correlation effects in metallic glass alloys. J. Phys. F. Metal Phys. **14**, L25–L31 (1984). https://doi.org/10.1088/0305-4608/14/3/001

81. V. Ambegaokar, B.I. Halperin, J.S. Langer, Hopping conductivity in disordered systems. Phys. Rev. B **4**, 2612–2620 (1971). https://doi.org/10.1103/PhysRevB.4.2612

82. F.R. de Boer, R. Boom, A.R. Miedema, A.K. Niessen, Cohesion in metals, in *Cohesion and Structure*, ed. by F. R. de Boer, D. G. Pettifor, (North-Holland, 1988)

Part V
Technology Trends and Future Perspectives

Chapter 21
New Material Developments/High-Entropy Alloys

Yannick Champion

1 Introduction

This chapter is dedicated to the development of new materials, more specifically new metallic alloys called high-entropy alloys (HEA) [1]. A very first definition is that HEA are solid solutions containing at least five metallic elements in equi-atomic composition. We shall see that HEAs will deviate from this strict definition and eventually extend to complex concentrated alloys (CCAs) which have higher degrees of flexibility in chemical composition and microstructure. The chapter reports on the main characteristics and properties of a new class of alloys, discovered in 2004, then having no applications so far but many perspectives. Beyond the objective of being informative, obvious perspectives for these alloys are crucially related to their development, and the importance of investigations and measurements such those performed in space and parabolic flights are of course no longer to be demonstrated.

With the word "new" in the title of this chapter, there is a strong temptation to start with a frequent question, which is whether with a 5000 years history since the bronze age, something new is still possible in metallurgy. An extension to this question is whether novelties in metallurgy is still necessary for our society. The questioning here is contrasted with materials that may appear to the public as the product of (more) modern science (and technology), for example, superconducting ceramic, liquid crystals, functional glass, blue LED, photovoltaic silicon, conductive polymers, carbon nanotubes, and graphene. One (metallurgists) may wonder why such a feeling. It is true that metallic alloys are common to everyone, present everywhere in our environment, in car, plane, building, devices. In addition, among all exceptional nonmetallic materials, some are recent discoveries highly

Y. Champion (✉)
Univ. Grenoble Alpes, CNRS, Grenoble INP, SIMaP, Grenoble, France
e-mail: yannick.champion@simap.grenoble-inp.fr
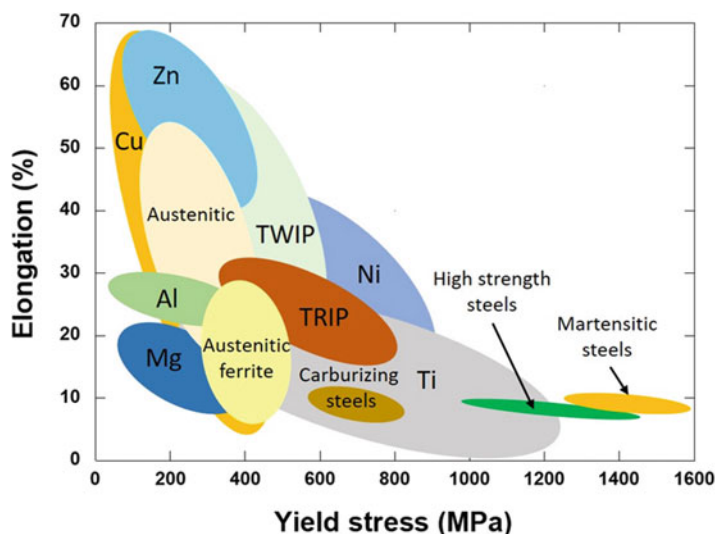
Fig. 21.1 The conflict between fracture elongation and yield stress. Different classes of main metal-based alloys show reduction in fracture elongation with increasing yield stress by the various hardening mechanisms

publicized for the disruptions they produce in their properties and potential applications or by prestigious awards. Note that there are only two Nobel Prizes strictly in the field of metallurgy, Charles Edouard Guillaume in 1920 for INVAR (FeNi alloy) and Dan Shechtman in 2011 for metallic quasicrystals. Without claiming being exhaustive, another reason is sometimes coming from a confusion between material and product. Glass is an excellent example, nearly as old as bronze, discovered by the Mesopotamians about BC 4500 and intensively developed by the Egyptian about BC 3000. Nowadays, window glass is an incredible material allowing tactile transmission of information to the smartphone, while an association with an invisible tin-indium-oxide layer performs the function.

Metallurgy has a long history and has contributed to mainstream advances in materials science and technology. It has produced for decades tremendous amounts of data, methods, experiences, and expertise, transferred to other phases studies and processing (ceramic, glass, semiconductors, etc.). One may emphasize the rather highly flexible character of metals and metallic alloys. Low- to medium-range melting points and plasticity allow large varieties of thermomechanical treatments and forming. Phase transformations are contributing to a large range of microstructures, phases, and properties. Possibilities in chemical combination lead to extremely large varieties of alloys from simple solid solutions to very complex ones; the large variety of steels is an emblematic example. The flexibility of metallic alloys is one of the origins of their strong impact on industry, economy, and society development and improvements, and ruptures in the field have still a lot to do. To illustrate, the main challenge in metallurgy is probably to overpass the conflict between strength

and toughness [2] (Fig. 21.1), but there are many others, such as conflict between strength and electrical conductivity.

HEA are part of new materials discovered in 2004 simultaneously in Taiwan and Oxford [3, 4]. They are also in some ways the products of a new concept in the formation of metallic alloys [5], which open new perspectives for novel properties and forthcoming applications.

In this chapter, we shall address an overview on thermophysical properties of the HEA and CCA, in particular those measured in parabolic flight, and emphasis of the necessary need of these properties for future theoretical understanding and technical developments. The chapter is introduced by a short overview on metallic alloys design and novelty brought by the HEA and CCA as well as their main properties.

2 Metallic Alloys and Alloy Design

The ranges of metallic materials are so large that alloys are traditionally separated in classes with their specificities and their science and engineering experts groups. To make it more complex, the classes are changing, depending on the scientific and technological domains. For materials science, the class is the alloy composition and microstructure, often in relation with the mechanical properties (with subclasses for chemical and physical metallurgy, mechanical properties): pure metal, solid solution, and multiphase alloy. For engineering, the class is related to alloys processing, depending on melting point range and forming ability. For the physics or functional applications, classes are physical properties: magnetic (with subclasses soft, hard, ferromagnetic alloys, etc.), electric, dielectric, etc.

Nevertheless, it is fortunate that all agree on a classification based on the main metal constituting an alloy family: iron-based alloys (note that steel, Fe with small C content constitutes its own class), aluminum (with industrial subclasses: 1000 series, 2000, 8000, etc.), titanium, copper, and nickel. It is emphasized that such classification is a strong feature of the standard approach of the alloys design. The principle consists in adding elements to the base metal, starting from low content and gradually increasing it. Initially, this is done empirically through trial and error, and then through long-term experience. The method lasts since the bronze age with addition of tin to copper to make it stronger. It suggests quasi-infinite possibilities and is guided by desired properties. Hence, appropriate additions identified in the long history of metallurgy have led, after discovery and incremental improvement, to the all-common alloys used today. Sometimes, some alloys with exceptional properties were obtained by chance and lost, as for the case of the Damascus steel (wootz) [6]. But technically high standard alloys are the results of long-term research and development. Steel is probably one of the most extraordinary class of alloys. The large variety of its metallurgical states is based on the unusual bcc low-temperature-fcc high-temperature allotropic transition and large difference in carbon solubility between the two crystallographic states. Then stabilizing fcc austenite at lower temperature by adding nickel, varying thermal treatment to produce martensite and

bainite, and adding chromium for oxidation resistance (stainless steel) generate diversity. With time, appropriate additions led to complex microstructures, duplex (austenite/ferrite), dual phase (ferrite/martensite), and TWIP/TRIP alloys. Browsing the various classes of modern metallic alloys, one notices their high degree of chemical and structural complexities. Duplex steels contain up to 10 elements with fractions from about 0.1 to 22 atomic %. The bcc βTi are quaternary and quinary alloys with vanadium content up to 15 atomic %. The new generation βTi for medical applications contains up to 29 atomic % of Nb, 13% Ta, and 4.6% Zr [7].

In the search for novelty, elemental addition has been extended to metallic compounds. The most emblematic example is the intermetallic NiAl superalloys, with high creep resistance for turbine blades of jet engines or steam turbines. Nowadays, active researches are devoted to TiAl and other alloys are of interest for their high strength such as FeAl. Motivation as starting point for alloys development is also based on specific property of compounds. To illustrate, a first example is the metallic glass [8, 9]. These are multi-elementary metallic materials obtained by rapid cooling (from 10 to 10^6 K·s^{-1}) to avoid crystallization and then forming long-range atomic disordered structures. These alloys are brittle but present extreme strength. Most metallic glasses are generated from a so-called deep eutectic in a binary phase diagram, that is, that the eutectic temperature is low compared to melting points of the constituting elements. High viscosity in the supercooled domain and eutectic structure alternating the two elements are much favorable to form disordering. Then strategy of elements additions is applied to the eutectic composition as for addition to a base metal, to improve the properties. The CuZr eutectic has been intensively studied producing amorphous which glass-forming ability is gradually improved by Al addition up to 10 atomic %. Then subsequent addition of Ti and Ni led to ZrCu-based bulk metallic glass giving part with few centimeters dimensions. Other metallic glasses were discovered not based on eutectic but still characterized by high viscosity in the supercooled domain related to metal-metalloid interactions. The starting point for metallurgical development of this class of alloy is then the property of "glass-forming ability." A second example is the shape memory alloy that shows the property of shape recovery after plastic deformation by thermal treatment. Here, the starting point is an alloy composition exhibiting the martensitic transformation. The reference alloy finding dental applications is NiTi. Then various alloying has been studied to focus on the desired properties leading, for example, to high-concentration NiTiPd, NiTiPt, NiTiHf, etc. [10].

To sum up, alloy design strategy can be defined as gradual additions of atomic elements to a main metal or a compound, generally a binary alloy showing specific properties. The main metal/simple compounds constitute the solvent. It is emphasized that the processing in the design process is based on the main metal (or the simple compounds) properties (thermophysical, mechanical, physical, and chemical).

As one has seen, metallic alloys are already very complex in terms of composition and microstructure (Fig. 21.2). So what is different with high-entropy alloy and derived complex concentrated alloys?

20 nm   Cu Ni Mn Si C
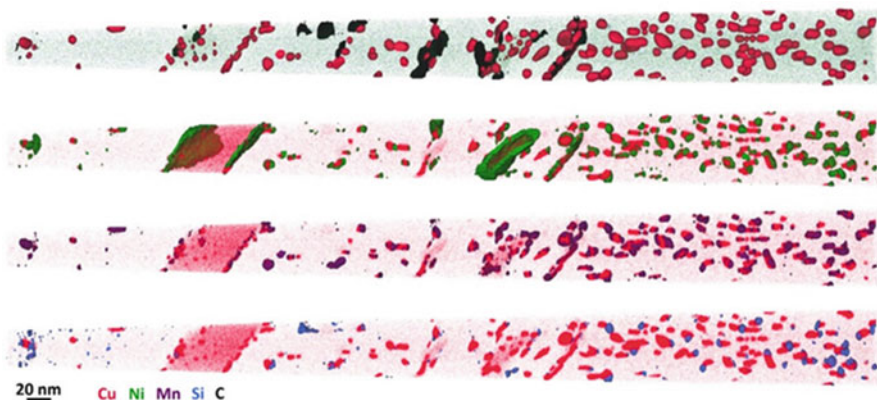
Fig. 21.2 Metallic alloys are already in complexity. Illustration with variation in phases and composition with thermal treatments in martensitic stainless steel 15-5-PH observed with atom probe tomography. (Adapted from Couturier Materialia 2020)

Fig. 21.3 Illustration of alloy design strategies on a ternary phase diagram for simplification. Traditional alloys start from a corner or specific composition of the phase diagram. HEA and CCA start from a solid solution in the middle of the phase diagram
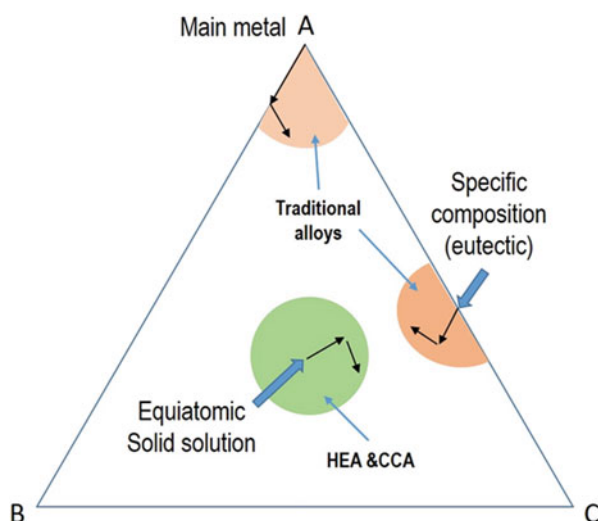
For HEA and CCA alloys, the design is starting from equi-atomic multi-elementary solid solution (quinary alloys and more) which constitutes the solvent. Then the properties are probed by variations of the HEA composition and elementary additions from the "middle" of the phase diagram while "traditional" alloys are probed from the corner or specific composition. The two different approaches are schemed in Fig. 21.3. This is a clear rupture in metallic alloy design and a novel fertile ground for innovation since the solvent has new complex properties in relation to multi-atomic interactions. The emblematic example of HEA and the first one discovered by Cantor and collaborators is FeCrMnCoNi [4]. The same year, Yeh and collaborators studied series of multi-elementary solid solutions and proposed the

name of high-entropy alloy for this class of alloys [3]. In a critical review on HEA and CCA, Gorsse, Couzinié, and Miracle pointed out the difference in motivation of the two groups [5]. The group of Oxford focused on the unexplored central region of the phase diagram and the fact that multicomponent, highly concentrated alloys open to extreme large numbers of new alloys. The group of Taiwan was working on possibilities from thermodynamics considerations to avoid intermetallics formation, responsible of low fracture resistance in alloys solid solution. The two motivations eventually converged to a unique new alloy concept. In some sense and unusually, a new material concept came from two different origins as pointed out by Miracle [11].

Design of HEA and CCA needs to deal to their chemical complexity to which must be added the timescale in materials discovery. The world and its societal issues need "smart" and ethical (friendly, recyclable, etc.) materials in shorter and shorter timescale. Hence, alloy design must be thought in an "accelerated form" which needs development and implementation of up-to-date combinatorial high throughput experimental techniques [12], supported by artificial intelligence tools and modelling such as DFT [13], thermophysical data calculation, phase diagram CALPHAD modelling [14, 15], etc.

3   Definitions

3.1   High-Entropy Alloys

The idea of the Oxford group was exploration of the very large possibilities in composition and phases of multi-elementary and concentrated regions of the phase diagrams. From that, a first definition is that alloys are composed of five or more elements with atom fraction between 0.05% and 35%.

In the other approach of the Taiwan group, HEA are derived from a stricter criterion, that is, that the formation of solid solution is predominant over intermetallic compounds. Here is one of the main motivations in metallurgy, which is avoiding intermetallic formation well known for alloy embrittlement effect. Some quantification is then derivable from the free enthalpy of phase formation in thermodynamic equilibrium condition, $\Delta G = \Delta H - T\Delta S$. In an ideal view, as assumed by Yeh and collaborators [3], solid solution formation is dominated by the entropy, $\Delta G_{ss} \approx -T\Delta S_{ss}$. In contrast for ordered intermetallic $\Delta S_{im} \approx 0$ and the formation is dominated by the mixing enthalpy $\Delta G_{im} \approx \Delta H_{im}$. It naturally results that solid solution is as much favored as $-T\Delta S_{ss}$ is much more negative than ΔH_{im}. Ideal solid solution means that the entropy is given by the ideal configurational contribution uniquely defined by the Boltzmann relation: $S_c = k \ln \Omega$, with k the Boltzmann constant and Ω the number of microstates configurations. For an alloy composed of n elements with atom fraction x_i of the ith, the ideal configurational entropy is $S_c = -k \sum_1^n x_i \ln x_i$. One notices that the maximum of S_c is given by $\forall i$ and j, $x_i = x_i$ and $S_c = k \ln n$. Then S_c is increasing with the number of elements following, respectively, $n = 4, 5$, and 6 and $S_c = 1.39k, 1.61k$, and $1.79k$. From

such consideration, Yeh and collaborators have proposed the condition that HEA is solid solution that respects $S_c > 1.5k$. Strictly speaking, equi-atomic HEAs need at least five elements to respect the definition. However, increasing the number of elements allows respecting the rule with some deviation from equi-atomic composition. This joins the Oxford definition and is the first step toward CCA. Again, as already emphasized for these alloys design, definition shows the dominant role of thermodynamics in HEA.

3.2 The Four Core Effects

The multi-elementary and highly concentrated composition leads to four specificities for the HEA, called the four core effects. Originally conjectured from the HEA atomic structure, these effects were the subject of numerous discussions and controversies since HEA discovery. The extended number of works so far have seem to comfort some of the original ideas, bringing interesting perspectives as discussed in detail by Miracle [11].

3.2.1 The High Entropy

A first core effect is straightforward since it is deduced from the definition, which is that HEA is as stable as its configurational entropy is high. It is here an opportunity to comment this strict definition with respect to possibility in HEA solid solution formation. Again, in such ideal view, HEA pioneers acknowledge that high entropy would not be able to compete with extreme stable compounds having large negative formation enthalpies (in the range of -30 kJ/mol to -120 kJ/mol) such as carbides (SiC, TaC, TiC), boride (TaB2), nitrides (Si3N4), etc. Another strong fact discussed by Miracle [11] is the decreasing probability of forming solid solution or increasing probability of binary intermetallics formation with increase of the number of elements, which is contrary to the high-entropy core effect. This is supported by experimental observations and modellings and can be simply argued by that facts that with increasing the number of elements, the configurational entropy is increasing more slowly following $\ln n$ than the number of potential binary systems, varying following $n/2(n-1)$.

An interesting experiment has consisted in substituting successively one element of the Cantor FeCrMnCoNi and then keeping the configurational entropy [16]. In this work, substitutions (Ti for Co, Mo or V for Cr, V for Fe, and Cu for Ni) were such that elements have the same room temperature, structure, size, and electronegativity. Multiphase formation observed proved that entropy is not alone the criterion for solid solution formation and that enthalpy has to be considered.

From the pioneering work of Yeh and Cantor, other criteria have then added to design HEA derived from the empirical Hume-Rothery rules for binary solid solutions formation and based on the following defined parameters:

– The mixing enthalpy: $\Delta H_{\text{mix}} = \sum_{i=1}^{n} \sum_{j=i+1}^{n} 4c_i c_j \Delta H_{\text{mix}}^{ij}$

n is the number of elements constituting the alloy.
c_i and c_j are the i and j elements content.
$\Delta H_{\text{mix}}^{ij}$ is the mixing enthalpy of the binary alloy i and j.

– The atomic size difference: $\delta = 100 \sqrt{\sum_{i=1}^{n} c_i \left(1 - \frac{r_i}{\bar{r}}\right)^2}$

r_i and $\bar{r}$, respectively, are the atomic radius of element i and average atomic radius.

– The valence electron concentration: $\text{VEC} = \sum_{i=1}^{n} c_i \text{VEC}_i$

VEC_i is the valence electron concentration of element i.

These parameters would predict favorable solid solutions formation [17] but in a very empirical way still although they constitute a first evaluation and guide to start in the so-complex domain.

3.2.2   The Lattice Distortion

Lattice distortions are responsible for properties variations in pure metals, and the phenomenon is exploited for adjusting and improving properties since the origin of metallic alloys development. It is also sometimes responsible for unwanted degrading of properties. With respect to the pure metal with perfect lattice as depicted in Fig. 21.4a, distortion is produced by the difference in size between the solvent atoms and the added solute one. As shown in Fig. 21.4b, with the example of a substitution solid solution, the orange atom is larger than the blue hosts producing long-range displacement. Lattice distortion is well known for strengthening; it is shown that the yield stress varies with solute atom concentration, c following, $Y_s \propto Ec^n$, with E the solvent Young modulus and the exponent $1/3 < n < 1$ depending on atomic interactions and concentration range. The necessary increase of stress for plasticity to occur is explained by larger difficulty for dislocations to move in the long-range distorted lattice. To pass, the distortion dislocation must bend increasing its length, the line tension, and then energy.
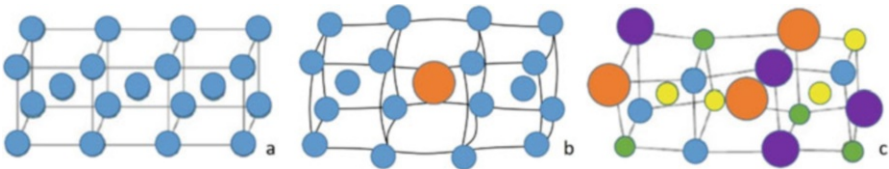
Fig. 21.4 Schematic illustration of the lattice distortion hypothesis. (**a**) Pure metal with perfect lattice. (**b**) Diluted substitutional solid solution with long-range distortion gradient produced by a larger atom in size. (**c**) Short-range (atomic distance) and homogenous distortions in HEA

Fig. 21.5 Strengthening of Au-Ag solid solution
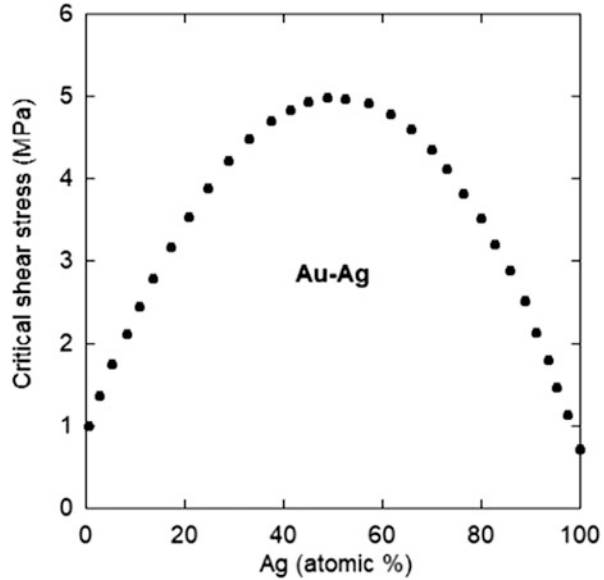
In the model system where Au and Ag are miscible in all content, strength varies linearly when Ag (respectively Au) is solvent and Au (respectively Ag) is solute, reaching the maximum strength for 50 atomic % (Fig. 21.5).

In HEA, the lattice distortion is due to atomic size difference at each node of the crystal lattice as schemed in Fig. 21.4c. Crucial difference with "standard" dilute solid solution is that there is no quantifiable distortion gradient. Distortion is true at any point, corresponding to small difference from perfect lattice translation. It is interesting to note that as distortion means difference from a reference perfect lattice, HEA distortion should be then redefined at any point of the crystal as the difference between two adjacent cells. But a full description would then need to define variations in this cells difference at each point of the crystal lattice. In a more simple way, this is what happened for Au-Ag when the alloy is close to 50 at %. On any side of the plot (Fig. 21.5), none of the metals is the relevant reference.

Easier way of "quantification" is an evaluation of lattice distortion with respect to an average crystal lattice, which can be determined from the maximum of X-ray diffraction peaks, for example. The average value of lattice distortion is then given by the relation previously mentioned for designing alloys with respect to Hume-Rothery rules, $\delta = 100\sqrt{\sum_{i=1}^{n} c_i \left(1 - \frac{r_i}{\bar{r}}\right)^2}$.

Quantitative structural characterization is obviously required for properties understanding, and specific analyses might be useful as the pair distribution function [18]. Another disruptive approach would be to describe the alloy from the local energy variations (potential energy landscape, PEL) ignoring atoms as proposed, for example, for glass description [19, 20]. It is emphasized here that though HEA are crystals, their structural definition contains a statistical component, which naturally

affects their properties. This statistical component is a supplementary parameter, compared to "standard" alloys, which could advantageously be used for novel properties development as far as it is understood and controlled.

3.2.3 Sluggish Diffusion

Diffusion is a thermally activated process occurring owing to the formation of an atomic and vacancies gradient and displacement by atomic jump into a nearby vacancy. Atomic diffusion is characterized by the temperature-dependent diffusion coefficient: $D = D_0 \exp\left(-\frac{Q}{RT}\right)$, D_0 is the jump frequency, Q is the activation energy, and R is the gas constant. Roughly, D_0 and Q are as low as disorder is large in crystal lattice. One feels that jump is more difficult from place to place, when the atomic position (lattice translation) is not well defined. In addition, activation energy related to bonding energy should be lower in disorder lattice where there are less bonds to cut for vacancy formation. A good illustration is the difference between diffusion coefficient in bulk crystal and grain boundary. Accordingly, with possibly decrease of D_0 and increase of $\exp\left(-\frac{Q}{RT}\right)$, predictions are not straightforward. To this, it is emphasized that disorder in HEA is not only of structural type but also of short-range atomic change and then of energy density disorder type (nonperiodic potential energy landscape).

Sluggish diffusion was originally attributed to lattice distortions and observations of nanocrystals in as cast HEA, elevated recrystallization temperature, and formation of amorphous phase [21]. The first relevant measurements on the FeCoCrMnNi HEA were reported in 2013 [22] and, though seemingly proving sluggish diffusion, was the subject of controversy. The couple method was used to measure diffusion coefficient of each metal in the HEA and comparison with diffusion in the reference metal. Systematic higher activation energy was found as well as higher normalized activation energy Q/T_m where T_m is the melting temperature. This work showed that Q/T_m is increasing with the number of elements in the alloy in connection with higher fluctuation of the lattice potential energy. Measuring diffusion in complex alloys and comparison with appropriate references are very challenging. Various investigations and analyses, so far, seem to show that in absolute, diffusion in HEA can be lower or higher and a sluggish effect is not only related to the number of elements. However, as generally observed, the mixings show lower T_m and higher resulting Q/T_m which, in this normalized context, places HEA sluggish for diffusion (see the comment in [11]).

3.2.4 The Cocktail Effect

This is probably the most intriguing effect and the one that cannot be quantifiable. Cocktail effect means the birth of unpredictable properties from the mixing of elements. In other words, the properties of the mixing are not predictable from the

properties of each component. Such effect occurring from complex mixing was first emphasized by Ranganathan [23]. In this article, the *cocktail effect* is not directly mentioned, but the author gives an interesting opinion at the time, on relatively novel metallurgy approach based on complex multi-elementary mixing, he called multimetallic cocktail, with the examples of metallic glasses, gum metals, and newly discovered HEA.

An interesting and straightforward illustration was reported by Laurent-Brocq and collaborators [24]. Lattice parameter variation was studied from deviation of the "Cantor" alloy NiFeCrCoMn on the alloy series $Ni_{1-4x}(FeCrCoMn)_x$. From the binary alloys NiA, with A = Fe, Cr, Co, Mn and the mixture of the later four metals, the linear Vegard's law should be expected. As shown in Fig. 21.6, except for Co, the other metals lie close onto the Vegard trend. However, experimental measurements using X-ray diffraction show deviation as soon as 40 atomic % of (FeCrCoMn) seemingly indicating a strong influence of Co. This might be pure feeling, and the lattice parameter variation is most likely depending on the cocktail mixture properties. It must be emphasized that in their study, authors verified absence of magnetic property effect as well as consideration of bcc structure of Cr.

The work also shows a decrease of the Young modulus with increasing the four (FeCrCoMn) elements content. Another peculiar behavior, considering that for the pure element having close Young moduli, a decrease of lattice cell should predict an increase of the alloy Young modulus (increase of the local energy density).

3.3 Toward Complex Concentrated Alloys

Soon after the discovery of HEAs, a solid solution of five or more equi-atomic elements was found to be very restrictive and potentially limiting in discovery of interesting high prospect alloys. Research focuses on the improvement and

Fig. 21.6 Deviation from Vegard's law for $Ni_{1-4x}(FeCrCoMn)_x$ alloys. (From Ref. [24])

Vegard's law
$$a = 1.527 \cdot 10^{-3} \cdot 4x + 3.5238$$
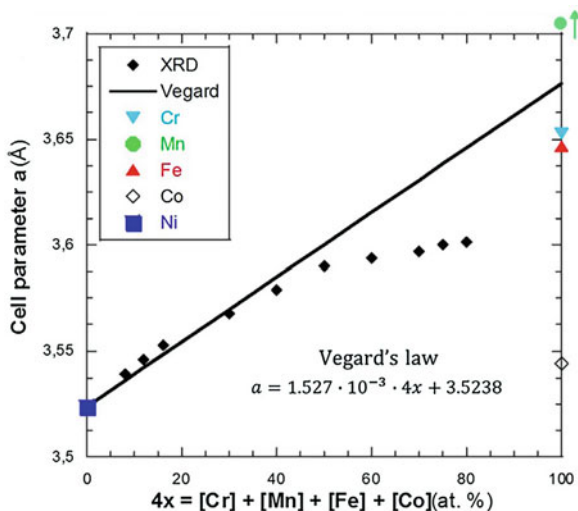
discovery of new properties. It has been found more productive releasing certain restrictions in particular on the composition and phase formation while retaining the HEA approach of studying the alloy from the middle of the phase diagram (no principal element), as shown in Fig. 21.3. For example, study of deviation in Ni content from the exact "Cantor" NiFeCrCoMn alloy shows that the maximum hardness is obtained for 60 atomic % of Ni instead of the maximum entropy at 20% (Fig. 21.7) [24].

HEA then derived toward complex concentrated alloys (CCA) also called some-times multi-principal element alloys (MPEA). Coupling the concentration concept to element addition, phase mixing properties (as in dual phase), and phase transformation ext. leads to extremely wide domain of alloys just waiting for being investigated. A recent article reports on a multi-concept approach conjugating face-centered cubic (fcc) and body-centered cubic (bcc) phases, grain refinement, and transformation-induced plasticity (TRIP) effect in a $Ti_{35}Zr_{27.5}Hf_{27.5}Nb_5Ta_5$ CCA (Fig. 21.8). This CCA shows high strength in the ranges of 950–1150 MPa and reasonable ductility of 12%.

4 HEA and CCA Properties and Perspectives

There is obviously no pretention to detail all properties of the HEA and CCA in this paragraph, and the readers will find appropriate reviews on the various topics. The objective here is to show perspectives focusing mainly on mechanical (structural) and functional properties. It must be emphasized again that HEA and CCA are still novel metallic alloys, and then the results are still scarce not showing obvious trends

Fig. 21.7 Hardness as function of the composition for $Ni_{1-4x}(FeCrCoMn)_x$ alloys. (From Ref. [24])

Mott-Nabarro-Labush
$H = 1.91 + 0.73 \cdot (4x)^{2/3}$
$R^2 = 0.92$

● Nanoindentation
— MNL

Hardness H (GPa)

$4x = [Cr] + [Mn] + [Fe] + [Co]$(at. %)
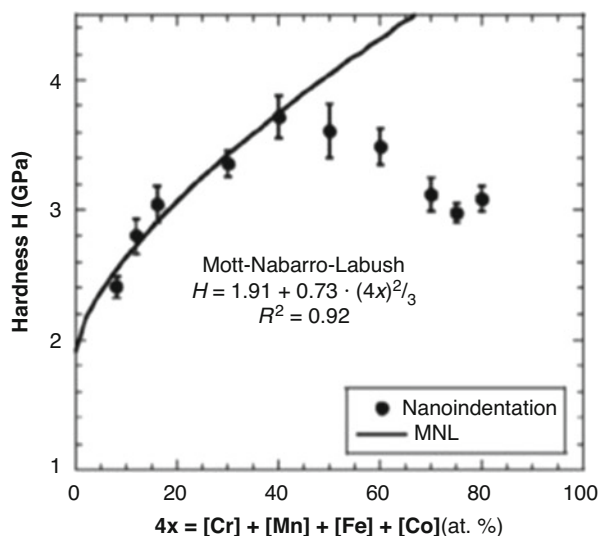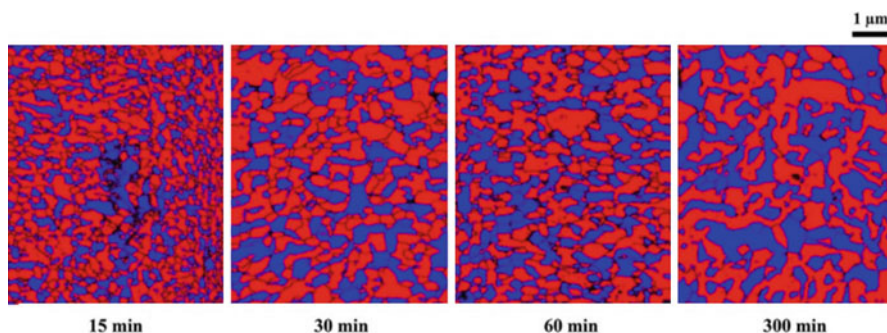
Fig. 21.8 $Ti_{35}Zr_{27.5}Hf_{27.5}Nb_5Ta_5$ CCA formed of nano-grains of fcc phase in red and bcc phase in blue with various size depending on the annealing time at 650 °C. Scanning electron microscopy in electron backscatter diffraction mode. (From Ref. [25])

and straightforward comparison with standard alloys. It is also currently a natural trend to (too soon to my opinion) envisage applications for any kind of materials, and then questioning on sustainability and recycling are quickly arising. HEA and CCA are in their teen age, and deep evaluation regarding these aspects is most likely premature. However, it is clear that in the future, properties such as resistance to oxidation, corrosion, fatigue, etc., will be dominant issues.

This book is devoted to measurements carried out in microgravity on metallic alloys. I then made the choice to focus in this paragraph on HEA and CCA for hydrogen storage, since alloys for such application are studied in microgravity. Eventually and also in relation with the book topic, the thermophysical properties of HEA and CCA will be the subject of a specific paragraph ending this chapter.

4.1 Mechanical Properties

Mechanical properties are dominant in metallurgy since alloys find major use as structural materials as well as in applications where mechanical integrity (fatigue, plasticity, etc.) is required (electrotechnics, microelectronics, packaging, etc.). In their seminal paper [3], Yeh and collaborators report on hardness and yield strength of their newly discovered HEA showing this main concern. Solid solutions were historically produced to strengthen metals, and then as some sort of ultimate and complex solid solution, HEA have been soon seen promising for strength improvement. Then varying either composition or/and producing multiphase toward CCA should lead to even more mechanical behaviors improvement such as high strength, ductility, etc. As a new alloy concept, HEA and CCA have been soon regarded as potential candidates to meet issues in relation to energy saving in transportation, for example. Higher temperature and more efficient airplane engines need novel alloys
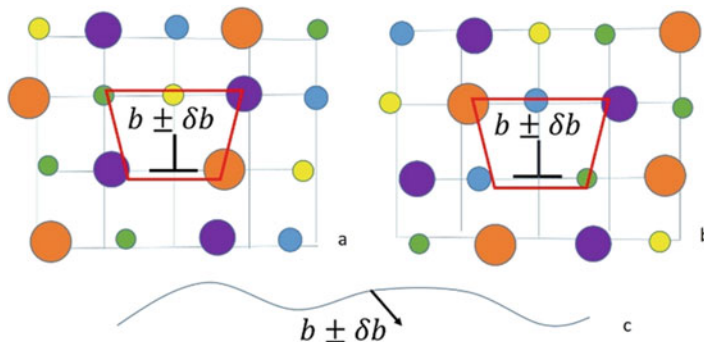
Fig. 21.9 Scheme of two successive cross sections, (**a**) and (**b**), perpendicular to a dislocation line showing that environment around the line is continuously changing. This is producing fluctuation of the Burgers vector and the shear modulus. (**c**) is a scheme of a dislocation line with the fluctuating Burgers vector

to replace superalloys, and lighter and high-strength alloys are necessary for structure lightening.

As previously discussed, atomic structure of HEA/CCA is characterized by lattice distortion. In addition, although atomic organization is not clearly defined (possible local clusters formation, nano-phases, etc.), it should be close to a random atom distribution on the crystal lattice (maximum configurational entropy). From that description, all defects involved in the micro-mechanisms controlling the mechanical properties are to be revisited with consideration of the small and local differences with respect to an average crystal lattice. High-temperature diffusion-like mechanism has been discussed in the "sluggish diffusion section." At low temperature, the deformation is controlled by dislocation dynamics. There are two interesting structural aspects concerning this defect. First, if a dislocation line is well defined on an average crystal lattice, the distortion along the line is producing fluctuation in the magnitude of an average Burgers vector such that the Burgers vector b varies continuously along the line by a small amount comprised in $\pm \delta b$ (Fig. 21.9). This means that dislocation energy, which is also modulated by a fluctuating shear modulus, varies along the dislocation line, $E \approx (G \pm \delta G) \cdot (b \pm \delta b)^2$.

A second feature is that there is no conservation of the local chemical structure of the moving dislocation at any point of the line and then no local energy conservation. This can be seen as a solute-(average) dislocation interaction (as punctually in a standard alloy) occurring continuously. Varvenne and collaborators proposed such description to model the yield strength with good comparison to the fcc NiFeCrCoMn HEA properties [26]. These authors have also examined interaction of dislocation with dilute solute atom in the HEA medium [27]. Here is pointed out the principal feature of plasticity and strengthening that is dislocation interactions with structural characteristics most likely all affected by distortions and atomic random distribution. The work hardening (Taylor relation) is controlled by
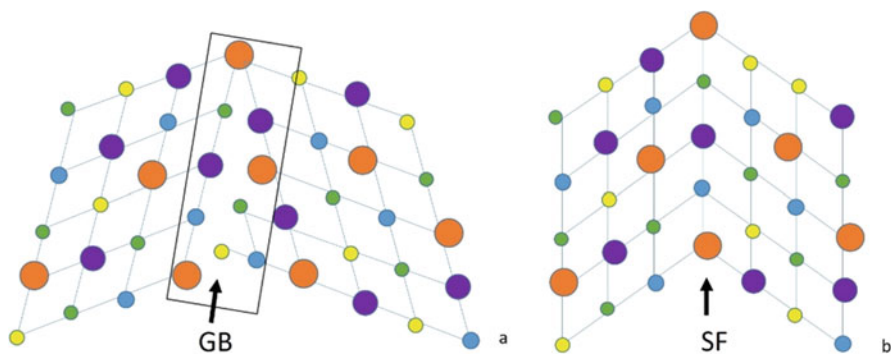
Fig. 21.10 Scheme of (**a**) grain boundary and (**b**) twin boundary

dislocation-dislocation interaction. The Hall-Petch (grain size) effect is controlled by dislocation-grain boundary interaction. The deformation twinning is controlled by dislocation dissociation and stacking fault energy. The grain and twin boundaries are characterized by a lattice disorder but not chemical disorder with respect to the reference random atom distribution (Fig. 21.10). One notices that the stacking fault energy reported for the HEA NiFeCrCoMn is consistent with the observation of decreasing the value with alloying. Stacking fault energy for this alloy is measured of about 20–30 mJ/m^2, for comparison Ni is 90 mJ/m^2.

From all these structural features, different behaviors and/or better performance with respect to common alloys have to be expected. As mentioned in main reviews [1, 28], direct comparison of available data from various HEA and CCA is still difficult owing to difference in composition and thermomechanical treatments. The most recent review on the mechanical properties reports on an extended data analysis available since 2019 [28], and one focuses only from this review on the emblematic strength-deformation behavior. Fig. 21.11 from [28] shows that HEA and CCA are mapping all the domain of the tensile strength vs. elongation properties of common metallic alloys. In compression, the properties are far better with larger values for compression strength up to twice as large (4 GPa), with still reasonable deformation (30%).

These results may be seen modest without the expected clear rupture, but it must be emphasized again that the field of HEA/CCA is still young and that time is needed to find relevant exploitation of all the novel structural features. In support of this argument, probably one of the most remarkable results has been reported by Gludovatz et al. [29]. It is well known that by any process, including by lowering the temperature, the increase in resistance leads to a decrease in ductility of alloys, due to the reduction in dislocations activity, decreasing work hardening and then earlier localization. These authors carried out tensile tests on the NiFeCrCoMn HEA at 293 K, 200 K, and 77 K and showed unexpected (cocktail effect) improved properties with increase in strength and elongation with decreasing temperature
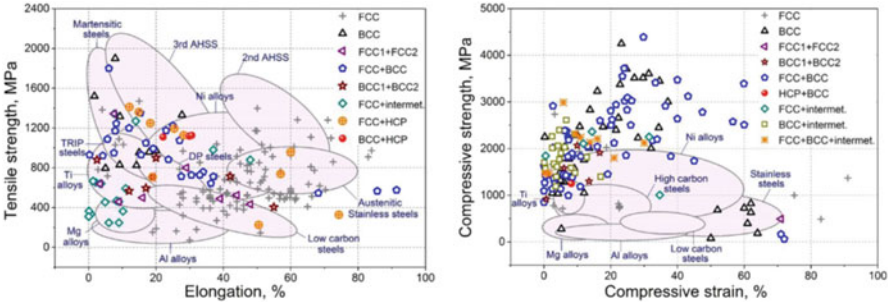
Fig. 21.11 Tensile/compressive strength vs. elongation/compressive strain for various HEA and CCA compared to standard alloys. (From Ref. [28])
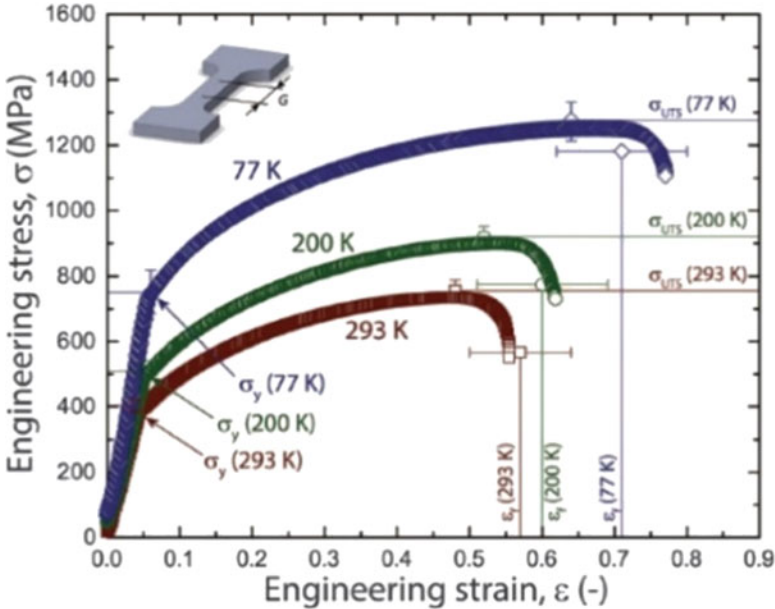
Fig. 21.12 Tensile stress vs. strain for HEA at 293 K, 200 K, and 77 K. (From Ref. [29])

(Fig. 21.12). Constant fracture toughness in the range of 220 MPa·m$^{1/2}$ is also reported.

These properties are associated to a change in deformation mechanism from dislocation glide at room temperature to gradually nano-twinning at 77 K which the atomic structure of HEA is able to do. Obviously, other such unexpected behaviors are to be found.

4.2   Functional Properties

In their critical review [1], Miracle and Senkov pointed out that main functional properties are reported on the 3D transition metal alloys family. Hence, one finds some results on electrical (conductivity), thermal (conductivity), magnetic (soft), and chemical for catalysts and reaction (mainly hydrogen storage). This latter is detailed in the next specific section. With combined effects, one finds thermoelectricity, shape memory, irradiation resistance, functional films for diffusion barrier, and solar absorber. As for mechanical properties, specificities and difference with standard metallic alloys are attributed to atomic distribution and lattice distortions. Main references for detailed reviews on functional properties are reported in [1] with an interesting viewpoint in [30].

Electrical resistivity investigated on $Al_xCoCrFeNi$ ($0 \leq x \leq 2$) is the range of 100–200 $\mu\Omega\cdot$cm. This is similar to the resistivity of the Vitreloy, Zr-based metallic glass, and two order of magnitude larger than the reference copper 1.7 $\mu\Omega\cdot$cm. For other comparison, bronze (CuSn) alloy has resistivity of 42 $\mu\Omega\cdot$cm. The electrical resistivity varies linearly with the temperature. Linear variation is also observed with Al content but with a gradual change owing to crystallographic transition from FCC to BCC. Other element additions have been studied such as Ti in $Al_xCoCrFeNi$. These alloys show large variation in the resistivity from 60 to 400 $\mu\Omega\cdot$cm depending on annealing. Interpretation in terms of HEA and/or CCA properties is not straightforward owing to the formation of B2 and various intermetallic phases. Refractory alloys have been studied such as $Hf_8Nb_{33}Ta_{34}Ti_{11}Zr_{14}$, showing resistivity of 46 $\mu\Omega$. cm at room temperature and 36 $\mu\Omega\cdot$cm at 8K and then drop to zero at 7.3 K.

Thermal conductivity was studied in $Al_xCoCrFeNi$ ($0 \leq x \leq 2$) annealed at 1273K and water quenched and as cast $Al_xCrMnFe_{1.5}Ni_{0.5}Mo_y$ ($x = 0.3$, 0.5 and $y = 0$, 0.1). Respectively, thermal conductivity and diffusivity of these alloys are in the range of 10–27 $Wm^{-1}k^{-1}$ and 2.8–3.5 $mm^{-2}s^{-1}$. These values are lower than pure metals but similar to steels and Ni superalloys. The thermal conductivity decreases with Al content, which is attributed to increase in the lattice distortions. Linear thermal expansion is rather classical compared to highly alloyed metallic materials such as austenitic steels.

Soft magnetic properties are investigated for electrical transformer application, with search for the combination of low coercive field, high-saturation induction, and high electrical conductivity for low loss at high frequency. Then the starting point is naturally FCC solid solutions of Fe, Ni, and Co alloys. The complexity toward CCA has been found by adding Al to form FCC + BCC/B2 phase and adding Si to form FCC + silicides. These alloys are all ferromagnetic with, respectively, saturation magnetization (M_s) of 102 emu/g and 80.5 emu/g with Al and Si additions. For comparison, M_s is 151 emu/g for FeNiCo, 218 emu/g for Fe, and 55 emu/g for Ni. The complex FeNiCoAl and FeNiCoSi alloys show very small magnetostriction effect which is of particular interest when subjected to external magnetic field. More complexity was tested with combining FeNiCo with AlCrCu leading to AlCoCrCuFeNi ferromagnetic in the as-cast state. The alloy exhibits very complex

distribution of paramagnetic FCC Cu and AlNi B2 phases and ferromagnetic FCC CoCrFe and BCC CrFe phases. The mixing of Al_xCrTi to FeNiCo ($0 \leq x \leq 2$) produces as-cast ferromagnetic with also complex phase mixing.

4.3 Hydrogen Storage

Hydrogen is the most efficient and potentially a clean energy carrier for transportation, nomad, and static devices. Currently (twenty twenties), researches in relation with hydrogen know unprecedented funding around the world for technological development related to energy and ecological societal needs. The growing number of hydrogen fuel cell public buses, trains, and private cars in European countries is emblematic. For improving and increasing hydrogen use, hydrogen storage is probably among the key challenges with at least the following specifications: the carrier must be efficient for storage and restitution, sustainable, high capacity, safe, and lightweight for mobile applications. Several technologies involving materials are studied (see, e.g., for review [31, 32]) as porous materials (metal-organic frameworks), liquid hydrides (cyclic alkane compounds, ammonia), and metallic hydrides such as aluminum-based and Mg-based alloys and intermetallics (ZrNi). Discovery of $LaNi_5$ led to significant development of solid materials for this application. The intermetallic storage is reversible, occurring around atmospheric pressure and with reasonable capacity of 1 H/M (hydrogen per metal). The conditions allow using $LaNi_5$ as negative electrode in batteries, electrochemically charged in hydrogen. However, in spite of excellent capacity, the performance is decreasing drastically with cycling, owing to decrepitating-related stress during hydrogenation and release and then corrosion in the KOH electrolyte. In the search for improving sustainability, a first level of complexity was used with partial substitution of La and Ni leading to $La_{0.8}Nd_{0.2}Ni_{2.5}Co_{2.4}Si_{0.1}$ showing drastic improvement in cycling with less decrepitating.

In this context, HEA and mainly CCA have appeared as potential interesting solutions for solid hydrogen storage materials because of their structural and chemical flexibility and tunable properties. In particular, the local lattice strain and fluctuation should possibly allow large interstitials sites for hydrogen occupation. The lattice strain may also allow higher resistance to decrepitating with less cycling-induced strain. In addition, metallic elements mixing in solid solution is more easily adjusted for hydrogen affinity compared to intermetallics. In connection with composition and then a relevant parameter for designing, the valence electron concentration (VEC) shows correlation with hydrogen storage capacity. Generally, degrading capacity is known for increasing the VEC above a certain limit for bcc alloys [33]. From experimental works on various ternary, quaternary, and quinary refractory alloys, a linear correlation was observed between the VEC and hydrides stability [34]. Among a simple capacity indicator, VEC and its relation with electronic structure opens interesting starting point for understanding hydrogen sorption properties in HEA and CCA. In contrast, the relationship between the lattice

distortion and capacity is not so clear and would need further investigations. For example, the group of Nigard studied series of bcc alloys $TiVZr_{(1-x)}NbTa_x$, where the lattice distortion is tuned by the Zr content. Nevertheless, interpretation is not straightforward since the various alloys have different lattice parameter and stability, with some alloys showing phase separation after hydrogen sorption/desorption [35].

Perspectives are now obvious, though research works are still few and focused mainly on lightweight bcc HEA. The first work was reported in 2014 by Kunce et al. on the bcc solid solution TiZrNbMoV showing low capacity of 0.6 weight % [36]. Soon after, Sahlberg et al. reported on an outstanding capacity of 2.5 H/M (2.7 weight %), larger than capacity of the single elements (2 H/M) for the TiVZrNbHf alloy [37]. Interestingly, hydrogenation is a single step reversible bcc-bct reaction, and such high hydrogen uptake has never been observed in transition metal, indicating that tetrahedral and octahedral sites are occupied in the crystal lattice [38].

Initially, researches focused on elemental substitution in HEA revealing interesting phenomena. For example, isoelectronic change of V by Ta leads to TiTaZrNbHf showing unexpectedly two-phase transformations bcc-bct-fcc in hydrides formation [39]. Such type of results incite to extend toward the CCAs for improving, with elements content variations such as Zr-deficient TiVNb-Zr [40] and elemental doping with the same VEC as TiVNb-(Cr, Ni, or Co) [41]. Interestingly, comparisons between the various alloys in terms of hydrogen capacity and structural properties (phase transformations) put the lattice distortion at the first level in dominant parameters along with VEC for designing relevant hydrogen storage materials.

Beside alloy design, preparation, processing, implementation, and integration will be soon a great challenge for the development of HEA/CCA. Alloys containing light metals like in $MgZrTiFe_{0.5}Co_{0.5}Ni_{0.5}$ [42] and MgAlTiFeNi [43] are rather challenging. The difference in melting points between elements and high-vapor tension of Mg is dealt in these works by solid-state ball milling syntheses. The refractory alloys containing Ti, V, Zr, Nb, Hf, Mo, and Ta are prepared by melting and solidification, for which thermophysical properties (viscosity, thermal capacity, surface tension, etc.) are key data.

As a general remark, it must be emphasized that the capacity of the refractory HEA/CCA is similar to those of rare earth metal hydrides (H/M >2.3), which are strategic elements and have a high geopolitical issue.

5 Thermophysical Properties

Previous pages attempt to define HEA and CCA and to show their novelties and perspectives. As any metallic alloys, their development with specific performances will need to control processing steps. The properties strongly depend on the history of the material, and solidification is one of the crucial steps for metallic alloys all the more crucial with the chemical complexity of the alloys. During solidification,

structural evolution and conditions will lead to final microstructure and phase formation with various possible features such as grain size, micro- and macro-segregation, dendrite, clustering, gradient, phase separation, stress relaxation, growth twinning, etc. Understanding structural evolution during solidification demands the knowledge of thermophysical properties of the melt. Additionally, the necessary precise thermophysical properties for theory and modelling require measuring them in microgravity [44]. This justifies the paramount importance of parabolic flight and space experiments.

Thermophysical properties of HEA and CCA are still very few. Ground experiments are reported for temperature surface tension. For example, on CuSnBiInPb [45], the same group in Russia published viscosity measurement on the same alloy in Russian language only [46].

The available data for HEA/CCA from microgravity experiments are reported in the next paragraph. With their specific multi-elementary high concentration, character-specific behaviors are expected. With available techniques (described in this book), measurements are for surface tension as function of temperature and undercooling, specific heat, thermal conductivity, emissivity, heat capacity, electrical conductivity, density, coefficient of thermal expansion, and viscosity.

5.1   Parabolic Flight Experiments

The very first experiments on HEA were carried out during the DLR/ESA (German space center/European space agency) parabolic flight campaign 2018. The studies were supervised by M. Mohr, R. K. Wunderlich, and H. J. Fecht of the Institute of Functional Nanosystems of Ulm University and part of the DLR ThermoLab and ESA ThermoProp projects. The works were performed on a FeCrNiCo-0.1Al alloy with three parabolas to measure the surface tension and viscosity undercooling of about 100 K and one parabola for electrical resistivity and sample radius measurements.

The equipment is consisting in a process and a sample chamber, connected to a vacuum pump system and a gas circulation unit. The sample is heated and positioned by radio frequency (rf-) electromagnetic fields. A dipole field for heating and a quadrupole field for positioning are superimposed using a single coil system operating at frequencies of 330 kHz (heating) and 170 kHz (positioning). The process chamber is equipped with two high-speed cameras. The axial camera is additionally equipped with an optical pyrometer with a measurement range between 300 and 2100 °C. A second camera is positioned in radial direction. In addition, the sample coupling electronics (SCE), developed by Georg Lohöfer from DLR, Institut für Materialphysik im Weltraum, Cologne, is used to measure the current, voltage, phase shift, and frequency of the rf-heating voltage with high accuracy and a data rate of 400 Hz. Then the changed sample coupling due to the varying sample diameter during oscillations is measured to determine surface tension and viscosity.
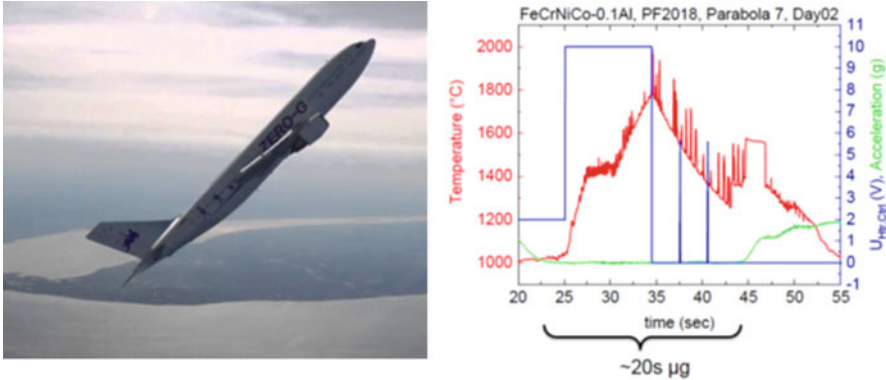
Fig. 21.13 Airplane for experiments close to Bordeaux, France, and representative temperature-time profile during parabola flight

Parabolic flights allow about 20 s of reduced gravity, which is sufficient for most alloys to heat the sample until melting, overheat the melt, and cool it down until solidification. The cooling period is the time span where the heater is turned off, and therefore, only minimal forces act on the sample. Hence, short heater pulses are applied to initiate surface oscillations. The oscillation frequency is measured in order to obtain the surface tension, and the damping time constant of the surface oscillations is used to obtain the viscosity of the sample.

The acceleration on the sample is shown as a function of time, in green in Fig. 21.13. The μ-g phase is about 20 s. The heater control voltage is shown in blue, showing the time duration when the sample is heated until melting, followed by further overheating in the beginning of the μ-g phase. Afterward, the heater is turned off and only two short pulses are used to initiate surface oscillations. In red, the sample temperature is shown as a function of time. After 10 s, the sample is already molten and overheated to the maximum temperature of around 1700 °C. Afterward, the sample undercools by about 100 K and solidifies during levitation. From the three working parabolas, the first one was performed without heater pulses to be able to measure the sample electrical resistivity and diameter by the sample coupling electronics (SCE). The analysis of the electrical resistivity and the sample radius was done by Georg Lohöfer from DLR, Institut für Materialphysik im Weltraum, Cologne.

The surface tension σ is evaluated from the surface oscillation frequency ν_R and the sample mass M using $\sigma = \frac{3}{8}\pi\nu_R^2 M$.

However, applicability of this relation is subjected to some constraints. The surface oscillation frequency, characterized by ν_R the Rayleigh frequency, pertains to the oscillations of a force-free spherical droplet. Under 1-g electromagnetic levitation, the sample is not force free and deformed. A correction was developed to account for the effect of the magnetic pressure on the surface oscillation frequency and was successfully proven by comparison with micro-g ground-based surface
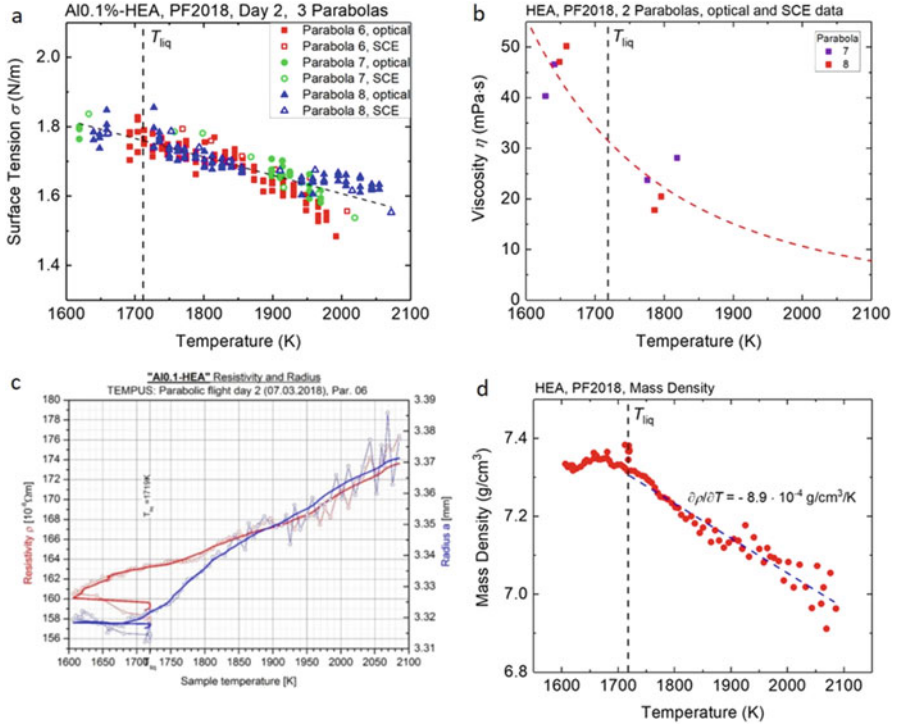
Fig. 21.14 Results of the parabolic flight experiments as a function of temperature. (**a**) Surface tension (measured by the SCE and optical method), (**b**) viscosity, (**c**) resistivity and sample radius, and (**d**) mass density

tension measurements in an EML device. Under reduced gravity conditions such as present in a parabolic flight, the sample is nearly force free and spherical. Under this condition, application of the so-called Cummings and Blackburn correction results in a reduction of the surface tension values in the range between 2% and 3% when the measured surface oscillation frequency instead of ν_R is used in the formula for the evaluation of the surface tension. This correction was not yet applied to the data presented here. It is only weakly temperature dependent. The temperature dependance of the surface tension from Fig. 21.14a is given, with T in K by

$$\sigma(T) = (1.7559 \pm 0.004) - (5.31 \pm 0.21) \times 10^{-4}\,(T - 1719)\,\text{N} \cdot \text{m}^{-1}$$

The viscosity is determined by the damping time constant of the surface oscillations following $\eta = \frac{3}{20\pi}\frac{M}{R}\nu_R^2\tau^{-1}$, where R is the sample radius and is τ the time constant. Small amount of data was obtained for viscosity of the HEA, due to the small numbers of parabolas with heater pulses (two). The temperature-dependent viscosity is shown in Fig. 21.14b. At liquidus temperature, the viscosity is

$\eta = 33$ mPa·s which is particularly high compared to viscosity of constituting elements at liquidus, 5.6 for Fe, 5.7 for Cr, 4.7 for Ni, and 5.4 for Co.

Eventually, the electrical resistivity and sample radius as a function of temperature were measured, shown in Fig. 21.12c. It can be seen that both resistivity and expansion coefficient vary strongly between the solid and liquid phase. The measurement was done from the highest temperature during cooling into the undercooled liquid and in the solid phase. Specific resistivity at liquidus temperature is obtained of the order of $\rho \approx 164$ $\mu\Omega$·cm. From mass density derived from the sample radius variations, the mass density changed is obtained, $\partial\rho/\partial T \approx -8.9 \times 10^{-4}$ g·cm^{-3}.

The first results and unusual thermophysical properties have convinced to pursuing in further investigations. In summer 2021, the FeCrNiCo quaternary alloy will be analyzed in the upcoming Batch#3 on board the ISS. Furthermore, at the same period, measurements will start on TiVCrZrNb HEA and $Ti_{0.3}V_{0.25}Zr_{0.1}Nb_{0.25}Ta_{0.1}$ CCA for H-storage, in the 2021 parabolic flight campaign.

6   Concluding Remarks

High-entropy alloys (HEA) and complex concentrated alloys (CCA) form a new class of metallic materials based on their design approach. Conventional in particular modern alloys can be complex in composition, microstructure, and phase distribution, but always, design is starting from a single metallic element ("corner" of the phase diagram). HEA and CCA bring a real breakthrough in design with, as a starting point, the multi-elementary mixing of at least five elements (middle of the phase diagram). This novel approach leads to tremendous possibilities, from which novel properties are expected in particular in relation with the "cocktail" core effect.

In this chapter, the need for novel metallic alloys and alloy design are discussed. Definitions of HEA and CCA are detailed with the specific four core effects, high entropy, lattice distortions, sluggish diffusion, and cocktail effect. Then a quick overview is given on the mechanical and functional properties with a focus on hydrogen storage since CCA alloys for this application will be soon studied in parabolic flights.

The chapter ends with the first thermophysical measurements carried out in parabolic flights on a FeCrNiCo-0.1Al alloy. The results of surface tension, viscosity, resistivity, sample radius, and mass density are reported showing in particular high viscosity. Along with interesting fundamental aspects, the perspectives of HEA and CCA for applications make essential to measure their thermophysical properties for the control of microstructure during the solidification stage of the processing.

References

1. D.B. Miracle, O.N. Senkov, A critical review of high entropy alloys and related concepts. Acta Mater. **122**, 448–511 (2017)
2. R.O. Ritchie, The conflicts between strength and toughness. Nat. Mater. **10**, 817–822 (2011)
3. J.W. Yeh, S.K. Chen, S.J. Lin, J.Y. Gan, T.S. Chin, T.T. Shun, C.H. Tsau, S.Y. Chang, Nanostructured high-entropy alloys with multiple principal elements: Novel alloy design concepts and outcomes. Adv. Eng. Mater. **6**, 299–303 (2004)
4. B. Cantor, I.T.H. Chang, P. Knight, A.J.B. Vincent, Microstructural development in equiatomic multicomponent alloys. Mater. Sci. Eng. A Struct. Mater. Properties Microstruct. Process. **375**, 213–218 (2004)
5. S. Gorsse, J.P. Couzinie, D.B. Miracle, From high-entropy alloys to complex concentrated alloys. Comptes Rendus Physique **19**, 721–736 (2018)
6. J.D. Verhoeven, The mystery of Damascus blades. Sci. Am. **284**, 74–79 (2001)
7. R.P. Kolli, A. Devaraj, A review of metastable beta titanium alloys. Metals **8**, 41 (2018)
8. C.A. Schuh, T.C. Hufnagel, U. Ramamurty, Overview No.144 – Mechanical behavior of amorphous alloys. Acta Mater. **55**, 4067–4109 (2007)
9. M.M. Khan, A. Nemati, Z.U. Rahman, U.H. Shah, H. Asgar, W. Haider, Recent advancements in bulk metallic glasses and their applications: A review. Crit. Rev. Solid State Mater. Sci. **43**, 233–268 (2018)
10. J.M. Jani, M. Leary, A. Subic, M.A. Gibson, A review of shape memory alloy research, applications and opportunities. Mater. Des. **56**, 1078–1113 (2014)
11. D.B. Miracle, High-entropy alloys: A current evaluation of founding ideas and core effects and exploring "nonlinear alloys". JOM **69**, 2130–2136 (2017)
12. A. Deschamps, F. Tancret, I.E. Benrabah, F. De Geuser, H.R. Van Landeghem, Combinatorial approaches for the design of metallic alloys. Comptes Rendus Physique **19**, 737–754 (2018)
13. J. Schmidt, M.R.G. Marques, S. Botti, M.A.L. Marques, Recent advances and applications of machine learning in solid-state materials science. npj Comput. Mater. **5**, 36 (2019)
14. S. Gorsse, F. Tancret, Current and emerging practices of CALPHAD toward the development of high entropy alloys and complex concentrated alloys. J. Mater. Res. **33**, 2899–2923 (2018)
15. G. Bracq, M. Laurent-Brocq, C. Varvenne, L. Perriere, W.A. Curtin, J.M. Joubert, I. Guillot, Combining experiments and modeling to explore the solid solution strengthening of high and medium entropy alloys. Acta Mater. **177**, 266–279 (2019)
16. F. Otto, Y. Yang, H. Bei, E.P. George, Relative effects of enthalpy and entropy on the phase stability of equiatomic high-entropy alloys. Acta Mater. **61**, 2628–2638 (2013)
17. Y. Zhang, Y.J. Zhou, J.P. Lin, G.L. Chen, P.K. Liaw, Solid-solution phase formation rules for multi-component alloys. Adv. Eng. Mater. **10**, 534–538 (2008)
18. L.R. Owen, H.J. Stone, H.Y. Playford, The assessment of local lattice strains in alloys using total scattering. Acta Mater. **170**, 38–49 (2019)
19. P.G. Debenedetti, F.H. Stillinger, Supercooled liquids and the glass transition. Nature **410**, 259–267 (2001)
20. Y. Champion, N. Thurieau, The sample size effect in metallic glass deformation. Sci. Rep. **10**, 7 (2020)
21. J.W. Yeh, Recent progress in high-entropy alloys. Ann. De Chimie-Sci. Des Mater. **31**, 633–648 (2006)
22. K.Y. Tsai, M.H. Tsai, J.W. Yeh, Sluggish diffusion in Co-Cr-Fe-Mn-Ni high-entropy alloys. Acta Mater. **61**, 4887–4897 (2013)
23. S. Ranganathan, Alloyed pleasures: Multimetallic cocktails. Curr. Sci. **85**, 1404–1406 (2003)
24. M. Laurent-Brocq, L. Perriere, R. Pires, F. Prima, P. Vermaut, Y. Champion, From diluted solid solutions to high entropy alloys: On the evolution of properties with composition of multi-components alloys. Mater. Sci. Eng. A Struct. Mater. Properties Microstruct. Process. **696**, 228–235 (2017)
25. I. Guillot, M. Tyrman, L. Perriere, J.P.P. Couzinie, L. Lilensten, F. Prima, G. Dirras, Ultrafine-grained two-phase high-entropy alloy microstructures obtained via recrystallization: Mechanical properties. Front. Mater. **7**, 11 (2020)

26. C. Varvenne, A. Luque, W.A. Curtin, Theory of strengthening in fcc high entropy alloys. Acta Mater. **118**, 164–176 (2016)

27. C. Varvenne, W.A. Curtin, Strengthening of high entropy alloys by dilute solute additions: CoCrFeNiAlx and CoCrFeNiMnAlx alloys. Scr. Mater. **138**, 92–95 (2017)

28. E.P. George, W.A. Curtin, C.C. Tasan, High entropy alloys: A focused review of mechanical properties and deformation mechanisms. Acta Mater. **188**, 435–474 (2020)

29. B. Gludovatz, A. Hohenwarter, D. Catoor, E.H. Chang, E.P. George, R.O. Ritchie, A fracture-resistant high-entropy alloy for cryogenic applications. Science **345**, 1153–1158 (2014)

30. X.H. Yan, Y. Zhang, Functional properties and promising applications of high entropy alloys. Scr. Mater. **187**, 188–193 (2020)

31. L.J. Bannenberg, M. Heere, H. Benzidi, J. Montero, E.M. Dematteis, S. Suwarno, T. Jaron, M. Winny, P.A. Orlowski, W. Wegner, et al., Metal (boro-) hydrides for high energy density storage and relevant emerging technologies. Int. J. Hydrog. Energy **45**, 33687–33730 (2020)

32. M. Hirscher, V.A. Yartys, M. Baricco, J.B. von Colbe, D. Blanchard, R.C. Bowman, D.P. Broom, C.E. Buckley, F. Chang, P. Chen, et al., Materials for hydrogen-based energy storage – Past, recent progress and future outlook. J. Alloys Compd. **827**, 39 (2020)

33. K. Sakaki, H. Kim, K. Asano, Y. Nakamura, Hydrogen storage properties of Nb-based solid solution alloys with a BCC structure. J. Alloys Compd. **820**, 6 (2020)

34. M.M. Nygard, G. Ek, D. Karlsson, M.H. Sorby, M. Sahlberg, B.C. Hauback, Counting electrons – A new approach to tailor the hydrogen sorption properties of high-entropy alloys. Acta Mater. **175**, 121–129 (2019)

35. M.M. Nygard, G. Ek, D. Karlsson, M. Sahlberg, M.H. Sorby, B.C. Hauback, Hydrogen storage in high-entropy alloys with varying degree of local lattice strain. Int. J. Hydrog. Energy **44**, 29140–29149 (2019)

36. I. Kunce, M. Polanski, J. Bystrzycki, Microstructure and hydrogen storage properties of a TiZrNbMoV high entropy alloy synthesized using Laser Engineered Net Shaping (LENS). Int. J. Hydrog. Energy **39**, 9904–9910 (2014)

37. M. Sahlberg, D. Karlsson, C. Zlotea, U. Jansson, Superior hydrogen storage in high entropy alloys. Sci. Rep. **6**, 6 (2016)

38. D. Karlsson, G. Ek, J. Cedervall, C. Zlotea, K.T. Moller, T.C. Hansen, J. Bednarcik, M. Paskevicius, M.H. Sorby, T.R. Jensen, et al., Structure and hydrogenation properties of a HfNbTiVZr high-entropy alloy. Inorg. Chem. **57**, 2103–2110 (2018)

39. C. Zlotea, M.A. Sow, G. Ek, J.P. Couzinie, L. Perriere, I. Guillot, J. Bourgon, K.T. Moller, T.R. Jensen, E. Akiba, M. Sahlberg, Hydrogen sorption in TiZrNbHfTa high entropy alloy. J. Alloys Compd. **775**, 667–674 (2019)

40. J. Montero, C. Zlotea, G. Ek, J.C. Crivello, L. Laversenne, M. Sahlberg, TiVZrNb multi-principal-element alloy: Synthesis optimization, structural, and hydrogen sorption properties. Molecules **24**, 14 (2019)

41. B. Hessel Silva, C. Zlotea, Y. Champion, W.J. Botta, G. Zepon, Design of TiVNb-(Cr, Ni or Co) multicomponent alloys with the same valence electron concentration for hydrogen storage. J. Alloys Compd. **865**, 158767 (2021)

42. G. Zepon, D.R. Leiva, R.B. Strozi, A. Bedoch, S.J.A. Figueroa, T.T. Ishikawa, W.J. Botta, Hydrogen-induced phase transition of MgZrTiFe0.5Co0.5Ni0.5 high entropy alloy. Int. J. Hydrog. Energy **43**, 1702–1708 (2018)

43. K.R. Cardoso, V. Roche, A.M. Jorge, F.J. Antiqueira, G. Zepon, Y. Champion, Hydrogen storage in MgAlTiFeNi high entropy alloy. J. Alloys Compd. **858**, 9 (2021)

44. M. Mohr, H.J. Fecht, Investigating thermophysical properties under microgravity: A review. Adv. Eng. Mater. **23**, 15 (2021)

45. V.V. V'Yukhin, O.A. Chikova, V.S. Tsepelev, Surface tension of liquid high-entropy equiatomic alloys of a Cu-Sn-Bi-In-Pb system. Russ. J. Phys. Chem. A **91**, 613–616 (2017)

46. O.A. Chikova, K.Y. Shmakova, V.S. Tsepelev, Kinetic viscosity of molten high entropy alloys Cu–Sn–In–Bi–Pb. Izvestiya Vysshikh Uchebnykh Zavedenij Tsvetnaya Metallurgiya, 57–60 (2015)

Chapter 22
Laser-Assisted Additive Manufacturing of Ni-Based Superalloy Components

Manoj Kumar, Jyotsna Dutta Majumdar, Hans-Jörg Fecht, and Indranil Manna

1 Engineering Materials

The progress of human civilization is intimately related to discovering or developing new materials and exploiting the same for specific purpose. At the very beginning, this "new" possibly was as rudimentary as stone (harder, sharper, heavier, and more durable than clay or wood) in the Stone Age and as exotic as steel, glass, silicon, diamond, carbon nanotube, or cubic boron nitride in the modern times. No wonder why different era of early stages of human civilization is identified with specific solids (such as stone, copper, or iron) or the level of proficiency of utilization of them that made living better in some way or the other. History proves that a new material, compositionally or structurally, has often led to a crucial breakthrough in performance and functionality and enabled translation of innovative ideas and design into new components, devices, and machines and eventually opening up a new possibility (e.g., electrical machines and semiconductor devices) or greater level of efficiency (e.g., internal combustion and turbine engines). Materials science, engineering, and technology have been the key enabler in this journey as this

M. Kumar
Metallurgical & Materials Engineering, IIT Kharagpur, Kharagpur, West Bengal, India

CSIR-IMMT, Bhubaneswar, Odisha, India

J. D. Majumdar
Metallurgical & Materials Engineering, IIT Kharagpur, Kharagpur, West Bengal, India

H.-J. Fecht
Institute for FNS, University of Ulm, Ulm, Germany

I. Manna (✉)
Metallurgical & Materials Engineering, IIT Kharagpur, Kharagpur, West Bengal, India

BIT Mesra, Ranchi, India
e-mail: imanna@metal.iitkgp.ac.in

seamless caucus has continuously endowed human society with improved standard of living and security against exigencies. Survival, growth, and prosperity of mankind, therefore, have hugely depended on the level of exploitation of engineering materials, be it for developing rudimentary tools or weapons in the pre-historic period to the most sophisticated components, devices, machines, and systems in the modern era. One must admit advancement in processing of materials plays a key role, too.

All the solids materials may not be used for engineering application. The materials needed for any engineering purpose, naturally occurring or synthesized, and useful to fabricate an engineering component, device, appliance, structure, amenity, or a complete system can only qualify to be engineering materials. Imagination and innovation allow exploitation of engineering materials to design and develop a new and novel solution that either nature does not offer as a ready solution or does not exist as yet. Water that ensures existence of life on earth is not an engineering material, but steam from water needed to generate electricity or locomotion certainly qualifies as engineering material. Frankly, almost all matter in any physical state can offer some utility and hence qualify as engineering materials.

Undoubtedly, metals should head that list not just for historical legacy but purely because of the sheer volume of application and utility. From the oldest metal artifact, a copper awl [1] (a drill or a conical tool) unearthed in Tel Tsaf village of Israel dating more than 7000 years, all the way to the most wonderful and useful metal of modern era, the superalloys (material for aeroengine turbine blades) that has survived even after sustained use in the most challenging conditions and has still been evolving since its earliest formulation nearly a century ago, the history of metals or more precisely metallic alloys is replete with an amazing number and fascinating documentary of development over centuries. Let us take superalloy as an example.

2   History of Superalloy

All crystalline solids, pure element or multicomponent alloys, soften as they approach and eventually melt or liquefy above the respective melting, fusion, or liquidus temperatures. Retaining strength at elevated temperatures, not necessarily close to fusion but even above half of its melting temperature, is an ambition that alloy designers have always keenly pursued. This challenge arises because strengthening mechanism of crystalline solids undergoes a major change from boundary dominated to grain body-controlled regime at such high temperatures. The principal motivation for developing alloys with high-temperature strength comes from the applications that demand operating at high temperature for the sake of enhancing efficiency, conducting specific jobs or functions, and exploring operations not feasible at ambient conditions. In case of steel, the most widely exploited workhorse metallic solid used for structural applications has undergone a series of experimentation over the years with the primary objective of retaining strength at elevated temperature. The outcome was evolution of a series of structural materials like alloy

steels, tools steels, stainless steels, high-speed steels, maraging steels, and superalloys, though the last two being technically more appropriate to be called nonferrous alloys than steels going by composition.

Superalloys are based on a multicomponent recipe with nickel, nickel-iron, or cobalt as the main or matrix element, offering excellent combination of mechanical strength, creep, and fatigue properties and resistance to oxidation and corrosion at elevated temperature. These heat-resisting alloys are practically the ultimate choice for aircraft jet engines, gas turbines, chemical process industries, heat exchanger tubes, nuclear reactors, coal conversion and gasification plants, and all other applications operating at temperatures well above half of their melting/fusion temperatures [2]. Superalloys are classified into three groups based on the major or matrix element present, namely, (a) Fe-based superalloys, (b) Ni-based superalloys, and (c) Co-based superalloys. The usual alloying elements include Cr, Al, Ti, Nb, V, Mo, etc.

Fe- or Fe+Ni-based superalloys with up to 25 wt.% Ni are essentially austenitic or face-centered cubic (FCC) matrix alloys strengthened both by solid solution and precipitation hardening that offer good mechanical strength at room temperature as well as at elevated temperature [2]. These alloys are also characterized by resistance to oxidation, wear, creep, and hot corrosion. Fe-based superalloys are relatively cheaper compared to Ni- or Co-based superalloys.

On the other hand, Ni-based superalloys are the most widely used in the hottest parts of turbine and similar applications. More than 50% by weight of the aircraft engine components are made from Ni-based superalloys due to greater phase stability of Ni-rich FCC matrix and associated ordered precipitates that arise following precipitation hardening [2]. Presence of alloying elements like Cr and Al readily enhances the corrosion and oxidation resistance. Ni-based superalloys usually retain strength up to about 1100 °C.

In comparison, Co-based superalloys can retain their strength at even higher temperature, though offering strength slightly inferior to that of Ni-based superalloys. Presence of refractory metal carbides (e.g., WC, Mo_2C) along grain boundaries is the main reason for retaining strength at higher, nearly close to melting temperatures in these alloys. Higher level of Cr makes these alloys more corrosion and oxidation resistant (through formation of Cr_2O_3 film on the surface). Co-based superalloys are also fairly thermal shock resistant.

Inconel series of alloys, say Inconel 718 (55Ni-21Cr-5Nb-3Mo), belong to Ni-Cr-based superalloys and are available in a wide composition range (containing varying amounts of Fe, Al, Nb, Ti, and Mo). These superalloys offer very attractive combination of mechanical properties mainly due to solid solution and precipitation hardening. The key allotriomorphic or idiomorphic precipitates in the Ni-rich γ matrix (FCC) are γ″ (Ni_3Nb) and γ′ (Ni_3TiAl), along with some amounts of interstitial carbide compounds of Ti or Nb, despite having very low C content. Mo enhances solid solution hardening. Inconel 718 (IN718) is very effective in registering steady diffusion-controlled parabolic-rate oxidation resistance at atmospheric pressure in air over a large temperature range (950–1300 °C) [3]. At still higher temperature, strength deteriorates rapidly and oxidation is almost catastrophic

[4]. Inconel alloys are suitable for several applications like nuclear reactors, aero/gas turbines, and rocket motors, as already stated, because of significant resistance to creep, thermal fatigue, oxidation, hot corrosion, and erosion. Further extension of life and reliability is often ensured at elevated temperatures by providing a protective layer at the surface, called thermal barrier coating [5].

3   Laser Additive Manufacturing (LAM)

Additive manufacturing is an innovative approach based on sequential integration of microscale melting and solidification events in one-, two-, and three-dimensional space following a definite design and geometry. Laser is useful for a wide variety of materials processing like cutting, joining, fabricating, surface engineering, and repairing of components [5]. As a logical extension, laser-assisted additive manufacturing (LAM) has now emerged as the most versatile, flexible, and effective method of additive manufacturing widely applied for direct manufacturing of finished net shape or near-net shape metallic components with the aid of computer-aided design tools. LAM adopts two main approaches: laser-based powder bed fusion (LPBF) and laser-assisted direct energy deposition (LDED) techniques [6]. LPBF process may be conducted by selective laser melting (SLM), selective laser sintering (SLS), or laser metal fusion (LMF) methods, while LDED may involve laser-engineered net shaping (LENS), direct metal deposition (DMD), or laser metal deposition (LMD) methods, respectively [7].

Historically, the concept of additive manufacturing including LAM can be considered as an extension of rapid prototyping of polymeric materials and rapid tooling technology of metallic components [8]. The process sequence in additive manufacturing involves computer-aided design (CAD) of the component → creation of three-dimensional (3D) view with two-dimensional (2D) slices in standard template library of digital files → transfer of design to LAM machine console → development and adoption of manufacturing routine → cleaning and withdrawal from the powder bed in the machine → post processing operations, if any. In general, additive manufacturing process may be classified into the following categories: vat photo-polymerization, binder jetting, materials jetting, sheet lamination, materials extrusion, powder bed fusing, and direct energy deposition [9].

As narrated above, the final product, miniature or large, is never made all in one single operation like metal casting or ceramic powder sintering but in multiple identical steps with provisions for changing the composition, process parameters, and accompanying thermal history. In simple words, like in calculus, integration is a mathematical process of joining multiple small differentials, and in engineering, additive manufacturing is a similar physical process of integration of infinitesimally small steps that eventually delivers a finished product. The overall scope and novelty of LAM lies not just in producing a finished product of intricate and novel geometry and functionality but also in developing a product with microstructure, phase aggregate, and properties quite different from what is expected from an engineering

solid fabricated by conventional processing techniques of melting, solidification, sintering, or deposition.

Imagine a machine tool, a bone or dental implant, a metallic valve or nozzle, or an expensive die that needs a change in design for customized fabrication or repair after severe wear and tear. It will not be an easy proposition by conventional route even if it appears simple. This is because conventional manufacturing offers limited freedom to fabricate components of complex shapes, change in dimensions or geometry, vary raw material and composition, and repair a worn or broken component with a fracture surface of irregular or random contour. Even if such improvisation is possible, it will not be economical or convenient, particularly when the number or volume of product or cost per component is small. However, change in shape, dimension, contour, and even composition, partially or wholly, may be necessary, that too in small volumes or quantity say, for a human patient with cancer-afflicted bone or a brake pad or bearing of an expensive racing car. In this respect, additive manufacturing, popularly called 3D printing, is a very attractive proposition for direct fabrication of a wide range of solid structures with variable size, shape, geometry, and complexity from the corresponding 3D CAD model in terms of flexibility, precision, cost, space, time, and novelty. As already explained, the process of LAM will simply involve integration of droplets and successive deposition or printing of successive layers as per the predetermined design.

The pioneering effort of developing such 3D products of polymers by Charles Hull in 1986 using stereo-lithography (SLA) of polymeric precursor was the earliest precursor of additive manufacturing [10]. Though the concept of additive manufacturing using polymers may be fairly old, the exponential growth in the interest and application of this processing route, not just for prototyping but for direct manufacturing of engineering components and products using metallic alloys, is barely a decade old. Once proven feasible, use of metallic powders to develop metallic components was vigorously pursued by powder bed fusion, fused deposition modelling, inkjet printing, and contour crafting approaches. Obviously, application of laser has made the process much more versatile and precise. As a result, LAM is now adopted in almost all sectors of engineering like metal manufacturing, aerospace, automobile, defense, electronics, civil construction, biomedical prosthesis, and many more.

Some of the potential benefits and novelty of LAM products can be (a) direct translation of design to finished product with minimum lead or development time; (b) direct manufacturing of components to final or near-net dimension and shape with minimal or no additional processing; (c) scope of greater customization with no additional tooling or manufacturing cost; (d) introduction of design novelty of retaining hollow volume, complex contour, controlled porosity, and special internal features; (e) approach to a practically zero-waste manufacturing practice; (f) improvisation on demand with no or minimal cost or downtime; and (g) linear scalability. However, it is important to note that LAM products do suffer from inherent flaws, deficiencies, and defects ranging from porosity, cracks, shrinkage, inclusion, contamination, segregation, surface roughness, distortion, and poor mechanical properties as compared to those achievable by conventional practices.

Established components developed and utilized in large scale by additive manufacturing of metals are mostly based on various grades of steel and aluminum alloys for limited structural (load-bearing) and functional (non-load-bearing) applications in ambient condition. Since most components made by additive manufacturing possess metastable microstructure which may transform toward equilibrium state when exposed to high temperature for extended period continuously or in cycles, application of additively manufacture components at elevated temperature is rare and sparsely explored. However, superalloys are meant for prolong use at elevated temperature under constant or cyclic loading condition. Presence of aggressive environment like air, dust, and combustion products demands even more rugged resistance against environmental and mechanical degradation. Thus, studies on development and evaluation of performance and reliability of additively manufactured superalloy components are warranted before fresh attempts are made to employ superalloy-based components in hitherto unexplored critical applications and even substitute the conventional products.

4 Additive Manufacturing of Ni-Based Superalloys

As a group of Ni-/Co-/Fe-based multicomponent alloys with a unique ability to retain mechanical strength at temperatures close to melting or fusion temperature, superalloys find wide and ever-increasing application for key structural components in aviation, aerospace, and power generation industry. Melting to final fabrication of superalloy component requires elaborate, multistage, expensive, and time-consuming processes that is neither common nor easy to practice. Single crystal or even directionally solidified Ni-based superalloy blades for aero-turbine engine are possibly one of most sophisticated and challenging material processing exercises that can easily be cited as a triumph of material technology of recent times. For the advantage of shortening the production time, minimizing the material waste and manufacturing cost, additive manufacturing is gradually becoming the most sought tool for development and repairing of components in various sectors like aerospace, automotive, and medical sectors. In particular, LAM provides the flexibility to fabricate components with controlled microstructure, composition, and texture with minimum defects by proper selection of laser parameters. The extremely rapid cooling rate associated with LAM can create novel and finer microstructure with minimal segregation that can compete with superalloy components developed by conventional methodology of melting and casting. Despite significant success in recent times, the technology concerning LAM is far from being matured enough to foresee the possibility of LAM altogether replacing conventional processing route to develop the entire gamut of all superalloy components currently in use in various industry sectors. In order to understand the current status of developing and exploiting superalloy-based engineering components by LAM and hurdles faced or anticipated by the user industry, an attempt will now be made to review the literature and examine the key advancements and challenges with regard to

microstructural evolution, mechanical properties, dimensional compliance, defects, processing difficulties, reliability, and life assessment.

4.1 Powder Bed Processing by LAM

Broadly, LAM can be conducted either by fixed powder bed or loose powder fed systems where the laser-matter interaction in micro-millisecond period allows melting and solidification in a small volume. As Fig. 22.1 shows, this process in a typical powder bed system creates a solid layer of limited depth and continues in directions guided by the computer-aided design that drives the laser beam [11]. Each new layer on solidification welds with the preceding one laterally and vertically. The phase aggregate of this layer will depend on the laser (wavelength, beam profile, and intensity), process parameters (power density, interaction time/speed, focus position, powder composition, size, shape, and packing density), and material properties (melting/fusion point, specific heat, density, surface energy, thermal conductivity, reflectivity, absorptivity). The resultant microstructure for a given powder bed composition is a complex function of the thermophysical parameters like heating/cooling rate, thermal gradient, melt pool geometry and convection, etc. The main handle to control the microstructure and properties of the product developed by LAM are the two independent process parameters, namely, laser power density and interaction time.
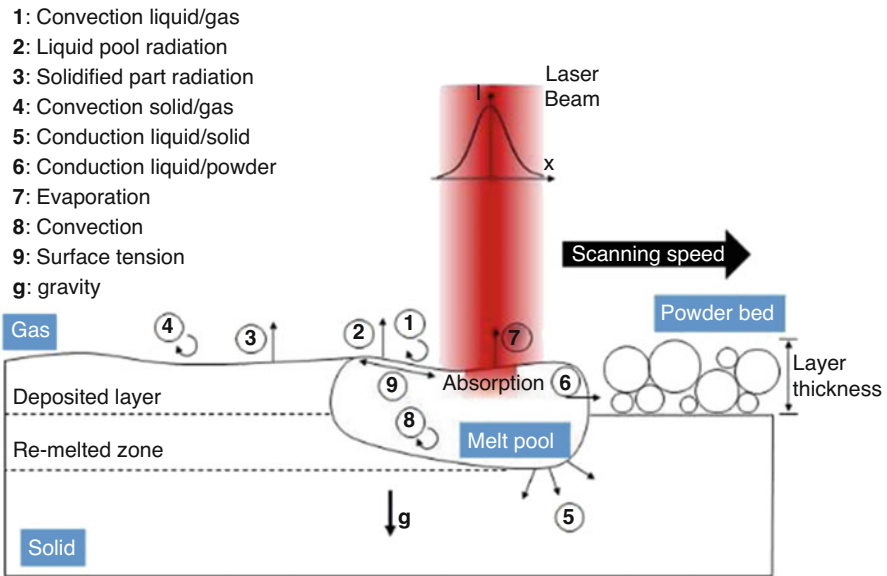
Fig. 22.1 Schematic of various physical phenomenon taking place in SLM process during laser interaction with pre-sprayed powder bed [11]

4.2   Effect of Process Parameters

Selective laser melting (SLM) and direct energy deposition (DED) are the two major techniques for additive manufacturing of metals and alloys. Jia and Gu [4] have shown that inadequate power density tends to spheroidize or ball up powder particles and reduces relative density of the solid. A reasonable power density is needed for near-full densification. The typical microstructures of SLM-processed IN718 parts may manifest morphological changes from coarsened columnar dendrites to clustered dendrites or even thin and uniformly distributed columnar dendrites. This resulted in uniform microhardness distribution, reduced wear rate, and low friction coefficient [12].

Xia et al. [13] have reported that scanning speed or interaction time largely determines the size, shape, and distribution of porosities in the SLM-processed IN718 components. It appears that open porosities form on the surface and also between the layers when laser is processed with a high scanning speed of 500 mm/s due to limited or incomplete melting and wetting of powder. In contrast, laser processing with relatively lower scanning speed of 200 mm/s results in formation of smooth surface with lower porosity on the top surface and cross-sectional plane indicating good metallurgical bonding between successive layers in the growth direction.

Figure 22.2 shows a process or weldability map for IN718 as a function of the independent process parameters of effective laser power and beam velocity [14]. It is apparent that an appropriate choice of laser power and scan speed is essential for
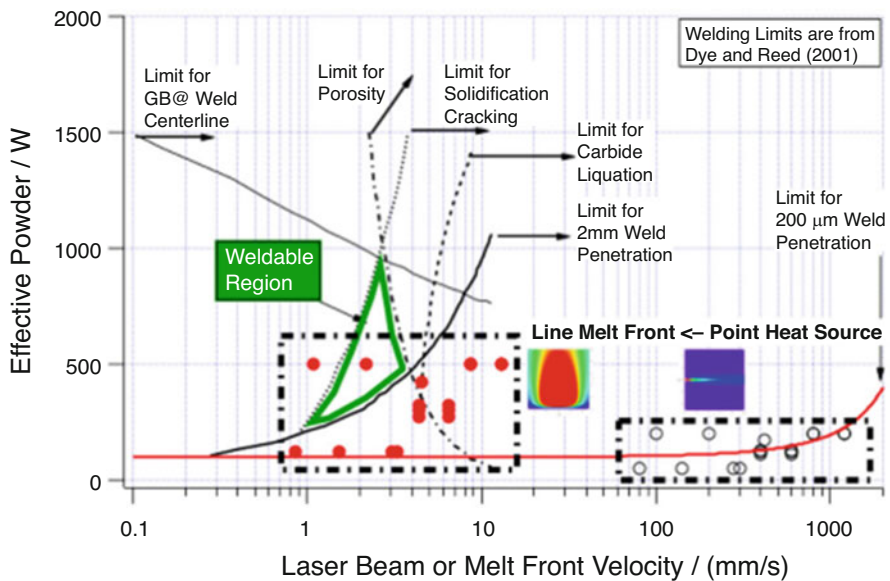
Fig. 22.2   Weldability process map for IN718 [14]

fabricating a smooth and dense solid by LAM. LAM is usually carried out in an enclosed chamber either in air or in positive inert gas atmosphere. Though melting happens in a miniscule small volume (compared to the full bed size) at a time, both experimental data and thermodynamic analysis suggest that partial oxidation of the powder cannot be completely ruled out during beam-powder interaction. The fracture surfaces reveal the presence of both Al_2O_3 and Cr_2O_3 films in LAM coupons of IN718 [15], which leads to poor wetting and bonding between layers and, hence, formation of internal cracks. In case of proper wetting, the oxide film may develop intermetallic compound layer, such as Laves phases, δ-Ni_3Nb, Nb-rich MC, and γ' compounds.

4.3   Macro- and Microdefects

The process of LAM, as opposed to bulk processing, involves transient melting and solidification in small volume integrated over space and time to develop a 3D product. While flexibility and novelty are advantages, several micro- and macroscale defects are inevitable, perhaps in greater variety and density than that in conventional products, and are undeniable disadvantages of LAM. Insufficient melting and wetting of powders cause entrapment of porosity and cracks, reducing density and bulk mechanical properties. Fig. 22.3 shows that apparent or relative density improves with higher laser power density simply because of greater degree of melting and intermixing in the melt pool [12]. Besides porosity or voids, other common defects include segregation, inclusion, anisotropy or directionality, hot cracks, precipitation of intermetallic compounds/phases, internal oxidation, etc. (Fig. 22.4).

Elemental segregation is very common in LAM due to solute rejection and redistribution during rapid solidification. Post LAM stress-relief or homogenization heat treatment of LAM-produced Inconel 625 (IN625) parts is reported to produce undesirable precipitation of δ-phase with a rapid kinetics (<5 min) [16].

Dimensional precision and surface finish is better in powder bed (e.g., SLS, SLM) processing than that direct energy deposition (DED) methods. In some cases, post LAM processing is needed like annealing, homogenization, surface polishing, densification by hot isostatic pressing, etc.

4.4   Evolution of Microstructure and Phase Aggregate

LAM produces cast microstructure characteristics of nonequilibrium solidification mainly comprising of dendritic and columnar features of varying length, width, morphology, and population density. Zhang et al. [18] compared the microstructures of IN718 produced by powder bed LAM and conventional casting and indicated that SLM produced microstructure with dendritic morphology and with different
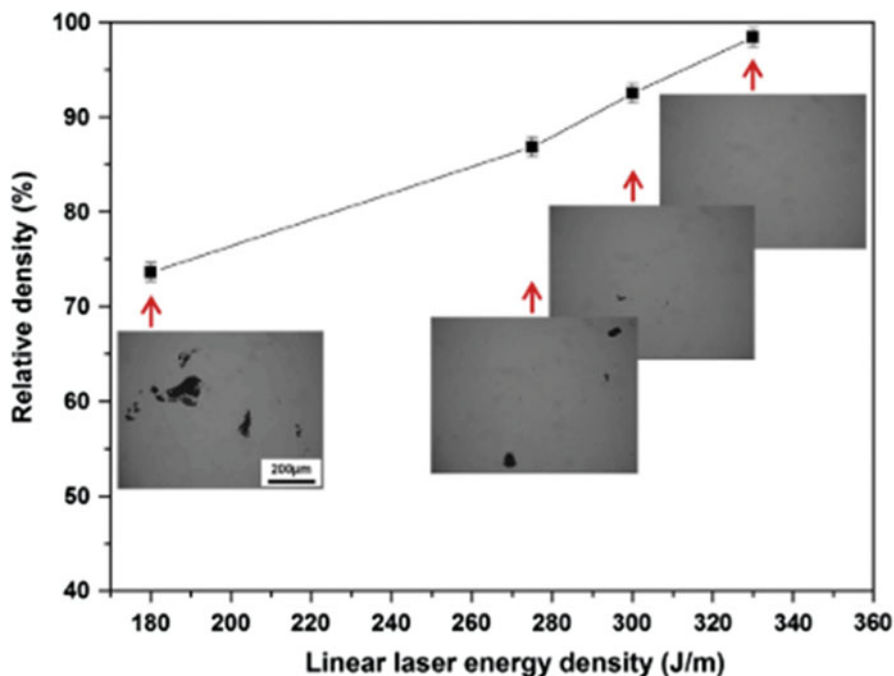
Fig. 22.3 Effect of laser parameter (energy density) on production of densified components of IN718 by SLM [12]

inter-dendritic arm spacing and length depending on the process parameters. Nie et al. [19] found that small dendrite arm spacing obtained by high cooling rate and low temperature gradient to growth rate (G/R) ratio was beneficial for forming discrete Laves-phase particles in solidification during LAM of Nb-bearing Ni-based superalloy. In contrast, large columnar dendrite arm spacing under a low cooling rate and high G/R ratio tends to produce continuously distributed coarse Laves phase particles that are known to adversely affect the bulk mechanical properties. Chen et al. [20] reported that forced cooling imposed by continuous water flow below the substrate during LAM of IN718 was effective to produce highly directional and ordered columnar dendrites; however, directionality was found to be reduced by decreasing the supplementary cooling rate (Fig. 22.5).

Dinda et al. [21] have reported that unidirectional laser beam scanning pattern develops a fiber crystallographic orientation or texture, while a reciprocating (back and forth) scanning leads to development of a rotated cube texture in the IN718 DED deposit over IN718 substrate. Besides IN718, IN625 also develop elongated columnar crystal in the <001> preferred direction (fiber component) due to possible epitaxial growth and heat conduction [22]. Following post LAM annealing, this microstructure changes into two morphologically distinct aggregates, namely, rectangular grains formed within the molten pool and equiaxed grains with triangular-shaped carbides along the molten boundaries. Long et al. [23] have confirmed that
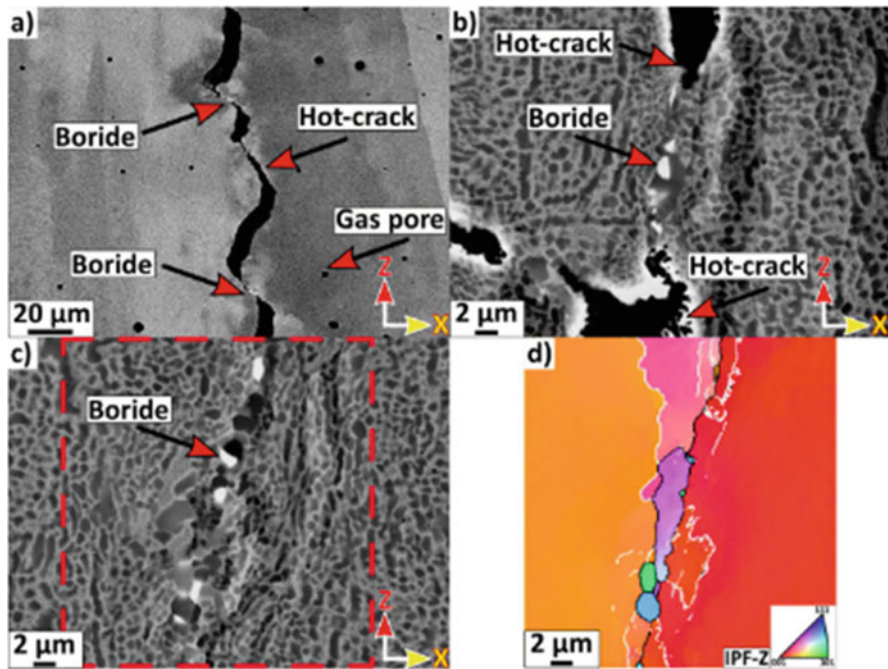
Fig. 22.4 Defects in AM-produced parts of nickel-based superalloy [17]

faster cooling can suppress segregation of Nb and reduce formation of brittle Laves phase in LAM of IN718.

Ni et al. [24] have observed ultrafine columnar grains with randomly dispersed γ'' allotriomorphs as well as idiomorphs in as-fabricated IN718 by SLM. Consequently, the as-fabricated longitudinal samples show lower ultimate tensile strength (about 1101 MPa) with higher elongation (24.5%) in comparison to the transverse samples which register higher tensile strength (1167 MPa) and lower elongation (21.5%). The improved mechanical properties can be attributed to grain refinement due to high cooling rate associated with SLM. The anisotropy in across longitudinal and transverse direction is attributed to the {100} fiber texture and columnar grain morphology.

Huebner et al. [25] have demonstrated that LAM allows not only deposition of atomized powder of the base composition but also blending of incoherent ex situ interstitial, intermetallic, and even oxide phases by blending the powder appropriately prior to LAM. In laser composite surfacing of IN625 + 30 wt.% WC, partial dissolution of WC in IN625 matrix leads to formation of topologically close-packed (TCP) phases along grain boundaries. Subsequently, WC, W_2C, NbC, $W_6C_{2.54}$, and $(W,Cr,Ni)_{23}C_6$ have been detected by XRD including faceted carbides and spherical oxide phases.

Superalloys attain peak strength not in as-cast or grown condition but following suitable precipitation annealing. Diepold et al. [26] have discussed in detail the effect
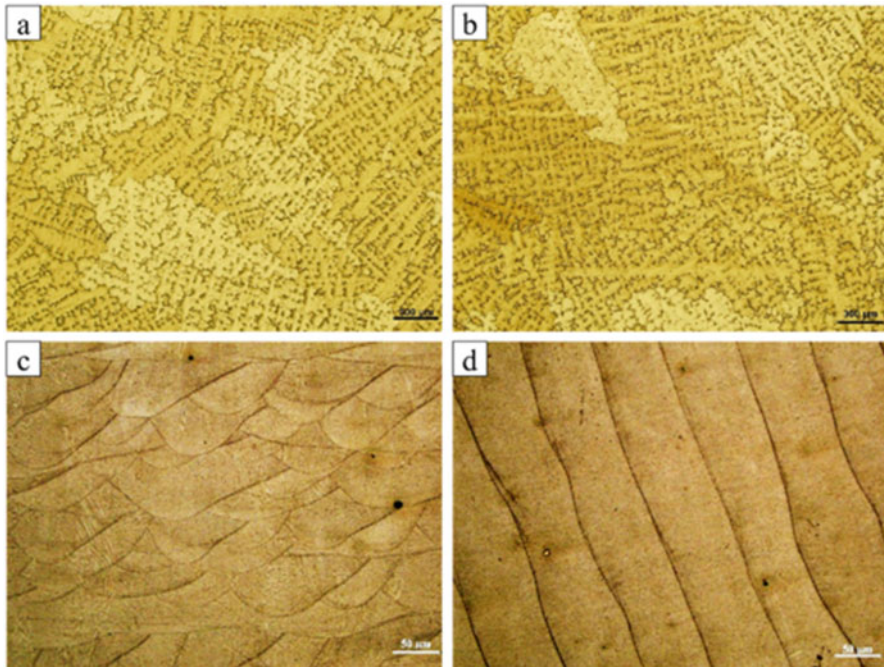
Fig. 22.5 Optical micrographs of IN718 casting sample in (**a**) transverse, (**b**) vertical cross section, and SLM-produced sample in (**c**) vertical cross section parallel to building direction and (**d**) transverse to building direction [18]

of post LAM heat treatment on the evolution of microstructure and mechanical properties, as summarized in Fig. 22.6. During LAM, rapid solidification at 10^4 K/s or higher in combination with a thermal gradient of around 10^7 K/m leads to introduction of large tensile residual stresses that may cause hot cracking. Preheating the base plate or stage may reduce residual stresses. The ratio of thermal gradient (G) to solidification rate (R), i.e., G/R ratio, determines columnar or equiaxed/cellular morphology of the primary phase. Presence of a large dislocation density, small dendritic size, high dissolved solute content, and coherent precipitates all contributes to overall strengthening of the LAM product. However, as-cast (in conventional) or as-deposited (in LAM) condition yields softer product, and coherent γ''- and γ'-precipitates form only after precipitation aging. This aging treatment is usually conducted in two stages, at 620 °C for 8 h followed by 720 °C for 8 h. A prior solution heat treatment at between 930 and 1070 °C may dissolve Laves phase, homogenize Nb-content, and reduce residual stresses.
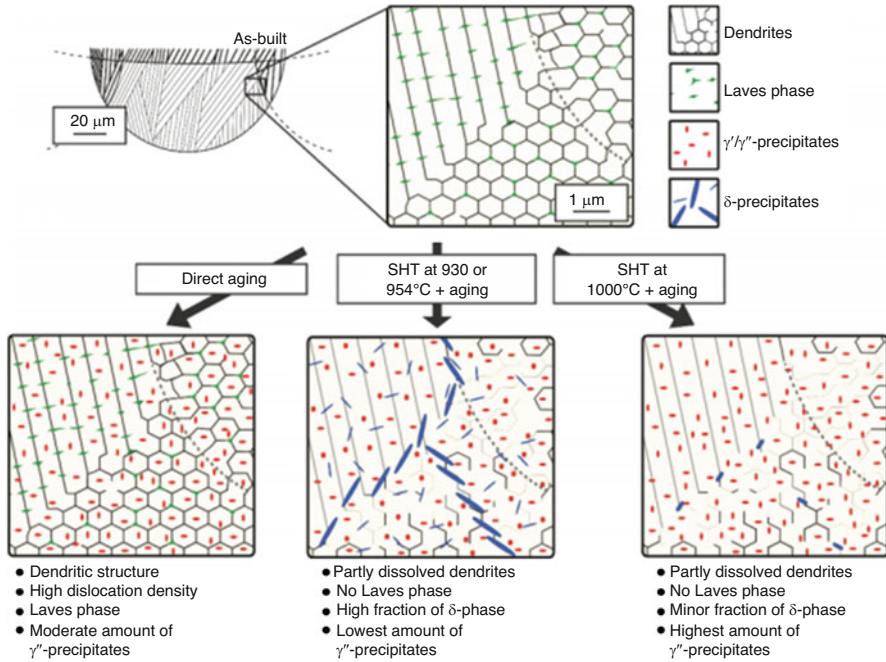
Fig. 22.6 Schematic of evolution of the microstructure and phases of SLM-produced IN718 parts [26]

4.5 Mechanical Properties

Figure 22.7 shows the range of mechanical properties of IN718 measured after proper heat treatment of products made by LAM. Directional columnar microstructure with Laves phases and carbides in the inter-dendritic spaces characterize the microstructure of LAM products of IN718 after aging. Popovich et al. [27] suggested that post LAM processing by hot isostatic pressing improves mechanical properties due to dissolution of undesirable Laves/δ-phase and collapsing of pores. This way, LAM or SLM can yield mechanical properties better than that produced by conventional processes. Furthermore, solution aging and hot isostatic pressing at 900–1000 °C of IN718 after SLM can show improved oxidation resistance [28]. Standard heat treatment schedule (solution treatment at 2 h at 1150 °C, water quench, and aging at 800 °C for 8 h then air cooling) solutionizes and, subsequently, develops precipitate hardening alloy. The microstructure consisted of about 10–12% of nano-dimension (30 nm diameter) γ'-Ni$_3$(Al,Ti) precipitates with the presence of M$_{23}$C$_6$ carbides in the grain boundary regions. On the other hand, in the as-processed samples, there were presence of the high dislocation density in the microstructure with the presence of ultrafine precipitates of γ' -Ni$_3$(Al,Ti) in <10 nm size at the dislocation cores [29]. Heat treatment at 600 °C for 8 h. was beneficial in relieving the residual stresses developed due to laser processing.
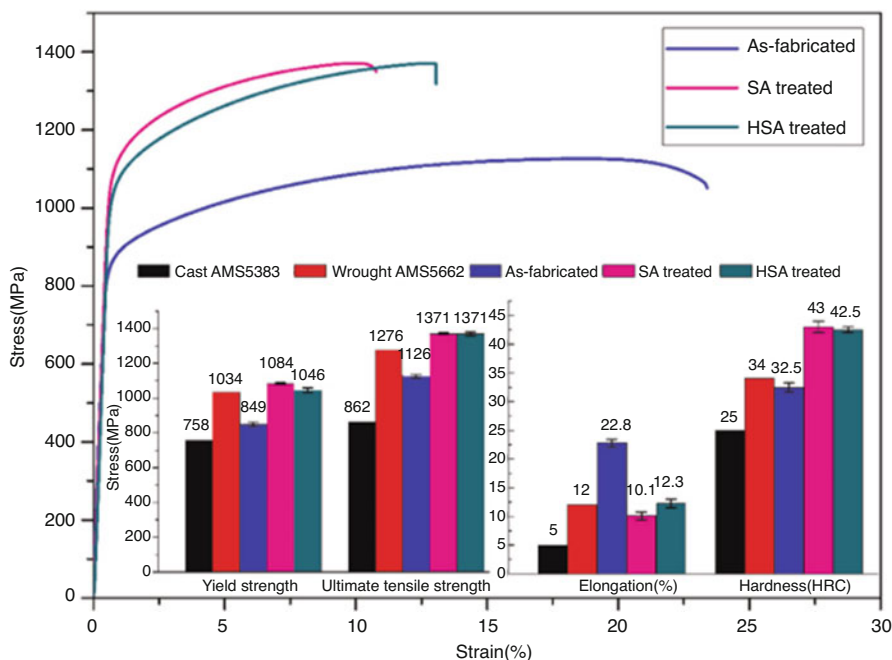
Fig. 22.7 Mechanical properties of IN718 processed by SLM in as-fabricated, solution and aging (SA)-treated, and homogenization, solution, and aging (HAS)-treated states [30]

5 Successful Fabrication of Engineering Components by LAM

LAM is no longer a concept under exploration. Several engineering sectors have successfully developed and commercialized a number of engineering components or even complete systems mostly for structural applications based on steel and stainless steel, superalloys, Al-alloys, Ti-alloys, polymers, and composites. These components cover a wide range of applications like heat exchangers, bearing assembly, ordinary or mountain bikes and bicycles, dental and orthopedic implants, space and aircraft components, footwear manufacturing, electronic devices and parts, polycarbonate lenses and glasses, decorative pieces, hydraulic machine components, automobile parts, power generation and turbine parts, and many more.

5.1 Turbomachinery Parts

LAM as one of the most flexible and innovative alternatives to casting and machining is widely exploited to manufacture several routine and special components for

Fig. 22.8 Photograph of a turbomachine (isometric view) showing various important parts [31]
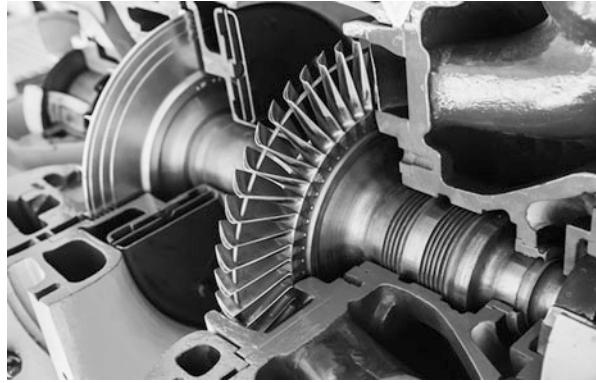
turbomachinery components such as impellers, rotors, swirlers, burners, pumps, and compressors used in rockets, jet engines, power plants, windmills, and hydropower plants, both for prototyping as well as direct manufacturing. The incentives for LAM emanate from faster product development and production, flexibility in design and manufacturing, and scope for rapid repair and refurbishment. By constant innovation and improvisation, LAM technology is nearing its limit of perfection to create defect-free, high-performance, direct, printed, multifunctional components capable of enduring high thrust, temperatures, and stress cycles with minimal distortion and damage. Figure 22.8 shows an isometric view of a part of a typical turbo-engine with impellers, blades, shafts, nozzles, etc. [31]. Many of these parts are now manufactured by LAM.

5.2 Anti-scatter Grids

Computed tomography (CT) scanners are now routinely used to visualize various parts of a human body in order to monitor and diagnose disorder, disease, or injury, in addition to conducting medical, surgical, or radiation treatment. One of the critical components of CT scanners is anti-scatter grids meant for absorbing and reducing unwanted scattered radiation that only enhances background noise and enhancing image resolution. These grids are usually tungsten-based metallic structures with high precision shape and geometry (with a thickness of about 100 μm and a positional accuracy of 25 μm). Tungsten is used because of its high melting point (3422 °C), wear resistance, and absorptivity. However, tungsten is very strong and hard posing immense difficulty in processing through usual melting, casting, and machining route and, hence, is ideally suited to fabrication by LAM that ensures a very precise and reliable manufacturing with micrometer-level resolution [32]. Anti-scatter grids are now more in demand due to developing precision CT systems to fight the coronavirus. Figure 22.9 shows the 3D-printed anti-scatter grid made of tungsten developed by LAM.

Fig. 22.9 Additive-
manufactured anti-scatter
grid of tungsten used in CT
scanning device [32]
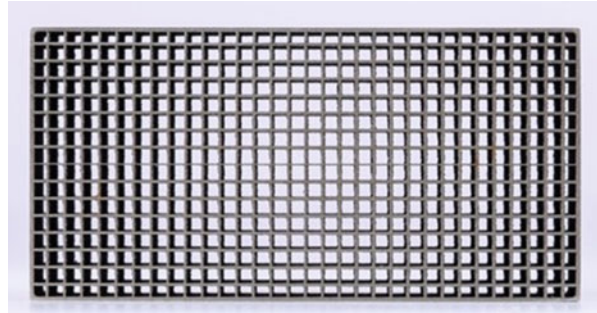
5.3 Bimetallic Combustion Chamber

LAM now enables manufacturing of a 10-ton-force liquid rocket engine combustion
chamber and injector assembly as a single component, made of Cu-Cr-Zr alloy, as
per customized design for space launching vehicles. Besides smooth changes in
diameter and curvature, the combustor also contains geometrically distributed holes
for air passage and cooling across the wall. Subsequently, this entire assembly is
coated by laser deposition or cladding with IN625 to enhance oxidation resistance
[33]. Initially, a prototype was developed using AlSi10Mg alloy powders for
examining dimensional accuracy and design compliance. The final CuCrZr alloy
component is used in the first stage of orbital launch vehicle to install minisatellite to
geostationary orbit (Fig. 22.10) [33].

5.4 Hybrid Laser Processing Technology

Though selected laser melting (SLM) is a popular technique, however, SLM is a
relatively slow process and requires a finite-size powder bed and, hence, a larger
chamber dimension than the final component. In comparison, direct energy deposi-
tion (DED) with powder feeding nozzles is a much faster process that does not suffer
from the limitation of maximum chamber or component size. However, DED is
inferior to SLM in terms of dimensional accuracy and control and final mechanical
properties of the component. A novel hybrid approach combining both SLM and
DED techniques is capable of developing products with the maximum efficiency and
superior quality as compared to the same developed independently by either of the
techniques. The advantages associated with application of hybrid technology include
faster processing rate, economy, and flexibility in processing. This hybrid technique
is more appropriate for large and complex components with compositional variation
or difference in functions [34]. Hybrid SLM and DED technology has successfully
been applied for the development of strut end filling part made of IN718 for space
application (Fig. 22.11).

Fig. 22.10 3D-printed combustion chamber of CuCrZr [33]

Fig. 22.11 Strut end filling part made of IN718 fabricated by hybrid SLM and DED technique [34]
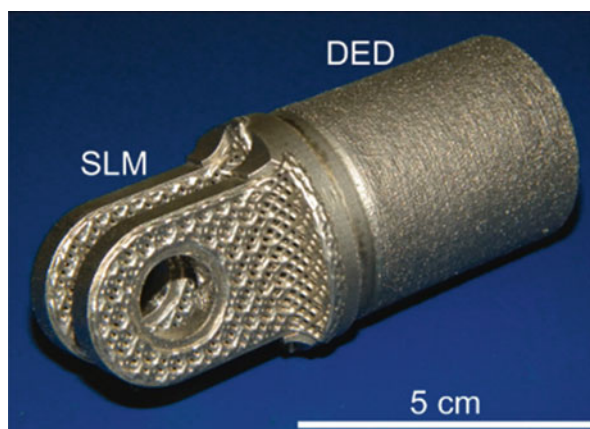
5.5 Injector Head for Rockets

Additive manufacturing of metals is drawing increasing attention for designing and developing tailored components for aerospace industry to improve efficiency and introduce design innovation without incurring large time and cost penalty. Development of injector head for Ariane 6 is one of the earliest and most notable successes in that direction [35]. Usually, injector heads are developed from a large number of independent or separate parts, requiring elaborate machining and joining. As a result, time, cost, skill, and manpower requirements are high. In contrast, LAM enables manufacturing of these components by a single-step processing. Figure 22.12 shows the LAM-processed injector head of Ariane 6 launcher. In this case, adoption of LAM significantly reduced the processing complexity and time of development from 3 months in conventional processing to 30–40 h by LAM. As a result, overall cost was reported to be reduced nearly by half.

5.6 Fuel Nozzle Tip

Another very successful example of developing a complex finished component by LAM is the fuel nozzle tip based on Co- or Ni-based superalloy, routinely used in the LEAP engine for aircrafts developed by General Electric, USA [36]. Figure 22.13 shows the schematic of fuel injector nozzle tip for LEAP aero-turbine engine developed by LAM [36]. Instead of using 20 different parts to be assembled,

Fig. 22.12 Image of an actual injector head for Ariane 6 launcher fabricated by LAM [35]

Fig. 22.13 Fuel injector nozzle tip for LEAP aero-turbine engine developed by LAM [36]

LAM allows developing this geometrically and functionally complex component for rocket or satellite launching vehicle by single-step processing without any machining, welding, or brazing. This product was successfully developed and deployed over 30,000 in field application by General Electric. LAM accounted for nearly 25% weight reduction in addition to process flexibility, product novelty, and cost benefits [36].

5.7   Combustor Based on Inconel 718 Alloy

Ni-based superalloys like IN625, IN718, IN939, and HX alloys are ideally suited materials for component development by LAM for a wide range of applications [37]. To ensure good flowability and weldability, atomized powder is essential in LAM. It is established that LAM-fabricated parts made of IN718 or IN625 possess superior tensile property, creep and rupture strength, and heat and corrosion resistance properties compared to that of the conventionally processed ones. As a result, the process may be applied for developing parts for aerospace, energy, and marine sectors. Figure 22.14 shows the real-time photograph of a combustor made of IN718 using LAM.

6   Concluding Remarks – A New Proposition

It is now well accepted that the true utility and novelty of LAM is not just confined to fabrication of finished products by a single-step manufacturing operation but lies in its ability to seamlessly vary the composition along a given dimension or direction

Fig. 22.14 Combustor
based on IN718 made by
LAM [37]
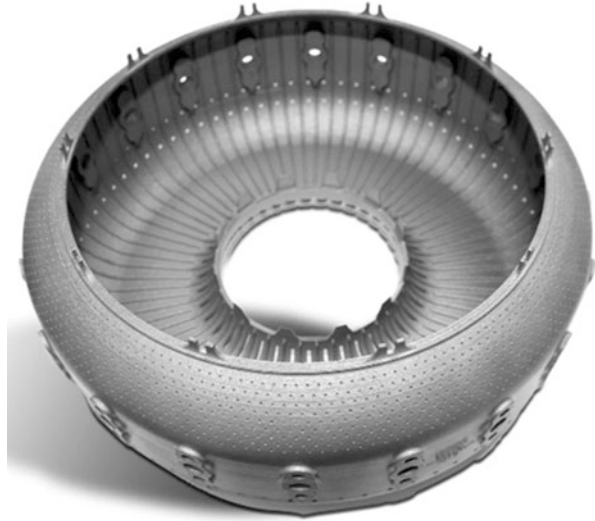
and, thereby, achieve functional gradation. Even for a given alloy subjected to LAM, the microstructure and phase aggregate can be significantly varied as a function of thermophysical conditions governed by LAM parameters. This novelty of material processing by LAM can be exploited to pursue a very novel and interesting issue, namely, to investigate origin of solid in space.

Creation of matter in outer space has always evoked questions and curiosity in the scientific community. Properties of solids on earth crucially depend on structure, composition, and prior history. Similar paradigm, even if true, is not yet established or verified about matter in outer space or outside the earth's environment. For instance, the theories on nucleation and growth; evolution of shape, size, and morphology of solid on solidification; values of diffusion coefficient; interfacial energy; thermal or electrical conductivity; density; principles of phase transition, solubility, and solute transport; response to thermal, mechanical, or any other activation; and many more such phenomena intimately related to structure and properties of solids are not known or inadequately understood as they happen in space. In other words, knowledge about all these phenomena needs systematic evaluation with regard to the difference or similarity between behavior in earth's gravitational environment and zero-/microgravity condition in the outer space.

Some, if not all, of these issues may be systematically pursued and resolved by designing complementary experiments on ground and in space using either International Space Station (ISS) facility or parabolic test flight operations simulating micro or reduced gravity condition using laser as a contactless source of heating for material processing or manufacturing as in LAM. The advantage of using laser lies in the fact that (i) heat input in pulse or continuous mode can be totally quantified, (ii) the heating/cooling rate and solidification velocity can be measured and controlled, and furthermore, (iii) all usual manufacturing operations like heating,

melting, joining, cladding, machining, and forming can be conducted in small volume using the same setup by varying only two independent process parameters (interaction time and power density), as explained in this review article on LAM of Ni-based superalloys, cited as a model multicomponent system.

Typical LAM experiments that can provide important clues of material behavior with different model systems, not just superalloy, may cover (i) melting or solidification of glassy solids (isomorphous or phase separated), (ii) invariant phase changes (eutectic/peritectic/eutectoid), (iii) solubility limit or its extension, (iv) miscibility or segregation behavior, (v) size dependence of first-order changes (e.g., melting point), and (vi) measurement of thermophysical properties (surface energy, conductivity, diffusivity, density, viscosity, etc.). Since condition in outer space is likely to be different and away from equilibrium due to ultrahigh to ultralow temperature, rarefied atmosphere, and zero- to-microgravity, laser-based experiments on ground and repeated in space through parabolic flights or in ISS can reveal important differences and produce excellent repository of knowledge to understand the origin and behavior of matter in outer space vis-à-vis on earth.

References

1. Y. Garfinkel, F. Klimscha, S. Shalev, D. Rosenberg, The beginning of metallurgy in the southern Levant: A late 6th millennium CalBC copper Awl from Tel Tsaf, Israel. PLoS One. **9**, e92591 (2014). https://doi.org/10.1371/journal.pone.0092591
2. E. Akca, A. Gürsel, A review on superalloys and IN718 nickel-based INCONEL superalloy. Period. Eng. Nat. Sci **3** (2015). https://doi.org/10.21533/pen.v3i1.43
3. G.A. Greene, C.C. Finfrock, Oxidation of Inconel 718 in air at high temperatures. Oxid. Met. **55**, 505–521 (2001). https://doi.org/10.1023/A:1010359815550
4. Q. Jia, D. Gu, Selective laser melting additive manufactured Inconel 718 superalloy parts: High-temperature oxidation property and its mechanisms. Opt. Laser Technol. **62**, 161–171 (2014). https://doi.org/10.1016/j.optlastec.2014.03.008
5. J. Dutta Majumdar, I. Manna, Laser material processing. Int. Mater. Rev. **56**, 341–388 (2011). https://doi.org/10.1179/1743280411Y.0000000003
6. C.K. Yong, G.J. Gibbons, C.C. Wong, G. West, A critical review of the material characteristics of additive manufactured IN718 for high-temperature application. Metals (Basel) **10**, 1576 (2020). https://doi.org/10.3390/met10121576
7. B. Graf, A. Gumenyuk, M. Rethmeier, Laser metal deposition as repair technology for stainless steel and titanium alloys. Phys. Procedia. **39**, 376–381 (2012). https://doi.org/10.1016/j.phpro.2012.10.051
8. J.-Y. Lee, J. An, C.K. Chua, Fundamentals and applications of 3D printing for novel materials. Appl. Mater. Today. **7**, 120–133 (2017). https://doi.org/10.1016/j.apmt.2017.02.004

9. T. DebRoy, H.L. Wei, J.S. Zuback, T. Mukherjee, J.W. Elmer, J.O. Milewski, A.M. Beese, A. Wilson-Heid, A. De, W. Zhang, Additive manufacturing of metallic components – Process, structure and properties. Prog. Mater. Sci. **92**, 112–224 (2018). https://doi.org/10.1016/j.pmatsci.2017.10.001

10. T.D. Ngo, A. Kashani, G. Imbalzano, K.T.Q. Nguyen, D. Hui, Additive manufacturing (3D printing): A review of materials, methods, applications and challenges. Compos. Part B Eng. **143**, 172–196 (2018). https://doi.org/10.1016/j.compositesb.2018.02.012

11. K. Moussaoui, W. Rubio, M. Mousseigne, T. Sultan, F. Rezai, Effects of selective laser melting additive manufacturing parameters of Inconel 718 on porosity, microstructure and mechanical properties. Mater. Sci. Eng. A **735**, 182–190 (2018). https://doi.org/10.1016/j.msea.2018.08.037

12. Q. Jia, D. Gu, Selective laser melting additive manufacturing of Inconel 718 superalloy parts: Densification, microstructure and properties. J. Alloys Compd. **585**, 713–721 (2014). https://doi.org/10.1016/j.jallcom.2013.09.171

13. M. Xia, D. Gu, G. Yu, D. Dai, H. Chen, Q. Shi, Porosity evolution and its thermodynamic mechanism of randomly packed powder-bed during selective laser melting of Inconel 718 alloy. Int. J. Mach. Tools Manuf. **116**, 96–106 (2017). https://doi.org/10.1016/j.ijmachtools.2017.01.005

14. S.S. Babu, N. Raghavan, J. Raplee, S.J. Foster, C. Frederick, M. Haines, R. Dinwiddie, M.K. Kirka, A. Plotkowski, Y. Lee, R.R. Dehoff, Additive manufacturing of nickel superalloys: Opportunities for innovation and challenges related to qualification. Metall. Mater. Trans. A. **49**, 3764–3780 (2018) 10.1007/s11661-018-4702-4

15. Y.N. Zhang, X. Cao, P. Wanjara, M. Medraj, Oxide films in laser additive manufactured Inconel 718. Acta Mater. **61**, 6562–6576 (2013). https://doi.org/10.1016/j.actamat.2013.07.039

16. F. Zhang, L.E. Levine, A.J. Allen, M.R. Stoudt, G. Lindwall, E.A. Lass, M.E. Williams, Y. Idell, C.E. Campbell, Effect of heat treatment on the microstructural evolution of a nickel-based superalloy additive-manufactured by laser powder bed fusion. Acta Mater. **152**, 200–214 (2018). https://doi.org/10.1016/j.actamat.2018.03.017

17. P. Kontis, E. Chauvet, Z. Peng, J. He, A.K. da Silva, D. Raabe, C. Tassin, J.-J. Blandin, S. Abed, R. Dendievel, B. Gault, G. Martin, Atomic-scale grain boundary engineering to overcome hot-cracking in additively-manufactured superalloys. Acta Mater. **177**, 209–221 (2019). https://doi.org/10.1016/j.actamat.2019.07.041

18. D. Zhang, Z. Feng, C. Wang, W. Wang, Z. Liu, W. Niu, Comparison of microstructures and mechanical properties of Inconel 718 alloy processed by selective laser melting and casting. Mater. Sci. Eng. A **724**, 357–367 (2018). https://doi.org/10.1016/j.msea.2018.03.073

19. P. Nie, O.A. Ojo, Z. Li, Numerical modeling of microstructure evolution during laser additive manufacturing of a nickel-based superalloy. Acta Mater. **77**, 85–95 (2014). https://doi.org/10.1016/j.actamat.2014.05.039

20. Y. Chen, F. Lu, K. Zhang, P. Nie, S.R. Elmi Hosseini, K. Feng, Z. Li, Dendritic microstructure and hot cracking of laser additive manufactured Inconel 718 under improved base cooling. J. Alloys Compd. **670**, 312–321 (2016). https://doi.org/10.1016/j.jallcom.2016.01.250

21. G.P. Dinda, A.K. Dasgupta, J. Mazumder, Texture control during laser deposition of nickel-based superalloy. Scr. Mater. **67**, 503–506 (2012). https://doi.org/10.1016/j.scriptamat.2012.06.014

22. S. Li, Q. Wei, Y. Shi, Z. Zhu, D. Zhang, Microstructure characteristics of Inconel 625 Super-alloy manufactured by selective laser melting. J. Mater. Sci. Technol. **31**, 946–952 (2015). https://doi.org/10.1016/j.jmst.2014.09.020

23. Y. Long, P. Nie, Z. Li, J. Huang, X. Li, X. Xu, Segregation of niobium in laser cladding Inconel 718 superalloy. Trans. Nonferrous Met. Soc. China. **26**, 431–436 (2016). https://doi.org/10.1016/S1003-6326(16)64131-6

24. M. Ni, C. Chen, X. Wang, P. Wang, R. Li, X. Zhang, K. Zhou, Anisotropic tensile behavior of in situ precipitation strengthened Inconel 718 fabricated by additive manufacturing. Mater. Sci. Eng. A. **701**, 344–351 (2017). https://doi.org/10.1016/j.msea.2017.06.098

25. J. Huebner, D. Kata, J. Kusiński, P. Rutkowski, J. Lis, Microstructure of laser cladded carbide reinforced Inconel 625 alloy for turbine blade application. Ceram. Int. **43**, 8677–8684 (2017). https://doi.org/10.1016/j.ceramint.2017.03.194

26. B. Diepold, N. Vorlaufer, S. Neumeier, T. Gartner, M. Göken, Optimization of the heat treatment of additively manufactured Ni-base superalloy IN718. Int. J. Miner. Metall. Mater. **27**, 640–648 (2020). https://doi.org/10.1007/s12613-020-1991-6

27. V.A. Popovich, E.V. Borisov, A.A. Popovich, V.S. Sufiiarov, D.V. Masaylo, L. Alzina, Impact of heat treatment on mechanical behaviour of Inconel 718 processed with tailored microstructure by selective laser melting. Mater. Des. **131**, 12–22 (2017). https://doi.org/10.1016/j.matdes.2017.05.065

28. Y.-J. Kang, S. Yang, Y.-K. Kim, B. AlMangour, K.-A. Lee, Effect of post-treatment on the microstructure and high-temperature oxidation behaviour of additively manufactured inconel 718 alloy. Corros. Sci. **158**, 108082 (2019). https://doi.org/10.1016/j.corsci.2019.06.030

29. T. Vilaro, C. Colin, J.D. Bartout, L. Nazé, M. Sennour, Microstructural and mechanical approaches of the selective laser melting process applied to a nickel-base superalloy. Mater. Sci. Eng. A **534**, 446–451 (2012). https://doi.org/10.1016/j.msea.2011.11.092

30. D. Zhang, W. Niu, X. Cao, Z. Liu, Effect of standard heat treatment on the microstructure and mechanical properties of selective laser melting manufactured Inconel 718 superalloy. Mater. Sci. Eng. A **644**, 32–40 (2015). https://doi.org/10.1016/j.msea.2015.06.021

31. Application Spotlight: 3D Printing for Turbine Parts – AMFG, (n.d.). https://amfg.ai/2020/02/06/application-spotlight-3d-printing-for-turbine-parts/. Accessed 28 May 2021

32. 3D printer for medical. Anti-Scatter Grids for CT equipment (n.d.). https://www.eos.info/en/landing-pages/distributed-production-additive-manufacturing/local-level/3d-printer-tungsten-anti-scatter-grids. Accessed 28 May 2021

33. Launching into space with 3D printed rocket engines | AMCM (n.d.). https://amcm.com/success-stories/customized-large-frame-system-for-launcher-aerospace. Accessed 28 May 2021

34. M. Godec, S. Malej, D. Feizpour, Č. Donik, M. Balažic, D. Klobčar, L. Pambaguian, M. Conradi, A. Kocijan, Hybrid additive manufacturing of Inconel 718 for future space applications. Mater. Charact. **172**, 110842 (2021). https://doi.org/10.1016/j.matchar.2020.110842

35. Industrial Applications of 3D Printing: The Ultimate Guide – AMFG (n.d.). https://amfg.ai/industrial-applications-of-3d-printing-the-ultimate-guide/. Accessed 28 May 2021

36. Manufacturing Milestone: 30,000 Additive Fuel Nozzles | The GE Aviation Blog | Aerospace & Flight News (n.d.). https://blog.geaviation.com/manufacturing/manufacturing-milestone-30000-additive-fuel-nozzles/. Accessed 28 May 2021

37. Nickel alloys for industrial 3D printing | EOS GmbH (n.d.). https://www.eos.info/en/additive-manufacturing/3d-printing-metal/dmls-metal-materials/nickel-alloys. Accessed 28 May 2021

Annex: Related Publications of the Last Decade

Fecht H.-J.; "Materials Science"; Laboratory Science with Space Data: Accessing and Using Space-Experiment Data (eds. Beysens D., Carotenuto L., Van Loon J. J.W.A., Zell M.); Springer (2011): 81–97

Egry I.; "Containerless processing for thermophysical property measurements of liquid metals: review and outlook"; High Temperatures – High Pressures, 40/3–4 (2011): 203–214

Lohöfer G., Pottlacher G.; "Inductive measurement of thermophysical properties of electromagnetically levitated melts"; High Temperatures – High Pressures 40/3–4 (2011): 237–248

Tóth G.I., Morris J.R., Gránásy L.; "Ginzburg-Landau-type multiphase field model for competing fcc and bcc nucleation"; Physical Review Letters 106/4 (2011): 045701 (https://doi.org/10.1103/physrevlett.106.045701)

Schetelat P., Etay J.; "A new approach for non-contact calorimetry: System identification using pseudo-white noise perturbation"; Heat and Mass Transfer 47/7 (2011): 759–769 (https://doi.org/10.1007/s00231-010-0711-6)

Wunderlich R.K., Fecht H.J., Schick M., Egry I.; "Time dependent effects in surface tension measurements of an industrial Fe-alloy"; Steel Research International 82/6 (2011): 746–752 (https://doi.org/10.1002/srin.201000156)

Wunderlich R.; "Surface tension and viscosity measurements of metallic alloys on TEXUS sounding rocket flights"; 20th ESA Symposium on European Rocket and Balloon Programmes & Related Research; Hyères, Switzerland (2011)

Novakovic R.; "Bulk and surface properties of liquid Al-Cr and Cr-Ni alloys"; Journal of Physics: Condensed Matter 23/23 (2011): 235107 (https://doi.org/10.1088/0953-8984/23/23/235107)

Tourret D., Gandin Ch.-A., Volkmann T., Herlach D.M.; "Multiple non-equilibrium phase transformations: Modeling versus electro-magnetic levitation experiment"; Acta Materialia 59/11 (2011): 4665–4677 (https://doi.org/10.1016/j.actamat.2011.04.013)

Kolbe M., Lierfeld T., Wu Z., Galenko P., Eggeler G., Herlach D. M.; "Microstructure analysis of undercooled Ni-Ta alloys"; 3rd International Conference on Advances in Solidification Processing; Kerkrade, Netherlands (2011)

Chen J., Dahlborg U., Bao C.M., Calvo-Dahlborg M., Henein H.; "Microstructure evolution of atomized Al-0.61 Wt Pct Fe and Al1.90 Wt Pct Fe alloys"; Metallurgical and Materials Transactions B 42/3 (2011): 557–567 (https://doi.org/10.1007/s11663-011-9485-6)

Lee G.W., Gangopadhyay A.K., Kelton K.F.; "Phase diagram studies of Ti-Zr-Ni alloys containing less than 40 at.% Ni and estimated critical cooling rate for icosahedral quasicrystal formation from the liquid"; Acta Materialia 59/12 (2011): 4964–4973 (https://doi.org/10.1016/j.actamat.2011.04.045)

Gandin Ch.-A., Rivaux B., Bellet M., Herlach D., Volkmann T., Johannsen N., Bobadilla M., Bontems N.; "Chill cooling for the electromagnetic levitator in relation with continuous casting"; International Symposium on Physical Sciences in Space; Bonn, Germany (2011)

Schneider S., Engelhardt M., Heuskin D., Diefenbach A.; "Support tools for TEMPUS / EML campaigns"; 4th International Symposium on Physical Sciences in Space (ISPS-4); Bonn, Germany (2011)

Schneider S., Engelhardt M., Heuskin D., Diefenbach A.; "Electromagnetic levitation in microgravity: EML on parabolic flights, TEXUS and ISS – Mission overview"; 4th International Symposium on Physical Sciences in Space (ISPS-4); Bonn, Germany (2011)

Etay J., Courtessole C., Schetelat P.; "Mesure de propriétés thermophysiques par lévitation électromagnétique utilisation d'une technique d'identification"; 20ème Congrès Français de Mécanique (2011)

Wunderlich R.K., Fecht H.-J.; "Surface tension and viscosity of NiAl catalytic precursor alloys from microgravity experiments"; International Journal of Materials Research 102/9 (2011): 1164–1173 (https://doi.org/10.3139/146.110572)

Herlach D., Galenko P.K., Forthaus M., Davydov E., Kolbe M., Parfeniev R.V., Volkov M.P., Dreier W., Kuhl R.; "Multiphase transformations of glass-forming alloys investigated on Earth and in reduced gravity"; Proceedings of IAC-11: 62nd International Astronautical Congress (2011): IAC-11.A2.7.2

Löser W., Woodcock T.G., Shuleshova O., Hermann R., Lindenkreuz H.-G., Gehrmann B., Schneider S., Volkmann T.; "Metastable solidification in undercooled liquid droplets of Fe-Ni based soft-magnetic alloys under terrestrial and microgravity conditions"; Journal of Physics: Conference Series 327 (2011): 012005 (https://doi.org/10.1088/1742-6596/327/1/012005)

Ilbagi A., Henein H., Chen J., Herlach D.M., Lengsdorf R., Gandin C.A., Tourret D., García-Escorial A.; "Containerless solidification and characterization of industrial alloys (NEQUISOL)"; Journal of Physics: Conference Series 327 (2011): 012007 (https://doi.org/10.1088/1742-6596/327/1/012007)

Matson D.M., Hyers R.W., Volkmann T., Fecht H.J.; "Phase selection in the mushy-zone: LODESTARS and ELFSTONE projects"; Journal of Physics: Conference Series 327 (2011): 012009 (https://doi.org/10.1088/1742-6596/327/1/012009)

Ilbagi A., Khatibi P.D., Henein H., Lengsdorf R., Herlach D.M.; "Effect of cooling rate on solidification of Al-Ni alloys"; Journal of Physics: Conference Series 327 (2011): 012010 (https://doi.org/10.1088/1742-6596/327/1/012010)

Hyers R.W., Matson D.M., Kelton K.F., Holland-Moritz D., Volkmann T.; "Fluid-flow effects on phase selection and nucleation in undercooled liquid metals"; Journal of Physics: Conference Series 327 (2011): 012013 (https://doi.org/10.1088/1742-6596/327/1/012013)

Seidel A., Soellner W., Stenzel C.; "Materials science investigations using electromagnetic levitation"; Journal of Physics: Conference Series 327 (2011): 012015 (https://doi.org/10.1088/1742-6596/327/1/012015)

Egry I.; "The viscosity of eutectic Pd-Si alloys"; Journal of Physics: Conference Series 327 (2011): 012022 (https://doi.org/10.1088/17426596/327/1/012022)

Easter S., Bojarevics V., Pericleous K.; "Numerical modelling of liquid droplet dynamics in microgravity"; Journal of Physics: Conference Series 327 (2011): 012027 (https://doi.org/10.1088/1742-6596/327/1/012027)

Seidel A., Soellner W., Stenzel C.; "EML – An electromagnetic levitator for the International Space Station"; Journal of Physics: Conference Series 327 (2011): 012057 (https://doi.org/10.1088/1742-6596/327/1/012057)

Etay J.; "Présentation du groupe ThermoLab de l'ESA"; Journées annuelles du GDR solidification des alliages métalliques et de la commission thématique de la SF2M; Paris, France (2011)

Krivilyov M., Volkmann T., Gao J., Fransaer J.; "Multiscale analysis of the effect of competitive nucleation on phase selection in rapid solidification of rare-earth ternary magnetic materials"; Acta Materialia 60/1 (2012): 112–122 (https://doi.org/10.1016/j.actamat.2011.09.009)

Tóth G.I., Tegze G., Pusztai T., Gránásy L.; "Heterogeneous crystal nucleation: The effect of lattice mismatch"; Physical Review Letters 108/2 (2012): 025502 (https://doi.org/10.1103/physrevlett.108.025502)

Novakovic R., Giuranno D., Ricci E., Tuissi A., Wunderlich R., Fecht H., Egry I.; "Surface, dynamic and structural properties of liquid Al-Ti alloys"; Applied Surface Science 258/7 (2012): 3269–3275 (https://doi.org/10.1016/j.apsusc.2011.11.080)

Matson D.M.; "Controlled convection during microgravity solidification"; Proceedings of the 50th AIAA Aerospace Science Meeting (2012): AIAA-2012-0592 (https://doi.org/10.2514/6.2012-592)

Wunderlich R.K., Fecht H.J., Egry I., Etay J., Battezzati L., Ricci E., Matsushita T., Seetharaman S.; "Thermophysical Properties of a Fe-Cr-Mo Alloy in the Solid and Liquid Phase"; Steel Research International 83/1 (2012): 43–54 (https://doi.org/10.1002/srin.201100156)

Kao A., Pericleous K.; "A numerical model coupling thermoelectricity, magnetohydrodynamics and dendritic growth"; Journal of Algorithms & Computational Technology 6/1 (2012): 173–201 (https://doi.org/10.1260/1748-3018.6.1.173)

Seidel A., Soellner W., Stenzel C.; "Studies of thermophysical properties of metals and semiconductors by containerless processing under microgravity"; TMS2012 141st Annual Meeting & Exhibition; Orlando FL, USA (2012)

Brillo J., Fritze H., Lohöfer G., Schulz M., Stenzel C.; "Advanced measurement devices for the microgravity electromagnetic levitation facility EML"; TMS2012 141st Annual Meeting & Exhibition; Orlando FL, USA (2012)

Fecht H.-J., Wunderlich R.K., Battezzati L., Ricci E., Etay J., Seetharaman S., Brillo J., Watanabe M., Kelton K., Matson D.M., Hyers R.W.; "Thermophysical property measurements under reduced gravity conditions: Evolution and status of the ThermoLab project"; TMS2012 141st Annual Meeting & Exhibition; Orlando FL, USA (2012)

Etay J., Egry I., Pericleous K., Wunderlich R.K.; "Status of viscosity measurements by the oscillating drop method in an electromagnetic levitation device under reduced gravity conditions"; TMS2012 141st Annual Meeting & Exhibition; Orlando FL, USA (2012)

Kelton K.; "Ground-based studies of the structure and properties of high temperature liquids for upcoming ISS experiments"; TMS2012 141st Annual Meeting & Exhibition; Orlando FL, USA (2012)

Watanabe M., Ozawa S., Mizuno A., Hibiya T., Kawauchi H., Murai K., Takahashi S.; "Thermophysical properties measurement of high-temperature liquids under microgravity conditions in controlled atmospheric conditions"; TMS2012 141st Annual Meeting & Exhibition; Orlando FL, USA (2012)

Herlach D.; "Dendrite growth into undercooled melts: Investigated on Earth and in reduced gravity"; TMS2012 141st Annual Meeting & Exhibition; Orlando FL, USA (2012)

Gandin C.-A., Tourret D., Volkmann T., Herlach D., Ilbagi A., Henein H.; "Solidification modeling: From electromagnetic levitation to atomization processing"; TMS2012 141st Annual Meeting & Exhibition; Orlando FL, USA (2012)

Lee J., Matson D., Hyers R.; "Containerless measurements of density and viscosity of Fe-Co alloys"; TMS2012 141st Annual Meeting & Exhibition; Orlando FL, USA (2012)

Schneider S., Willnecker R., Diefenbach A.; "Containerless processing on ISS: Ground support program for EML"; TMS2012 141st Annual Meeting & Exhibition; Orlando FL, USA (2012)

Seidel A., Soellner W., Stenzel C.; "EML – A multi-user electromagnetic levitation facility for containerless processing experiments onboard the ISS"; TMS2012 141st Annual Meeting & Exhibition; Orlando FL, USA (2012)

Lohöfer G., Brillo J.; "Inductive measurement device for microgravity electromagnetic levitator"; TMS2012 141st Annual Meeting & Exhibition; Orlando FL, USA (2012)

Wunderlich R., Fecht H.-J.; "Surface tension and viscosity of Ni-Al catalytic precursor alloys measured by the oscillating drop method on different microgravity platforms"; TMS2012 141st Annual Meeting & Exhibition; Orlando FL, USA (2012)

Schneider S., Willnecker R., Diefenbach A.; "Containerless processing on ISS: Ground support program for EML"; TMS2012 141st Annual Meeting & Exhibition; Orlando FL, USA (2012)

Bojarevics V., Pericleous K.; "Modeling magnetically excited and magnetically damped liquid metal flow"; CFD Modeling and Simulation in Materials Processing (2012): 243–252 (https://doi.org/10.1002/9781118364697.ch29)

Wunderlich R.K., Fecht H.-J.; "Surface tension and viscosity of NiAl catalytic precursor alloys from microgravity experiments"; 18th Symposium on Thermophysical Properties; Boulder CO, USA (2012)

Kao A., Pericleous K.; "Using thermoelectric magnetohydrodynamics to control microstructural evolution"; IOP Conference Series: Materials Science and Engineering 33 (2012): 012045 (https://doi.org/10.1088/1757-899x/33/1/012045)

Ilbagi A., Tourret D., Henein H., Gandin Ch.-A.; "Neutron diffraction analysis and solidification modeling of impulse-atomized Al36 wt%Ni"; IOP Conference Series: Materials Science and Engineering 33 (2012): 012060 (https://doi.org/10.1088/1757899x/33/1/012060)

Zhang H., Gandin C.A., He J., Nakajima K.; "Prediction of solidification path and carbide precipitation in Fe-CV-Cr-Mo-W high speed steels"; IOP Conference Series: Materials Science and Engineering 33 (2012): 012061 (https://doi.org/10.1088/1757899x/33/1/012061)

Herlach D.M.; "Containerless undercooling of drops and droplets"; Solidification of Containerless Undercooled Melts (eds. Herlach D.M., Matson D.M.); Wiley (2012): 1–30 (https://doi.org/10.1002/9783527647903.ch1)

Hyers R.W.; "Computer-aided experiments in containerless processing of materials"; Solidification of Containerless Undercooled Melts (eds. Herlach D.M., Matson D.M.); Wiley (2012): 31–50 (https://doi.org/10.1002/9783527647903.ch2)

Kolbe M.; "Demixing of Cu-Co alloys showing a metastable miscibility gap"; Solidification of Containerless Undercooled Melts (eds. Herlach D.M., Matson D.M.); Wiley (2012): 51–68 (https://doi.org/10.1002/9783527647903.ch3)

Holland-Moritz D.; "Short-range order in undercooled melts"; Solidification of Containerless Undercooled Melts (eds. Herlach D.M., Matson D.M.); Wiley (2012): 69–86 (https://doi.org/10.1002/9783527647903.ch4)

Kelton K.F., Lindsay Greer A.; "Ordering and crystal nucleation in undercooled melts"; Solidification of Containerless Undercooled Melts (eds. Herlach D.M., Matson D.M.); Wiley (2012): 87–112 (https://doi.org/10.1002/9783527647903.ch5)

Krivilyov M., Fransaer J.; "Effects of transient heat and mass transfer on competitive nucleation and phase selection in drop tube processing of multicomponent alloys"; Solidification of Containerless Undercooled Melts (eds. Herlach D.M., Matson D.M.); Wiley (2012): 139–160 (https://doi.org/10.1002/9783527647903.ch7)

Löser W., Shuleshova O.; "Nucleation and solidification kinetics of metastable phases in undercooled melts"; Solidification of Containerless Undercooled Melts (eds. Herlach D.M., Matson D.M.); Wiley (2012): 187–212 (https://doi.org/10.1002/9783527647903.ch9)

Matson D.M.; "Nucleation within the mushy zone"; Solidification of Containerless Undercooled Melts (eds. Herlach D.M., Matson D.M.); Wiley (2012): 213–238 (https://doi.org/10.1002/9783527647903.ch10)

Volkmann T.; "Measurements of crystal growth velocities in undercooled melts of metals"; Solidification of Containerless Undercooled Melts (eds. Herlach D.M., Matson D.M.); Wiley (2012): 239–260 (https://doi.org/10.1002/9783527647903.ch11)

Bojarevics V., Kao A., Pericleous K.; "Modeling the fluid dynamics and dendritic solidification in EM-levitated alloy melts"; Solidification of Containerless Undercooled Melts (eds. Herlach D.M., Matson D.M.); Wiley (2012): 321–348 (https://doi.org/10.1002/9783527647903.ch15)

Galenko P.K., Binder S., Ehlen G.J.; "Forced flow effect on dendritic growth kinetics in a binary nonisothermal system"; Solidification of Containerless Undercooled Melts (eds. Herlach D.M., Matson D.M.); Wiley (2012): 349–362 (https://doi.org/10.1002/9783527647903.ch16)

Gandin Ch.-A., Tourret D., Volkmann T., Herlach D.M., Ilbagi A., Henein H.; "Solidification modeling: From electromagnetic levitation to atomization processing"; Solidification of Containerless Undercooled Melts (eds. Herlach D.M., Matson D.M.); Wiley (2012): 403–424 (https://doi.org/10.1002/9783527647903.ch19)

Henein H., Ilbagi A., Gandin C.-A.; "Quantitative analysis of alloy structures solidified under limited diffusion conditions"; Solidification of Containerless Undercooled Melts (eds. Herlach D.M., Matson D.M.); Wiley (2012): 451–481 (https://doi.org/10.1002/9783527647903.ch21)

Seidel A., Soellner W., Stenzel C.; "Studies of thermophysical properties of metals and semiconductors by containerless processing under microgravity"; Materials Research in Microgravity 2012; NASA/CP-2012-217,466 (2012) 12–20

Brillo J., Fritze H., Lohöfer G., Schulz M., Stenzel C.; "Advanced measurement devices for the microgravity electromagnetic levitation facility EML"; Materials Research in Microgravity 2012; NASA/CP-2012-217,466 (2012): 21–28

Watanabe M., Ozawa S., Mizuno A., Hibiya T., Kawauchi H., Murai K., Takahashi S.; "Thermophysical properties measurement of high-temperature liquids under microgravity conditions in controlled atmospheric conditions"; Materials Research in Microgravity 2012; NASA/CP-2012-217,466 (2012): 41–47

Capuano G., Titomanlio D., Soellner W., Seidel A.; "Innovative video diagnostic equipment for material science"; Materials Research in Microgravity 2012; NASA/CP-2012-217,466 (2012): 88–96

Lee J., Choufani P., Bradshaw R.C., Hyers R.W., Matson D.M.; "Containerless measurements of density and viscosity of Fe-Co alloys"; Materials Research in Microgravity 2012; NASA/CP-2012-217,466 (2012): 97-014

Diefenbach A., Schneider S., Willnecker R.; "Containerless processing on ISS: Ground support program for EML"; Materials Research in Microgravity 2012; NASA/CP-2012-217,466 (2012): 163–169

Wunderlich R.; "Thermophysical properties of industrial alloys in the liquid phase under microgravity – The ThermoLab project"; 5th China-Germany Workshop

on Microgravity and Space Life Sciences; Rottach-Egern/Tegernsee, Germany (2012)

Wunderlich R.; "High temperature calorimetry of industrial alloys with conventional and containerless methods"; HI TEMP 2012 Conference; Munich, Germany (2012)

Matson D.M.; "Materials science in reduced gravity"; JOM 64/9 (2012): 1087–1088 (https://doi.org/10.1007/s11837-012-0425-y)

Bojarevics V., Hyers R.W.; "Levitated liquid dynamics in reduced gravity and gravity-compensating magnetic fields"; JOM 64/9 (2012): 1089–1096 (https://doi.org/10.1007/s11837-012-0417-y)

Schulz M., Brillo J., Stenzel C., Fritze H.; "Oxygen partial pressure control for microgravity experiments"; Solid State Ionics 225.SI (2012): 332–336. (https://doi.org/10.1016/j.ssi.2012.04.008)

Diarra A., Gagnoud A., Etay J., Stein A., Wunderlich R.; "Simulation numérique de l'ecoulement à l'Intérieur d'une goutte de métal liquide placée dans un inducteur parcouru par deux courants différents"; Journées Annuelles de la SF2M 2012; Paris, France (2012)

Diarra A., Gagnoud A., Etay J., Stein A., Wunderlich R.; "Numerical simulation of fluid flow inside a molten liquid metal droplet located in an electromagnetic induction generated by two different inducting currents"; 7th International Conference on Electromagnetic Processing of Materials (EPM2012); Beijing, China (2012)

Bojarevics V., Pericleous K., Roy A.; "Levitated liquid dynamics in gravity compensating magnetic fields"; Journal of Iron and Steel Research International 19/S1 (2012): 1058–1062

Kao A., Pericleous K.; "Investigating magnetic field orientation as an operational parameter in thermoelectric MHD solidification"; Journal of Iron and Steel International 19/S1 (2012): 260–264

Kao A., Pericleous K.; "A multiscale method for thermoelectric MHD in dendritic solidification"; Journal of Iron and Steel Research International 19/S1 (2012): 317–321

Emmerich H., Löwen H., Wittkowski R., Gruhn T., Tóth G.I., Tegze G., Gránásy L.; "Phase-field-crystal models for condensed matter dynamics on atomic length and diffusive time scales: An overview"; Advances in Physics 61/6 (2012): 665–743 (https://doi.org/10.1080/00018732.2012.737555)

Matson D.M.; "Containerless processing of molten metal alloys on the ISS"; 28th Annual Meeting of the American Society for Gravitational and Space Research (ASGSR); New Orleans LA, USA (2012)

Lohöfer G., Egry I.; "Heat balance in levitation melting"; High Temperatures-High Pressures 42/3 (2013): 175–202 Kelton K.F.; "Crystal nucleation in supercooled liquid metals"; International Journal of Microgravity Science and Application 30/1 (2013): 11–18

Kelton K.F.; "Crystal nucleation in supercooled liquid metals"; International Journal of Microgravity Science and Application 30/1 (2013): 11–18

Etay J.; "Electromagnetic levitation white-noise measurement protocol for modulated calorimetry"; International Journal of Microgravity Science and Application 30/1 (2013): 50–55

Pericleous K., Bojarevics V., Roy A; "Modeling of EML in combined AC/DC magnetic fields as the basis for microgravity experiments"; International Journal of Microgravity Science and Application 30/1 (2013): 56–63

Davidoff E., Galenko P.K., Herlach D.M., Kolbe M., Wanderka N.; "Spinodally decomposed patterns in rapidly quenched Co-Cu melts"; Acta Materialia 61/4 (2013): 1078–1092 (https://doi.org/10.1016/j.actamat.2012.10.010)

Lee J., Xiao X., Matson D.M., Hyers R.W.; "Characterization of fluid flow inside electromagnetically-levitated molten iron-cobalt droplets for ISS experiment"; TMS2013 142nd Annual Meeting & Exhibition – Supplemental Proceedings; Wiley (2013): 469–476 (https://doi.org/10.1002/9781118663547.ch58)

Zhang H., Nakajima K., Gandin C.A., He J.; "Prediction of carbide precipitation using partial equilibrium approximation in Fe-C-VW-Cr-Mo high speed steels"; ISIJ international 53/3 (2013): 493–501 (https://doi.org/10.2355/isijinternational.53.493)

Chen J., Lengsdorf R., Henein H., Herlach D.M., Dahlborg U., Calvo-Dahlborg M.; "Microstructure evolution in undercooled Al8wt%Fe melts: Comparison between terrestrial and parabolic flight conditions"; Journal of Alloys and Compounds 556 (2013): 243–251 (https://doi.org/10.1016/j.jallcom.2012.11.182)

Etay J., Gaganoud A., Diarra A., Garnier Ch., Massucci S., Alamir M., Sulpice A., Rivoirard S.; "Un nouveau dispositif de mesure de capacité calorifique et conductivité hermique d'alliages métalliques par lévitation électromagnétique"; 44e Journeés de calorimétrie; Lyon, France (2013)

Zhang Y.K., Gao J., Kolbe M., Klein S., Yang C., Yasuda H., Herlach D.M., Gandin Ch.-A.; "Phase selection and microstructure formation in undercooled Co-61.8at % Si melts under various containerless processing conditions"; Acta Materialia 61/13 (2013): 4861–4873 (https://doi.org/10.1016/j.actamat.2013.04.061)

Etay J.; "Non-contact thermophysical properties measurements in reduced gravity using inductive levitation"; Workshop on Advanced Electromagnetic Technology in Metallurgy; Baotou, China (2013)

Fecht H.J., Wunderlich R.K.; "THERMOLAB – An international microgravity laboratory for the measurement of thermophysical properties of liquid metallic alloys"; ELGRA Biennial Symposium and General Assembly; Rome, Italy (2013)

Diefenbach A., Schneider S., Willnecker R.; "Containerless processing on ISS: Experiment preparation for EML"; ELGRA Biennial Symposium and General Assembly; Rome, Italy (2013)

Binder S., Galenko P.K., Herlach D.M.; "Faceting of a rough solid-liquid interface of a metal induced by forced convection"; Philosophical Magazine Letters 93/10 (2013): 608–617 (https://doi.org/10.1080/09500839.2013.830201)

Bogno A.A., Khatibi P.D., Henein H., Gandin C.A; "Quantification of primary dendritic and secondary eutectic undercoolings of rapidly solidified Al-Cu droplets"; Materials Science & Technology 2 (2013): 1153–1160

Gránásy L., Rátkai L., Szállás A., Korbuly B., Tóth G.I., Környei L., Pusztai T.; "Phase-field modeling of polycrystalline solidification: From needle crystals to spherulites – A review"; Metallurgical and Materials Transactions A 45/4 (2014): 1694–1719 (https://doi.org/10.1007/s11661-013-1988-0)

Gránásy L., Podmaniczky F., Tóth G.I., Tegze G., Pusztai T.; "Heterogeneous nucleation of/on nanoparticles: A density functional study using the phase-field crystal model"; Chemical Society Reviews 43/7 (2014): 2159–2173 (https://doi.org/10.1039/c3cs60225g)

Bojarevics V., Pericleous K.; "Dual frequency AC and DC magnetic field levitation melting of metals"; International Journal of Applied Electromagnetics and Mechanics 44/2 (2014): 147–153 (https://doi.org/10.3233/JAE-141754)

Podmaniczky F., Toth G.I., Pusztai T., Granasy L.; "Free energy of the bcc–liquid interface and the Wulff shape as predicted by the phase-field crystal model"; Journal of Crystal Growth 385 (2014): 148–153 (https://doi.org/10.1016/j.jcrysgro.2013.01.036)

Binder S., Galenko P.K., Herlach D.M.; "The effect of fluid flow on the solidification of Ni2B from the undercooled melt"; Journal of Applied Physics 115/5 (2014): 053511 (https://doi.org/10.1063/1.4864151)

Battezzati L., Dalla Fontana G.; "Thermodynamics and fragility of glass-forming alloys"; Journal of Alloys and Compounds 586 (2014): S9–S13 (https://doi.org/10.1016/j.jallcom.2012.10.027)

Costa C., Delsante S., Borzone G., Zivkovic D., Novakovic R.; "Thermodynamic and surface properties of liquid Co-Cr-Ni alloys"; The Journal of Chemical Thermodynamics 69 (2014): 73–84 (https://doi.org/10.1016/j.jct.2013.09.034)

Amore S., Giuranno D., Novakovic R., Ricci E., Nowak R., Sobczak N.; "Thermodynamic and surface properties of liquid Ge-Si alloys"; Calphad 44 (2014): 95–101 (https://doi.org/10.1016/j.calphad.2013.07.014)

Ricci E., Amore S., Giuranno D., Novakovic R., Tuissi A., Sobczak N., Nowak R., Korpala B., Bruzda G.; "Surface tension and density of Si-Ge melts"; The Journal of Chemical Physics 140/21 (2014): 214704 (https://doi.org/10.1063/1.4879775)

Galenko P.K., Kolbe M., Herlach D.M., Rettenmayr M.; "Kinetics of dendrite growth and dendritic fragmentation in the undercooled Co 81.2 Cu 18.8 alloy's melt"; Revue de Métallurgie – International Journal of Metallurgy 111/5 (2014): 295–303 (https://doi.org/10.1051/metal/2014019)

Lee J., Matson D.M., Binder S., Kolbe M., Herlach D., Hyers R.W.; "Magnetohydrodynamic modeling and experimental validation of convection inside electromagnetically levitated Co-Cu droplets"; Metallurgical and Materials Transactions B 45/3 (2014): 1018–1023 (https://doi.org/10.1007/s11663-013-9995-5)

Ricci E., Amore S., Valenza F., Giuranno D., Novakovic R.; "Thermophysical properties of Ni based superalloys"; International Conference on Thermophysical and Mechanical Properties of Advanced Materials (THERMAM 2014); Izmir, Turkey (2014)

Lee J., Matson D.M.; "Prediction of mass evaporation of Fe50Co50 during measurements of thermophysical properties using an electrostatic levitator";

International Journal of Thermophysics 35/9–10 (2014): 1697–1704 (https://doi.org/10.1007/s10765-014-1662-9)

Valloton J., Herlach D.M., Henein H.; "Dendrite growth kinetics in undercooled melts of D2 tool steels"; 4th International Conference on Advances in Soldification Processing (ICASP4); Old Windsor, UK (2014)

Kolbe M., Goldschmidt F., Menke D., Neumann C., Drescher J., Kargl F., Meyer A.; "Liquid-liquid demixing of Co-Cu alloys on MAPHEUS rocket flight"; 4th International Conference on Advances in Solidification Processing; Old Windsor, UK (2014)

Alexandrov D.V., Galenko P.K.; "Dendrite growth under forced convection: Analysis methods and experimental tests"; Physics Uspekhi 57/8 (2014): 771–786 (https://doi.org/10.3367/UFNe.0184.201408b.0833)

Valloton J., Herlach D.M., Henein H.; "Dendrite growth kinetics in undercooled melts of D2 tool steels"; Space Exploration Symposium 2014; Alberta, Canada (2014)

Diefenbach A., Willnecker R., Schneider S.; "Containerless processing on ISS: Experiment preparation for EML"; 65th International Astronautical Congress (IAC-14); Toronto ON, Canada (2014): IAC-14.A2.7.2

Matson D.M.; "NASA materials science onboard the International Space Station"; 10th Asian Microgravity Society Symposium; Seoul, Korea (2014)

Matson D.; "Numerical prediction of the accessible convection range for electromagnetically levitated metallic melts in microgravity"; 30th Annual Meeting of the American Society for Gravitational and Space Research (ASGSR); Pasadena CA, USA (2014)

Jiang J.Z., Hofmann D., Jarvis D.J., Fecht H.J.; "Low-density high-strength bulk metallic glasses and their composites: A review"; Advanced Engineering Materials 17/6 (2015): 761–780 (https://doi.org/10.1002/adem.201400252)

Novakovic R., Brillo J.; "Thermodynamics, thermophysical and structural properties of liquid Fe-Cr alloys"; Journal of Molecular Liquids 200/B (2014): 153–159 (https://doi.org/10.1016/j.molliq.2014.09.053)

Fecht H.-J.; "Materials Science"; Generation and applications of extra-terrestrial environments on earth (2015): 211–218 (https://doi.org/10.13052/rp-9,788,793,237,544)

Velasco V., Crespo P., Marín P., García-Escorial A., Lieblich M., González-Calbet J.M., Ynduráin F., Hernando A.; "Short range order fluctuations and itinerant ferromagnetism in Ni3Al"; Solid State Communications 201 (2015): 111–114 (https://doi.org/10.1016/j.ssc.2014.10.026)

Lee J., Hyers R.W.; "Numerical estimation of convection in a molten zirconium droplet processed by electromagnetic levitation in microgravity"; International Journal of Microgravity Science and Application 32/1 (2015): 320105

Saad A., Gandin C.A., Bellet M.; "Temperature-based energy solver coupled with tabulated thermodynamic properties – Application to the prediction of macrosegregation in multicomponent alloys"; Computational Materials Science 99 (2015): 221–231 (https://doi.org/10.1016/j.commatsci.2014.12.009)

Lee J., Xiao X., Matson D.M., Hyers R.W.; "Numerical prediction of the accessible convection range for an electromagnetically levitated Fe50Co50 droplet in space"; Metallurgical and Materials Transactions B 46/1 (2015): 199–207 (https://doi.org/10.1007/s11663014-0178-9)

Blodgett M.E., Gangopadhyay A.K., Kelton K.F.; "Thermal evaporation loss measurements on quasicrystal (Ti-Zr-Ni) and glass forming (Vit 106 and Vit 106a) liquids"; International Journal of Thermophysics 36/4 (2015): 701–708 (https://doi.org/10.1007/s10765-0141663-8)

Wang H., Galenko P.K., Zhang X., Kuang W., Liu F., Herlach D.M.; "Phase-field modeling of an abrupt disappearance of solute drag in rapid solidification"; Acta Materialia 90 (2015): 282–291 (https://doi.org/10.1016/j.actamat.2015.02.0211359-6462)

Lohöfer, G., Schneider, S.; "Heat balance in levitation melting: The influence of sample cooling by heat conduction"; High Temperatures – High Pressures 44/2 (2015): 147–162

Giuranno D., Amore S., Novakovic R., Ricci E.; "Surface tension and density of RENE N5 and RENE 90 Ni-based superalloys"; Journal of Materials Science 50 (2015): 3763–3771 (https://doi.org/10.1007/s10853-015-8941-0)

Maitre A., Bogno A.A., Bedel M., Reinhart G., Henein H.; "Heterogeneous nucleation of the primary phase in the rapid solidification of Al-4.5 wt% Cu alloy droplet"; IOP Conference Series: Materials Science and Engineering 84 (2015): 012013 (https://doi.org/10.1088/1757-899x/84/1/012013)

Saad A., Gandin C.A., Bellet M., Shevchenko N., Eckert S.; "Simulation of channel segregation during directional solidification of In-75 wt pct Ga: Qualitative comparison with in situ observations"; Metallurgical and Materials Transactions A 46/11 (2015): 4886–4897 (https://doi.org/10.1007/s11661-015-2963-8)

Podmaniczky F., Tóth G.I., Tegze G., Gránásy L; "Recent developments in modeling heteroepitaxy/heterogeneous nucleation by dynamical density functional theory"; Metallurgical and Materials Transactions A 46/11 (2015): 4908–4920 (https://doi.org/10.1007/s11661-015-2986-1)

Dalla Fontana G., Castellero A., Battezzati L.; "Thermodynamics and fragility of Fe-based glass forming melts"; Journal of NonCrystalline Solids 433 (2016): 103–108 (https://doi.org/10.1016/j.jnoncrysol.2015.06.006)

Kuang W., Karrasch C., Wang H., Liu F., Herlach D.M.; "Eutectic dendrite growth in undercooled Fe83B17 alloy: Experiments and modeling"; Scripta Materialia 105 (2015): 34–37 (https://doi.org/10.1016/j.scriptamat.2015.04.022)

Glaubitz B., Kullack K., Dreier W., Seidel A., Soellner W., Diefenbach A., Schneider S.; "The electro-magnetic levitator (EML) on board the ISS – An overview and outlook"; Deutscher Luft- und Raumfahrtkongress (2015): 370222

Herlach D.M.; "Dendrite growth kinetics in undercooled melts of intermetallic compounds"; Crystals 5/3 (2015): 355–375 (https://doi.org/10.3390/cryst5030355)

Matson D.M.; "Electromagnetic levitation experiments on the ISS"; 6th International Symposium on Physical Sciences in Space (ISPS-6); Kyoto, Japan (2015)

Herlach D.M.; "Nicht-Gleichgewichtserstarrung: Modellierung für das Materialdesign industrieller Werkstoffe (NEQUISOL)"; Nationales Symposium Forschung unter Weltraumbedingungen; Bonn, Germany (2015)

Herlach D.M., Binder S., Galenko P., Gegner J., Holland-Moritz D., Klein S., Kolbe M., Volkmann T.; "Containerless undercooled melts: Ordering, nucleation, and dendrite growth"; Metallurgical and Materials Transactions A 46/11 (2015): 4921–4936 (https://doi.org/10.1007/s11661-015-3052-8)

Lohöfer G., Scheinder S.; "Heat balance in levitation melting: Sample cooling by forced gas convection in helium"; High Temperatures – High Pressures 44/6 (2015): 429–450

Lee J., Rodriguez J.E., Hyers R.W., Matson D.M.; "Measurement of density of Fe-Co alloys using electrostatic levitation"; Metallurgical and Materials Transactions B 46/6 (2015): 2470–2475 (https://doi.org/10.1007/s11663-015-0434-7)

Lomaev S., Krivilyov M., Fransaer M.; "Exact analytical solution based on the vector potential technique for a conjugated hydrodynamic and Joule heating problem in an electromagnetically levitated drop"; Magnetohydrodynamics 52/1–2 (2016):105–116 (https://doi.org/10.22364/mhd.52.1-2.12)

Karrasch C.; Solidification kinetics in undercooled pure Fe and Fe-B alloys under different fluid flow conditions; Ruhr University of Bochum; PhD thesis (2016)

Amore S., Valenza F., Giuranno D., Novakovic R., Dalla Fontana G., Battezzati L., Ricci E., "Thermophysical properties of some Ni-based superalloys in the liquid state relevant for solidification processing"; Journal of Materials Science 51 (2016): 1680–1691 (https://doi.org/10.1007/s10853-015-9452-8)

Saad A., Gandin C.A., Bellet M., Volkmann T., Herlach D.; "Simulation of shrinkage-induced macrosegregation in a multicomponent alloy during reduced-gravity solidification"; TMS2016 145th Annual Meeting & Exhibition – Supplemental Proceedings (2016): 35–42 (https://doi.org/10.1007/978-3-319-48,254-5_5)

Valloton J., Bogno A.A., Chen J., Lengsdorf R., Henein H., Herlach D.M., Dahlborg U., Calvo-Dahlborg M.; "Microstructural evolution in undercooled Al-8 wt% Fe melts"; TMS2016 145th Annual Meeting & Exhibition – Supplemental Proceedings (2016): 51–57 (https://doi.org/10.1007/978-3-319-48,254-5_7)

Wunderlich R.K., Fecht H.-J.; "Recent results from calorimetry on the bulk metallic glass forming alloy VIT106a with the electromagnetic levitation device on ISS"; TMS2016 145th Annual Meeting & Exhibition; Nashville TN, USA (2016)

Saad A.; Numerical modelling of macrosegregation formed during solidification with shrinkage using a level set approach; PSL Research University; PhD thesis (2016)

Karrasch C., Volkmann T., Valloton J., Kolbe M., Herlach D.M.; "Bent dendrite growth in undercooled Fe-B alloy melts"; IOP Conference Series: Materials Science and Engineering 117/1 (2016): 012015 (https://doi.org/10.1088/1757-899x/117/1/012015)

Valloton J., Herlach D.M., Henein H.; "Effect of convection on the dendrite growth kinetics in undercooled melts of D2 tool steels"; IOP Conference Series:

Materials Science and Engineerin g 117/1 (2016): 012058 (https://doi.org/10.1088/1757899x/117/1/012058)

Matson D.M., Xiao X., Rodriguez J., Wunderlich R.K.; "Preliminary experiments using electromagnetic levitation on the International Space Station"; International Journal of Microgravity Science and Application 33/2 (2016): 330206 (https://doi.org/10.15011/jasma.33.330206)

Matson D.; "Thermophysical property measurement using containerless techniques in microgravity"; 11th International Workshop on SubSecond ThermoPhysics; Krakow, Poland (2016)

Wunderlich R.K., Lohöfer G., Fecht H.-J.; "Surface tension and viscosity of the Ni-based superalloys LEK94 and CMSX-10 measured by the oscillating drop method on board a parabolic flight"; 11th International Workshop on SubSecond ThermoPhysics; Krakow, Poland (2016)

Wunderlich R.K., Fecht H.-J.; "Specific heat capacity in the liquid phase of reactive metallic alloys – Containerless processing in an electromagnetic levitation device on board the ISS"; 11th International Workshop on SubSecond ThermoPhysics (IWSSTP11); Krakow, Poland (2016)

Matson D.M., Watanabe M., Pottlacher G., Lee G.W., Fecht H.-J.; "Thermophysical property measurement: A call to action"; International Journal of Microgravity Science and Application 33/3 (2016): 330304 1–7 (https://doi.org/10.15011/ijmsa.33.330304)

Lohöfer G., Schneider S.; "Heat Balance in levitation melting: Sample cooling by forced gas convection in argon"; High Temperatures – High Pressures 45/4 (2016): 255–271

Podmaniczky F., Tóth G.I., Pusztai T., Gránásy L.; "Investigating nucleation using the phase-field method"; Journal of the Indian Institute of Science 96/3 (2016): 161–177

Bogno A.A., Khatibi P.D., Henein H., Gandin C.A.; "Quantification of primary dendritic and secondary eutectic nucleation undercoolings in rapidly solidified hypo-eutectic Al-Cu droplets"; Metallurgical and Materials Transactions A 47/9 (2016): 4606–4615 (https://doi.org/10.1007/s11661-016-3594-4)

Diefenbach A., Schneider S., Schumann S., Willnecker R.; "Containerless processing in ISS: Status of experiments in ESA's EML, the electromagnetic levitator"; 67th International Astronautical Congress (IAC-16); Guadalajara, Mexico (2016): IAC-16.A2.6.5

Kolbe M.; "Liquid-liquid demixing of Co-Cu alloys under various convective conditions"; XVI Liquid and Amorphous Metals Conference; Bonn-Bad Godesberg, Germany (2016)

Diarra A.; Mesures de propriétés thermiques des métaux par procédé électromagnétique; Université Grenoble Alpes, PhD thesis (2016)

Xiao X., Wunderlich R., Fecht H.-J., Matson D.; "Optimizing containerless viscosity measurement techniques using the MSL-EML facility on the ISS for a molten FeCrNi alloy"; 32nd Annual Meeting of the American Society for Gravitational and Space Research (ASGSR); Cleveland OH, USA (2016)

Barlow S., Wunderlich R., Fecht H.-J., Matson D.M.; "Containerless measurement of thermophysical properties of the melt for industrial nickel-based turbine blade alloys"; 32nd Annual Meeting of the American Society for Gravitational and Space Research (ASGSR); Cleveland OH, USA (2016)

Hyers R., Zhao J., Lee J., SanSoucie M., Rogers J., Wunderlich R., Fecht H.-J.; "Thermophysical properties of zirconium-oxygen alloys: Comparison of flight and ground data"; 32nd Annual Meeting of the American Society for Gravitational and Space Research (ASGSR); Cleveland OH, USA (2016)

Matson D.; "Electromagnetic levitation on the International Space Station"; 32nd Annual Meeting of the American Society for Gravitational and Space Research (ASGSR); Cleveland OH, USA (2016)

Gangopadhyay A.K., Kelton K.F.; "Measurements of the temperature-dependent total hemispherical emissivity using an electrostatic levitation facility"; International Journal of Thermophysics 38/1 (2017): 3 (https://doi.org/10.1007/s10765-016-2138-x)

Wunderlich R.K., Fecht H.J., Lohöfer G.; "Surface tension and viscosity of the Ni-based superalloys LEK94 and CMSX-10 measured by the oscillating drop method on board a parabolic flight"; Metallurgical and Materials Transactions B 48/1 (2017):237–246 (https://doi.org/10.1007/s11663-016-0847-y)

Luo Y., Damaschke B., Schneider S., Lohöfer G., Abrosimov N., Czupalla M., Samwer K.; "Contactless processing of SiGe-melts in EML under reduced gravity"; npj Microgravity 2 (2016): 1 (https://doi.org/10.1038/s41526-016-0007-3)

Herlach D. M., Palberg T., Klassen I., Klein S., Kobold R.; "Overview: Experimental studies of crystal nucleation: Metals and colloids"; The Journal of Chemical Physics 145/21 (2016): 211703 (https://doi.org/10.1063/1.4963684)

Podmaniczky F., Tóth G.I., Tegze G., Pusztai T., Gránásy L.; "Phase-field crystal modeling of heteroepitaxy and exotic modes of crystal nucleation"; Journal of Crystal Growth 457 (2017): 24–31 (https://doi.org/10.1016/j.jcrysgro.2016.06.056)

Galenko P.K., Danilov D.A., Reuther K., Alexandrov D.V., Rettenmayr M., Herlach D.M.; "Effect of convective flow on stable dendritic growth in rapid solidification of a binary alloy"; Journal of Crystal Growth 457 (2017): 349–355 (https://doi.org/10.1016/j.jcrysgro.2016.07.042)

Rodriguez J.E., Kreischer C., Volkmann T., Matson D.M.; "Solidification velocity of undercooled Fe-Co alloys"; Acta Materialia 122 (2017): 431–437 (https://doi.org/10.1016/j.actamat.2016.09.047)

Delshad Khatibi P., Henein H.; "Estimation of droplet solidification temperature in rapid solidification using in-situ measurements"; Canadian Metallurgical Quarterly 56/1 (2017): 76–84 (https://doi.org/10.1080/00084433.2016.1259711)

Bogno A.A., Valloton J., Henein H., Gallerneault M., Herlach D.; "Effect of hypoeutectic Sc additions to Al-4.5 wt% Cu under different cooling rates"; Proceedings of the 3rd Pan American Materials Congress (2017): 355–363 (https://doi.org/10.1007/978-3-31,952,132-9_36)

Zhao J., Lee J., Wunderlich R.K., Fecht H.J., Schneider S., SanSoucie M., Rogers J., Hyers R.; "Influence of oxygen on surface tension of zirconium"; Materials Processing Fundamentals 2017: 47–54 (https://doi.org/10.1007/978-3-319-51,580-9_5)

Gangopadhyay A.K., Pueblo C.E., Dai R., Johnson M.L., Ashcraft R., Van Hoesen D., Sellers M., Kelton K.F.; "Correlation of the fragility of metallic liquids with the high temperature structure, volume, and cohesive energy"; The Journal of Chemical Physics 146/15 (2017): 154506 (https://doi.org/10.1063/1.4981011)

Galenko P.K., Hanke R., Paul P., Koch S., Rettenmayr M., Gegner J., Herlach D.M., Dreier W., Kharanzhevski E.V.; "Solidification kinetics of a Cu-Zr alloy: Ground-based and microgravity experiments"; IOP Conference Series: Materials Science and Engineering 192/1 (2017): 012028 (https://doi.org/10.1088/1757-899x/192/1/012028)

Ankudinov V., Galenko P.K.; "The diagram of phase-field crystal structures: an influence of model parameters in a two-mode approximation"; IOP Conference Series: Materials Science and Engineering 192/1 (2017): 012019 (https://doi.org/10.1088/1757899X/192/1/012019)

Kazak O.V., Galenko, P.K., Alexandrov D.V.; "Influence of tiny amounts of impurity on dendritic growth in undercooled melts''; IOP Conference Series: Materials Science and Engineering 192/1 (2017): 012030 (https://doi.org/10.1088/1757-899x/192/1/012030)

Salhoumi A., Galenko P. K.; "Analysis of interface kinetics: solutions of the Gibbs-Thomson-type equation and of the kinetic rate theory"; IOP Conference Series: Materials Science and Engineering 192/1 (2017): 012014 (https://doi.org/10.1088/1757899x/192/1/012014)

Etay J., Diarra A., Gagnoud A., Garnier C., Massucci S., Al Amir M., Sulpice A., Rivoirard S.; "Measuring thermal conductivity and heat capacity of molten metallic alloys by electromagnetic levitation in DC field"; Magnetohydrodynamics 53/2 (2017): 289–298 (https://doi.org/10.22364/mhd.53.2.7)

Gangopadhyay A.K., Kelton K.F.; "Recent progress in understanding high temperature dynamical properties and fragility in metallic liquids, and their connection with atomic structure"; Journal of Materials Research 32/14 (2017): 2638–2657 (https://doi.org/10.1557/jmr.2017.253)

Herlach D.M., Galenko P.K., Rettenmayr M.; "Design of metastable materials: Experimental results and modelling of nonequilibrium solidification"; Proceedings of the 6th Decennial International Conference on Solidification Processing (2017): 26–29

Reinartz M., Burggraf S., Rettenmayr M., Herlach D.M.; "Rapid solidification of aluminium-nickel melts in Earth and space environments"; 6th Decennial International Conference on Solidification Processing; Old Winsor, United Kingdom (2017)

Valloton J., Herlach D.M., Henein H., Sediako D.; "Microstructural quantification of rapidly solidified undercooled D2 tool steel"; Metallurgical and Materials Transactions A 48/10 (2017): 4735–4743 (https://doi.org/10.1007/s11661-017-4249-9)

Fecht H.-J., Wunderlich R.K.; "Fundamentals of liquid processing in low Earth orbit: From thermophysical properties to microstructure formation in metallic alloys"; JOM 69/8 (2017): 1261–1268 (https://doi.org/10.1007/s11837-017-2417-4)

Lee J., SanSoucie M.P.; "Experiments using a ground-based electrostatic levitator and numerical modeling of melt convection for the iron-cobalt system in support of space experiments"; JOM 69/8 (2017): 1298–1302 (https://doi.org/10.1007/s11837-017-2387-6)

Herlach D.M., Burggraf S., Galenko P., Gandin C.-A., Garcia-Escorial A., Henein H., Karrasch C., Mullis A., Rettenmayr M., Valloton J.; "Solidification of undercooled melts of Al-based alloys on Earth and in space"; JOM 69/8 (2017): 1303–1310 (https://doi.org/10.1007/s11837-017-2402-y)

Matson D., Xiao X., Rodriguez J.E., Lee J., Hyers R.W., Shuleshova O., Kaban I., Schneider S., Karrasch C., Burggraf S., Wunderlich R.K., Fecht H.-J.; "Use of thermophysical properties to select and control convection during rapid solidification of steel alloys using electromagnetic levitation on the space station"; JOM 69/8 (2017): 1311–1318 (https://doi.org/10.1007/s11837-017-2396-5)

Lohöfer G., Pottlacher G.R.; "Inductive measurement of electrical resistivity and thermal expansion of molten $Zr64Ni36$ alloy"; 21st European Conference on Thermophysical Properties (ECTP2017); Graz, Austria (2017)

Matson D.M.; 'In-situ property measurement for selection and control of convection in EML space experiments"; 21st European Conference on Thermophysical Properties (ECTP2017); Graz, Austria (2017)

Jeon S., Matson D.M.; "Formation of cellular structure on metastable solidification of undercooled eutectic CoSi 62 at%"; Crystals 7/10 (2017): 295 (https://doi.org/10.3390/cryst7100295)

Schneider S.; "Installation and operation of the electromagnetic levitator on ISS and experiment preparation"; 7th ISPS & 25th ELGRA Biennial Symposium and General Assembly; Juan-les-Pins, France (2017)

Volkmann T., Kreischer C., Gao J., Shuleshova O., Löser W.; "Metastable phase formation in undercooled Nd-Fe-B alloy melts"; 7th ISPS & 25th ELGRA Biennial Symposium and General Assembly; Juan-les-Pins, France (2017)

Shuleshova O.; "Transient formation of the metastable bcc phase in Ti-Al and Fe-Co systems"; 7th ISPS & 25th ELGRA Biennial Symposium and General Assembly; Juan-les-Pins, France (2017)

Wunderlich R.K., Fecht H.J, Hecht U., Hediger F.; "Surface tension and viscosity of titanium alloys: Application of oscillating drop method in an electromagnetic processing device on board parabolic flights and the ISS"; 7th ISPS & 25th ELGRA Biennial Symposium and General Assembly; Juan-les-Pins, France (2017)

Lohöfer G.; "Inductive measurement of thermophysical properties of metallic melts in microgravity EML facilities"; 7th ISPS & 25th ELGRA Biennial Symposium and General Assembly; Juan-les-Pins, France (2017)

Aalilija A., Hachem E., Gandin C.-A.; "Numerical modelling of a levitated steel melt in microgravity"; 7th ISPS & 25th ELGRA Biennial Symposium and General Assembly; Juan-les-Pins, France (2017)

Wunderlich R., Fecht H.J., Ricci E., Novakovic R., Etay J., Budenkova O., Battezzati L., Brillo J., Kelton K.F., Matson D.M., Hyers R., Neels A., Dommann A., Prades-Roedel S., Blatter A.; "Thermophysical properties of metallic alloys in the liquid phase: Results of containerless electromagnetic processing on the International Space Station"; 7th ISPS & 25th ELGRA Biennial Symposium and General Assembly; Juan-les-Pins, France (2017)

Wang Y., Gao J., Kolbe M., Chuang A.C.-P., Ren Y., Matson D.; "Metastable solidification of hypereutectic Co2Si-CoSi composition: Microstructural studies and in-situ observation"; Acta Materialia 142 (2018): 172–180 (https://doi.org/10.1016/j.actamat.2017.09.037)

Herlach D.M., Simons D., Pichon P.-Y.; "Crystal growth kinetics in undercooled melts of pure Ge, Si and Ge-Si alloys"; Philosophical Transactions A 376 (2018): 20170205 (https://doi.org/10.1098/rsta.2017.0205)

Matson D.M., Xiao X.; "Identifying metastable interface potency limits during steel alloy transformations"; Materials Letters 212 (2018): 256–258 (https://doi.org/10.1016/j.matlet.2017.10.098)

Wunderlich R.K., Hecht U., Fecht H.-J.; "Surface tension and viscosity of gamma-TiAl alloys and Ti6Al4V measured in containerless electromagnetic processing under reduced gravity conditions"; TMS2018 147th Annual Meeting & Exhibition; Phoenix AZ, USA (2018)

Faraji M., Kolbe M., Lierfeld T., Eggeler G., Herlach D. M.; "Influence of Ta on the solidification behaviour of undercooled Ni-Ta alloys"; TMS2018 147th Annual Meeting & Exhibition; Phoenix AZ, USA (2018)

Herlach D.M., Kolbe M., Reinartz M., Galenko P.K., Rettenmayr M.; "Anomalous dendrite growth in undercooled melts of Al-Ni alloys"; TMS2018 147th Annual Meeting & Exhibition; Phoenix AZ, USA (2018)

Kolbe M., Dreissigacker C., Burggraf S., Wegener M., Kargl F.; "Liquid demixing in undercooled Co-Cu alloys"; TMS2018 147th Annual Meeting & Exhibition; Phoenix AZ, USA (2018)

Wunderlich R., Mohr M., Fecht H.-J.; "Specific heat capacity in the liquid phase of metallic alloys measured by non-contact calorimetry in a containerless electromagnetic processing device on board the International Space Station"; 20th International Symposium on Thermophysical Properties; Boulder CO, USA (2018)

Wunderlich R., Mohr M., Hecht U., Fecht H.-J.; "Surface tension and viscosity of Ti-6Al-4 V, Ti-48Al-2Nb-2Cr, Ti46Al-8Nb and Ti46Al8Ta from measurements with the oscillating drop method in an electromagnetic processing device on board the International Space Station and on board parabolic flights"; 20th International Symposium on Thermophysical Properties; Boulder CO, USA (2018)

Zhang Sh., Guillemot G., Gandin Ch.-A., Bellet M.; "A partitioned two-step resolution algorithm for solid-mushy-liquid interaction modelling in solidification

processes"; 6th European Conference on Computational Mechanics – 7th European Conference on Computational Fluid Dynamics (ECCM-ECFD 2018); Glasgow, UK (2018)

Schulz M., Fritze H., Zell U., Aicher W.; "Oxygen pump and oxygen sensor as extension of the electromagnetic levitator on International Space Station"; ITG-Fb. 281: Sensoren und Messsystemen, GMA (2018): 143–146

Xiao X., Hyers R.W., Wunderlich R.K., Fecht H.-J., Matson D.; "Deformation induced frequency shifts of oscillating droplets during molten metal surface tension measurement"; Applied Physics Letters 113 (2018): 011903 1–4 (https://doi.org/10.1063/1.5039336)

Rettenmayr M.; "Solidification of Al-Ni melts under terrestrial and microgravity conditions"; Seventh International Conference on Solidification and Gravity; Miskolc, Hungary (2018)

Reinartz M., Burggraf S., Kolbe M., Paul P., Galenko P., Herlach D.M., Rettenmayr M.; "Solidification of Al-Ni melts under terrestrial and microgravity conditions"; Seventh International Conference on Solidification and Gravity; Miskolc, Hungary (2018)

Aalilija A., Hachem E., Gandin Ch.-A.; "Numerical simulation of chill cooling and solidification of a levitated steel droplet in microgravity"; Seventh International Conference on Solidification and Gravity; Miskolc, Hungary (2018)

Koch S., Galenko P., Shuleshova O., Kobold R., Rettenmayr M.; "Solidification behavior and microstructure analysis of ternary Zr.Cu.(Al6Ni) alloys"; Seventh International Conference on Solidification and Gravity; Miskolc, Hungary (2018)

Soellner, W., Aicher, W., Winter, C.; "The electromagnetic levitator (EML) on-board the ISS: Capabilities, on-orbit performance and recent enhancements"; Deutscher Luft- und Raumfahrtkongress 2018; Friedrichshafen, Germany (2018)

Wunderlich, R.K., Hecht, U., Hediger, F., Fecht, H. "Surface tension, viscosity, and selected thermophysical properties of Ti48Al48Nb2Cr2, Ti46Al46Nb8, and Ti46Al46Ta8 from microgravity experiments"; Advanced Engineering Materials 20 (2018): 1800346 (https://doi.org/10.1002/adem.201800346)

Aicher W.; "Future capabilities of the electromagnetic levitator (EML) on-board the ISS: Oxygen sensing and control system (OCS)"; 69th International Astronautical Congress (IAC-18); Bremen, Germany (2018): IAC-18.A2.5.7

Soellner W.; "The electromagnetic levitator (EML) on-board the ISS: Capabilities, on-orbit performance and recent enhancements"; 69th International Astronautical Congress (IAC-18); Bremen, Germany (2018): IAC-18.A2.6.10

Schumann S., Diefenbach A., Schneider S., Willnecker R.; "Containerless processing on ISS: Experiment operations in ESA's EML – the electromagnetic levitator"; 69th International Astronautical Congress (IAC-18); Bremen, Germany (2018): IAC-18.A2.6.11

Fecht, H.-J., Mohr, M., Wunderlich, R.K.; "Thermophysical properties of metallic alloys in the liquid phase: Recent results of containerless electromagnetic processing on the International Space Station ISS"; 69th International Astronautical Congress (IAC-18); Bremen, Germany (2018): IAC-18.A2.6.12

Wunderlich, R.K., Mohr, M., Fecht, H.-J.; "The Materials Science Laboratory – Electromagnetic Levitator on the International Space Station (ISS-EML): Thermophysical properties of a g-TiAl alloy in the liquid phase"; 69th International Astronautical Congress (IAC-18); Bremen, Germany (2018): IAC-18. A2.6.13

Matson D.M.; "Retained free energy as a driving force for phase transformation during rapid solidification of stainless steel alloys in microgravity"; npj Microgravity 4 (2018): 22 (https://doi.org/10.1038/s41526-018-0056-x)

Nawer J., Matson D.M.; "Measurement of mass evaporation and density of Ni-based super alloy by electrostatic levitation (ESL)"; 34th Annual Meeting of the American Society for Gravitational and Space Research (ASGSR); Bethesda MD, USA (2018)

Lohöfer G.; "High-resolution inductive measurement of electrical resistivity and density of electromagnetically levitated liquid metal droplets"; Review of Scientific Instruments 89 (2018): 124709 (https://doi.org/10.1063/1.5065482)

Zhang Sh., Guillemot G., Gandin Ch.-A., Bellet M.; "Numerical simulation of mechanical interactions between liquid and solid in casting processes"; Journées Annuelles du GdR Solidification des Alliages Métalliques; Lille, France (2018)

Hearn W., Bogno A.-A., Spinelli J., Valloton J., Henein H.; "Microstructure solidification maps for Al-10 Wt Pct Si alloys"; Metallurgical and Materials Transactions A 50/3 (2019): 1333–1345 (https://doi.org/10.1007/s11661-018-5093-2)

Krivilyov M., Afyatunova D., Lebedev V., Galenko P.K.; "Phase-field simulation of non-isothermal phase separation in rapidly quenched Co-Cu melts"; Computational Materials Science 158 (2019): 289–295 (https://doi.org/10.1016/j.commatsci.2018.11.010)

Mohr M., Wunderlich R.K., Zweiacker K., Prades-Rödel S., Sauget R., Blatter A., Logé R., Dommann A., Neels A., Johnson W.L., Fecht H.-J.; "Surface tension and viscosity of liquid Pd43Cu27Ni10P20 measured in a levitation device under microgravity"; npj Microgravity 5 (2019): 4 (https://doi.org/10.1038/s41526-019-0065-4)

Bracker G., Xiao X., Lee J., Reinartz M., Burggraf S., Herlach D., Rettenmayr M., Matson D., Hyers R.; "Modeling of fluid flow effects on experiments using electromagnetic levitation in reduced gravity"; Materials Processing Fundamentals 2019: 171–180 (https://doi.org/10.1007/978-3-030-05728-2_16)

Xiao X., Lee J., Hyers R.W., Matson D.M.; "Numerical representations for flow velocity and shear rate inside electromagnetically levitated droplets in microgravity"; npj Microgravity 5 (2019): 7 (https://doi.org/10.1038/s41526-019-0067-2)

Mohr M., Wunderlich R., Liaw P., Battezzati L., Fecht H.-J.; "Surface tension and viscosity of FeCoCrNiTa and Al0.1CoCrFeNi measured by the oscillating drop method in an electromagnetic processing device under reduced gravity"; TMS2019 148th Annual Meeting & Exhibition; San Antonio TX, USA (2019)

Wunderlich R., Mohr M., Hecht U., Hyers R.W., Matson D.M., Lohöfer G., Shuleshova O., Fecht H-J; "The materials science laboratory – Electromagnetic levitator on the International Space Station: A case study with the alloy Ti48Al-

2Cr-2Nb"; TMS2019 148th Annual Meeting & Exhibition; San Antonio TX, USA (2019)

Bracker G., Xiao X., Lee J., Herlach D.M.; Rettenmayr M., Reinartz M., Burggraf S., Matson D.M., Hyers R.W.; "Modeling of fluid flow effects on experiments using electromagnetic levitation in reduced gravity"; TMS2019 148th Annual Meeting & Exhibition; San Antonio TX, USA (2019)

Wunderlich R., Mohr M.; "Investigation of non-linear effects in viscosity measurements by the oscillating drop method in an electromagnetic levitation device under reduced gravity conditions"; TMS2019 148th Annual Meeting & Exhibition; San Antonio TX, USA (2019)

Hyers R., Zhao J., Bracker G., Wunderlich R., Fecht H.; "Anomalous nucleation in undercooled melts processed by electromagnetic levitation"; TMS2019 148th Annual Meeting & Exhibition; San Antonio TX, USA (2019)

Mohr M., Wunderlich R.K., Koch S., Galenko P.K., Gangopadhyay A.K., Kelton K. F., Jiang J.Z., Fecht H.-J.; "Surface tension and viscosity of Cu50Zr50 measured by the oscillating drop technique on board the International Space Station"; Microgravity Science and Technology 31/2 (2019): 177–184 (https://doi.org/10.1007/s12217-019-9678-1)

Galenko P.K., Ankudinov V., Reuther K., Rettenmayr M., Salhoumi A., Kharanzhevskiy E.V.; "Thermodynamics of rapid solidification and crystal growth kinetics in glass-forming alloys", Philosophical Transactions of Royal Society A 377/2143 (2019): 20180205 (https://doi.org/10.1098/rsta.2018.0205)

Krivilyov M., Lomaev S., Fransaer J., Matson D.M., Volkmann T.; "Numerical simulation of heat and mass transport in the containerless solidification experiment PARSEC onboard of the International Space Station"; 8th International Conference on Solidification – Computer Simulation, Experiments and Technology; Izhevsk, Russia (2019)

Wunderlich R.K., Mohr M.; "Non-linear effects in the oscillating drop method for viscosity measurements"; High Temperatures – High Pressures 48/3 (2019): 253–277 (https://doi.org/10.32908/hthp.v48.648)

Matson D.M., Xiao X., Jeon S.; "Optimization strategies for identifying the controlling mechanism for solid state transformation in FeCrNi during rapid solidification"; IOP Conference Series: Materials Science and Engineering 529 (2019): 012012 (https://doi.org/10.1088/1757-899X/529/1/012012)

Zhang Sh., Guillemot G., Gandin Ch.-A., Bellet M.; "A partitioned solution algorithm for fluid flow and stress-strain computations applied to continuous casting"; IOP Conference Series: Materials Science and Engineering 529 (2019): 012082 (https://doi.org/10.1088/1757-899X/529/1/012082)

Lomaev S., Krivilyov M., Fransaer J., Lee L., Volkmann T., Matson D.M; "Simulation of fluid flow in levitated Fe-Co droplets electromagnetically processed onboard the ISS"; Magnetohydrodynamics 55/1–2 (2019): 251–260 (https://doi.org/10.22364/mhd.55.12.30)

Xiao X., Hyers R.W., Matson D.M.; "Surrogate model for convective flow inside electromagnetically levitated molten metal droplet using magnetohydrodynamic

simulation and feature analysis"; International Journal of Heat and Mass Transfer 136 (2019): 531–542 (https://doi.org/10.1016/j.ijheatmasstransfer.2019.03.028)

Mohr M., Wunderlich R., Fecht H.-J.; "Surface tension, viscosity and specific heat capacity of Ni-based superalloys MC2, LEK94 and CMSX-10 measured in the electromagnetic levitator (EML) on board the International Space Station (ISS)"; 12th International Workshop on Subsecond Thermophysics; Cologne, Germany (2019)

Mohr M., Wunderlich R., Koch S., Galenko P.K., Gangopadhyay A.K., Kelton K.F., Fecht H.-J.; "A correction method to enable surface tension measurements on rotating samples using the oscillating drop technique"; 12th International Workshop on Subsecond Thermophysics; Cologne, Germany (2019)

Luo Y., Damaschke B., Lohöfer G., Samwer K.; "Processing SiGE melts on board the ISS"; 12th International Workshop on Subsecond Thermophysics; Cologne, Germany (2019)

Reinartz M., Burggraf S., Kolbe M., Paul P., Koch S., Galenko P., Herlach D.M., Rettenmayr M.; "Study of nucleation and growth in rapidly solidifying Al-Ni alloys"; 5th International Conference on Advances in Solidification Processes (ICASP-5); Salzburg, Austria (2019)

Srirangam P., Mohr M., Fecht H.-J.; "Thermophysical properties of iron alloys under microgravity conditions"; 1st International Conference on Materials Science and Engineering (ICMSE 2019); Jalandhar, India (2019)

Herlach D.M., Burggraf S., Reinartz M., Galenko P.K., Rettenmayr M., Gandin Ch.-A., Henein H., Mullis A., Ilbagi A., Valloton J.; "Dendrite growth in undercooled Al-rich Al-Ni melts measured on Earth and in Space"; Physical Review Materials 3/7 (2019):073402 (https://doi.org/10.1103/PhysRevMaterials.3.073402)

Galenko P., Jou D.; "Rapid solidification as non-ergodic phenomenon"; Physics Reports 818 (2019): 1–70 (https://doi.org/10.106/j.physrep.2019.06.002)

Brillo J., Wessing J., Kobatake H., Fukuyama H.; "Surface tension of liquid Ti with adsorbed oxygen and its prediction"; Journal of Molecular Liquids 290 (2019): 111226 (https://doi.org/10.1016/j.molliq.2019.111226)

Jeon S., Kolbe M., Kaban V., String G., Cleaver A., Kaban I., Shuleshova O., Gao J., Matson D.M.; "Metastable solidification pathways of undercooled eutectic CoSi–CoSi2 alloys"; Acta Materialia 176/9 (2019): 43–52 (https://doi.org/10.1016/j.actamat.2019.06.048)

Mohr M., Dong Y., Wunderlich R., Fecht H.-J.; "The electromagnetic levitator (ISS-EML) on the International Space Station – Containerless electromagnetic processing on the International Space Station ISS – The ThermoProp/ThermoLab project"; 26th ELGRA Biennial Symposium and General Assembly; Granada, Spain (2019)

Mohr M., Dong Y., Wunderlich R., Fecht H.-J.; "The electromagnetic levitator (ISS-EML) on the International Space Station – Thermophysical properties of Ni-based superalloys MC2, LEK94, CMSX-10"; 26th ELGRA Biennial Symposium and General Assembly; Granada, Spain (2019)

Cao Q., Chen L., Mohr M., Wunderlich R., Fecht H., Wang X., Zhang D., Yang Y., Jiang J.; "Correlation of viscosity with atomic packing in Cu50Zr50 melt"; 26th ELGRA Biennial Symposium and General Assembly; Granada, Spain (2019)

Novakovic R., Giuranno D., Ricci E., Brillo J., Plevachuk Y., Egry I., Wunderlich R., Mohr M., Fecht H.-J.; " THERMOLAB and THERMOPROP projects: Thermophysical properties of liquid Al-Ni alloys"; 26th ELGRA Biennial Symposium and General Assembly; Granada, Spain (2019)

Mohr M., Dong Y., Wunderlich R., Fecht H.-J.; "The electromagnetic levitator (ISS-EML) on the International Space Station – Precise measurement of thermophysical properties of the titanium alloy Ti-Al6-V4 (Ti64)"; 26th ELGRA Biennial Symposium and General Assembly; Granada, Spain (2019)

Mohr M., Wunderlich R.K., Fecht H.-J.; "Surface tension, viscosity and specific heat capacity of Ni-based superalloys MC2, LEK94 and CMSX-10 in the liquid phase measured in the Electromagnetic Levitator (EML-ISS) on board the International Space Station"; Proceedings of the Liquid Metal Processing & Casting Conference (LMPC 2019): 407–416

Mohr M., Wunderlich R., Hofmann D.C., Fecht H.-J.; "Thermophysical properties of liquid Zr52.5Cu17.9Ni14.6Al10Ti5 – Prospects for bulk metallic glass manufacturing in Space"; npj Microgravity 5 (2019): 24 (https://doi.org/10.1038/s41526-019-0084-1)

Bracker G.P.; Computational fluid dynamics models of electromagnetic levitation experiments in reduced gravity; University of Massachusetts Amherst, Amherst MA, USA; MSc Thesis 821 (2019)

Chen L.Y., Mohr M., Wunderlich R.K., Fecht H.-J., Wang X.D., Cao Q.P., Zhang D.X., Yang Y., Jiang J.Z.; "Correlation of viscosity with atomic packing in Cu50Zr50 melt"; Journal of Molecular Liquids 293 (2019): 111544 (https://doi.org/10.1016/j.molliq.2019.111544)

Van Hoesen D.C., Gangopadhyay A.K., Lohöfer G., Sellers M.E., Pueblo C.E., Koch S., Galenko P.K., Kelton K.F.; "Resistivity saturation in metallic liquids above a dynamic crossover temperature observed in measurements aboard the International Space Station"; Physical Review Letters 123 (2019): 226601 (https://doi.org/10.1103/PhysRevLett.123.226601)

Zhang Sh., Guillemot G., Gandin Ch.-A., Bellet M.; "A partitioned two-step solution algorithm for concurrent fluid flow and stress-strain numerical simulation in solidification processes"; Computer Methods in Applied Mechanics and Engineering 356 (2019): 294–324 (https://doi.org/10.1016/j.cma.2019.07.006)

Valloton J., Bogno A.-A., Henein H., Herlach D.M., Sediako D.; "Scandium effect on undercooling and dendrite morphology of Al4.5 wt pct Cu droplets"; Metallurgical and Materials Transactions A 50/12 (2019): 5700–5706 (https://doi.org/10.1007/s11661-019-05463y)

Sumaria K.J., Hyers R.W., Lee J.; "Numerical prediction of oscillation behaviors of a multiphase core-shell droplet during interfacial tension measurement"; Metallurgical and Materials Transactions B 50/6 (2019): 3012–3019 (https://doi.org/10.1007/s11663-019-01680-3)

Su Y., Mohr M., Wunderlich R., Wang X.D., Cao Q.P., Zhang D.X., Yang Y., Fecht H.-J., Jiang J.Z.; "The relationship between viscosity and local structure in liquid zirconium via electromagnetic levitation and molecular dynamics simulations"; Journal of Molecular Liquids (2019): 111992 (https://doi.org/10.1016/j.molliq.2019.111992)

Lohöfer G.; "Viscosity measurements by the oscillating drop method: The case of strongly damped oscillations"; International Journal of Thermophysics 41 (2020): 30 (https://doi.org/10.1007/s10765-020-2608-7)

Aalilija A., Gandin Ch.-A., Hachem E.; "On the analytical and numerical simulation of an oscillating drop in zero-gravity"; Computers and Fluids 197 (2020): 104362 (https://doi.org/10.1016/j.compfluid.2019.104362)

Schneider S., Beckers M., Diefenbach A.; "Experiment preparation and operation of the electromagnetic levitator EML on the ISS"; TMS2020 149th Annual Meeting & Exhibition; San Diego CA, USA (2020)

Mohr M., Wunderlich R., Fecht H.; "Thermophysical properties of bulk metallic glasses measured in the liquid phase on board the International Space Station"; TMS2020 149th Annual Meeting & Exhibition; San Diego CA, USA (2020)

Bojarevics V.; "Modelling liquid droplet oscillation and laminar damping in reduced gravity conditions"; TMS2020 149th Annual Meeting & Exhibition; San Diego CA, USA (2020)

Reinartz M., Burggraf S., Kolbe M., Galenko P., Herlach D.M., Rettenmayr M.; "Nucleation fronts growing in Al-Ni melts under reduced gravity"; TMS2020 149th Annual Meeting & Exhibition; San Diego CA, USA (2020)

Valloton J., Volkmann T., Henein H.; "Chill-cooling of D2 tool steel under reduced gravity conditions"; TMS2020 149th Annual Meeting & Exhibition; San Diego CA, USA (2020)

Koch S., Silva Pinto M. da, Wilde G., Galenko P.; "Kinetics of solidification in glass forming alloys under microgravity conditions"; TMS2020 149th Annual Meeting & Exhibition; San Diego CA, USA (2020)

Shuleshova O., Löser W., Volkmann T., Matson D.; "Metastable phase formation in peritectic systems under terrestrial and reduced gravity conditions"; TMS2020 149th Annual Meeting & Exhibition; San Diego CA, USA (2020)

Baker E., Jeon S., Matson D.; "Effect of convection on Co-Si solidification pathway: Insights from advanced photon source synchrotron XRD"; TMS2020 149th Annual Meeting & Exhibition; San Diego CA, USA (2020)

Xiao X., Matson D.; "Viscosity measurement of liquid alloys in microgravity and experiment parameters optimization"; TMS2020 149th Annual Meeting & Exhibition; San Diego CA, USA (2020)

Mohr M., Wunderlich R., Fecht H.; "Containerless measurement of thermophysical properties of Ni-based superalloys LEK94, MC2 and CMSX-10 in the liquid phase on board the International Space Station"; TMS2020 149th Annual Meeting & Exhibition; San Diego CA, USA (2020)

Bracker G., Hyers R.; "Modeling magnetohydrodynamics in microgravity electromagnetic levitation experiments"; TMS2020 149th Annual Meeting & Exhibition; San Diego CA, USA (2020)

Nawer J., Gossé S., SanSoucie M., Matson D.; "Effect of inert gas atmosphere on evaporation losses and density measurement for electromagnetically levitated superalloys"; TMS2020 149th Annual Meeting & Exhibition; San Diego CA, USA (2020)

Luo Y., Damaschke B., Lohöfer G., Samwer K.; "Thermophysical properties of SiGe melts measured on board the ISS"; TMS2020 149th Annual Meeting & Exhibition; San Diego CA, USA (2020)

Betzou A., Mohr M., Wunderlich R., Santillana B., Fecht H., Seetharaman S., Srirangam P.; "Thermo-physical properties of Fe-Si alloys under microgravity"; TMS2020 149th Annual Meeting & Exhibition; San Diego CA, USA (2020)

Luo Y., Damaschke B., Lohöfer G., Samwer K.; "Thermophysical properties of a Si50Ge50 melt measured on board the International Space Station"; npj Microgravity 6 (2020): 10 (https://doi.org/10.1038/s41526-020-0100-5)

Nawer J., Xiao X., SanSouci M.P., Matson D.; "Effect of mass evaporation on measurement of liquid density of Ni-based super alloys using ground and space levitation techniques"; High Temperatures – High Pressures 49/1–2 (2020): 17–29

Bracker G.P., Baker E.B., Nawer J., Sellers M.E., Gangopadhyay A.K., Kelton K.F., Xiao X., Lee J., Reinartz M., Burggraf S., Herlach D.M., Rettenmayr M., Matson D., Hyers R.W.; "The effect of flow regime on surface oscillations during electromagnetic levitation experiments"; High Temperatures – High Pressures 49/1–2 (2020): 49–60 (https://doi.org/10.32908/hthp.v49.817)

Brillo J., Wessing J., Kobatake H., Fukuyama H.; "Surface tension of liquid Ti with adsorbed oxygen and a simple associate model for its prediction"; High Temperatures – High Pressures 49/1–2 (2020): 89–105 (https://doi.org/10.32908/hthp.v49.849)

Baker E.B., Nawer J., Xiao X., Matson D.M.; "MHD surrogate model for convection in electromagnetically levitated molten metal droplets processed using the ISS-EML facility"; npj Microgravity 6/1 (2020): 9 (https://doi.org/10.1038/s41526-020-0099-7)

Diefenbach A., Schneider S., Volkmann T.; "Experiment preparation and performance for the electromagnetic levitator (EML) onboard the International Space Station"; Preparation of Space Experiments (ed. Pletzer V.); IntechOpen (2020): chapter 7, 1–29 (https://doi.org/10.5772/intechopen.93470)

Mohr M., Wunderlich R., Novakovic R., Ricci E., Fecht H.-J.; "Precise measurements of thermophysical properties of liquid Ti-6Al4V (Ti64) on board the International Space Station"; Advanced Engineering Materials 22/7 (2020): 2000169 (https://doi.org/10.1002/adem.202000169)

Mohr M., Wunderlich R., Dong Y., Furrer D., Fecht H.-J.; "Thermophysical properties of advanced Ni-based superalloys in the liquid state measured on board the International Space Station"; Advanced Engineering Materials 22/4 (2020): 1901228 (https://doi.org/10.1002/adem.201901228)

Cover-Page: Mohr M., Wunderlich R., Dong Y., Furrer D., Fecht H.-J.; "Thermophysical properties of advanced Ni-based superalloys in the liquid

state measured on board the International Space Station"; Advanced Engineering Materials 22/4 (2020): 2070016 (https://doi.org/10.1002/adem.202070016)

Zhang S., Guillemot G., Gandin C.-A., Bellet M.; "Concurrent and coupled resolution of fluid flow and solid deformation in solidification processes"; IOP Conference Series: Materials Science and Engineering 861 (2020) 012068 (https://doi.org/10.1088/1757-899X/861/1/012068)

Reinartz M.; Study on the growth anomaly in Al-Ni melts under gravity and microgravity conditions; Friedrich-Schiller Universität Jena, Jena, Germany; PhD thesis (2020)

Matson D.M.; "Maximizing scientific return from shared facilities working in space: ESA's investigator working group for the ISS-EML facility"; International Journal of Microgravity Science and Application 37/3 (2020): 370301 (https://doi.org/10.15011/jasma.37.3.370301)

Nawer J., Gossé S., Matson D.M.; "Tracking evaporation during levitation processing of nickel-based superalloys on the ISS"; JOM 72/09 (2020): 3132–3139 (https://doi.org/10.1007/s11837-020-04256-8)

Bracker G.P., Schneider S., Wunderlich R., Fecht H., Zhao J., Hyers R.W.; "Confirmation of anomalous nucleation in zirconium"; JOM 72/09 (2020): 3140–3146 (https://doi.org/10.1007/s11837-020-04257-7)

Novakovic R., Mohr M., Giuranno D., Ricci E., Brillo J., Wunderlich R., Egry I., Plevachuk Y., Fecht H.-J.; "Surface properties of liquid Al-Ni alloys: Experiments vs theory"; Microgravity Science and Technology 32 (2020): 1049–1064 (https://doi.org/10.1007/s12217020-09832-w)

Castellero A., Fiore G., Van Steenberge N., Battezzati L.; "Processing a Fe67Mo4.5Cr2.3Al2Si3C7P8.7B5.5 metallic glass: Experimental and computed TTT and CCT curves"; Journal of Alloys and Compounds 843 (2020): 156061 (https://doi.org/10.1016/j.jallcom.2020.156061)

Matson D.M.; "Influence of induced convection on transformation kinetics during rapid solidification of steel alloys: The retained damage model"; JOM 72/11 (2020) 4109–4116

Kang Y., Brillo J., Han J., Kim H.G., Giuranno D., Novakovic R., Ricci E., Arato E., Lee J.; "Oxygen adsorption of molten Ag-Cu eutectic alloy and its associated surface modification"; Journal of Molecular Liquids, 319 (2020): 114294 (https://doi.org/10.1016/j.molliq.2020.114294)

Aalilija A.; Numerical modelling of chill cooling and solidification of a levitated drop in the International Space Station; Ecole Nationale Supérieure des Mines de Paris, Sophia Antipolis, France, PhD thesis (2020)

Zhang Sh.; Numerical simulation of mechanical interactions between liquid and solid phases in solidification processes; Ecole Nationale Supérieure des Mines de Paris, Sophia Antipolis, France; PhD thesis (2020)

Kreischer C.; Crystallization and transformation of metastable phases in undercooled metallic melts; Rheinisch Westfälische Technische Hochschule Aachen, Aachen, Germany; PhD thesis (2020)

Mohr M., Fecht H.-J.; "Investigating thermophysical properties under microgravity: A review"; Advanced Engineering Materials 23/2 (2021): 2001223 (https://doi.org/10.1002/adem.202001223)

Mohr M., Hofmann D.C., Fecht H.-J.; "Thermophysical properties of Fe57.75Ni19.25Mo10C5B8 glass-forming alloy measured in microgravity"; Advanced Engineering Materials 23/3 (2021): 2001143 (https://doi.org/10.1002/adem.202001143)

Baker E.B., Jeon S., Shuleshova O., Kaban I., Wang Y., Gao J., Kolbe M., SanSoucie M.P., Matson D.M.; "Dendrite remelting during rapid solidification of undercooled CoSi-CoSi2 eutectic alloys quantified by in situ synchrotron X-ray diffraction"; Scripta Materialia 194 (2021): 113645 (https://doi.org/10.1016/j.scriptamat.2020.113645)

Zhang S., Guillemot G., Gandin C.-A., Bellet M.; "A partitioned solution algorithm for concurrent computation of stress-strain and fluid flow in continuous casting process"; Metallurgical and Materials Transactions B 52/2 (2021): 978–995 (https://doi.org/10.1007/s11663-021-02070-4)

Mitic V., Serpa C., Ilic I., Mohr M., Fecht H.-J.; "Fractal nature of advanced Ni-based superalloys solidified on board the International Space Station"; Remote Sensing 13 (2021): 1724 1–22 (https://doi.org/10.3390/rs13091724)

Beckers M., Schneider S., Engelhardt M.; "Containerless measurement of temperature-dependent viscosity and surface tension of liquid Al69.1Cu12.8Ag18.1 eutectic alloy under microgravity conditions using the oscillating-drop-method"; High Temperatures – High Pressures 50/3 (2021): 167–184

Gangopadhyay A.K., Sellers M.E., Bracker G.P., Holland-Moritz D., Van Hoesen D.C., Koch S., Galenko P.K., Hyers R.W., Kelton K.F.; "Demonstration of stirring effect on nucleation from electro-magnetic levitation experiments on the International Space Station"; npj Microgravity (to be submitted)

Aalilija A., Gandin Ch.-A., Hachem E.; "A simple and efficient numerical model for thermal contact resistance based on diffuse interface immersed boundary method"; International Journal of Thermal Sciences 166 (2021): 106817 (https://doi.org/10.1016/j.ijthermalsci.2020.106817)

Index